Imperial College London

Nonlinear Analysis of Post-tensioned Timber Elements

Carlos Javier Melchor Placencia

Department of Civil and Environmental Engineering

Imperial College London

A thesis submitted for the degree of

Doctor of Philosophy

April 2024

Statement of Originality

I confirm that this submission is my own work. In it, I give references and citations whenever I refer to, describe or quote from the published, or unpublished, work of others.

Carlos Melchor-Placencia

Copyright Statement

The copyright of this thesis rests with the author. Unless otherwise indicated, its contents are licensed under a Creative Commons Attribution-Non Commercial 4.0 International Licence (CC BY-NC).

Under this licence, you may copy and redistribute the material in any medium or format. You may also create and distribute modified versions of the work. This is on the condition that: you credit the author and do not use it, or any derivative works, for a commercial purpose.

When reusing or sharing this work, ensure you make the licence terms clear to others by naming the licence and linking to the licence text. Where a work has been adapted, you should indicate that the work has been changed and describe those changes.

Please seek permission from the copyright holder for uses of this work that are not included in this licence or permitted under UK Copyright Law.

Acknowledgements

First of all, I would like to thank God Almighty for giving me several moments of enlightenment during the development of this thesis and guiding my hand in overwhelming situations. Thanks Lord for making me analytical and accurate in the key moments of this research journey.

I would like to thank my supervisor, Dr. Christian Málaga-Chuquitaype, for giving me the opportunity to be part of his research group and for believing in the outcome of this thesis. I appreciated the freedom I had during the development of this work and the vibrant discussions we shared during our meetings.

I would also like to acknowledge the financial support provided by the Peruvian governmental institution PRONABEC (National Program of Scholarships and Educational Loan) to perform my PhD studies in a prestigious educational institution.

Special thanks to my wife Deysi who had always listen to all my dreams and concerns during this journey. Without her support and encouragement, this work couldn't be completed.

I want to dedicated the outcome of this work to my beloved son Salvador who accompanied me throughout the development of this project. I feel so lucky to have you in my life.

Finally, I want express my deepest gratitude to my parents, sister, brother, and other family members who always showed me their kind support, encouragement and good will. To conclude, I would like to thanks the friends I made during my stay in UK for the unforgettable experience.

Abstract

This thesis deals with the numerical simulation of the short- and long-term response of post-tensioned structural elements. It proposes and implements a numerical framework with particular orientation towards timber members and draped tendon profiles. The modelling approach employs beam-column finite elements with a fiber-based approach to incorporate the material nonlinearity and a corotational formulation to address the large displacements of the hosting member. Displacement-based beam-column elements considering traditional and enhanced-strain formulations as well as beam-column formulations with internal nodeless degrees of freedom were included in the proposed modelling approach. The proposed numerical framework incorporates the inelastic and time-dependent behaviour of wood and the prestressing steel. Prior to tackle the time-dependent response of the timber members, a moisture diffusion analysis using a finite difference scheme is carried out to assess the spatial and temporal distribution of moisture inside the members.

The intricate behavior of unbonded tendons induce strain incompatibility and second-order effects adding more complexities into the numerical framework. To address these complexities, a constantly updated equivalent load scheme along with a resisting tendon element formulation involving the explicit derivation of a material and geometric tangent stiffness matrix were adopted. Additionally, a robust numerical formulation to assess the equilibrium state just after the prestress transfer is evaluated. As post-tensioned structures can experience sharp variations in their tangent stiffness matrices, robust numerical solvers were adopted to trace the whole global and local responses of interest. After validating the capabilities of the proposed numerical approach and carrying out several simulations to assess the influence of deviator spacing on the short- and long-term response of post-tensioned timber beams, this thesis demonstrates that the proposed modelling approach features versatility, numerical robustness and computational efficiency to a greater extent.

Contents

1 Introduction **21**

1.1 Background 21

1.2 Research objectives 23

1.3 Thesis outline 24

2 Literature Review **26**

2.1 Transient Moisture Diffusion Analysis 26

2.2 Nonlinear Numerical Modelling of the Short-Term Response of Timber Structures 33

2.3 Nonlinear Numerical Modelling of the Long-Term Response of Timber Structures 40

2.4 Short-Term Response and Numerical Modelling of Post-tensioned Timber Structures 47

2.5 Long-Term Response and Numerical Modelling of Post-tensioned Timber Structures 51

2.6 Concluding Remarks 58

3 Transient Moisture Diffusion Analysis **61**

3.1 Governing Differential Equations 61

3.2 Numerical Methods 63

3.2.1 Finite Element Method 64

3.2.2 Finite Difference Method 65

3.3 Finite Difference Equations 69

3.3.1 Solid Rectangular Section 71

3.3.2 Hollow Rectangular Section 72

3.4 Verification Examples 75

3.4.1 Solid Square Section under Constant Conditions 75

3.4.2 Solid Square Section under Changing Conditions 78

3.4.3 Hollow Square Section under Constant Conditions 80

3.4.4 Hollow Square Section under Changing Conditions 83
3.4.5 Cross-Laminated Timber Panel 85
3.5 Concluding Remarks 90

4 Nonlinear Modelling of Timber Beam-Column Elements 91
4.1 Beam–Column Finite Element Formulation 91
4.1.1 Virtual Work Equation 94
4.1.2 Derivation of the Global Force and Tangent Stiffness at the Element Level 96
4.1.3 Euler-Bernoulli Beam-Column Element 98
4.1.4 Euler-Bernoulli Beam-Column Element with Enhanced-Strain Formulation 100
4.1.5 Timoshenko Beam-Column Element 103
4.1.6 Timoshenko Beam-Column Element with Enhanced-Strain Formulation . 106
4.2 Material Constitutive Laws 108
4.2.1 Inelastic Model 109
4.2.2 Rheological Model 110
4.3 Incremental Finite Element Equations 114
4.4 Validation Examples 115
4.4.1 Cantilever Beam with an End Moment 115
4.4.2 Lee's Frame 116
4.4.3 Williams Toggle Frame 119
4.4.4 Four-Point Bending Tests 120
4.4.5 Viscoelastic Cantilever Beam 124
4.4.6 Hoyle's test 126
4.5 Concluding Remarks 129

5 Nonlinear Solution Algorithms 131
5.1 Nonlinear Equation Solvers 131
5.1.1 Krylov Subspace Accelerated Newton Algorithm 132
5.1.2 Two-level Consistent Quasi Newton–Raphson Algorithm 133
5.1.3 Lyapunov-Based Nonlinear Solution Algorithm 134
5.2 Study Cases 135
5.2.1 Single DOF System 135
5.2.2 Two DOF System with Two Springs 139
5.2.3 Two DOF System with Three Springs 144

5.3 Concluding Remarks . . . 148

6 Nonlinear Modelling of Unbonded Post-tensioned Timber Beam-Column Elements 150

6.1 Unbonded Tendon Modelling . . . 150
6.1.1 Equivalent Load Scheme . . . 154
6.1.2 Load Resisting Element . . . 159
6.2 Tendon Constitutive Laws . . . 165
6.2.1 Nonlinear Elastic Model . . . 166
6.2.2 Rheological Model . . . 166
6.3 Incremental Finite Element Equations . . . 168
6.3.1 Stage at the Transfer of the Post-tensioning Force . . . 169
6.3.2 Stage after the Transfer of the Post-tensioning Force . . . 170
6.4 Validation Examples . . . 171
6.4.1 Simply-Supported RC Beams Post-Tensioned with External Tendons . . . 172
6.4.2 Continuous RC Beams Post-tensioned with Internal Tendons . . . 177
6.4.3 Externally Post-tensioned Timber Beams . . . 181
6.4.4 Simply-Supported RC Beams Post-Tensioned with Internal Tendons . . . 188
6.5 Concluding Remarks . . . 193

7 Numerical Case Studies 195

7.1 Influence of Deviator Spacing on Ultimate Response . . . 195
7.2 Influence of Deviator Spacing on Long-Term Response . . . 206
7.3 Concluding Remarks . . . 214

8 Conclusions and Recommendations for Future Research 215

8.1 Conclusions . . . 215
8.2 Suggestions for Future Work . . . 220

Bibliography 222

A 248

B 256

C 267

C.1 Single DOF System . . . 267

C.2 Two DOF System with Two Springs 270
C.3 Two DOF System with Three Springs 273

D **277**

List of Figures

2.1 Hierarchical representation of softwood in the macroscale, microscale and cellular scale (Figure taken from Thybring et al. [9]). 27
2.2 Absorption and desorption isotherms in the hygroscopic and over-hygroscopic moisture ranges (Figure taken from Thybring et al. [9]). 28
2.3 Experimental stress–strain curves for Scandinavian Spruce Glulam specimens (Figure taken from Karagiannis et al. [39]). 34
2.4 Wood beam subjected to different moisture conditions and stress levels (Figure taken from Frandsen [61]). 40
2.5 Description of the microstructure and nanostructure of wood (Figure modified from Bengtsson et al. [65]). 42

3.1 Control volume of an interior node. 67
3.2 Boundary nodes in the edges of a solid rectangular section. 71
3.3 Boundary nodes in the corners of a solid rectangular section. 72
3.4 Boundary nodes in the internal edges of a hollow rectangular section. 73
3.5 Boundary nodes in the internal corners of a hollow rectangular section. 73
3.6 Grid generated for the solid square section. 76
3.7 Moisture content variation in the solid square section under constant environmental conditions. 76
3.8 Moisture content distribution in the solid square section after 1 day of exposure under constant environmental conditions. 77
3.9 Moisture content distribution in the solid square section after 40 days of exposure under constant environmental conditions. 77
3.10 Moisture content variation in the solid square section under cyclic variations in the environmental conditions. 78
3.11 Moisture content distribution in the solid square section after 6 days of exposure under cyclic variations in the environmental conditions. 79

3.12 Moisture content distribution in the solid square section after 10 days of exposure under cyclic variations in the environmental conditions. 79
3.13 Moisture content distribution in the solid square section after 34 days of exposure under constant environmental conditions. 80
3.14 Moisture content distribution in the solid square section after 38 days of exposure under constant environmental conditions. 80
3.15 Grid generated for the Hollow square section. 81
3.16 Moisture content variation in the hollow square section under constant environmental conditions. 81
3.17 Moisture content distribution in the hollow square section after 1 day of exposure under constant environmental conditions. 82
3.18 Moisture content distribution in the hollow square section after 40 days of exposure under constant environmental conditions. 82
3.19 Moisture content variation in the hollow square section under cyclic variations in the environmental conditions. 83
3.20 Moisture content distribution in the hollow square section after 6 days of exposure under cyclic variations in the environmental conditions. 84
3.21 Moisture content distribution in the hollow square section after 10 days of exposure under cyclic variations in the environmental conditions. 84
3.22 Moisture content distribution in the hollow square section after 34 days of exposure under constant environmental conditions. 85
3.23 Moisture content distribution in the hollow square section after 38 days of exposure under constant environmental conditions. 85
3.24 Mesh of the CLT panel. 86
3.25 Moisture content variation in the CLT panel under a constant variation in the environmental conditions. 87
3.26 Moisture content contour distribution in the CLT panel under constant environmental conditions. 88
3.27 Moisture content surface distribution in the CLT panel under constant environmental conditions. 89

4.1 Reference systems of the beam-column element. 94
4.2 Stress-strain curve for wood. 109
4.3 Toratti's rheological constitutive model. 111

4.4 Cantilever beam under an end moment. 115
4.5 Normalized load-displacement curves for a cantilever beam with an end moment. 116
4.6 Lee's frame. 117
4.7 Load-displacement curves for Lee's frame in the elastic range. 118
4.8 Load-displacement curves for Lee's frame in the inelastic range. 118
4.9 Williams toggle frame. 119
4.10 Load-displacement curves for Williams toggle frame with and without shear effects.119
4.11 Four-point bending failure test. 120
4.12 Load–deflection curves of timber beam B1. 121
4.13 Load–deflection curves of timber beam DF1. 122
4.14 Load–deflection curves of timber beam FS0. 122
4.15 Load–deflection curves of timber beam HS0-1. 123
4.16 Load–deflection curves of timber beam HS0-7. 123
4.17 Cantilever beam under an end point load. 124
4.18 Time-dependent deflection by considering linear geometric effects. 125
4.19 Time-dependent deflection by considering nonlinear geometric effects. 126
4.20 Five-point bending creep test. 127
4.21 Variation over time of the creep coefficient for weekly humidity cycles. 128
4.22 Variation over time of the creep coefficient for daily humidity cycles. 128

5.1 One degree of freedom spring system. 136
5.2 Newton-Raphson iterative equilibrium search for $r = \frac{1}{3}$. 136
5.3 Modified Newton-Raphson iterative equilibrium search for $r = \frac{1}{3}$. 137
5.4 Krylov-Newton iterative equilibrium search for $r = \frac{1}{3}$. 137
5.5 Quasi Newton iterative equilibrium search with origin operator for $r = \frac{1}{3}$. 138
5.6 Quasi Newton iterative equilibrium search with incremental operator for $r = \frac{1}{3}$. . 138
5.7 Lyapunov iterative equilibrium search for $r = \frac{1}{3}$. 139
5.8 Two degree of freedom system with two springs. 140
5.9 Newton-Raphson iterative equilibrium search for inconsistent Jacobian matrix. . 141
5.10 Modified Newton-Raphson iterative equilibrium search for inconsistent Jacobian matrix. 141
5.11 Krylov-Newton iterative equilibrium search for inconsistent Jacobian matrix. . . 142
5.12 Quasi Newton iterative equilibrium search with origin operator for inconsistent Jacobian matrix. 142

5.13 Quasi Newton iterative equilibrium search with incremental operator for inconsistent Jacobian matrix. . . . 143
5.14 Lyapunov iterative equilibrium search for inconsistent Jacobian matrix. . . . 143
5.15 Two degree of freedom system with three springs. . . . 144
5.16 Newton-Raphson iterative equilibrium search for inconsistent Jacobian matrix. . 145
5.17 Modified Newton-Raphson iterative equilibrium search for inconsistent Jacobian matrix. . . . 146
5.18 Krylov-Newton iterative equilibrium search for inconsistent Jacobian matrix. . . 146
5.19 Quasi Newton iterative equilibrium search with origin operator for inconsistent Jacobian matrix. . . . 147
5.20 Quasi Newton iterative equilibrium search with incremental operator for inconsistent Jacobian matrix. . . . 147
5.21 Lyapunov iterative equilibrium search for inconsistent Jacobian matrix. . . . 148

6.1 Tendon and hosting member in the undeformed and deformed configuration. . . 156
6.2 Procedure to update the tendon eccentricity. . . . 157
6.3 Post-tensioning load in a tendon segment. . . . 159
6.4 Tendon and hosting member in the undeformed and deformed configuration. . . 161
6.5 Stress-strain curves for the strand material. . . . 166
6.6 Simply-supported post-tensioned RC beam layouts: (a) No deviators; (b) One deviator; (c) Two deviators. . . . 173
6.7 Rectangular section of the post-tensioned simply-supported RC beams. . . . 173
6.8 FE discretization used in the EQL: (a) No deviators; (b) One deviator; (c) Two deviators. . . . 174
6.9 FE discretization used in the LRE: (a) No deviators; (b) One deviator; (c) Two deviators. . . . 175
6.10 Load-deflection response for single concentrated load obtained with the EQL scheme. . . . 175
6.11 Load-deflection response for uniform load obtained with the EQL scheme. . . . 176
6.12 Load-deflection response for single concentrated load obtained with the LRE formulation. . . . 176
6.13 Load-deflection response for uniform load obtained with the LRE formulation. . 177
6.14 Continuous post-tensioned RC beam layouts. . . . 179
6.15 Section and reinforcement layout of the continuous beam YLA2. . . . 179

6.16 Section and reinforcement layout of the continuous beam YLB2. 179
6.17 FE discretization of the continuous post-tensioned RC beams. 180
6.18 Load-displacement responses: (a) Specimen YLA2; (b) Specimen YLB2. 181
6.19 Externally post-tensioned timber beam layouts: (a) Beam 2; (b) Beam 3; (c) Beam 4. 183
6.20 Box section layouts: (a) Beam 2; (b) Beam 3; (c) Beam 4. 183
6.21 FE discretization: (a) Beam 2; (b) Beam 3; (c) Beam 4. 184
6.22 Load-midspan displacement response for the ENH EB : (a) Beam 2; (b) Beam 3; (c) Beam 4. 186
6.23 Load-midspan displacement response for the ENH TB : (a) Beam 2; (b) Beam 3; (c) Beam 4. 187
6.24 Simply-supported post-tensioned RC beam layout. 188
6.25 Section layout of the post-tensioned simply-supported RC beam. 189
6.26 FE discretization of the simply-supported post-tensioned RC beam. 189
6.27 Long-term deflections under self-weight loads obtained with the LRE formulation. 190
6.28 Long-term deflections under self-weight loads obtained with the EQL scheme. . . 190
6.29 Long-term prestress losses under self-weight loads obtained with the LRE formulation. 191
6.30 Long-term prestress losses under self-weight loads obtained with the EQL scheme. 191
6.31 Long-term deflection under self-weight and four-point bending loads obtained with the LRE formulation. 191
6.32 Long-term deflection under self-weight and four-point bending loads obtained with the EQL scheme. 192
6.33 Long-term prestress losses self-weight and four-point bending loads obtained with the LRE formulation. 192
6.34 Long-term prestress losses self-weight and four-point bending loads obtained with the EQL scheme. 192

7.1 Fine mesh discretization adopted for FE models 1 and 2: (a) $S_{dev}/L = 0$; (b) $S_{dev}/L = 1/9$; (c) $S_{dev}/L = 1/3$; (d) $S_{dev}/L = 2/3$; (e) $S_{dev}/L = 1$. 197
7.2 Coarse mesh discretization adopted for FE models 3 and 4: (a) $S_{dev}/L = 0$; (b) $S_{dev}/L = 1/9$; (c) $S_{dev}/L = 1/3$; (d) $S_{dev}/L = 2/3$; (e) $S_{dev}/L = 1$. 198
7.3 Ultimate responses obtained for loading scenario 1 using FE Model 1. 199
7.4 Ultimate responses obtained for loading scenario 1 using FE Model 2. 200

7.5 Ultimate responses obtained for loading scenario 1 using FE Model 3. 201
7.6 Ultimate responses obtained for loading scenario 1 using FE Model 4. 202
7.7 Ultimate responses obtained for loading scenario 2 using FE Model 1. 203
7.8 Ultimate responses obtained for loading scenario 2 using FE Model 2. 204
7.9 Effects of deviator spacing on ultimate load capacities: (a) Euler-Bernoulli formulations; (b) Timoshenko formulations. 205
7.10 Effects of deviator spacing on ultimate tendon stress increase: (a) Euler-Bernoulli formulations; (b) Timoshenko formulations. 206
7.11 FE discretization: (a) $S_{dev}/L = 0$; (b) $S_{dev}/L = 1/3$; (c) $S_{dev}/L = 1$. 207
7.12 Grid generated for the Hollow square section. 208
7.13 Average moisture content under weekly and daily relative humidity cycles. . . . 209
7.14 Time-dependent responses under self-weight load for weekly climatic variations. 210
7.15 Time-dependent responses under self-weight and four-point bending loads for weekly climatic variations. 211
7.16 Time-dependent responses under self-weight load for daily climatic variations. . 212
7.17 Time-dependent responses under self-weight and four-point bending loads for daily climatic variations. 213

A.1 Descriptive Flow Chart of Finite Difference Framework. 248
A.2 Descriptive Flow Chart of Finite Element Framework. 249
A.3 Descriptive Flow Chart of Traditional Euler-Bernoulli Formulation. 250
A.4 Descriptive Flow Chart of Enhanced Euler-Bernoulli Formulation. 251
A.5 Descriptive Flow Chart of Timoshenko Formulation. 252
A.6 Descriptive Flow Chart of Enhanced Timoshenko Formulation. 253
A.7 Descriptive Flow Chart of Tendon Equivalent Load Method. 254
A.8 Descriptive Flow Chart of Tendon Load-Resisting Method. 255

B.1 History of normal forces obtained in the EB elements for Beam B1. 256
B.2 History of normal forces obtained in the ENH EB elements for Beam B1. 257
B.3 History of Bending Moments obtained in the EB elements for Beam B1. 257
B.4 History of Bending Moments obtained in the ENH EB elements for Beam B1. . 258
B.5 History of normal forces obtained in the EB elements for Beam DF1. 258
B.6 History of normal forces obtained in the ENH EB elements for Beam DF1. . . . 259
B.7 History of Bending Moments obtained in the EB elements for Beam DF1. 259
B.8 History of Bending Moments obtained in the ENH EB elements for Beam DF1. 260

B.9 History of normal forces obtained in the EB elements for Beam FS0. 260
B.10 History of normal forces obtained in the ENH EB elements for Beam FS0. . . . 261
B.11 History of Bending Moments obtained in the EB elements for Beam FS0. 261
B.12 History of Bending Moments obtained in the ENH EB elements for Beam FS0. . 262
B.13 History of normal forces obtained in the EB elements for Beam HS01. 262
B.14 History of normal forces obtained in the ENH EB elements for Beam HS01. . . . 263
B.15 History of Bending Moments obtained in the EB elements for Beam HS01. . . . 263
B.16 History of Bending Moments obtained in the ENH EB elements for Beam HS01. 264
B.17 History of normal forces obtained in the EB elements for Beam HS07. 264
B.18 History of normal forces obtained in the ENH EB elements for Beam HS07. . . . 265
B.19 History of Bending Moments obtained in the EB elements for Beam HS07. . . . 265
B.20 History of Bending Moments obtained in the ENH EB elements for Beam HS07. 266

C.1 Newton-Raphson iterative equilibrium search for $r = 2$. 267
C.2 Modified Newton-Raphson iterative equilibrium search for $r = 2$. 268
C.3 Krylov-Newton iterative equilibrium search for $r = 2$. 268
C.4 Quasi Newton iterative equilibrium search with origin operator for $r = 2$. 269
C.5 Quasi Newton iterative equilibrium search with incremental operator for $r = 2$. . 269
C.6 Lyapunov iterative equilibrium search for $r = 2$. 270
C.7 Newton-Raphson iterative equilibrium search for consistent Jacobian matrix. . . 270
C.8 Modified Newton-Raphson iterative equilibrium search for consistent Jacobian matrix. 271
C.9 Krylov-Newton iterative equilibrium search for consistent Jacobian matrix. . . . 271
C.10 Quasi Newton iterative equilibrium search with origin operator for consistent Jacobian matrix. 272
C.11 Quasi Newton iterative equilibrium search with incremental operator for consistent Jacobian matrix. 272
C.12 Lyapunov iterative equilibrium search for consistent Jacobian matrix. 273
C.13 Newton-Raphson iterative equilibrium search for inconsistent Jacobian matrix. . 273
C.14 Modified Newton-Raphson iterative equilibrium search for inconsistent Jacobian matrix. 274
C.15 Krylov-Newton iterative equilibrium search for inconsistent Jacobian matrix. . . 274
C.16 Quasi Newton iterative equilibrium search with origin operator for inconsistent Jacobian matrix. 275

C.17 Quasi Newton iterative equilibrium search with incremental operator for inconsistent Jacobian matrix. 275
C.18 Lyapunov iterative equilibrium search for inconsistent Jacobian matrix. 276

D.1 History of normal forces obtained in the ENH EB elements for Beam B2 and f_{tu} =47.0 MPa. 278
D.2 History of Bending Moments obtained in the ENH EB elements for Beam B2 and f_{tu} =47.0 MPa. 278
D.3 History of normal forces obtained in the ENH EB elements for Beam B2 and f_{tu} =35.2 MPa. 279
D.4 History of Bending Moments obtained in the ENH EB elements for Beam B2 and f_{tu} =35.2 MPa. 279
D.5 History of normal forces obtained in the ENH EB elements for Beam B3 and f_{tu} =47.0 MPa. 280
D.6 History of Bending Moments obtained in the ENH EB elements for Beam B3 and f_{tu} =47.0 MPa. 280
D.7 History of normal forces obtained in the ENH EB elements for Beam B3 and f_{tu} =35.2 MPa. 281
D.8 History of Bending Moments obtained in the ENH EB elements for Beam B3 and f_{tu} =35.2 MPa. 281
D.9 History of normal forces obtained in the ENH EB elements for Beam B4 and f_{tu} =47.0 MPa. 282
D.10 History of Bending Moments obtained in the ENH EB elements for Beam B4 and f_{tu} =47.0 MPa. 282
D.11 History of normal forces obtained in the ENH EB elements for Beam B4 and f_{tu} =35.2 MPa. 283
D.12 History of Bending Moments obtained in the ENH EB elements for Beam B4 and f_{tu} =35.2 MPa. 283
D.13 History of normal forces obtained in the ENH TB elements for Beam B2 and f_{tu} =47.0 MPa. 284
D.14 History of Bending Moments obtained in the ENH TB elements for Beam B2 and f_{tu} =47.0 MPa. 284
D.15 History of normal forces obtained in the ENH TB elements for Beam B2 and f_{tu} =35.2 MPa. 285

D.16 History of Bending Moments obtained in the ENH TB elements for Beam B2 and f_{tu} =35.2 MPa. 285
D.17 History of normal forces obtained in the ENH TB elements for Beam B3 and f_{tu} =47.0 MPa. 286
D.18 History of Bending Moments obtained in the ENH TB elements for Beam B3 and f_{tu} =47.0 MPa. 286
D.19 History of normal forces obtained in the ENH TB elements for Beam B3 and f_{tu} =35.2 MPa. 287
D.20 History of Bending Moments obtained in the ENH TB elements for Beam B3 and f_{tu} =35.2 MPa. 287
D.21 History of normal forces obtained in the ENH TB elements for Beam B4 and f_{tu} =47.0 MPa. 288
D.22 History of Bending Moments obtained in the ENH TB elements for Beam B4 and f_{tu} =47.0 MPa. 288
D.23 History of normal forces obtained in the ENH TB elements for Beam B4 and f_{tu} =35.2 MPa. 289
D.24 History of Bending Moments obtained in the ENH TB elements for Beam B4 and f_{tu} =35.2 MPa. 289

List of Tables

3.1 Coefficients for a solid rectangular section using an explicit scheme. 71
3.2 Coefficients for a solid rectangular section using an implicit scheme. 72
3.3 Coefficients for a hollow rectangular section using an explicit scheme. 74
3.4 Coefficients for a hollow rectangular section using an implicit scheme. 74
3.5 Geometry and material property data adopted for the solid square section. . . . 75
3.6 Geometry and material property data of the CLT panel. 87

4.1 Material property data and dimensions of the timber beams. 121
4.2 Adopted material parameters for Toratti's rheological model. 127

6.1 Number of iterations performed during the analysis. 177
6.2 Material properties for timber beams. 182
6.3 Material properties for steel strands. 184

7.1 Adopted material parameters for Toratti's rheological model. 208

Chapter 1

Introduction

This thesis deals with the short- and long-term response of post-tensioned timber structures by incorporating the intrinsic and intricate behaviour of unbonded tendons along with the large displacement effects and material nonlinearities undergone by the hosting member. Furthermore, the characteristic hygroscopic response of wood is considered throughout the assessment of the long-term response of these structures. This research is motived by the current rise in popularity of post-tensioned timber structures around the world. The aim of this work is to contribute in the development of a cost-effective modelling approaches for these complex structures. This introductory chapter includes a brief description of the background motivating this research, followed by the main objectives and an outline of the thesis.

1.1 Background

Traditional materials such as concrete and steel are associated with large amounts of embodied energy, specially during their fabrication process, which results the emissions of large quantities of greenhouses gases contributing to global warming (John et al. [1]). Motivated by the need to limit carbon emissions, sustainable materials such as timber have experienced a growing interest in the construction industry. Despite of the good structural performance (Van De Lindt [2]) of traditional structures built with sawn timber, the resisting system of these structures is not able to provide sufficient strength and stiffness to withstand the high gravitational and lateral loads associated with mid- and high-rise buildings or long-span structures.

As an alternative to sawn timber, a new generation of timber products, denominated as engineered wood products, emerged in the construction industry. Timber members with larger section sizes and lengths, along with enhanced features such as: high strength characteristics, reduced natural defects, uniformity, high strength-mass ratio, dimensional stability, have been

attained (Harte [3]). These timber products experienced another wave of popularity at the beginning of the 2000s due to the development of a damage-control seismic resisting systems denominated as Pres-Lam (Palermo et al. [4]). These systems consisted of post-tensioned engineered timber products with unbonded tendons that provide recentering capacity after a major earthquake. However, in the majority of experimental programmes and numerical studies, only concentric straight tendons have been considered for these emerging systems.

The use of eccentric and draped tendon profiles in post-tensioned timber members leads to the possibility of creating a precamber and increasing of the load-carrying capacity of timber beams and frames. As a result, longer spans for the case of designing open-space building plans and short-to-medium span bridges can be achieved than adopting traditional timber solutions (Palermo et al. [5]). Nevertheless, an accurate numerical modelling of these post-tensioned structures with draped tendon profiles under short- and long-term loading involves the consideration of material nonlinearity and large displacement effects, being the last one also denominated as geometric nonlinear effects. Material nonlinearity address the complex inelastic and time-dependent behaviour of wood whereas the incorporation of large displacement effects allows an accurate description of the tendon and hosting member deformed configurations under considerable displacements and rotations. The consideration of these geometric nonlinear effects enables the modelling of intricate features introduced by the unbonded tendons such as strain incompatibility and eccentricity variation.

Various semi-analytical iterative procedures (Lago et al. [6],van Beerschoten et al. [7]) and continuum-based finite element (FE) models (van Beerschoten et al. [7],Quiquero et al. [8]) have been proposed to assess the short-term response of post-tensioned members. Despite considering geometric nonlinear effects and being suitable for typical design purposes, semi-analytical approaches lack versatility for modelling general tendon profiles and beam layouts, and only accounts for linear-elastic behavior. In case of continuum models, large displacement effects and material nonlinear behavior can be incorporated, however, these models involve high computational cost and complexity. Regarding the long-term assessment of post-tensioned timber structures, eccentric and draped unbonded tendon layouts, and large displacements effects have not been addressed. Therefore, there is a lack of numerical modelling approaches to assess the short- and long-term response of these post-tensioned timber structures that incorporate the complex nonlinear behavior of wood and large displacement effects from the tendon and hosting member motions, and are suitable for carrying out design-oriented parametric studies.

This research work proposes a novel numerical modelling approach that can address the inelastic and time-dependent behavior of wood, as well as strain incompatibility and eccentricity

variation for different unbonded tendon profiles by fully including large displacement effects during the assessment of the response of post-tensioned timber beam-like structures under short- and long-term loading conditions. Moreover, this novel modelling approach features robustness, versatility and efficiency which allows performing parametric studies for design-oriented purposes.

1.2 Research objectives

This thesis deals with the numerical assessment of the short- and long-term response of post-tensioned timber structures, with a specific focus on post-tensioned beam-like structures. Its aim is the development of a robust, versatile and efficient numerical framework that captures the complex material behavior of wood and the intricate features of unbonded tendons by incorporating large displacement effects. The development of this novel approach would constitute a first step towards a cost-effective FE model that allows performing parametric analyses for typical design purposes. To achieve this goal, the following objectives were pursued:

- The implementation of efficient beam-column FE formulations to simulate the large displacement and material nonlinearities undergone by timber hosting members enabling the straightforward assessment of global and local responses of interest for the structural design and assessment practice.

- Adopting modelling approaches featuring numerical efficiency which enables the simulation of the intricate behaviour of unbonded tendons such as strain incompatibility and eccentricity variation (second-order effects) for eccentric and draped tendon profiles.

- Examination of simple constitutive models to capture with sufficient accuracy the material inelasticity and time-dependent behaviour of timber and the prestressing steel in the particular case of longitudinal post-tensioned beams.

- Adoption of an efficient finite difference (FD) scheme to solve the moisture transfer equations governing the intrinsic hygroscopic behaviour of timber enabling the determination of the temporal and spatial distribution of moisture content over the timber element for different climatic conditions.

- Rigorous assessment of the equilibrium state of the post-tensioned beam immediately after prestress force transfer by considering a specific stress level, denominated as effective stress, in the tendon following its anchoring at the hosting member ends.

- Evaluation of robust numerical solvers to tackle material and geometric nonlinearities inducing sharp changes in the structural tangent stiffness enabling the overall tracking of the ultimate or time-dependent response of post-tensioned timber members.

1.3 Thesis outline

As stated above, the main aim of this research work is the development of a versatile, robust and efficient numerical modelling approach to assess the short- and long-term response of post-tensioned timber beams by capturing the intrinsic and intricate behavior of these complex structures. To this end, a general finite element framework along with a finite difference solver were implemented. The FE and FD discrete equations comprising the framework and solver are described throughout the thesis. It should be mentioned that the FE framework and FD solver were developed as a stand-alone implementation for their general use in any programming language. However, the code implementation was performed in MATLAB due to the its friendly debugging interface and versatility in dealing with diverse and large matrix operations.

As first step to conceive the proposed numerical modelling approach, a comprehensive literature review of the current modelling techniques used in post-tensioned timber beams and frames, and the essential features describing the response of these post-tensioned structures observed from experimental programmes and numerical studies was performed in chapter 2. This first stage allowed the identification of the research gaps to be addressed and to justify the adopted assumptions throughout the thesis.

In chapter 3, a single Fickian diffusion equation is adopted to encompass the transport mechanism of all different water phases occurring inside the timber member. This nonlinear differential equation was solved by implementing a finite difference code to assess the transient moisture distribution in rectangular and hollow sections. To validate the finite difference solver, a series of numerical examples under different climatic conditions were carried out and were then compared with the obtained results from a nonlinear finite element solver like Abaqus.

From the literature review was determined that timber beam members without openings and notches, and non-predominant local defects can be accurately represented by uniaxial stress states as the orthotropic behavior can be disregarded. As result, chapter 4 examines a set of different beam-column (BC) FE formulations that incorporates large displacements, shear deformations and material nonlinearities such as inelasticity and time-dependent behavior. Regarding the material nonlinearities, a fiber based approach was adopted along with uniaxial constitutive models. To incorporate shear deformations, BC element with a bubble or

nodeless degrees of freedom were considered. With the aim of evaluating local responses with higher accuracy and relative less computational effort, BC elements with enhanced-strain formulations are also described and implemented in the numerical framework. The incorporation of large displacements is tackled by considering a corotational approach to describe the deformed configuration of the hosting member. The corresponding geometric stiffness matrix for each BC formulation was deduced and presented in this chapter. Finally, a series of benchmark results were reproduced to validate the capability of the implemented framework to tackle all the previously mentioned features.

In chapter 5 a brief description of all the numerical nonlinear solvers adopted and implemented into the numerical framework was performed first. The implementation of this solvers allowed tracking the whole global and local nonlinear response of timber beams with and without post-tensioning. A series of numerical examples were performed to attest the numerical robustness of each solver under different challenging conditions.

Two numerical modelling approaches were presented in chapter 6 to simulate the intricate nonlinear behavior of unbonded tendons comprising strain incompatibility and second order effects. These methods consisted of a equivalent load scheme that is constantly updated in magnitude and orientation, and a load resisting FE formulation of the tendon element that involved the deduction of material and geometric stiffness matrices. In this chapter, also a robust numerical procedure was employed to assess the initial post-tensioning force before the stress transfer to the hosting member. As a result, an augmented system of the original linearized finite element equations was obtained. Depending on the modelling approach adopted for the unbonded tendons, two different numerical procedures were used to solve the resulting linearized equations. Following the description of the adopted numerical procedures, a set of numerical examples were carried out to validate the implemented framework in performing short- and long-term analysis of beams post-tensioned with different tendon profiles.

Finally, after performing a series of validation cases in the previous chapters, in chapter 7 the numerical framework was used to perform a numerical study of the short- and long-term response of a post-tensioned timber reference beam. In this particular case, the distance between deviators was selected as the parameter to study its influence on the ultimate and time-dependent response of the post-tensioned beam. This numerical study demonstrated versatility, robustness and numerical efficiency of the adopted modelling approach to tackle large deflections, material nonlinearity, interaction of different time-dependent deformations, hygroscopic behavior of timber, shear deformations, as well as strain incompatibility and changing eccentricity related to unbonded tendons.

Chapter 2

Literature Review

Post-tensioning of timber members as a construction technique or retrofitting method has been studied over many decades, more specifically since the 1960s. However, since the 2000s a resurgence in post-tensioned timber structures has emerged as engineered timber structural components have become popular in the construction industry. The post-tensioning action can potentially improve the serviceability and ultimate loading capacity of timber elements. Besides, post-tensioning can provide a self-centering capacity to timber structures upgrading their seismic performance. However, the complex nature of timber and the challenging modelling features of unbonded post-tensioned elements configure a demanding task, particularly when the short-term or long-term response of these structures in the nonlinear range need to be assessed. In these cases, a comprehensive knowledge of the hygro-mechanical behavior of wood, the nonlinear behaviour of the hosting members and effects introduced by the slipping behaviour of unbonded tendons is required. In this chapter, an extensive review of these topics is performed.

2.1 Transient Moisture Diffusion Analysis

Like other biological materials, wood features a complex and sophisticated structure on several length scales. Wood is a porous material composed of cell walls, lumens and pits as depicted in Fig. 2.1 (Thybring et al. [9]). The cell walls are made up of fundamental polymers such as cellulose, hemicelluloses and lignin which are present in all wood species. In the case of softwood, the cell walls form a kind of honeycomb structure which in turn comprises a series of tracheids which are long tubular macrovoids, also denominated as cell lumens, following the stem axis of the tree. This honeycomb-like microstructure ensures the mechanical bearing capacity and the transport of water and nutrients along the tree. The transport of water inside

wood is possible due to the presence of pits which are round holes interconnecting the tracheids. At the macrostructure scale, the tracheids of different sizes are set in a concentric array forming the growth rings of the heartwood and sapwood regions (Thybring et al. [9], Eitelberger et al. [10]).

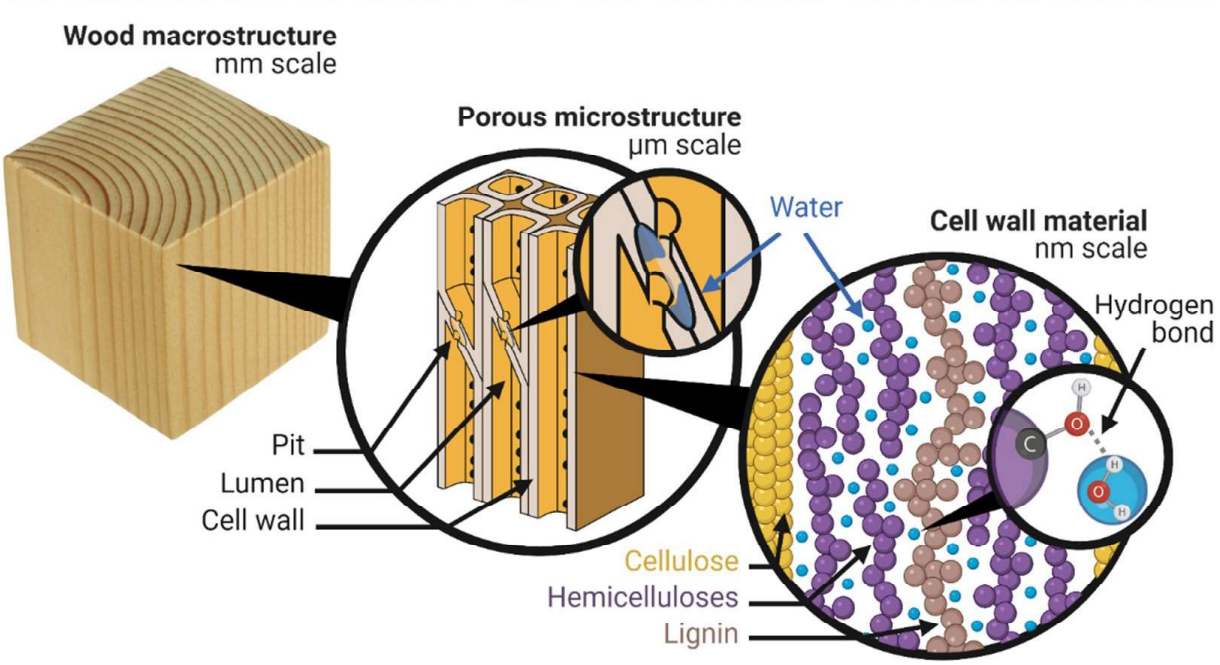


Figure 2.1: Hierarchical representation of softwood in the macroscale, microscale and cellular scale (Figure taken from Thybring et al. [9]).

Generally, water inside wood can be found in three states: i) as liquid water and ii) water vapor, both within the macrovoid structure (cell lumens); and as iii) bound water interacting with the cell wall polymers. Liquid water, which interacts with the boundary surface of the cell walls by capillary condensation or capillary action, is only found in living trees or in wood directly exposed to water like during rainfall and leakage situations. However, wood products are generally exposed to air and are usually being bellow the fiber saturation point (defined as the moisture state where significant amounts of capillary water are present) meaning that water vapor and bound water are the only existing phases (Thybring et al. [9]).

The transport of water in wood can be classified in general in three coupled processes: i) water vapor diffusion, ii) bound water diffusion and iii) capillary liquid transport. In the case of water vapor diffusion, the mean free path of water molecules, a measure of the average distance these molecules travel between collisions with other molecules, and the connectivity layout through pits among the tracheids play a key role. For bound water diffusion, the tortuosity of the nano-pores located inside the cell walls and the hydrogen bond between the cell wall polymers and water molecules are the governing factors. Similarly, the flow of liquid wa-

ter depends on the connectivity between different tracheids through pits, but the gradient in capillary pressure is also a relevant aspect (Thybring et al. [9]).

Commonly, the transport of water starts when a wood specimen is in contact with the ambient air which has a specific relative humidity (RH) and temperature. This triggers the uptake of ambient water vapor by a sorption mechanism leading to the gain of water mass until equilibrium is reached with the ambient conditions. This sorption process is related to the transition of water from a vapor phase to a condensed phase within the cell walls or in the cell lumens. However, sorption can also refer to a change of water state from a condensed phase as bound water to a vapor phase. Both processes are commonly known as absorption and desorption, respectively (Thybring et al. [9]).

The equilibrium moisture content (EMC) obtained for certain environmental conditions can be assessed by means of water vapor sorption isotherms describing the relationship between the EMC and the RH of the ambient for a specific temperature as depicted in Fig. 2.2 (Thybring et al. [9]). Sorption isotherms cover the hygroscopic and over-hygroscopic ranges, and have different relationships for the absorption and desorption processes. In a strict sense, the EMC depends on the moisture history due to changes in RH. This dependency on the moisture history can be reflected by a series of relationships called sorption hysteresis. These hysteretic relationships encompass the sorption mechanics of phase change from a vapor or liquid phase to a bound water phase or vice versa related to the hygroscopic and over-hygroscopic regime, respectively.

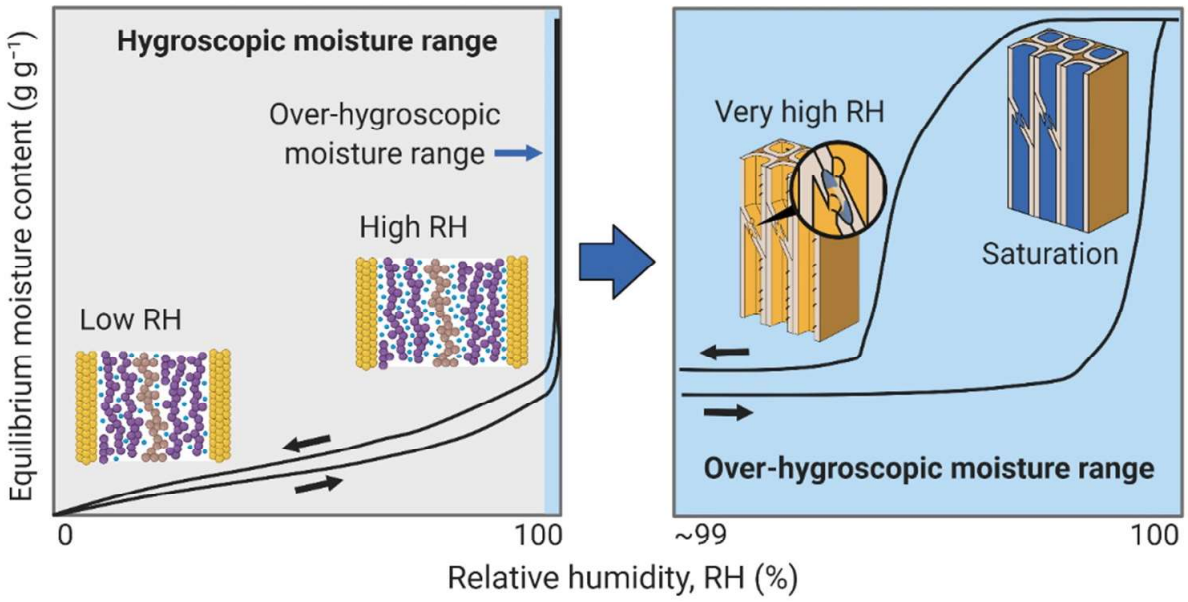


Figure 2.2: Absorption and desorption isotherms in the hygroscopic and over-hygroscopic moisture ranges (Figure taken from Thybring et al. [9]).

Moisture content and moisture concentration gradients inside wood could have serious repercussions in the serviceability and safety of timber elements. Fungal growth as a consequence of elevated levels of moisture content in the elements could degrade wood material properties. In the case of moisture gradients with notable spatial variations, they could produce a non-uniform restraining of the swelling and shrinkage between the external and inner parts of the timber element. This situation leads to the build-up of additional internal stresses denominated moisture induced stresses (MIS) producing cracks in the surface of the elements. On the other hand, moisture fluctuations over time due to a continuously varying climate could induce large deformations due to the rheological behavior of wood. Therefore, the temporal and spatial distribution of moisture content in timber elements need to be carefully assessed using a moisture transport model. A series of macroscopic mathematical models for describing the moisture transport process in wood has been proposed over the last decades. These models are reviewed and described in the following part.

The denominated single Fickian moisture transport approach relies on considering a unique total flux that encompasses all water phases together so the whole process can be represented by a single Fickian diffusion equation (Kollmann and Cote Jr [11]). This approach is based on Fick's laws (Fick [12]). The flux is assessed by means of the first law of Fick by using the gradient of the moisture content and diffusion coefficients. On the other hand, the variation of the moisture content over time is evaluated through Fick's second law using the divergence of the gradient of the moisture content. In this approach is assumed that under transient conditions the water vapor and bound water phase are always in equilibrium meaning that there is no a rate of sorption (Krabbenhoft and Damkilde [13]). The single-Fickian diffusion approach has been widely adopted in different types of hydro-mechanical analyses to assess the response of timber elements under changing climatic conditions. Some of these studies are described below.

Fortino et al. [14] extended a well-known unidimensional viscoelastic-mechano-sorptive model to a three-dimensional orthotropic model to study the hygro-mechanical response of wood under service loads and varying humidity conditions. To evaluate the moisture-dependent response, the rheological model was coupled with a single-Fickian diffusion model. This Model allowed the evaluation of the long-term deformation of wood specimens which were in agreement with the experimental responses. The development of internal stresses perpendicular to the grain due to an internal moisture gradient was also assessed for the case of a beam subjected to a step increase in relative humidity. This rheological model coupled with a single-Fickian diffusion equation has also been used to describe the creep and relaxation tests performed in Norway

Spruce specimens compressed perpendicular to the grain and subjected to constant and variable humidity loads (Massaro and Malo [15]). A numerical study of a simple supported curved timber beam using the same previous coupled hygro-mechanical model in conjunction with a heat transfer analysis was performed by Zhou et al. [16]. The aim was to evaluate the induced stresses perpendicular to the grain in the curved beam under daily variations of relative humidity and temperature. Their results pointed out that the environmental conditions were the primary sources in the development of these stresses which could lead to a potential cracking of the surface as the tensile strength of wood perpendicular to the grain could be surpassed.

A single-Fickian approach was also used to assess the rheological behavior of cross-laminated timber (CLT) panels of three and five layer specimens (Nguyen et al. [17]). In this study, a series of moisture diffusion tests were performed to calibrate the moisture diffusion coefficients in the direction perpendicular to the surface panel. As part of this calibration process, several numerical diffusion analysis were performed in order to obtain the best-fitted diffusion coefficients to match the experimental results. Likewise, a rheological model at the macroscopic level was calibrated with a number of creep test carried out on CLT specimens. Finally, to assess the long-term behavior of a CLT panel subjected to four-day length cycles with square wave shape, a numerical analysis was performed with the calibrated models. The results showed that the panels with three layers underwent larger axial strain variations than the five-layer panels.

The single-Fickian diffusion approach was also used to model the short-term coupled hygro-mechanical behavior of wood specimens (Saft and Kaliske [18]). The authors proposed a three-dimensional constitutive model considering a hygroscopic behavior through a moisture dependency of the mechanical properties describing the elastic behaviour and material strengths, and a ductile behaviour by means of a multi-surface plasticity model. Latter this model was extended to consider a more comprehensive hygro-mechanically coupled approach to include the linear viscoelastic, non-linear viscoelastic–viscoplastic, hygro-expansional and mechano-sorptive behaviour of wood (Reichel and Kaliske [19]). Similarly, Hassani et al. [20] presented a moisture-dependent rheological model encompassing elastic, plastic, hygro-expansion, visco-elastic creep, and mechano-sorption deformations in wood coupled to a single-Fickian diffusion equation.

The study of the moisture induced stresses in wood elements has been addressed by a number of authors using the single-Fickian diffusion approach. Gereke et al. [21] studied the dimensional stability of three-layered cross-laminated solid wood panels under a moisture gradient along their thickness. The results showed good agreement with the experimental results and it was concluded that the annual growth ring orientation of the board layers and the layer ratio related to the outers play a key role in the hygroscopic warping of the panels. Then, additional studies

were performed (Gereke et al. [22] Gereke and Niemz [23]) on possible solutions to alleviate the moisture-induced stresses and hygroscopic distortions on three-layered panels. These solutions involved the use of wood composite in the middle layers (Gereke et al. [22]) and compressive prestress in the outer layers (Gereke and Niemz [23]).

In the same way, Fragiacomo et al. [24] analysed a series of timber elements under different European climates using a single Fickian moisture transfer model coupled to a three-dimensional rheological model (Fortino et al. [14]) to evaluate the moisture-induced stresses perpendicular to grain. From, the results it was noticed that the cross section size of the element, the type of climate and protective coatings have a major effect on the variation of the moisture content inside the element. Moreover, it was found that the Northern European climates generated the higher moisture-induced stress due to their larger humidity variations.

Moisture induced stresses perpendicular to the grain have been also evaluated by means of simplified numerical models (Angst and Malo [25]). These models uses an unidimensional single-Fickian diffusion approach integrated with a two-dimensional model of the cross section of the timber element in which a two-dimensional orthotropic hygro-mechanical model is incorporated. This model has been applied to study the developed internal stresses due to restricted swelling and shrinkage in glulam sections of different widths and piths location within the laminates comprising the section exposed wetting conditions (Angst and Malo [26]). It was noticed that wider cross sections had a risk of cracking when the wetting cycles have a long period. The same model (Angst and Malo [25]) has also been used to study the moisture induced stresses in glulam sections of different widths and heights under wetting, drying and European climatic conditions (Franke et al. [27]). The results pointed out that under wetting conditions wider cross sections with the same height can reduce the inner tension due to the moisture induced stresses whereas in drying conditions the geometry does not have a effect in the tension stresses as they develop in the area near the surface.

Single-Fickian approaches coupled with one-dimensional rheological models have been widely used to study the long-term behavior of beam-column elements. Khorsandnia et al. [28] performed the long-term analyses of timber–concrete composite beams integrating an implicit finite difference scheme with a one-dimensional force-based finite element formulation. It was concluded that the proposed frame finite element model can capture with sufficient accuracy the long-term behaviour of timber and timber–concrete composite beams. Ormarsson and Gíslason [29] developed a frame element capable of considering the modulus of elasticity and shrinkage coefficient of each wood laminate comprising the element. This finite element model was used in conjunction with a Single-Fickian approach and Rheological material model to assess the

long-term behaviour of a statically indeterminate curved frame structure subjected to mechanical loading and Norwegian climatic conditions. The results showed that the curved frame experienced a significant stress redistribution due to the its statically indeterminate nature and changing humidity.

The hygroscopic and rheological behaviour of wood plays a key role in the assessment of the long-term tendon force losses in post-tensioned timber elements. Granello et al. [30] described a procedure to assess the long-term behaviour of post-tensioned timber beams and frames under controlled and uncontrolled environmental conditions. In this procedure a single-Fickian diffusion analysis in the cross section of the element is performed first to assess the moisture distribution and then these calculated values of moisture are used as input parameters in the constitutive model defining the rheological behavior of wood. Finally, the time-dependent deformations are evaluated and the post-tensioned force is updated. The model demonstrated its ability to simulate with enough accuracy the post-tensioning loss in the specimens under laboratory and real-case scenarios.

When considering the diffusion of water vapor and bound water separately, it is possible to model both diffusion processes by two Fickian equations coupled by a sorption term accounting for the phase change from one state to another (Krabbenhoft and Damkilde [13]). This mathematical description is called multi-Fickian moisture transport model (Frandsen et al. [31]). The model developed by Frandsen et al. [31] is based on the approach introduced by Krabbenhoft and Damkilde [13]. Further efforts were done by Eitelberger et al. [32] to obtain a more comprehensive macroscopic description of the moisture transport process below the fiber saturation point. In this approach, the change in internal energy involved in the phase changes of water in the sorption process is considered by including a third equation representing the conservation of energy. Thus, three coupled differential equations are obtained.

Over the last decade, multi-Fickian approaches have been extended to incorporate new features in the assessment of moisture distribution under different varying ambient conditions. Svensson et al. [33] carried out a series of numerical analysis incorporating a sorption hysteresis into this approach to evaluate the influence of the features describing a sinusoidal humidity load on the build-up of moisture induced stresses in timber elements. Similarly, the multi-Fickian hygro-thermal approach Eitelberger et al. [32] was upgraded to include a hysteresis describing the attainment of equilibrium moisture content to assess the moisture states in a monitored timber beam of a pedestrian bridge in a natural environment (Fortino et al. [34]). Later, the hygro-thermal approach was modified to adopt a sorption depending on temperature though an average temperature-dependent sorption curve to evaluate the moisture state in bridge

members under Northern European climates exposed to temperatures above and below zero degrees Celsius (Fortino et al. [35]).

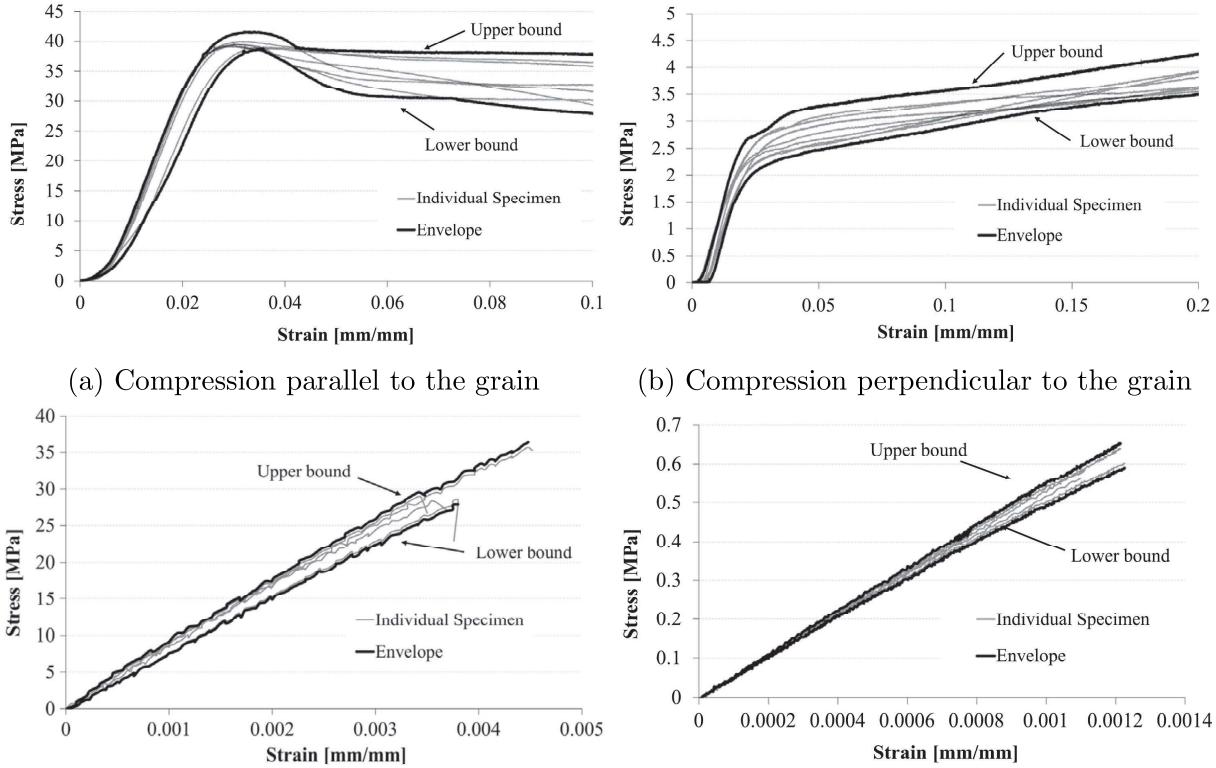
In cases in which free or liquid water is present in the moisture transport mechanism, the three phases of water which are interacting with each other can be described by combining the multi-Fickian approach with Darcy's law (Autengruber et al. [36]). The multi-Fickian approach describes the diffusion of the water vapor in the lumens and bound water in the cell walls bellow the fiber saturation point (FSP), whereas Darcy's law describes the transport of free water above the FSP. In Darcy's law the driving force starting the transport of free water is the gradient of capillary pressure. To describe the interaction between the water vapor and free water phase, a evaporation rate is introduced. This modelling approach has the potential to study timber elements directly expose to water which could lead to the potential risk of local cracking or delamination.

2.2 Nonlinear Numerical Modelling of the Short-Term Response of Timber Structures

Besides wood's hygroscopic behavior inducing water transport inside wood as stated in the previous section, the orthotropic nature of wood along with the presence of natural defects and geometric irregularities in timber members constitute an additional set of intricate features that should be carefully considered as them strongly influence the short-term response of timber beams and columns. The short-term assessment of these timber elements usually involves the calculation of load-deflection curves under ultimate loads. In the case of modelling these timber elements, a wide variety of different finite element (FE) models can be used to assess their load-carrying capacity. Specifically, nonlinear continuum-based FE models by means of brick or membrane elements have demonstrated their versatility and accuracy when geometric irregularities such as holes and notches, or growth characteristics such as knots play a major role at the ultimate state of loading. Under these circumstances, a multiaxial constitutive model considering the orthotropic behavior of timber should be adopted (Khorsandnia and Crews [37]).

Wood constitutive models should be able to reflect the directionality (orthotropy) of wood mechanical properties (differing along and perpendicular to the grain directions) and capture the failure modes observed in different experimental campaigns. In general, these failure modes can be categorized as brittle failure due to tension parallel or perpendicular to the grain, ductile

softening failure due to compression parallel to the grain, and ductile failure with slight hardening (material densification) due to compression perpendicular to the grain (Oudjene and Khelifa [38]). Fig. 2.3 (Karagiannis et al. [39]) illustrates the experimental strain-stress relationships related to these failure modes obtained for Scandinavian Spruce specimens. The constitutive models developed to encompass the behaviour of clear wood can be categorized as orthotropic elastic models, elasto-plastic models, elasticity-damage models and coupled plasticity-damage models (Khorsandnia and Crews [37]). A review of the existing constitutive models available in the literature can be found in previous works (Khorsandnia and Crews [37],Gharib et al. [40],Zhang et al. [41],Sirumbal Zapata [42]).



(a) Compression parallel to the grain

(b) Compression perpendicular to the grain

(c) Tension parallel to the grain

(d) Tension perpendicular to the grain

Figure 2.3: Experimental stress–strain curves for Scandinavian Spruce Glulam specimens (Figure taken from Karagiannis et al. [39]).

The size and distribution of defects such as knots influence the ultimate loading capacity of timber members due to the local deviation of the grains around the knots. Baño et al. [43] developed a modelling technique to take into account the effects of knots in the bending load capacity of sawn timber beams as well as to predict the position of the rupture. In their numerical assessment, three different models considering the local grain deviation were proposed to characterize the knots using plane stress quadrilateral elements along with a yield criterion for orthotropic materials. By comparing their results with the experimental data, they found that the model considering holes instead of knots predicted most accurately results. The

same authors then performed a numerical study, using the validated FE model, to quantify the influence of different knot sizes and positions along the depth of the beam on its bending strength (Baño et al. [44]). After analysing 165 virtual beam cases, it was observed that the knot size reduces the bending strength, in proportion to the separation distance from the centroidal beam axis. In the case of knots located in the tension side, it was highlighted that the tension parallel and perpendicular to the grain play a major role in the rupture of the element when the knots are closer to the bottom edge of the beam whereas the shear stresses are relevant when the knots are set apart from the bottom edge. Recently, a three-dimensional FE model was developed using brick elements to replicate the geometrical features of knots in timber beams (Saad and Lengyel [45]). Through a destructive approach, the conical shape of the knots and three-dimensional fiber pattern surrounding the knot region was replicated. In this simulation, the knots were represented by bonded contact elements and openings, and a failure criterion including the orthotropy and interaction of stresses among the fibre deviations was adopted. It was noticed that the simulations replicated well the measured load-deflection curves while modelling of the knot itself was not as significant as an accurate representation of the fibre deviations.

Openings in timber members are required due to construction requirements to facilitate building services to pass through. However, the presence of these openings could affect the ultimate load carrying capacity of timber members as the build-up of tensile stresses perpendicular to the grain direction and longitudinal splitting shear stresses can initiate and propagate cracks. Guan and Zhu [46] performed a numerical simulation of timber composite I-beams using oriented strand boards in the webs with circular and square openings in conjunction with a experimental campaign. A FE model was built using iso-parametric solid elements incorporating a orthotropic elasto-plastic constitutive model along with a modelling procedure that attempted to replicate the crack initiation and growth by removing damaged elements. The results were compared with the experimental data which showed a good agreement and that the element removal procedure was capable of replicating efficiently the crack growth. The numerical and experimental results also confirmed a drop of the ultimate load capacity in these timber members, especially in the case of square openings. A less computationally demanding approach was proposed by Khorsandnia et al. [47] to assess the global and local behavior of timber members including beams with notches and holes. This 2D continuum-based FE model adopted a piecewise continuous orthotropic failure envelope in a simplified way. This model used isotropic layers along with interface elements to represent the behaviour of timber perpendicular to the grain. The comparison of the numerical and experimental results attested

the ability of the proposed technique to simulate the ultimate response of these beams at the local and global level.

Valipour et al. [48] proposed another 2D continuum-based FE model in which timber is considered as a composite material comprising a matrix with smeared fictitious reinforcing fibers aligned parallel and perpendicular to the grain. The behaviour of the matrix is simulated through a simplified version of a previous presented orthotropic failure envelope (Khorsandnia et al. [47]). It was found that the simple modelling strategy proposed can capture the global and localised failures modes in the case of timber beams with web openings and notched timber beams strengthened with carbon-fibre-reinforced polymer (CFRP) strips/sheets. Due to the quasi-brittle failure modes in tension and/or shear of beam-like timber members with openings, the softening branches incorporated on the constitutive models lead to spurious mesh sensitivity in the results if a localisation limiter is not adopted. In order to avoid this numerical issues, Karimi-Nobandegani and Valipour [49] incorporated a nonlocal integral averaging technique into a continuum damage model as a regularization technique. Using this modified constitutive model in conjunction with a three dimensional FE model allowed a reasonable prediction of the local and global response of timber beams with square and circular opening layouts under ultimate loads.

More complex FE modelling techniques have also been introduced to study the ultimate response of timber beams with openings. The use of cohesive elements allows the simulation of crack propagation under gradually increasing loads. Ardalany et al. [50] considered solid elements and predefined cohesive layers with bilinear traction-separation relationships located in the hole edge where maximum normal stress are developed to assess the failure modes and load-carrying capacity of timber beams with holes. Sophisticated models by means of the Extended Finite Element Method can also be employed to simulate automatically crack nucleation, propagation and branching. Gebhardt and Kaliske [51] assessed crack initiation or propagation by employing a multi-surface failure criterion based on a failure envelope for anisotropic materials.

The complexity involved in developing nonlinear continuum 2D/3D FE models could be a overwhelming task as a large number of input parameters are required to define a constitutive model, whose calibration process and the computational time could be significantly demanding. However, if there are no openings or notches, and local defects such as knots are considered negligible, the influence of multi-axial stress state within wood and its orthotropic behaviour can be small for the assessment of the global response of timber structures (Khorsandnia and Crews [37]). As a result, unidimensional beam-column elements along with uniaxial constitutive

laws can be used to assess the nonlinear response of beam-like timber members at the ultimate state of loading with enough accuracy. The use of fiber beam-column elements adopting the Euler–Bernoulli beam theory seems to be a reliable modelling option as it has been employed in the assessment of the short-term global behaviour of timber and timber-concrete composite beams as it will be described bellow.

Lukaszewska et al. [52] explored the nonlinear response of timber-concrete composite beams using prefabricated concrete slabs with various types of shear connectors. In this study, sixteen fiber beam elements were used to describe the behavior of the concrete slab and timber beams employing quadratic and cubic interpolation functions to describe the axial and flexural displacement field in each element. With regard to the modelling of the concentrated connectors linking the concrete and timber beams elements, a smeared connection assumption was considered by means of a continuous horizontal spring system. The behavior of the timber fibers was modelled through a uniaxial stress-strain relationship in which a elasto-brittle and elasto-plastic model were used in the tension and compression, respectively. By comparing with experimental results obtained from four-point bending tests, the unidimensional FE model was capable of simulating the failure load and mid-span deflection with less than 10% discrepancy. After this validation, a parametric study was performed to investigate the response of these composite beams with other configurations of shear connectors.

Apart from fibre beam-column elements based on displacement formulations, force-based formulations have also been used in the nonlinear analysis of timber beam-like structures. Valipour and Crews [53] assessed the global response of timber beams strengthened with externally bonded fibre reinforced polymer (FRP) sheets and bars using a fiber force-based frame finite element following a total secant approach. In this modelling procedure, a uni-axial material law was adopted to describe the nonlinear behavior of the timber fibers parallel to the grain using the compression stress–strain law presented by Glos [54] and a linear elastic-brittle relationship in tension. Additionally, bond shear-slip effects were considered between timber and FRP surfaces. A high correlation between experiments and simulations with low dispersion among the results was observed for ultimate load capacities. A three dimensional FE model incorporating contact elements was also built to compare its results with the obtained from the proposed frame FE model and its similar level of accuracy and superior efficiency was demonstrated.

The force-based formulation developed by Valipour and Crews [53] was extended by Khorsandnia et al. [55] to study the ultimate capacity of timber–concrete composite and timber–timber composite beams. In this model, the FE element consist of two or three layers connected through a shear transfer mechanism between them represented by lumped-nonlinear springs

located at each end of the interlayer edge. This modelling technique uses the same uniaxial constitutive law for timber layer as in their previous work (Valipour and Crews [53]). However, a quasi-brittle behavior was consider in the tension regime by means of a linear softening branch. The efficiency and accuracy of the proposed FE element was demonstrated by comparing the numerically predicted global response of composite beams, such as load-deflection response, midspan stresses and strain profiles, with experimental data. Moreover, the developed model showed similar accuracy to the FE model proposed by Lukaszewska et al. [52].

A comparative analysis of a 2D continuum-based FE model, 1D frame FE model and manual calculation based on Eurocode procedure was carried out by Khorsandnia et al. [56] to predict the global behaviour of timber-concrete composite structures at serviceability and ultimate limit state. The force-based frame FE model proposed by Khorsandnia et al. [55] to study the nonlinear behavior of two and three-layered composite beams was employed in this comparative study. The continuum-based model adopted a constitutive law to describe the failure modes of timber under bi-axial stress states and lumped nonlinear springs to model the full shear-slip behaviour of the mechanical fasteners. It was observed that the 2D FE model attained the highest level of accuracy. Nevertheless, the 1D FE model predicted the global responses with adequate accuracy as reflected in the estimation of the ultimate loading capacity and ultimate deflection with average errors of 8% and 6%, respectively. Moreover, it was found out that the manual procedure stated in the Eurocode can capture the serviceability and ultimate response of these composite beams with reasonable accuracy.

Khorsandnia and Crews [37] performed a comparative numerical study of unidimensional (1D), bidimensional (2D) and three-dimensional (3D) non-linear FE models to evaluate their efficacy and accuracy in capturing the load-deflection response and failure load of flexural dominated timber elements. The force-based 1D FE model presented by Valipour and Crews [53] was adopted in this work. In the case of the 2D and 3D continuum-based FE models, quasi-brittle constitutive laws adopted for describing the isotropic behavior of concrete were used to describe the nonlinear behavior of timber as these laws require fewer material parameters than the typical timber constitutive laws. A very good correlation was observed betweem numerical and experimental results in terms of global response when notches, holes and knots were not considered in the analysis. Otherwise, an overestimation of strength capacity was noted. It was stressed that the 1D FE model showed greater efficacy from a computational point of view.

The frame FE model developed by Khorsandnia et al. [56] was used by Khorsandnia et al. [57] to assess the behaviour of deconstructable timber-concrete composite beams with panelized reinforced concrete slabs considering a number of different connections. In this assessment, an

analytical method and a 2D continuum-based FE model were also employed with the aim of contrasting the efficacy and accuracy of these methods. In the 1D and 2D FE models, concentrated nonlinear springs were adopted to consider the load-slip curve relationships of the mechanical connections. It was noticed that the 1D FE model in general overestimates the stiffness and strength of the composite beams when the effect of the gaps between the slab panels weights in the structural response. Otherwise, this model describes with enough accuracy the global response of these structures. Nevertheless, the continuum-based model was the most accurate in all the cases as it can include the effect of the gaps and contacts between the precast panelised slabs.

Tao et al. [58] carried out a comparative numerical analysis of 1D, 2D and 3D non-linear FE models to estimate their ability to predict the failure modes and load-deflection response of timber-concrete composite beams adopting four types of interfacial connections. The 1D FE model presented consisted of two parallel fiber beam elements linked through continuous nonlinear spring elements incorporating a representative load-slip relationship of the shear connections. In this 1D model, a ideal elasto-plastic behavior was assumed for the compression range whereas a elasto-brittle law was adopted for tension. From the selected analysis cases, it was observed that three of them experienced a first peak load related to the failure of the end connections followed by a sequence of peak loads related to the remaining connections up to the failure of the timber beam bottom. On the other hand, one of the composite beam showed only one peak load related to the fracture of the bottom of the beam. A comparison between the numerical results and experimental data showcased the capability of the 1D and 2D FE models of capturing the global nonlinear response up to the first peak load related to the failure of the end connections or timber failure at the beam bottom. These models were not able to describe the subsequent stages of failure due to convergence issues. Nevertheless, only the 3D model was able of replicate the failure models observed in the experimental campaign.

As described in this section, a wide variety of modelling techniques have been employed to assess the short-term ultimate-load response of timber elements. However, not only these ultimate state scenarios can compromise the integrity, safety and functionality of timber structures. Long-term effects plays also an important role, specially in terms of functionality. Likewise, a number of modelling approaches have been undertaken to assess the long-term response of these structures. In what follows, a summary of these approaches is performed.

2.3 Nonlinear Numerical Modelling of the Long-Term Response of Timber Structures

As was pointed out in section 2.1, the hygroscopic nature of wood can compromise the safety and serviceability of timber structures due to the build-up of moisture induced stresses and strains under moisture content variations. However, if the timber members are subjected to sustained load besides to continuously varying climate, large deformations can be induced in these members due to the rheological behavior of wood which could potentially affect their service life. Besides the normal viscoelastic creep experienced at constant humidity conditions, an additional delayed deformation denominated mechano-sorptive (MS) creep is experienced as a result of the moisture fluctuation. This additional deformation can be comparable to the result of superimposing the hygroexpansion and basic viscoelastic creep deformations (Hanhijärvi [59]). From previous experimental results, Mårtensson [60] described a series of observed features related to MS phenomenon. Among some of these features, it can be mentioned that the MS deformation rates at absorption and desorption presents distinct behaviours. A MS deformation increase is observed when the first humidity variation is related to an absorption process. Besides moisture history dependency on previous attained thresholds, partial recovery of MS deformations after unloading, and a limit on MS creep are all observed features of the response. Some of these features are depicted in Fig. 2.4 (Frandsen [61]) from the experimental results carried out by Hearmon and Paton [62].

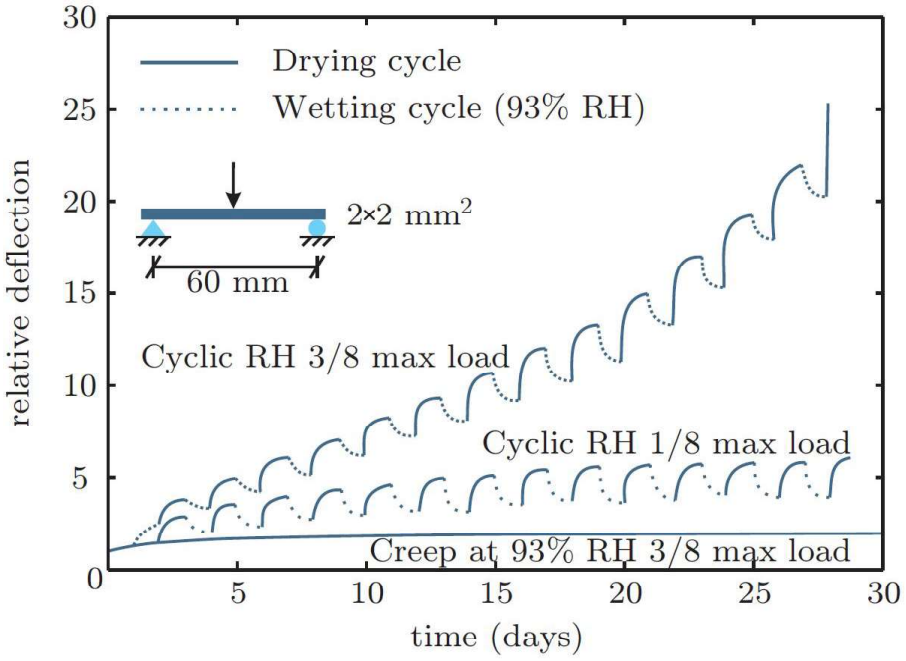
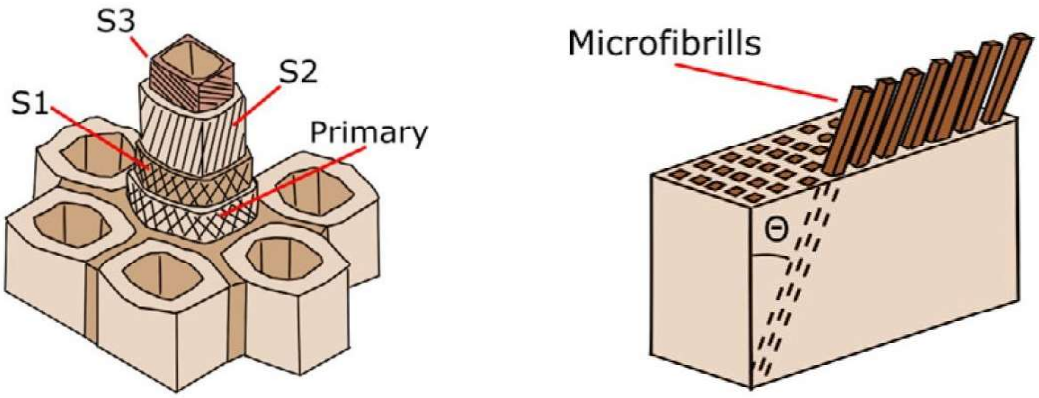


Figure 2.4: Wood beam subjected to different moisture conditions and stress levels (Figure taken from Frandsen [61]).

The complex rheological behavior of wood has led to the development of multiple explanatory theories based on the physical and chemical interactions taking place at the micro- and nano-structural levels (Schänzlin [63],Chassagne et al. [64]). The microstructure and nanostructure of wood is depicted in Fig. 2.5 (Bengtsson et al. [65]). From this figure, it can be seen that the cell wall consists of a primary and secondary wall, and that last one comprises three layers labelled as S1, S2 and S3. These layers are formed by of fibril networks denominated microfibrils and composed by cellulose, hemicellulose, and lignin chains. An important feature of the microfibrils is that the ones comprising the primary wall are not closely arranged and have a random alignment whereas the ones forming the secondary wall are closely placed and aligned parallel to each other. Moreover, the S2 layer comprising more than 75 % of the cell walls has a microfibril alignment almost parallel to the cell wall direction is considered to have a key play role in influencing the mechanical response of wood. Nevertheless, reflecting this structure on structural engineering level simulations is impractical due to their complexity and great number of parameters involved.

On the other hand, phenomenological approaches to describe the rheological behavior have demonstrated to be a feasible modelling technique to incorporate the mechano-sorptive (MS) features observed (Mårtensson [60]) to a practical extent. Some of the uniaxial models developed are mentioned here. Models considering Kelvin-Voigt components in series to describe the viscoelastic and MS creep were proposed by Toratti [66], Hanhijärvi [67] and Svensson and Toratti [68]. Particular features among these models are the inclusion of dashpots activated by moisture increments to represent the MS deformations (Toratti [66], Hanhijärvi [67], Svensson and Toratti [68]), MS dashpots interacting in parallel to plastic elements (Hanhijärvi [67]) to describe the irrecoverable deformations due to high moisture changes in drying conditions and dashpots driven by moisture increments related to moisture levels not previously attained (Svensson and Toratti [68]) to simulate the irrecoverable deformations. Models constructed by assembling Maxwell elements in parallel were proposed by Hanhijärvi [69] and Bou Said [70]. The model developed by Bou Said [70] considers separated Maxwell units to represent the viscoelastic and MS deformations where the dashpots are nonlinear functions of the stress levels, moisture rates and accumulated moisture variations. In contrast, the model proposed by Hanhijärvi [69] encompasses the viscoelastic and MS mechanism together in the Maxwell units through a nonlinear dashpot that couples the viscoelastic creep and hygroexpansion deformation. The generalization of these uniaxial models into a multiaxial rheological models was carried out by Fortino et al. [14], Hanhijärvi and Mackenzie-Helnwein [71], Chassagne et al. [64], Vidal-Sallé and Chassagne [72] and Hassani et al. [20]. More rheological models of wood can

be found in the literature review of previous works (Hanhijärvi [59], Schänzlin [63], Vidal-Sallé and Chassagne [72], Yu et al. [73]).



(a) Cell wall layers (b) S2 wall

Figure 2.5: Description of the microstructure and nanostructure of wood (Figure modified from Bengtsson et al. [65]).

Multiaxial rheological constitutive models have been widely applied in numerous long-term assessments of timber members under sustained load and variable climate conditions using three- and bi- dimensional continuum finite element models. For instance, Huč et al. [74] proposed a detailed FE model of wood boards including features such as the growth rings, spiral grain and conical shape to study the development of the deformations during a drying scenario of relative short-period duration. In this analysis, the mechano-sorptive strains were estimated using the model developed by Santaoja et al. [75] which is a multiaxial extension of the uniaxial model proposed by Ranta-Maunus et al. [76]. The same authors then performed a numerical study (Ormarsson et al. [77]) concluding that the hygroexpansion and mechano-sportive parameters had a high degree of influence in the assessment of the distortions.

Similarly, Florisson et al. [78] analysed the long-term behavior of small and medium sized timber beams under controlled and natural climatic conditions, respectively, by developing detailed 3D FE models of the timber beams with the fibre orientations were included. These orientations comprised the curvature of annual rings due to the pith location, the conical angle and spiral grain angle of the log. The authors adopted the mechano-sorptive model proposed by Salin [79] in a multiaxial stress state. It was observed that the spiral grain angle had a negligible influence in the variation of the longitudinal stresses and deflections whereas in the case of the tangential stresses the influence of the angle is noticeable. The calibrated material parameters were subsequently used to simulate the response of the medium specimens. The numerically predicted deflection was in good agreement with the experimental results.

Detailed FE models have also been employed to determine the rheological parameters of wood samples based on the results of long-term tests. In these simulations, the pith location of each lamella comprising the timber element were taken into account and the parameters were obtained through a fitting procedure against the simulated and experimental response. Huč et al. [74] simulated the long-term behavior of European oak blocks under a constant and variable relative humidity conditions during 180 hours. The numerical work adopted a rheological model based on proposal of Frandsen [61] and a multi-Fickian moisture transport model for the diffusion analysis. Similarly, Massaro and Malo [15] analysed the long-term response of Norway Spruce blocks under compression perpendicular to the grain. In this case, the rheological model proposed by Fortino et al. [14] was employed in conjunction with a single-Fickian approach for the diffusion analysis. In this study, a creep tests were performed first under constant and variable moisture conditions to calibrate the material parameters. Then a relaxation test was carried out to further validate the calibrated model.

Regarding engineering applications, Fortino et al. [80] performed a long-term analysis of a mass timber girder of a bridge subjected to Northern European climates with temperatures above and below zero-degree Celsius. In their assessment, the goal was to predict the moisture-induced stresses, strains and deflections during a 10-year period under real climate conditions. Only one slice of the cross-section beam located at the mid-span was simulated employing a 3D FE model including the modelling the pith locations of the different lamellas comprising the beam. Previous to the mechanical analysis, a hygro-thermal multi-Fickian approach was employed to assess the moisture content, relative humidity and temperature fields inside the member. In a sequential analysis, these results were then used in conjunction with the orthotropic rheological model proposed by Fortino et al. [14] to assess the long-term deformations in the section. These deformations were then used to calculate the vertical deflection of the beam by performing a second integration of the estimated curvature from the modelled cross-section. The moisture induced stresses perpendicular to the grain highlighted the risk faced by the bridge under the assumed environmental conditions as the tension strength of wood could be exceeded.

Other applications of 3D FE models was found in the strengthening of timber beams. The long-term behavior of strengthened timber beams with aramid fibre-reinforced polymer (AFRP) sheets was analysed by Yahyaei-Moayyed and Taheri [81]. A three-dimensional (3D) Finite Element (FE) model was built using brick elements for wood and the FRP laminates joined by multi-point constraints to simulate the interaction at the bonding interface. The viscoelastic behavior of the FRP composite and the viscoelastic-mechano-sorptive behavior of

wood were fitted to creep tests performed under tension and flexural stresses, respectively, using a power law model. The numerically simulated results showed a good agreement with the experimental data in depicting the improved response of strengthened timber beam in terms of reduced mid-span deflections.

A study on the long-term performance of timber beams strengthened with bonded carbon fiber reinforced polymer (CFRP) bars embedded near the bottom of the beam was carried out by Xu et al. [82]. A 3D model using solid, shell and truss elements was built to simulate the long-term mid-span deflections of one unreinforced reference and two reinforced timber beams under sustained load and ambient relative humidity ranging between 40% to 65% for 1200 days. Previously, a calibration was performed on the reference beam by using a five-parameter model and assuming that timber was the only material undergoing long-term effects. Their results showed that the numerical model was able to capture the primary and secondary creep phases well.

Similarly, O'Ceallaigh et al. [83] employed a three dimensional model to assess the long-term effects on timber beams strengthened with basalt fibre reinforced polymer (BFRP) rods under constant and cyclic variations of the environmental humidity conditions. Solid elements were used to model the reinforcing bars and beam, and timber was considered as the only material affected by long-term effects. Additionally, a modification was performed in the rheological model proposed by Fortino et al. [14] to take into account the irrecoverable mechano-sorptive creep effects in the longitudinal direction. The numerical results replicated with enough accuracy the deflections and longitudinal strains obtained in the laboratory test showing the beneficial effects of using BRFP bars in reducing the undergoing deflection and strains.

Three-dimensional FE models have also been employed in the assessment of the time-dependent behavior of timber-concrete composite beams. Bou Said [70] simulated the medium- and long-term response of composite beams using shear crown connectors and metal rods at the interface layer adopted from experimental campaigns at full and reduced scale, respectively. The uniaxial model originally proposed by the author was extended to a multiaxial stress state to allow the 3D analysis. The comparison of experimental and numerical results showed the capability of the 3D model to capture the development of time-dependent deflections over time with good accuracy. Similarly, Fragiacomo et al. [84] also performed a 3D simulation of timber-concrete composite beams using notched shear key connectors. An extension of the model proposed by Toratti [66] was developed by assuming that the creep of wood perpendicular to the grain is four timers greater than the experienced along the grain. The numerically simulated results indicated good agreement with the experimental data highlighting the benefit

of a 3D model as there was no need to model the rheological behavior of the shear connectors compared with a fiber beam model. Moreover, the 3D modelling technique was shown adequate to simulate long-term push-out (slip) tests with enough accuracy.

Timber-timber composite (TTC) beams were also assessed by means of 3D continuum-based FE models. Nie [85] performed a long-term assessment of TTC connections and beams with screw shear connectors. Brick elements were used to model the mass timber slabs and beams as well as the steel crews and the orthotropic model proposed by Fortino et al. [14] was adopted to model the rheological behaviour of wood. In this simulation, a surface-to-surface contact modelling technique was employed to represent the contact interface between the different materials involved by considering a penalty friction and soft contact method in the tangential and normal directions to the interface face, respectively. Moreover, cohesive zones with traction-separations laws were used to model the failure of the epoxy adhesives employed in the interface of some connection and composite beam specimens. The 3D models were validated against seven push-out and eight composite beams specimens monitored for 523 and 540 days, respectively. From the results, it was noticed that the numerically simulated responses were able to capture the trend of the relative slips and mid-span deflections over time with reasonable accuracy overall.

On the other hand, beam-like timber structures in which openings, notches and knots do not play a key role in the governing behaviour can be analysed with sufficient reliability and accuracy employing fiber beam-column elements. Fragiacomo [86] used two parallel fiber beams in conjunction with a longitudinal continuous spring system simulating an smeared connection to perform the long-term analysis of timber-concrete composite (TCC) beams. The well-known uniaxial rheological model proposed by Toratti [66] was employed to include the long-term behavior of wood under sustained load and changing humidity conditions. In this work, a trapezoidal rule was used to solve the integral form equations defining the constitutive law obtained for each incremental step. A similar process was followed to solve the constitutive laws adopted to represent the rheological behavior of the concrete slabs and connection system. In the finite element formulation, cubic and quadratic interpolation functions were used to represent the transverse and axial displacement fields. The model was able to satisfactorily depict the global long-term response of a simple supported timber beam and a TCC beam with dowel shear connectors under controlled environmental conditions through cyclic and step changes in humidity variations, respectively.

The former model proposed by Fragiacomo [86] was employed in the assessment of the long-term deflection of two timber-concrete composite (TCC) beams with corrugated steel bars

and inclined screws as shear connectors, respectively, under outdoor environmental conditions by Fragiacomo and Ceccotti [87]. The simulated results showed a good approximation of the experimental data of the tests recorded during almost five years. The same model was then employed by Fragiacomo [88] to perform a parametric study to determine the most influential rheological mechanisms and environmental conditions on the beam deflection and connection slip of TCC beams. Based on the obtained numerical results, a simplified approach was proposed to evaluate the long-term response of these composite structures. Further validation of the unidimensional model to perform long-term analysis of TCC beams addressing different connection systems and construction techniques was conducted by Fragiacomo et al. [89], Fragiacomo [90], Fragiacomo and Lukaszewska [91], and Fragiacomo and Lukaszewska [92].

Another unidimensional beam element was developed by Khorsandnia et al. [28] to study the long-term behavior of timber-concrete composite (TCC) beams. The beam model is an extension of the model formulated by Khorsandnia et al. [55] to study the nonlinear short-term behavior of TCC beams. The FE formulation is derived using a force-based approach in conjunction with a total secant stiffness approach which then is sequentially coupled to a finite difference analysis that estimates the variation of moisture content over the cross section. In this case, the model allows to consider the nonlinear shear-slip behavior of the shear connectors. The uniaxial rheological model proposed by Toratti [66] was also included in the long-term analysis. The model's ability to capture the variation trend and values of the long-term deflections with satisfactory accuracy under outdoor uncontrolled environmental conditions was verified. The same authors carried out further validations of the model and then used the verified model to calibrate, by means of parametric and sensitivity analyses, the input parameters to adequately describe the long-term response of a TCC beam made of laminated veneer lumber (Khorsandnia et al. [93]). In this study, Toratti [66] rheological model, its modified version (Schänzlin [63]) and the model proposed by Hanhijärvi [69] were considered in the numerical analysis. In contrast, a different finite element formulation was followed by Chiniforush et al. [94] to develop a unidimensional beam element allowing the long-term analysis of steel-timber composite (STC) beams. Similar to former developments, this model allows the simulation of discrete connectors through lumped springs which can incorporate the shear-slip relationships calibrated from long-term push out tests. In this model also the rheological law proposed by Toratti [66] was considered to describe the long-term behavior of the timber slabs.

Finally, it can be mentioned that Ormarsson and Dahlblom [95] proposed a unidimensional beam element in which the inhomogeneous properties of the laminations comprising the timber members can be considered in the long-term analysis. In this work, the variations of stiff-

ness and hygroexpansion properties of each wood lamella constituting the cross section were considered by allowing a piecewise and linear variation of these properties and moisture content distributions over the beam depth. Linear and cubic shape functions were employed to describe the longitudinal and transverse displacement fields. Subsequently, this beam model was employed by Ormarsson and Gíslason [29] to perform the long-term analysis of a statically indeterminate curved frame structure under sustained load and outdoor climate conditions. However, high order interpolation functions were included to describe the displacement fields in this analysis case. The model demonstrated a good ability to depict the long-term deflections and complex stress profile variations over the service life of the structure under real climatic conditions with computational efficiency.

2.4 Short-Term Response and Numerical Modelling of Post-tensioned Timber Structures

The feasibility of applying post-tensioning to timber members was addressed by Bohannan [96] in the early 1960s. Unbonded high-strength strands passing through internal pre-cut holes were located in the tensile zone of the beams and then anchored to the beam ends by means of bearing plates. The results showcased an average increase in load carrying capacity of 31% in comparison to the unreinforced beams along with no significant change in the stiffness. Further studies in sawn timber beams carried out by Lantos [97] and Bond and Sidwell [98] in the mid 1960s, demonstrated the feasibility of using unbonded strands to reduce the permanent deflections. Later on, in the late 1970s, Taylor and Csagoly [99] proposed the retrofitting of a nail-laminated timber bridge deck by means of transverse post-tensioning. According to Oliva and Dimakis [100], this retrofitting created the alternative of building economic bridges by using stress-laminated timber decks to cover short spans. These bridge decks consists of timber laminations placed side by side compressed together by using high-strand steel bars located transversely. As a result of the post-tensioning, the deck behaves as an orthotropic plate as frictional forces resist the vertical shear between the laminates.

As mentioned in chapter 1, since the mid of 2000s there has been a resurgence of interest in longitudinally post-tensioned timber members driven by the introduction of wood-based engineered materials and Pres-Lam technology (Palermo et al. [4]). Experimental campaigns and numerical studies performed by several authors have shown that post-tensioning can be used to achieve longer beam spans. Generally, the design of these members is governed by

deflection limit states due to the low values of the elastic modulus of wood. Longitudinal post-tensioning can effectively enhance the deflection and ultimate load carrying capacity of timber beams by balancing the permanent loads, and even increase the stiffness of these beams. As a result, open-space building plans and medium bridge spans can be designed. Some references corroborating these claims are described bellow.

Experimental campaigns carried out by Deam et al. [101] on a series of innovative solutions for composite timber-concrete beams for the construction of medium- to long-span flooring systems. In the experimental tests, two full scale specimens with straight and draped tendon profiles using stiff and flexible connections, respectively, were studied. It was concluded that the initial precamber induced by the post-tensioning enhanced the serviceability performance with regard to the deflection criteria which is crucial in the design of long-span floors.

The potential of engineered timber in conjunction with longitudinal post-tensioning to design medium span bridges was investigated by Palermo et al. [5]. In this proposal, mono-box and multi-box-girder solutions were deployed to obtain efficient and feasible dimensions in accordance with engineered timber products provided by the manufactures. The extension of post-tensioning techniques employed in precast concrete bridges allowed the possibility of constructing continuous spans by linking longitudinally the single segments with full-length post-tensioning tendons. Additionally, a description of longitudinal and transversal post-tensioning layouts for short-span bridges was also discussed.

Bending tests on post-tensioned timber beams ranging from service loads up to the failure were carried out by McConnell et al. [102] to assess the level of strengthening obtained by using unbonded steel tendons. The results attested to the benefits of post-tensioning in terms of increasing the bending stiffness and flexural strength in comparison with unreinforced timber specimens. Similarly, the same authors (McConnell et al. [103]) also performed bending tests using basalt fibre-reinforced polymer tendons which possess a relatively low elastic modulus. The test results showed similar benefits to those previously reported. However, the use of tendons with stiffer materials was suggested to obtain an overall enhanced performance.

The results obtained by Lago et al. [6], based on experimental tests and parametric design analysis of simply supported and two-span continuous beams, show the enhanced service performance attained by using different unbonded tendon profiles. In the parametric studies, it was noticed that the use of longitudinal post-tensioning enables the reduction of section depth obtained by traditional timber solutions. As a result of the material savings and long-span beams, competitive construction costs and greater architectural benefits can be obtained.

van Beerschoten et al. [7] performed four-point bending tests on four full-scale timber specimens up to failure. In their study, three beam were post-tensioned with straight or draped tendons, whereas one of the specimens was not post-tensioned and was used as benchmark. It was concluded that the applied post-tensioning can enhance the load-carrying capacity of the timber beams to different degrees depending on the tendon layout adopted. Furthermore, the introduction of post-tensioning can influence the failure modes of the beams, specifically, by transitioning from a brittle tension failure to a compression failure mechanisms with ductile behaviour.

Innovative post-tensioning systems have also been proposed over the last two decades to achieve longer spans, enhanced load-carrying capacity and deflection serviceability in timber structures. Al-Hayek and Svecova [104] proposed a solution in which the tendons were attached to external anchor plates with the aim of retrofitting on-site timber beams. Another innovative solution developed by Negrão [105] consists of a mechanical anchorage system relying on nuts allowing the tendons to be re-tightened after s given period of time. A new technology patented by D'Aveni and D'Agata [106] was devised to include continuous concordant tendon paths inside the post-tensioned members. It consisted of milled multi-layered engineered timber that are then glued and assembled to conform a single structural element. Li et al. [107] proposed new types of anchorage systems in conjunction with adjustable devices to control the level of post-tensioning force. Based on the previous control devices, a group led by Li et al. [107] developed a connection device to joint two simple supported beams to form continuous beams with sufficient stiffness. Among these innovative solutions, Otero-Chans et al. [108] proposed a self-tensioning system exerting a force of variable intensity depending on the magnitude of the applied forces. This promising alternative can be employed to build long-span timber flooring systems as stated by Bazli et al. [109].

Among timber beam-like structures, post-tensioned connections have also been proposed to achieve long-span timber frames. In these post-tensioned structures, continuos unbonded tendons are passed trough columns and beams and anchored at the exterior columns. The post-tensioning effects clamp the beam-column timber joints allowing the generation of semi-rigid moments resisting connections. In this way, the load-carrying capacity is enhanced as well as the serviceability limit state deflections as precamber are created after the post-tensioning operation (Buchanan et al. [110]). Experimental tests carried out by Wanninger and Frangi [111] on a post-tensioned beam-column timber joint, and van Beerschoten et al. [112] on one-bay and two-bay post-tensioned timber frames attested to the possibility of obtaining a system with enhanced structural performance. In both tests, different reinforcement strategies were adopted

to improve the connection strength governed by the limited compressive strength provided by the column in its direction perpendicular to the grain.

It is worth noting that the relatively low elastic and shear modulus of wood could induce large deflections in post-tensioned timber beams leading to non negligible geometrical nonlinearities under service and failure conditions. As a result, the assessment of the elongation in unbonded tendons, which is member-dependent rather than section-dependent, must consider the deformed configuration of the beam. In order to address this geometrical nonlinear problem under service loads, a semi-analytical iterative procedure was proposed by Palermo et al. [113] and validated through experimental tests performed on simple supported and two span continuous beams post-tensioned with internal tendons having straight and draped profiles, and external tendons placed outside the beam section. Similarly, van Beerschoten et al. [7] proposed a semi-analytical iterative procedure incorporating second-order effects to evaluate the tendon elongation at the ultimate limit state.

Regarding the numerical modelling of post-tensioned timber beam-like structures, the use of high-fidelity finite element (FE) models is currently a viable option. van Beerschoten et al. [7] developed a three-dimensional (3D) model to study the short-term response of post-tensioned timber beams. In this model, the planks conforming the built-up box section, the deviator blocks and anchorage plates comprising the beam were modeled using solid brick elements. In order to represent the complex behavior of timber, an orthotropic elasto-plasticity constitutive model was adopted. For modelling the unbonded tendons, 3D beam elements were used along with multi-freedom constraints such as Lagrange multipliers and penalty-based methods to simulate the contact interaction between the contact surfaces of tendons and deviators. In this way, the strain incompatibility complexity can be addressed. Other modelling challenges such as second-order effects are also considered in the analysis by incorporating geometrical nonlinearity. Similarly, Quiquero et al. [8] developed a 3D FE model to assess the response of post-tensioned timber beams under ambient and fire conditions. However, it should be mentioned that these models generally tend to be overwhelming and intimidating for design practitioners.

In the case of post-tensioned timber frames, an additional modelling complexity is added to the strain incompatibility and second order effects as the joint connection needs to be considered. An accurate modelling of these connections is crucial to assess the deflections at service conditions and moment distributions at ultimate conditions. Van Beerschoten [114] proposed modelling the joint deformation by means of three separated mechanism: joint panel shear deformation, interface compression deformation and gap opening. The author adopted full frame

models with rotational springs to represent the previous deformation mechanisms. Additionally, simplified procedures were used to estimate the parameters defining the rotational springs which were validated with experimental results performed on post-tensioned timber beam-column joints. On the other hand, Wanninger [115] developed a simplified model to simulate the post-tensioned joint behaviour by adopting the analogy of a rigid foundation resting on a flexible soil. Moreover, a two-dimensional continuum-based FE model was developed in which zones were defined with orthotropic-plasticity behavior along with discrete elements without tension allowed to simulate the embedment and gap opening at the contact zone between the column and beams. The predicted response of the simplified and detailed FE model, and the experimental results were in good agreement. However, the authors claimed that extensive validation is still needed.

2.5 Long-Term Response and Numerical Modelling of Post-tensioned Timber Structures

In the 20th century, timber was employed to a limited extent, mainly in low-rise buildings and short-span bridges, due to concerns regarding its strength, durability, and moisture-dependent and long-term behaviour. As mentioned in the previous section, post-tensioning was considered as an alternative to enhance the load-carrying capacity and deflection serviceability of timber members. However, the assessment of the long-term behavior of post-tensioned timber members in the previous century was scarce. A preliminary long-term test on longitudinal post-tensioned laminated timber specimens during eight years was carried out by Bohannan [116]. The experimental results showed benefits in terms of a modest enhanced deflection and low post-tension force losses, specifically less than 5% after eight years. Nevertheless, in the case of stress-laminated timber bridges with transverse post-tensioning, high force losses were found due to the rheological properties of wood perpendicular to the grain direction and the use of high-strength unbonded post-tensioning bars. An experimental campaign performed by Taylor [117] studied the effects of considering different wood species, stiffness ratio, post-tensioning sequence and levels of relative humidity. Losses not exceeding the 50% of the initial post-tensioning force were observed. Measurements carried out by Oliva and Dimakis [100] evaluated higher force losses of the order of 60% in less than a year due to drying and shrinkage deformations.

From the references described in section 2.3, it can be appreciated that several studies have been carried out on the rheological behaviour of wooden samples made of different sawn timber

species since the 1960s. However, it was not until the late 2000s that attention was turned the long-term behaviour of engineered timber sub-assemblies using post-tensioned connections suitable for the development of mid- and high-rise timber buildings as well as medium-span timber bridges. Concerns arose regarding the long-term behavior of these post-tensioned timber structures as the post-tension force losses could affect considerably the serviceability performance and the self-centering capacity provided by the post-tensioned connections.

Among the first experimental tests carried out to study the long-term behaviour of post-tensioned timber specimens made of engineered timber was the study conducted by Davies and Fragiacomo [118]. In this experimental programme, post-tensioned beams and frame sub-assemblies with unbonded cables running trough the centroidal axis were monitored in controlled and uncontrolled heated indoor conditions. The timber specimens were subjected to sustained loads for approximately one year and the deflections, moisture content, level of post-tensioning force, as well as the environmental temperature and relative humidity were continuously measured. During the test, different post-tensioning sequences were performed to assess their influences on the post-tension force losses. At the end of the test, total force losses of 2.9% and 8.4% were estimated for the beam and frame specimens, respectively. Based on the obtained experimental results, an estimation of the post-tension force losses at the end of a 50-year service life period was performed. From the extrapolated results, force losses in range of 6-10% and 27-39% for the beam and frame specimen, respectively, were expected. It was concluded that the main factor influencing the reduction of post-tensioning forces was the volume of timber loaded perpendicular to the grain. In the case of the frame sub-assemblies, the post-tensioning force was applied parallel to the grain of the beams and perpendicular to the grain of the columns.

The post-tensioning force in post-tensioned beam-column connections could exert high compressions perpendicular to the surface of the columns at service and ultimate conditions. As a result, the column surface can experience considerable long-term deformations and local crushing. In order to avoid these issues, a research team in Switzerland proposed the use of hardwood as local strengthening in the contact region of the column instead of other reinforcement options such as steel plates with self-tapping screws. Wanninger et al. [119] carried out laboratory tests on several post-tensioned joint and beam specimens under controlled and uncontrolled environmental conditions for just over a year. On the basis of the experimental results, it was predicted that the percentage of post-tension force losses in the timber joint was likely to reach a value of 26% at the end of a 50-year service life which is larger than the losses expected in post-tensioned concrete members. It was also observed that the column depth did not play a

key role on the amount of post-tensioning losses.

Laboratory tests performed by Smith et al. [120] on full-scale post-tensioned beam-column joint specimens reflected the effect of post-tensioning force variations on the overall performance of these post-tensioned systems. To this end, several quasi-static cyclic tests were carried out using post-tensioned specimens with or without dissipation devices. In the case of post-tensioned-only layouts, the total moment capacity of the connection was observed to decrease with lower levels of initial post-tensioning forces. Similarly, the moment contribution of the post-tensioning was reduced with decreasing initial post-tensioning values in specimens incorporating dissipation devices. These reductions led to larger and earlier gap openings at the connection interface which resulted in earlier yielding and higher ductility demands in the dissipative devices, and residual drifts in the specimens.

In previous experimental tests, the unbonded post-tensioning cables ran through the centroid of the timber sections. With the aim of studying alternative cable configurations, Granello et al. [121] performed a long-term test on two full-scale simply supported engineered timber beams post-tensioned with eccentric unbonded cable. During the four-year test under uncontrolled environmental conditions, one post-tensioned specimen was subjected to permanent loads whereas the other specimen was just post-tensioned without carrying a load. Relevant data related to the variation of the post-tensioning force, midspan deflections, timber strains, end rotations, environmental temperature and relative humidity were continuously recorded. After processing the results, it was observed that the unloaded and loaded post-tensioned specimen experienced post-tensioning losses of 3.4% and 4.5%, respectively, at the end of the four-year test. Regarding the long-term deflections, it was noticed that the unloaded specimen underwent an increasing camber whereas the loaded specimen experienced a decreasing camber due to the effect of the permanent loads. These results confirmed the reduction of long-term deflections due to post-tensioning. However, the authors called to review the effects of the shear forces on the long-term response of timber beams.

The monitoring of post-tensioned timber structural members during their construction and operative stage is a useful alternative to complement the limited data related to the long-term performance of these post-tensioned solutions. Granello et al. [30] monitored a set of two-story post-tensioned timber frames reinforced with hardwood in the beam-column joints for almost two and a half years. It was observed during the monitoring that the environmental conditions transitioned gradually from outdoor to indoor conditions having an influence on the variation of the post-tensioning forces. From the collected data, it was noticed that the post-tensioned frames experienced an average post-tensioning loss of around 7% with a scatter of $\pm$ 3%.

Two-story post-tensioned timber frames and walls reinforced with steel plates and screws at the beam-column connection interfaces were monitored by Granello and Palermo [122] during three years. An average and maximum post-tensioning loss of the order of 5% and 7%-8%, respectively, were measured. It should be mentioned that environmental conditions inside the monitored buildings reflected the service class I conditions stated in the Eurocode.

A series of shaking table tests on a two-third-scale three-story timber building utilizing post-tensioned beam-column connections was carried out by Di Cesare et al. [123]. The purpose of this experimental programme was to study the feasibility of considering other engineered timber products in Pres-Lam technology along with innovate dissipative steel angles placed in the beam-column and column-foundation interfaces. After being dynamically tested, the building specimen was subjected to a monitoring programme during four years in the laboratory facilities to evaluate the tension losses in the post-tensioning bars. In the first stage of the monitoring, the post-tensioning losses of the building configuration without energy dissipation were recorded during 321 days. In the second stage, the configuration with dissipative steel angles was monitored during 1101 days. From the gathered data, Di Cesare et al. [124] reported post-tensioning losses in the range of 13%-29% in less than one year for the first stage and a reduction of 22%-43% in the post-tensioning force during the second stage. It should be noted that these losses are higher than the previous recorded values in laboratory tests and monitoring programmes performed in operative timber structures.

Long-term experimental tests on two unreinforced post-tensioned timber beam-column joints under uncontrolled environmental conditions, which can be considered as service class II conditions according to the Eurocode, were performed by Li et al. [125]. In these tests, one specimen was just subjected to post-tensioning effects, whereas the other specimen was withstanding the post-tension and gravity loads. After 140 days of testing, the unloaded and loaded specimens experienced a maximum post-tensioning loss of 11.4% and 19.1%, respectively. From the recorded data, it was observed that in the case of the unloaded specimen the environmental deformations in the beam and column strongly affected the post-tensioning force in the joint specimen. Regarding the loaded specimen, it was noticed that the non-uniform stress distribution in the beam-column interface led to an increase of joint rotations over time. As a result, the joint experienced an increase of 7.56 times the elastic rotation and a vertical deflection at the end of the beam of 1.55 times the elastic deflection. It was concluded that local reinforcement is needed to enhance the long-term performance of these post-tension joints as significant long-term deformations are expected.

A set of nine unloaded post-tensioned timber beam-column joint specimens with different

structural details along with two environmental specimens were tested by Zheng et al. [126] to assess the loss of post-tensioning force after 750 days of monitoring. This experimental campaign was a continuation of the tests performed by Li et al. [125], so the same geometric layout and environmental conditions were employed. However, different prestressing ratios and the incorporation of two types of local reinforcement were studied during the experimental test. In the case of the unreinforced specimens, it was observed that an increasing prestressing ratio influenced the variation in the post-tensioning forces by rising the average loss and reducing the average increase. Regarding the post-tensioning losses, average losses in the range of 11.3% to 23.9% were found for the prestressing ratios employed. From the results of these set of unreinforced specimens, it was observed that the time-dependent deformations were dominated by the deformations perpendicular to the grain and the fluctuation of the variations in the post-tensioning forces was strongly linked to the environmental conditions. In the case of the reinforced specimens, reinforcement with self-tapping screws reduced the losses to the 7.8%-13.7% range whereas the reinforcement with steel rods induced higher reductions. Moreover, the reinforced specimens showed lower fluctuations in the variations of the post-tensioning force due to the environmental conditions.

An analytical solution was derived by Fragiacomo and Davies [127] using a well-known moisture-dependent rheological constitutive model. This derivation involved the following simplifications: neglection of the dependency of the Young's modulus on the moisture content, cyclic annual history of the moisture content was assumed, consideration of an average moisture content over the entire section instead of a local variation, disregard of the irrecoverable mechano-sorptive effects, linearization of the nonlinear expression governing the relaxation phenomenon of prestressing tendons and use of the age-adjusted effective modulus method to solve the integral equations defining the time-dependent constitutive relations for timber and steel strands. Although the analytical solution was able to represent the trend of prestress losses obtained in the previous experimental results, some differences were noticed. The model underestimated the prestress losses obtained in the beam specimens whereas it overestimated the losses obtained in the frame specimens. However, the inherent variability in timber material properties and their influence in the scatter of the experimental results made the analytical results acceptable. A further simplification of the analytical solution was made by disregarding the inelastic or environmental deformations, and assuming a null value for the aging coefficient of the prestressing tendons and a unity values for the aging coefficients relate to timber. After rewriting the simplified equation in a non-dimensional form, it was found that the amount of long-term losses is highly influenced by the ratio between the axial stiffness of the the frame

and the steel strands.

The simplified close-form expression proposed by Fragiacomo and Davies [127] to assess the post-tension losses in post-tensioned timber beam and frames was modified by Wanninger et al. [119] by neglecting the relaxation effects related to the prestressing tendon and including the environmental deformations (shrinkage and swelling). Regarding the post-tensioned frame specimens, the modified solution was able to reproduce the recorded data from the tendon force for the different column depths and even the re-stressing case with reasonable accuracy during the first 300 days of the test. After this period, the prediction started to underestimate the tendon forces. In the case of the beam specimen, the losses were slightly overestimated. Subsequently, the modified solution was employed to perform a parametric study to investigate the benefits of using hardwood and steel reinforcements in terms of reduced amount of post-tensioning losses in the joint specimen.

In the case of post-tensioned timber beams with tendon layouts incorporating eccentric and draped profiles, Giorgini et al. [128] proposed a modified version of the analytical solution developed by Fragiacomo and Davies [127] to assess the long-term losses by neglecting the intrinsic relaxation of the prestressing tendons. This modified analytical model was employed by Granello et al. [121] to estimate the post-tensioning losses in two simply supported beams with eccentric tendon profiles under uncontrolled environmental conditions. In terms of the evolution of the post-tensioning forces over time, the predicted results showed good agreement with the observed post-tensioning trends. However, the calculated post-tension losses for a service life period of 50 years were slightly lower (7-8%) than the extrapolated values (11-13%) from the experimental results.

With the aim of applying in the design practice the closed-form expressions developed by Fragiacomo and Davies [127] to predict the post-tensioning loss, Granello et al. [129] performed calibrations on the parameters describing the moisture content variations in the members. Before performing the calibrations, environmental conditions were defined based on the three categories described in the Eurocode standards. After defining these conditions, a series of parametric diffusion analyses were carried out to determine the variation of the yearly moisture accumulation and maximum moisture content attained, for a 50 years period, with respect the wet perimeter of the section. Based on the previous assessed moisture variations and calibrated material parameters found in the literature, a range of values were determined for the aging coefficients by solving numerically the time-dependent stress-strain relationship. From comparisons with the recorded data in operative post-tensioned timber structures, it was observed that the closed-form expressions were able to describe reasonable well the trend of the

post-tension losses despite of not capturing the observed fluctuations. This same methodology was employed by Li et al. [125] to predict the variation of the post-tensioning force over time in post-tensioned beam-column joint specimens. Comparisons with the recorded experimental data demonstrated the accuracy that can be attained with the closed-form solutions along with further calibrated parameters.

A numerical modelling approach to assess the long-term response of post-tensioned timber beams and frames was proposed by Granello et al. [130]. In this numerical approach a moisture diffusion analysis following a single Fickian model was coupled with a fibre-based finite element analysis employing a linear viscoelastic constitutive law. The adoption of a single Fickian model and a linear viscoelastic constitutive law allowed the use of fewer material parameters and reduced the computational effort as the complexity of moisture transfer process was simplified and the Boltzmann's superposition principle could be employed, respectively. The computational efficiency of the model was also enhanced by assuming that moisture content distribution along the length of the member was constant. In this approach the time and moisture dependent strain-stress relationships were numerically integrated by subdividing the time domain into a number of steps along with a section subdivision to solve the moisture diffusion equations through a finite difference scheme and to obtain the section response by means of a fiber-based approach. The timber members were also discretized along their lengths to approximate the axial and transverse displacement field by adopting linear and Hermitian cubic polynomials as the interpolation functions. Regarding the modelling of the post-tensioning tendons, the well-know equivalent loads technique was adopted to take into account the action of different tendon profiles. In this approach, the post-tensioning force was evaluated by imposing displacement compatibility at the anchorages and its value was updated at the end of each time step. Lastly, the relaxation phenomenon related to the steel strands was neglected and its stress-strain relationship was considered linear-elastic.

In order to assess the accuracy of the numerical model proposed by Granello et al. [130], the long-term response of two unloaded and loaded post-tensioned timber beam specimens with eccentric straight tendons tested during four years under uncontrolled environmental conditions were numerically simulated. The numerical results were able of reproducing the post-tensioning loss trend with good accuracy. However, the predicted mid-span deflections differed from the experimental measurements. Similarly, the numerical model was also used to predict the response of post-tensioned timber frames from an operative post-tensioned building monitored for two and a half years by covering the construction, transition and operation stages. Measurements of the real environmental conditions, timber moisture content and force variations in

the tendons were recorded by Granello et al. [30]. A comparison between the numerical results and gathered data showed that the model was able to simulate with sufficient accuracy the trend of average moisture content and post-tensioning forces over time. However, it should be noted that the calibration of the material parameters, used in the constitutive law, had been performed using post-tensioned beam and beam-column sub-assembly specimens instead of conventional block specimens.

The previous numerical model proposed by Granello et al. [130] was also employed by Zheng et al. [126] to predict the long-term response of unreinforced post-tensioned beam-column timber connection specimens with different prestressing ratios tested over 750 days under unloaded conditions. However, the authors employed an equivalent stress to capture the effects of the different stress distribution regions in the beams and columns members due to the application of the post-tensioning forces. The numerical model was able to depict the variation of the moisture content at different locations and the post-tensioning forces with enough accuracy. The model was then used to predict the maximum post-tensioning losses of unreinforced and reinforced joint specimens during a service life period of 50 years. Later on, Zheng et al. [131] performed a numerical study using the same numerical model to assess the post-tensioning losses on unreinforced and reinforced post-tensioned timber joints under different climatic conditions which can be categorized as Service Class 2 conditions according to the Eurocode.

2.6 Concluding Remarks

The following remarks are complied from the extensive literature review presented above:

- section 2.1 pointed out that multi-Fickian models offer a comprehensive description of the transport mechanism of different water phases and their interaction. It was also stressed that a large number of input parameters and details regarding wood morphology and/or composition need to be known in advance to use these complex models. Last but not least, the material properties of wood present an intrinsic variability between different species and even between wood specimens of the same specie. Therefore, as the goal of assessing moisture content variations is aimed at the long-term response of wood members, the present work will adopt the simple global diffusion equation as this approach in conjunction with some well-known rheological models was able to capture the global response of timber members with adequate accuracy, see section 2.3.

- section 2.2 and section 2.3 emphasized that onedimensional (1D) beam-column elements

have the potential to describe well the short- and long-term global response of timber beam-like structures if the effects of knots, notches and holes do not dominate their axial–flexural response. Moreover, validated 1D FE models are computationally efficient and therefore are well suited for parametric and sensitivity studies.

- Regarding the onedimensional (1D) beam-column elements described in section 2.2 and section 2.3, in most cases the kinematic description employed in these elements is based on the Euler–Bernoulli beam theory, hence neglecting shear deformations that are know to be important in timber structures. Despite of having large span/depth ratio, timber beams can experience shear distortions due to the low shear modulus and type of cross section. Therefore, 1D FE elements describing the short- and long-term response should incorporate in their kinematic formulation the Timoshenko beam theory to obtain accurate results under different beam layouts.

- Following section 2.2 and section 2.3, force-based and traditional displacement-based approaches have been employed to study the short- and long-term response of timber beam-like structures. As emphasized in chapter 4, traditional displacement-based formulations only allow a weak satisfaction of equilibrium. This feature demands a fine mesh discretization and hence large time-consuming computations. In order to overcome this drawback, force-based approaches where equilibrium is enforced have been used. However, the convergence of iterative process performed in the element state determination is not always guaranteed. Therefore, opportunity exist for the use of more robust and efficient onedimensional beam elements in the simulation of timber structures.

- Continuum-based FE models have demonstrated high versatility to simulate the short- and long-term response of post-tensioned members with improved accuracy since the strain incompatibility between the tendon and host member, the progressive change in tendon eccentricity with host deformation and complex material behavior can be modeled extensively. These modelling features render continuum-based models a reliable option for simulating the local and global response of post-tensioned timber members. Nevertheless, the benefits of these detailed models comes with high computational costs, complex constitute laws difficult to implement, the requirement of several material parameters to characterize specific wood species and potential convergence issues. As a result of these demands, continuum-based models are less suitable for design-oriented parametric studies of large post-tensioned timber structures. On the basis of this, less computationally

demanding models including strain incompatibility, varying eccentricity and nonlinear material behaviour should be adopted.

- The numerical modelling strategy depicted in section 2.5 consists on a coupled moisture diffusion analysis with a fiber-based finite element analysis to numerically simulate the long-term response of post-tensioned timber members. In this approach, the tendon elongation is assessed by considering displacement compatibility at the anchorages, large displacement effects are not considered, the post-tensioning effects are included through a system of equivalent loads acting on the hosting member and the intrinsic relaxation of the steel strands is neglected. However, there is a lack of generalization to incorporate different tendon layouts and profiles, and to automatically update of the post-tensioning force over each time step. Moreover, as mentioned before, large displacements effects in long-span post-tensioned timber members can be significant under serviceability conditions. Therefore, a more robust and efficient modelling approach is needed to address these particular aspects.

Chapter 3

Transient Moisture Diffusion Analysis

The assessment of moisture diffusion inside timber elements has become a key step to assess the long-term performance of timber structures as the moisture content and moisture gradients directly affect their serviceability and safety. Moisture values are used as input parameters in the constitutive laws defining the hygro-mechanical behaviour of timber elements. In this chapter, a moisture diffusion analysis is conducted by solving a single Fickian diffusion equation defined by a nonlinear partial differential equation of the parabolic type. This equation is solved for solid and hollow rectangular cross sections using the finite difference code OpenMoist developed by Melchor and Málaga [132]. A schematic description of the implementation is shown in Appendix A.

3.1 Governing Differential Equations

As described in chapter 2, different moisture transport models have been proposed over the last decades to assess the distribution of moisture content in timber elements. Single-Fickian and multi-Fickian approaches are among the most popular models to describe the moisture diffusion below the fibre saturation point. As stated by Frandsen et al. [31], the flux of the water phases can be described by means of Fickian type gradient laws of the following form:

$$\boldsymbol{J}_b = -\boldsymbol{D}_b \nabla c_b \tag{3.1}$$

$$\boldsymbol{J}_v = -\boldsymbol{D}_v \nabla c_v \tag{3.2}$$

where $\boldsymbol{J}_b$ and $\boldsymbol{J}_v$ are the flux vectors, $\boldsymbol{D}_b$ and $\boldsymbol{D}_v$ are the diffusion tensors, and c_b and c_v are the mass concentrations of the bound water and water vapor, respectively. Based on a particular

case of the convection-diffusion relations, the following coupled diffusion equations (Frandsen et al. [31]) were used:

$$\frac{\partial c_b}{\partial t} = \nabla \cdot (\boldsymbol{D}_b \nabla c_b) + \dot{s} \tag{3.3}$$

$$\frac{\partial c_v}{\partial t} = \nabla \cdot (\boldsymbol{D}_v \nabla c_v) + \dot{s} \tag{3.4}$$

where $\dot{s}$ represents the sorption rate which enables the change of water phase. Latest developments consider an additional coupled differential equation related to the conservation of energy (Eitelberger et al. [32]) as described in chapter 2. The boundary condition setting the normal flux vector of vapor through the boundary layer driven by the difference in vapor pressure is:

$$\boldsymbol{n} \cdot \boldsymbol{J}_v = k_v \left(p_v^s - p_v^a\right) \tag{3.5}$$

where $\boldsymbol{n}$ is the normal vector, k_v is the surface emission coefficient, and p_v^s and p_v^a are the vapour pressure at the surface and in the ambient air, respectively.

If the moisture transport process of all the water phases can be considered together as one, the whole process can be simplified to a single Fickian diffusion equation (Kollmann and Cote Jr [11]). In this case, the flux is represented by a single Fickian type gradient law:

$$\boldsymbol{J} = -\boldsymbol{D}\,\nabla c \tag{3.6}$$

where $\boldsymbol{J}$ is the moisture flux, $\boldsymbol{D}$ is diffusion tensor and c is the water concentration. Similarly, the diffusion process is expressed by a single equation following Fick's second law (Fick [12]):

$$\frac{\partial c}{\partial t} = \nabla \cdot (\boldsymbol{D}\,\nabla c) \tag{3.7}$$

Eqs. (3.1) to (3.7) are formulated in cylindrical coordinates due the cylindrical orthotropic nature of wood. However, it is mainstream engineering practice to disregard the growth rings of the wood layers in timber elements. Moreover, if the timber elements have a dominant dimension, as in the case of beam–columns elements (along their longitudinal axis), the diffusion equations can be set in a two-dimensional Cartesian coordinate system over the cross section of the element. The resulting diffusion equation describing the time-dependent diffusion problem

is a parabolic partial differential equation:

$$\frac{\partial m}{\partial t} = \frac{\partial}{\partial x}\left(D_x \frac{\partial m}{\partial x}\right) + \frac{\partial}{\partial y}\left(D_y \frac{\partial m}{\partial y}\right) \tag{3.8}$$

where m is the moisture content, and D_x and D_y are the moisture-dependent diffusion coefficients along the x and y axes, respectively. In order to solve Eq. (3.8), a set of initial conditions in time setting the initial moisture content and boundary conditions at the edges of the section are needed. In this case a convective surface, categorized as a third type boundary condition, is considered by means of the following equation:

$$-\left(D_x \frac{\partial m}{\partial x} n_x + D_y \frac{\partial m}{\partial y} n_y\right) = S(m - m_{equil}) \tag{3.9}$$

where S is the moisture-dependent surface emissivity coefficient, n_x and n_y are unit vectors normal to the boundary surface pointing outwards of the section, and m_{equil} is the moisture content in equilibrium with the environmental conditions. Eq. (3.9) represents the flux vector perpendicular to the boundary surface driven by the difference in water concentration between the wood surface and ambient air.

During the last years, multi-Fickian approaches has been increasingly employed in the assessment of moisture content in timber members as described in chapter 2. However, the large number of input parameters required for these complex moisture transfer models along with wood's intrinsic variability make them not suitable for design-oriented parametric studies which is one of the main goals of this thesis. In order to meet this goal and for the sake of simplicity, only the single-Fickian moisture diffusion approach is adopted. Additionally, the moisture transfer analysis of timber elements performed in this research work is restricted to bi-dimensional cases.

3.2 Numerical Methods

The assessment of the moisture content distribution inside one-dimensional timber elements can be described by Eq. (3.8) and Eq. (3.9). Analytical solution methods are limited to very few cases involving simple geometries and specific environmental variations. Therefore, numerical solution methods such as the finite difference and finite element methods are widely used to solve these equations allowing for complex geometries, nonlinearities and a wide variety of environmental variations. A brief description of these methods is presented in this section.

3.2.1 Finite Element Method

Classical variational and weighted-residual methods are the basis of the traditional finite element method. The main idea behind this method is to subdivide the entire domain in subregions referred as finite elements in which approximation functions are used to estimate the desired unknown field in each corresponding subregion. The approximation functions are a linear combination of appropriately selected functions and unknown parameters determined after setting the finite element model, a set of algebraic equations, of the original differential equations. These algebraic equations are the result of using approximated solutions to satisfy the governing differential equations in a weighted-integral sense.

To establish the corresponding finite element equations of each subregion (i.e., element) with regard to Eq. (3.8) and Eq. (3.9), the weak-form Galerkin formulation is employed. The resulting element residual equation [133] in the subregion Ω^e is:

$$\int_{\Omega^e} \left[w \frac{\partial m}{\partial t} + D_x \frac{\partial w}{\partial x} \frac{\partial m}{\partial x} + D_y \frac{\partial w}{\partial y} \frac{\partial m}{\partial y} \right] dx\, dy - \oint_{\partial\Omega^e} J_n\, w\, ds = 0 \tag{3.10}$$

where w is the weight function and J_n is the flux normal to the edge boundaries. In the derivation of the finite element equations, it is assumed that the approximation functions of the unknown field can be represented in separated time-dependant and space-dependant terms [133, 134]:

$$m\,(x, y, t) = \sum_{i=1}^{n_e} m_i^e\,(t)\, N_i^e\,(x, y) \tag{3.11}$$

where m_i^e and N_i^e are the unknown moisture value and shape function (or interpolation function) at node i, and n_e is the total numbers of nodes in the element. Besides, the weight function is assumed to have the same shape functions as the approximated moisture field:

$$w\,(x, y) = \sum_{i=1}^{n_e} \omega_i^e N_i^e\,(x, y) \tag{3.12}$$

where ω_i^e are the unknown weight values at node i. After inserting Eq. (3.9), Eq. (3.11) and Eq. (3.12) into Eq. (3.10), the following equations [133] are obtained:

$$\sum_{j=1}^{n_e} \left(C_{ij}^e \frac{dm_j^e}{dt} + K_{ij}^e\, m_j^e \right) - F_i^e = 0 \tag{3.13}$$

$$C_{ij}^e = \int_{\Omega^e} N_i^e N_j^e\, dx\, dy \tag{3.14}$$

$$K_{ij}^{e} = \int_{\Omega^e} \left(D_x \frac{\partial N_i^e}{\partial x} \frac{\partial N_j^e}{\partial x} + D_y \frac{\partial N_i^e}{\partial x} \frac{\partial N_j^e}{\partial x} \right) dx\, dy + \oint_{\partial\Omega^e} N_i^e S N_j^e\, ds \tag{3.15}$$

$$F_i^e = \oint_{\partial\Omega^e} N_i^e\, S\, m_{equil}\, ds \tag{3.16}$$

And the element residual equation Eq. (3.13) can be rewritten in the following matrix form:

$$\mathbf{C}^e \dot{\mathbf{m}}^e + \mathbf{K}^e \mathbf{m}^e - \mathbf{F}^e = 0 \tag{3.17}$$

where $\mathbf{m}^e$ is the vector collecting the nodal values of the moisture content field. To solve Eq. (3.13) a direct integration can be performed using a finite difference technique. For instance, the generalized trapezoidal algorithm can be applied. Labelling the vector containing the assembled nodal moisture content values at instant t_n and t_{n+1} as $\mathbf{m}_n$ and $\mathbf{m}_{n+1}$, respectively, and Δt as the time step between the previous instants, the following approximation (Reddy and Gartling [133],Bergheau and Fortunier [134]) can be adopted to estimate the rate of change of the moisture field:

$$\mathbf{m}_{n+1} = \mathbf{m}_n + \Delta t \left[(1-\alpha)\, \dot{\mathbf{m}}_n + \alpha \dot{\mathbf{m}}_{n+1} \right] \tag{3.18}$$

If Eq. (3.18) is replaced in the assembled version of Eq. (3.17) and a linearization of the resulting equations is performed, the following incremental system of equations (Bergheau and Fortunier [134]) is obtained:

$$\hat{\mathbf{K}}\, \Delta\mathbf{m} = \hat{\mathbf{F}} \tag{3.19}$$

In order to solve Eq. (3.19), an iterative process has to be performed. Moreover, in the case of strong nonlinearities, nonlinear solver algorithms should be used. Some of these algorithms are described in chapter 5.

3.2.2 Finite Difference Method

Contrarily to the finite element method in which the approximate solution is continuous in the domain, the finite difference method approximates the unknown field only at discrete (nodal) points. In this method, the discretization equations are obtained by replacing the derivates of the unknown field in the governing differential equations by finite difference approximations. The resulting set of algebraic equations is then solved to obtain a discrete solution of the

unknown field.

For this, a control volume approach is adopted (Patankar [135]). In this approach, Eq. (3.8) is integrated over a time interval $[t, t+\Delta t]$ and a non-overlapping control volume surrounding a particular grid point (i, j). In the case of an interior node whose control volume is shown in Fig. 3.1, the following integration (Patankar [135]) is carried out:

$$\int_{i-\frac{1}{2}}^{i+\frac{1}{2}}\int_{j-\frac{1}{2}}^{j+\frac{1}{2}}\int_{t}^{t+\Delta t}\frac{\partial m}{\partial t}\,dx\,dy\,dt = \int_{i-\frac{1}{2}}^{i+\frac{1}{2}}\int_{j-\frac{1}{2}}^{j+\frac{1}{2}}\int_{t}^{t+\Delta t}\frac{\partial}{\partial x}\left(D_x\,\frac{\partial m}{\partial x}\right)\,dx\,dy\,dt + \int_{i-\frac{1}{2}}^{i+\frac{1}{2}}\int_{j-\frac{1}{2}}^{j+\frac{1}{2}}\int_{t}^{t+\Delta t}\frac{\partial}{\partial x}\left(D_x\,\frac{\partial m}{\partial x}\right)\,dx\,dy\,dt \quad (3.20)$$

In the resulting equations, the derivative terms regarding the spatial variations and the homogeneous moisture-dependent coefficients are replaced with piece-wise linear and constant approximations, respectively. An approximation for the variation of the moisture content field over the time interval of analysis is still required. Usually, a weighted approximation (Patankar [135]) is adopted for this purpose as follows:

$$m_{i,j} = \left[f\,m_{i,j}^{t+\Delta t} + (1-f)\,m_{i,j}^{t}\right] \quad (3.21)$$

where f is the time approximation weighting factor. This factor defines a unique finite difference scheme ranging from explicit ($f = 0$) to fully implicit schemes ($f = 1$). Replacing Eq. (3.21) into the expressions for the derivatives associated with the spatial variations of the equations resulting from integrating Eq. (3.20) leads to the following expressions (Majumdar [136]):

$$D_x\frac{\partial m}{\partial x}\Big|_{i+\frac{1}{2},j} = f\frac{D_{x_{i+\frac{1}{2},j}}(m_{i+1,j}^{t+\Delta t} - m_{i,j}^{t+\Delta t})}{\Delta x_{i+\frac{1}{2}}} + (1-f)\frac{D_{x_{i+\frac{1}{2},j}}(m_{i+1,j}^{t} - m_{i,j}^{t})}{\Delta x_{i+\frac{1}{2}}} \quad (3.22)$$

$$D_x\frac{\partial m}{\partial x}\Big|_{i-\frac{1}{2},j} = f\frac{D_{x_{i-\frac{1}{2},j}}(m_{i,j}^{t+\Delta t} - m_{i-1,j}^{t+\Delta t})}{\Delta x_{i+\frac{1}{2}}} + (1-f)\frac{D_{x_{i-\frac{1}{2},j}}(m_{i,j}^{t} - m_{i-1,j}^{t})}{\Delta x_{i+\frac{1}{2}}} \quad (3.23)$$

$$D_y\frac{\partial m}{\partial y}\Big|_{i,j+\frac{1}{2}} = f\frac{D_{y_{i,j+\frac{1}{2}}}(m_{i,j+1}^{t+\Delta t} - m_{i,j}^{t+\Delta t})}{\Delta y_{j+\frac{1}{2}}} + (1-f)\frac{D_{y_{i,j+\frac{1}{2}}}(m_{i,j+1}^{t} - m_{i,j}^{t})}{\Delta y_{j+\frac{1}{2}}} \quad (3.24)$$

$$D_y\frac{\partial m}{\partial y}\Big|_{i,j-\frac{1}{2}} = f\frac{D_{y_{i,j-\frac{1}{2}}}(m_{i,j}^{t+\Delta t} - m_{i,j-1}^{t+\Delta t})}{\Delta y_{j+\frac{1}{2}}} + (1-f)\frac{D_{y_{i,j-\frac{1}{2}}}(m_{i,j}^{t} - m_{i,j-1}^{t})}{\Delta y_{j+\frac{1}{2}}} \quad (3.25)$$

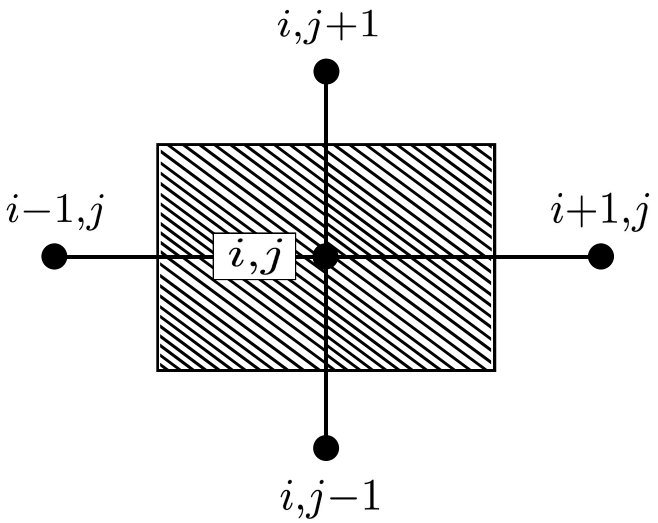


Figure 3.1: Control volume of an interior node.

where $\Delta x_{i+\frac{1}{2}}$ and $\Delta y_{j+\frac{1}{2}}$ are the discretizations along the x and y axes, respectively. To obtain the discretization equation or finite difference equation for the interior grid point (i, j), a finite difference approximation of the first-order time derivative of Eq. (3.8) is needed. A forward difference approximation is adopted here. Considering an explicit finite difference scheme, the discretization equation for an interior node (i, j) can be expressed in closed-form (Majumdar [136]) as:

$$m_{i,j}^{t+\Delta t} = c_{i+1,j}^{t} m_{i+1,j}^{t} + c_{i-1,j}^{t} m_{i-1,j}^{t} + c_{i,j+1}^{t} m_{i,j+1}^{t} + c_{i,j-1}^{t} m_{i,j-1}^{t} + c_{i,j}^{t} m_{i,j}^{t} \tag{3.26}$$

$$c_{i+1,j}^{t} = \frac{\Delta t \, D_{x_{i+\frac{1}{2},j}}^{t}}{\Delta x_{i+\frac{1}{2}}^{2}} \tag{3.27}$$

$$c_{i-1,j}^{t} = \frac{\Delta t \, D_{x_{i-\frac{1}{2},j}}^{t}}{\Delta x_{i+\frac{1}{2}}^{2}} \tag{3.28}$$

$$c_{i,j+1}^{t} = \frac{\Delta t \, D_{y_{i,j+\frac{1}{2}}}^{t}}{\Delta y_{j+\frac{1}{2}}^{2}} \tag{3.29}$$

$$c_{i,j-1}^{t} = \frac{\Delta t \, D_{y_{i,j-\frac{1}{2}}}^{t}}{\Delta y_{j+\frac{1}{2}}^{2}} \tag{3.30}$$

$$c_{i,j}^{t} = 1 - c_{i+1,j}^{t} - c_{i-1,j}^{t} - c_{i,j+1}^{t} - c_{i,j-1}^{t} \tag{3.31}$$

Similarly, the discretization equation for an interior node (i, j) adopting a fully implicit

finite difference scheme [136] can be expressed as:

$$m_{i,j}^{t} = c_{i+1,j}^{t+\Delta t} m_{i+1,j}^{t+\Delta t} + c_{i-1,j}^{t+\Delta t} m_{i-1,j}^{t+\Delta t} + c_{i,j+1}^{t+\Delta t} m_{i,j+1}^{t+\Delta t} + c_{i,j-1}^{t+\Delta t} m_{i,j-1}^{t+\Delta t} + c_{i,j}^{t+\Delta t} m_{i,j}^{t+\Delta t} \tag{3.32}$$

$$c_{i+1,j}^{t+\Delta t} = -\frac{\Delta t \, D_{x_{i+\frac{1}{2},j}}^{t+\Delta t}}{\Delta x_{i+\frac{1}{2}}^{2}} \tag{3.33}$$

$$c_{i-1,j}^{t+\Delta t} = -\frac{\Delta t \, D_{x_{i-\frac{1}{2},j}}^{t+\Delta t}}{\Delta x_{i+\frac{1}{2}}^{2}} \tag{3.34}$$

$$c_{i,j+1}^{t+\Delta t} = -\frac{\Delta t \, D_{y_{i,j+\frac{1}{2}}}^{t+\Delta t}}{\Delta y_{j+\frac{1}{2}}^{2}} \tag{3.35}$$

$$c_{i,j-1}^{t+\Delta t} = -\frac{\Delta t \, D_{y_{i,j-\frac{1}{2}}}^{t+\Delta t}}{\Delta y_{j+\frac{1}{2}}^{2}} \tag{3.36}$$

$$c_{i,j}^{t+\Delta t} = 1 - c_{i+1,j}^{t+\Delta t} - c_{i-1,j}^{t+\Delta t} - c_{i,j+1}^{t+\Delta t} - c_{i,j-1}^{t+\Delta t} \tag{3.37}$$

A set of similar discretization equations have to be developed for the nodes at the boundary surfaces. All the discretization equations form a system of algebraic equations. If an explicit scheme is used, this system of equations can be expressed as:

$$\mathbf{m}^{t+\Delta t} = \mathbf{A}^{t} \, \mathbf{m}^{t} + \mathbf{b}^{t} \tag{3.38}$$

Eq. (3.38) is solved directly to obtain the solution in the next time step. In case of an implicit scheme, the system of equations is:

$$\mathbf{m}_{k}^{t+\Delta t} = \mathbf{A}_{k-1}^{t+\Delta t} \, \mathbf{m}_{k-1}^{t+\Delta t} + \mathbf{b}_{k-1}^{t+\Delta t} \tag{3.39}$$

Eq. (3.39) requires an iterative procedure. In the next section the remaining finite difference equations for a solid and hollow rectangular section are presented.

3.3 Finite Difference Equations

As it was mentioned in the previous section, a set of algebraic equations involving the boundary surfaces are needed to establish the complete set of finite difference equations required to solve the moisture diffusion problem. To obtain the finite difference equation of a boundary node (i, j) an integration similar to Eq. (3.20) is performed over Eq. (3.8) with the limits of integration corresponding to the control volume surrounding the grid node. In the resulting equations, the derivatives terms and moisture-diffusion coefficients are approximated in the same way as in case of an interior node. However, the boundary equation (Eq. (3.9)) is also used in the development of the final discretization equations.

The discretization equation of the boundary nodes using an explicit scheme can be set in a general form as:

$$m_{i,j}^{t+\Delta t} = c_{i+1,j}^{t} m_{i+1,j}^{t} + c_{i-1,j}^{t} m_{i-1,j}^{t} + c_{i,j+1}^{t} m_{i,j+1}^{t} + c_{i,j-1}^{t} m_{i,j-1}^{t} + c_{i,j}^{t} m_{i,j}^{t} + p_{i,j}^{t} m_{equil}^{t} + q_{i,j}^{t} m_{equil}^{t} \quad (3.40)$$

$$c_{i+1,j}^{t} = \frac{a_{i+1,j}^{es}\, \Delta t\, D_{x_{i+\frac{1}{2},j}}^{t}}{\Delta x_{i+\frac{1}{2}}^{2}} \quad (3.41)$$

$$c_{i-1,j}^{t} = \frac{a_{i-1,j}^{es}\, \Delta t\, D_{x_{i-\frac{1}{2},j}}^{t}}{\Delta x_{i+\frac{1}{2}}^{2}} \quad (3.42)$$

$$c_{i,j+1}^{t} = \frac{a_{i,j+1}^{es}\, \Delta t\, D_{y_{i,j+\frac{1}{2}}}^{t}}{\Delta y_{j+\frac{1}{2}}^{2}} \quad (3.43)$$

$$c_{i,j-1}^{t} = \frac{a_{i,j-1}^{es}\, \Delta t\, D_{y_{i,j-\frac{1}{2}}}^{t}}{\Delta y_{j+\frac{1}{2}}^{2}} \quad (3.44)$$

$$p_{i,j}^{t} = \frac{r_{i,j}^{es}\, \Delta t\, S_{i,j}^{t}}{\Delta x_{i+\frac{1}{2}}} \quad (3.45)$$

$$q_{i,j}^{t} = \frac{s_{i,j}^{es}\, \Delta t\, S_{i,j}^{t}}{\Delta y_{j+\frac{1}{2}}} \quad (3.46)$$

$$c_{i,j}^{t} = 1 - c_{i+1,j}^{t} - c_{i-1,j}^{t} - c_{i,j+1}^{t} - c_{i,j-1}^{t} - p_{i,j}^{t} - q_{i,j}^{t} \quad (3.47)$$

where $a^{es}_{i+1,j}$, $a^{es}_{i-1,j}$, $a^{es}_{i,j+1}$, $a^{es}_{i,j-1}$, $r^{es}_{i,j}$ and $s^{es}_{i,j}$ are coefficients whose values depend on the position of the nodal point (i, j) along the boundary surface for an explicit scheme. The values of these coefficients for solid and hollow rectangular sections are presented in the next section. Similarly, the discretization equation of boundary nodes for an implicit scheme can be expressed in a closed form as:

$$m^{t}_{i,j} = c^{t+\Delta t}_{i+1,j} m^{t+\Delta t}_{i+1,j} + c^{t+\Delta t}_{i-1,j} m^{t+\Delta t}_{i-1,j} + c^{t+\Delta t}_{i,j+1} m^{t+\Delta t}_{i,j+1} + c^{t+\Delta t}_{i,j-1} m^{t+\Delta t}_{i,j-1} + c^{t+\Delta t}_{i,j} m^{t+\Delta t}_{i,j} + p^{t+\Delta t}_{i,j} m^{t+\Delta t}_{equil} + q^{t+\Delta t}_{i,j} m^{t+\Delta t}_{equil} \quad (3.48)$$

$$c^{t+\Delta t}_{i+1,j} = -\frac{a^{is}_{i+1,j}\, \Delta t\, D^{t+\Delta t}_{x_{i+\frac{1}{2},j}}}{\Delta x^{2}_{i+\frac{1}{2}}} \quad (3.49)$$

$$c^{t+\Delta t}_{i-1,j} = -\frac{a^{is}_{i-1,j}\, \Delta t\, D^{t+\Delta t}_{x_{i-\frac{1}{2},j}}}{\Delta x^{2}_{i+\frac{1}{2}}} \quad (3.50)$$

$$c^{t+\Delta t}_{i,j+1} = -\frac{a^{is}_{i,j+1}\, \Delta t\, D^{t+\Delta t}_{y_{i,j+\frac{1}{2}}}}{\Delta y^{2}_{j+\frac{1}{2}}} \quad (3.51)$$

$$c^{t+\Delta t}_{i,j-1} = -\frac{a^{is}_{i,j-1}\, \Delta t\, D^{t+\Delta t}_{y_{i,j-\frac{1}{2}}}}{\Delta y^{2}_{j+\frac{1}{2}}} \quad (3.52)$$

$$p^{t+\Delta t}_{i,j} = -\frac{r^{is}_{i,j}\, \Delta t\, S^{t+\Delta t}_{i,j}}{\Delta x_{i+\frac{1}{2}}} \quad (3.53)$$

$$q^{t+\Delta t}_{i,j} = -\frac{s^{is}_{i,j}\, \Delta t\, S^{t+\Delta t}_{i,j}}{\Delta y_{j+\frac{1}{2}}} \quad (3.54)$$

$$c^{t+\Delta t}_{i,j} = 1 - c^{t+\Delta t}_{i+1,j} - c^{t+\Delta t}_{i-1,j} - c^{t+\Delta t}_{i,j+1} - c^{t+\Delta t}_{i,j-1} - p^{t+\Delta t}_{i,j} - q^{t+\Delta t}_{i,j} \quad (3.55)$$

where $a^{is}_{i+1,j}$, $a^{is}_{i-1,j}$, $a^{is}_{i,j+1}$, $a^{is}_{i,j-1}$, $r^{is}_{i,j}$ and $s^{is}_{i,j}$ are coefficients related the nodal boundary point (i, j) for an implicit scheme. The value of these coefficients rely on the grid location of the nodal point. The values of these coefficients regarding solid and hollow rectangular sections are presented in the next section.

3.3.1 Solid Rectangular Section

In the case of a solid rectangular section, the boundary surface consist of four edges and four corners. Fig. 3.2 and Fig. 3.3 depict the edges and corners of the section and the corresponding control volumes for each boundary node, respectively.

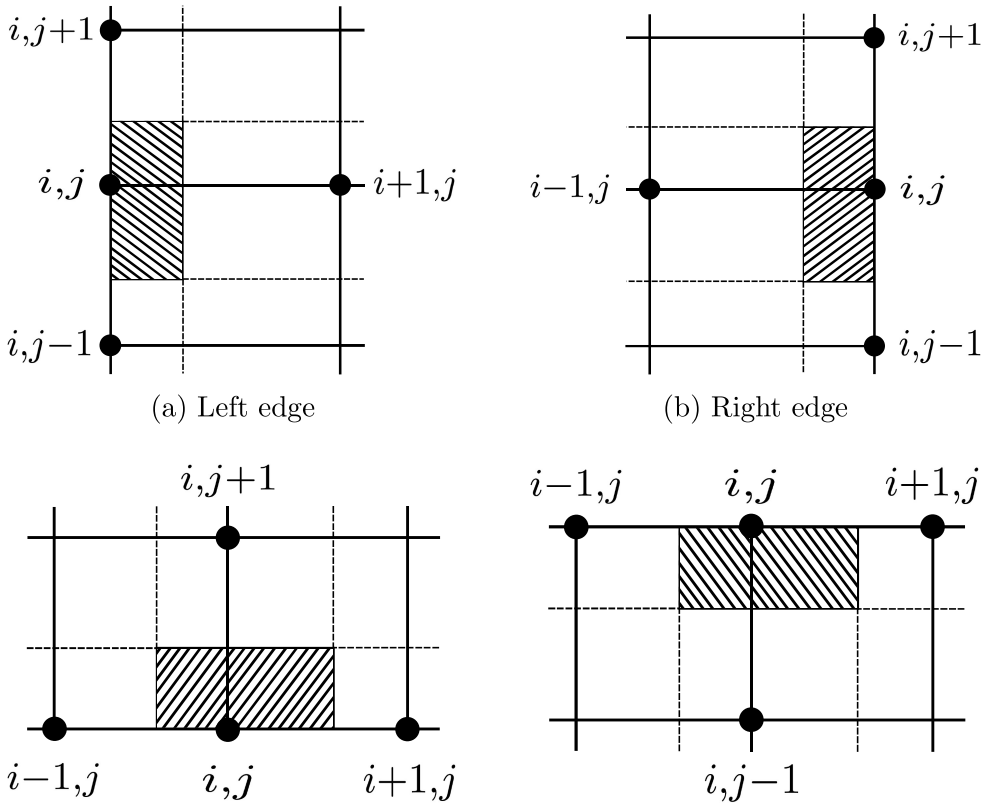
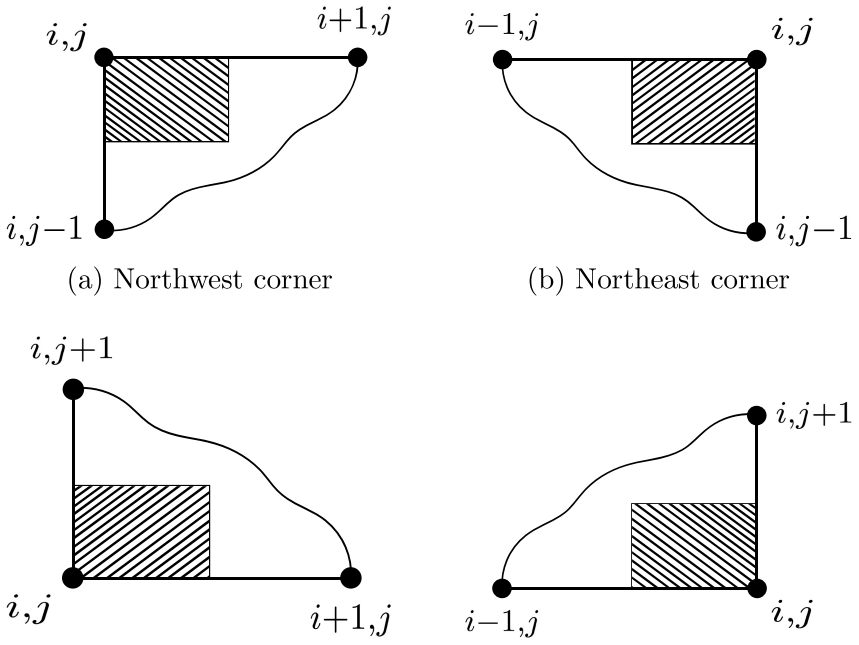


Figure 3.2: Boundary nodes in the edges of a solid rectangular section.

The values of the coefficients employed in Eqs. (3.41) to (3.46) for an explicit scheme and Eqs. (3.49) to (3.54) for an implicit scheme are summarized in Table 3.1 and Table 3.2, respectively.

Boundary surface position	$a^{es}_{i+1,j}$	$a^{es}_{i-1,j}$	$a^{es}_{i,j+1}$	$a^{es}_{i,j-1}$	$r^{es}_{i,j}$	$s^{es}_{i,j}$
Right-Hand Edge	0	2	1	1	2	0
Left-Hand Edge	2	0	1	1	2	0
Top Edge	1	1	0	2	0	2
Bottom Edge	1	1	2	0	0	2
Northeast Corner	0	2	0	2	2	2
Southeast Corner	0	2	2	0	2	2
Northwest Corner	2	0	0	2	2	2
Southwest Corner	2	0	2	0	2	2

Table 3.1: Coefficients for a solid rectangular section using an explicit scheme.



(a) Northwest corner (b) Northeast corner

(c) Southwest corner (d) Southeast corner

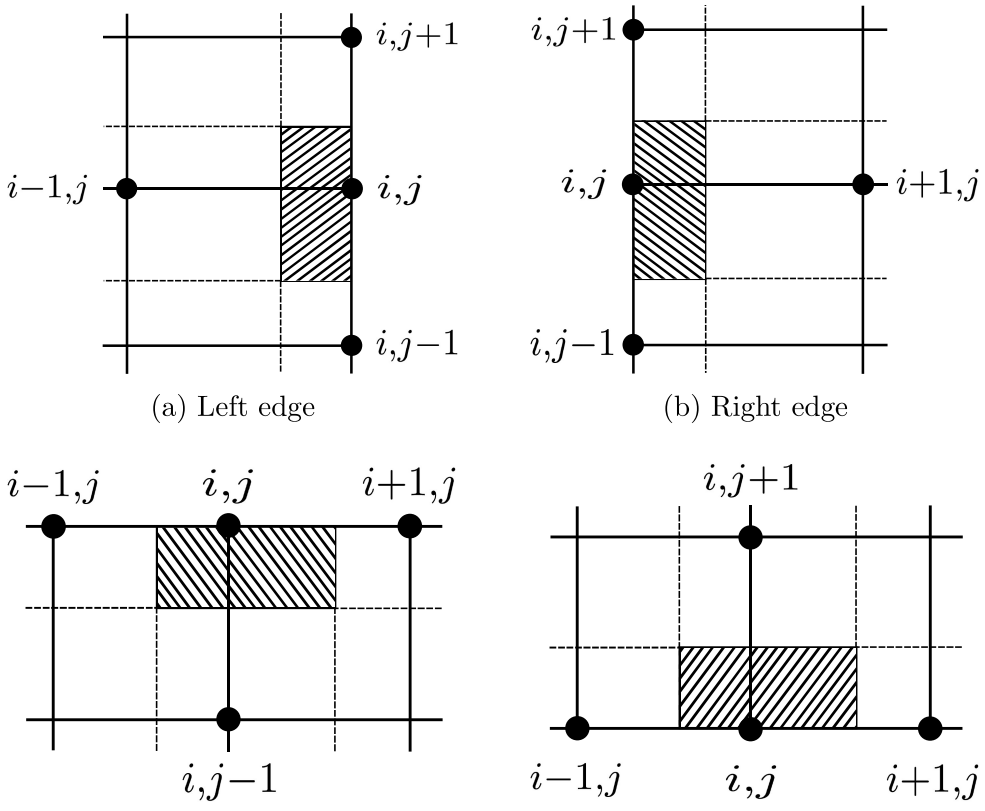
Figure 3.3: Boundary nodes in the corners of a solid rectangular section.

Boundary surface position	$a^{is}_{i+1,j}$	$a^{is}_{i-1,j}$	$a^{is}_{i,j+1}$	$a^{is}_{i,j-1}$	$r^{is}_{i,j}$	$s^{is}_{i,j}$
Right-Hand Edge	0	2	1	1	2	0
Left-Hand Edge	2	0	1	1	2	0
Top Edge	1	1	0	2	0	2
Bottom Edge	1	1	2	0	0	2
Northeast Corner	0	2	0	2	2	2
Southeast Corner	0	2	2	0	2	2
Northwest Corner	2	0	0	2	2	2
Southwest Corner	2	0	2	0	2	2

Table 3.2: Coefficients for a solid rectangular section using an implicit scheme.

3.3.2 Hollow Rectangular Section

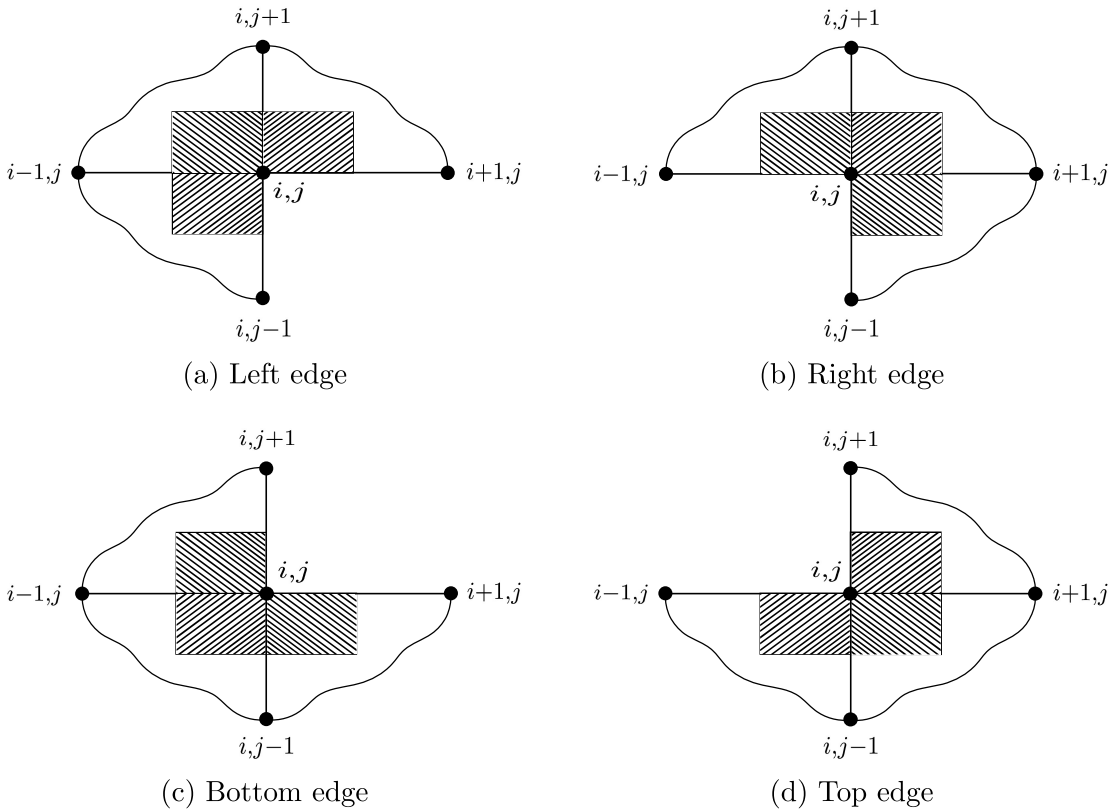
The distinct feature of a hollow rectangular section is the presence of two separate boundary surfaces which could be referred to as exterior and interior surfaces. Both surfaces are comprised of four edges and four corners. The exterior surface is identical to the boundary surface of a solid rectangular section and Fig. 3.2 and Fig. 3.3 depict the corresponding control volumes for each boundary node in this surface. However, in the case of the internal boundary the control volumes surrounding the corner nodes are different whereas the control volumes of the edge nodes are similar to the external boundary but with different locations. The locations of the internal edge and corner nodes and their corresponding control volumes are shown in Fig. 3.4 and Fig. 3.5, respectively.



(a) Left edge (b) Right edge

(c) Bottom edge (d) Top edge

Figure 3.4: Boundary nodes in the internal edges of a hollow rectangular section.



(a) Left edge (b) Right edge

(c) Bottom edge (d) Top edge

Figure 3.5: Boundary nodes in the internal corners of a hollow rectangular section.

Table 3.3 and Table 3.4 show the coefficient for Eqs. (3.41) to (3.46) and Eqs. (3.49) to (3.54) for an explicit and implicit scheme, respectively.

Boundary surface position	$a^{es}_{i+1,j}$	$a^{es}_{i-1,j}$	$a^{es}_{i,j+1}$	$a^{es}_{i,j-1}$	$r^{es}_{i,j}$	$s^{es}_{i,j}$
Exterior Right-Hand Edge	0	2	1	1	2	0
Exterior Left-Hand Edge	2	0	1	1	2	0
Exterior Top Edge	1	1	0	2	0	2
Exterior Bottom Edge	1	1	2	0	0	2
Exterior Northeast Corner	0	2	0	2	2	2
Exterior Southeast Corner	0	2	2	0	2	2
Exterior Northwest Corner	2	0	0	2	2	2
Exterior Southwest Corner	2	0	2	0	2	2
Interior Right-Hand Edge	2	0	1	1	2	0
Interior Left-Hand Edge	0	2	1	1	2	0
Interior Top Edge	0	1	2	0	0	2
Interior Bottom Edge	1	1	0	2	0	2
Interior Northeast Corner	$\frac{4}{3}$	$\frac{2}{3}$	$\frac{4}{3}$	$\frac{2}{3}$	$\frac{2}{3}$	$\frac{2}{3}$
Interior Southeast Corner	$\frac{4}{3}$	$\frac{2}{3}$	$\frac{2}{3}$	$\frac{4}{3}$	$\frac{2}{3}$	$\frac{2}{3}$
Interior Northwest Corner	$\frac{2}{3}$	$\frac{4}{3}$	$\frac{4}{3}$	$\frac{2}{3}$	$\frac{2}{3}$	$\frac{2}{3}$
Interior Southwest Corner	$\frac{2}{3}$	$\frac{4}{3}$	$\frac{2}{3}$	$\frac{4}{3}$	$\frac{2}{3}$	$\frac{2}{3}$

Table 3.3: Coefficients for a hollow rectangular section using an explicit scheme.

Boundary surface position	$a^{is}_{i+1,j}$	$a^{is}_{i-1,j}$	$a^{is}_{i,j+1}$	$a^{is}_{i,j-1}$	$r^{is}_{i,j}$	$s^{is}_{i,j}$
Exterior Right-Hand Edge	0	2	1	1	2	0
Exterior Left-Hand Edge	2	0	1	1	2	0
Exterior Top Edge	1	1	0	2	0	2
Exterior Bottom Edge	1	1	2	0	0	2
Exterior Northeast Corner	0	2	0	2	2	2
Exterior Southeast Corner	0	2	2	0	2	2
Exterior Northwest Corner	2	0	0	2	2	2
Exterior Southwest Corner	2	0	2	0	2	2
Interior Right-Hand Edge	2	0	1	1	2	0
Interior Left-Hand Edge	0	2	1	1	2	0
Interior Top Edge	0	1	2	0	0	2
Interior Bottom Edge	1	1	0	2	0	2
Interior Northeast Corner	$\frac{4}{3}$	$\frac{2}{3}$	$\frac{4}{3}$	$\frac{2}{3}$	$\frac{2}{3}$	$\frac{2}{3}$
Interior Southeast Corner	$\frac{4}{3}$	$\frac{2}{3}$	$\frac{2}{3}$	$\frac{4}{3}$	$\frac{2}{3}$	$\frac{2}{3}$
Interior Northwest Corner	$\frac{2}{3}$	$\frac{4}{3}$	$\frac{4}{3}$	$\frac{2}{3}$	$\frac{2}{3}$	$\frac{2}{3}$
Interior Southwest Corner	$\frac{2}{3}$	$\frac{4}{3}$	$\frac{2}{3}$	$\frac{4}{3}$	$\frac{2}{3}$	$\frac{2}{3}$

Table 3.4: Coefficients for a hollow rectangular section using an implicit scheme.

3.4 Verification Examples

This section shows the moisture diffusion analysis of five illustrative cases. These analyses were performed using the finite difference code OpenMoist (Melchor and Málaga [132]) implemented in Python and MATLAB as well. The first four case studies describes the moisture diffusion analysis of two section geometries widely used in current design practice. The results of these analyses were compared to the results obtained using the commercial finite element software ABAQUS [137] to further validate the capabilities of the developed finite difference code. ABAQUS solves the nonlinear finite element equations described in subsection 3.2.1. The last analysis case describes the moisture diffusion analysis of a cross-laminated timber (CLT) panel under a sudden change of moisture in the environment.

3.4.1 Solid Square Section under Constant Conditions

A numerical diffusion analysis was carried out by Fragiacomo [86], Schänzlin [63] and Khorsandnia et al. [28] to assess the moisture content distribution in a timber beam of square cross section under cyclic environmental conditions. The diffusion process was considered isotropic. Here the same section is analysed but under a sudden change of humidity remaining constant thereafter. The case with cyclic environmental conditions is presented in the next section. The section geometry and properties of the wood section are summarized in Table 3.5. The surface emissivity coefficients are constant along the perimeter whereas the diffusion coefficient varies exponentially with the moisture content according to the model proposed by Toratti [66].

Type of input data	Parameter	Value
Geometry	Height (cm)	8.9
	Width (cm)	8.9
Surface emissivity coefficient	Right-Hand Side Boundary (cm/day)	1.1232
	Left-Hand Side Boundary (cm/day)	1.1232
	Top Boundary (cm/day)	1.1232
	Bottom Boundary (cm/day)	1.1232
Diffusion coefficient	Parameter multiplying the base (cm^2/day)	0.10368
	Parameter multiplying the exponent	2.28

Table 3.5: Geometry and material property data adopted for the solid square section.

In the finite difference analysis, a implicit scheme was chosen together with 1 hour time steps. Also, a spaced grid of 24x24 as shown in Fig. 3.6 was adopted. An initial uniformly distributed moisture content of 0.108 corresponding to a relative humidity level of 40% was considered in the analysis.

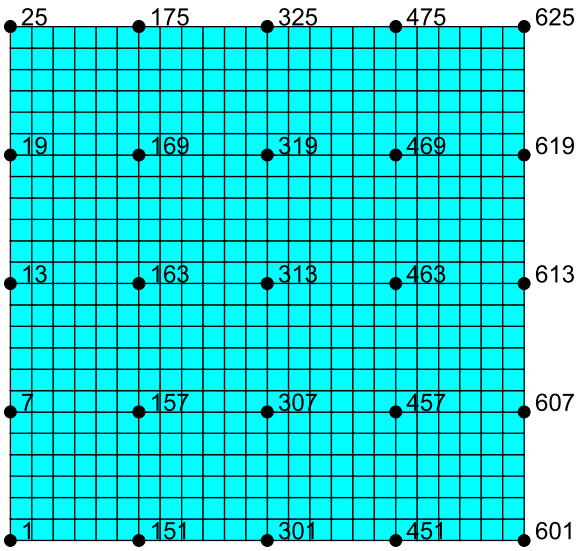


Figure 3.6: Grid generated for the solid square section.

The imposed new relative humidity in the wood section is 90%. The corresponding equilibrium moisture content was assessed based on the sorption isotherm proposed by Toratti [66] comprising the average of the absorption and desorption curves, i.e., the sorption hysteresis of wood was not considered. The results of the analysis are depicted in Fig. 3.7. The results are compared with the ones obtained by the software ABAQUS. The average moisture content in the section and the localized moisture in nodes 13 (Exterior node), 163 (Mid node) and 313 (centre node) are plotted in Fig. 3.7. From the comparison, it can be concluded that the results are almost identical.

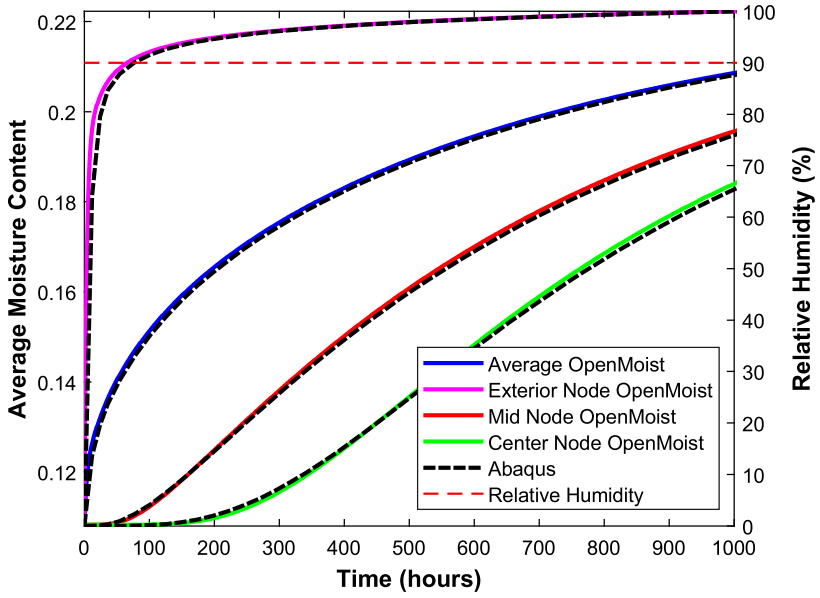
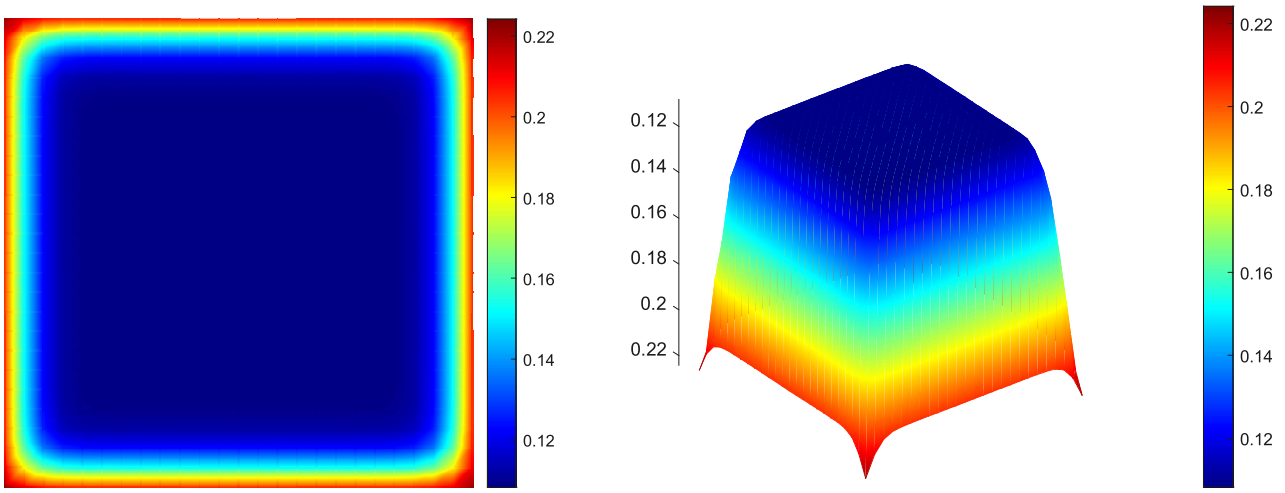


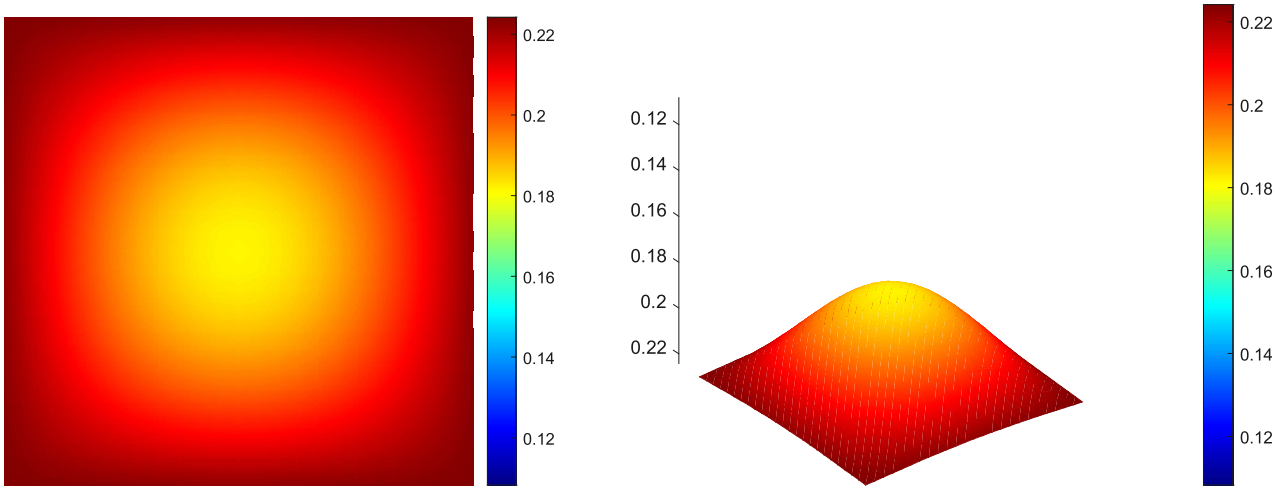
Figure 3.7: Moisture content variation in the solid square section under constant environmental conditions.

In order to have a better overview of the changing moisture distribution over the section, Fig. 3.8 and Fig. 3.9 are generated. From Fig. 3.8, it can be noticed that after 1 day of exposure the section experiences a sharp change of the moisture content just along its perimeter. However, after 40 days the moisture content has increased over the whole section but at a slower rate at the centre of the section.



(a) Contour (b) Surface

Figure 3.8: Moisture content distribution in the solid square section after 1 day of exposure under constant environmental conditions.



(a) Contour (b) Surface

Figure 3.9: Moisture content distribution in the solid square section after 40 days of exposure under constant environmental conditions.

3.4.2 Solid Square Section under Changing Conditions

The numerical analysis performed by Fragiacomo [86], Schänzlin [63] and Khorsandnia et al. [28] considered a cyclic variation of the moisture content. The changing environmental conditions consisted of weekly cycles of square waves with amplitudes ranging between 40% and 90% as shown in Fig. 3.10.

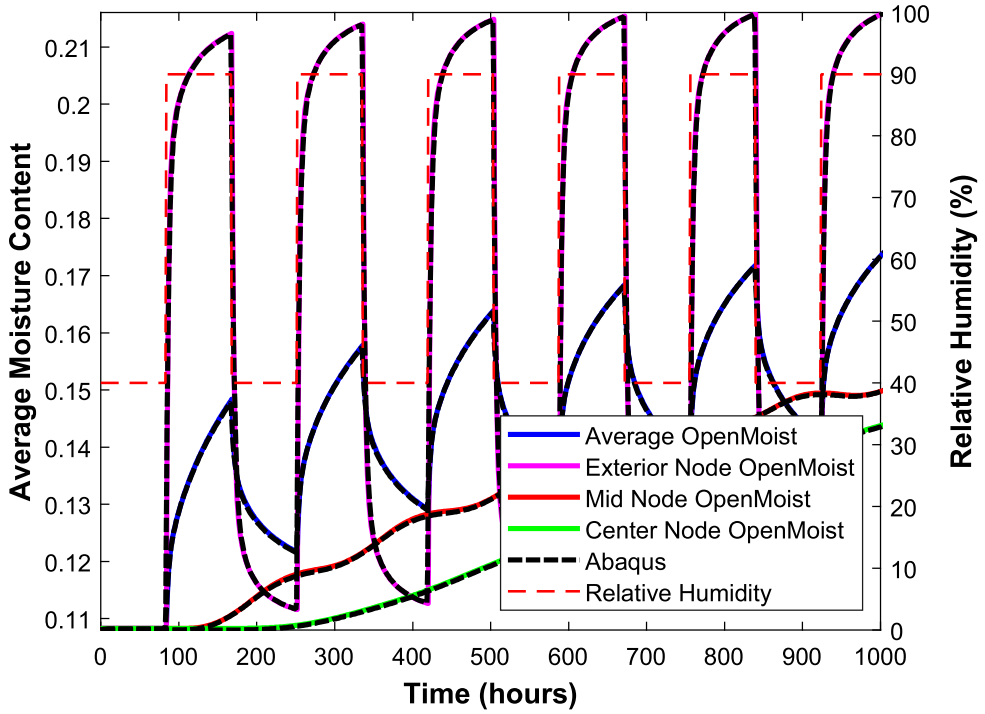
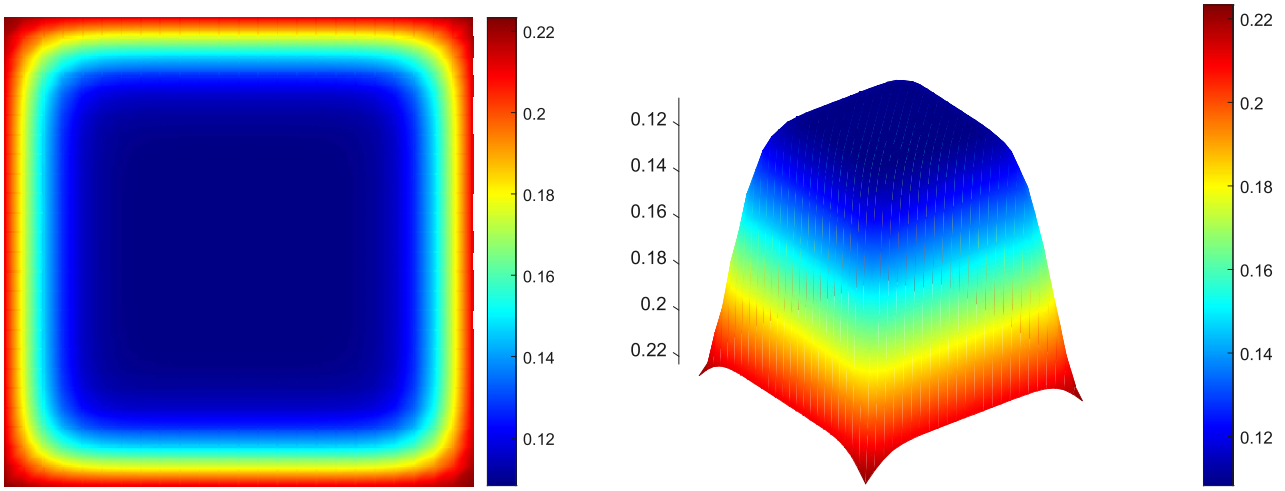


Figure 3.10: Moisture content variation in the solid square section under cyclic variations in the environmental conditions.

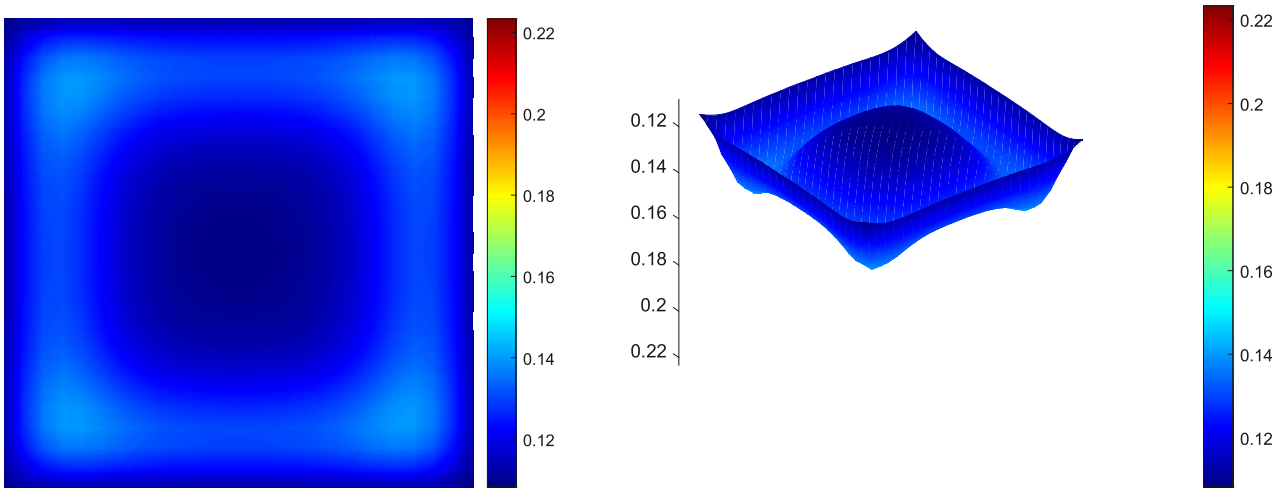
The average moisture content and nodal moisture in the same monitoring nodes (nodes 13, 163 and 313) as in the previous case are plotted in Fig. 3.10. The results indicate that the exterior node experiences higher variations than the internal nodes. From the average results, it is observed that the moisture in the section varies cyclically and gains moisture over the time. These same results were also obtained using ABAQUS.

To have a better idea of the moisture variation and distribution in the section, moisture contours and surfaces after 6, 10, 43 and 38 days are generated and presented in Figs. 3.11 to 3.14. Fig. 3.11 depicts the gain of moisture in the section when subjected to the first peak cycle variation. It can be observed that the perimeter experiences high variations of moisture whereas the internal nodes almost remain with the same initial moisture content. In contrast, Fig. 3.12 describes the lose of moisture just after the first wave. It can be noticed that the whole section returns roughly to the initial moisture scenario.



(a) Contour (b) Surface

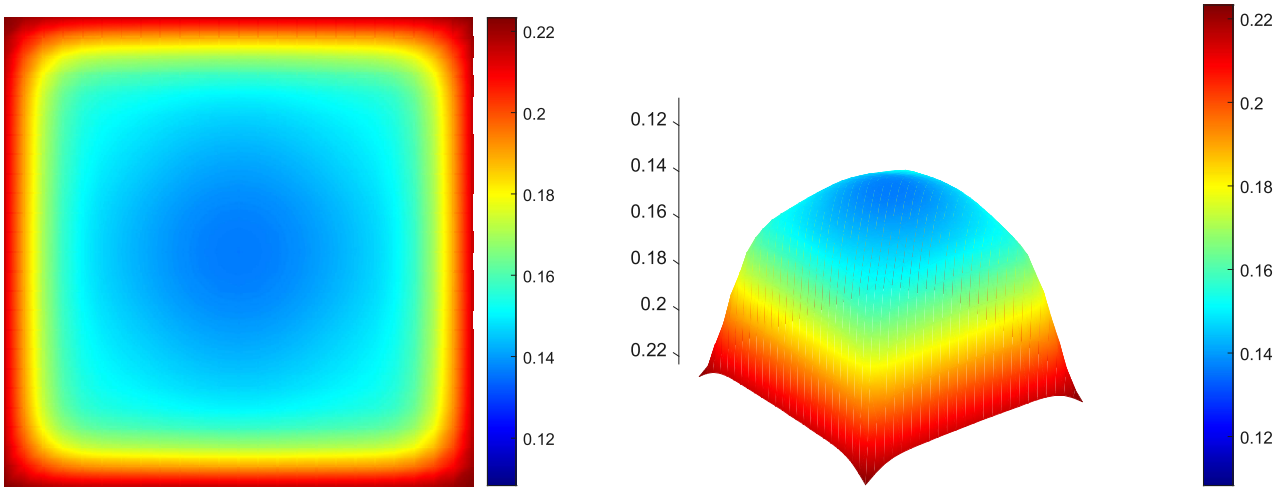
Figure 3.11: Moisture content distribution in the solid square section after 6 days of exposure under cyclic variations in the environmental conditions.



(a) Contour (b) Surface

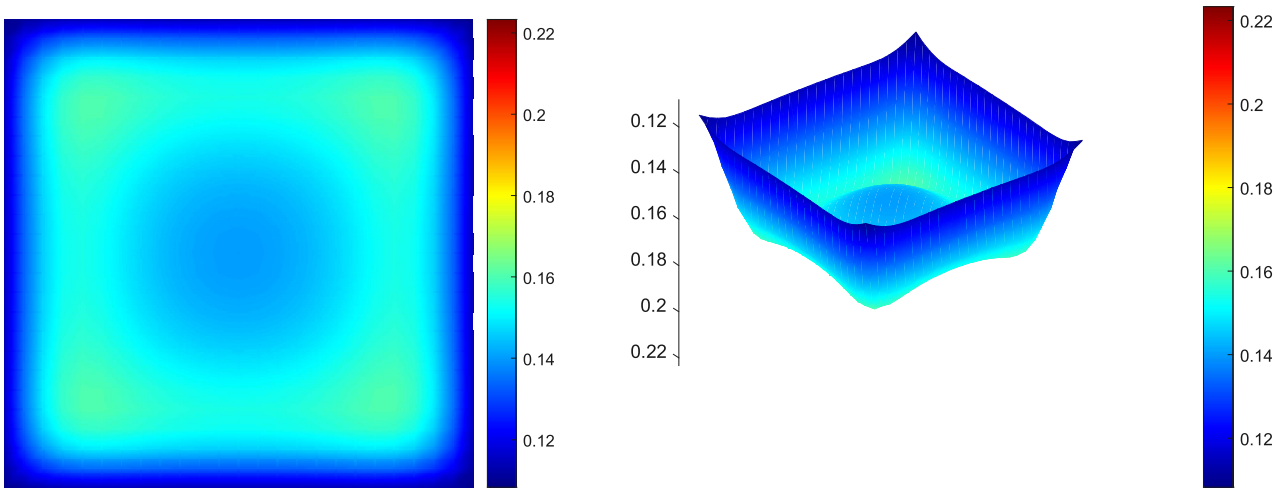
Figure 3.12: Moisture content distribution in the solid square section after 10 days of exposure under cyclic variations in the environmental conditions.

Fig. 3.13 shows the moisture distributions when the section experiences the fifth wave. As in the first wave, the perimeter undergoes higher variations whereas the internal nodes experiences lower rates of moisture gain. However, the variation rates in the perimeter are smaller in comparison with the first wave. From the pictures, it can be noticed that perimeter experiences a drop of moisture content to the levels of the initial moisture content. But in contrast to the lose scenario after the first wave (Fig. 3.14), the whole interior area of the section remains at moisture levels higher than the initial moisture content.



(a) Contour (b) Surface

Figure 3.13: Moisture content distribution in the solid square section after 34 days of exposure under constant environmental conditions.



(a) Contour (b) Surface

Figure 3.14: Moisture content distribution in the solid square section after 38 days of exposure under constant environmental conditions.

3.4.3 Hollow Square Section under Constant Conditions

The moisture diffusion inside a timber beam-colum element with hollow square section is studied in this section. The same material properties, sorption isotherm relationship, external height and width of the section, and initial moisture content as in the previous section are used. However, a uniform thickness of 1.78 cm and an equally spaced grid of 20x20, as shown in Fig. 3.15, was adopted. The specimen was initially in equilibrium with the surrounding air at a relative humidity of 40%. Then the external perimeter of the section was subjected to a sudden change in the ambient humidity level of 90%. This value was keep constant over the whole analysis whereas the internal perimeter remained steady at a humidity level of 40%.

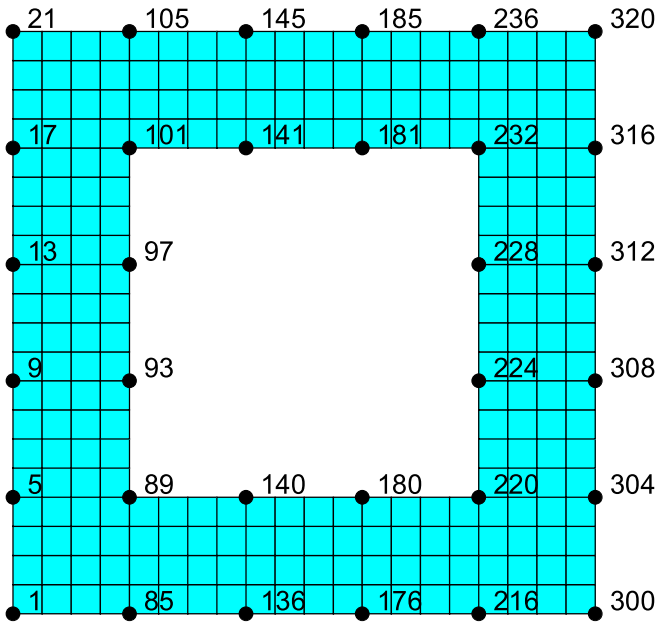


Figure 3.15: Grid generated for the Hollow square section.

The nodes along the middle of the web or flange length are chosen to study the variation of the moisture content in the section. Specifically, the nodes located at the internal and external boundary surface (nodes 11 and 53) as well as the middle node (node 95) are selected. The nodal moisture variations along with the average moisture in the section are depicted in Fig. 3.16.

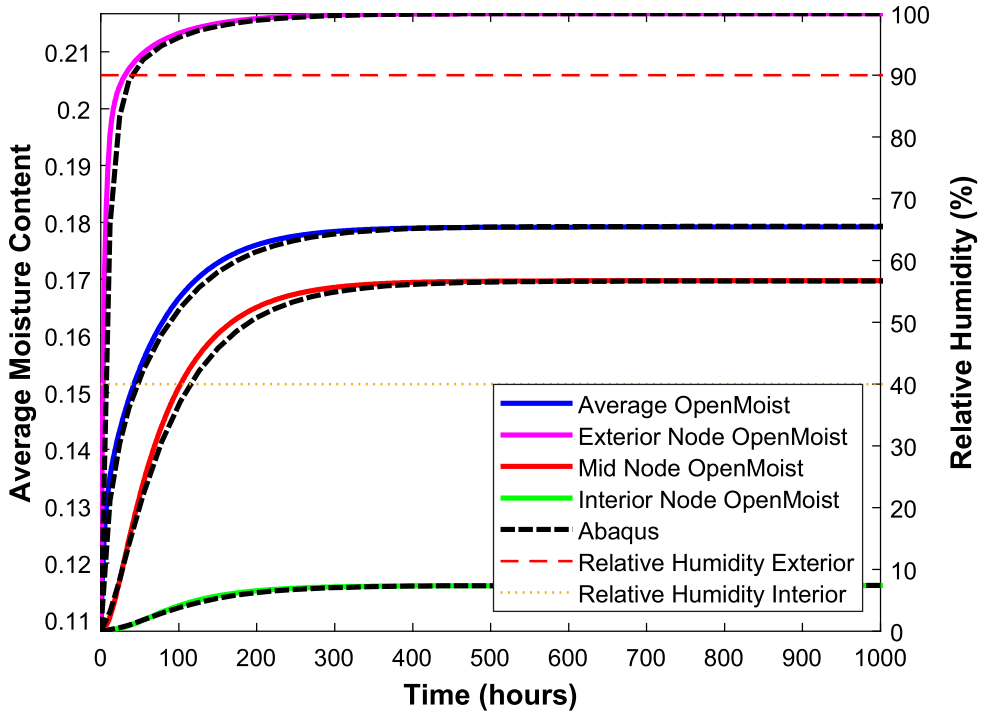
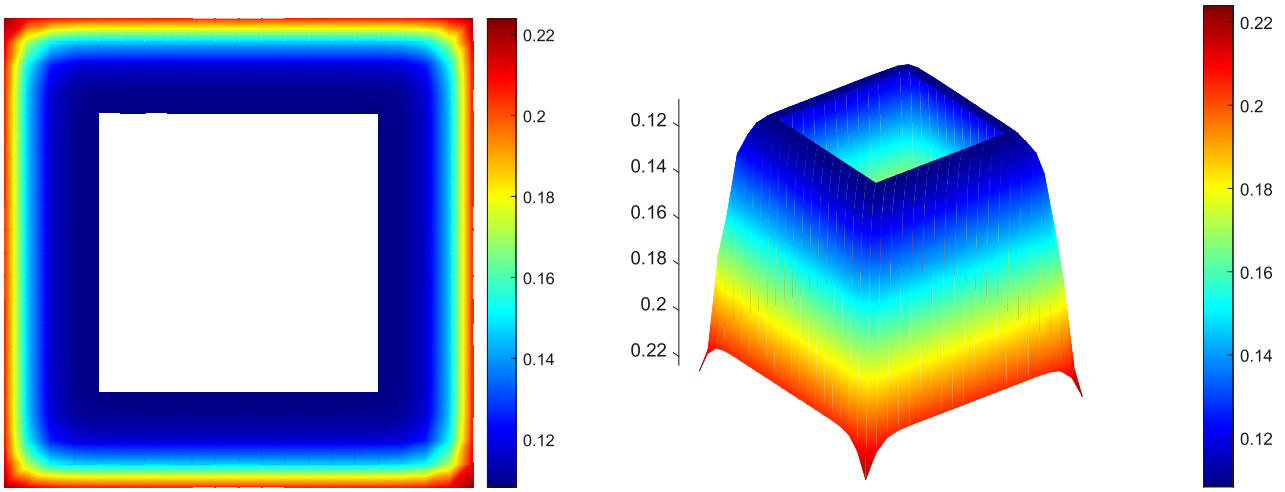


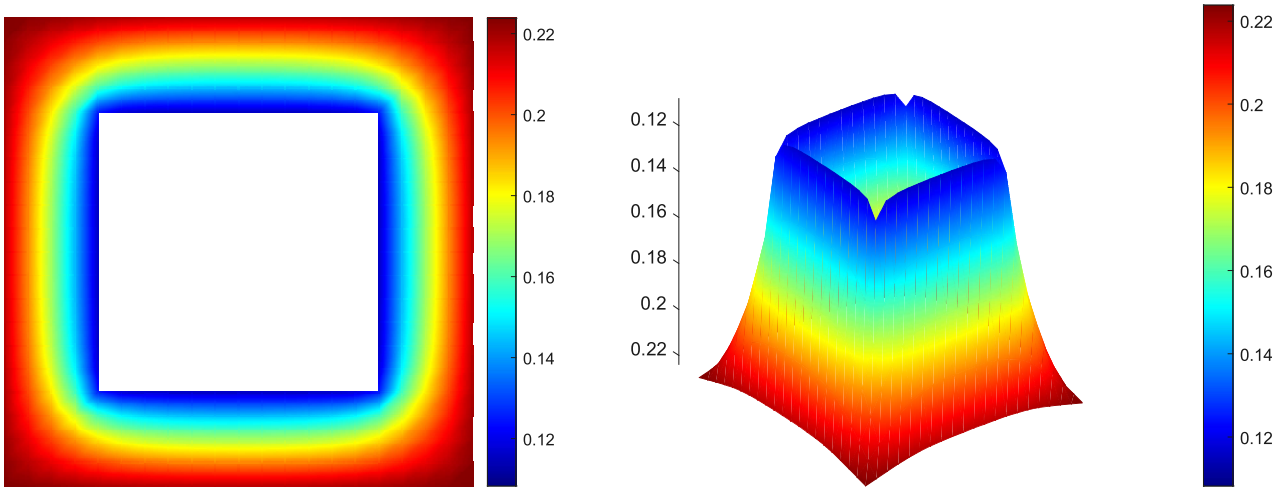
Figure 3.16: Moisture content variation in the hollow square section under constant environmental conditions.

From these results, it can be noticed that the moisture in the section reaches equilibrium after 18 days of exposure. Additionally, the results match perfectly the results obtained with the software ABAQUS. Fig. 3.17 shows the moisture distribution after 1 day of exposure, where high rate variations are experienced close to the external perimeter whereas the area close to the internal perimeter experiences slower rates. After 40 days of the exposure to the new climatic conditions (Fig. 3.18), a steady gradient is reached along the thickness of the section.



(a) Contour (b) Surface

Figure 3.17: Moisture content distribution in the hollow square section after 1 day of exposure under constant environmental conditions.



(a) Contour (b) Surface

Figure 3.18: Moisture content distribution in the hollow square section after 40 days of exposure under constant environmental conditions.

3.4.4 Hollow Square Section under Changing Conditions

The same hollow section described in the previous case is analysed here but subjected to the same cyclic variations of the moisture content as those described in Section 3.4.2 whereas the environmental condition in the internal perimeter stays unchanged at constant relative humidity of 40%. The same data used in the former model is also employed here. Similarly, the same monitoring nodes in the mesh (nodes 11, 53 and 95) are used in this analysis to depict the moisture variation in the section.

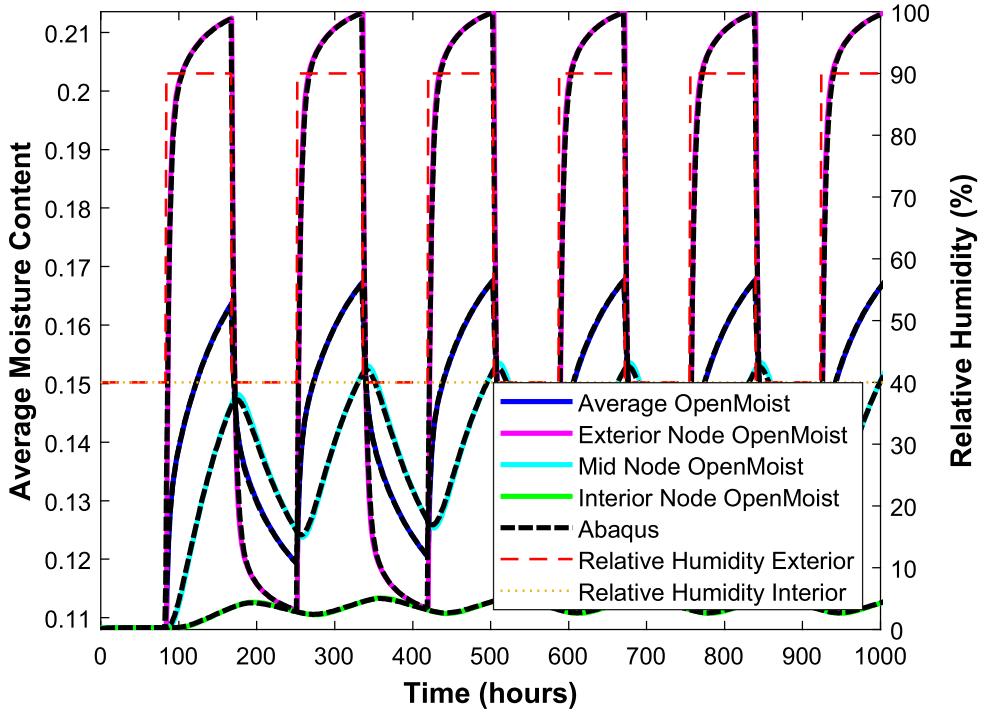
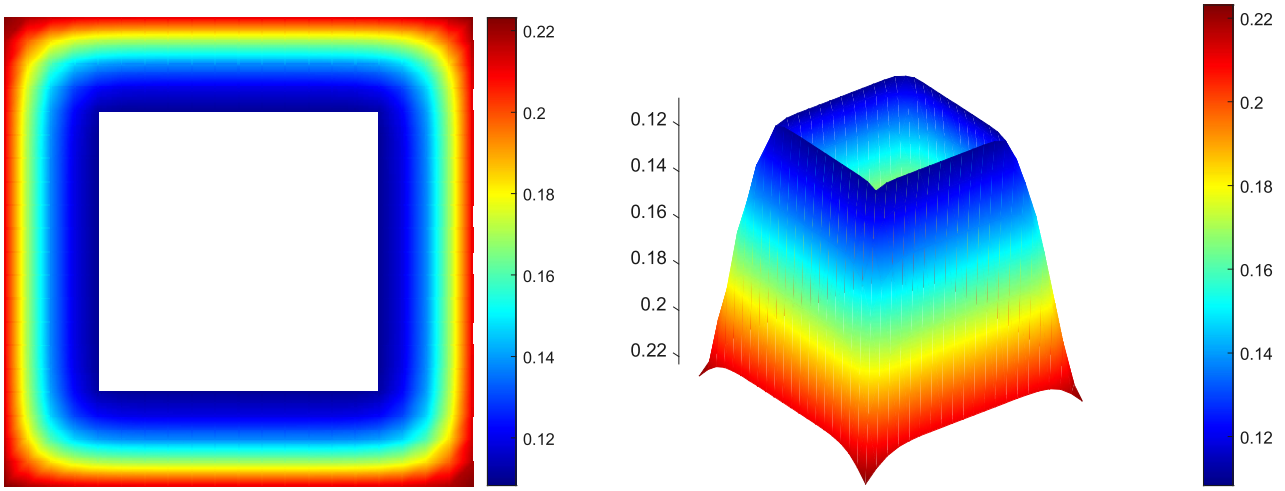


Figure 3.19: Moisture content variation in the hollow square section under cyclic variations in the environmental conditions.

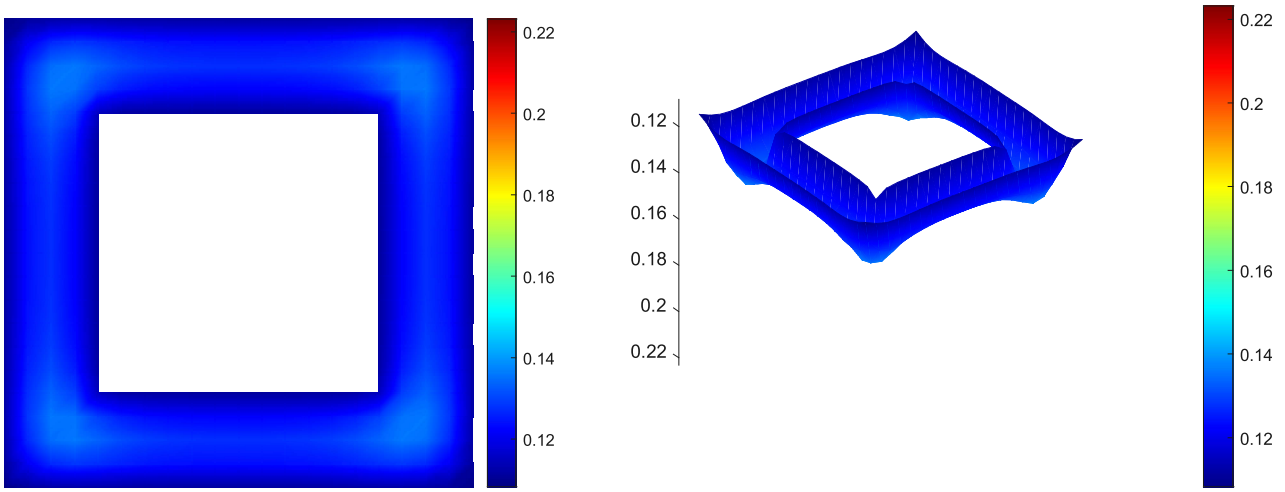
The obtained results ate plotted in Fig. 3.19, it can be observed that the node in the external boundary surface undergoes a high variation of moisture in contrast to the interior and mid nodes. Besides, the average moisture over the section shows that the there is a negligible gain of moisture content over time. The results are identical to those obtained with the ABAQUS software.

Fig. 3.20 and Fig. 3.21 presents the moisture distribution in the first wave and just after the first wave, respectively. It is noticed that the external boundary experiences larger variation rates under the first wave. After the ambient load is removed, a losing scenario of moisture is generated leading the section to moisture levels roughly similar to the initial equilibrium scenario.



(a) Contour (b) Surface

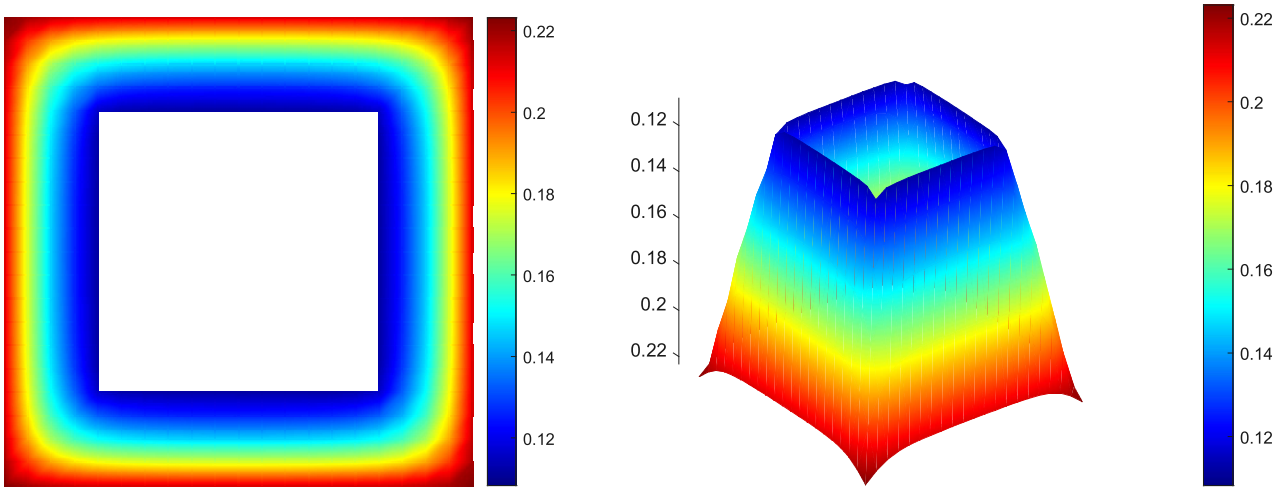
Figure 3.20: Moisture content distribution in the hollow square section after 6 days of exposure under cyclic variations in the environmental conditions.



(a) Contour (b) Surface

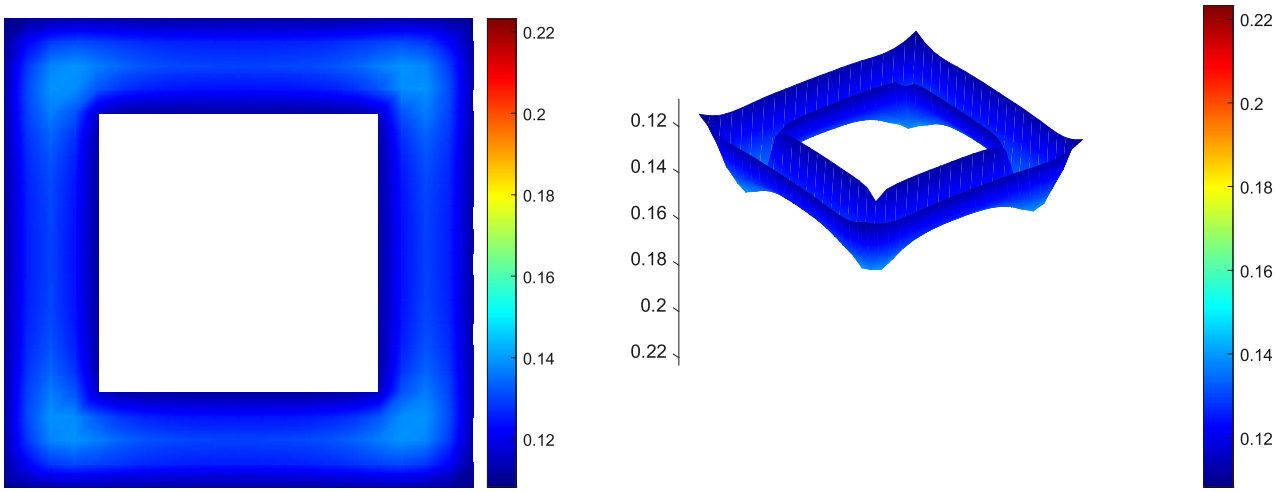
Figure 3.21: Moisture content distribution in the hollow square section after 10 days of exposure under cyclic variations in the environmental conditions.

Fig. 3.22 and Fig. 3.23 show the moisture distribution over the section under and just after the fifth wave. They describe almost the same variation observed in the first wave. In comparison with the solid square section under the same ambient load conditions (Section 3.4.2), the hollow section has a marginal gain of moisture after being subject to various moisture waves. This is due to the geometry of the section. The thickness of the web and flange does not allow a steady moisture gradient in these lengths.



(a) Contour (b) Surface

Figure 3.22: Moisture content distribution in the hollow square section after 34 days of exposure under constant environmental conditions.



(a) Contour (b) Surface

Figure 3.23: Moisture content distribution in the hollow square section after 38 days of exposure under constant environmental conditions.

3.4.5 Cross-Laminated Timber Panel

A transient moisture diffusion analysis of a CLT panel is performed as an illustration of insulated boundary conditions. This simulation is based on the numerical and experimental test performed by Nguyen et al. [17]. In the setup of this test, two opposite boundary surfaces of the CLT specimens were insulated. Generally, when the moisture distribution in CLT panels needs to be assessed, a three-dimensional moisture diffusion analysis should be performed to consider all the complexity involved. However, in this analysis case due to the CLT dimensions and test setup, it can be assumed that the main moisture diffusion process is perpendicular to the panel

surface. Therefore, the complexity of the model can be reduced to a one-dimensional problem. To perform this type of analysis, insulated boundary conditions are set in the two insulated boundary surfaces. The dimensions and material properties of the CLT specimen analysed can be found in Nguyen et al. [17]. These parameter values are summarized in Table 3.6. From the laboratory results, it was concluded that the moisture diffusion coefficients vary according to different ranges of relative humidity levels. In regard to the non-insulated boundary conditions, convective boundary conditions are considered in this analysis using the same surface emissivity coefficients of the previous examples. A mesh size of 12 elements in the direction of the diffusion process and 2 elements in the perpendicular direction are adopted. The mesh is shown in Fig. 3.24.

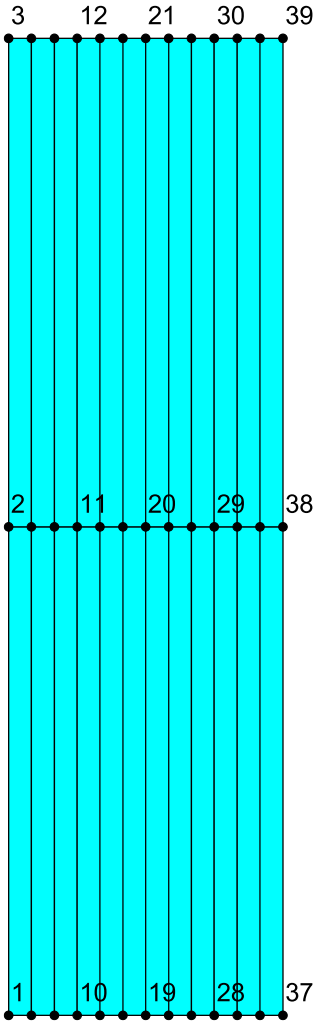


Figure 3.24: Mesh of the CLT panel.

Type of input data	Parameter	Value
Geometry	Height (cm)	60.9
	Width (cm)	17.1
Surface emissivity coefficient	Right-Hand Side Boundary (cm/day)	1.1232
	Left-Hand Side Boundary (cm/day)	1.1232
	Top Boundary (cm/day)	0.0
	Bottom Boundary (cm/day)	0.0
Diffusion coefficient	Relative humidity 50 % - 70 % (cm^2/day)	0.110
	Relative humidity 70 % - 90 % (cm^2/day)	0.217

Table 3.6: Geometry and material property data of the CLT panel.

An initial moisture content of 0.106 was considered for the CLT specimen. This initial value corresponds to an initial relative humidity of 50%. Then, the environmental conditions surrounding the specimen are suddenly changed to a relative humidity level of almost 80%. The equilibrium moisture content related to this relative humidity value is 0.161 (Nguyen et al. [17]).

To have an overview of the moisture diffusion process inside the element, the transient nodal moisture contents related to the boundary node (node 2), and the interior nodes located at the mid point (node 11) and center point (node 20), shown in Fig. 3.24, are plotted in Fig. 3.25. From the results, it is observed that the exterior node experiences the highest rate variation of moisture content, whereas the centre node does not show a meaningful moisture variation.

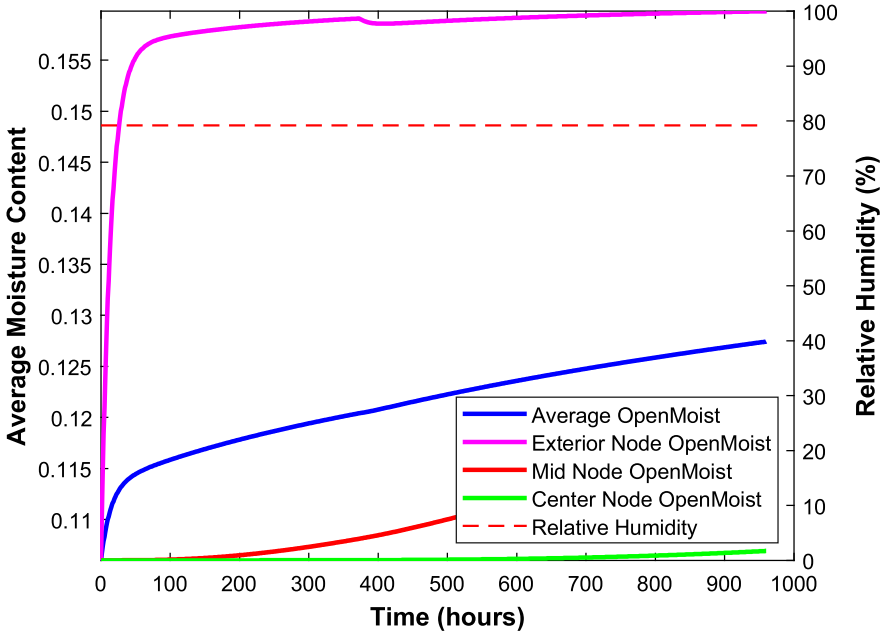
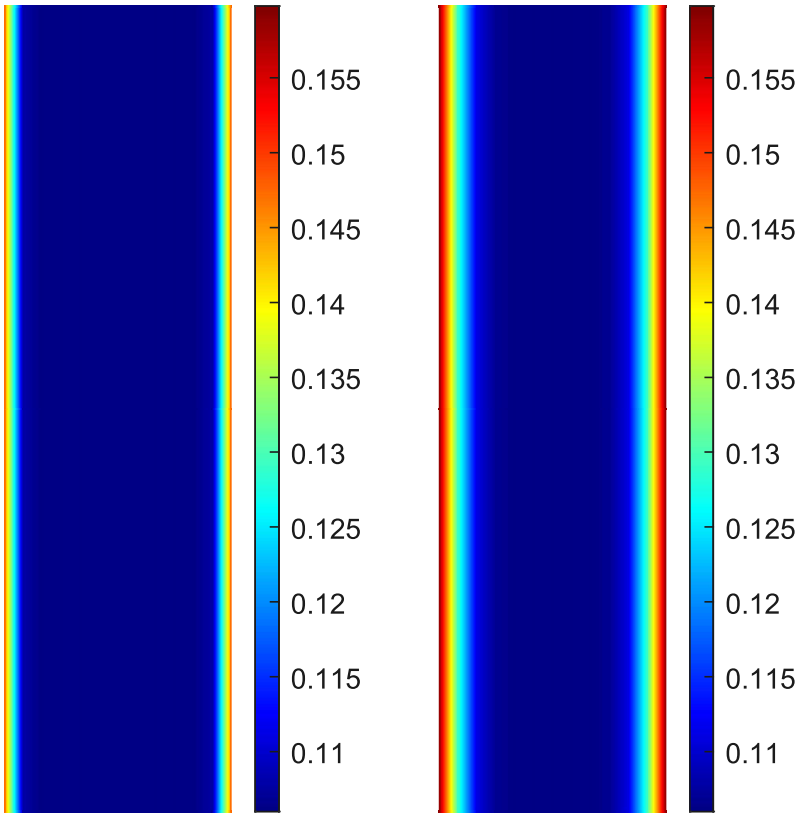
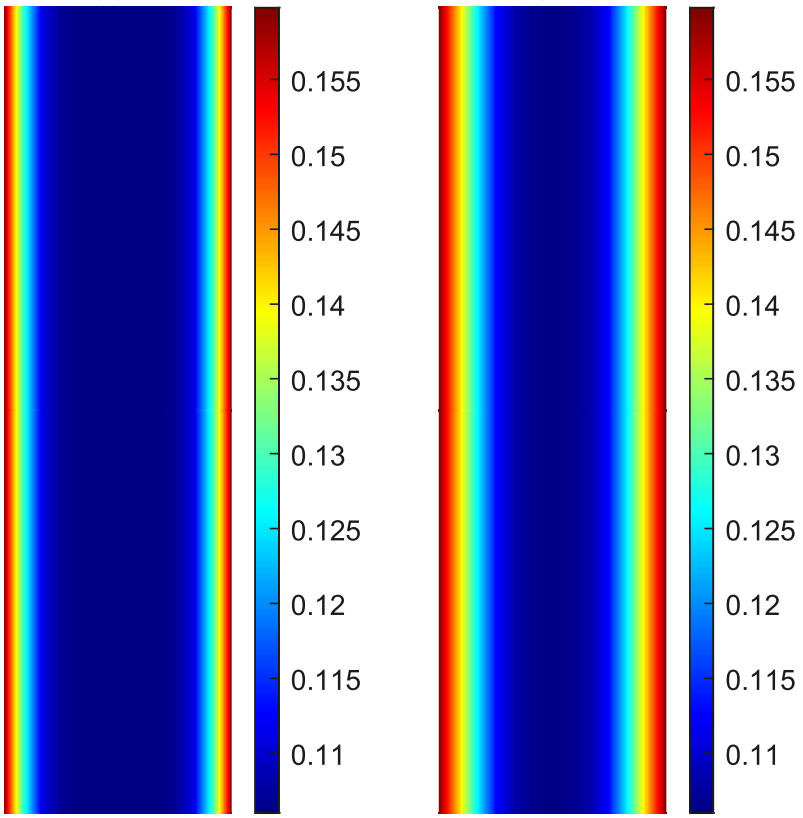


Figure 3.25: Moisture content variation in the CLT panel under a constant variation in the environmental conditions.



(a) after 1 day

(b) after 10 days

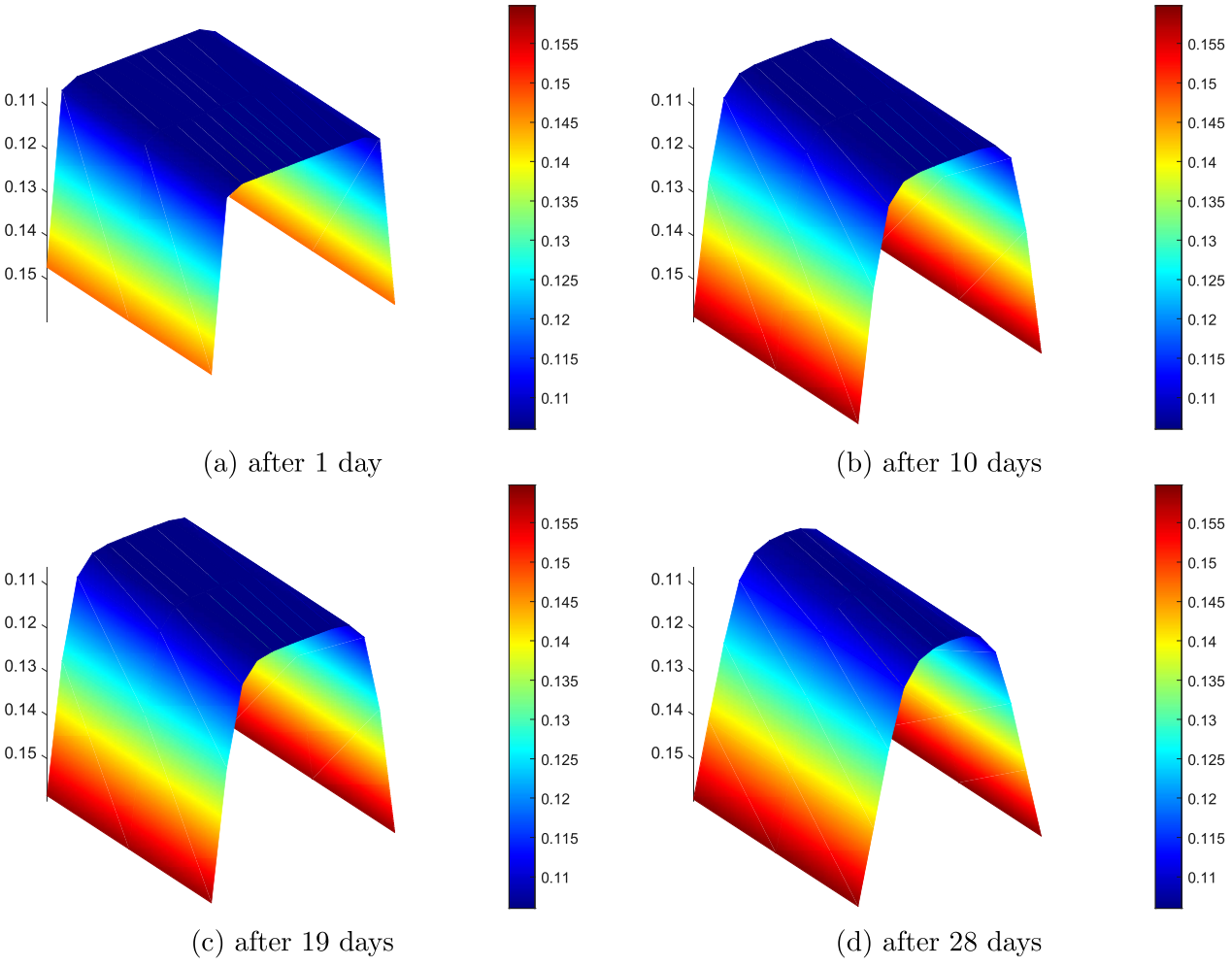


(c) after 19 days

(d) after 28 days

Figure 3.26: Moisture content contour distribution in the CLT panel under constant environmental conditions.

To gain a comprehensive understanding of the moisture distribution in the CLT panel, Fig. 3.26 and Fig. 3.27 are generated. From these plots, it can be noticed that the moisture variation in the panel is abrupt after 1 day having a moisture gradient concentration along the perimeter. However after 28 days, the moisture gradient variation over the panel smoothens. The moisture contours shown in Fig. 3.26 have a good agreement with the contours plotted by Nguyen et al. [17].



(a) after 1 day

(b) after 10 days

(c) after 19 days

(d) after 28 days

Figure 3.27: Moisture content surface distribution in the CLT panel under constant environmental conditions.

3.5 Concluding Remarks

From the finite difference equations derived and results obtained, it can be highlighted that:

- The derived discretization equations includes moisture-dependent diffusion and surface emissivity coefficients resulting in a series of algebraic nonlinear equations. Solving these equations for the transient non-linear moisture diffusion analysis cases presented in this chapter produced results which are almost identical to the results obtained with the software ABAQUS which performed a nonlinear finite element analysis.

- From the results of timber elements subjected to single humidity steps, it can be observed that in the case of the hollow section the equilibrium is almost reached long before the exposed time period. On the other hand, in the case of the solid section a longer period of the humidity load is needed to reach equilibrium in the section. This can be explained as a consequence of the moisture penetration depth which in the case of solid sections is longer.

- When the sections are exposed to cyclic humidity loads, it can be noticed that the solid section after experiencing a number of cycles gains higher moisture levels than its initial moisture distribution. In contrast, the hollow section returns to moisture levels close to its initial distribution. This result is also an implication of the moisture penetration depth.

- The assessment of the moisture spatial and temporal distributions allows the generation of the input data required in the evaluation of the rheological constitutive model.

Chapter 4

Nonlinear Modelling of Timber Beam-Column Elements

This chapter focuses on the modelling of the short- and long-term response of unidimensional beam-column (BC) elements with geometric and material non-linearity. First, the finite element (FE) formulation of different two-node BC elements adopted is described. These formulations are derived within a corotational framework restricted to a two dimensional space. This is followed by a description of material constitutive laws used to describe the short- and long-term behaviour of wood under monotonic loading. In the context of material non-linearity, the stress-strain relationships describing the short-term behaviour are considered. Similarly, the rheological behaviour of timber can be categorized as material non-linearity because the strain-stress laws describing the aging or hygroscopic effects have to be set in a rate form to comply with the fundamental laws of thermodynamics [Bažant [138]]. Finally, the linearized equations to be solved are presented and then a series of short- and long-term analysis involving small or large displacements were performed to validate the numerical framework.

4.1 Beam–Column Finite Element Formulation

Fibre BC elements have been widely used over the last decade to assess the ultimate load capacity of structural components comprising building and bridges under monotonic, cyclic and dynamic loading scenarios. The popularity of these elements springs form their low computational cost in comparison with 2D/3D continuum elements despite their comparable accuracy in the case of modelling beam and column structural components. Generally, the plane section hypothesis encompassing the Euler-Bernoulli and Timoshenko beam theories are the most

common kinematic assumption adopted. Regarding Euler-Bernoulli theory, displacement-based formulations were among the earliest developments, assuming polynomial shape function to approximate the field displacements inside the elements (Kang and Scordelis [139], Hellesland and Scordelis [140], Scordelis [141]). However, due to the shortcomings of displacement-based formulations requiring large mesh refinements to represent complex inelastic deformations, alternative formulations were developed. Force-based and mixed formulations were developed as an alternative based on the principle of virtual forces and mixed variational principles, respectively (Spacone et al. [142], Neuenhofer and Filippou [143], Spacone et al. [144], Petrangeli and Ciampi [145], Alemdar and White [146]). Lastly, enhanced formulations of the traditional displacement-based approaches have been proposed to overcome the weak enforcement of equilibrium (Koutromanos and Bowers [147], Tarquini et al. [148]). All these fiber element formulations based on the Euler-Bernoulli theory are capable of capturing the axial-flexure coupling effects of flexure-dominant members.

When non-negligible transverse shear deformations are expected in BC members, the Timoshenko beam theory which considers a constant shear strain distribution over the cross section can be adopted. It is worthwhile to mention that higher-order theories to describe the section kinematics including warping and distortion can also be considered to obtain more accurate shear strain distributions, however, they are beyond the scope of this work. Timoshenko fibre BC element formulations also comprise displacement-based, forced-based and mixed-based approaches. With regard to forced-based and mixed formulations, different elements have been proposed considering axial-flexure-shear interactions (Ranzo and Petrangeli [149], Taylor et al. [150], Filippou and Saritas [151], Marini and Spacone [152], Saritas and Filippou [153], Jafari et al. [154], Feng et al. [155], Feng and Ren [156], Feng et al. [157]). One common feature of these formulations is that they do not experience shear locking problems in contrast to displacement-based formulations. However, several alternatives to avoid this numerical issue can be found in the literature. Well-known techniques such as reduced integration if independent polynomial interpolations of equal order for the transverse displacement and rotation fields are used (Ferreira et al., [158], Hughes et al., [159]), modification of the shear-strain energy (Guedes et al., [160], Donea and Lamain, [161]) and the use of consistent interpolation functions (Reddy, [162]) are among these alternatives. Further developments include the use of material-dependent interpolation functions based on the exact solutions of the homogeneous differential equations defining the equilibrium of a Timoshenko beam (Kotronis and Mazars [163], Stramandinoli and La Rovere [164], Li et al. [165]). An alternative approach to overcome the shear locking issue in displacement-based Timoshenko fibre frame elements is the addition

of bubble terms to the interpolation functions of transverse displacements and rotations (Ceresa et al. [166], Khalid [167], Jukić et al. [168], Caillerie et al. [169], Li et al. [170], Feng et al. [171], Liu et al. [172]). Assuming the FE approximation of the displacement or rotation field in the element is $u(x)$, this approach can be expressed as:

$$u(x) = \sum_{i=1}^{n} u_i \, \phi_i(x) + \sum_{j=1}^{m} a_j \, \psi_j(x) \tag{4.1}$$

where the parameters u_i in the first term of the equation represent the nodal values of the approximate field, whereas the parameters a_j in the second term are nodeless parameters without physical meaning. Meanwhile, ϕ_i and ψ_j are interpolation functions.

Similar to the displacement-based Euler-Bernoulli fibre frame elements, displacement-based Timoshenko fibre frame elements only satisfy the equilibrium in an average sense due to the weak-form formulation employed in these elements. As a result, Feng and Wu [173] developed an improved formulation of the displacement-based Timoshenko frame element to enforce equilibrium.

From the literature review presented in section 2.2 and section 2.3, force-based and displacement-based Euler-Bernoulli frame elements were employed in most cases. Only in one of these studies (Tao et al. [58]), a displacement-based Timoshenko BC element was adopted with linear independent shape functions and a reduced integration scheme. Despite the well-known robustness of force-based formulations, the element state determination of these formulations can result in cumbersome iterative algorithms that not always guarantee convergence. Moreover, even if non-iterative schemes are used, there is no certainty that the residuals of the global equilibrium and weak compatibility conditions will be satisfied simultaneously [Koutromanos and Bowers [147]]. Therefore, displacement-based formulations are adopted in this thesis in light of their easier element state determination. With the aim of capturing the nonlinear response of timber BC members with different slenderness ratios and cross-sections, Timoshenko fiber BC FE formulations without shear locking are also adopted in this work. It should be mentioned that shear locking problems could arise specially in the case of post-tensioned timber members as the shear forces and deformations in the elements can be drastically reduced due to the lift effect provided by the post-tensioning system (Lyu et al. [174]). More specifically, the FE formulation adopted by Feng et al. [171] and its enhanced version developed by Feng and Wu [173] are considered in the fibre-based FE analysis framework implemented in this work. Besides, the traditional Euler-Bernoulli fibre BC formulation and its enhanced version are also included in this analysis framework. A schematic description of the implemented FE framework and BC

elements comprising it are shown in Appendix A.

4.1.1 Virtual Work Equation

The conventional consistent corotational approach which assumes large displacements in conjunction with small-strain theory is adopted to describe the nonlinear geometric effects in BC elements (De Borst et al. [175]). In this approach, the large displacements undergone by the element can be separated in rigid and stretching displacements. For that reason, the element deformations are assessed through a basic reference system, which is an auxiliary isostatic configuration that does not allow rigid motions, attached to a continuously rotating configuration in which the material nonlinearities can be isolated. Meanwhile, the large displacements are related to the rigid motion undergone by the attached rotating frame described in a global reference system. Fig. 4.1 shows the global, local and basic reference system used in transforming the element displacement and force vectors, and stiffness matrices from one system to another. In contrast, the reference configuration in the updated and total Lagrangian approaches are related to the last calculated or initial undeformed configurations, respectively [Yang and Kuo [176], McGuire et al. [177]].

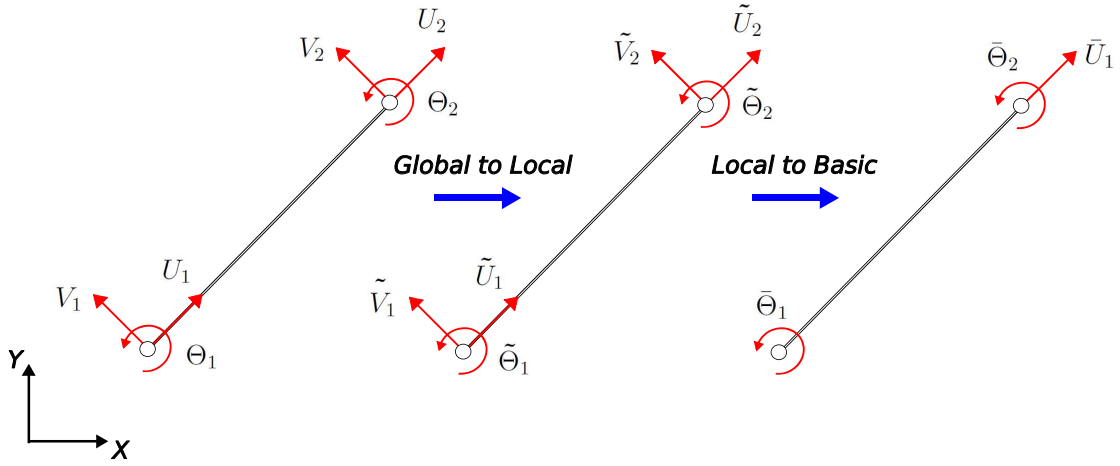


Figure 4.1: Reference systems of the beam-column element.

The transformation relation between the virtual nodal displacements of the element in the global reference system $\delta \boldsymbol{U}_e$ and the basic one $\delta \bar{\boldsymbol{U}}_e$ can be expressed as:

$$\delta \bar{\boldsymbol{U}}_e = \boldsymbol{T}\, \delta \boldsymbol{U}_e \tag{4.2}$$

where $\boldsymbol{T}$ is the global to basic transformation matrix which depends on the number of degrees of freedom adopted. In the case of displacement-based Timoshenko fibre elements, the generalized

displacement field is approximated as follows:

$$\begin{bmatrix} u(x) \\ v(x) \\ \theta(x) \end{bmatrix} = \boldsymbol{N}(x)\,\tilde{\boldsymbol{U}}_e \tag{4.3}$$

where $u(x)$, $v(x)$ and $\theta(x)$ are the axial and transversal displacements of the centroidal axis, and the section rotation, respectively; and $\boldsymbol{N}(x)$ is the matrix array containing the interpolation functions. When Euler-Bernoulli fibre elements are considered, the section rotation is discarded from Eq. (4.3) as it can be evaluated from the transversal displacement field.

In the case of BC elements is convenient to describe the undergone strain deformations in terms of section deformations in an array called generalized strain vector, $\hat{\boldsymbol{\varepsilon}}$. If a Timoshenko element is employed, the section deformations can be calculated from the generalized displacement field as follows:

$$\hat{\boldsymbol{\varepsilon}} = \begin{bmatrix} \varepsilon_0(x) \\ \kappa(x) \\ \gamma(x) \end{bmatrix} = \begin{bmatrix} \dfrac{\partial\, u(x)}{\partial\, x} \\ \dfrac{\partial\, \theta(x)}{\partial\, x} \\ \dfrac{\partial\, v(x)}{\partial\, x} - \theta(x) \end{bmatrix} \tag{4.4}$$

where $\varepsilon_0\,(x)$, $\kappa\,(x)$, and $\gamma\,(x)$ are the longitudinal extension, curvature and shear deformation of the section, respectively. In case of Euler-Bernoulli fibre elements, the shear deformations are zero as the section rotation is perpendicular to the longitudinal axis.

An important relationship derived from Eq. (4.3) and Eq. (4.4) is the linear relation between the generalized strain vector and the basic nodal displacement vector, $\bar{\boldsymbol{U}}_e$, described by:

$$\hat{\boldsymbol{\varepsilon}} = \bar{\boldsymbol{B}}\,\bar{\boldsymbol{U}}_e \tag{4.5}$$

where $\bar{\boldsymbol{B}}$ is known as the compatibility or strain-displacement matrix and its terms and size depend on the type of displacement-based FE formulation employed. It should be noted that this linear relationship reflects the small strain theory assumed in the basic reference system.

An alternative formulation of the equilibrium state of a BC element in its deformed configuration can be derived following the standard principle of virtual work in terms of virtual displacements (Bathe [178]). Adopting the derivation presented by De Borst et al. [175], the internal work in the element after a linearization of the virtual work equations can be stated as:

$$\delta \mathcal{W}_{int} = \delta \boldsymbol{U}_e^T \int_l \boldsymbol{T}^T \, \bar{\boldsymbol{B}}^T \, \boldsymbol{D}_T \, \bar{\boldsymbol{B}} \, \boldsymbol{T} \, dx \, \Delta \boldsymbol{U}_e + \delta \boldsymbol{U}_e^T \int_l \frac{\partial \boldsymbol{T}}{\partial \boldsymbol{U}_e}^T \, \bar{\boldsymbol{B}}^T \, \hat{\boldsymbol{\sigma}} \, dx \, \Delta \boldsymbol{U}_e + \delta \boldsymbol{U}_e^T \int_l \boldsymbol{T}^T \, \bar{\boldsymbol{B}}^T \, \hat{\boldsymbol{\sigma}} \, dx \tag{4.6}$$

where $\Delta \boldsymbol{U}_e$ is the incremental nodal displacement vector, $\boldsymbol{D}_T$ is the section tangent stiffness matrix, $\hat{\boldsymbol{\sigma}}$ is the generalized stress vector containing the stress resultants, and l is the length of the BC element.

4.1.2 Derivation of the Global Force and Tangent Stiffness at the Element Level

The assessment of the element internal force vector and tangent stiffness matrix in the global reference system is an important step in the assemblage of the linearized nonlinear equations at the structural level. A midpoint method is applied to perform the numerical integration along the fibre-based sections of the element. In the case of the internal force vector, the generalized stress vector (also denominated section force vector) needs to be evaluated previously. Considering that the axial-bending and shear response are decoupled at the section level, the section force vector for a Timoshenko fibre element can be obtained as:

$$\hat{\boldsymbol{\sigma}}(x) = \begin{bmatrix} N(x) \\ M(x) \\ Q(x) \end{bmatrix} = \begin{bmatrix} \sum \sigma_k \, A_k \\ -\sum \sigma_k \, A_k \, y_k \\ Q(x) \end{bmatrix} \tag{4.7}$$

where N, Q, and M are the stress resultants: the section axial force, shear force and bending moment, respectively; and σ_k, A_k, and y_k are the stress, area and position with respect to the centroidal axis of the k-th fibre, respectively. In this case, the shear force is obtained separately from a phenomenological constitutive law dependent on the shear deformation, γ. Regarding the Euler–Bernoulli fibre elements, the shear force is not assessed at the section level. Instead, the shear force is evaluated at the element level from the nodal internal forces.

Similarly, the element tangent stiffness matrix depends on the evaluation of the section tangent stiffness matrix. If uncoupled axial-flexure-shear behaviour is considered, the section

stiffness matrix of a Timoshenko element is evaluated as follows:

$$\boldsymbol{D}_T = \begin{bmatrix} \sum E_k\, A_k & -\sum E_k\, A_k\, y_k & 0 \\ -\sum E_k\, A_k\, y_k & \sum E_k\, A_k\, y_k^2 & 0 \\ 0 & 0 & \dfrac{\partial Q(\gamma)}{\partial \gamma} \end{bmatrix} \tag{4.8}$$

where E_k is the tangent modulus of the k-th fibre and $\partial Q(\gamma)/\partial\gamma$ represents the shear tangent stiffness assessed from the derivative of the shear constitutive law. For Euler–Bernoulli elements, the assessment of the shear stiffness term in Eq. (4.8) is not considered.

It is worth mentioning that the integrals comprising the right-hand side of the internal virtual work equation Eq. (4.6) represent the stiffness matrices and force vector of the BC element. Specifically, the first term represents the element material stiffness matrix, $\boldsymbol{K}^e_m$, the second term the element geometric stiffness matrix, $\boldsymbol{K}^e_g$, and the last term the element internal force vector, $\boldsymbol{F}^e_{int}$. It should be mentioned that all these matrix arrays refers to the global coordinate system and the tangent stiffness matrix is the sum of the material and geometric stiffness matrices. On the other hand, these matrix arrays are denoted as $\bar{\boldsymbol{K}}^e_m$, $\bar{\boldsymbol{K}}^e_g$, and $\bar{\boldsymbol{F}}^e_{int}$, respectively, in a basic reference system . The evaluation of these integrals to determine the previous matrix arrays is carried out by employing the fibre-based approach in conjunction with a Gauss-Legendre integration scheme along the element length to include the section stress variations and distributed inelasticity within the element.

In what follows, the general method described by Khalid [167] to obtain the global internal force vector and tangent stiffness matrix, including the case with bubble or nodeless degrees of freedom, is adopted.

For convenience, the transformation matrix in Eq. (4.2) can be rewritten as follows:

$$\boldsymbol{T} = \begin{bmatrix} \boldsymbol{T}_{bb} & \boldsymbol{T}_{ba} \\ \boldsymbol{T}_{ab} & \boldsymbol{T}_{aa} \end{bmatrix} \tag{4.9}$$

where $\boldsymbol{T}_{bb}$ and $\boldsymbol{T}_{aa}$ represents the transformation of the mesh node and nodeless degrees of freedom, while $\boldsymbol{T}_{ba}$ and $\boldsymbol{T}_{ab}$ are zero rectangular matrices. Similarly, the element material stiffness matrix and internal force vector in the basic reference system as well as the element geometric stiffness matrix in the global reference system, are rewritten as:

$$\bar{\boldsymbol{K}}^e_m = \begin{bmatrix} \bar{\boldsymbol{K}}^e_{m\,bb} & \bar{\boldsymbol{K}}^e_{m\,ba} \\ \bar{\boldsymbol{K}}^e_{m\,ab} & \bar{\boldsymbol{K}}^e_{m\,aa} \end{bmatrix} \tag{4.10}$$

$$\bar{\boldsymbol{F}}^e_{int} = \begin{bmatrix} \bar{\boldsymbol{F}}^e_{int\,bb} \\ \bar{\boldsymbol{F}}^e_{int\,aa} \end{bmatrix} \tag{4.11}$$

$$\boldsymbol{K}^e_g = \begin{bmatrix} \boldsymbol{K}^e_{g\,bb} & \boldsymbol{K}^e_{g\,ba} \\ \boldsymbol{K}^e_{g\,ab} & \boldsymbol{K}^e_{g\,aa} \end{bmatrix} \tag{4.12}$$

Finally, the global internal force vector and tangent stiffness matrix are assessed as follows:

$$\boldsymbol{F}^e_{int} = \begin{bmatrix} \boldsymbol{T}^T_{bb}\,\bar{\boldsymbol{F}}^e_{int\,bb} \\ \bar{\boldsymbol{F}}^e_{int\,aa} \end{bmatrix} \tag{4.13}$$

$$\boldsymbol{K}^e = \begin{bmatrix} \boldsymbol{T}^T_{bb}\,\bar{\boldsymbol{K}}^e_{m\,bb}\,\boldsymbol{T}_{bb} + \boldsymbol{K}^e_{g\,bb} & \boldsymbol{T}^T_{bb}\,\bar{\boldsymbol{K}}^e_{m\,ba} \\ \bar{\boldsymbol{K}}^e_{m\,ab}\,\boldsymbol{T}_{bb} & \bar{\boldsymbol{K}}^e_{m\,aa} \end{bmatrix} \tag{4.14}$$

If using only interpolation functions associated with nodal values, based on the previous equations, the internal force vector and tangent stiffness matrix in a global coordinate system are evaluated as:

$$\boldsymbol{F}^e_{int} = \boldsymbol{T}^T\,\bar{\boldsymbol{F}}^e_{int} \tag{4.15}$$

$$\boldsymbol{K}^e = \boldsymbol{T}^T\,\bar{\boldsymbol{K}}^e_m\,\boldsymbol{T} + \boldsymbol{K}^e_g \tag{4.16}$$

4.1.3 Euler-Bernoulli Beam-Column Element

This two-node element is the simplest and most well-known BC formulation. The nodal displacement vector comprises three degrees of freedom per node, two translations and one rotation, in the global reference system:

$$\boldsymbol{U}_e = \begin{bmatrix} U_1 & V_1 & \Theta_1 & U_2 & V_2 & \Theta_2 \end{bmatrix}^T \tag{4.17}$$

In contrast, the nodal displacement vector in a basic reference system consists of three degrees of freedom in total:

$$\bar{\boldsymbol{U}}_e = \begin{bmatrix} \bar{U}_1 & \bar{\Theta}_1 & \bar{\Theta}_2 \end{bmatrix}^T \tag{4.18}$$

The traditional interpolation functions consist of linear and Hermitian cubic polynomials to approximate the axial and transverse displacement field, respectively. The adoption of Her-

mitian interpolation functions allows continuity in the transverse displacements and rotations over the entire element and between elements. The interpolation functions can be summarized as follow:

$$\boldsymbol{N}_e = \begin{bmatrix} 1-\dfrac{x}{l} & 0 & 0 & \dfrac{x}{l} & 0 & 0 \\ 0 & 1-\dfrac{3x^2}{l^2}+\dfrac{2x^3}{l^3} & x-\dfrac{2x^2}{l}+\dfrac{x^3}{l^2} & 0 & \dfrac{3x^2}{l^2}-\dfrac{2x^3}{l^3} & -\dfrac{x^2}{l}+\dfrac{x^3}{l^2} \end{bmatrix} \tag{4.19}$$

From the previous interpolation functions, the strain-displacement matrix in a basic reference system can be evaluated as:

$$\bar{\boldsymbol{B}} = \begin{bmatrix} \dfrac{1}{l} & 0 & 0 \\ 0 & -\dfrac{4}{l}+\dfrac{6x}{l^2} & -\dfrac{2}{l}+\dfrac{6x}{l^2} \end{bmatrix} \tag{4.20}$$

The transformation matrix from global to basic coordinates can be assessed as:

$$\boldsymbol{T} = \begin{bmatrix} -\cos(\alpha) & -\sin(\alpha) & 0 & \cos(\alpha) & \sin(\alpha) & 0 \\ -\dfrac{\sin(\alpha)}{l} & \dfrac{\cos(\alpha)}{l} & 1 & \dfrac{\sin(\alpha)}{l} & -\dfrac{\cos(\alpha)}{l} & 0 \\ -\dfrac{\sin(\alpha)}{l} & \dfrac{\cos(\alpha)}{l} & 0 & \dfrac{\sin(\alpha)}{l} & -\dfrac{\cos(\alpha)}{l} & 1 \end{bmatrix} \tag{4.21}$$

Despite of evaluating the integrals in Eq. (4.6) by numerical integration, a set of closed-form expressions of the material and geometric stiffness matrices can be obtained in a local reference system as a preliminary validation of the adopted numerical integration scheme. Each fibre stress and tangent modulus variations are assumed constant along the element. With the aim of building closed-form expressions, the terms of the section stiffness matrix are rewritten as follows:

$$\boldsymbol{D}_T = \begin{bmatrix} \sum E_k\, A_k & -\sum E_k\, A_k\, y_k \\ -\sum E_k\, A_k\, y_k & \sum E_k\, A_k\, y_k^2 \end{bmatrix} = \begin{bmatrix} D_{T_{11}} & D_{T_{12}} \\ D_{T_{12}} & D_{T_{22}} \end{bmatrix} \tag{4.22}$$

By adopting the previous notation and carrying out the integrations, the tangent stiffness matrix can be evaluated in terms of its material and geometric matrices with reference to the

local coordinate system as:

$$\tilde{\boldsymbol{K}}_m^e = \begin{bmatrix} \frac{D_{T_{11}}}{l} & 0 & \frac{D_{T_{12}}}{l} & -\frac{D_{T_{11}}}{l} & 0 & -\frac{D_{T_{12}}}{l} \\ 0 & \frac{12D_{T_{22}}}{l^3} & \frac{6D_{T_{22}}}{l^2} & 0 & -\frac{12D_{T_{22}}}{l^3} & \frac{6D_{T_{22}}}{l^2} \\ \frac{D_{T_{12}}}{l} & \frac{6D_{T_{22}}}{l^2} & \frac{4D_{T_{22}}}{l} & -\frac{D_{T_{12}}}{l} & -\frac{6D_{T_{22}}}{l^2} & \frac{2D_{T_{22}}}{l} \\ -\frac{D_{T_{11}}}{l} & 0 & -\frac{D_{T_{12}}}{l} & \frac{D_{T_{11}}}{l} & 0 & \frac{D_{T_{12}}}{l} \\ 0 & -\frac{12D_{T_{22}}}{l^3} & -\frac{6D_{T_{22}}}{l^2} & 0 & \frac{12D_{T_{22}}}{l^3} & \frac{6D_{T_{22}}}{l^2} \\ -\frac{D_{T_{12}}}{l} & \frac{6D_{T_{22}}}{l^2} & \frac{2D_{T_{22}}}{l} & \frac{D_{T_{12}}}{l} & -\frac{6D_{T_{22}}}{l^2} & \frac{4D_{T_{22}}}{l} \end{bmatrix} \tag{4.23}$$

$$\tilde{\boldsymbol{K}}_g^e = \begin{bmatrix} 0 & \frac{Q}{l} & 0 & 0 & -\frac{Q}{l} & 0 \\ \frac{Q}{l} & \frac{N}{l} & 0 & -\frac{Q}{l} & -\frac{N}{l} & 0 \\ 0 & 0 & 0 & 0 & 0 & 0 \\ 0 & -\frac{Q}{l} & 0 & 0 & \frac{Q}{l} & 0 \\ -\frac{Q}{l} & -\frac{N}{l} & 0 & \frac{Q}{l} & \frac{N}{l} & 0 \\ 0 & 0 & 0 & 0 & 0 & 0 \end{bmatrix} \tag{4.24}$$

Similarly, under the same previous assumption, the internal force vector can be calculated (in a local reference system) through:

$$\tilde{\boldsymbol{F}}_{int}^e = \begin{bmatrix} -\sum \sigma_k A_k \\ 0 \\ \sum \sigma_k A_k y_k \\ \sum \sigma_k A_k \\ 0 \\ -\sum \sigma_k A_k y_k \end{bmatrix} \tag{4.25}$$

4.1.4 Euler-Bernoulli Beam-Column Element with Enhanced-Strain Formulation

Despite of the simplicity of traditional Euler-Bernoulli BC formulations that facilities the assessment of internal force and tangent stiffness at the element level, a drawback concerning these elements is the weak satisfaction of equilibrium. In a nonlinear analysis, this feature could lead

to the need for extensively reduced element sizes to obtain accurate results (Calabrese et al. [179]). This can also be reflected in the difference between the section stress resultants and the internal basic forces (Pugh et al. [180], Almeida et al. [181]). The Euler-Bernoulli BC element proposed by Koutromanos and Bowers [147] can overcome these equilibrium-related issues by adopting a enhanced-strain formulation in the axial strain field and carrying out a modified integration rule. This formulation which does not consider distributed axial and transverse loads is describe bellow.

As mentioned before, the standard strain in displacement-based elements calculated in Eq. (4.5) is enhanced by adding a strain enhancement, $\check{\boldsymbol{\varepsilon}}$. As a result, the strain field is evaluated as:

$$\hat{\boldsymbol{\varepsilon}} = \bar{\boldsymbol{B}} \begin{bmatrix} \bar{U}_1 \\ \bar{\Theta}_1 \\ \bar{\Theta}_2 \end{bmatrix} + \check{\boldsymbol{\varepsilon}} \tag{4.26}$$

where $\bar{\boldsymbol{B}}$ is the same as Eq. (4.20). The strain enhancement is obtained as:

$$\check{\boldsymbol{\varepsilon}} = e \begin{bmatrix} 1 - \dfrac{2x}{l} \\ 0 \end{bmatrix} \tag{4.27}$$

where e is constant parameter determined iteratively at the element level. A requirement of the strain enhancement is that it should be orthogonal to the stress vector. This condition is satisfied through the following expression:

$$\int_l \check{\boldsymbol{\varepsilon}}^T \begin{bmatrix} N \\ M \end{bmatrix} dx = 0 \tag{4.28}$$

Before introducing the modified integration rule, a set of notations for the section force vector and section stiffness matrix are adopted to represent the value of these at the left and right end sections, they are:

$$\hat{\boldsymbol{\sigma}}|_{x=0} = \begin{bmatrix} N|_{x=0} \\ M|_{x=0} \end{bmatrix} \tag{4.29}$$

$$\hat{\boldsymbol{\sigma}}|_{x=l} = \begin{bmatrix} N|_{x=l} \\ M|_{x=l} \end{bmatrix} \tag{4.30}$$

$$\boldsymbol{D}_T|_{x=0} = \begin{bmatrix} D_{T_{11}}|_{x=0} & D_{T_{12}}|_{x=0} \\ D_{T_{12}}|_{x=0} & D_{T_{22}}|_{x=0} \end{bmatrix} \tag{4.31}$$

$$\boldsymbol{D}_T|_{x=l} = \begin{bmatrix} D_{T_{11}}|_{x=l} & D_{T_{12}}|_{x=l} \\ D_{T_{12}}|_{x=l} & D_{T_{22}}|_{x=l} \end{bmatrix} \tag{4.32}$$

As stated before, a modified integration rule is adopted to assess the internal force vector and material stiffness matrix associated to the basic reference system. This modification is performed by introducing a linear interpolation to approximate the generalized stress vector using the resultant stresses at both end sections. This approximation assumes the following form:

$$\hat{\boldsymbol{\sigma}} \approx \left(1 - \frac{x}{l}\right) \hat{\boldsymbol{\sigma}}|_{x=0} + \left(\frac{x}{l}\right) \hat{\boldsymbol{\sigma}}|_{x=l} \tag{4.33}$$

The adoption of the previous approximation yields the following expressions to assess the basic internal force and basic material tangent stiffness matrix:

$$\bar{\boldsymbol{F}}^e_{int} = \int_l \bar{\boldsymbol{B}}^T \left[\left(1 - \frac{x}{l}\right) \begin{bmatrix} N|_{x=0} \\ M|_{x=0} \end{bmatrix} + \left(\frac{x}{l}\right) \begin{bmatrix} N|_{x=l} \\ M|_{x=l} \end{bmatrix} \right] dx \tag{4.34}$$

$$\begin{aligned} \bar{\boldsymbol{K}}^e_m = \int_l \bar{\boldsymbol{B}}^T \Bigg[& \left(1 - \frac{x}{l}\right) \boldsymbol{D}_T|_{x=0} \left(\bar{\boldsymbol{B}}|_{x=0} + \left[1 - \frac{2x}{l} \right] \Bigg|_{x=0} \boldsymbol{B}_e \right) \\ & + \left(\frac{x}{l}\right) \boldsymbol{D}_T|_{x=l} \left(\bar{\boldsymbol{B}}|_{x=l} + \left[1 - \frac{2x}{l} \right] \Bigg|_{x=l} \boldsymbol{B}_e \right) \Bigg] dx \end{aligned} \tag{4.35}$$

where

$$\begin{aligned} \boldsymbol{B}_e &= \begin{bmatrix} B_{e\,1} & B_{e\,2} & B_{e\,3} \end{bmatrix} \\ B_{e\,1} &= \frac{D_{T_{11}}|_{x=l} - D_{T_{11}}|_{x=0}}{l \left(D_{T_{11}}|_{x=0} + D_{T_{11}}|_{x=l} \right)} \\ B_{e\,2} &= \frac{4\, D_{T_{12}}|_{x=0} + 2\, D_{T_{12}}|_{x=l}}{l \left(D_{T_{11}}|_{x=0} + D_{T_{11}}|_{x=l} \right)} \\ B_{e\,3} &= \frac{2\, D_{T_{12}}|_{x=0} + 4\, D_{T_{12}}|_{x=l}}{l \left(D_{T_{11}}|_{x=0} + D_{T_{11}}|_{x=l} \right)} \end{aligned} \tag{4.36}$$

A robust iterative process is performed to assess the element state determination. In this process, convergence is achieved when the axial force at both end sections of the BC element are almost equal. If this is not the case, an update of the parameter e is performed. By considering the current iteration as i, the following expression is employed:

$$e_{i+1} = e_i - \frac{N|_{x=0,\, e=e_i} - N|_{x=l,\, e=e_i}}{D_{T_{11}}|_{x=0,\, e=e_i} + D_{T_{11}}|_{x=l,\, e=e_i}} \tag{4.37}$$

The geometric tangent stiffens matrix of the element, can be evaluated using the same stiffness matrix used for the Traditional Euler-Bernoulli BC element shown in Eq. (4.24).

4.1.5 Timoshenko Beam-Column Element

Timoshenko beam theory, which is a first-order shear deformation theory, assumes a linear warping and a constant distortion to describe the section kinematics. In contrast to Euler-Bernoulli beam theory, Timoshenko theory does not enforce the normality assumption. As mentioned in section 4.1, a common numerical issue of displacement-based BC formulations is the proneness to shear locking. An alternative to overcome this issue is the adoption of BC formulations including nodeless or bubble degrees of freedom. In this section the methodology described by Feng et al. [171] for a locking-free Timoshenko fiber BC element based on the enhanced interpolations developed by Ehrlich and Armero [182] is adopted. However, the axial-bending and shear behaviour are considered to be decoupled.

The element consist of two nodes comprising three degrees of freedom per node and one nodeless or bubble rotation, Θ_3, at the middle of the element in a global reference system. The nodal displacement vector is:

$$\boldsymbol{U}_e = \begin{bmatrix} U_1 & V_1 & \Theta_1 & U_2 & V_2 & \Theta_2 & \Theta_3 \end{bmatrix}^T \tag{4.38}$$

In a basic coordinate system, the degrees of freedom are:

$$\bar{\boldsymbol{U}}_e = \begin{bmatrix} \bar{U}_1 & \bar{\Theta}_1 & \bar{\Theta}_2 & \bar{\Theta}_3 \end{bmatrix}^T \tag{4.39}$$

The shape functions of the element involves mixed interpolations of the transverse and rotations fields. The use of these interpolations allows the description of a constant shear strain distribution and linear distribution of the curvature deformation. These interpolations

are defined as:

$$\boldsymbol{N}_e = \begin{bmatrix} 1-\frac{x}{l} & 0 & 0 & \frac{x}{l} & 0 & 0 & 0 \\ 0 & 1-\frac{x}{l} & \frac{x}{2}\left(1-\frac{x}{l}\right) & 0 & \frac{x}{l} & -\frac{x}{2}\left(1-\frac{x}{l}\right) & \frac{2x}{3}\left(\frac{2x}{l}-1\right)\left(1-\frac{x}{l}\right) \\ 0 & 0 & 1-\frac{x}{l} & 0 & 0 & \frac{x}{l} & \frac{4x}{l}\left(1-\frac{x}{l}\right) \end{bmatrix} \tag{4.40}$$

Based on the previous interpolation functions, the strain-displacement matrix in terms of the basic coordinate system can be obtained as:

$$\bar{\boldsymbol{B}} = \begin{bmatrix} \frac{1}{l} & 0 & 0 & 0 \\ 0 & -\frac{1}{l} & \frac{1}{l} & \frac{4l-8x}{l^2} \\ 0 & -\frac{1}{2} & -\frac{1}{2} & -\frac{2}{3} \end{bmatrix} \tag{4.41}$$

And the transformation matrix from global to basic reference system is given by:

$$\boldsymbol{T} = \begin{bmatrix} -\cos(\alpha) & -\sin(\alpha) & 0 & \cos(\alpha) & \sin(\alpha) & 0 & 0 \\ -\frac{\sin(\alpha)}{l} & \frac{\cos(\alpha)}{l} & 1 & \frac{\sin(\alpha)}{l} & -\frac{\cos(\alpha)}{l} & 0 & 0 \\ -\frac{\sin(\alpha)}{l} & \frac{\cos(\alpha)}{l} & 0 & \frac{\sin(\alpha)}{l} & -\frac{\cos(\alpha)}{l} & 1 & 0 \\ 0 & 0 & 0 & 0 & 0 & 0 & 1 \end{bmatrix} \tag{4.42}$$

As in the case of the traditional Euler-Bernoulli element, a set closed-form expressions can be developed to verify the numerical integrations. For convenience, the section stiffness matrix terms are rewritten as:

$$\boldsymbol{D}_T = \begin{bmatrix} \sum E_k\, A_k & -\sum E_k\, A_k\, y_k & 0 \\ -\sum E_k\, A_k\, y_k & \sum E_k\, A_k\, y_k^2 & 0 \\ 0 & 0 & \frac{\partial Q(\gamma)}{\partial \gamma} \end{bmatrix} = \begin{bmatrix} D_{T_{11}} & D_{T_{12}} & 0 \\ D_{T_{12}} & D_{T_{22}} & 0 \\ 0 & 0 & D_{T_{33}} \end{bmatrix} \tag{4.43}$$

Following the same assumption adopted in subsection 4.1.3, the expressions for the tangent

material and geometric stiffness matrix are given by:

$$\tilde{\boldsymbol{K}}_m^e = \begin{bmatrix} \frac{D_{T_{11}}}{l} & 0 & \frac{D_{T_{12}}}{l} & -\frac{D_{T_{11}}}{l} & 0 & -\frac{D_{T_{12}}}{l} & 0 \\ 0 & \frac{D_{T_{33}}}{l} & \frac{D_{T_{33}}}{2} & 0 & -\frac{D_{T_{33}}}{l} & \frac{D_{T_{33}}}{2} & \frac{2D_{T_{33}}}{3} \\ \frac{D_{T_{12}}}{l} & \frac{D_{T_{33}}}{2} & \frac{lD_{T_{33}}}{4} + \frac{D_{T_{22}}}{l} & -\frac{D_{T_{12}}}{l} & -\frac{D_{T_{33}}}{2} & \frac{lD_{T_{33}}}{4} - \frac{D_{T_{22}}}{l} & \frac{lD_{T_{33}}}{3} \\ -\frac{D_{T_{11}}}{l} & 0 & -\frac{D_{T_{12}}}{l} & \frac{D_{T_{11}}}{l} & 0 & \frac{D_{T_{12}}}{l} & 0 \\ 0 & -\frac{D_{T_{33}}}{l} & -\frac{D_{T_{33}}}{2} & 0 & \frac{D_{T_{33}}}{l} & -\frac{D_{T_{33}}}{2} & -\frac{2D_{T_{33}}}{3} \\ -\frac{D_{T_{12}}}{l} & \frac{D_{T_{33}}}{2} & \frac{lD_{T_{33}}}{4} - \frac{D_{T_{22}}}{l} & \frac{D_{T_{12}}}{l} & -\frac{D_{T_{33}}}{2} & \frac{lD_{T_{33}}}{4} + \frac{D_{T_{22}}}{l} & \frac{lD_{T_{33}}}{3} \\ 0 & \frac{2D_{T_{33}}}{3} & \frac{lD_{T_{33}}}{3} & 0 & -\frac{2D_{T_{33}}}{3} & \frac{lD_{T_{33}}}{3} & \frac{16D_{T_{22}}}{3l} + \frac{4D_{T_{33}}}{9} \end{bmatrix} \tag{4.44}$$

$$\tilde{\boldsymbol{K}}_g^e = \begin{bmatrix} 0 & \frac{Q}{l} & 0 & 0 & -\frac{Q}{l} & 0 & 0 \\ \frac{Q}{l} & \frac{N}{l} & 0 & -\frac{Q}{l} & -\frac{N}{l} & 0 & 0 \\ 0 & 0 & 0 & 0 & 0 & 0 & 0 \\ 0 & -\frac{Q}{l} & 0 & 0 & \frac{Q}{l} & 0 & 0 \\ -\frac{Q}{l} & -\frac{N}{l} & 0 & \frac{Q}{l} & \frac{N}{l} & 0 & 0 \\ 0 & 0 & 0 & 0 & 0 & 0 & 0 \\ 0 & 0 & 0 & 0 & 0 & 0 & 0 \end{bmatrix} \tag{4.45}$$

In the same way, under the same assumption made in subsection 4.1.3, the internal force vector in the local coordinate system can be evaluated as:

$$\tilde{\boldsymbol{F}}_{int}^e = \begin{bmatrix} -\sum \sigma_k A_k \\ -Q(\gamma) \\ \sum \sigma_k A_k y_k - \frac{Q(\gamma)\, l}{2} \\ \sum \sigma_k A_k \\ Q(\gamma) \\ -\sum \sigma_k A_k y_k - \frac{Q(\gamma)\, l}{2} \\ \frac{2\, Q(\gamma)\, l}{3} \end{bmatrix} \tag{4.46}$$

4.1.6 Timoshenko Beam-Column Element with Enhanced-Strain Formulation

As stated in subsection 4.1.4, displacement-based BC formulations only satisfy the equilibrium weakly or in average sense leading to the use of fine FE meshes. For this reason, Feng and Wu [173] extended the enhanced-strain formulation proposed by Koutromanos and Bowers [147] for Euler-Bernoulli fiber BC elements to the Timoshenko fibre BC formulation developed by Feng et al. [171] described in the previous section.

In this case, a strain enhancement, $\check{\boldsymbol{\varepsilon}}$, is added to the standard strain in Eq. (4.5). Hence, the final strain field is evaluated as:

$$\hat{\boldsymbol{\varepsilon}} = \bar{\boldsymbol{B}} \begin{bmatrix} \bar{U}_1 \\ \bar{\Theta}_1 \\ \bar{\Theta}_2 \\ \bar{\Theta}_3 \end{bmatrix} + \check{\boldsymbol{\varepsilon}} \tag{4.47}$$

where $\bar{\boldsymbol{B}}$ is given by Eq. (4.41). The proposed strain enhancement for the Timoshenko element is expressed as:

$$\check{\boldsymbol{\varepsilon}} = e \begin{bmatrix} 1 - \dfrac{2x}{l} \\ 0 \\ 0 \end{bmatrix} \tag{4.48}$$

where e is the parameter that determines the element state determination. Similarly, the stress vector of the Timoshenko element should be orthogonal to the strain enhancement. This requirement can be expressed as:

$$\int_l \check{\boldsymbol{\varepsilon}}^T \begin{bmatrix} N \\ M \\ Q \end{bmatrix} dx = 0 \tag{4.49}$$

The section force vector and section stiffness matrix at the end sections following the next notation are:

$$\hat{\boldsymbol{\sigma}}|_{x=0} = \begin{bmatrix} N|_{x=0} \\ M|_{x=0} \\ Q \end{bmatrix} \tag{4.50}$$

$$\hat{\boldsymbol{\sigma}}|_{x=l} = \begin{bmatrix} N|_{x=l} \\ M|_{x=l} \\ Q \end{bmatrix} \tag{4.51}$$

$$\boldsymbol{D}_T|_{x=0} = \begin{bmatrix} D_{T_{11}}|_{x=0} & D_{T_{12}}|_{x=0} & 0 \\ D_{T_{12}}|_{x=0} & D_{T_{22}}|_{x=0} & 0 \\ 0 & 0 & D_{T_{33}}|_{x=0} \end{bmatrix} \tag{4.52}$$

$$\boldsymbol{D}_T|_{x=l} = \begin{bmatrix} D_{T_{11}}|_{x=l} & D_{T_{12}}|_{x=l} & 0 \\ D_{T_{12}}|_{x=l} & D_{T_{22}}|_{x=l} & 0 \\ 0 & 0 & D_{T_{33}}|_{x=l} \end{bmatrix} \tag{4.53}$$

Similarly, the material stiffness matrix and internal force vector in the basic coordinate system are evaluated using a modified integration scheme. In this integration, the generalized stress vector is assessed by interpolating linearly the force values at the end sections. The same expression in Eq. (4.33) can be used for this case. As a result, the following expressions are obtained:

$$\bar{\boldsymbol{F}}^e_{int} = \int_l \bar{\boldsymbol{B}}^T \left[\left(1 - \frac{x}{l}\right) \begin{bmatrix} N|_{x=0} \\ M|_{x=0} \\ Q \end{bmatrix} + \left(\frac{x}{l}\right) \begin{bmatrix} N|_{x=l} \\ M|_{x=l} \\ Q \end{bmatrix} \right] dx \tag{4.54}$$

$$\begin{aligned} \bar{\boldsymbol{K}}^e_m = \int_l \bar{\boldsymbol{B}}^T \Bigg[& \left(1 - \frac{x}{l}\right) \boldsymbol{D}_T|_{x=0} \left(\bar{\boldsymbol{B}}|_{x=0} + \begin{bmatrix} 1 - \dfrac{2x}{l} \\ 0 \\ 0 \end{bmatrix} \Bigg|_{x=0} \boldsymbol{B}_e \right) \\ & + \left(\frac{x}{l}\right) \boldsymbol{D}_T|_{x=l} \left(\bar{\boldsymbol{B}}|_{x=l} + \begin{bmatrix} 1 - \dfrac{2x}{l} \\ 0 \\ 0 \end{bmatrix} \Bigg|_{x=l} \boldsymbol{B}_e \right) \Bigg] dx \end{aligned} \tag{4.55}$$

In which

$$
\begin{aligned}
\boldsymbol{B}_e &= \begin{bmatrix} B_{e\,1} & B_{e\,2} & B_{e\,3} & B_{e\,4} \end{bmatrix} \\
B_{e\,1} &= \frac{D_{T\,11}|_{x=l} - D_{T\,11}|_{x=0}}{l\,(D_{T\,11}|_{x=0} + D_{T\,11}|_{x=l})} \\
B_{e\,2} &= \frac{D_{T\,12}|_{x=0} - D_{T\,12}|_{x=l}}{l\,(D_{T\,11}|_{x=0} + D_{T\,11}|_{x=l})} \\
B_{e\,3} &= \frac{D_{T\,12}|_{x=l} - D_{T\,12}|_{x=0}}{l\,(D_{T\,11}|_{x=0} + D_{T\,11}|_{x=l})} \\
B_{e\,4} &= -4\,\frac{D_{T\,12}|_{x=l} + D_{T\,12}|_{x=0}}{l\,(D_{T\,11}|_{x=0} + D_{T\,11}|_{x=l})}
\end{aligned}
\tag{4.56}
$$

Similar to subsection 4.1.4, an iterative process has to be performed to assess the parameter e. Eq. (4.37) is used to update the value of the parameter. With regard to the assessment of the geometric stiffness matrix of the element, the matrix array in Eq. (4.45) can be used.

4.2 Material Constitutive Laws

In the assessment of the short-term response of timber BC elements, the uniaxial bilinear stress-strain relationship proposed by Bazan [183] and further improved by Buchanan [184] has been widely used (Schober et al. [185], Blank and Frangi [186] and Cao and Sebastian [187]). This model includes a linear softening branch for compression and a brittle response in tension. Other phenomenological relationships such as cubic (Lam and Oh [188]), quartic (Cao and Sebastian [187]), power law (Tomasi et al. [189]), and rational (Ehrhart et al. [190]) expressions have also been used to describe the compressive behaviour parallel to the grain. In this section, the rational algebraic expression proposed by Glos [191] is adopted following previous works (see section 2.2).

On the other hand, the long-term response of timber BC elements has been assessed by a wide variety of uniaxial rheological models as described in section 2.3. Among models incorporating the hygroscopic and mechano-sorptive creep behavior of wood, the model proposed by Toratti [66] is adopted herein as it is a well-know constitutive model.

4.2.1 Inelastic Model

The stress-strain relationship proposed by Glos [191] to describe the short-term compressive behaviour of wood is shown in Fig. 4.2. The expressions describing this relationship are:

$$\sigma\left(\varepsilon_c\right) = \frac{\varepsilon_c + \alpha_1 \varepsilon_c^n}{\alpha_2 + \alpha_3 \varepsilon_c + \alpha_4 \varepsilon_c^n} \quad for \;\; -\varepsilon_{cu} \leq \varepsilon_c \leq 0 \tag{4.57}$$

$$\alpha_1 = \frac{f_{cy}\,\alpha_0}{(n-1)\,E_t\,\varepsilon_{c_0}^{(n-1)}\left(1 - \dfrac{f_{cy}}{f_{cu}}\right)} \quad for \;\; f_{cy} \leq f_{cu} - 1 \;\; (MPa) \tag{4.58a}$$

$$\alpha_2 = \frac{1}{E_t} \tag{4.58b}$$

$$\alpha_3 = \frac{1}{f_{cu}} - \frac{n}{(n-1)\,E_t\,\varepsilon_{c_0}} \tag{4.58c}$$

$$\alpha_4 = \frac{\alpha_1}{f_{cy}} \tag{4.58d}$$

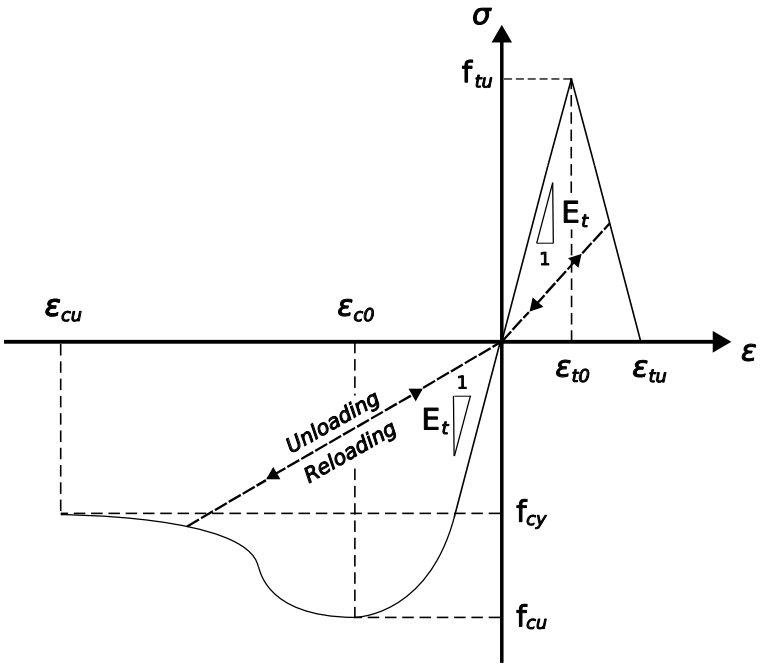


Figure 4.2: Stress-strain curve for wood.

where f_{cu}, ε_{c0}, f_{cy}, ε_{cu} and E_t are the compressive strength, strain at maximum strength, residual strength, residual strain, and initial elastic modulus of the timber material, respectively. Parameters α_0 and n are used to set up the slope at maximum strength, and the shape of the curve.

Regarding the short-term behaviour under tension, a linear-elastic relationship followed by a linear softening is considered to describe a quasi-brittle response. From Fig. 4.2, f_{tu} is the tensile strength attained at tensile strain ε_{t0}, and ε_{tu} is the ultimate strain.

After reaching the peak strength of the material, a softening stress-strain law is adopted in the stress-strain curve to describe the complex fracture process in the failure region. In order to avoid localization issues and consequently spurious mesh dependency in the assessment of global responses at the peak load and post-peak regime (Bažant et al. [192], Jirásek and Bauer [193]), a material parameter defined as the fracture energy is introduced to represent coherently the dissipated energy involved in the fracture process by means of a smeared equivalent response (Blank and Frangi [186], Blank et al. [194]). Other types of localization limiters, also called regularization techniques, can be reviewed in Jirasek and Bazant [195]).

Furthermore, a damage model with no plastic strains for unloading and reloading conditions is considered for the timber material as also assumed by previous researches like Khorsandnia et al. [55].

4.2.2 Rheological Model

The rheological constitutive relation based on the model developed by Toratti [66] and Svensson and Toratti [68] consists of several elements arranged in series comprising different deformation mechanisms as shown in Fig. 4.3. This constitutive model allows to decompose the total strain, ε, in different additive terms as follows:

$$\varepsilon = \varepsilon^{el} + \varepsilon^{hyg} + \sum_{i=1}^{p} \varepsilon_i^{ve} + \varepsilon^{ms,rec} + \varepsilon^{ms,irr} \tag{4.59}$$

where ε^{el} is the elastic strain, ε^{hyg} the hygroexpansion strain, ε_i^{ve} the ith element of the viscoelastic strain, $\varepsilon^{ms,rec}$ the recoverable mechano-sorptive strain, $\varepsilon^{ms,irr}$ the irrecoverable mechano-sorptive strain, and p is the number of viscoelastic Kelvin elements.

The hygroscopic nature of wood induces variations in the modulus elasticity with the variation of the moisture content. As a result, the elastic strain depends on stress changes as well as variations in Young's modulus. This dependency can be expressed as follows:

$$\varepsilon^{el} = \int_{t_0}^{t} J_0(m(\tau)) \frac{d\sigma(\tau)}{d\tau} d\tau + \int_{t_0}^{t} \sigma(\tau) \frac{dJ_0(m(\tau))}{dm(\tau)} dm(\tau) \tag{4.60}$$

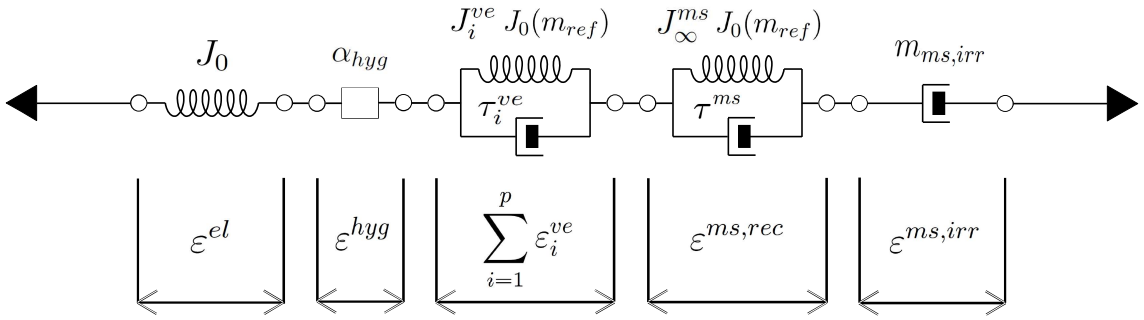


Figure 4.3: Toratti's rheological constitutive model.

where J_0, σ, m, t_0, t and τ are the elastic compliance, total stress, moisture content, initial time, final time and current time of analysis, respectively.

The hygroexpansion strain is assumed to be dependent on the total strain. Besides, timber shrinks and swells more under compression loads than under tension solicitations. This deformation mechanism can be written as:

$$\varepsilon^{hyg} = \int_{t_0}^{t} \alpha_{hyg}\, dm(\tau) = \int_{t_0}^{t} (\alpha_{hyg} - b\,\varepsilon(\tau))\, dm(\tau) \tag{4.61}$$

where α_{hyg} and b are material parameters determined experimentally.

The basic or normal viscoelastic strain under sustained loads and constant moisture conditions is represented by an arrange of Kelvin-Voigt bodies assembled in series as depicted in Fig. 4.3. The pure creep strains are given by:

$$\varepsilon^{ve} = \int_{t_0}^{t} J_{ve}(t,\tau)) \, \frac{d\sigma(\tau)}{d\tau}\, d\tau \tag{4.62}$$

where J_{ve} is the delayed component of the creep compliance J_{cr} defined as follows:

$$J_{cr}(t,\tau,m) = J_0(m) + J_{ve}(t,\tau) \tag{4.63}$$

$$J_{ve}(t,\tau) = J_0(m_{ref}) \sum_{i=1}^{p} J_i^{ve} \left(1 - exp\left(-\frac{t-\tau}{\tau_i^{ve}}\right)\right) \tag{4.64}$$

where τ_i^{ve} and J_i^{ve} are material parameters calibrated in experimental campaigns and m_{ref} is the reference moisture content. Replacing Eq. (4.64) into Eq. (4.62) results in:

$$\varepsilon^{ve} = J_0(m_{ref}) \sum_{i=1}^{p} \int_{t_0}^{t} J_i^{ve} \left(1 - exp\left(-\frac{t-\tau}{\tau_i^{ve}}\right)\right) \frac{d\sigma(\tau)}{d\tau}\, d\tau \tag{4.65}$$

Similarly, the recoverable mechano-sorptive strain consists of Kelvin-Voigt bodies arranged in series. However, the dashpots in these bodies are denominated as mechano-sorptive dashpots

as their flow rate is driven by the absolute value of the moisture increment, $|dm|$. This strain can be calculated by

$$\varepsilon^{ms,rec} = J_0(m_{ref}) \int_{t_0}^{t} J_{\infty}^{ms} \left(1 - exp\left(-c \int_{\tau}^{t} |dm|\right)\right) \frac{d\sigma(\tau)}{d\tau} \, d\tau \tag{4.66}$$

where c and J_{∞}^{ms} are material parameters fitted to experimental data.

The irrecoverable mechano-sorptive strain, can be modelled by means of an irrecoverable mechano-sorptive dashpot as follows:

$$\varepsilon^{ms,irr} = \int_{t_0}^{t} m_{ms,irr} \, \sigma(\tau) \, |M(\tau)| \, d\tau \tag{4.67}$$

where $m_{ms,irr}$ and $M(\tau)$ are the irrecoverable coefficient and the moisture levels exceeding the previous threshold during the preceding load history.

In what follows, Eq. (4.60), Eq. (4.61), Eq. (4.65), Eq. (4.66) and Eq. (4.67) are solved using the numerical integration schemes employed by Fortino et al. [14], Khorsandnia et al. [28] and Granello [196]. These integration schemes were included in the numerical framework. Consequently, the time is discretized in several time steps, Δt, comprising the discrete time instants t_n and t_{n+1} related to the previous time and current time in which quantities such as strains, stresses and the moisture content are known and unknown, respectively.

The elastic strain can be assessed by either of the following expressions:

$$\varepsilon_{n+1}^{el} = \varepsilon_{n}^{el} + J_0(m_n) \, \Delta\sigma + \sigma_n \left(J_0(m_{n+1}) - J_0(m_n)\right) \tag{4.68}$$

$$\varepsilon_{n+1}^{el} = J_0(m_0) \left(\sigma_n - \sigma_0\right) + J_0(m_n - m_0) \, \sigma_0 \tag{4.69}$$

The hygroexpansion strain can be evaluated by:

$$\varepsilon_{n+1}^{hyg} = \varepsilon_{n}^{hyg} + \left(\alpha_{hyg} - b \, \varepsilon_n\right) \Delta m \tag{4.70}$$

The *ith* viscoelastic strain value at the end of the time step can be calculated by either of the following equations:

$$\varepsilon_{i,n+1}^{ve} = \varepsilon_{i,n}^{ve} + \left(1 - \Lambda_i^{ve}\right) \Delta\sigma \, J_0(m_{ref}) \, J_i^{ve} + \left(1 - \Upsilon_i^{ve}\right) \left(\sigma_n \, J_0(m_{ref}) \, J_i^{ve} - \varepsilon_{i,n}^{ve}\right) \tag{4.71}$$

$$\varepsilon_{i,n+1}^{ve} = \Upsilon_i^{ve}\,\varepsilon_{i,n}^{ve} + J_0(m_{ref})\,J_i^{ve}\,(1-\Upsilon_i^{ve})\,(\sigma_n - \sigma_0) \tag{4.72}$$

where

$$\Lambda_i^{ve} = \frac{\tau_i^{ve}}{\Delta t}\left(1 - exp\left(-\frac{\Delta t}{\tau_i^{ve}}\right)\right) \tag{4.73}$$

$$\Upsilon_i^{ve} = exp\left(-\frac{\Delta t}{\tau_i^{ve}}\right) \tag{4.74}$$

In similar way, the recoverable mechano-sorptive strain can be obtained by either of the following expressions:

$$\varepsilon_{n+1}^{ms,rec} = \varepsilon_n^{ms,rec} + (1-\Lambda^{ms})\,\Delta\sigma\,J_0(m_{ref})\,J_\infty^{ms} + (1-\Upsilon^{ms})\,(\sigma_n\,J_0(m_{ref})\,J_\infty^{ms} - \varepsilon_n^{ms,rec}) \tag{4.75}$$

$$\varepsilon_{n+1}^{ms,rec} = \Upsilon^{ms}\,\varepsilon_n^{ms,rec} + J_0(m_{ref})\,J_\infty^{ms}\,(1-\Upsilon^{ms})\,(\sigma_n - \sigma_0) \tag{4.76}$$

where

$$\Lambda^{ms} = \frac{\tau^{ms}}{|\Delta m|}\left(1 - exp\left(-\frac{|\Delta m|}{\tau^{ms}}\right)\right) \tag{4.77}$$

$$\Upsilon^{ms} = exp\left(-\frac{|\Delta m|}{\tau^{ms}}\right) \tag{4.78}$$

Finally, the irrecoverable mechano-sorptive strain is given by:

$$\varepsilon_{n+1}^{ms,irr} = \varepsilon_n^{ms,irr} + m_{ms,irr}\,\sigma_n\,|\Delta M| \tag{4.79}$$

4.3 Incremental Finite Element Equations

The tangent stiffness matrices and internal force vectors of the BC elements presented in subsection 4.1.3, subsection 4.1.4, subsection 4.1.5 and subsection 4.1.6 are evaluated by means of a numerical integration scheme. In order to set up the incremental equilibrium equations of the whole structure, the stiffness matrices and force vectors from all the elements comprising the structure must be transformed to the global coordinate system to be assembled. The resulting incremental equations are nonlinear, therefore an incremental-iterative procedure is needed to solve them. For a specific step of the short- or long-term analysis, the resultant linearized system of equations can be written as (Bathe [178]):

$$\left(\boldsymbol{K}_m^i + \boldsymbol{K}_g^i\right) \Delta \boldsymbol{U}^{i+1} = \Delta\lambda^{i+1} \boldsymbol{F}_{ref} + \boldsymbol{F}_{ext}^i - \boldsymbol{F}_{int}^i \tag{4.80}$$

where the superscript i indicates the ith iteration, $\Delta\lambda$ is the increment of the load factor , $\boldsymbol{K}_m$ and $\boldsymbol{K}_g$ are the material and geometric stiffness matrices of the structure, respectively, $\boldsymbol{F}_{ext}$ and $\boldsymbol{F}_{int}$ are the force vectors acting on the structure due to external loads and internal stresses, respectively, $\boldsymbol{F}_{ref}$ is the reference vector of the external loads, and $\Delta\boldsymbol{U}$ is the increment of the displacement vector. Generally, Eq. (4.80) is compacted as follows (McGuire et al. [177]):

$$\boldsymbol{K}^i \, \Delta \boldsymbol{U}^{i+1} = \Delta\lambda^{i+1} \boldsymbol{F}_{ref} + \boldsymbol{R}^i \tag{4.81}$$

where $\boldsymbol{K}$ and $\boldsymbol{R}$ are the total tangent stiffness matrix and unbalanced force vector, respectively. It should be noticed that the iterative load ratio can be considered as an additional unknown in the system of equations defined in Eq. (4.81) making it underdetermined. Therefore, an additional equation imposed by a constraint condition is required to solve the system. In this numerical framework, the well-known load and displacement control strategy (Batoz and Dhatt [197]) as well as the cylindrical arc-length method (de Souza Neto and Feng [198]) adopting non-consistent scheme are considered to evaluate the load ratio.

Regarding the global convergence criteria, the well-known residual force, displacement and energy norm criterion were adopted here. It should be mentioned that the choice of criterion depends on the type of nonlinear response addressed. More details can be found in De Borst et al. [175].

In the solution process of incremental nonlinear equations in Eq. (4.81), traditional Newton-Raphson solution algorithms are adopted. However, if the tangent stiffness matrix presents sharp variations during the analysis, convergence could not be attained leading to the abortion

of the ongoing analysis. Therefore, more robust nonlinear solution algorithms are also examined in this thesis. The description and performance of these methods is described in the next chapter.

4.4 Validation Examples

A set of analytical and numerical benchmark results were selected to validate the implemented framework in performing material non-linear analysis, considering inelastic and rheological behaviour, and including geometric non-linear effects. In the following examples, the different implemented BC elements described in subsection 4.1.3, subsection 4.1.4, subsection 4.1.5 and subsection 4.1.6 are going to be abbreviated and referred as EB (Euler-Bernoulli formulation), ENH EB (Euler-Bernoulli enhanced formulation), TB (Timoshenko formulation) and ENH TB (Timoshenko enhanced formulation), respectively.

4.4.1 Cantilever Beam with an End Moment

This analysis case was chosen to validate the capability of the numerical framework to deal with large displacements involving highly deformed configurations. This nonlinear problem consists of a elastic cantilever beam subjected to a moment at its free end, as shown in Fig. 4.4, leading to a state of pure bending and constant curvature under each equilibrium configuration meaning that shear effects are null. Several authors (Epstein and Murray [199], Bathe and Bolourchi [200], Gummadi and Palazotto [201], Nanakorn and Vu [202]) studied this problem to test the accuracy of different FE formulations in the large displacement regime. In this nonlinear analysis, The four BC element formulations described in section 4.1 are used to assess the load-deflection curves or equilibrium paths related to this problem. The results are then compared with the analytical results used by Epstein and Murray [199]).

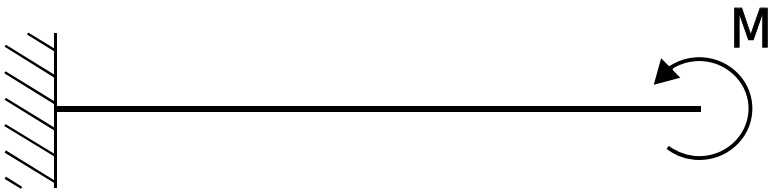


Figure 4.4: Cantilever beam under an end moment.

During the analysis, a mesh of eight elements in conjunction with a discretization of ten fibres along the section were employed for all the BC element formulations. In Fig. 4.5, the results are presented in their normalized versions using the beam length for the vertical and

horizontal displacements, and the analytical moment at a complete circle fold for the applied load. From the results, it can be observed that the numerical and analytical results are almost identical. Moreover, the TB element and its enhanced version (ENH TB) attest their shear locking-free nature under large displacements. In this analysis, the results are independent from the geometric and material properties chosen as long as a slender cantilever is modelled.

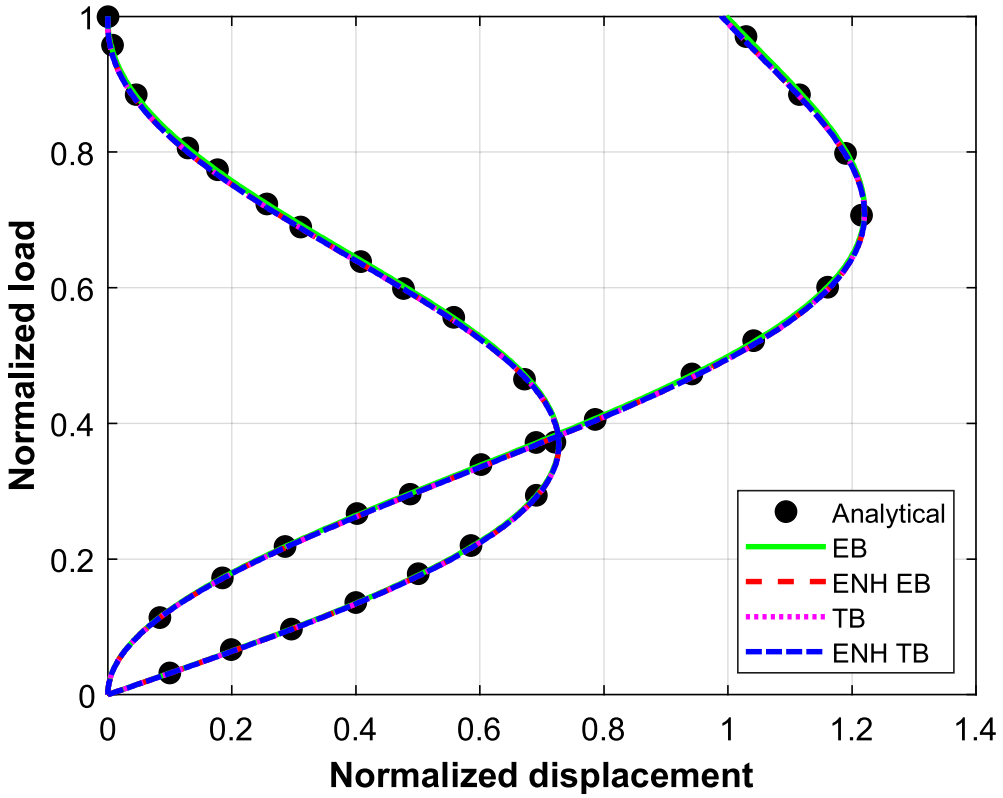


Figure 4.5: Normalized load-displacement curves for a cantilever beam with an end moment.

4.4.2 Lee's Frame

In order to test the capability of the implemented framework to address large displacements with inelastic behaviour, the well-known Lee's frame (Lee et al. [203]) depicted in Fig. 4.6 is analysed here. This L-shaped pin-supported frame consists of two members in which one of its members is subjected to a transverse load. The elastic and elasto-plastic response of this frame was widely analysed by several authors to validate their proposed FE formulations (Cichoń [204], Hsiao et al. [205], Waszczyszyn and Janus-Michalska [206], Park and Lee [207], Battini [208]). Regarding the geometric and material properties, the following data was considered: a member length, $L = 120\,cm$, area, $A = 6\,cm^2$, inertia, $I = 2\,cm^4$, elastic modulus, $E = 720\,tonf/cm^2$, yielding stress, $\sigma_y = 10.44\,tonf/cm^2$, and elasto-plastic tangent modulus, $E_T = 72\,tonf/cm^2$.

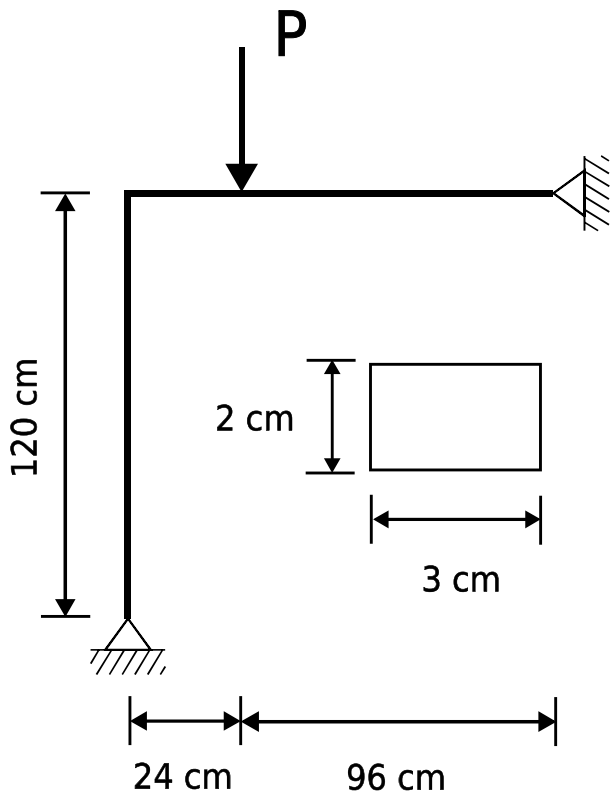


Figure 4.6: Lee's frame.

In this numerical analysis, the four BC element formulations described in section 4.1 are compared against the validated numerical results obtained by Battini [208]. In the assessment of the nonlinear elastic response of the frame, ten elements in total were employed. In contrast, a total of twenty elements were used for the inelastic case. Regarding the section discretization, 20 fibres along the depth were considered for both cases. In the case of the Timoshenko beam formulations, a shear correction factor of one and a shear modulus equal to the elastic modulus were adopted to prevent the shear effects. Fig. 4.7 and Fig. 4.8, show a very good agreement between the different formulations and the benchmark results for the vertical and horizontal displacements in the elastic and elasto-plastic regimes.

It should be mentioned that this example also allowed the validation of the implemented cylindrical arc-length method as the frame's response exhibits a snap-back behaviour.

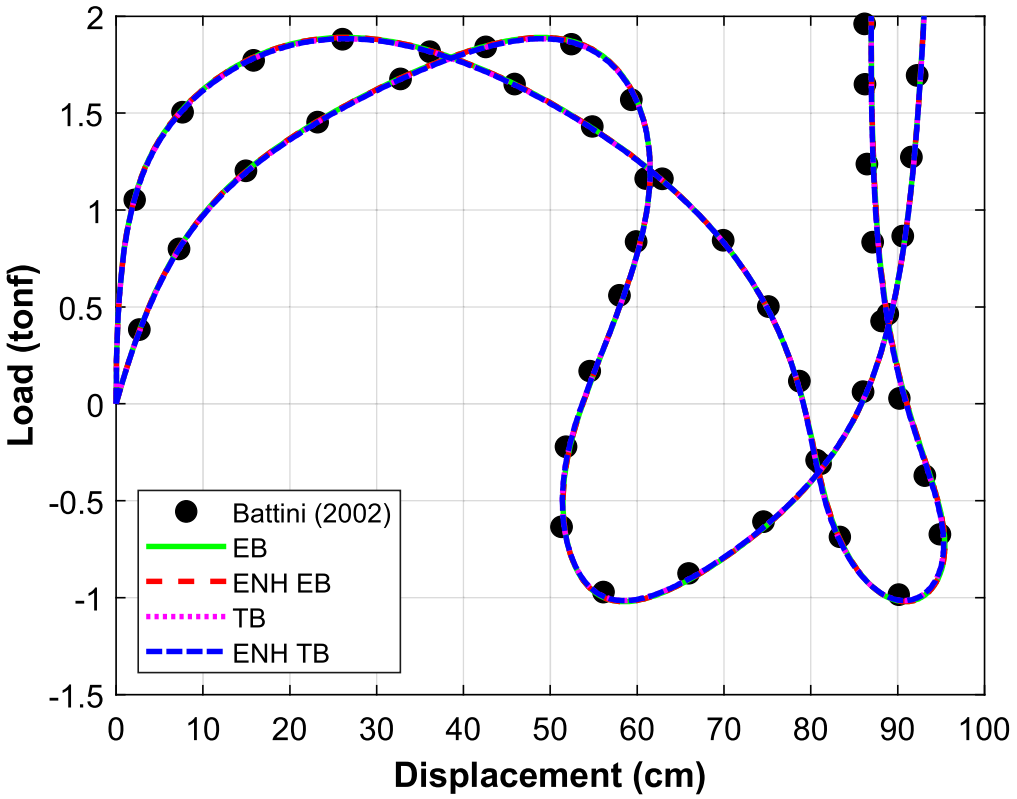


Figure 4.7: Load-displacement curves for Lee's frame in the elastic range.

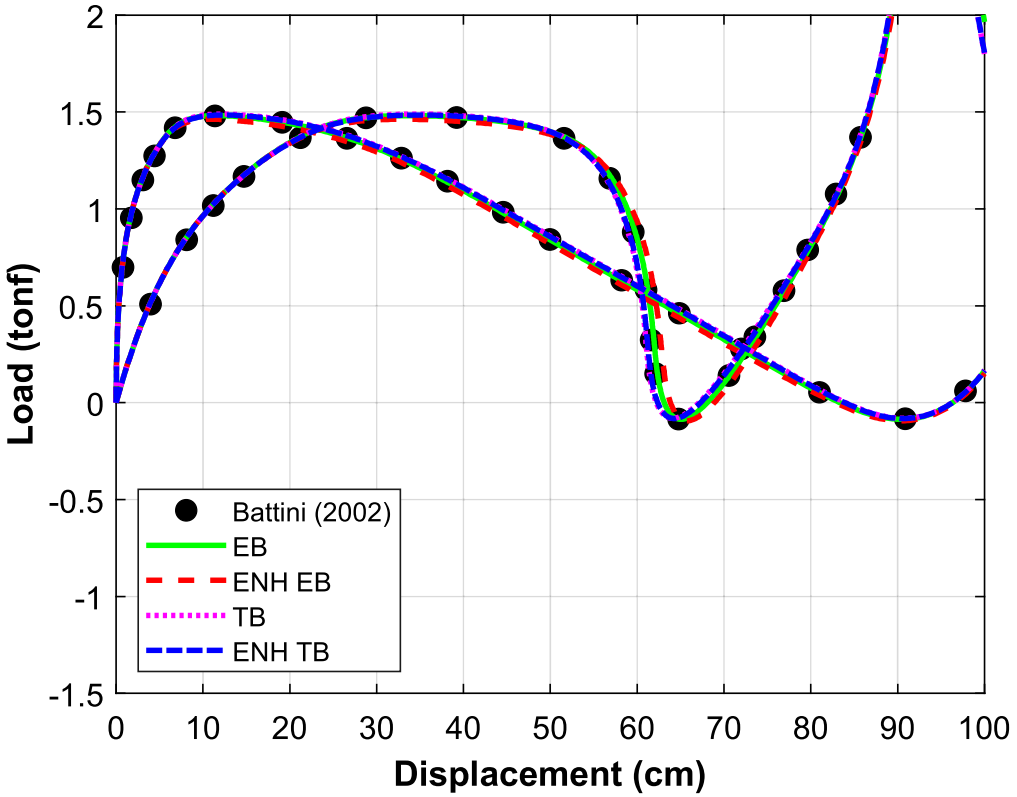


Figure 4.8: Load-displacement curves for Lee's frame in the inelastic range.

4.4.3 Williams Toggle Frame

This simple frame structure consist of two sloped members fixed at its two ends and subjected to a vertical load at its rigid joint as shown in Fig. 4.9. This nonlinear problem was first addressed by Williams [209] and then analysed by several authors (Jennings [210], Wood and Zienkiewicz [211], Chan [212], Tin-Loi and Misa [213], Teh and Clarke [214]) with the aim of testing the accuracy of different FE formulations in dealing with geometrical nonlinearities and snap-through behaviour. In this analysis case, the toggle frame proposed by Tang et al. [215] considering a hollow section with elastic behaviour is analysed as shear effects and large displacements are taken into account simultaneously. As is shown in Fig. 4.10, the problem is studied using BC elements following the Euler–Bernoulli and Timoshenko beam hypothesis.

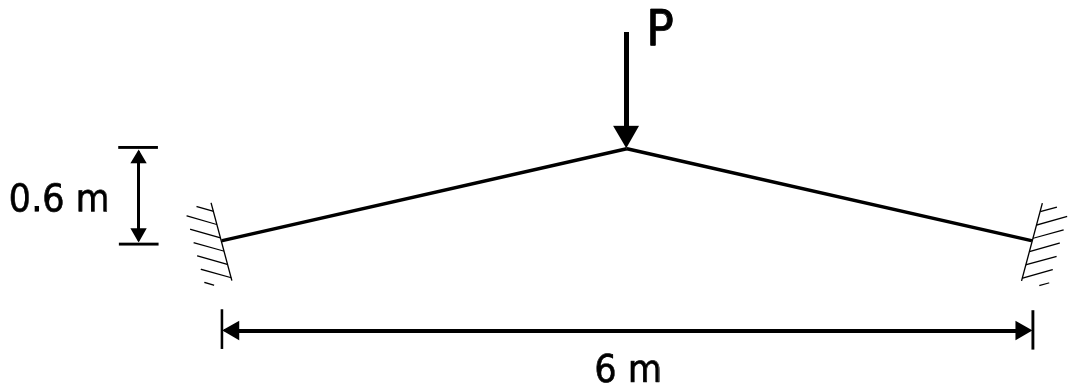


Figure 4.9: Williams toggle frame.

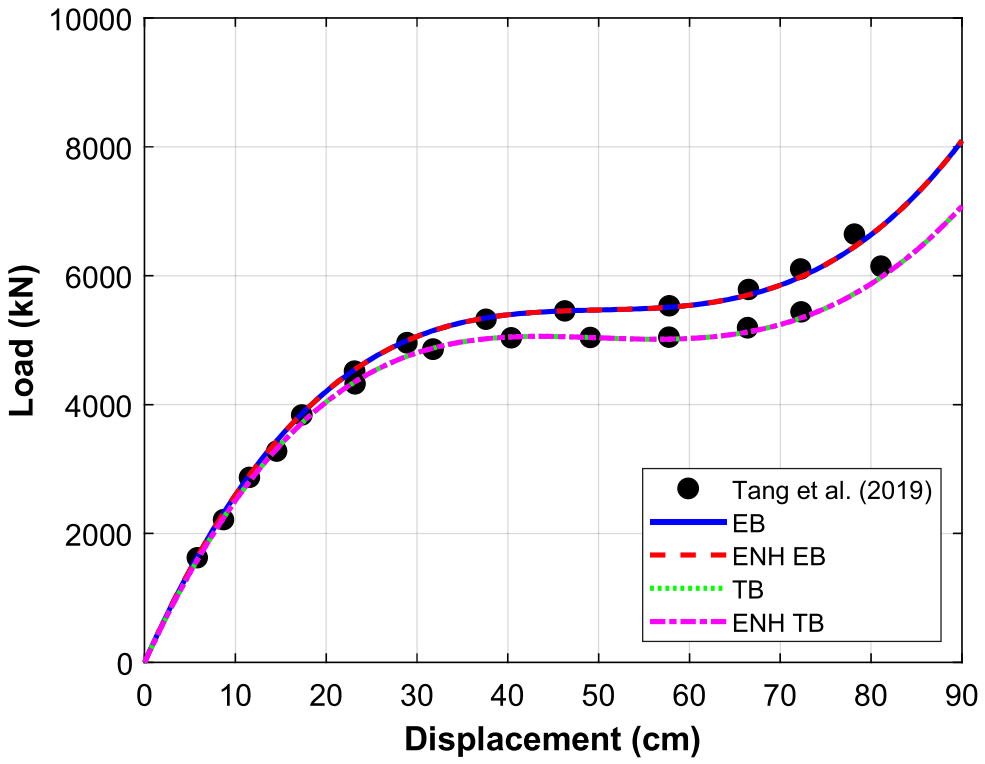


Figure 4.10: Load-displacement curves for Williams toggle frame with and without shear effects.

In this nonlinear analysis the following geometric and material properties were employed: horizontal projection length, $L = 6\,m$, vertical projection height, $h = 0.6\,m$, area, $A = 41.98\,cm^2$, inertia, $I = 6490.28\,cm^4$, elastic modulus, $E = 20000\,kN/cm^2$, shear modulus, $G = 7692.31\,kN/cm^2$, and shear correction factor of 0.5. In the modelling of the toggle frame, a mesh discretization of eight elements was employed along with fifteen fibres over the section depth. From Fig. 4.10, a good agreement between the benchmark and obtained numerical results is observed in both scenarios with and without shear effects. It should be mentioned that the BC formulations employed by Tang et al. [215] includes the shallow arch effect and a consistent axial displacement function (Tang et al. [216]). This fact could explain the slight differences in the large displacement regime.

4.4.4 Four-Point Bending Tests

A set of simply-supported timber beams subjected to 4-point bending tests as shown in Fig. 4.11 were analysed with the aim of predicting the ultimate loading capacity of these timber beams. The five beams analysed here were experimentally tested by Buell and Saadatmanesh [217], Kim and Harries [218] and Gentile et al. [219] and labelled as Beam B1, DF-1, FS0, HS0-1 and HS0-7. From their dimensions and experimental results, these beams can be categorized as flexure-nominated. As a result, the traditional Euler–Bernoulli BC element (BE) and its enhanced formulation (ENH-EB) are used in this analysis by considering only material nonlinearity. In this assessment, the short-term behavior of timber comprises a compressive branch governed by the stress-strain relationship proposed by Glos [191] and a brittle behavior in tension. A summary of the material properties and beam dimensions used in the numerical analysis is provided in Table 4.1. Regarding the dimensions, w and h are the width and height of the beam, L is the length of the beam, and b is the span of the flexure zone.

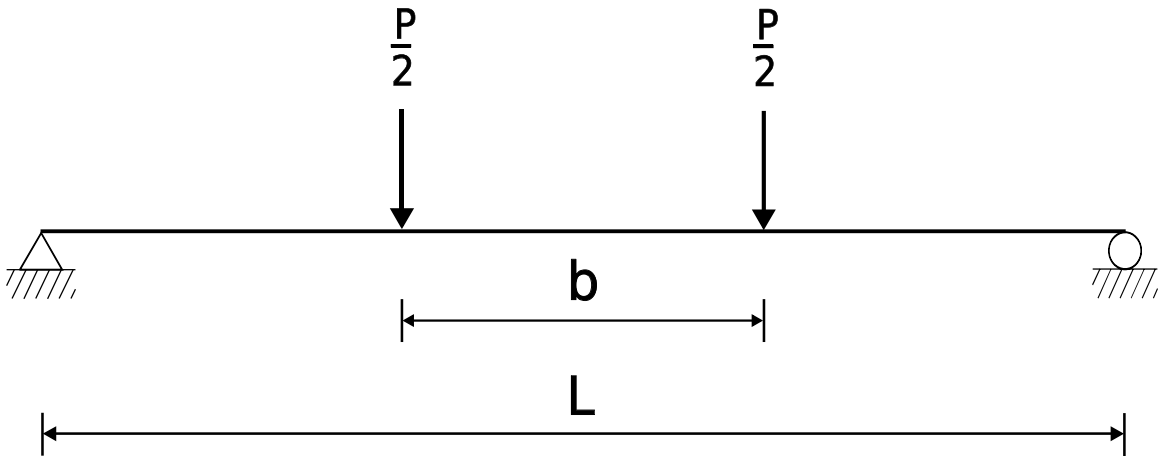


Figure 4.11: Four-point bending failure test.

Beam Label	E (GPa)	f_{cu} (MPa)	f_{tu} (MPa)	ε_{c_0}	$h \times w$ (mm x mm)	b (mm)	L (mm)
B1	13.2	34.0	34.0	0.004	300 x 100	1820	7620
DF1	12.8	43.0	43.0	0.004	138 x 38	430	2440
FS0	11.9	25.0	25.0	0.008	600 x 200	1300	10000
HS0-1	7.0	18.8	18.8	0.004	300 x 100	600	4000
HS0-7	14.7	44.0	44.0	0.008	300 x 100	600	4000

Table 4.1: Material property data and dimensions of the timber beams.

In Figs. 4.12 to 4.16 the obtained numerical results are contrasted with the measured experimental results and the numerical results determined by Khorsandnia and Crews [37]. These authors developed three-dimensional (3D) and two-dimensional (2D) continuum-based FE models along with one-dimensional (1D) force-based fiber beam-column elements to assess the ultimate loading capacity of the tested timber beams.

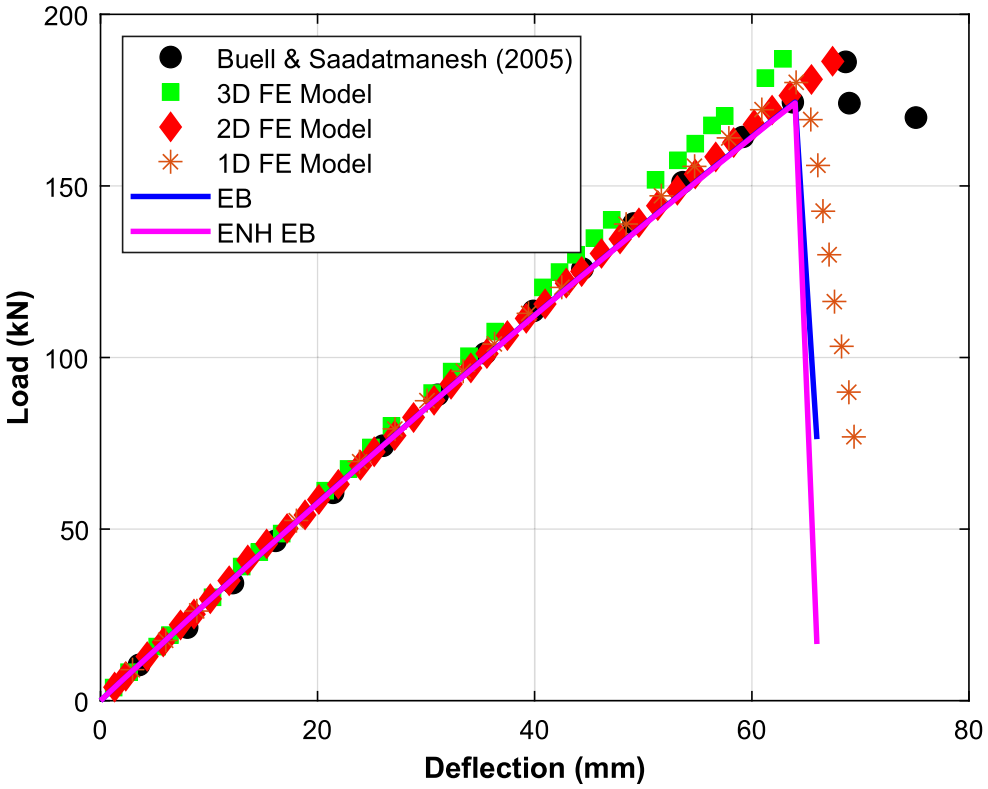


Figure 4.12: Load–deflection curves of timber beam B1.

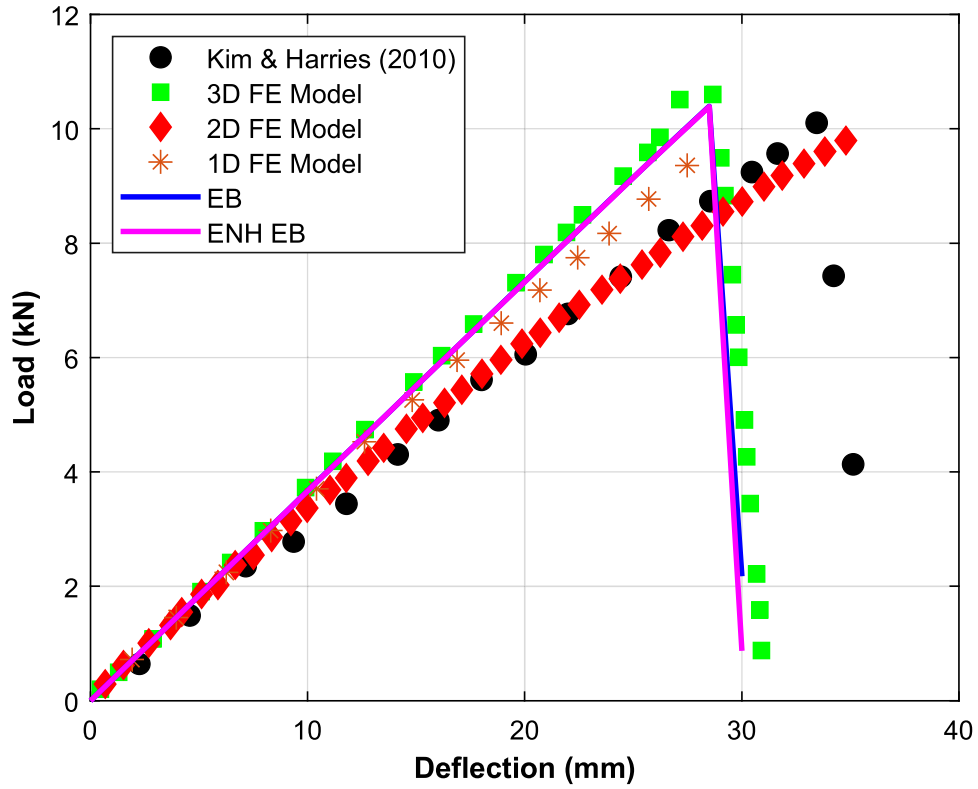


Figure 4.13: Load–deflection curves of timber beam DF1.

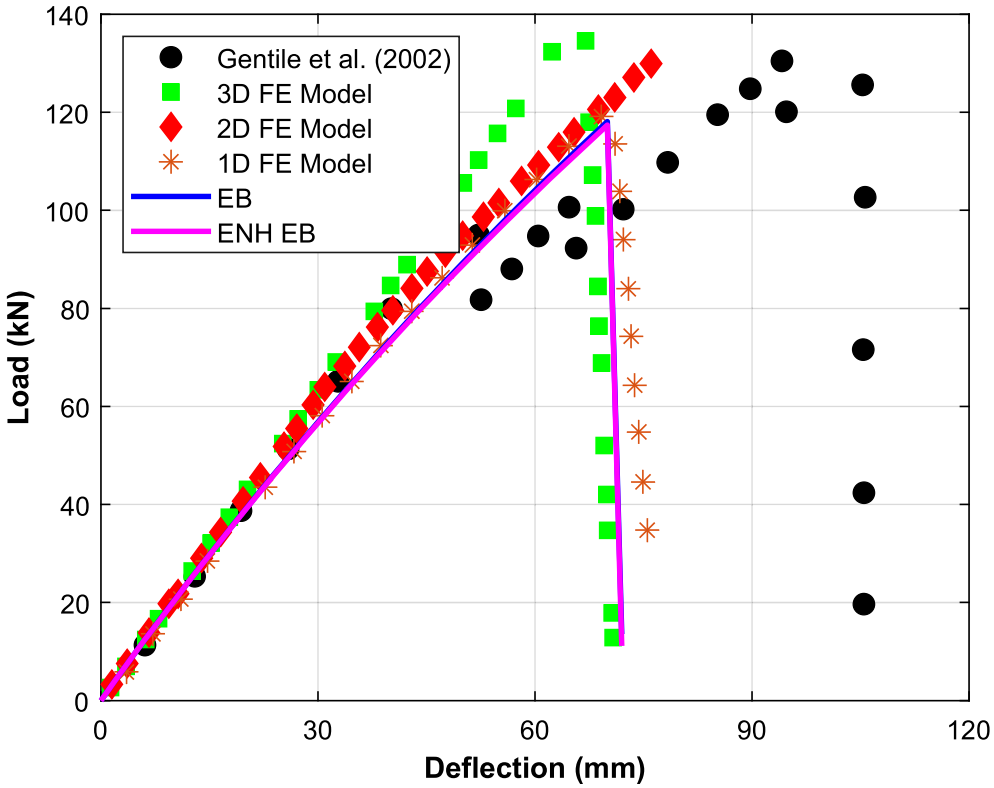


Figure 4.14: Load–deflection curves of timber beam FS0.

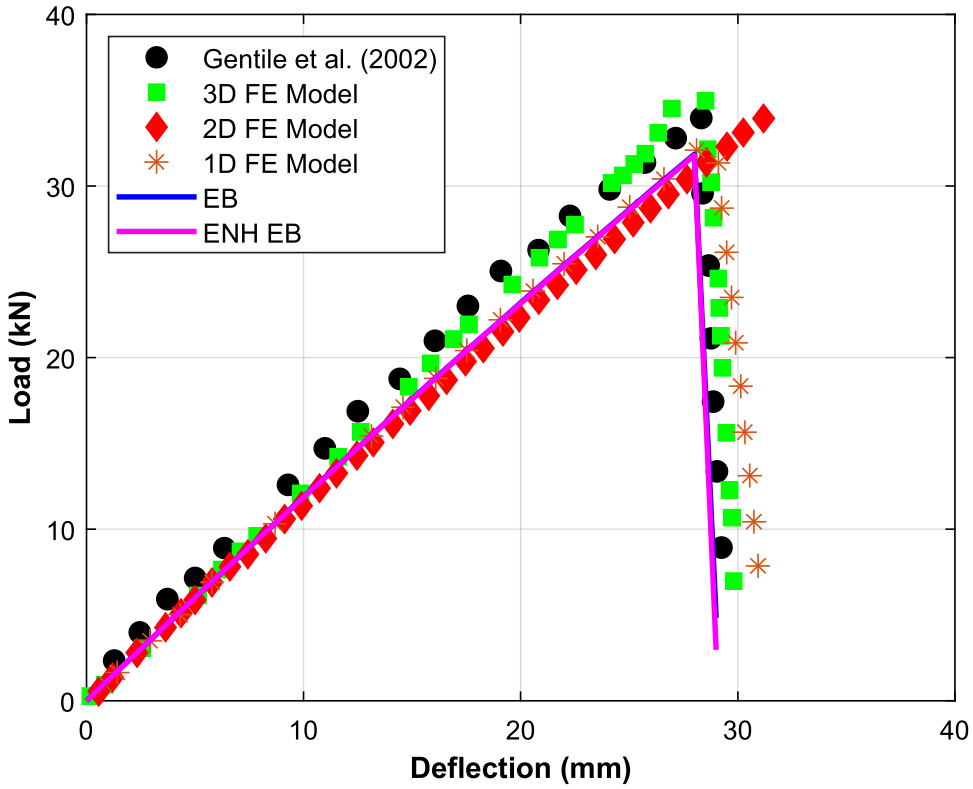


Figure 4.15: Load–deflection curves of timber beam HS0-1.

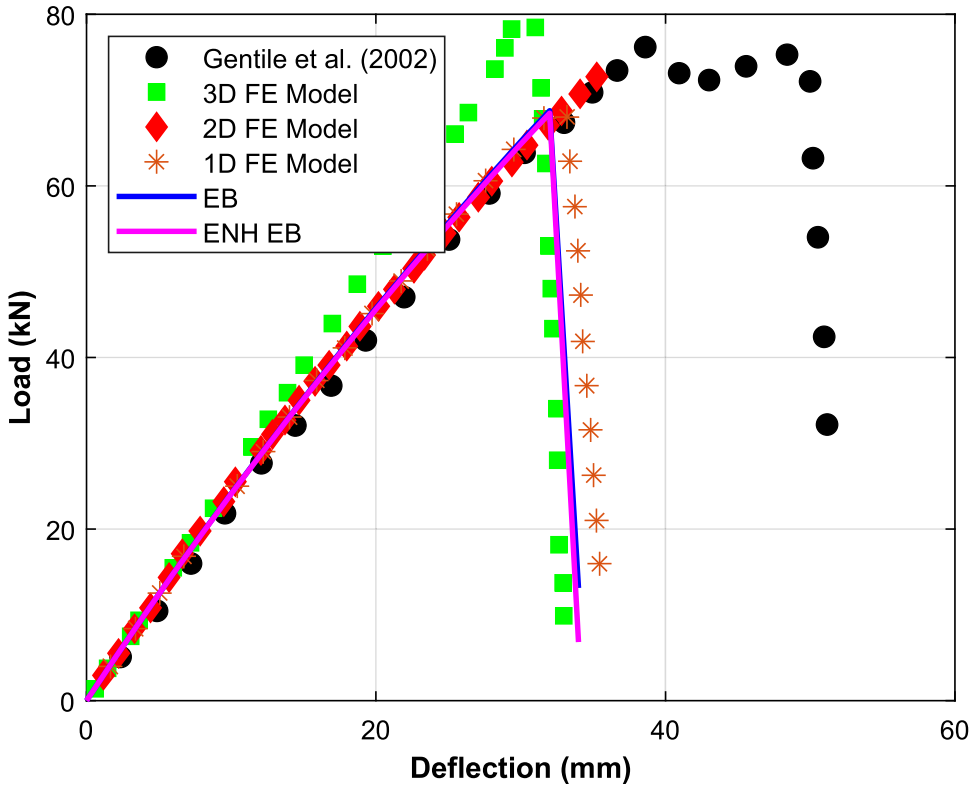


Figure 4.16: Load–deflection curves of timber beam HS0-7.

After performing a convergence analysis and modelling half of the structure due to its symmetry, four elements along the element length and thirty-five fibers for the section depth were determined to be sufficient in the assessment of the ultimate bearing capacity of the timber beams. In contrast, the benchmark 1D model employed only one element but with more than twenty five integration points. From the figures, it can be observed that the obtained numerical results are in good agreement with the benchmark numerical results attesting the computational efficiency of the analysis framework. Despite of obtaining almost equal results with both BC formulations, the numerical performance of these formulations differ in the assessment of the section and internal forces within the elements (local responses). These differences are depicted in Appendix B.

4.4.5 Viscoelastic Cantilever Beam

The viscoelastic cantilever beam illustrated in Fig. 4.17 studied first by Vaz and Caire [220] and then by Dadgar-Rad and Firouzi [221] is analysed here to validate the implemented numerical framework in addressing long-term effects and large displacements simultaneously. In this nonlinear analysis, a standard linear or three-parameter solid model was used to represent the rheological behaviour by adopting the Kelvin-Voigt representation.

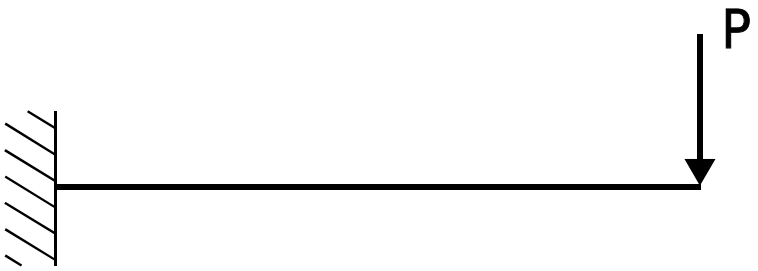


Figure 4.17: Cantilever beam under an end point load.

The viscoelastic beam is analysed based on the following non-dimensional parameters: the non-dimensional time normalized with respect to the characteristic relaxation time, $\bar{t}$, the non-dimensional relaxation modulus (NRM) which is the ratio of the impact to the asymptotic relaxation modulus, $\bar{\alpha}_R$, and the non-dimensional load normalized with respect to the ratio of the impact bending stiffness to the square of the beam length, $\bar{P}$. The adopted values of these non-dimensional parameters for the analysis are: sustained load time period, $\bar{t} \in [0, 10]$, unloading time period, $\bar{t} \in]10, 20]$, concentrated vertical load at the free end, $\bar{P} = 10$, and relation modulus, $\bar{\alpha}_R = 0.25$, 0.50 and 0.75. The variation of the beam deflection at the free end over time is normalized with respect the length of the beam.

In order to validate the numerical framework in handling with long-term effects, the cantilever beam is first analysed by considering only viscoelastic behaviour without large displacement effects. The long-term deflection of this beam with linear geometric effects can be evaluated analytically following the Correspondence Principle (Flügge [222]). As shear and inelastic deformations are not considered, the traditional Euler-Bernoulli BC element was employed to assess the long-term response. A total of ten elements along the longitudinal direction and fifteen fibers were used in this analysis. From Fig. 4.18, it can be noticed that the numerical and analytical results are almost identical.

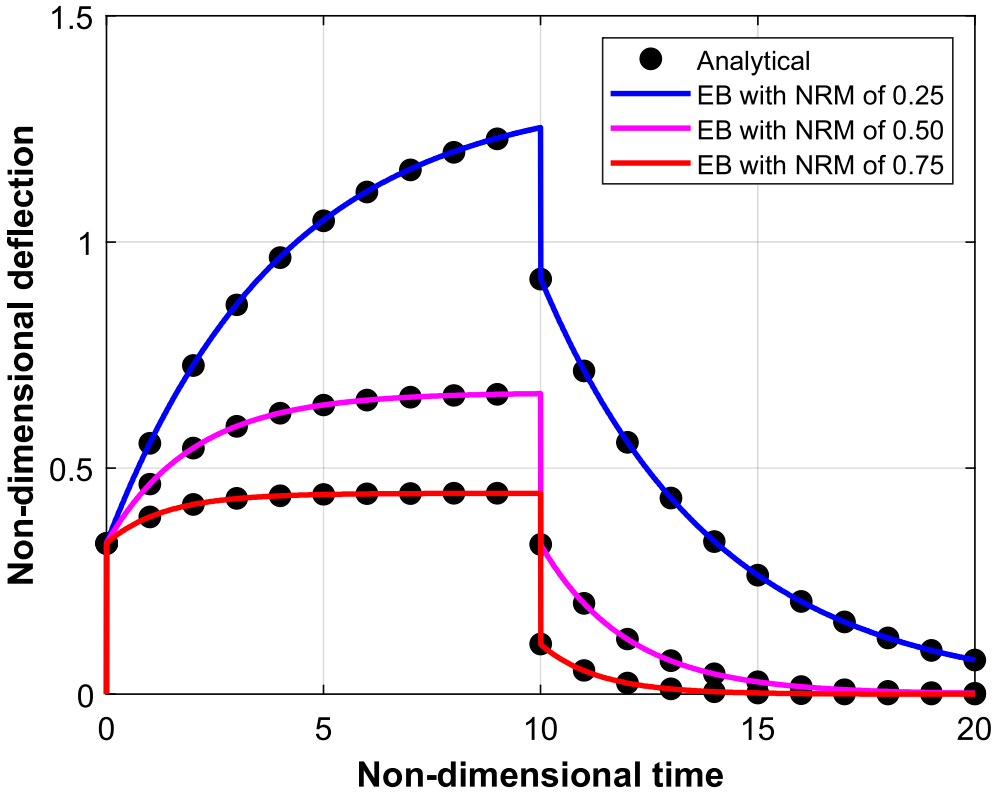


Figure 4.18: Time-dependent deflection by considering linear geometric effects.

In the case of incorporating nonlinear geometric effects and using the same mesh and fiber discretization than the previous linear case, the obtained variation over time of the deflection is shown in Fig. 4.19. From the figure, it can be observed that the numerical results are in close agreement with the benchmark results obtained by Vaz and Caire [220].

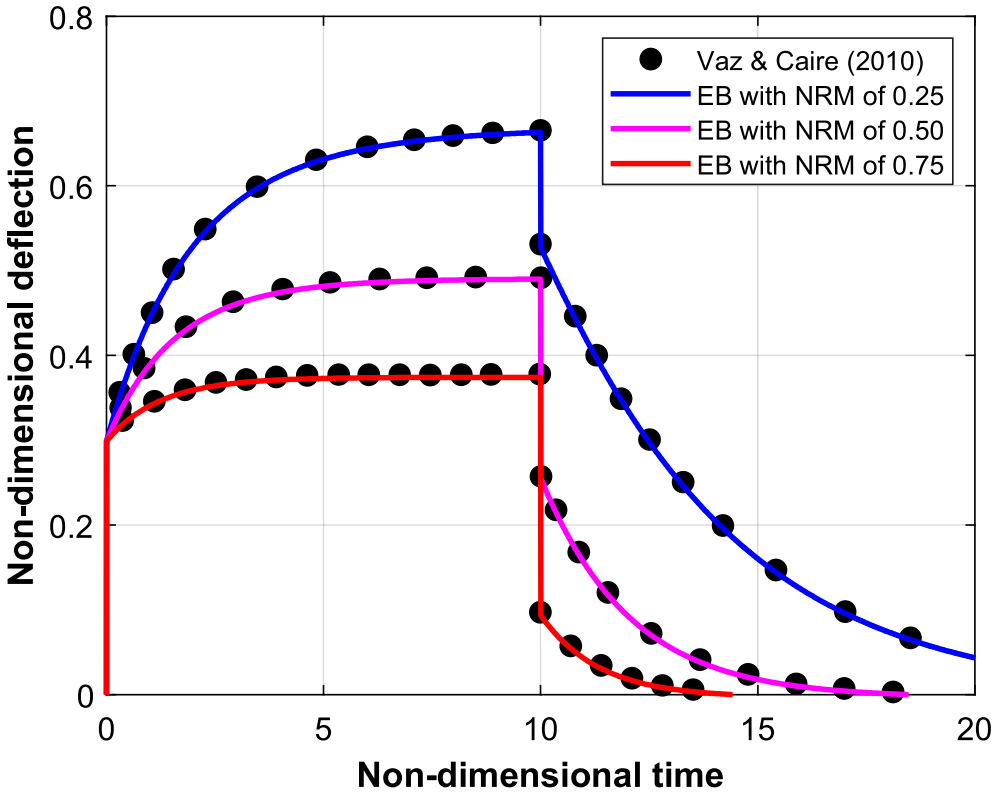


Figure 4.19: Time-dependent deflection by considering nonlinear geometric effects.

4.4.6 Hoyle's test

The purpose of this analysis case is to validate the capability of the implemented framework in performing a hygro-mechanical analysis by means of carrying out a coupled finite element-finite difference analysis. Hoyle et al. [223] performed a series of long-term test on simply supported timber beams subjected to three equally spaced vertical loads of the same value (Fig. 4.20) and cyclic humidity variations represented by square waves. The two groups of samples that were bearing a constant maximum stress level of 13.1 MPa are analysed here. One group was subjected to weakly cycles of relative humidity (RH) raging between 40% and 90% whereas the other was exposed to daily cycles raging between 40% and 88%. The dimensions of the specimens were a square section of 89 mm x 89 mm and a span length of 800 mm. Regarding the material parameters, the values summarized in Table 3.5 were used for the moisture transfer analysis whereas the ones in Table 4.2 were adopted for the rheological model described in subsection 4.2.2.

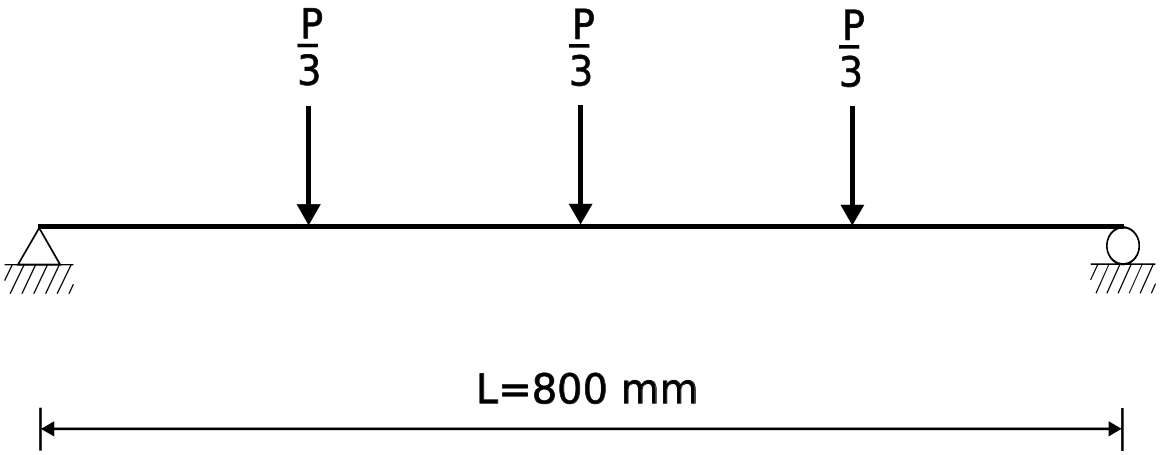


Figure 4.20: Five-point bending creep test.

Timber Materials Parameters					
τ_1^{ve}	0.01 days	J_1^{ve}	0.0686	c	2.5
τ_2^{ve}	0.1 days	J_2^{ve}	-0.0056	J_∞^{ms}	0.7
τ_3^{ve}	1. days	J_3^{ve}	0.0716	α^{hyg}	0.00625
τ_4^{ve}	10 days	J_4^{ve}	0.0404	b	1.3
τ_5^{ve}	100 days	J_5^{ve}	0.2073	m_{ref}	0.2
τ_6^{ve}	5000 days	J_6^{ve}	0.5503	E_0	14.0 GPa

Table 4.2: Adopted material parameters for Toratti's rheological model.

In this long-term analysis, the large displacement effects are disregarded and the traditional Euler-Bernoulli BC element was employed as shear and inelastic deformations were not expected. A discretization of twenty BC elements along with four hundred fibres over the section were used to perform the analysis. The adopted dense fibre discretization allowed the capture of the moisture variation over the height and width of the section. The obtained results are compared with the previously assessed by Schänzlin [63] and Fragiacomo [86] as shown in Fig. 4.21 and Fig. 4.22. From the results, it can be noticed that the obtained results are in close agreement with the numerical benchmark results.

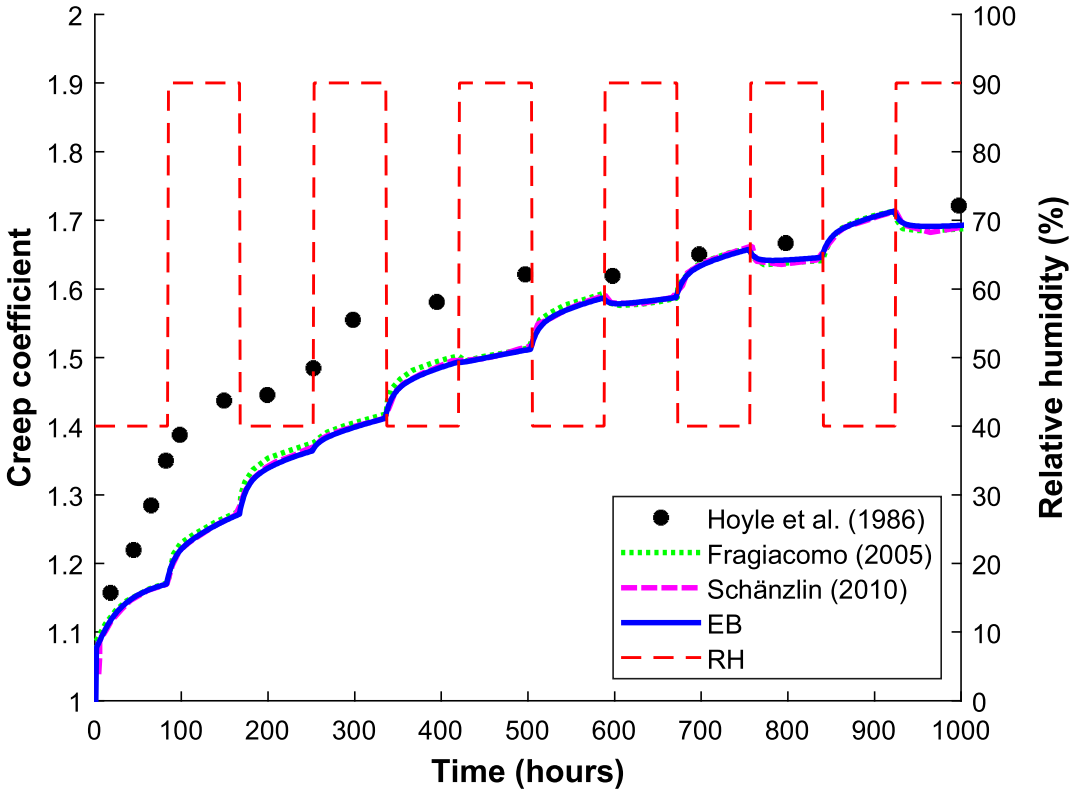


Figure 4.21: Variation over time of the creep coefficient for weekly humidity cycles.

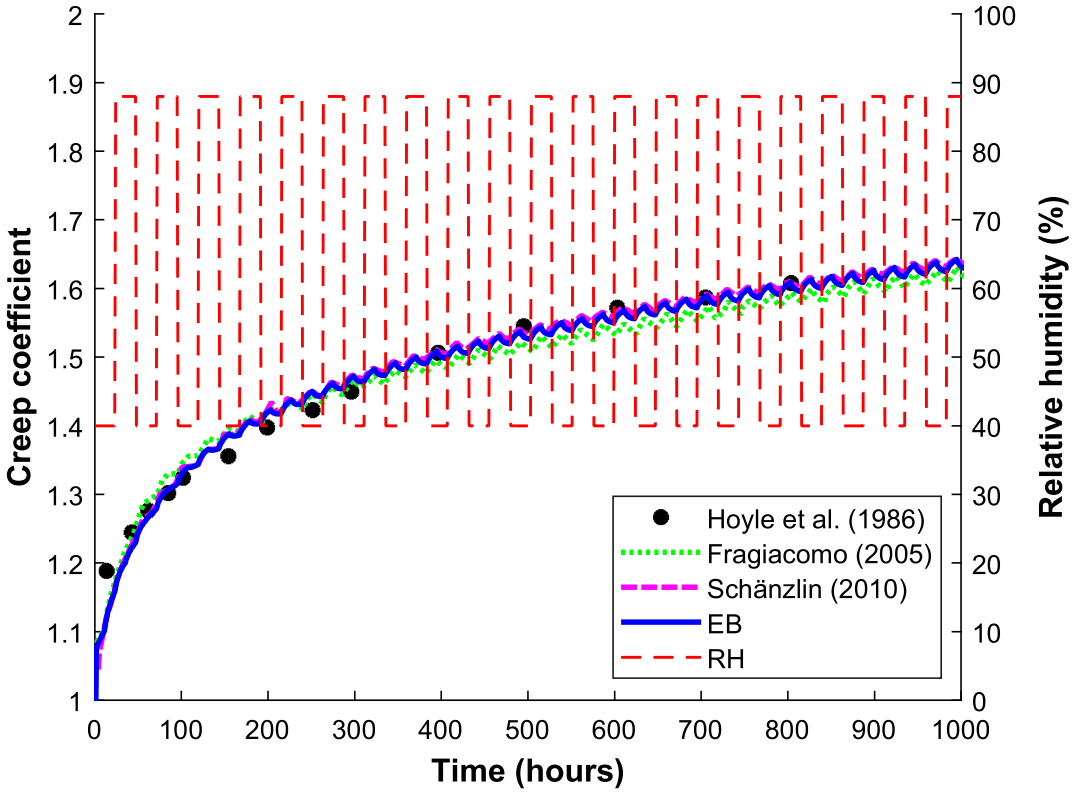


Figure 4.22: Variation over time of the creep coefficient for daily humidity cycles.

4.5 Concluding Remarks

From the obtained results in the validation examples, it can be highlighted the following:

- The use of bubble or nodeless degrees of freedom in the TB and ENH TB element formulation allowed the consideration of shear effects without incurring in shear locking problems even when large displacements are considered. This feature can be attested in subsection 4.4.1. Moreover, in this thesis, a closed-form matrix expression was derived for the geometric stiffness matrix of the Timoshenko element and its enhanced version using a corotational formulation. To the current knowledge of the authors, this expression was not provided before in the literature.

- From the obtained results in subsection 4.4.4, it was attested that the onedimensional BC elements described in section 4.1 along with the stress-strain relationship presented in subsection 4.2.1 can capture the global ultimate response of timber beams with similar accuracy as the obtained with 2D and 3D continuum-based FE models and the force-based BC fiber element. Therefore, the implementation of these BC elements into will contribute towards the aim of developing a cost-effective numerical approach.

- As was noted in subsection 4.4.4, traditional displacement-based BC formulations and their enhanced versions can attain the same level of accuracy in the assessment of the global ultimate response even if the same coarse discretization was employed. However, the numerical performance of the traditional formulations is poor in comparison with their enhanced version when local responses such as section forces need to be evaluated. This can be verified in Appendix B. In order to obtain accurate results, traditional formulations would require a finer mesh discretization.

- In subsection 4.4.4 it can be observed that the coarse mesh FE model using an enhanced formulation of the traditional Euler-Bernoulli BC element attained the same level of accuracy obtained with the single forced-based BC element in terms of assessing global ultimate responses. If the entire beam is modelled, the number of integration points used in the force-based element (at least 25 integration points) and enhanced displacement-based formulation (24 integration points) is very similar.

- In subsection 4.4.5 was attested that the inclusion of large displacement effects in the long-term analysis of structures can induce stiffening effects in the time-dependent deflections as a consequence of the geometrically nonlinear effects.

- In subsection 4.4.6, it was found that a fine discretization of the cross-section along its height and width was required to capture accurately the variation of the material properties with the moisture content. If this is not the case, the assessment of global responses such as of the time-dependent deflections can be determined inaccurately.

Chapter 5

Nonlinear Solution Algorithms

As pointed out in the previous chapter, incremental-iterative procedures are needed to solve the equilibrium equations obtained above. Among these procedures, the Newton-Raphson algorithm and its modified version are the most renowned and thus the most widely adopted solution algorithms. However, the presence of sharp variations in the tangent stiffness, even if they are associated with few degrees of freedom (DOF), could lead to nonconvergent and drifting away scenarios. As a result, more robust solution algorithms should be adopted to overcome these numerical issues. In this chapter, three solution algorithms are described and implemented. The convergence performance of these algorithms is compared to the traditional Newton-Raphson algorithms by analysing three case studies.

5.1 Nonlinear Equation Solvers

Newton-Raphson algorithms are widely used in solving the nonlinear equations of equilibrium due its quadratic rate of convergence. However, in the presence of drastic changes of the tangent stiffness matrix an overwhelming number of steps could be required and in the case of large structural systems this could lead to an excessive computational effort as the stiffness matrix of the structure has to be calculated and assembled at every iteration. On the contrary, the modified Newton-Raphson algorithm involves less computational effort as it only performs one computation of the tangent matrix at the beginning of the step, although it only achieves a linear rate of convergence. An improvement of this rate of convergence can be obtained if the computation of the tangent matrix is performed periodically after a determined number of iterations resulting in a superlinear convergence (Kelley [224]). Nevertheless, these traditional Newton-Raphson algorithms could not attain convergence even for simple structural systems if a numerically consistent tangent stiffness matrix is not attained due to the non-use of a

consistent tangent operator (Simo and Taylor [225]) or round-off errors near singularity, as shown in the case studies discussed in the next sections.

In order to obtain a convergent scenario (in the numerical assessment of the equilibrium paths), more robust and sophisticated solution algorithms should be adopted. In what follows, the Krylov subspace accelerated Newton algorithm, the two-level consistent quasi Newton–Raphson algorithms, and the Lyapunov-based nonlinear solution algorithm are described and implemented. Among other available algorithms, which are not reviewed here, the popular approach of adding artificial viscosity to the tangent stiffness matrix to bypass the involved numerical instabilities is worth mentioning. This viscous stabilisation method has been used in the simulation of structural failure (Dai et al. [226], Nzabonimpa and Hong [227]).

5.1.1 Krylov Subspace Accelerated Newton Algorithm

This algorithm, proposed by Scott and Fenves [228], aims to accelerate the rate of convergence of the improved modified Newton-Raphson algorithm with periodic updates by incorporating a Krylov subspace. In the derivation of this algorithm, the system of nonlinear equilibrium equations, which are a function of the global displacements, $\boldsymbol{U}$, are represented compactly in a residual form:

$$\boldsymbol{R}(\boldsymbol{U}) = \boldsymbol{0} \tag{5.1}$$

In the Krylov acceleration algorithm, the root of Eq. (5.1) is obtained for each analysis step by solving a modified version of this equation:

$$\hat{\boldsymbol{R}}(\boldsymbol{U}) = \left(\boldsymbol{K}^0\right)^{-1} \boldsymbol{R}(\boldsymbol{U}) = \boldsymbol{0} \tag{5.2}$$

where $\boldsymbol{K}^0$ is the initial tangent stiffness matrix at the beginning of the step and $\hat{\boldsymbol{R}}(\boldsymbol{U})$ contains the set of preconditioned residual equations. By performing a linearization process by means of Taylor series, the following approximation is obtained:

$$\hat{\boldsymbol{R}}_{k+1} = \hat{\boldsymbol{R}}_k + \left.\frac{\partial \hat{\boldsymbol{R}}}{\partial \boldsymbol{U}}\right|_{\boldsymbol{U}_k} \Delta \boldsymbol{U}_{k+1} \tag{5.3}$$

which can be rewritten as:

$$\hat{\boldsymbol{R}}_{k+1} = \hat{\boldsymbol{R}}_k - \boldsymbol{A}\, \Delta \boldsymbol{U}_{k+1} \tag{5.4}$$

In this solution algorithm, the displacement increment is conveniently decomposed into two vector components. As a result, Eq. (5.3) can be expressed as:

$$\hat{\boldsymbol{R}}_{k+1} = \hat{\boldsymbol{R}}_k - \boldsymbol{A}\,\Delta\boldsymbol{V}_{k+1} - \boldsymbol{A}\,\Delta\boldsymbol{W}_{k+1} \tag{5.5}$$

where $\Delta\boldsymbol{V}_{k+1}$ and $\Delta\boldsymbol{W}_{k+1}$ are the acceleration and standard modified Newton-Raphson component, respectively. Moreover, it is assumed that the acceleration component is the linear combination of the Krylov subspace conformed by the set of displacement increments previously attained during the iteration process. This combination can be given by:

$$\Delta\boldsymbol{V}_{k+1} = \sum_{i=1}^{m} c_i\,\Delta\boldsymbol{U}_i \tag{5.6}$$

where m is the number of the previous iterations. Following this notation, the second term in the right-hand side of Eq. (5.5) can be rewritten as:

$$\boldsymbol{A}\,\Delta\boldsymbol{V}_{k+1} = \sum_{i=1}^{m} c_i\,\boldsymbol{A}\,\Delta\boldsymbol{U}_i \tag{5.7}$$

To evaluate the acceleration component, the norm of the term $\hat{\boldsymbol{R}}_k - \boldsymbol{A}\,\Delta\boldsymbol{V}_{k+1}$ needs to be minimized by means of a low-rank least-square analysis. It should be noticed that the terms $\boldsymbol{A}\,\Delta\boldsymbol{U}_i$ can be implicitly assessed from Eq. (5.4). As a result, the coefficients c_i can be evaluated and the component $\Delta\boldsymbol{V}_{k+1}$ in Eq. (5.6) can be assessed. Finally, the standard component can be calculated from Eq. (5.5) as follows:

$$\Delta\boldsymbol{W}_{k+1} = \hat{\boldsymbol{R}}_k - \boldsymbol{A}\,\Delta\boldsymbol{V}_{k+1} \tag{5.8}$$

After conducting a number of iterations, the process is restarted along with an updated tangent stiffness matrix.

5.1.2 Two-level Consistent Quasi Newton–Raphson Algorithm

This algorithm, developed by Ren and Li [229], proposes the use of consistent secant operators at the structural and material level to attain a superlinear rate of convergence. This means that the linearization process performed at the structural level should be congruent with the linearization at the material level. According to this, the solution of the linearized nonlinear equations in Eq. (4.81) uses a secant stiffness matrix instead of a tangent matrix as is the case in the traditional Newton-Raphson methods. By adopting the quasi Newton–Raphson method

used by Matthies and Strang [230] based on the Broyden-Fletcher-Goldfarb-Shanno algorithm to update the inverse of the secant matrix, the following iterative expression which performs rank-two updates is employed:

$$\left(\boldsymbol{K}_{sec}^{i}\right)^{-1} = \left(\boldsymbol{I} - \frac{\Delta \boldsymbol{U}^{i} \left(\Delta \boldsymbol{F}_{int}^{i}\right)^{T}}{\left(\Delta \boldsymbol{F}_{int}^{i}\right)^{T} \Delta \boldsymbol{U}^{i}}\right) \left(\boldsymbol{K}_{sec}^{i-1}\right)^{-1} \left(\boldsymbol{I} - \frac{\Delta \boldsymbol{F}_{int}^{i} \left(\Delta \boldsymbol{U}^{i}\right)^{T}}{\left(\Delta \boldsymbol{F}_{int}^{i}\right)^{T} \Delta \boldsymbol{U}^{i}}\right) + \frac{\Delta \boldsymbol{U}^{i} \left(\Delta \boldsymbol{U}^{i}\right)^{T}}{\left(\Delta \boldsymbol{F}_{int}^{i}\right)^{T} \Delta \boldsymbol{U}^{i}} \tag{5.9}$$

where $\boldsymbol{I}$ is the identity matrix, i the current iteration, $\Delta \boldsymbol{U}$ is the displacement vector increment and $\Delta \boldsymbol{F}_{int}$ is the internal force increment. With the aim of maintaining the consistency at the material level, the element material stiffness matrices are evaluated as follows:

$$\bar{\boldsymbol{K}}_{m}^{e} = \int_{l} \bar{\boldsymbol{B}}^{T} \boldsymbol{D}_{sec} \, \bar{\boldsymbol{B}} \, dx \tag{5.10}$$

where $\boldsymbol{D}_{sec}$ is the section secant stiffness matrix also denominated as the secant operator. In the implementation of the analysis framework of this thesis, only two types of secant operators were considered: the origin and incremental operator.

After performing a certain number of iterations, the stiffness matrix is updated at the material level in order to reduce the bandwidth and cumulative errors of the updating process at the structural level related to the stiffness matrix.

5.1.3 Lyapunov-Based Nonlinear Solution Algorithm

Liang and Mosalam [231] proposed a solution algorithm based on Lyapunov stability theory by reframing the original nonlinear equilibrium equations of a structural system into a hypothetical dynamical system described by a set of first-order differential equations. The equilibrium points of the original structural system are assessed by solving the hypothetical dynamical system. The differential equations describing the hypothetical system are given by:

$$\dot{\boldsymbol{U}} = \boldsymbol{G}(\boldsymbol{U}) = -\check{\boldsymbol{K}} \left[\frac{\partial \boldsymbol{R}(\boldsymbol{U})}{\partial \boldsymbol{U}}\right]^{T} \boldsymbol{R}(\boldsymbol{U}) = -\check{\boldsymbol{K}} \, \boldsymbol{J}(\boldsymbol{U})^{T} \boldsymbol{R}(\boldsymbol{U}) \tag{5.11}$$

where $\check{\boldsymbol{K}}$ is a symmetric positive definite matrix that influences the convergence rate of the differential equations, $\boldsymbol{R}(\boldsymbol{U})$ is the residual form of the nonlinear equilibrium equations and $\boldsymbol{J}(\boldsymbol{U})$ is the Jacobian matrix. The corresponding Lyapunov function of the dynamical system

is defined as:

$$\upsilon(\boldsymbol{U}) = \frac{1}{2}\,\boldsymbol{R}(\boldsymbol{U})^T\boldsymbol{R}(\boldsymbol{U}) \tag{5.12}$$

To assess the equilibrium points of the original structural system, a numerical integration scheme should be used to solve the differential equations set in Eq. (5.11). The explicit Runge-Kutta formula proposed by Dormand and Prince [232] which combines expressions with truncation errors of fourth and fifth order is employed in this thesis. In order to attain a linear rate of convergence, matrix $\check{\boldsymbol{K}}$ is adopted as follows:

$$\check{\boldsymbol{K}} = \mu_0\,\boldsymbol{J}(\boldsymbol{U})^{-1}\boldsymbol{J}(\boldsymbol{U})^{-T} \tag{5.13}$$

where μ_0 is a positive scalar. One important feature of this solution algorithm is its global asymptotic stability.

5.2 Study Cases

Three nonlinear static systems are analysed in this chapter to compare the convergence performance of traditional Newton-Raphson algorithms against the three nonlinear algorithms previously described. The first example consists of a single degree-of-freedom (DOF) representing the scenario of a singular Jacobian matrix near the equilibrium point. The second and third benchmark problems describe a simple two DOF system with two and three resisting springs, respectively, in which a numerically inconsistent tangent stiffness matrix is generated. In these study cases, all units are omitted for convenience by assuming their consistent use throughout. Regarding the Krylov acceleration and Quasi Newton algorithms, the global tangent stiffness of the systems were updated after performing two iterative operations. In the case of the Lyapunov algorithm, a value of $\mu_0 = 15$ was employed in all cases.

5.2.1 Single DOF System

This benchmark example was analysed by Ren and Li [229]. It consists of a nonlinear single DOF system (Fig. 5.1) governed by the following restoring force:

$$f\,(u) = sign\,(u)\,|u|^r \tag{5.14}$$

where r is the exponent parameter and $sign$ represents the sign function.

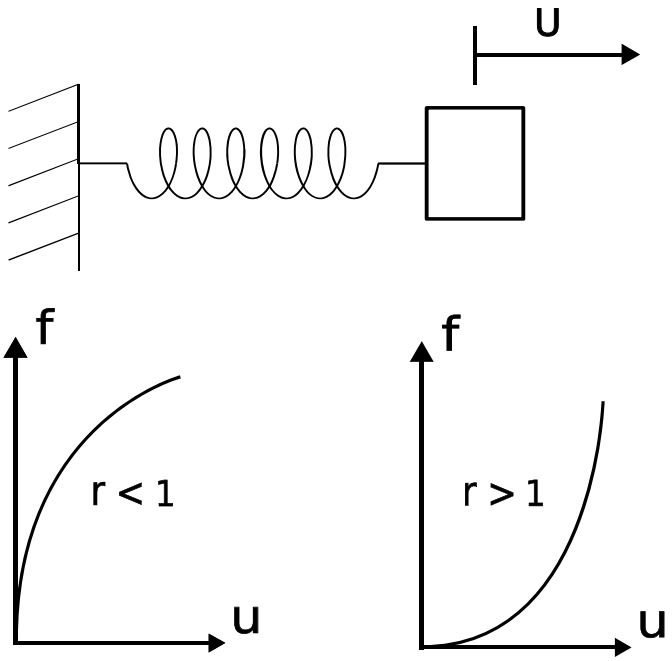


Figure 5.1: One degree of freedom spring system.

The initial displacement has a value of ten and the equilibrium point is associated with a null displacement. The system incurs singularity in the vicinity of its equilibrium point when the value of the exponent r in Eq. (5.14) is less than one, as shown in Fig. 5.1. The implication of this singularity in the solution algorithms is depicted in Figs. 5.2 to 5.7 for an exponent of $r = \frac{1}{3}$.

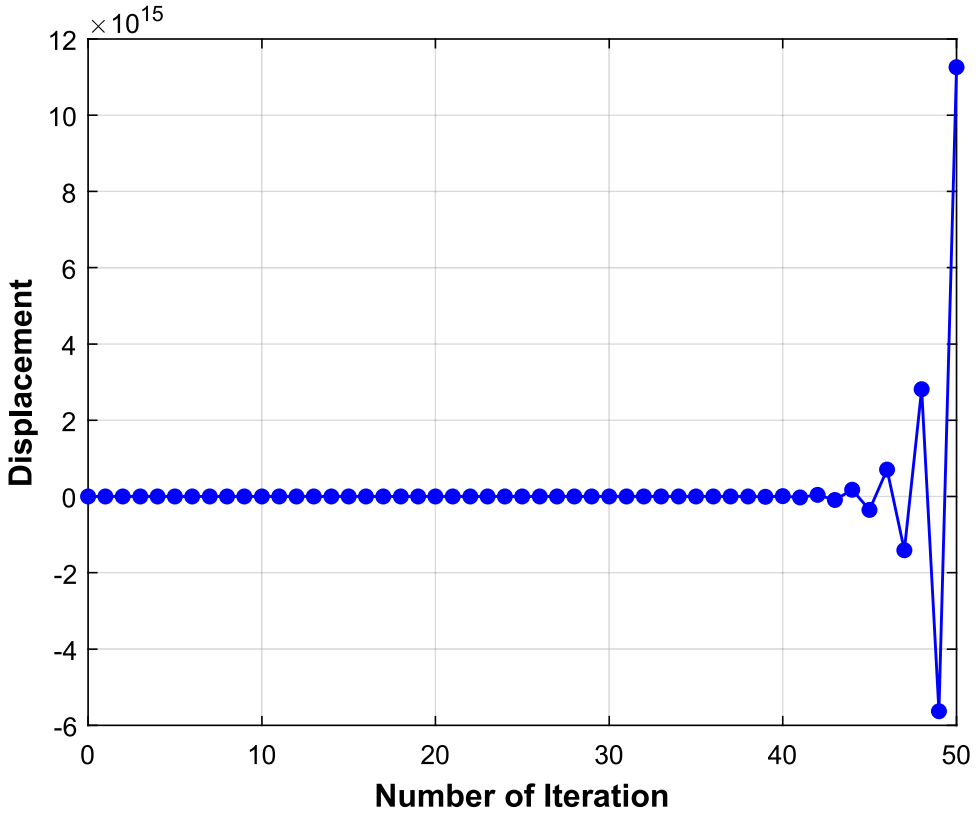


Figure 5.2: Newton-Raphson iterative equilibrium search for $r = \frac{1}{3}$.

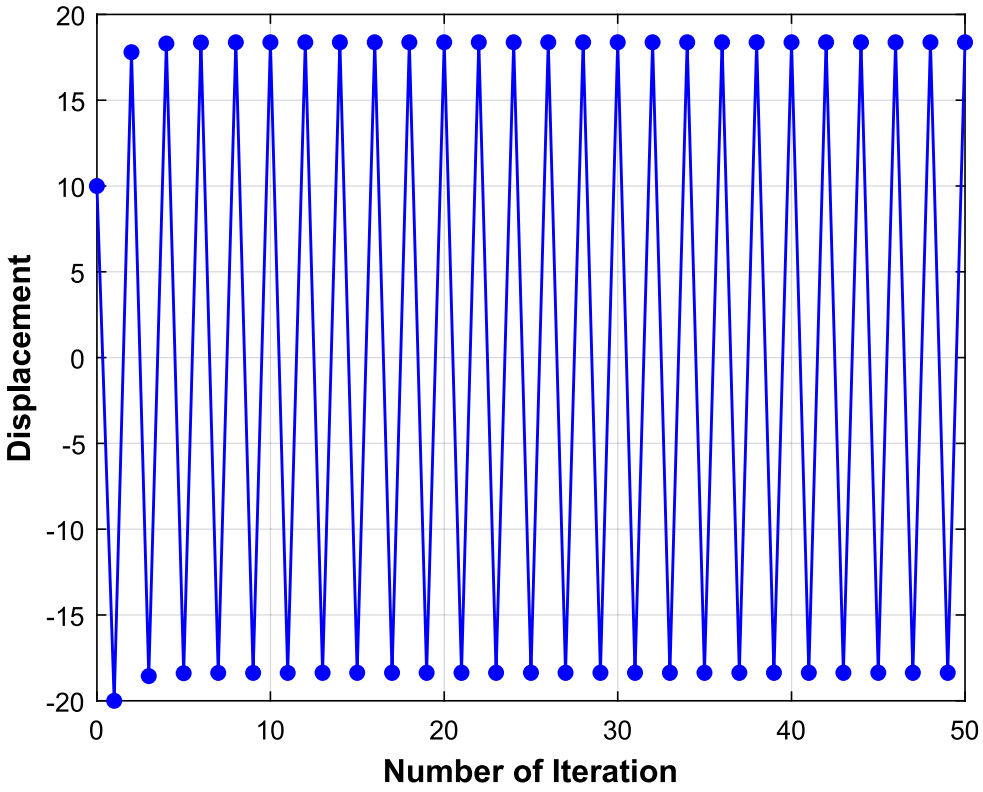


Figure 5.3: Modified Newton-Raphson iterative equilibrium search for $r = \frac{1}{3}$.

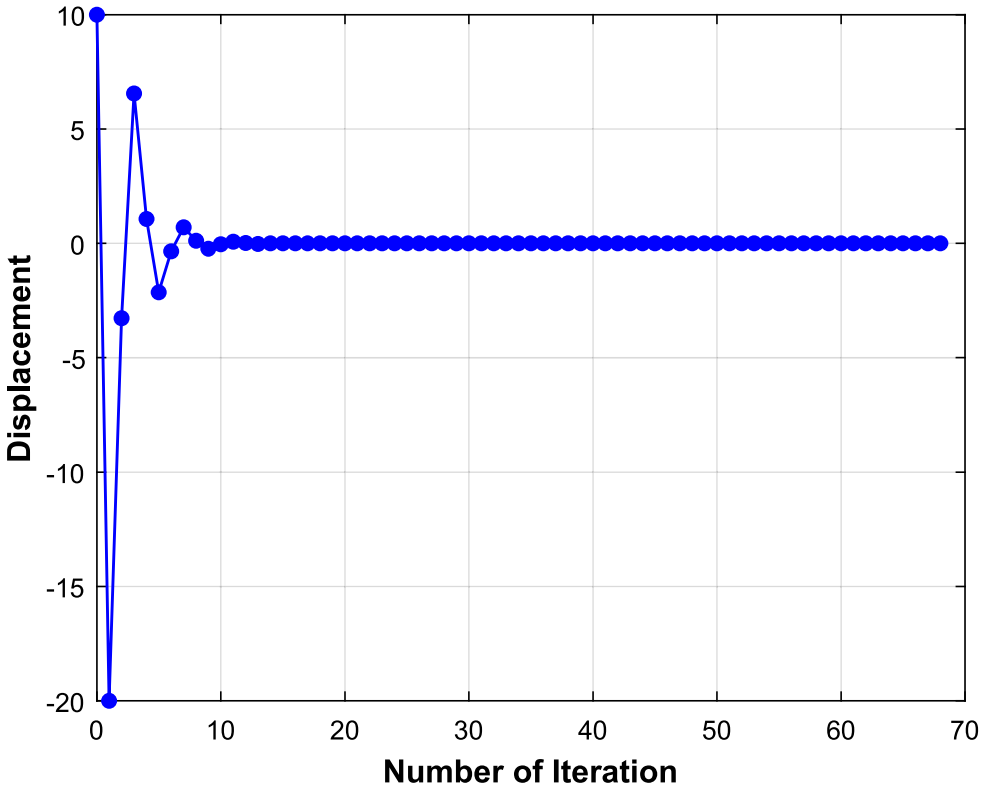


Figure 5.4: Krylov-Newton iterative equilibrium search for $r = \frac{1}{3}$.

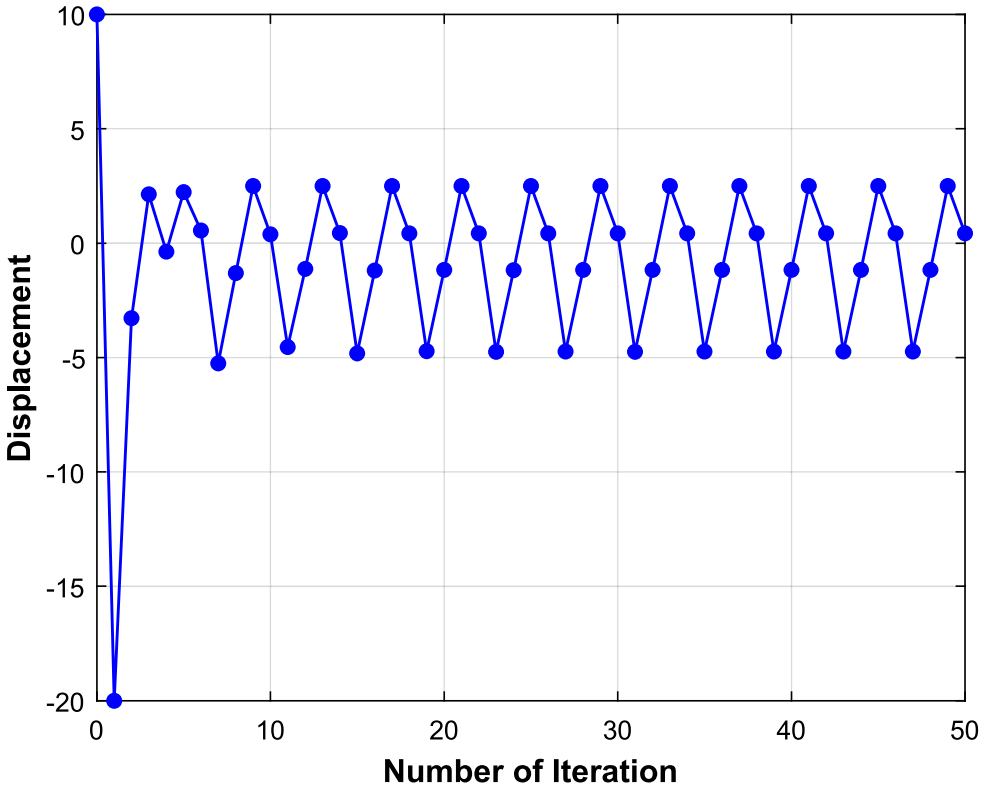


Figure 5.5: Quasi Newton iterative equilibrium search with origin operator for $r = \frac{1}{3}$.

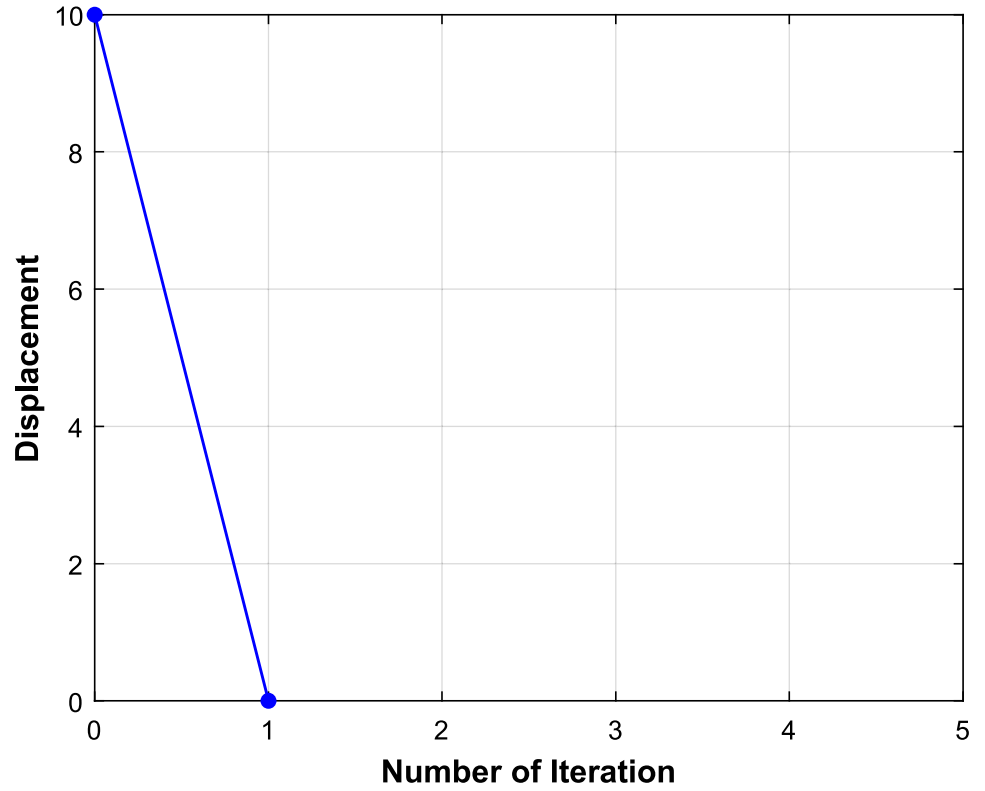


Figure 5.6: Quasi Newton iterative equilibrium search with incremental operator for $r = \frac{1}{3}$.

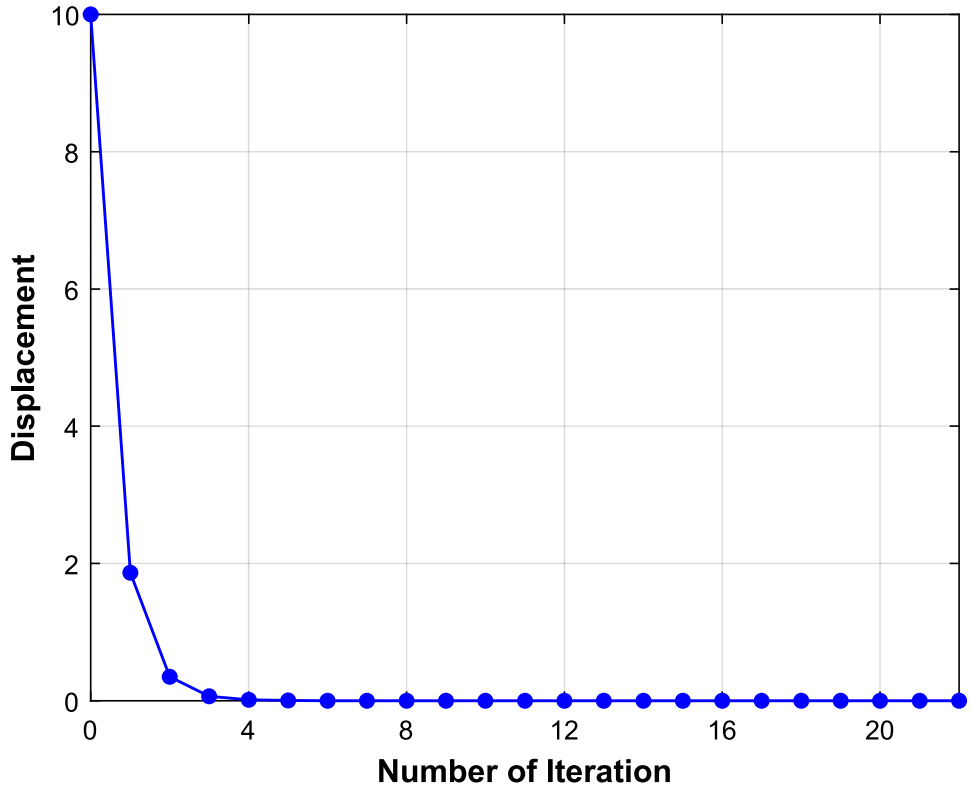


Figure 5.7: Lyapunov iterative equilibrium search for $r = \frac{1}{3}$.

From the above figures, it is observed that the full and modified Newton-Raphson methods diverge and oscillate, respectively, whereas the Krylov-Newton, Quasi Newton with incremental secant operator and Lyapunov algorithms converge to the true solution. In contrast, in the case of using an exponent of $r = 2$ there is no singularity and all the algorithms converge to the equilibrium point as shown in Appendix C. Regarding the results related to the singularity scenario, it can be noticed that the fastest convergence rate was achieved by the Quasi Newton algorithm which uses an origin secant operator just after 1 iteration. The Lyapunov and Krylov-Newton algorithms converged at lower rates by attaining 22 and 68 iterations, respectively. For the no singularity scenario, the modified Newton-Raphson method converged after the striking number of 6315 iterations.

5.2.2 Two DOF System with Two Springs

This benchmark problem was also proposed by Ren and Li [229]. The mechanical system shown in Fig. 5.8 comprises two uniaxial springs with bilinear force-deformation relationships as the resisting mechanism. If the system is subjected to a load of $\boldsymbol{P} = [10\ 20]^T$, the resulting displacement should be $\boldsymbol{U} = [21\ 39]^T$. In order to test the performance of the nonlinear algorithms, an initial displacement guess of $\boldsymbol{U}_0 = [100\ 50]^T$ is adopted.

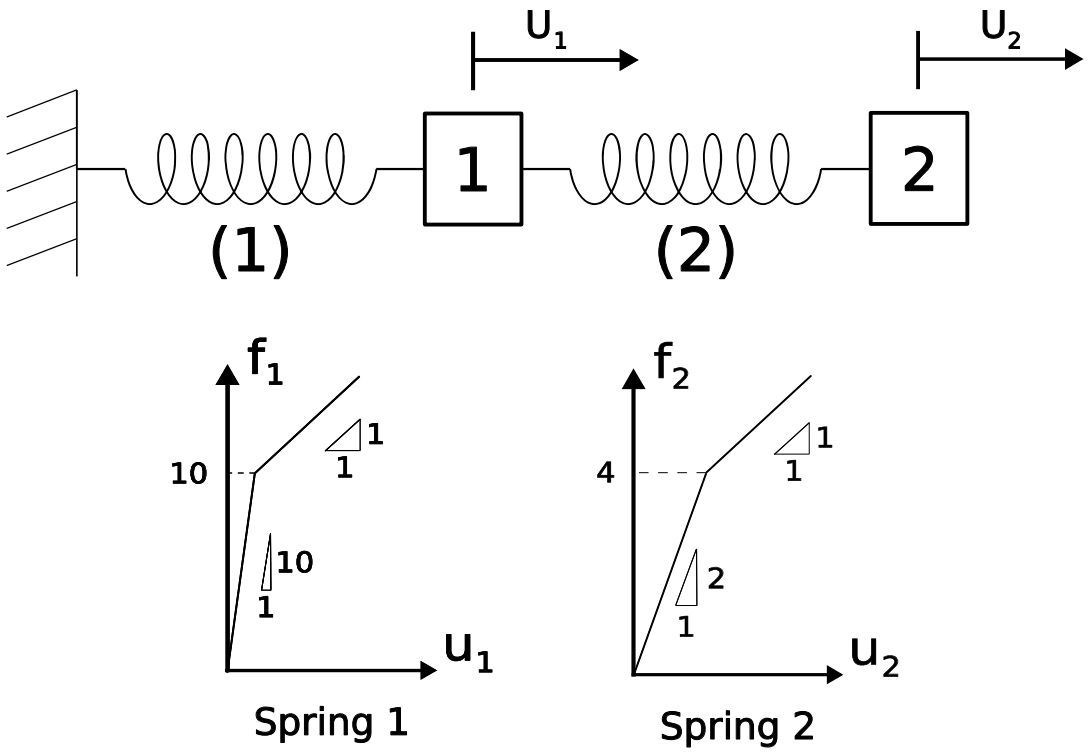


Figure 5.8: Two degree of freedom system with two springs.

For this simple mechanical system, the consistent tangent stiffness matrix can be expressed in a closed form as follows:

$$\boldsymbol{K} = \begin{bmatrix} k_1 + k_2 & -k_2 \\ -k_2 & k_2 \end{bmatrix} \tag{5.15}$$

where k_1 and k_2 are the spring stiffness. In order to study the performance of the numerical solvers, a numerically inconsistent tangent stiffness matrix is generated by introducing an artificial coupling in the springs resulting in the following tangent stiffness matrix:

$$\boldsymbol{K} = \begin{bmatrix} k_1 + k_2 - 1 & -k_2 + 0.5 \\ -k_2 + 0.5 & k_2 \end{bmatrix} \tag{5.16}$$

The modified stiffness matrix in Eq. (5.16) represents the scenario of having a complex constitutive model leading to the assessment of an inconsistent tangent operator or round-off errors during the computations. The results obtained for the case of using an inconsistent Jacobian matrix are depicted in Figs. 5.9 to 5.14. The results related to the use of the consistent tangent stiffness matrix in Eq. (5.15) are illustrated in Appendix C.

From the results, it can be noticed that under the consistent stiffness matrix scenario, all the numerical solvers converge. The faster rate of convergence is obtained with the full and modified Newton-Raphson methods after just 2 iterations.

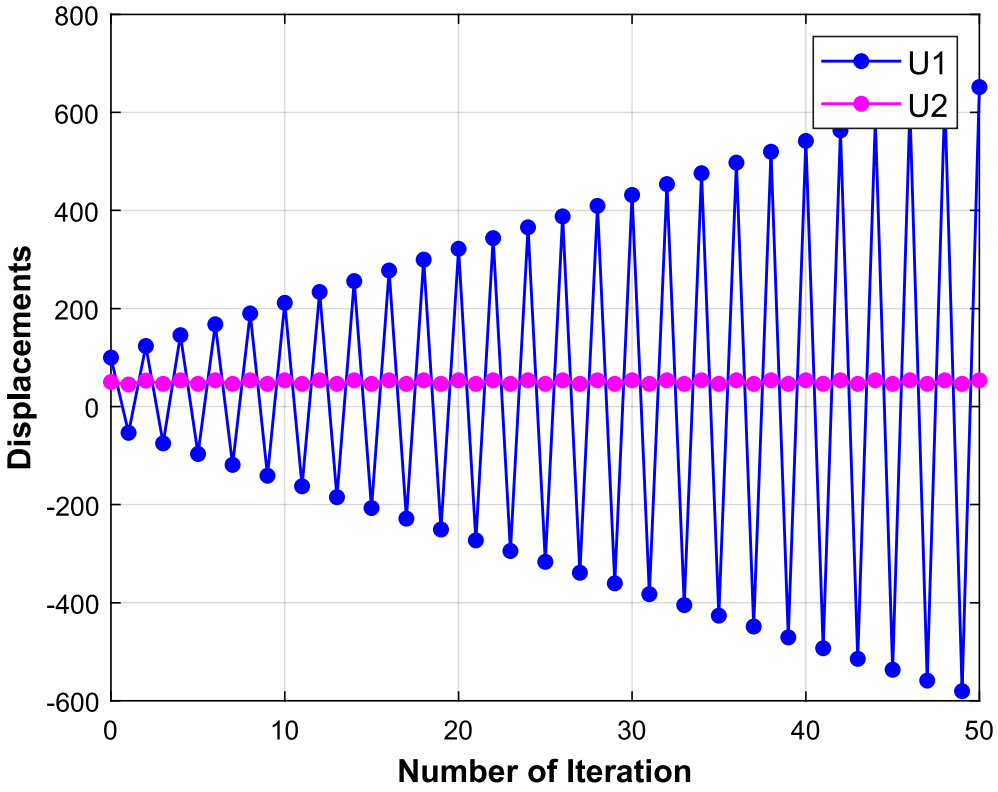


Figure 5.9: Newton-Raphson iterative equilibrium search for inconsistent Jacobian matrix.

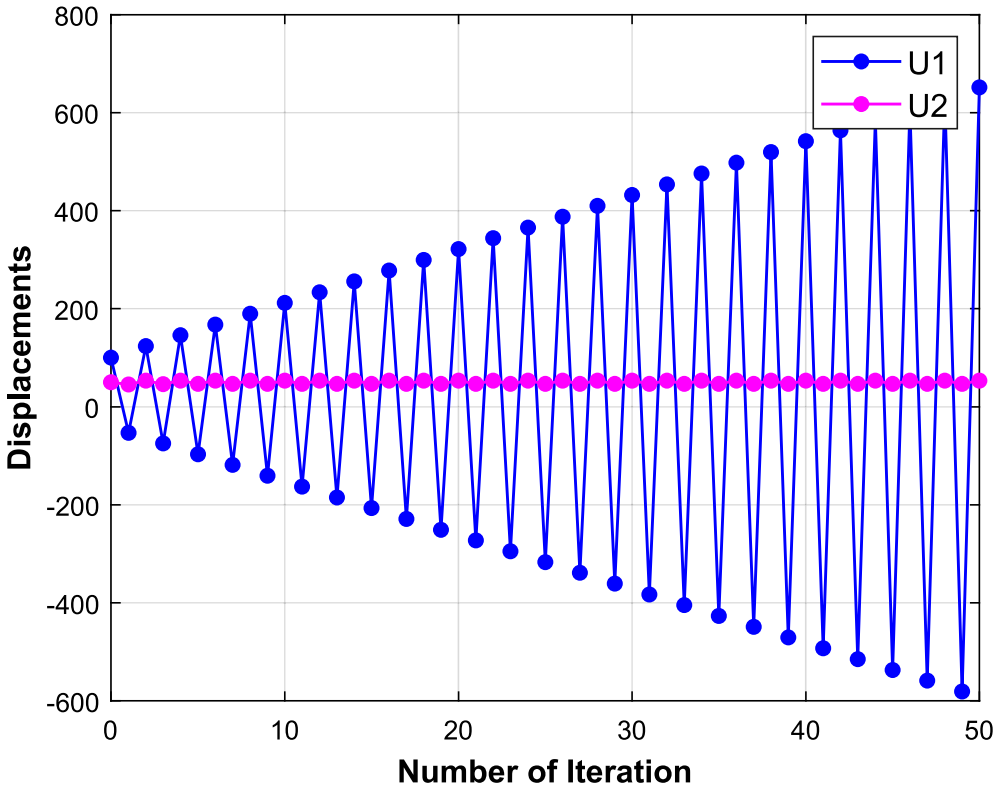


Figure 5.10: Modified Newton-Raphson iterative equilibrium search for inconsistent Jacobian matrix.

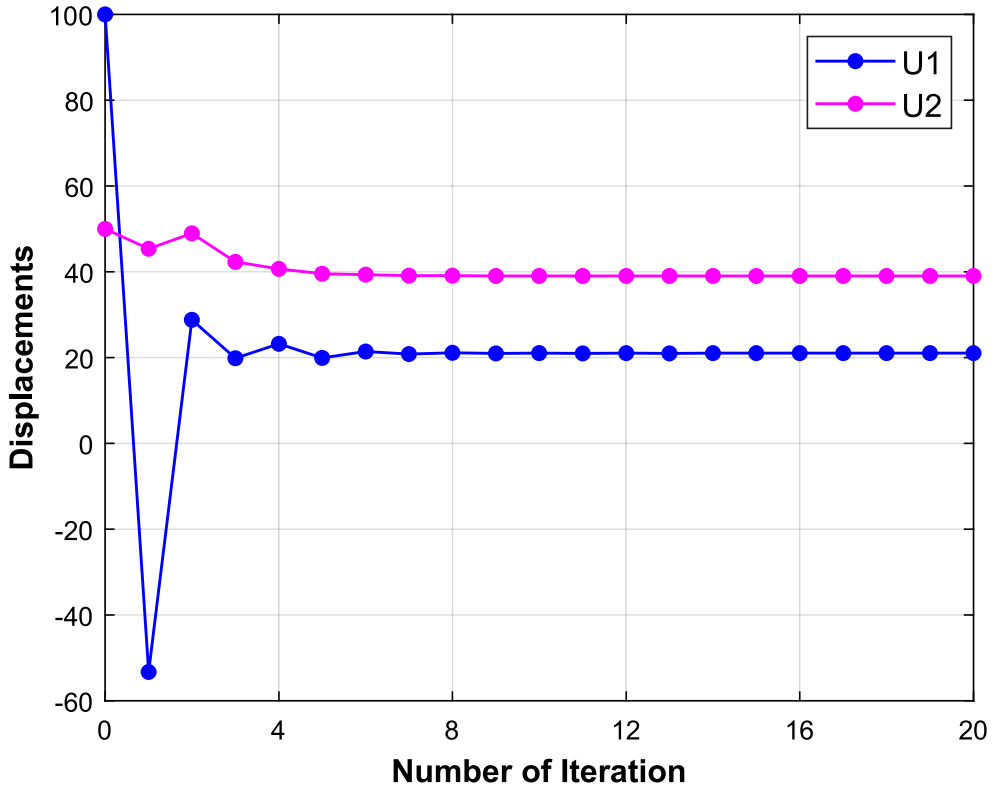


Figure 5.11: Krylov-Newton iterative equilibrium search for inconsistent Jacobian matrix.

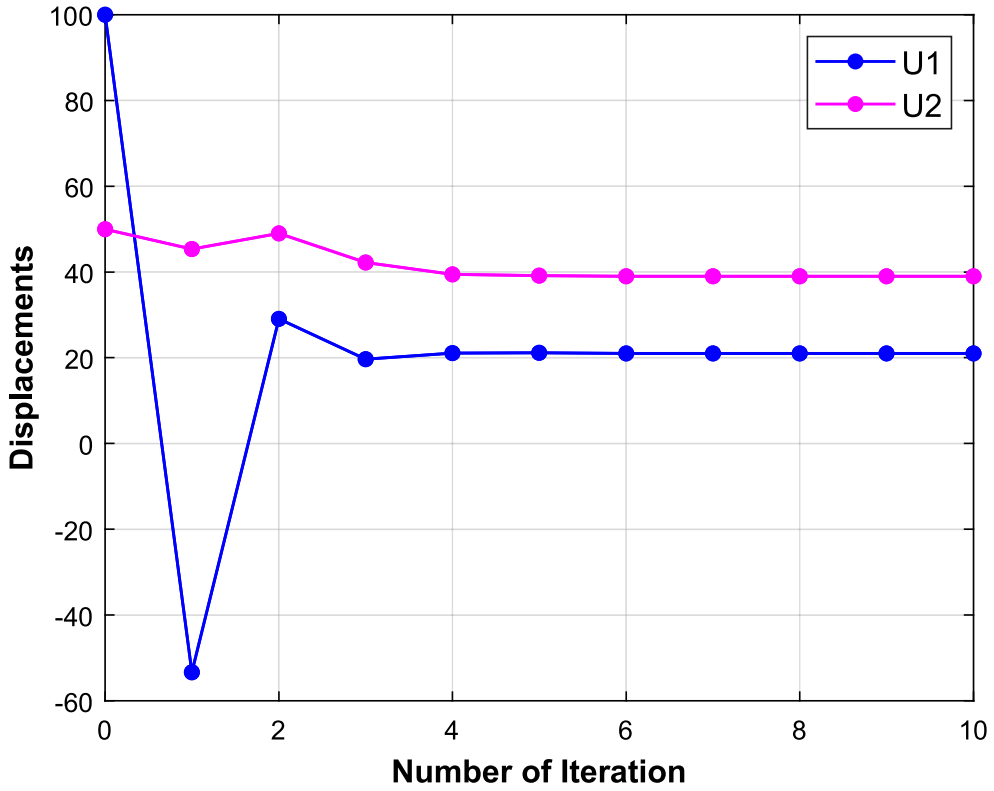


Figure 5.12: Quasi Newton iterative equilibrium search with origin operator for inconsistent Jacobian matrix.

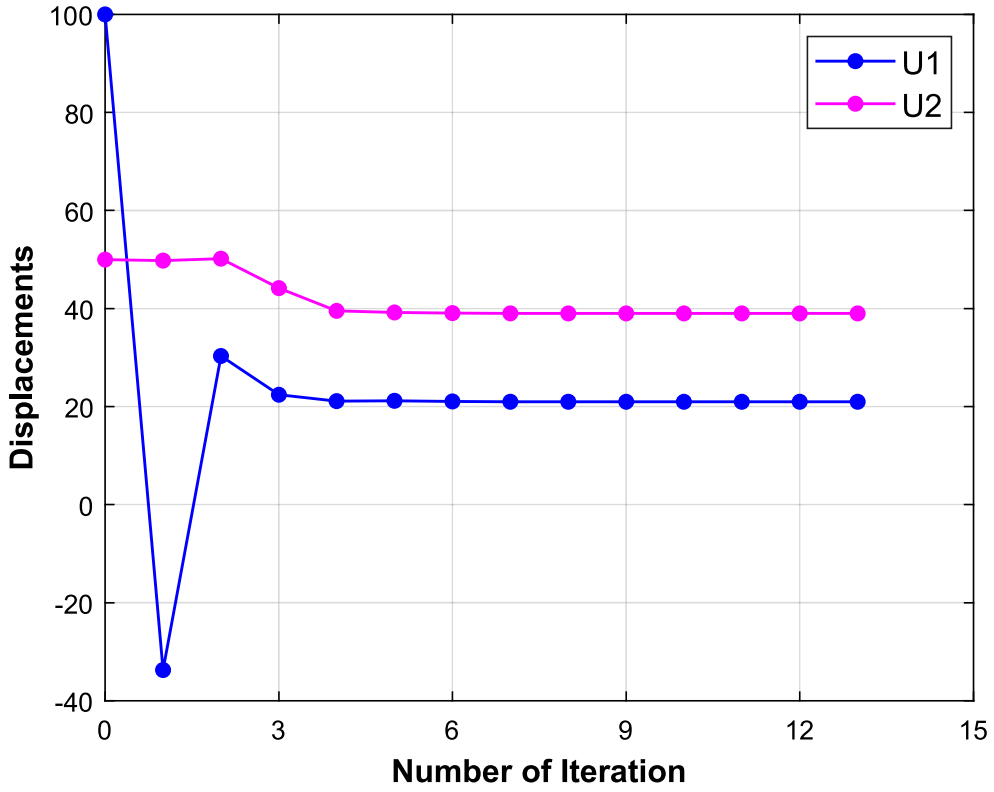


Figure 5.13: Quasi Newton iterative equilibrium search with incremental operator for inconsistent Jacobian matrix.

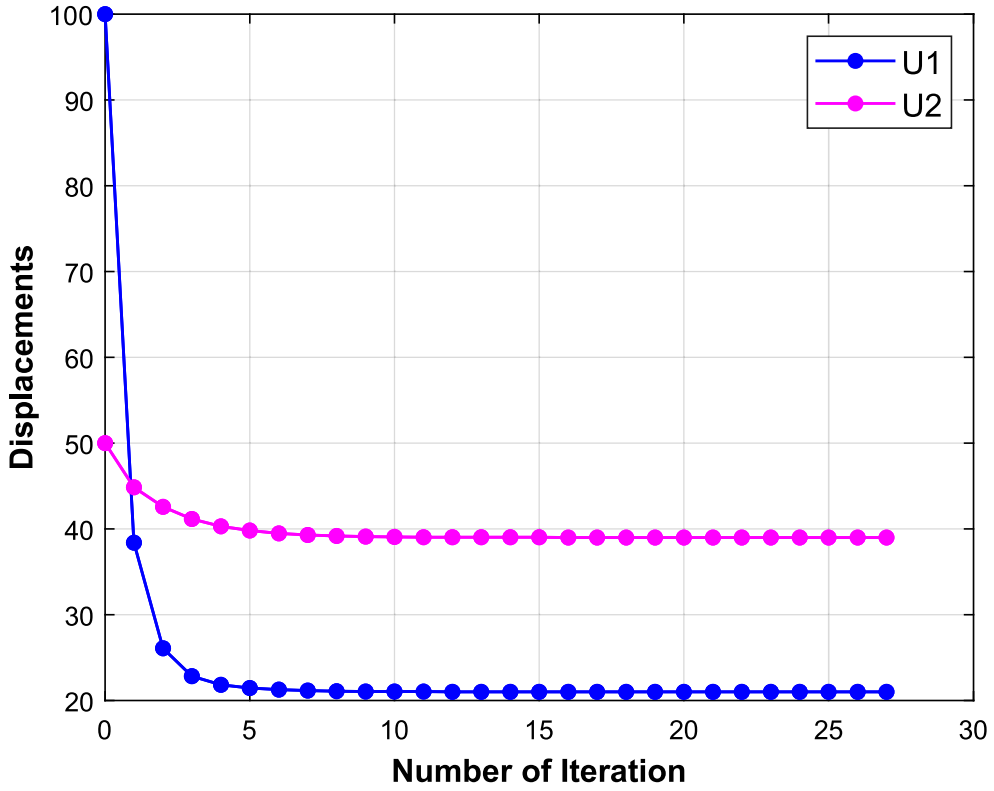


Figure 5.14: Lyapunov iterative equilibrium search for inconsistent Jacobian matrix.

For the case of an inconsistent tangent stiffness matrix, the displacements in the full and modified Newton-Raphson methods drift away and the system oscillates from/around the solution. Regarding the other numerical solvers, the faster convergence rate is achieved with the quasi Newton method using an origin secant operator after 10 iterations. The Lyapunov, quasi Newton method with incremental operator and Krylov-Newton algorithms converge after 27, 13, and 20 iterations.

5.2.3 Two DOF System with Three Springs

This analysis benchmark case was proposed and studied by Scott and Fenves [228] to study the effects of a numerically inconsistent tangent stiffness matrix due to approximation errors in the computational operations and not having a consistent tangent operator. The mechanical system depicted in Fig. 5.15 consists of three uniaxial springs with bilinear force-deformation relationships. In this problem, the system is subjected to a external load of $\boldsymbol{P} = [6\ 12]^T$ which leads to a nodal displacement of $\boldsymbol{U} = [2\ 5]^T$.

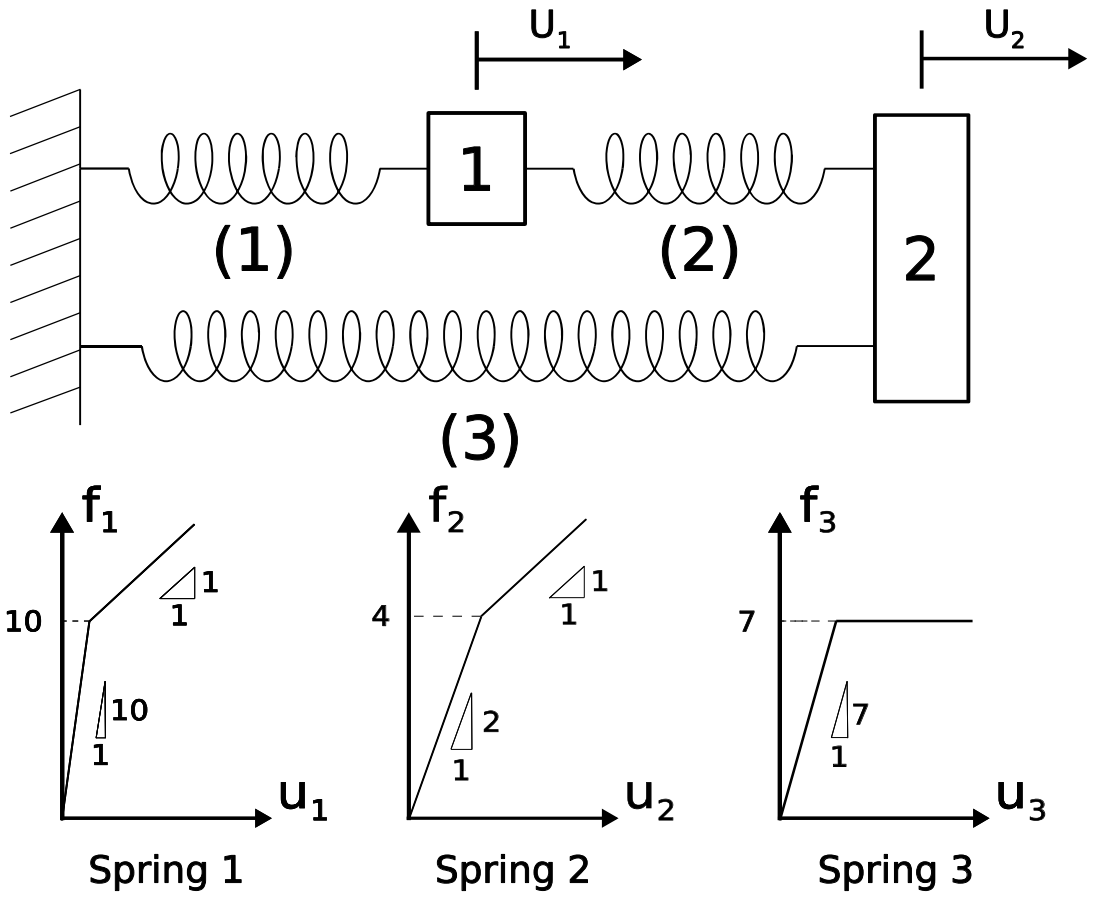


Figure 5.15: Two degree of freedom system with three springs.

The consistent tangent stiffness matrix of this mechanical system can be written in closed form as:

$$\boldsymbol{K} = \begin{bmatrix} k_1 + k_2 & -k_2 \\ -k_2 & k_2 + k_3 \end{bmatrix} \tag{5.17}$$

where k_1, k_2 and k_3 are the spring stiffnesses comprising the resisting mechanism. With the aim of studying the performance of the nonlinear algorithms, a numerically inconsistent tangent stiffness matrix is provided by introducing diagonal and off-diagonal terms in the tangent stiffness matrix of the system as follows:

$$\boldsymbol{K} = \begin{bmatrix} k_1 + k_2 - 1 & -k_2 + 0.5 \\ -k_2 + 0.5 & k_2 + k_3 \end{bmatrix} \tag{5.18}$$

The results related to the inconsistent tangent stiffness are shown in Figs. 5.16 to 5.21 whereas the ones corresponding to the consistent tangent stiffness are illustrated in Appendix C. In this analysis case, the results are presented by plotting the traces of equilibrium search with regard to the displacements.

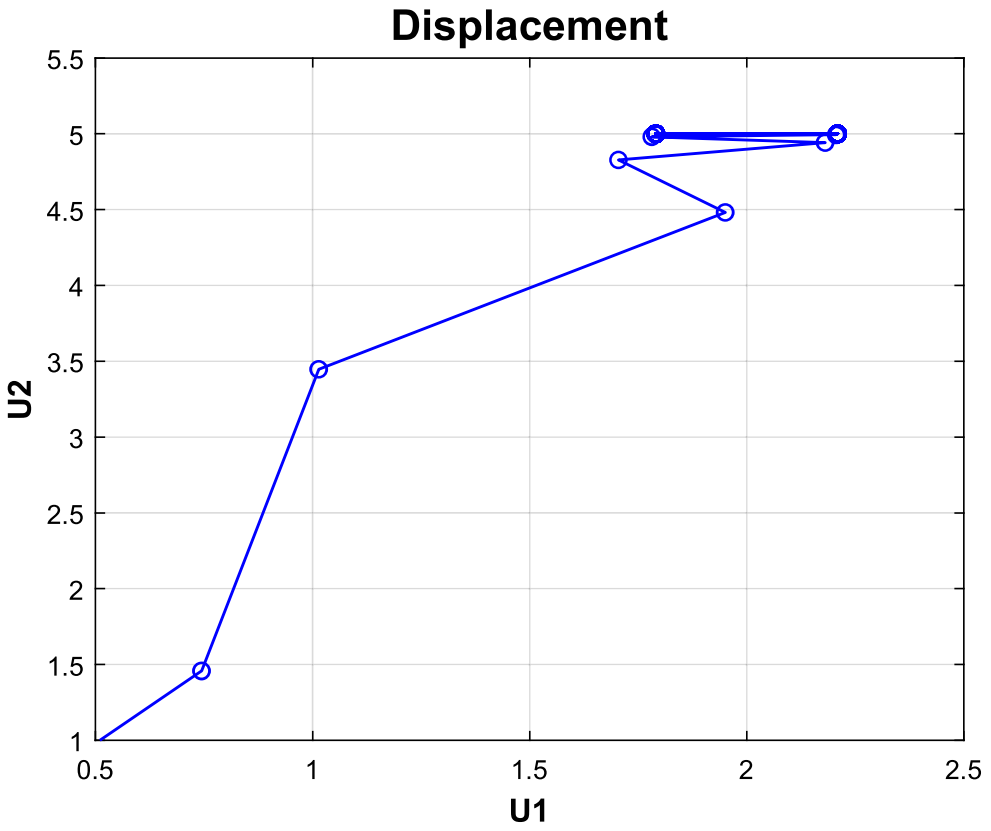


Figure 5.16: Newton-Raphson iterative equilibrium search for inconsistent Jacobian matrix.

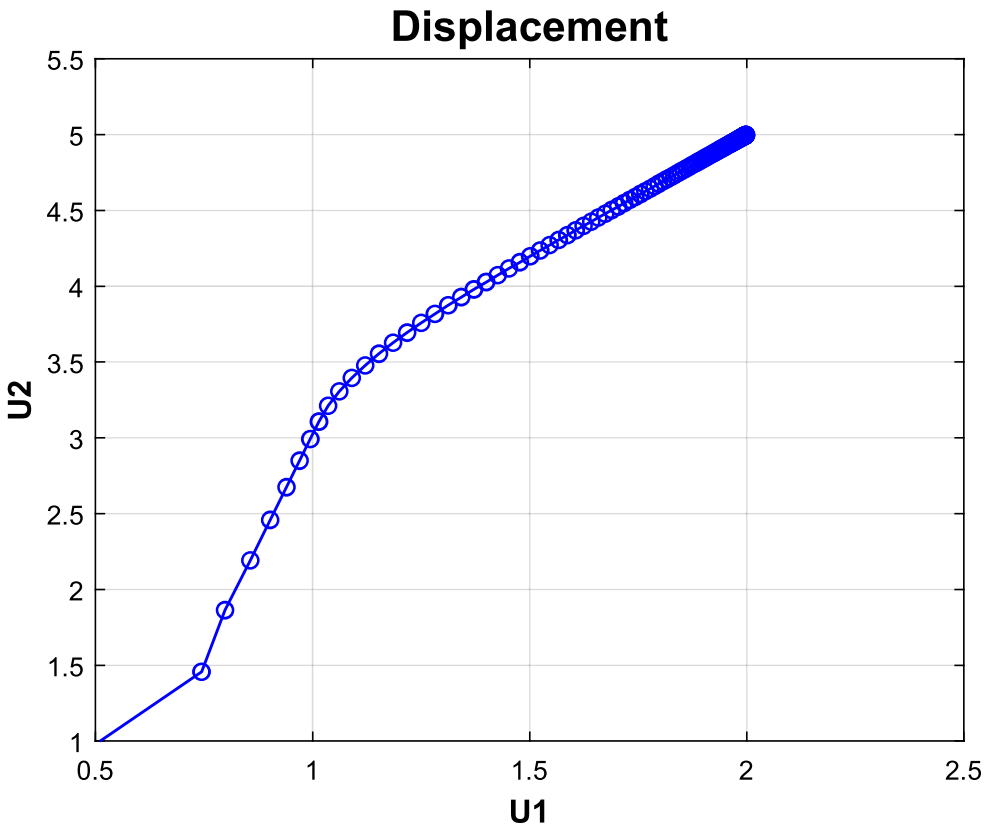


Figure 5.17: Modified Newton-Raphson iterative equilibrium search for inconsistent Jacobian matrix.

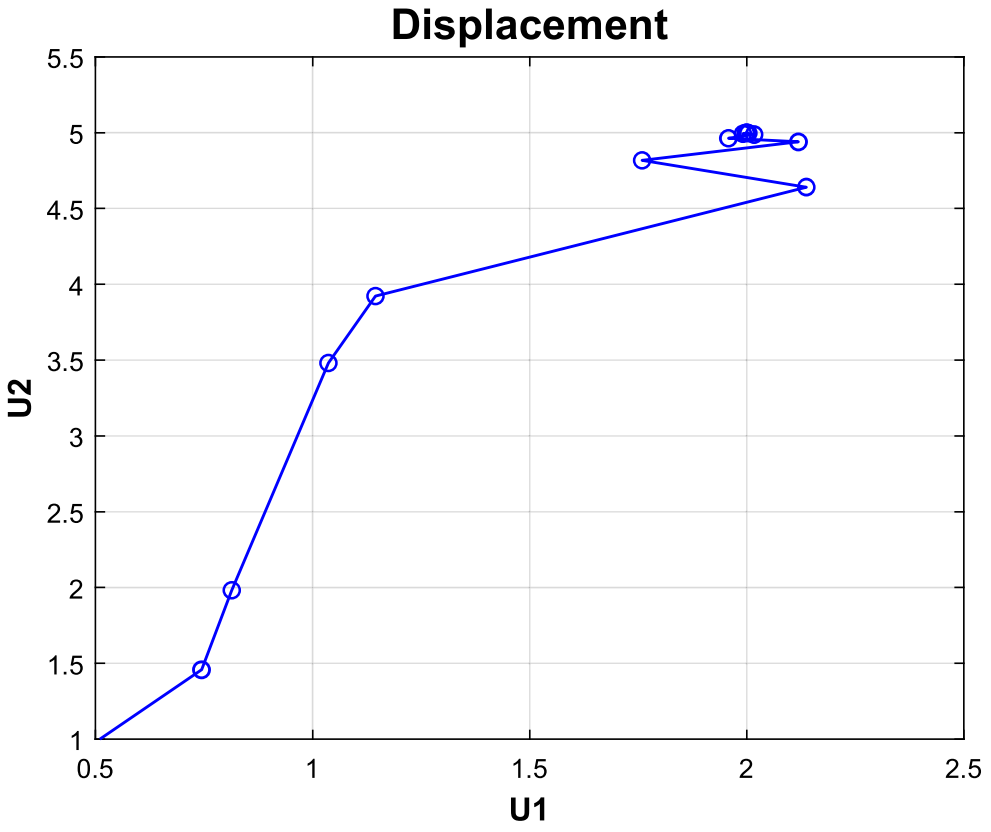


Figure 5.18: Krylov-Newton iterative equilibrium search for inconsistent Jacobian matrix.

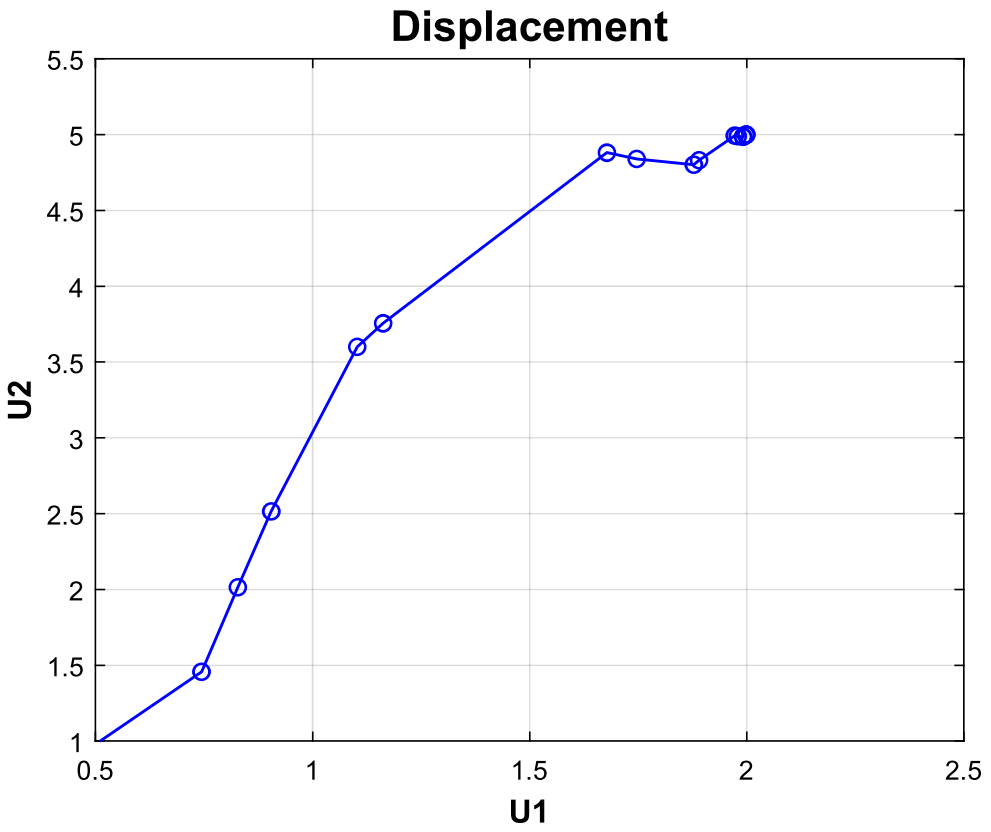


Figure 5.19: Quasi Newton iterative equilibrium search with origin operator for inconsistent Jacobian matrix.

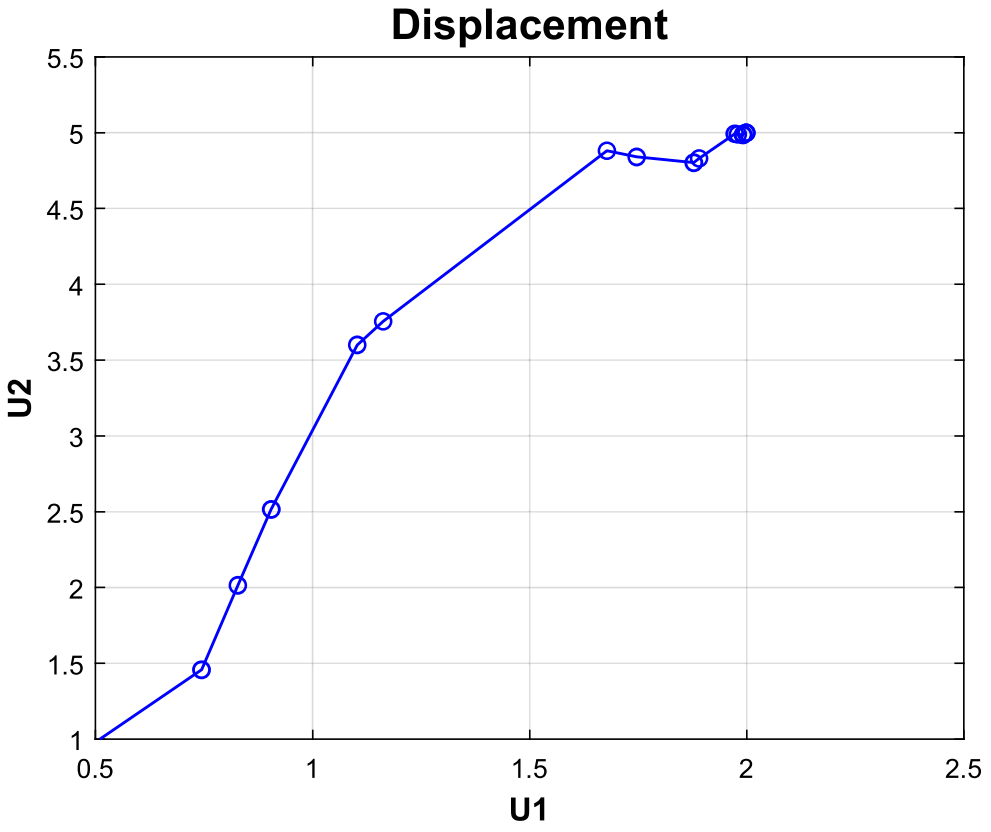


Figure 5.20: Quasi Newton iterative equilibrium search with incremental operator for inconsistent Jacobian matrix.

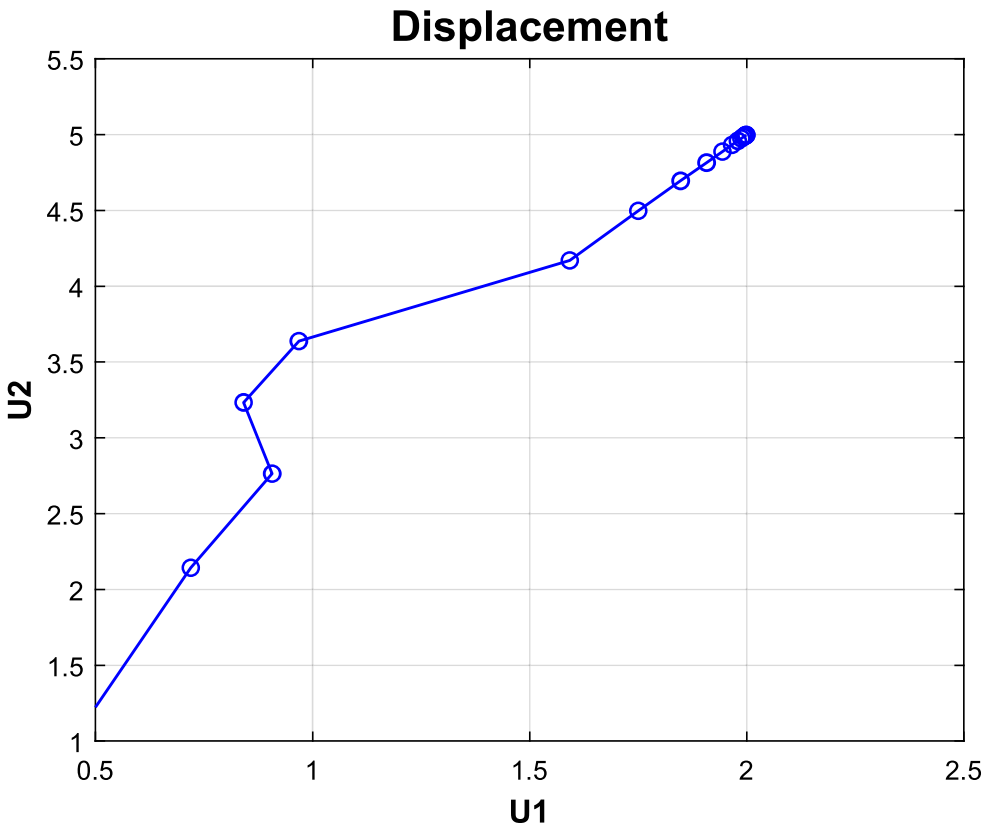


Figure 5.21: Lyapunov iterative equilibrium search for inconsistent Jacobian matrix.

When using an inconsistent tangent stiffness, the full Newton–Raphson algorithm fails to converge as it oscillates around the equilibrium point whereas its modified version converges after 143 iterations. In contrast, the other nonlinear algorithms reach convergence after performing fewer iterations. Specifically, the Krylov, quasi Newton and Lyapunov algorithms converge after 14, 16 and 18 iterations, respectively. On the contrary, for a consistent tangent stiffness, the full Newton–Raphson algorithm attained the fastest converge rate after just 3 iterations whereas its modified version achieved the slowest converge with 140 iterations. Regarding the Krylov, quasi Newton and Lyapunov algorithms their convergence required 5, 16 and 13 iterations, respectively.

5.3 Concluding Remarks

From the previous results, the following observations can be obtained:

- The numerical framework implemented in this thesis, based on fibre beam-column elements, is susceptible to convergence issues, specifically when phenomenological material constitutive laws defined by unsmooth force-deformation relationships are employed. Therefore, the use of robust numerical solvers is necessary to trace the whole equilibrium

paths.

- As observed, in general the assessment of the equilibrium points should start the iterative process by using the full Newton–Raphson method to attain fastest convergence when a numerically consistent tangent stiffness matrix is still used. If there are convergence issues, the solution strategy should choose any of the robust algorithms to continue the analysis. Once this issue has been overcome, the solution algorithm should return to full Newton–Raphson method to perform another cycle. This solution strategy was implemented in the analysis framework developed in this thesis. It is worth mentioning that this solution strategy enhances the computational efficiency of the implemented framework.

- Traditional Newton–Raphson methods failed when there was an scenario of singularity as a numerically inconsistent tangent stiffness matrix was assessed due to approximation errors. Similarly, the adoption of constitutive laws involving the assessment of an inconsistent tangent operator also induced no converging scenarios. In the absence of these drawbacks, the full Newton–Raphson method converges at a quadratic rate.

Chapter 6

Nonlinear Modelling of Unbonded Post-tensioned Timber Beam-Column Elements

As it has been mentioned before in section 2.4 and section 2.5, the modelling of post-tensioned beam-column structural components is a challenging task as unbonded post-tensioning tendons introduce strain incompatibilities and second order effects (eccentricity variation). To consider these features, two different modelling techniques are adopted and described in this chapter. One is based on a constantly updated equivalent load system whereas the other one relies on a load resisting element with a derived tangent stiffness matrix and internal force vector. Stress-strain relationships describing the short- and long-term behaviour of the post-tensioning strands comprising the tendons are presented together with a set of linearized nonlinear equations to assess the equilibrium state in two different stages. The first stage comprises the state just after the anchoring of the tendons whereas the second stage covers the states of the post-tensioned timber member under the action of short-or long-term external loads. Finally, a number of short- and long-term analyses are performed to validate the numerical framework.

6.1 Unbonded Tendon Modelling

In contrast to bonded post-tensioning tendons, unbonded tendons introduce a few additional modelling complexities such as strain incompatibility and gradual change in eccentricity. Strain incompatibility between the adjacent concrete and unbonded tendon implies that the displacements of the tendons are only compatible with the hosting member at the anchors and thus

the strain in the tendon is no longer section dependent. As a result, the assessment of strains is based on whole-member deformations (Dall'Asta et al. [233]). In the case of external post-tensioning tendons, the modelling complexities can be even more challenging as the tendon profile should remain straight between adjacent anchorages and/or deviators after deflection of the hosting member. This feature leads to second order effects as the eccentricity changes during the loading history (Harajli et al. [234]). An accurate determination of the equilibrium state after the force transfer or anchoring of the tendons is indispensable for modelling post-tensioned beam-column structural components as this state, after self-weight and post-tensioning loads self-equilibrate, establishes the initial condition for the next loading stage (Lou and Xiang [235]).

Within the various finite element (FE) models developed for post-tensioned reinforced concrete (RC) and composite members, unbonded tendons have been modeled as a system of equivalent loads or as a load resisting element. In the case of the equivalent load scheme, the tendon force components perpendicular and parallel to the centroidal axis of the hosting member are transferred to the member ends as tendon-eccentricity dependent moments. Earliest applications of this scheme to post-tensioned reinforced concrete structures can be referred to Kang and Scordelis [139], Ramos and Aparicio [236] and Aalami [237]. In this context, Lou and Xiang [238] proposed a method in which the tendon eccentricity and force are constantly updated with respect to the current position of member local axis by adopting an updated Lagrangian formulation. The eccentricity is assessed by means of a geometric method taking into account second order effects based on deformation compatibility of the whole member and kinematic assumptions of sliding behaviour between the tendon and the deviators.

The numerical method proposed by Lou and Xiang [238] has been used in a wide range of applications to study the effect of span-to-depth ratio on the flexural response of externally post-tensioned RC beams (Lou et al. [239]), the ultimate flexural behaviour of continuous RC beams post-tensioned with external tendons (Lou et al. [240]), the ultimate and long-term response of RC continuous beams with internal unbonded tendons (Lou et al. [241]), the moment redistribution in continuous post-tensioned RC members (Lou et al. [242]), the evolving eccentricities over time in externally post-tensioned beams (Lou et al. [243]), the short- and long-term response of post-tensioned steel–concrete composite (SCC) beams (Lou et al. [244],Lou and Karavasilis [245]), and the use of fibre reinforced polymer (FRP) composites as external tendons (Lou et al. [246],Lou and Karavasilis [247]). Páez and Sensale [248] and Páez and Sensale-Cozzano [249] have also employed the equivalent load scheme to study the time-dependent response of post-tensioned RC beams with internal tendons.

Regarding the modelling of unbonded post-tensioning tendons as load resisting elements, several approaches have been developed. According to Aalami [250] and El-Ariss [251], truss elements linked together by means of rigid arms to beam elements can be used to model post-tensioned RC beams. Similarly, Ariyawardena and Ghali [252] proposed the use of truss and beam elements connected through rigid arms to assess the ultimate response of post-tensioned RC beams with internal or external tendons. However, an iterative process is necessary to adjust the force in all tendon elements so that the converged force is the same throughout the tendon. Other authors have employed multi-freedom constraints in conjunction with truss and beam elements to simulate the ultimate response and progressive collapse response of post-tensioned RC beams (Nassif et al. [253]) and post-tensioned RC beam-column sub-assemblages (Feng et al. [254]), respectively. In these cases, the multi-freedom constraints are employed to impose the kinematic compatibility conditions between the tendon and its hosting elements. Sánchez et al. [255] adopted zero-length contact elements to model the slipping behavior of external tendons in post-tensioned SCC beams in which catenary and shell elements were employed to build a three-dimensional (3D) FE model.

Another FE modelling technique comprises the formulation of tendon elements incorporating a frictionless slipping behaviour whose benefits lays in the avoidance of multi-freedom constraints and contact elements to address the strain incompatibility between the unbonded tendons and hosting member. These techniques could potentially alleviate the numerical convergence issues faced during a nonlinear analysis. Wu et al. [256] and Wu and Lu [257] developed curved and straight sliding tendon elements embedded into bidimensional (2D) continuum elements to simulate the slipping behaviour of internal and external unbonded tendons at curved ducts and deviators, in post-tensioned RC beams, respectively. In the case of one-dimensional fibre beam-column elements, Dall'Asta and Zona [258] derived a sliding tendon element for externally post-tensioned SCC beams with deformable shear connection based on the work of Dall'Asta and Dezi [259]. In their derivation, the deformation of the sliding tendons, which consisted of piecewise linear segments, was assessed using a linearized expression of the deformed tendon length as the hosting member was assumed to undergo small deflections.

The derivation developed by Dall'Asta and Zona [258] was extended by Zona et al. [260] to introduce geometric nonlinearities. On the basis of the approximated nonlinear kinematic theory developed by Dall'Asta et al. [233], Zona et al. [260] derived a FE formulation for sliding tendons with piecewise configuration by adopting a total Lagrangian approach to set the equilibrium in the deformed configuration. Likewise, Moreira et al. [261] derived a sliding tendon formulation for post-tensioned RC beams with internal tendons of piecewise configuration by

describing the hosting member position with a total Lagrangian approach. However, Moreira et al. [261] employed different kinematic variables and simplifications to assess the tendon deformed length and deformation. Sousa Jr et al. [262] expanded this last formulation to evaluate the ultimate response of SCC beams with external post-tensioning and flexible shear connectors. Multi-node sliding elements were developed by Gao and Lu [263] to simulate the behaviour of self-centering connections by adopting a total Lagrangian approach in the element formulation. Yan et al. [264] derived also a multi-node sliding element to model the flexural response of precast RC segmental box girders post-tensioned with external tendons. Nonetheless, in the derivation of the element a corotational approach was used and rigid arms were used to connect the slipping tendon with the hosting member. The same research group then employed multi-node corotational slipping-tendon elements to assess the response of externally post-tensioned SCC beams with interfacial slip (Yan et al. [265]).

Another technique employed to model the complex behaviour of unbonded tendons includes the use of solid brick elements in conjunction with multi-freedom constraints. These constraints comprises Lagrange multiplier and penalty based methods that allow the simulation of the interaction between tendons and deviators/ducts along the normal and tangential directions of their contact surfaces. Regarding the normal direction, the constraints limit the penetration of the element contact surfaces into each other under compression stresses and restrict the development of tensile stresses between them to allow a gap. Otherwise, the constraints along with Coulomb friction models can be adopted to simulate the friction or even frictionless behavior between the tendons and deviators/ducts surfaces in the tangential direction. These models have been used to simulate the ultimate limit states of precast segmental RC beams post-tensioned with external (Tran et al. [266]) and internal (Tran et al. [267], Le et al. [268]) unbonded tendons.

As discussed in section 2.4 and section 2.5, to date, only solid brick elements and a conventional equivalent load scheme have been employed to simulate the short- and long-term behaviour of unbonded tendons in post-tensioned timber beam-column structural components, respectively. However, the use of solid elements leads to expensive computational cost and the employed equivalent load scheme has neglected second order effects. Therefore, in the analysis framework proposed in this chapter, a modified version of the constantly updated member-dependent equivalent load scheme proposed by Lou and Xiang [238] and an extended version of sliding tendon formulation derived by Moreira et al. [261] are adopted to address the strain incompatibility and second order effects as well as to attain computational efficiency. A schematic description of the implemented tendon modelling techniques are shown in Appendix A.

6.1.1 Equivalent Load Scheme

The numerical procedure for the modelling of unbonded tendons used herein is based on the preceding works of Lou and Xiang [238] which was continued and extended by Lou et al. [241] and Lou et al. [244]. Nevertheless, in the numerical approach formulated herein the deformed configuration of the hosting member is described by means of a corotational framework. Furthermore, in the assessment of the tendon coordinates the basic nodal end rotations and total rotation of the BC elements comprising the hosting member are used instead of the total nodal end rotations and initial inclination of the elements. In this procedure, the tendons are handled as equivalent loads applied to the centroidal axis of the hosting member and are constantly updated (in magnitude and orientation) as the hosting member deforms during the loading process. Moreover, a frictionless slipping behaviour between the tendon and deviators is assumed. Regarding the eccentricities, their variations due to the deformation of the hosting member are taken into account explicitly by means of a geometric method, described below, that permanently updates the tendon geometry. This procedure allows modelling internal unbonded tendons with different tendon profiles by considering them as conformed by piecewise segments.

It is worth noting that, unbonded external tendons refer to tendons that transfer the post-tensioning force to the hosting member through anchorages and deviators. By contrast, in the case of unbonded internal tendons, the tendon layouts have permanent contact with the internal duct that passes through the whole hosting member. In the description of the numerical procedure that follows, only the case of unbonded external tendons is considered as the unbonded internal case can be regarded as a particular instantiation of the unbonded external case by considering a sufficient number of deviators to describe the tendon profile.

A portion of a post-tensioned beam-column member between two contiguous deviators and/or anchorages is shown in Fig. 6.1. In this figure, the subscript 0 is associated with the initial or undeformed configuration before any self-weight and external loads are applied. As it has been mentioned previously, deformation compatibility between the tendon and hosting member occurs only at the anchorages. However, the deformed tendon length and orientation of the tendon force rely on the displacement of the deviators and anchorages with respect to the centroidal axis of the hosting member. In what follows, the deviator and anchorage coordinates in contact with the tendon are designated as deviator coordinates. If m and n are the left-end and right-end nodes of a portion of the post-tensioned member, respectively, a set of transformation equations linking the total displacements of the hosting member ends and

deviator coordinates can be established. To this end, the equations presented by Lou et al. [244] are modified as follows:

$$X_{pm} = X_{m_0} + U_m - e_m \bar{\Theta}_m \cos\alpha_l - e_m \sin\alpha_l \tag{6.1}$$

$$Y_{pm} = Y_{m_0} + V_m - e_m \bar{\Theta}_m \sin\alpha_l + e_m \cos\alpha_l \tag{6.2}$$

$$X_{pn} = X_{n_0} + U_n - e_n \bar{\Theta}_n \cos\alpha_r - e_n \sin\alpha_r \tag{6.3}$$

$$Y_{pn} = Y_{n_0} + V_n - e_n \bar{\Theta}_n \sin\alpha_r + e_n \cos\alpha_r \tag{6.4}$$

where (X_{pm}, Y_{pm}) and (X_{pn}, Y_{pn}) are the deviator coordinates, (X_m, Y_m) and (X_n, Y_n) are the hosting member coordinates in its deformed configuration, $\bar{\Theta}_m$ and $\bar{\Theta}_n$ are the basic rotations, e_m and e_n are the tendon eccentricities; and (U_m, V_m) and (U_n, V_n) are the displacements at nodes m and n, respectively. Besides, the angles α_l and α_r are the inclinations of left-end and right-end elements with respect to the global horizontal axis. The subscript 0 refers to the initial or undeformed configuration.

The transformation equations, Eqs. (6.1) to (6.4), describe the kinematic relationship linking the deviator nodes and end nodes of the hosting member. It is assumed that the deviators behave like rigid arms. As a result, the tendon eccentricities at the deviators remain unchanged whereas the eccentricities in between are subjected to continuos change as the hosting member deforms during the loading process. The use of these relationships allows the assessment of the deformed tendon length and thus the evaluation of tendon strain considered constant along the whole member due to the assumption of frictionless slippage behaviour between the tendon and deviators. It is worth mentioning that non multi-freedom constraints are required to link the deviator and hosting member nodes which may result in less computational effort.

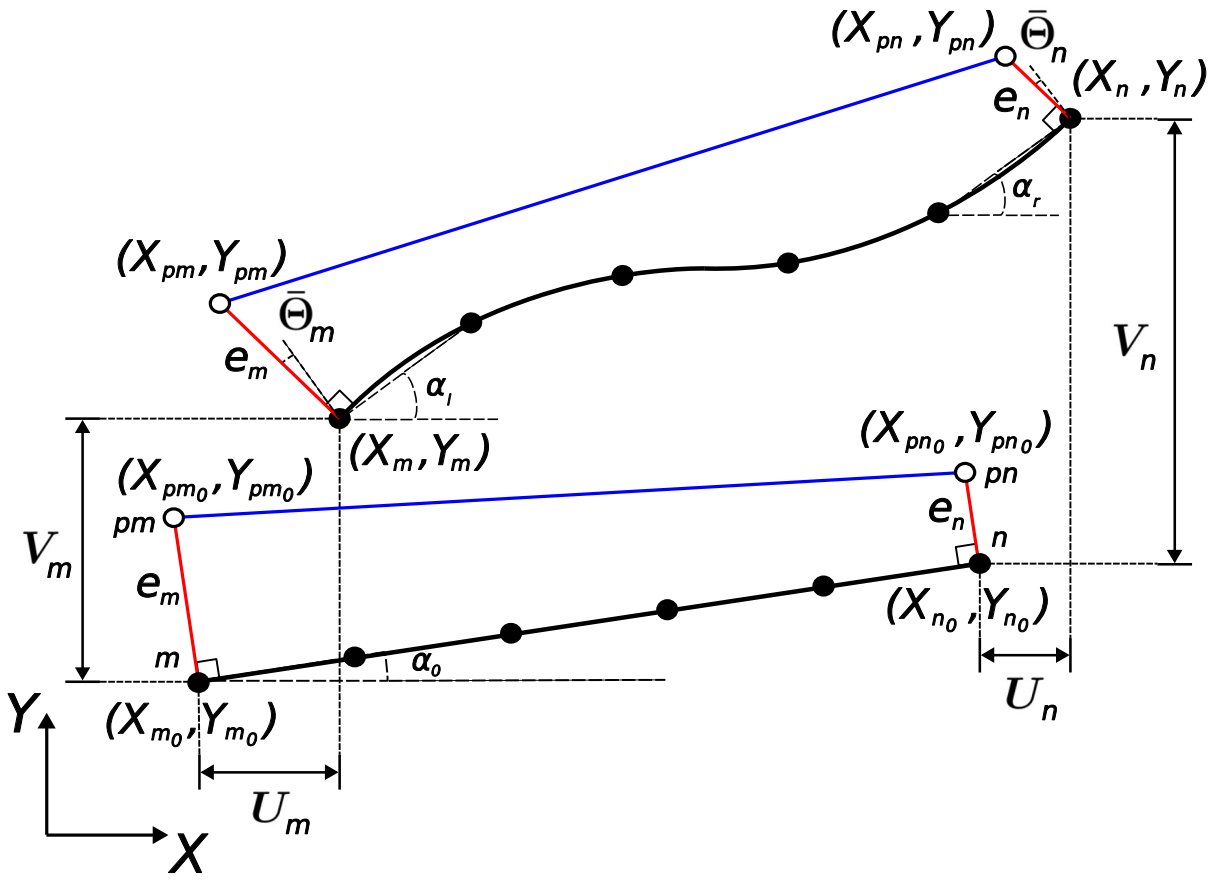


Figure 6.1: Tendon and hosting member in the undeformed and deformed configuration.

In the case of external unbonded tendons, the tendon eccentricity varies as the hosting member deforms. This phenomenon is known as second-order effects which are characteristic of externally post-tensioned members with tendon profiles inside and outside of the member section. The present methodology addresses the eccentricity variations in an explicit way and the corresponding numerical procedure is summarized in Fig. 6.2. To explain this procedure, the beam-column element with nodes i and j and the hosting member portion between nodes m and n are selected as the instance case. The initial tendon eccentricity of the element is determined by the initial coordinates of the deviators at the ends of the hosting member portion under consideration, and by the discretization of the tendon and hosting member in between these end nodes. It must be highlighted that the discretization of the tendon segment must correspond to each discretization of the member portion as shown in Fig. 6.2. After a deformation is imposed to the hosting member, the deviator coordinates are updated by means of Eqs. (6.1) to (6.4). Then, to calculate the updated values of the tendon eccentricities at nodes i and j, perpendiculars to the deformed configuration at these nodes are traced. This allows the determination of the intersections (points pi and pj) of these perpendiculars with the straight line that defines the position of the tendon. Finally, the tendon eccentricity is

the distance between these intersections points and the nodes of the beam-column element. To consider internal unbonded tendons within this numerical procedure, the deviators can be assumed to be located at every node of the hosting member. Therefore, the tendon eccentricity remains constant along the entire procedure which reflects the main difference between external and internal unbonded tendons.

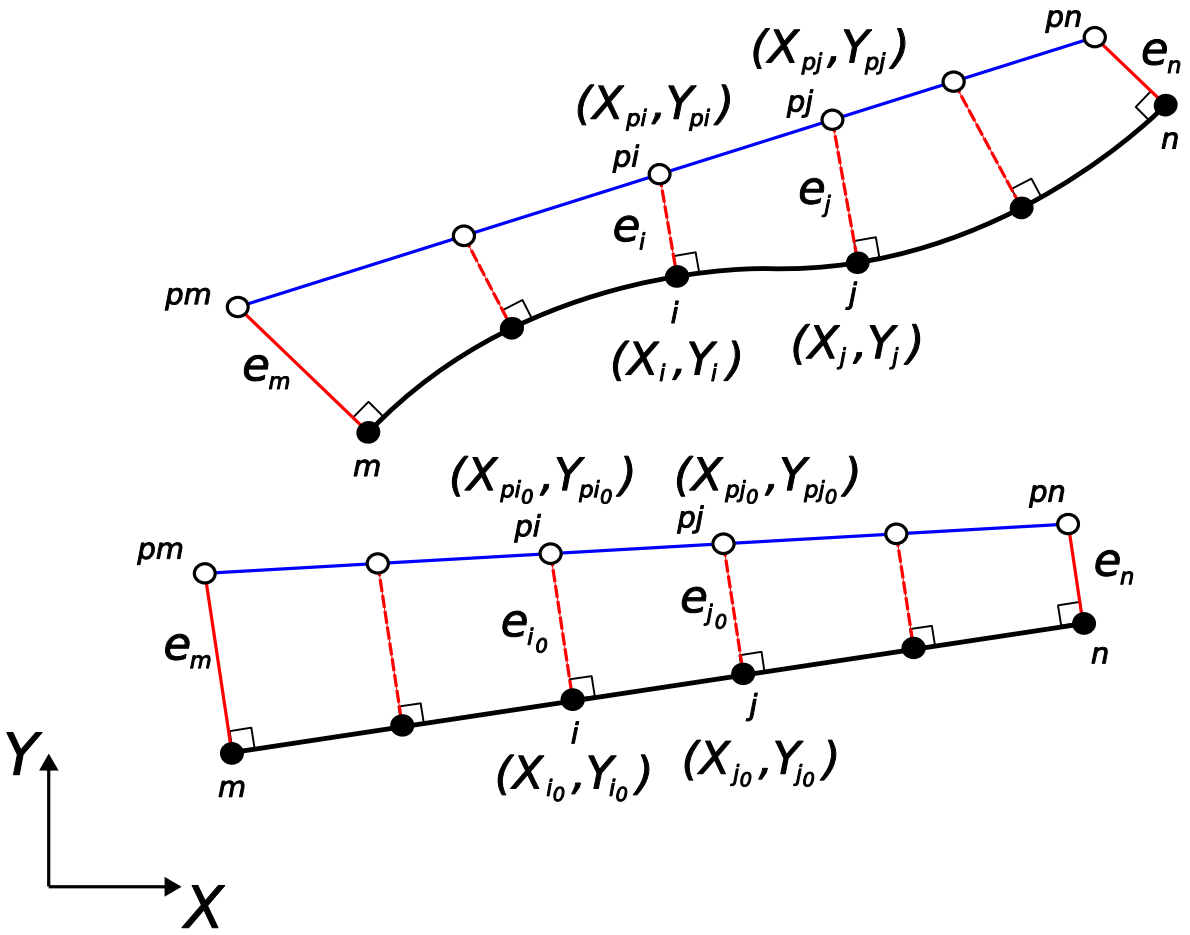


Figure 6.2: Procedure to update the tendon eccentricity.

Assuming that the tendon profile has a piecewise linear shape during the whole loading process, the deformed length of the tendon between two contiguous deviators, m and n, can be assessed as:

$$L_{p_{mn}} = \sqrt{(X_{pm} - X_{pn})^2 + (Y_{pm} - Y_{pn})^2} \tag{6.5}$$

The deformed length is constantly updated during the incremental iterative process. As the tendon is assumed to slip freely without friction between itself and the duct/deviator, the tendon strain can be regarded as constant along its full length. As a result, the strain increment in the tendon due to the deformation of the hosting member during the loading process can be

obtained as:

$$\Delta\varepsilon_p = \frac{\sum L_{p_{mn}} - L_{p_0}}{L_{p_0}} \tag{6.6}$$

where $\sum L_{p_{mn}}$ represents the sum of each tendon segment length in the deformed state and L_{p_0} is the total length in the initial or undeformed configuration.

The constant strain along the unbonded tendon for a specific state of post-tensioning and deformation can be calculated as:

$$\varepsilon_p = \Delta\varepsilon_p + \varepsilon_{p_0} \tag{6.7}$$

where ε_{p_0} is the initial tendon strain just after the post-tensioning operation or during the anchorage.

The force in the tendon can be straightforwardly assessed by multiplying the tendon stress by its area. To evaluate the stress in the tendon, the tendon strain [Eq. (6.7)] should be substituted in the constitutive stress-strain relationship, $f_p(\varepsilon_p)$, that governs the behaviour of the steel strands of the post-tensioning tendons. Then, the tendon force is obtained from:

$$F_p = f_p(\varepsilon_p) A_p \tag{6.8}$$

Once the tendon force and eccentricities related to a specific beam-column element are known, the post-tensioning equivalent load exerted by the tendon segment between nodes i and j can be determined as follows:

$$\boldsymbol{F}'_{post} = F_p \begin{bmatrix} -\cos\beta & \sin\beta & e_i\cos\beta & \cos\beta & -\sin\beta & -e_j\cos\beta \end{bmatrix}^T \tag{6.9}$$

where β is the angle between the current position of the element longitudinal axis and the corresponding tendon segment as depicted in Fig. 6.3. This angle can be evaluated as:

$$\tan\beta = \frac{e_i - e_j}{l_p} \tag{6.10}$$

where l_p is the length of the tendon segment.

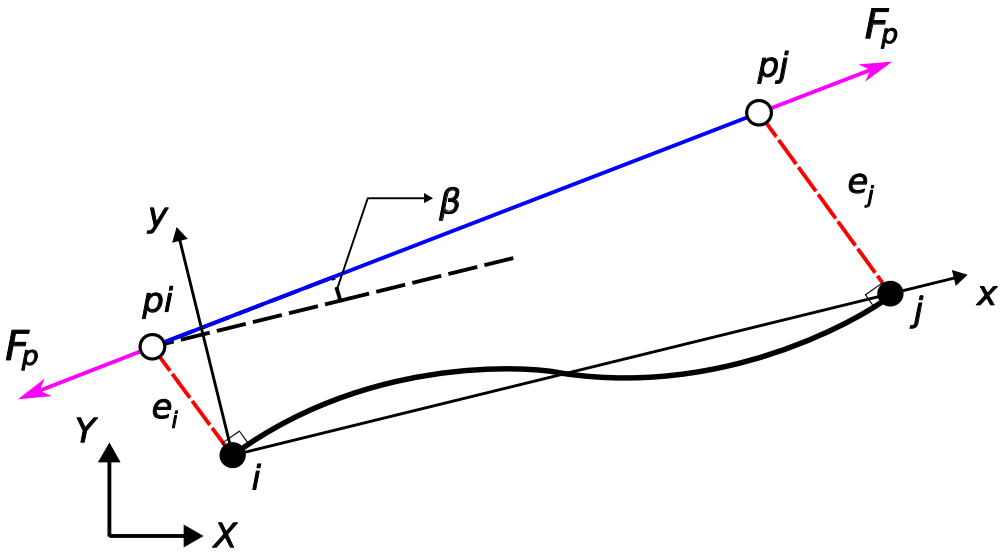


Figure 6.3: Post-tensioning load in a tendon segment.

It should be noted that the equivalent loads in Eq. (6.9) are defined within a local coordinate system. After the determination of the local equivalent loads, the total equivalent nodal load resisted by the tendon at the structural level is computed by assembling all the local contributions. During this assembling process, the contributions of all the tendon segments are transformed from the local coordinate system to the global coordinate system. These local equivalent loads are constantly changing in magnitude and direction throughout the incremental-iterative numerical procedure.

6.1.2 Load Resisting Element

Moreira et al. [261] derived a sliding tendon formulation for unbonded internal tendons on the basis of a frictionless slipping behaviour between the tendon and the duct. It was assumed that the tendon configuration consists of piecewise straight segments in contact with the duct and anchorages at discrete locations through rigid arms as considered by [244] and Lou et al.. Furthermore, the same kinematic relationships employed by Lou et al. [241] to link the nodes of the hosting member elements and rigid arms were adopted. In order to describe the deformed configuration of the hosting member, the authors employed a total Lagrangian description that considers large displacements and moderate rotations in conjunction with the Euler-Bernoulli beam theory. As a result, a sliding tendon element that does not require the modelling of rigid arms by means of multi-freedom constraints was formulated. The element was then extended by Sousa Jr et al. [262] to address external unbonded tendons. Nevertheless, The formulation was derived for hosting members without inclination and assuming a linearized kinematic relationship between the displacements of the hosting members and rigid arms. In

this section, the sliding element derived for internal and external tendons is extended to consider a hosting member with an initial inclination by means of non-linearized kinematic relationships. Furthermore, a corotational approach is adopted to describe the deformed configuration of the hosting member.

The same derivation process adopted by Moreira et al. [261] and Sousa Jr et al. [262] is followed here. The process consists first of setting a kinematic relationship in terms of global coordinates and displacements between the nodes of the post-tensioned hosting member in their undeformed and deformed configurations. These relationships are then used to assess the deformed tendon length and thus the deformation in the tendon element. Finally, an internal work expression is constructed for the tendon element with the aim of deriving its internal force vector and consistent tangent stiffness matrix.

A kinematic relationship is established to link the coordinates of rigid arms in contact with the tendon and hosting member. The rigid arms represent the deviators and/or anchorages employed in externally post-tensioned members to transfer the post-tensioning force to the hosting member. In the deformed configuration shown in Fig. 6.4, the following coordinate transformation equations can be set:

$$X_{pm} = X_{m_0} + U_m - e_m \sin\Theta_m \cos\alpha_0 - e_m \sin\alpha_0 \cos\Theta_m \tag{6.11}$$

$$Y_{pm} = Y_{m_0} + V_m - e_m \sin\Theta_m \sin\alpha_0 + e_m \cos\alpha_0 \cos\Theta_m \tag{6.12}$$

$$X_{pn} = X_{n_0} + U_n - e_n \sin\Theta_n \cos\alpha_0 - e_n \sin\alpha_0 \cos\Theta_n \tag{6.13}$$

$$Y_{pn} = Y_{n_0} + V_n - e_n \sin\Theta_n \sin\alpha_0 + e_n \cos\alpha_0 \cos\Theta_n \tag{6.14}$$

where Θ_m and Θ_n are the global rotations of left-end and right-end elements in the hosting member at nodes m and n, respectively, α_0 is the initial inclination angle of hosting elements with respect to the global horizontal axis, and the subscript 0 in the coordinates refers to the initial or undeformed configuration.

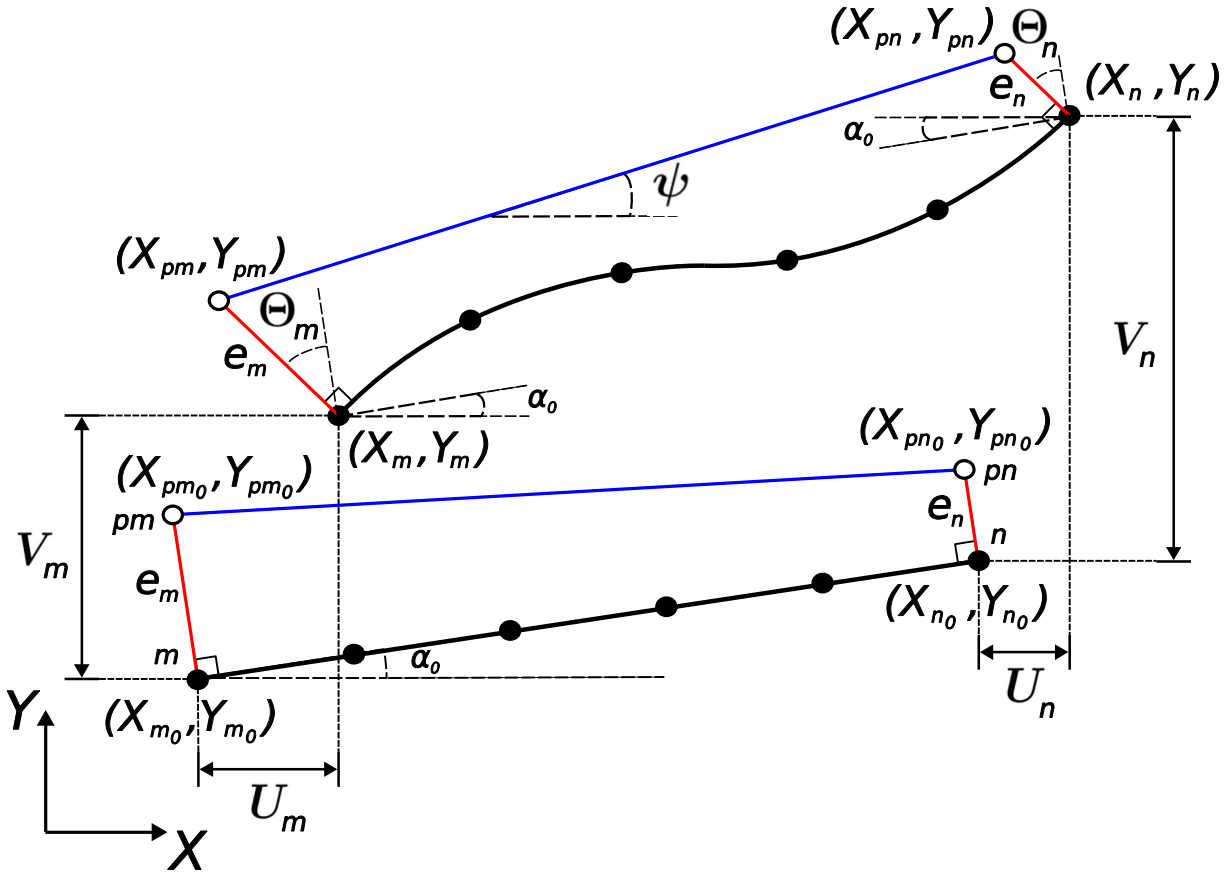


Figure 6.4: Tendon and hosting member in the undeformed and deformed configuration.

It is worth noting that the transformation equations derived (Eqs. (6.11) to (6.14)) are similar to the ones employed by Lou et al. [241]. However, the rotations in the hosting elements are not considered to be small enough in the kinematic relationships. This assumption allows the derivation of closed form expressions to assess the internal force vector and consistent tangent stiffness matrix of the sliding tendon element. Similarly, the displacements of the hosting elements at nodes m and n comprising the tendon segment k, $\boldsymbol{U}_k$, can be related to the displacement vector of the whole structure, $\boldsymbol{U}$, as follows:

$$\begin{bmatrix} U_m & V_m & \Theta_m & U_n & V_n & \Theta_n \end{bmatrix}^T = \boldsymbol{U}_k = \boldsymbol{L}_k \boldsymbol{U} \tag{6.15}$$

where $\boldsymbol{L}_k$ is the matrix relating the degrees of freedom (DOF) of the hosting member nodes linked to the tendon segment k and the DOF of the entire structure.

As a frictionless slipping behaviour is assumed, the tendon deformation is constant along the tendon length. As a result, the internal virtual work associated with the tendon deformation can be assessed in the following simplified way:

$$\delta \mathcal{W}_{int_p} = \int_{V_p} \delta\varepsilon_p \, \sigma_p \, d\, V_p = \delta\varepsilon_p \, F_p \, L_p \approx \delta\varepsilon_p \, F_p \, L_{p_0} \tag{6.16}$$

where L_p is the deformed length of the tendon and $\delta\varepsilon_p$ is the variation of the tendon strain. From this equation, it can be observed that the assessment of the virtual work for the tendon can be approximated by using the initial length of the tendon instead of the undeformed one. This approximation can be considered accurate enough if the strain experienced in the tendon is small.

From Eqs. (6.6) and (6.7), the variation of the tendon strain is given by:

$$\delta\varepsilon_p = \frac{\delta L_p}{L_{p_0}} \tag{6.17}$$

Considering that the current length of a tendon segment k is L_{pk}, the variation of the deformed length of the whole tendon can be assessed as:

$$\delta L_p = \sum_{k=1}^{n_p} \delta L_{pk} \tag{6.18}$$

where n_p is number of segments comprising the tendon. The current length of a tendon segment k can be evaluated using Eq. (6.5) which can be rewritten as:

$$L_{pk} = \sqrt{(L_{pk\,X})^2 + (L_{pk\,Y})^2} \tag{6.19}$$

where $L_{pk\,X}$ and $L_{pk\,Y}$ are the projections of the tendon segment in the axis X and Y, respectively. As a result, the variation of the current length of a specific tendon segment can be assessed through the following compact expression:

$$\delta L_{pk} = \delta L_{pk\,X} \cos\psi + \delta L_{pk\,Y} \sin\psi \tag{6.20}$$

where $\delta L_{pk\,X}$ and $\delta L_{pk\,Y}$ are the variation of the segment length projections, and ψ is the inclination angle of tendon segment in the deformed configuration as shown in Fig. 6.4.

From Eqs. (6.11) to (6.14), the variation of the segment length projections can be evaluated as:

$$\begin{aligned}\delta L_{pk\,X} = \delta U_n - \delta U_m &+ (\cos\Theta_m \cos\alpha_0 - \sin\alpha_0 \sin\Theta_m)\, e_m\, \delta\Theta_m \\ &- (\cos\Theta_n \cos\alpha_0 - \sin\alpha_0 \sin\Theta_n)\, e_n\, \delta\Theta_n\end{aligned} \tag{6.21}$$

$$\delta L_{pk_Y} = \delta V_n - \delta V_m + (\cos\Theta_m \sin\alpha_0 + \cos\alpha_0 \sin\Theta_m)\, e_m\, \delta\Theta_m \\ - (\cos\Theta_n \sin\alpha_0 + \cos\alpha_0 \sin\Theta_n)\, e_n\, \delta\Theta_n \tag{6.22}$$

After inserting Eqs. (6.21) and (6.22) into Eq. (6.20) and performing some manipulations, the variation of the tendon segment length can be conveniently arranged in the following matrix form:

$$\delta L_{pk} = \boldsymbol{W}_{pk}^T\, \delta\, \boldsymbol{U}_k \tag{6.23}$$

where

$$\boldsymbol{W}_{pk} = \begin{bmatrix} -\cos\psi \\ -\sin\psi \\ e_m \cos(\Theta_m + \alpha_0 - \psi) \\ \cos\psi \\ \sin\psi \\ -e_n \cos(\Theta_n + \alpha_0 - \psi) \end{bmatrix} \tag{6.24}$$

$$\delta\, \boldsymbol{U}_k = \begin{bmatrix} \delta U_m & \delta V_m & \delta\Theta_m & \delta U_n & \delta V_n & \delta\Theta_n \end{bmatrix}^T \tag{6.25}$$

If Eqs. (6.17), (6.18) and (6.23) are substituted into Eq. (6.16), the virtual work equation related to the tendon deformation can be evaluated as follows:

$$\delta\mathcal{W}_{int_p} = \sum_{k=1}^{n_p} \delta L_{pk}\, F_p = \sum_{k=1}^{n_p} F_p\, \boldsymbol{W}_{pk}^T\, \delta\, \boldsymbol{U}_k \tag{6.26}$$

From the previous equation, it can be established that internal force vector of the tendon segment can be assessed as:

$$\boldsymbol{g}_{pk} = F_p\, \boldsymbol{W}_{pk} \tag{6.27}$$

If Eq. (6.15) is replaced into Eq. (6.26), the contribution of the tendon element to the internal force vector of the whole structure can be evaluated as:

$$\boldsymbol{g}_p = \sum_{k=1}^{n_p} \boldsymbol{L}_k^T\, \boldsymbol{g}_{pk} \tag{6.28}$$

However, in the numerical framework implemented herein, the internal force vector of the tendon element at the structural level is obtained by a conventional assembling process of the contribution of each tendon segment. This process can be represented by using the following assembly operator:

$$\boldsymbol{g}_p = \mathop{\mathbf{A}}_{k=1}^{n_p} \boldsymbol{g}_{pk} \tag{6.29}$$

The tangent stiffness of the tendon element at the structural level, $\boldsymbol{K}_p$, can be obtained by differentiating the internal force vector, $\boldsymbol{g}_p$, with respect to the nodal displacements of the whole structure:

$$\boldsymbol{K}_p = \frac{\partial \boldsymbol{g}_p}{\partial \boldsymbol{U}} = \sum_{k=1}^{n_p} \boldsymbol{L}_k^T \frac{\partial \boldsymbol{g}_{pk}}{\partial \boldsymbol{U}} \tag{6.30}$$

After inserting Eq. (6.27) into the previous equation, the tangent stiffness can be rewritten as follows:

$$\boldsymbol{K}_p = \sum_{k=1}^{n_p} \boldsymbol{L}_k^T \boldsymbol{W}_{pk} \frac{\partial F_p}{\partial \boldsymbol{U}} + \sum_{k=1}^{n_p} \boldsymbol{L}_k^T \frac{\partial \boldsymbol{W}_{pk}}{\partial \boldsymbol{U}} F_p = \boldsymbol{K}_{mp} + \boldsymbol{K}_{gp} \tag{6.31}$$

In Eq. (6.31), the first and second term of the right hand side are denominated as the material and geometric stiffness of the tendon element. From Eqs. (6.8), (6.17), (6.18) and (6.23), the derivative of tendon force with respect the nodal displacement can be evaluated as follows:

$$\frac{\partial F_p}{\partial \boldsymbol{U}} = A_p \frac{\partial f_p(\varepsilon_p)}{\partial \varepsilon_p} \frac{\partial \varepsilon_p}{\partial \boldsymbol{U}} = \frac{E_p A_p}{L_{p0}} \sum_{j=1}^{n_p} \boldsymbol{W}_{pj}^T \boldsymbol{L}_j \tag{6.32}$$

As a result, the material stiffness of the tendon can calculated as:

$$\boldsymbol{K}_{mp} = \frac{E_p A_p}{L_{p0}} \sum_{k=1}^{n_p} \boldsymbol{L}_k^T \boldsymbol{W}_{pk} \sum_{j=1}^{n_p} \boldsymbol{W}_{pj}^T \boldsymbol{L}_j = \frac{E_p A_p}{L_{p0}} \boldsymbol{W}_p \boldsymbol{W}_p^T \tag{6.33}$$

where E_p is the tangent modulus of the strand material. The vector $\boldsymbol{W}_p$ can be assembled as follows:

$$\boldsymbol{W}_p = \sum_{k=1}^{n_p} \boldsymbol{L}_k^T \boldsymbol{W}_{pk} = \mathop{\mathbf{A}}_{k=1}^{n_p} \boldsymbol{W}_{pk} \tag{6.34}$$

The geometric stiffness of the tendon can be assessed as:

$$\boldsymbol{K}_{gp} = F_p \sum_{k=1}^{n_p} \boldsymbol{L}_k^T \frac{\partial \boldsymbol{W}_{pk}}{\partial \boldsymbol{U}_k} \frac{\partial \boldsymbol{U}_k}{\partial \boldsymbol{U}} = F_p \sum_{k=1}^{n_p} \boldsymbol{L}_k^T \frac{\partial \boldsymbol{W}_{pk}}{\partial \boldsymbol{U}_k} \boldsymbol{L}_k \tag{6.35}$$

The derivative of $\boldsymbol{W}_{pk}$ with respect to the nodal displacements of the hosting member at its end nodes can evaluated as:

$$\frac{\partial \boldsymbol{W}_{pk}}{\partial \boldsymbol{U}_k} = \frac{\partial \boldsymbol{W}_{pk}}{\partial \psi} \frac{\partial \psi}{\partial \boldsymbol{U}_k} \tag{6.36}$$

Taking the derivative of vector $\boldsymbol{W}_{pk}$ in Eq. (6.24) with respect to inclination angle of the tendon segment is given by:

$$\frac{\partial \boldsymbol{W}_{pk}}{\partial \psi} = \boldsymbol{Z}_{pk} = \begin{bmatrix} \sin\psi \\ -\cos\psi \\ e_m \sin\left(\Theta_m + \alpha_0 - \psi\right) \\ -\sin\psi \\ \cos\psi \\ -e_n \sin\left(\Theta_n + \alpha_0 - \psi\right) \end{bmatrix} \tag{6.37}$$

Besides, it can be deduced that:

$$\frac{\partial \psi}{\partial \boldsymbol{U}_k} = \frac{\boldsymbol{Z}_{pk}^T}{L_{pk}} \tag{6.38}$$

Therefore, after replacing Eqs. (6.37) and (6.38) in Eq. (6.36), the geometric stiffness matrix in Eq. (6.35) can be rewritten as follows:

$$\boldsymbol{K}_{gp} = \sum_{k=1}^{n_p} \boldsymbol{L}_k^T \frac{F_p}{L_{pk}} \boldsymbol{Z}_{pk} \boldsymbol{Z}_{pk}^T \boldsymbol{L}_k = \sum_{k=1}^{n_p} \boldsymbol{L}_k^T \boldsymbol{K}_{gp_k} \boldsymbol{L}_k \tag{6.39}$$

where $\boldsymbol{K}_{gp_k}$ is geometric tangent stiffness of a tendon segment. As a result, the total geometric tangent stiffness of the tendon element can be assembled as follows:

$$\boldsymbol{K}_{gp} = \mathop{\mathrm{A}}_{k=1}^{n_p} \boldsymbol{K}_{gp_k} \tag{6.40}$$

6.2 Tendon Constitutive Laws

Uniaxial stress-strain laws are adopted to model the short-term and long-term response of unbonded tendons to accurately represent non-linear material behavior of the steel strands that comprise the these tendons. A well-known stress-strain relationship is adopted to describe a nonlinear elastic behavior of the strands under short-term loading. For tendons under the action of long-term loading, two different numerical procedures are adopted to take into account the

time-dependent behaviour of the steel strands under different loading and interaction scenarios as described bellow.

6.2.1 Nonlinear Elastic Model

The stress-strain relationship for steel strands under short-term uniaxial tension devised by Menegotto and Pinto [269] is employed in this framework. The corresponding curve is depicted in Fig. 6.5 and can be assessed by employing the following expression:

$$\sigma_p\left(\varepsilon_p\right) = E_p\,\varepsilon_p \left(Q + \frac{1-Q}{\left(1+\left(\frac{E_p\varepsilon_p}{K f_{py}}\right)^R\right)^{\frac{1}{R}}} \right) \quad \leq \quad f_{pu} \tag{6.41}$$

where f_{pu}, f_{py} and E_p are the ultimate tensile strength, yield stress, and modulus of elasticity of the steel strand; and R, K and Q are empirical coefficients defined according to the type of steel strand employed. It is worth noting that this constitutive law does not allow inelastic deformation or damage in the material.

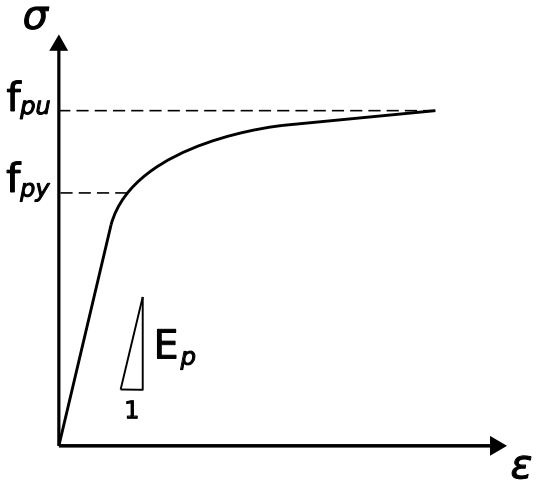


Figure 6.5: Stress-strain curves for the strand material.

6.2.2 Rheological Model

Regarding prestressing steel, two common expressions are widely adopted in the engineering practice to assess the prestress loss due to the stress relaxation phenomenon. In the case of the European practice, the CEB [270] considers the following equation:

$$\frac{\sigma_p(t_0) - \sigma_p(t)}{\sigma_p(t_0)} = \rho \left(\frac{t - t_0}{\lambda_1} \right)^k \tag{6.42}$$

where t is the time that passed since the transfer of the post-tensioning force, t_0 is the time at stress transfer process, σ_p is the axial stress in the steel strand or bar, $\lambda_1 = 1000\,h$, ρ is a parameter that depends of the initial stress and the class of prestressing steel, and k is an exponent parameter depending on the type of prestressing steel employed.

In the case of the North American practice, the equation proposed by Magura et al. [271] is adopted:

$$\frac{\sigma_p(t_0) - \sigma_p(t)}{\sigma_p(t_0)} = \ln\left(\frac{t - t_0}{\lambda_0}\right) \frac{\sigma_p(t_0) - s_0}{s_y} \tag{6.43}$$

where $\lambda_0 = 1\,h$, $s_0 = 0.55\,f_{py}$, $s_y = k_r\,ln(10)\,f_{py}$, f_{py} is the specified yield strength of the prestressing steel, and k_r is a parameter considering normal or low relaxation.

It is worth noting that Eqs. (6.42) and (6.43) assess the stress relaxation under test conditions meaning that the tendon length is kept constant and subjected to a single prestressing force variation. Nevertheless, under real loading scenarios, the stress applied in the tendon and its length can experience variations along the time due to different construction stages and the interaction between the distinct long-term deformations. Therefore, a more robust numerical procedure would be required to take into account these effects.

Alternatives such as the use of a linear Maxwell chain model as employed by Barbieri et al. [272] following the procedure proposed by Bažant and Wu [273] or an equivalent creep coefficient as describe by Au and Si [274] can be adopted to describe the long-term behaviour of the prestressing steel under real loading scenarios. However, these procedures do not incorporate the dependency of the stress relaxation on the initial prestress level. In the numerical framework implemented here, the widely adopted numerical procedure proposed by Hernandez and Gamble [275] and the realistic constitutive model for steel relaxation developed by Bažant and Yu [276] are incorporated.

The method proposed by Hernandez and Gamble [275] consists in the assessment of the prestress relaxation by employing an updated version of Eqs. (6.42) and (6.43). With this aim, the initial prestress $\sigma_p(t_0)$ is updated at each time step of the analysis. In this procedure, in order to assess the initial prestress, the prestress level at the beginning of each analysis step is taken as the result of the relaxation of this fictitious initial prestress. In case of using the expression proposed by Magura et al. [271], the amount of prestress relaxation $\Delta\sigma_{pr}^n$ taking place at time step n, comprising the time interval $[t_{n-1}, t_n]$, can be assessed as stated by Lou

et al. [277]:

$$\Delta\sigma_{pr}^{n} = \frac{\sigma_p^n(t_0)}{k_r}\left(\frac{\sigma_p^n(t_0)}{f_{py}} - 0.55\right)\left[\log_{10}(t_n - t_0) - \log_{10}(t_{n-1} - t_0)\right] \tag{6.44}$$

where $\sigma_p^n(t_0)$ is the fictitious initial prestress for the time step n of the analysis. Similarly, in case of using the expression proposed by the CEB [270], the following expression to assess the prestress relaxation can be used:

$$\Delta\sigma_{pr}^{n} = \sigma_p^n(t_0)\,\rho\left[\left(\frac{t_n - t_0}{\lambda_1}\right)^k - \left(\frac{t_{n-1} - t_0}{\lambda_1}\right)^k\right] \tag{6.45}$$

Regarding the procedure proposed by Bažant and Yu [276], in order to incorporate the dependency of the relaxation on the applied stress, the authors considered a viscoplastic constitutive model capable of describing Eqs. (6.42) and (6.43) for the case of constant deformation. Based on the equation adopted by the CEB [270], the following differential equation describes the viscoplastic behaviour of the prestressing steel:

$$\dot{\varepsilon_p} = \frac{\dot{\sigma}_p}{E_{pt}} + \frac{k\rho^{1/k}}{E_{pt}\lambda_1}\frac{F(\varepsilon_p)}{\left(1 - \sigma_p/F(\varepsilon_p)\right)^{1/k-1}} \tag{6.46}$$

where E_{pt} is the tangential modulus of the prestressing steel and $F(\varepsilon_p)$ is a monotonically increasing function describing the short-term stress-strain relationship of the steel strands. In case of describing the relaxation expression proposed by Magura et al. [271] under a constant deformation scenario, Bažant and Yu [276] suggested the following differential equation:

$$\dot{\varepsilon_p} = \frac{\dot{\sigma}_p}{E_{pt}} + \frac{F(\varepsilon_p)}{E_{pt}s_y\lambda_0}\left\langle F(\varepsilon_p) - s_0\right\rangle exp\left[-\frac{s_y}{\langle F(\varepsilon_p) - s_0\rangle}\left\langle 1 - \frac{\sigma_p}{F(\varepsilon_p)}\right\rangle\right] \tag{6.47}$$

To solve Eqs. (6.46) and (6.47), the Runge-Kutta explicit integration method comprising expressions with truncation errors of fourth and filth order are used (Dormand and Prince [232]).

6.3 Incremental Finite Element Equations

In order to solve the global incremental equilibrium equations of unbonded post-tensioned members over the entire loading range, the nonlinear analysis is performed in two stages. The first stage refers to the equilibrium state between the application of post-tensioning tendon forces and the self-weight of the hosting members. More specifically, this stage represents the state just after the stress transfer process in the post-tensioning operation. To estimate this

state of equilibrium accurately, the initial tendon strain ε_{p_0} in Eq. (6.7) should be known. In case this strain value is available the incremental equilibrium equations can be solved directly employing a load control method. However, in the majority of cases, only the tendon stress at the end of the prestress transfer is known. This final value of tendon stress is usually denominated as the effective prestress, σ_{pe}. Generally, the initial strain applied in the tendon is greater than the resulting strain after the transfer process. This larger strain is the result of the elastic shortening of the hosting member due to the post-tensioning force. Lou et al. [241] proposed an iterative trial-and-error method to assess the initial strain in the tendon. However, in this numerical framework a more robust method is implemented as described in the following subsections. Once the equilibrium state after the release of the tendon and transfer of the post-tensioned force is evaluated, a second stage is set to assess the effects of imposing additional external loads on the structure.

6.3.1 Stage at the Transfer of the Post-tensioning Force

As it has been mentioned before, generally only the effective prestress is available. To determine the initial strain in the tendon and thus any state of deformation in the tendon after the prestress transfer, Moreira et al. [261] and Sousa Jr et al. [262] proposed a robust numerical procedure which is followed in this work. This procedure consist in deriving a set of nonlinear equations by adding an additional equation to the incremental equilibrium equations of the structural system defining the equilibrium between the post-tensioning and self-weight loads. The resulting nonlinear equations can be written as follows:

$$\begin{bmatrix} \boldsymbol{r}\left(\boldsymbol{U}, \varepsilon_{p_0}\right) \\ F_p\left(\boldsymbol{U}, \varepsilon_{p_0}\right) - F_{pe} \end{bmatrix} = \begin{bmatrix} \mathbf{0} \\ 0 \end{bmatrix} \tag{6.48}$$

where $\boldsymbol{r}\left(\boldsymbol{U}, \varepsilon_{p_0}\right)$ is the residual force related to the structural system, which is a function of the global displacements, $\boldsymbol{U}$, and the initial tendon strain, ε_{p_0}; and F_{pe} is the corresponding tendon force for a given effective prestress in the tendon.

To solve the nonlinear equations in Eq. (6.48), a linearization procedure is performed resulting in the following nonlinear system of coupled equations:

$$\begin{bmatrix} \boldsymbol{K}_T & A_p\, E_{pt}\, \boldsymbol{W}_p \\ \dfrac{A_p\, E_{pt}}{L_{p_0}}\, \boldsymbol{W}_p^T & A_p\, E_{pt} \end{bmatrix} \begin{bmatrix} \Delta \boldsymbol{U} \\ \Delta \varepsilon_{p_0} \end{bmatrix} = - \begin{bmatrix} \boldsymbol{r} \\ F_p - F_{pe} \end{bmatrix} \tag{6.49}$$

where $\boldsymbol{K}_T$ is the tangent stiffness of the whole structure, E_{pt} is the tangent modulus of the prestressing steel and $\boldsymbol{W}_p$ is the vector defined in Eq. (6.34). The resulting tangent stiffness matrix of the system related to previous equation is going to be denominated as $\boldsymbol{K}_{TS}$.

It is worth noting that Eq. (6.49) is derived by considering the stiffness matrix and resisting internal force of the hosting members and tendon element. Therefore, traditional Newton-Raphson methods can be applied to solve these nonlinear equations. In case of employing the equivalent load scheme described in subsection 6.1.1, only the forces generated by the tendon segments are included. This feature implies that the evaluation of the true total tangent stiffness matrix of the system is not possible. In this case, Quasi-Newton methods can be employed to approximate the missing true stiffness matrix in the nonlinear system of equations. In this work, the well-known Broyden and Broyden–Fletcher–Goldfarb–Shanno (BFGS) methods (Dennis and Moré [278]) are adopted. The Broyden method consist on performing a first-order update of the stiffness matrix whereas the BFGS method conducts a rank-two update. To start these numerical algorithms, an initial guess of the tangent stiffness matrix $\boldsymbol{K}_{TS}^0$ has to be made. In this case, the following approximation was adopted:

$$\boldsymbol{K}_{TS}^0 = \begin{bmatrix} \boldsymbol{K}_T & \boldsymbol{0} \\ \boldsymbol{0} & A_p\, E_{pt} \end{bmatrix} \tag{6.50}$$

where $\boldsymbol{K}_T$ in this case only contains the stiffness matrix of the beam-column elements.

6.3.2 Stage after the Transfer of the Post-tensioning Force

The incremental equilibrium equations after the transfer stress process represents the equilibrium states when the structure is subjected to additional external loads besides the self-weight load. In the case of the assessment of the short-term response, the external loads are varied continuously in each step analysis up to the failure state and tracked into the post-failure regime. On the contrary, the external loads in the long-term assessment are only varied at specific steps of the analysis and then hold constant. As described in section 4.3, the stiffness matrices and

force vector of all the elements comprising the structure are assembled in a global coordinate system to set up the incremental equilibrium equations of the whole structural system. Similar to Eq. (4.80), to solve the resulting linearized equations comprising the incremental equilibrium equations, a incremental-iterative procedure is adopted. As a result, the linearized equations for a specific step of the short- or long-term analysis can be expressed as follows:

$$\left(\boldsymbol{K}_M^i + \boldsymbol{K}_G^i\right) \Delta \boldsymbol{U}^{i+1} = \Delta\lambda^{i+1} \boldsymbol{F}_{ref} + \boldsymbol{F}_{ext}^i - \boldsymbol{F}_{post}^i - \boldsymbol{F}_{int}^i \tag{6.51}$$

where the superscript i indicates the ith iteration, and $\boldsymbol{F}_{post}$ and $\boldsymbol{F}_{int}$ are the force vectors acting on the structure due to the post-tensioning load and internal stresses generated in the hosting members, respectively. It is worth noting that the tangent stiffness matrices $\boldsymbol{K}_M$ and $\boldsymbol{K}_G$ encompass the stiffness matrices of the hosting members and tendon element for the case of using the tendon formulation described in subsection 6.1.2. Otherwise, the tangent stiffness matrices only comprises the stiffness matrices of the hosting members when the equivalent load scheme is adopted. In the assessment of the vector $\boldsymbol{F}_{post}$, Eq. (6.9), referred to a local coordinate system, or Eq. (6.27), referred to a global coordinate system, are employed depending on the formulation adopted.

Similarly, the Eq. (6.51) can be compactly expressed as Eq. (4.81) and solved by imposing a constrain condition using a load or displacement control strategy or a continuation technique as the cylindrical arc-length method as described in section 4.3. Once a constraint conditions is adopted, Eq. (6.51) are solved using the nonlinear solution algorithms described in chapter 5. The iterative process is stopped when a global convergence criteria is satisfied. In the numerical framework of this thesis, the well-known force, displacement and energy norm criterion are adopted.

6.4 Validation Examples

The analysis framework detailed above was implemented to study the global behaviour of post-tensioned timber members under short and long-term loading. As described before, the finite element formulations of the hosting members and tendon element encompass material nonlinearity as well as large displacements while assuming the development of small strains inside the elements. To test the capabilities of the analysis framework, four benchmark test were replicated for validation purposes. Given the dearth of available experimental data on unbonded post-tensioned timber members with draped or eccentric tendon profiles using conventional

anchor systems tested up to failure or under long-term loading, numerical and experimental test performed on unbonded post-tensioned RC beams were also included. This will also serve to illustrate the capabilities of the framework and the versatility of the implementation. Regarding the study of the short-term response up to failure of post-tensioned members, two benchmark tests performed on RC beams and one test involving timber beams were analysed. In relation to the study of the long-term response of post-tensioned members, a benchmark test performed on a RC beam including the interaction of the different time-dependent effects is also analysed. As it has been mentioned before, unbonded tendons that depend on anchorages and deviators to transfer the prestress force to the hosting member are denominated external tendons, whereas the unbonded tendons passing through the hosting member through internal duct which are in permanent contact with the member are referred to as internal tendons. The numerical performance of the numerical procedures to address unbonded tendons presented in this chapter will also be compared in terms of computational effort in two specific examples. In these comparisons, the equivalent load scheme described in subsection 6.1.1 and the load resisting element presented in subsection 6.1.2 will be refereed to EQL and LRE, respectively.

6.4.1 Simply-Supported RC Beams Post-Tensioned with External Tendons

Lou and Xiang [235] performed a numerical test to assess the effects of using different deviator arrangements on the ultimate load capacity of externally post-tensioned simply-supported RC beams. The numerical framework developed by the authors had been previously extensively validated against experimental results (Lou and Xiang [238] Lou et al. [241] Lou et al. [244]). This particular numerical test is selected due to its challenging modelling features which include a varying eccentricity (in value and direction) as well as large displacements and material nonlinearity. In particular, the beam with a span of 16000 mm is selected as the test case. The external post-tensioning applied on the beam consists of straight horizontal tendons with an initial eccentricity of 200 mm and three different deviator configurations. These configurations include middle and one-third span locations as well as no deviators in between the anchorages as shown in Fig. 6.6. The beam section has a rectangular shape of 300 mm width and 600 mm height with a constant reinforcement layout top and bottom along its full length as shown in Fig. 6.7. Regarding the material properties, it was considered a concrete cylinder strength and elastic modulus of 40.0 MPa and 36.3 GPa were considered, respectively. Besides, an ordinary reinforcement with a yield strength and elastic modulus of 450.0 MPa and 200.0

GPa, respectively, a prestressing steel with a ultimate tensile strength and elastic modulus of 1860.0 MPa and 195.0 GPa, and, a specific weight of 25 kN per cubic meter was assumed. For this analysis, an effective prestress in the tendon of 1120.0 MPa was used. In the analysis, two loading scenarios were considered for the externally post-tensioned beams: uniform and midpoint loads denominated in the following as UL and PL, respectively.

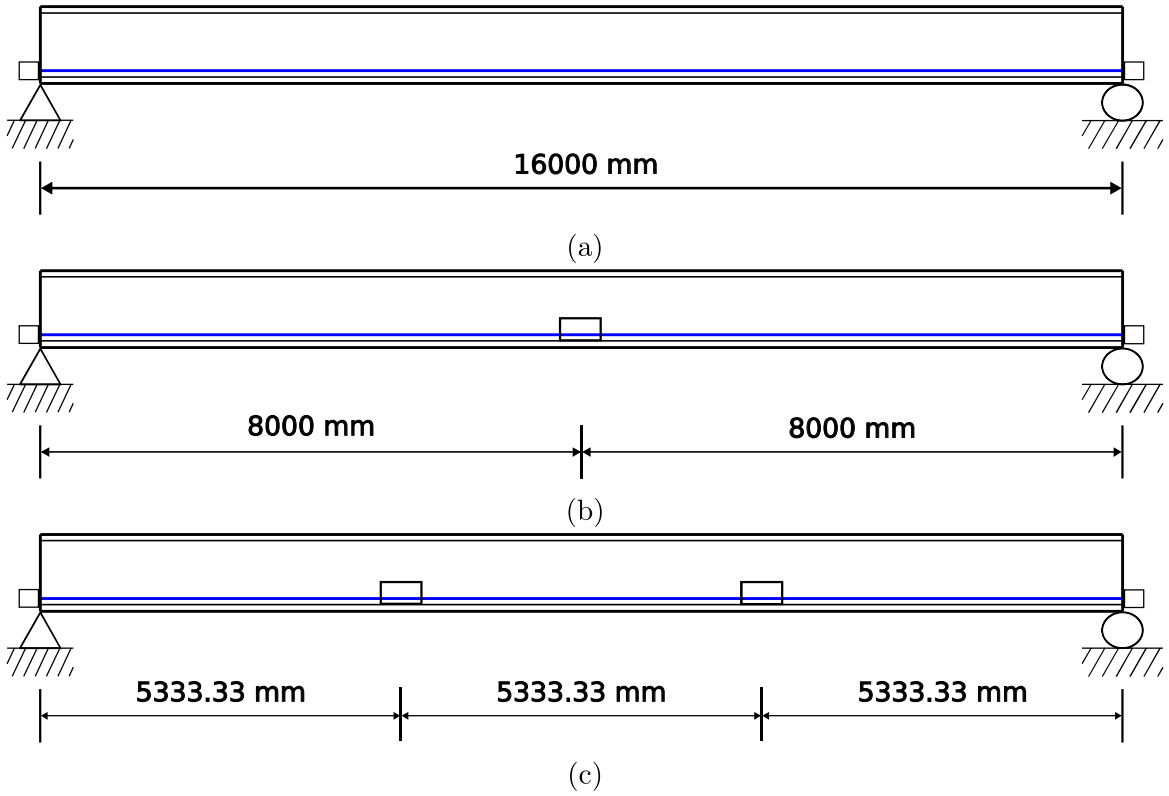


Figure 6.6: Simply-supported post-tensioned RC beam layouts: (a) No deviators; (b) One deviator; (c) Two deviators.

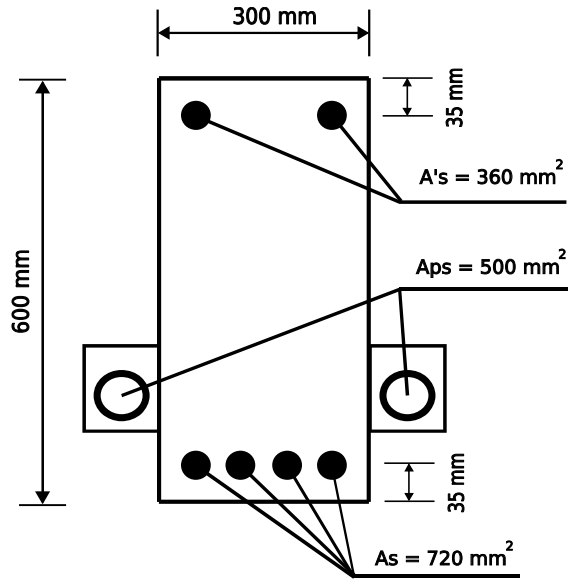


Figure 6.7: Rectangular section of the post-tensioned simply-supported RC beams.

The same discretization and type of beam column elements adopted by Lou and Xiang [235] were employed here for comparison purposes. The hosting member was discretized into 18 elements along the span using a traditional Euler-Bernoulli Beam-Column formulation whereas its section was subdivided into 10 layers. Similarly, for the EQL, the tendon was discretized into 18 segments corresponding to each beam-column element of the hosting member as depicted in Fig. 6.8. On the contrary, in the case of LRE, only one, two and three tendon segments were employed for the no deviator, one deviator and two deviators configurations, respectively, as shown in Fig. 6.9.

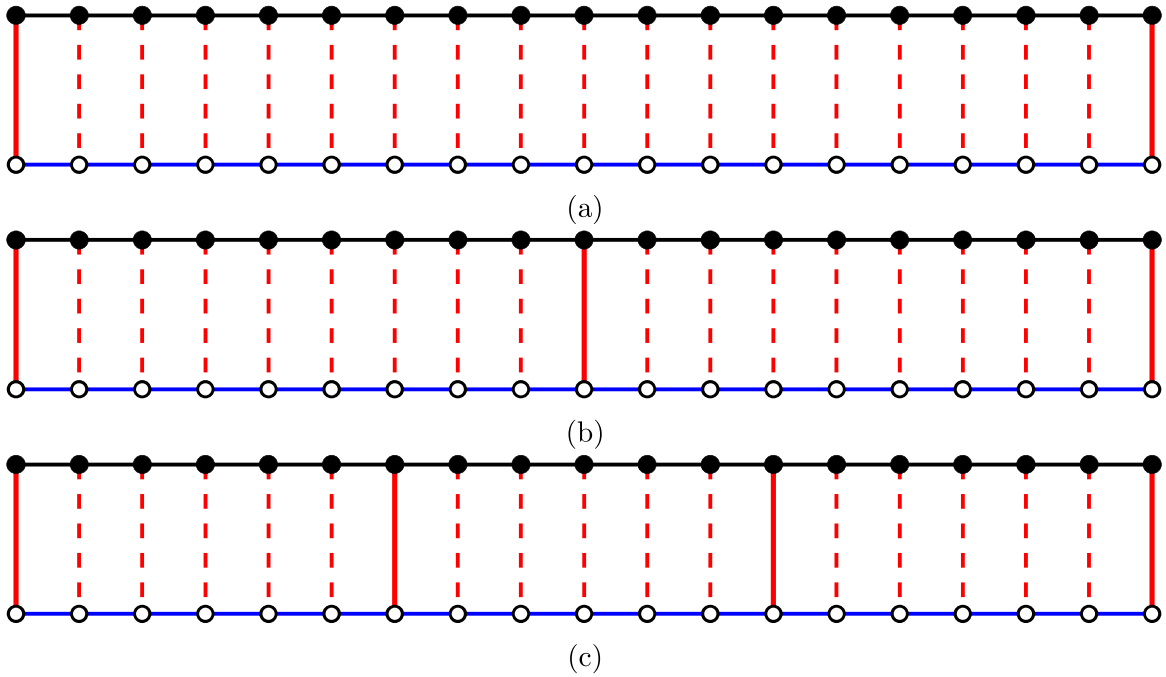


Figure 6.8: FE discretization used in the EQL: (a) No deviators; (b) One deviator; (c) Two deviators.

To consider the inelasticity of the materials, the Hognestad [279] and perfectly-plastic backbone envelopes were adopted for the unconfined concrete and reinforcing steel bars, respectively. For the prestressing steel, the strain-stress relationship proposed by Menegotto and Pinto [269] was adopted.

The results from the simulation are presented in Figs. 6.10 to 6.13, together with those of Lou and Xiang [235]. From these figures, it can be noticed that the results obtained for both tendon approximations are almost identical. However, the involved computational effort in terms of the total number of iterations to achieve convergence during the whole analysis for each tendon formulation and loading scenario is different as summarized in Table 6.1. It can be observed from this table that the performance of the LRE formulation is slightly superior in the majority of cases. However, for the specific case a one deviator configuration under UL,

the performance of the EQL is markedly superior. From Figs. 6.10 to 6.13 it can be noticed that the numerical framework used in this study is capable of accurately simulate the full load-deflection response of these test cases and that key response features like stiffness degradation and inflection points are well captured.

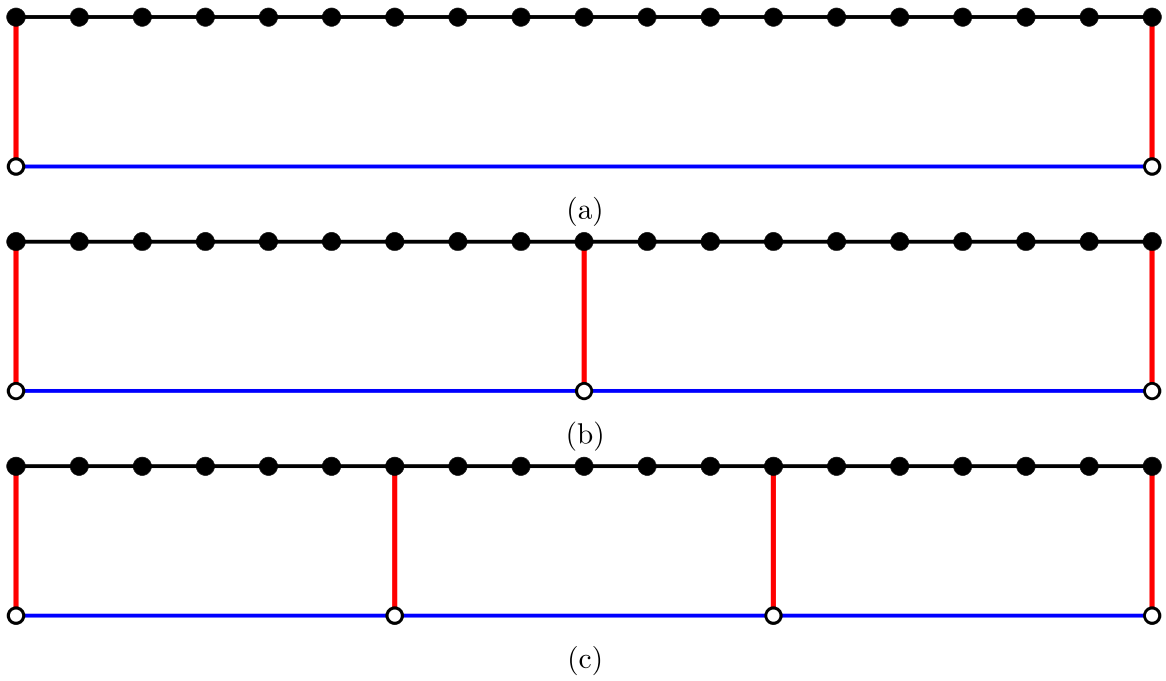


Figure 6.9: FE discretization used in the LRE: (a) No deviators; (b) One deviator; (c) Two deviators.

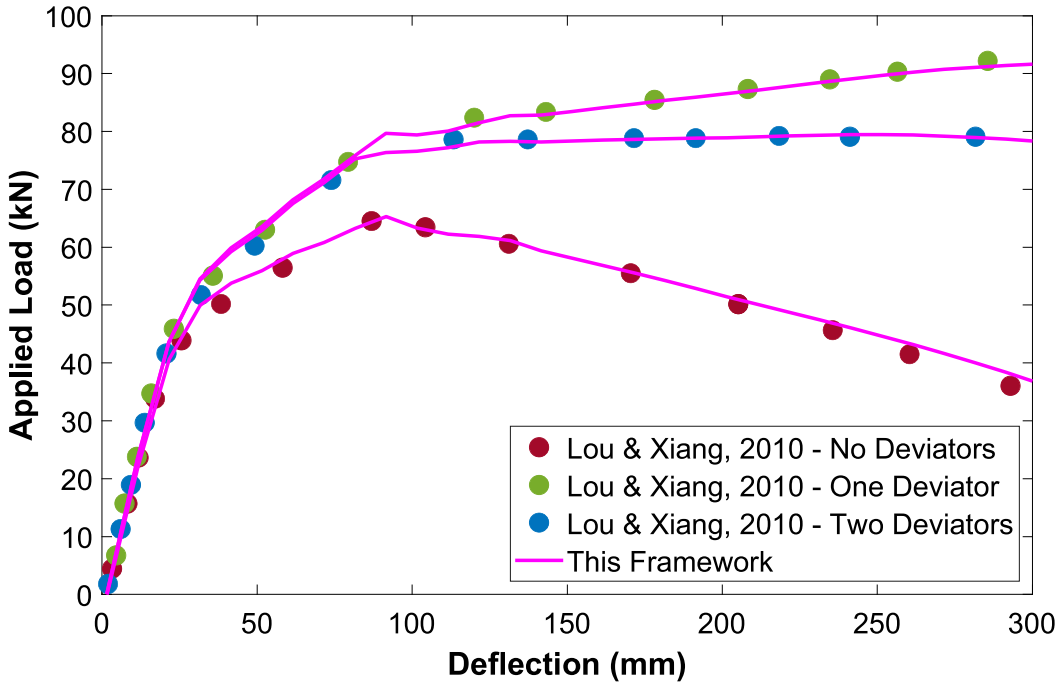


Figure 6.10: Load-deflection response for single concentrated load obtained with the EQL scheme.

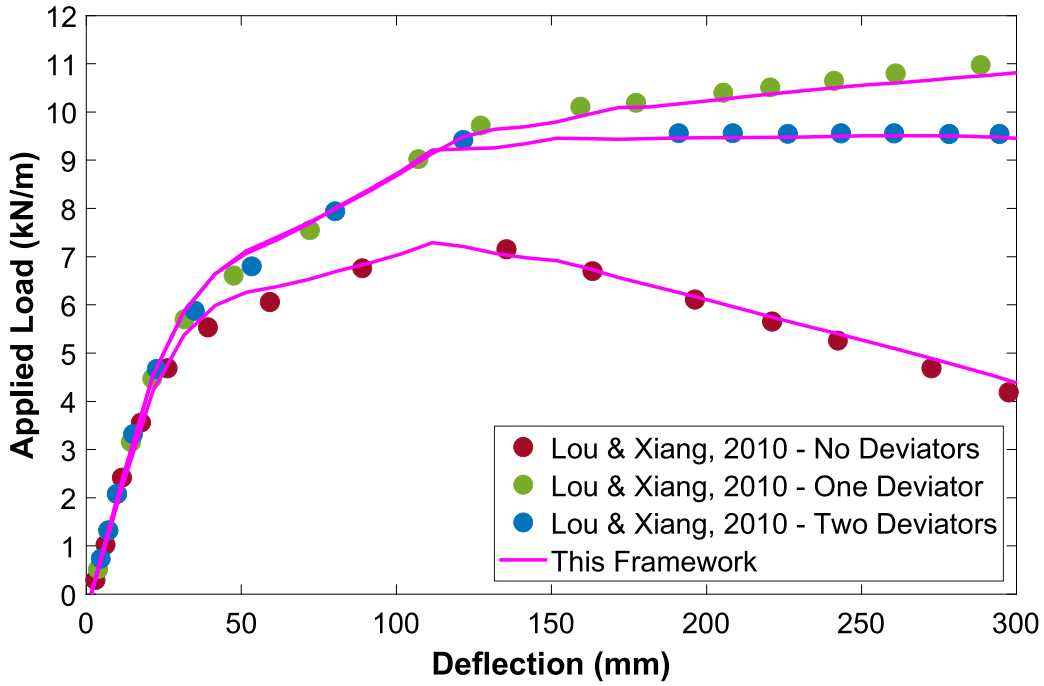


Figure 6.11: Load-deflection response for uniform load obtained with the EQL scheme.

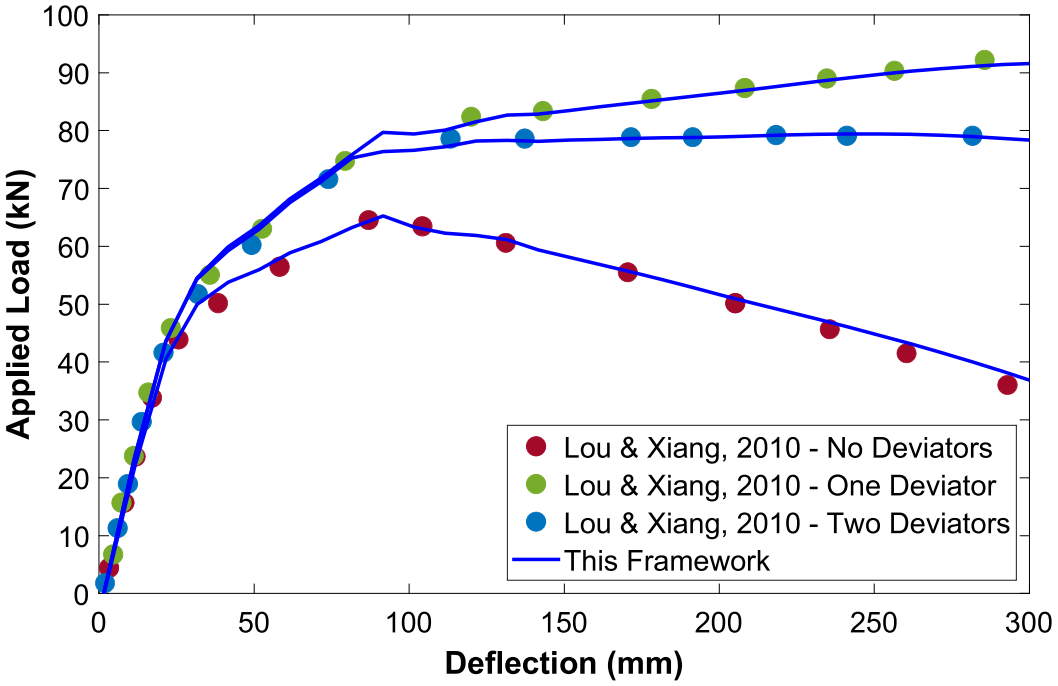


Figure 6.12: Load-deflection response for single concentrated load obtained with the LRE formulation.

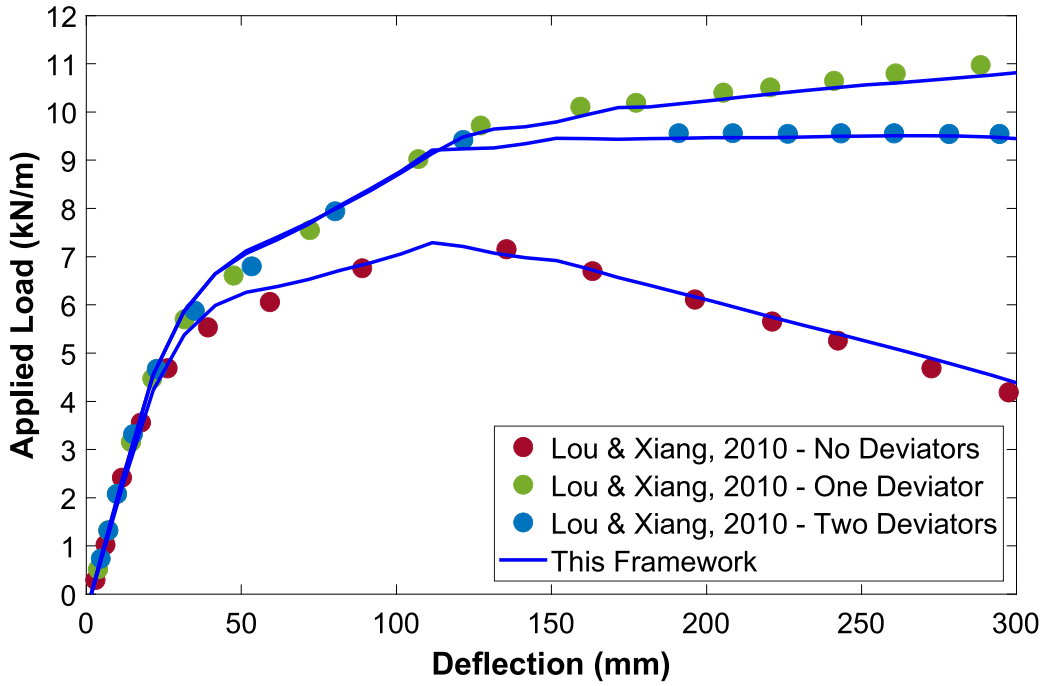


Figure 6.13: Load-deflection response for uniform load obtained with the LRE formulation.

	EQL-PL	LRE-PL	EQL-UL	LRE-UL
No Deviators	124	107	128	118
One Deviators	106	101	210	157
Two Deviators	126	102	132	121

Table 6.1: Number of iterations performed during the analysis.

6.4.2 Continuous RC Beams Post-tensioned with Internal Tendons

The second case study consists in the analysis of internally post-tensioned two-span continuous RC beams subjected to three-point loadings up to failure tested experimentally by Chen [280]. This experimental results were also simulated numerically by Lou et al. [241] from where the experimental test data was extracted. The aim of analysing this test is to attest the capability of the implemented framework to address the use of piecewise parabolic profiles in internally post-tensioned beams as shown in Fig. 6.14. The set of beams analysed have rectangular sections of 150 mm width and 300 mm depth, and total lengths of 10000 mm with each span covering 4800 mm. In this test, the layout of the internal unbonded tendons along the beam were the same for all the specimens. This layout that consisted of 15 mm seven-wire strands can be described by the following expressions:

$$\bar{y} = 2.5297 \times 10^{-5}\,\bar{x}^2 - 0.1006\,\bar{x} \quad 0 \leq \bar{x} \leq 1988\,mm \tag{6.52a}$$

$$\bar{y} = 3.0518 \times 10^{-5}\,\bar{x}^2 - 0.1214\,\bar{x} + 20.7 \quad 1988\,mm < \bar{x} \leq 4320\,mm \tag{6.52b}$$

$$\bar{y} = -1.4817 \times 10^{-4}\,\bar{x}^2 + 1.4225\,\bar{x} - 3313.9 \quad 4320\,mm < \bar{x} \leq 4800\,mm \tag{6.52c}$$

where $\bar{x}$ is the distance from the left end support of the beam and $\bar{y}$ is the vertical distance between the tendon layout and the beam centroidal axis. Regarding the small lengths of the beam outside the end supports, the tendon layout in these zones was considered as straight lines that follow the tangent to the tendon curve at the end support.

Two specimens of the experimental campaign, namely YLA2 and YLB2, are studied. The layout of the ordinary and prestressed reinforcement in the beam sections at the inner shear spans and the span comprising the outer shear and flexural spans as well as the reinforcement areas are shown in Figs. 6.15 and 6.16.

The reinforcing steel bars of 12, 16 and 18 mm have yield strengths of 361 MPa, 384 MPa and 364 MPa, respectively. In the case of the prestressing steel, a ultimate tensile strength of 1941 MPa, a yield strength of 1680 MPa and an elastic modulus of 197 GPa were reported. In regard to the reinforcing steel bars of 12, 16 and 18 mm, yielding strengths of 361 MPa, 384 MPa and 364 MPa, respectively, were employed. The shear reinforcement comprised 10 mm stirrups with a spacing of 150 mm in the outer shear spans and of 200 mm in the flexural spans. In the specific case of specimens YLA2 and YLB2, the stirrup spacing in the inner shear spans were 150 mm and 100 mm, respectively. Regarding the concrete material, a concrete cylinder strength, tensile strength and elastic modulus of 36.7 MPa, 2.8 MPa, 32.5 GPa and 33.0 MPa, 2.6 MPa, 31.5 GPa were used for specimens YLA2 and YLB2, respectively. The remaining material properties for the simulation were assumed as they were not provided, hence, a specific weight of 25 kN per cubic meter, an elastic modulus of 200 GPa for the longitudinal and transversal ordinary reinforcement, and a yield strength of 360.0 MPa for the transverse reinforcement were adopted.

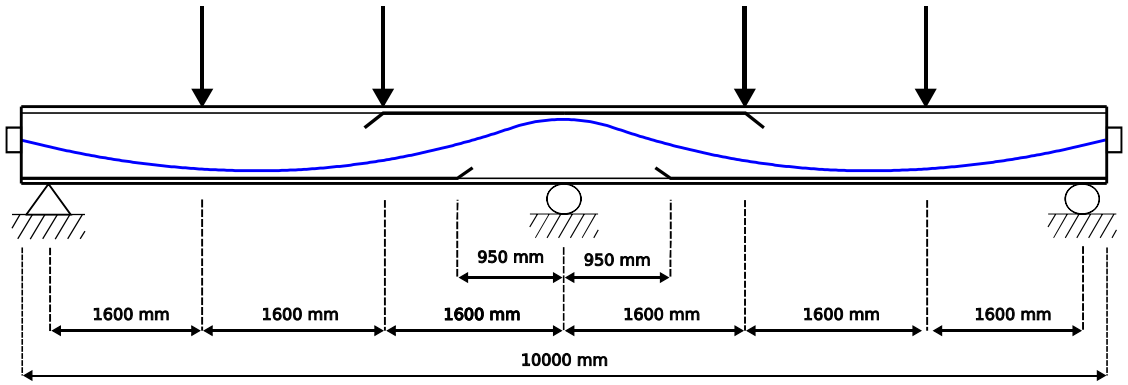


Figure 6.14: Continuous post-tensioned RC beam layouts.

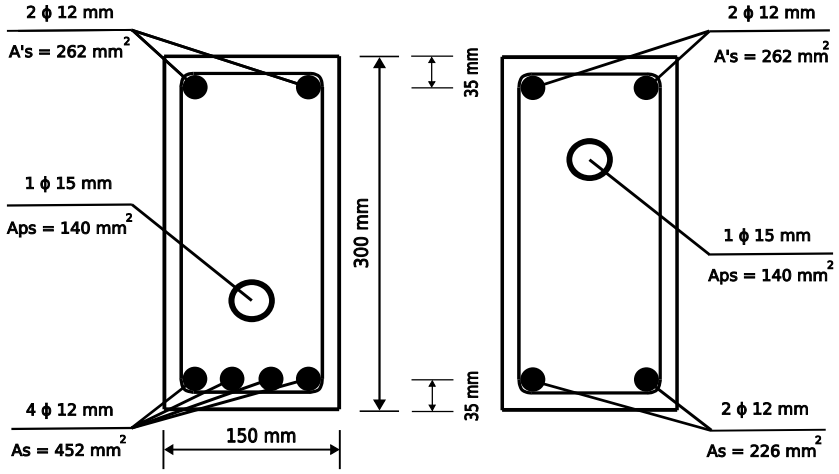


Figure 6.15: Section and reinforcement layout of the continuous beam YLA2.

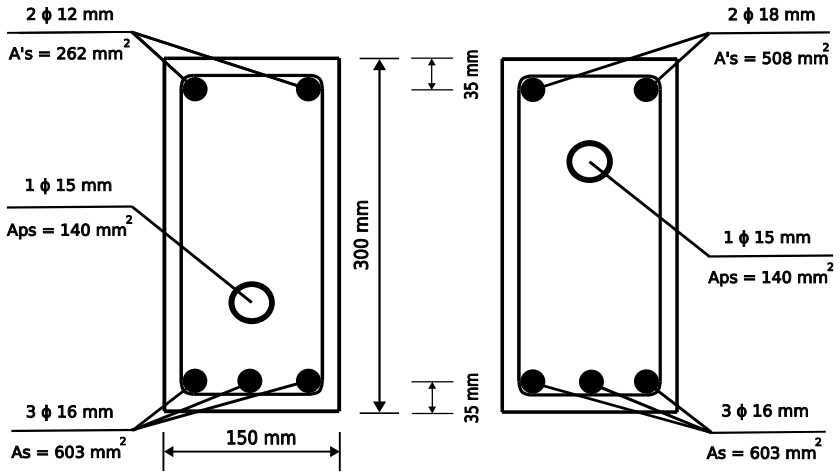


Figure 6.16: Section and reinforcement layout of the continuous beam YLB2.

The parabolic profile of the tendon was approximated by a set of linear segments as shown in Fig. 6.17. When using internal tendons, the mesh of the EQL and LRE formulations are the same. Therefore, the hosting member and the unbonded tendon were subdivided into 38 elements and segments, respectively. The cross section of the beam was discretized into

10 concrete layers. These subdivisions are the same employed by Lou et al. [241] during their simulation. For comparison purposes, the same type of beam-column element with a traditional Euler-Bernoulli formulation was also used during the simulation.

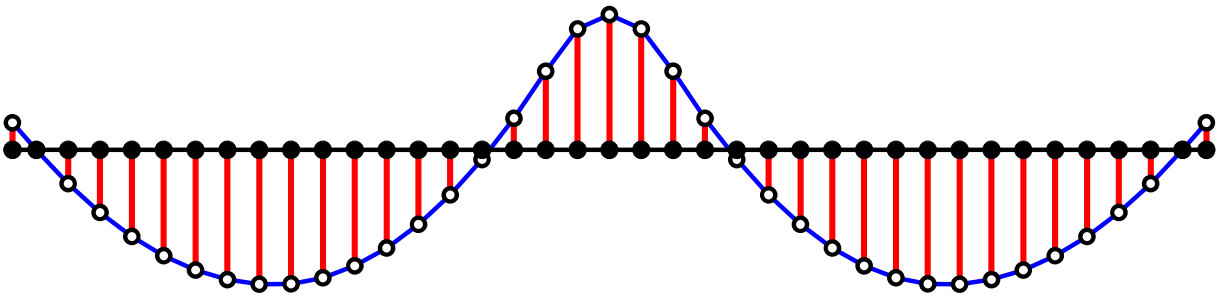
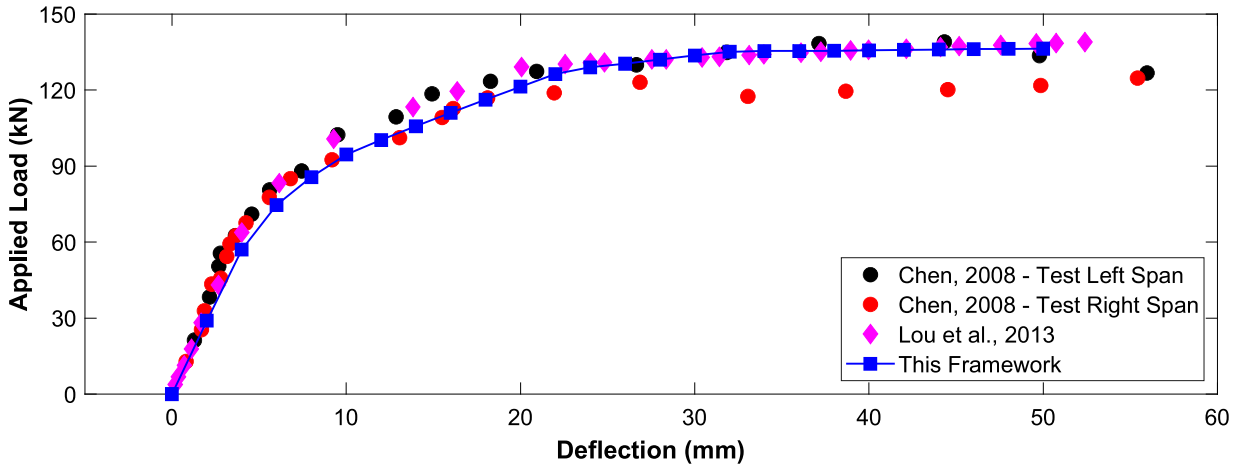


Figure 6.17: FE discretization of the continuous post-tensioned RC beams.

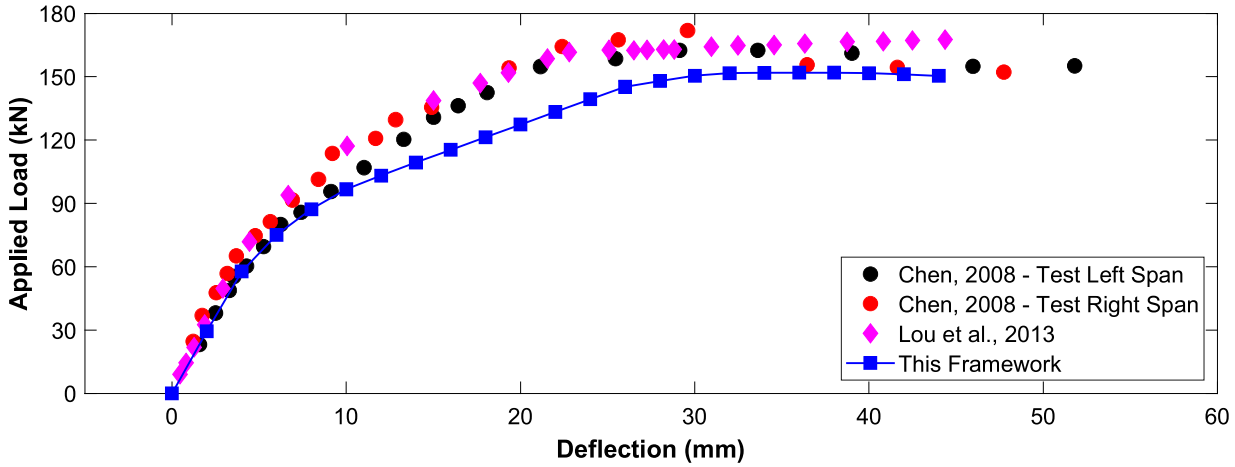
To reflect the behaviour of the tested specimens, the different levels of confinement along the beam provided by the stirrups were considered in the assessment of the concrete strain-stress curves. The variation in the layout of the top and bottom reinforcement bars over the length of the beam was taken into account. A perfectly-plastic, and modified Park et al. [281] backbone envelopes were adopted for the reinforcing steel bars and concrete, respectively. In the case of the steel strands, the backbone envelope curve described by Eq. (6.41) was employed. Effective prestress levels of 1196 MPa and 1193 MPa for the beam specimens YLA2 and YLB2, respectively, were considered in the analysis.

Fig. 6.18 presents the experimental force-displacement relationships recorded by Chen [280] along with numerical predictions by Lou et al. [241]. These results are contrasted with the numerical results obtained in the numerical framework of this thesis. In this validation case, only the EQL formulation is used in the assessment.

Despite using the same discretization, element type and material properties used by Lou et al. [241], the curves in Fig. 6.18 show some discrepancies between their numerical results and those obtained with the present framework. This mismatch could be explained by unintended differences in material parameters since these were not specified in Lou et al. [241] and had to be assumed from nominal values in the literature. Nevertheless, the results show a reasonable agreement with the experimental results.



(a)



(b)

Figure 6.18: Load-displacement responses: (a) Specimen YLA2; (b) Specimen YLB2.

6.4.3 Externally Post-tensioned Timber Beams

van Beerschoten et al. [7] conducted a series of experiments on full-scale simple supported timber beams with box section. These experimental results are taken here as the third validation set. Furthermore, the authors developed high-fidelity 3D FE models which were validated by comparing the numerically simulated results against the experimental ones. This numerical results are also used for comparison in the present case. The post-tensioned beam specimens; labelled as Beam 2, Beam 3 and Beam 4 in the experimental campaign, are the ones to be analysed herein up to their ultimate state. In the experimental test, the beam specimens were first subject to a post-tensioning force transferred through external tendons followed by the application of four-point bending loads.

Regarding the unbonded tendon layouts, the tendon in Beam 2 is straight with an initial constant eccentricity of 161 mm as shown in Fig. 6.19a. In contrast, the tendons in Beams 3 and 4 have a draped profile enforced through two deviators located at one-third of the span with

zero eccentricity at both ends and maximum eccentricities of 185 and 215 mm in the flexural spans, respectively, as depicted in Figs. 6.19b and 6.19c. The total span of the beams is 9150 mm and a box section of 426 mm width and 610 mm height overall were used in all cases. These sections are comprised of webs and flanges with 63 and 90 mm of thickness, respectively, for Beam 2 and 3 as illustrated in Figs. 6.20a and 6.20b, whereas the box section of Beam 4 has a top flange thickness of 180 mm as shown in Fig. 6.20c.

The compression strength of the timber material that comprises the full-scale beam specimens is adopted directly from experimental tests performed by van Beerschoten et al. [282] on scaled specimens analysed in parallel to the post-tensioned specimens. These strength values were employed during the construction of the high-fidelity 3D FE model developed by van Beerschoten et al. [7]. In the analysis performed herein, two tension strength values are adopted to set an upper and lower load-deflection response curves and to account for the natural variability associated with wood. The first set corresponds to tension values assumed to be the same than the compression values, similar to van Beerschoten et al. [7]. In the second case, the tension strength is obtained from the bending strength values provided by the manufacturer Nelson-Pine [283] as no test was performed to assess this strength during the original experimental campaign. To this end, a scale factor of 0.733 is used in accordance with the manufacturer's recommendation which includes consideration of potential size effects. On the contrary, the elastic properties of the box-section beams are obtained from the full-scale test on the beam specimens. All these material properties are summarized in Table 6.2. Finally, a specific weight of the timber beam of 5.7 kN per cubic meter was assumed.

Properties of timber material	Value
Ultimate bending strength	48 MPa
Ultimate compressive strength parallel to grain	47MPa
Modulus of elasticity Beam 2	10.9 GPa
Modulus of elasticity Beam 3	11.2 GPa
Modulus of elasticity Beam 4	11.4 GPa
Shear modulus Beam 2	631 MPa
Shear modulus Beam 3	703 MPa
Shear modulus Beam 4	757 MPa

Table 6.2: Material properties for timber beams.

For the case of the prestressing steel comprising the externally post-tensioned tendons, seven steel strands of 12.7 mm diameter are employed. Their material properties are summarized in Table 6.3. Once the strength values are defined, the uniaxial constitutive model for timber and steel strands can be assessed using Eq. (4.57) and Eq. (6.41), respectively.

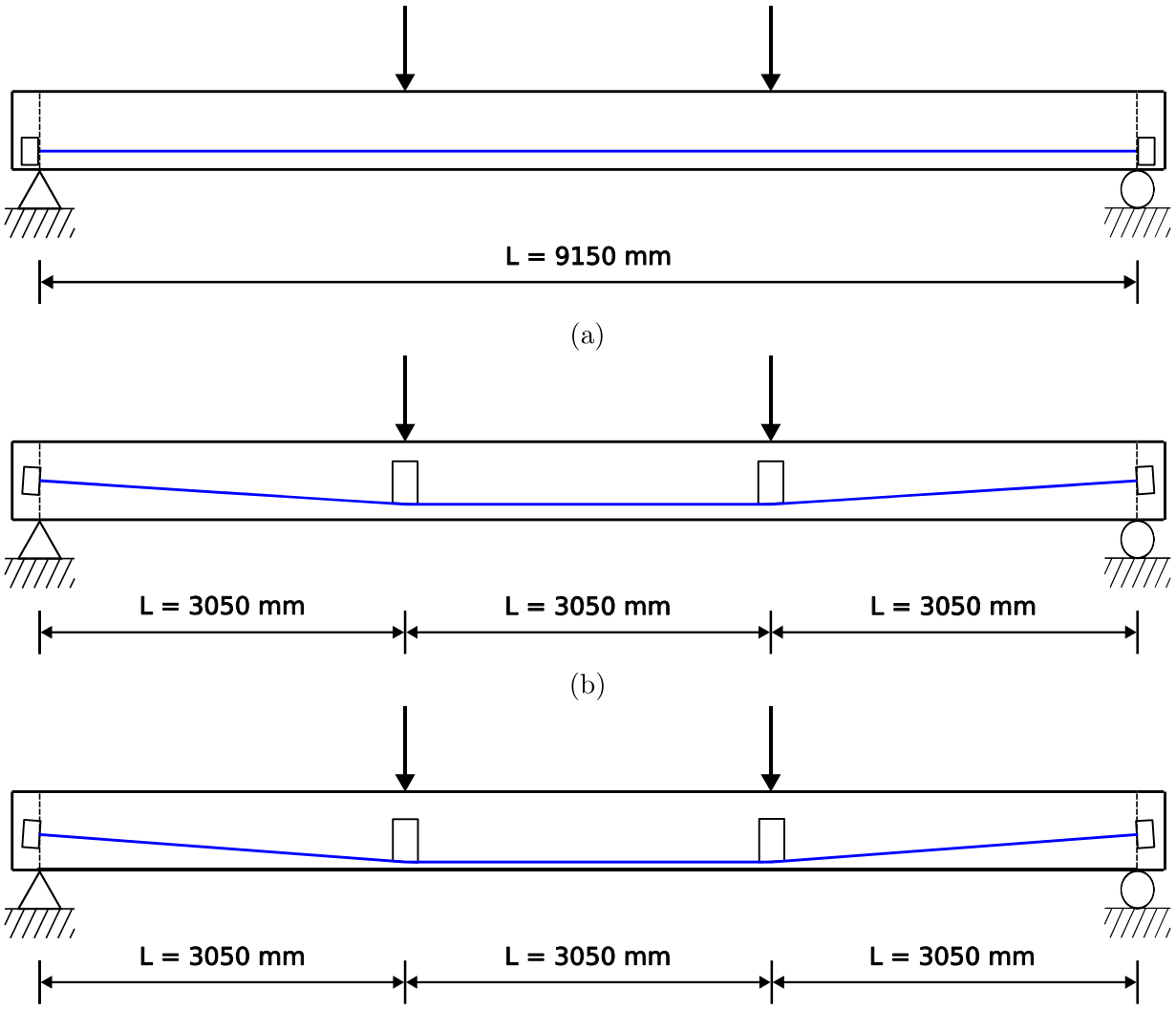


Figure 6.19: Externally post-tensioned timber beam layouts: (a) Beam 2; (b) Beam 3; (c) Beam 4.

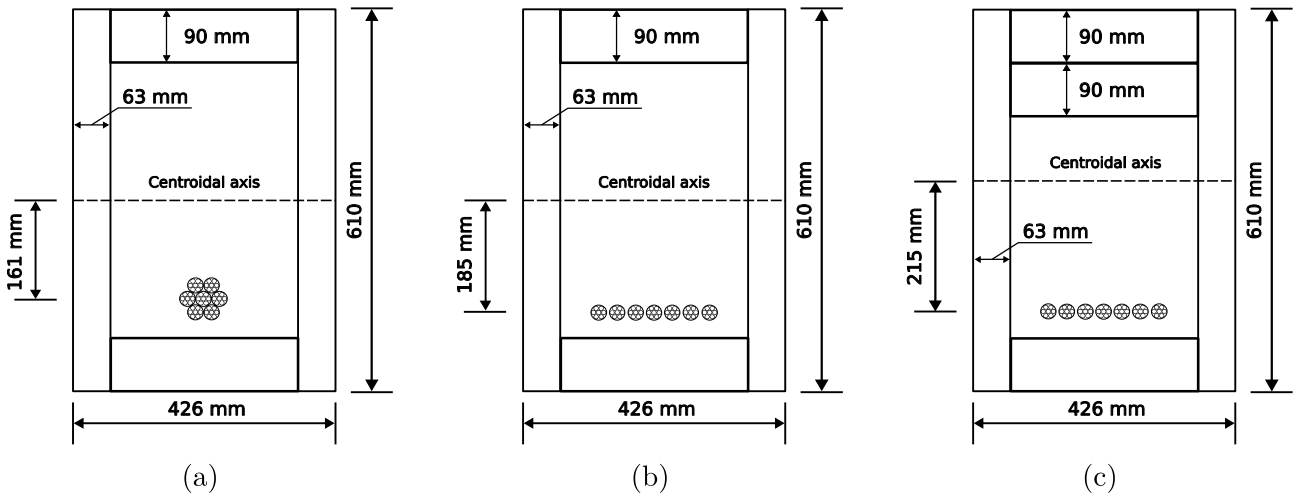


Figure 6.20: Box section layouts: (a) Beam 2; (b) Beam 3; (c) Beam 4.

Properties of steel strands	Value
Ultimate tensile strength	1860 MPa
Yield strength	1520 MPa
Modulus of elasticity	200 GPa

Table 6.3: Material properties for steel strands.

To assess the ultimate load capacity of the post-tensioned beams, two numerical models were constructed. In one model the enhanced formulation of the traditional Euler-Bernoulli beam-column element (subsection 4.1.4) is employed whereas in the other model the enhanced version of the Timoshenko beam-column element (subsection 4.1.6) is used for comparison purposes. These beam-column element formulations are denominated as ENH EB and ENH TB, respectively. Following a mesh sensitivity study, it was found that a discretization of 4 elements along the hosting member, as shown in Fig. 6.21, was sufficient to capture the failure load of the post-tensioned specimens in both formulations. On the other hand, the box sections of all beam specimens were divided in 14 fibers along the section depth. Regarding the modelling of the unbonded tendons, the LRE formulation was employed in this validation study as the aim was to use a coarse-mesh FE model. As it is depicted in Fig. 6.21, the tendon was discretized in one segment for Beam 2 and three segments for Beam 3 and 4.

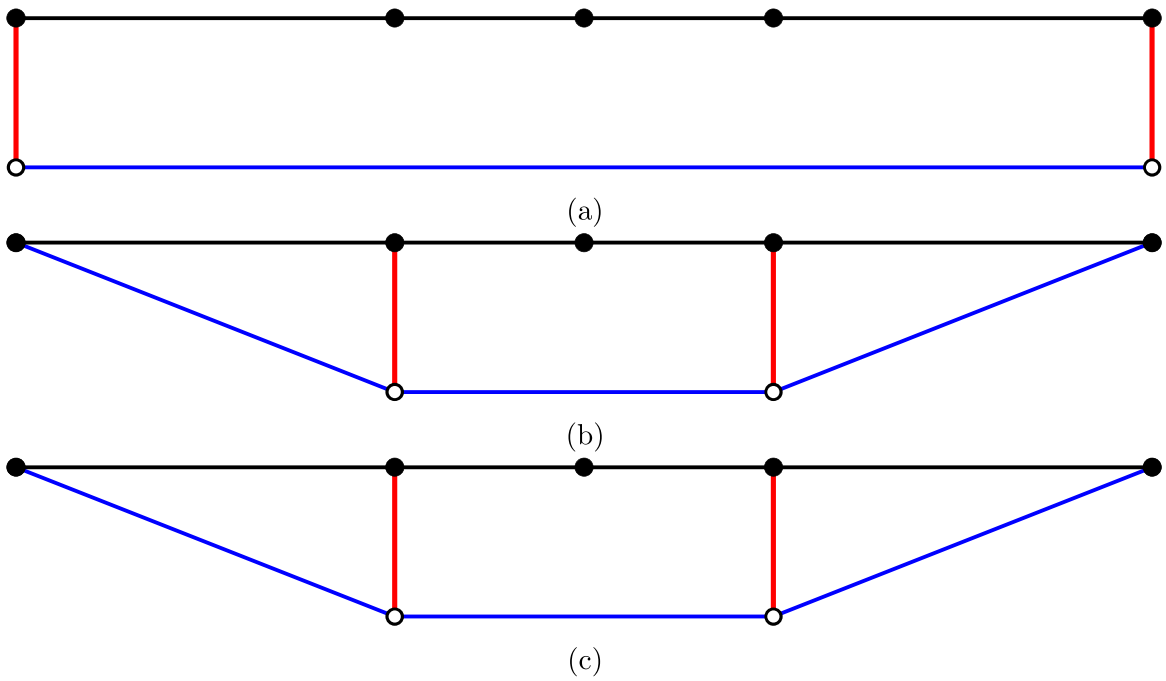
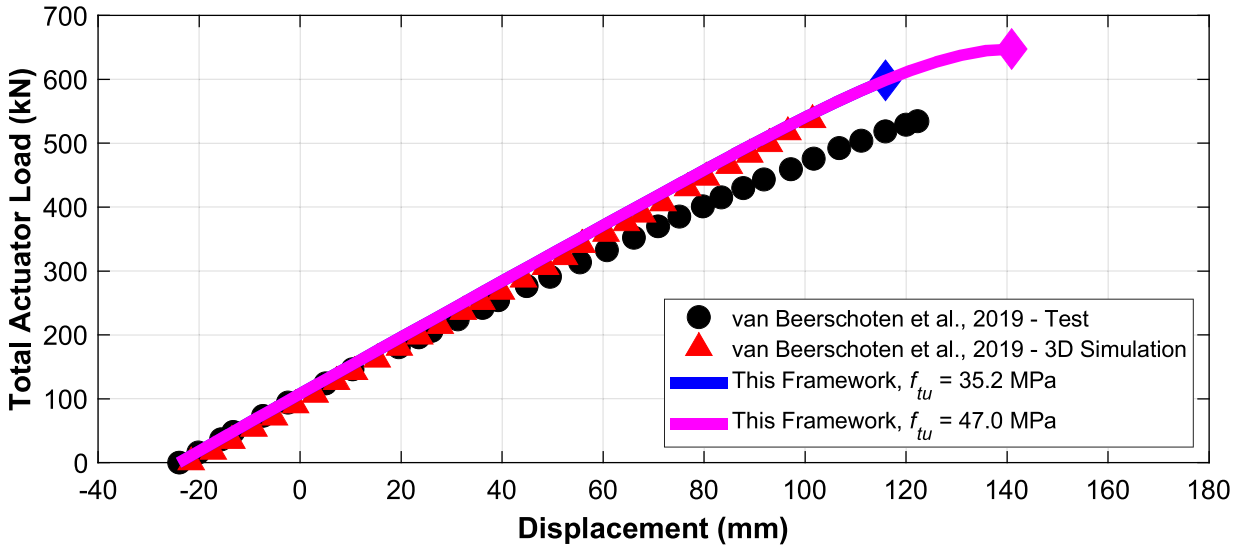


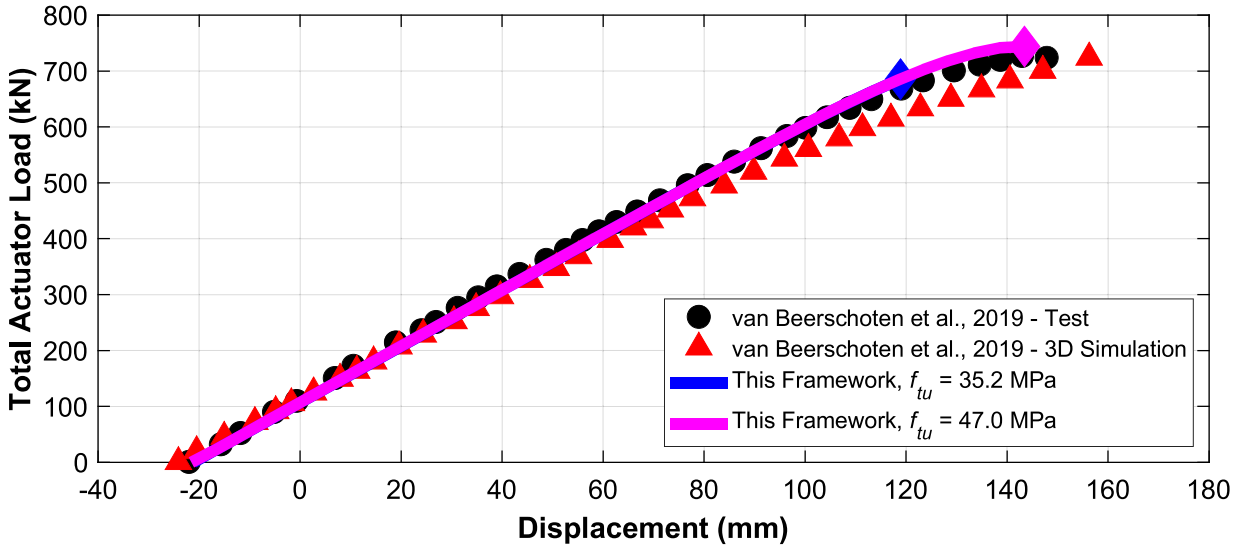
Figure 6.21: FE discretization: (a) Beam 2; (b) Beam 3; (c) Beam 4.

Figs. 6.22 and 6.23, presents and compares the numerical and experimental benchmark load-displacement responses of the post-tensioned timber beams with the ones obtained with the implemented numerical framework. It can be noticed from these figures that the global responses obtained with the proposed numerical framework for both beam-column formulations are in good agreement with the experimental and numerical results obtained by van Beerschoten et al. [7]. It is worth mentioning that the benchmark numerical results in the case of Beam 2 obtained from a 3D simulation (high-fidelity 3D FE model) were performed up to the same level of failure load observed during the experimental test. This is because the Beam 2 specimen experienced a premature failure during the physical testing due to an initial damage state induced on the specimen during the prestress transfer operation. Therefore, the performed simulation was also carried out up to the same premature failure load. However, this is not the case for beam specimens 3 and 4, where the full set of numerical results are plotted up to the limit point of failure. The numerically simulated results indicates a very good prediction of the ultimate failure capacities of the post-tensioned timber specimens. Besides, it can be noticed that the upper and lower load-deflection response curves obtained comprise the benchmark experimental and numerical results. The obtained results show that the ENH EB case presents a slightly stiffer behaviour in comparison with the ENH TB due to the absence of shear deformations. However, the discrepancies between both analysis cases are marginal for peak loads.

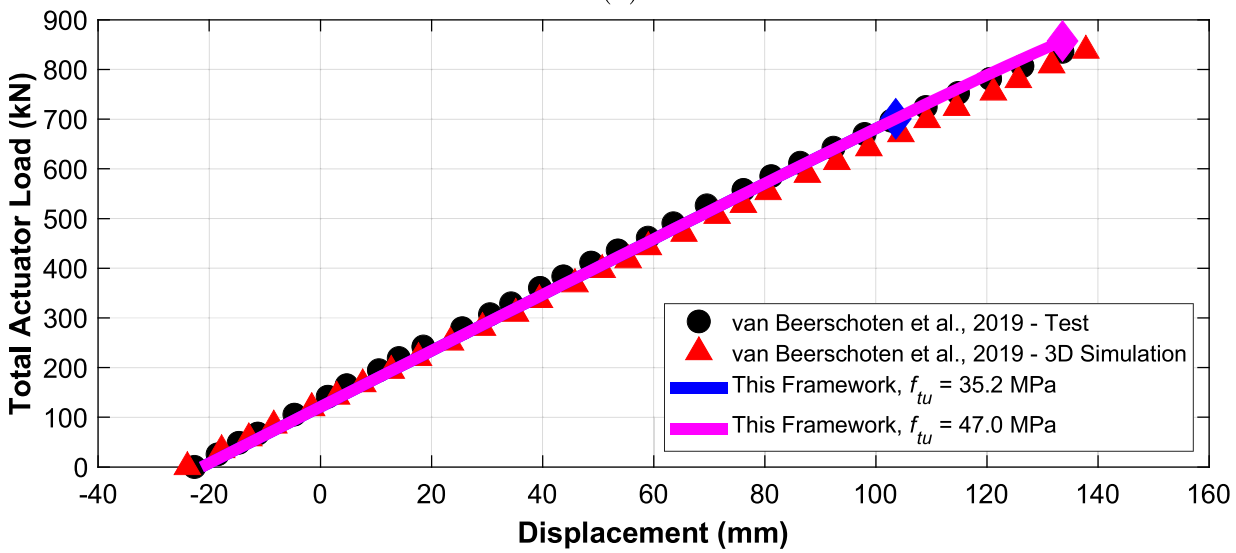
From the obtained results, it was noticed that the sectional forces at each integration points (IPs) of the elements are almost identical to the internal sectional forces up to the peak load. After reaching the failure point, the internal sectional started to slightly diverge in the post-peak range. This is illustrated in Appendix D for the most strained element located at the middle of the mesh. Therefore, the use of enhanced formulations in conjunction with the LRE tendon formulation offer a potential alternative to carry out a performance assessment of post-tensioned members up to the ultimate limit state with a relative coarse mesh. In case the post-peak response is of interest, a localisation limiter has to be considered to avoid spurious mesh sensitivity.



(a)

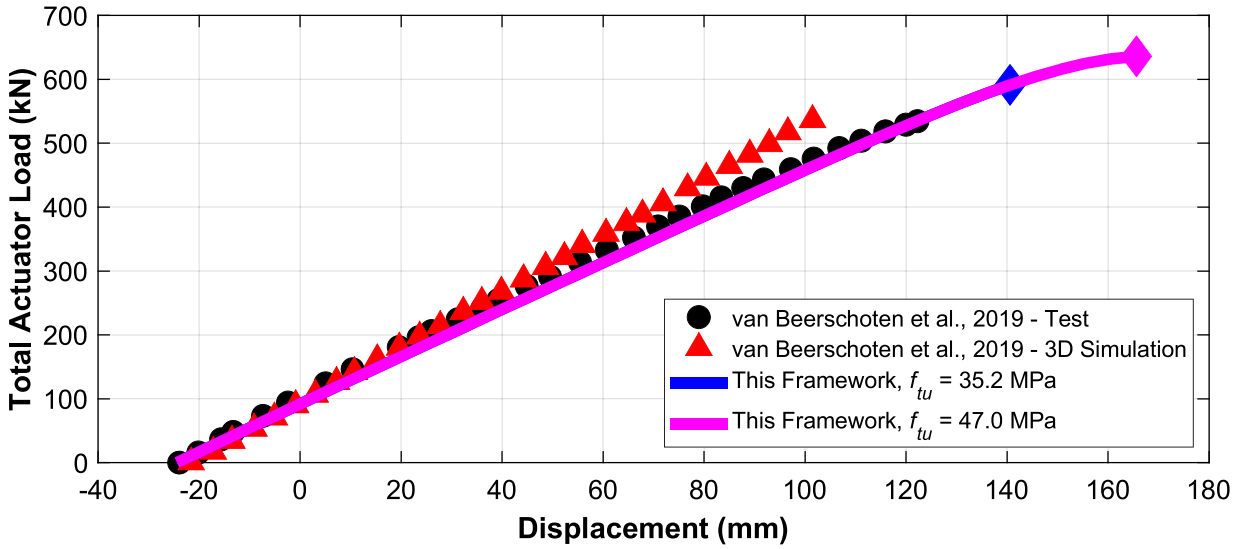


(b)

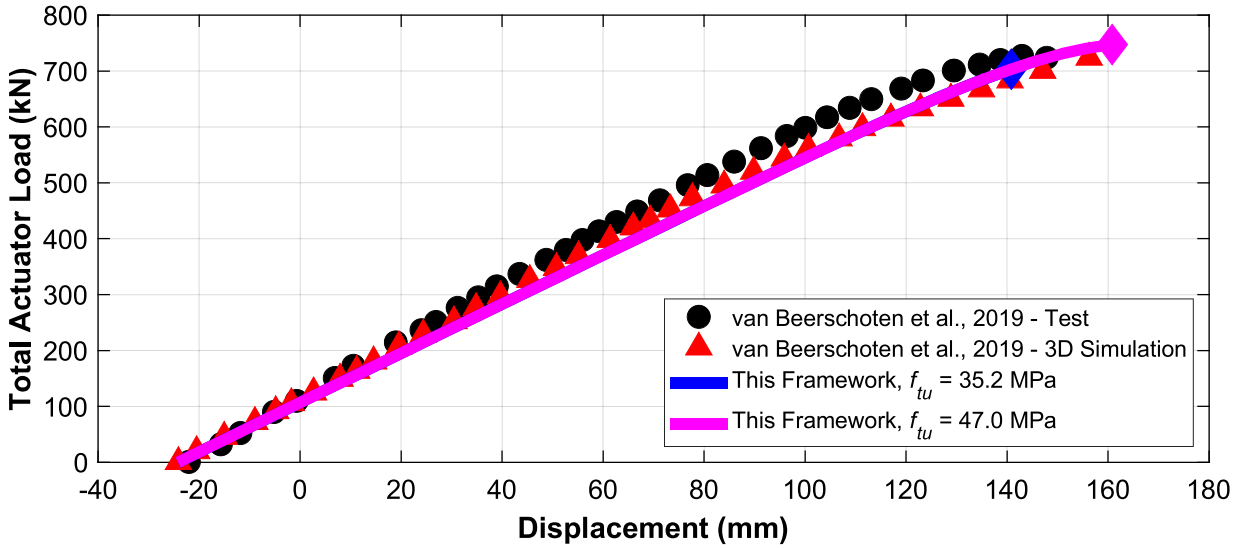


(c)

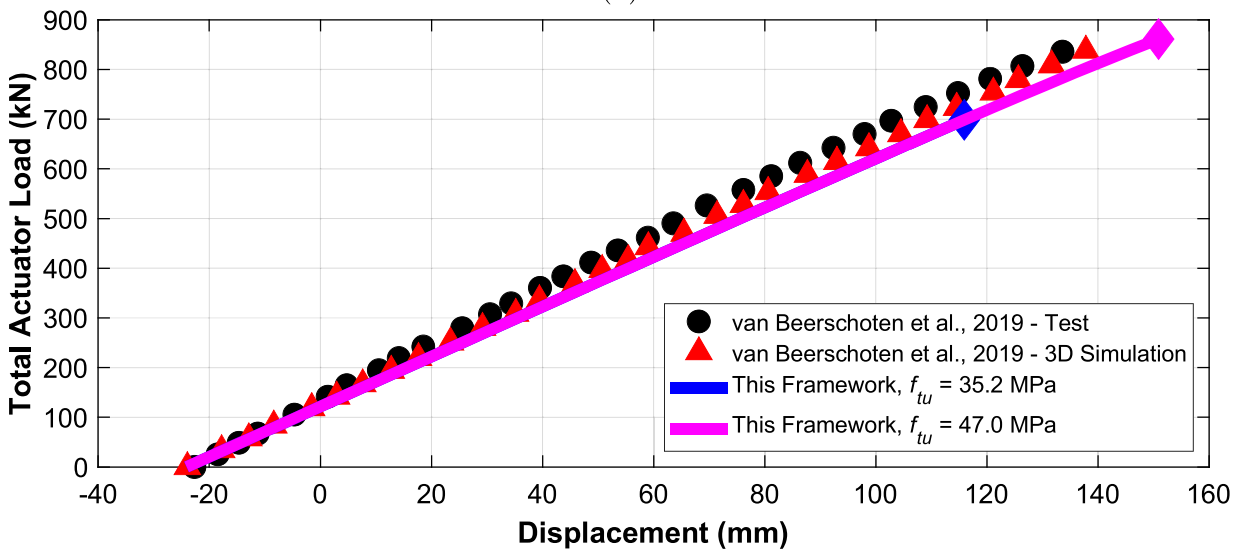
Figure 6.22: Load-midspan displacement response for the ENH EB : (a) Beam 2; (b) Beam 3; (c) Beam 4.



(a)



(b)



(c)

Figure 6.23: Load-midspan displacement response for the ENH TB : (a) Beam 2; (b) Beam 3; (c) Beam 4.

6.4.4 Simply-Supported RC Beams Post-Tensioned with Internal Tendons

The fourth validation test encompass the capabilities of the implemented numerical framework to address the long-term response of post-tensioned beam-like structures. For the sake of simplicity, the numerical results obtained by Lou and Karavasilis [284] are chosen as benchmark as they use a widely validated FE model. This numerical exercise consist of a simply-supported RC beam with a span of 12000 mm post-tensioned with a parabolic internal unbonded tendon subjected to self-weight and four-point bending loads as shown in Fig. 6.24. Regarding the parabolic profile of the tendon, a maximum eccentricity of 200 mm was considered at the mid-span and no eccentricities at the end anchorages. The numerical results offers a comprehensive benchmark as it includes the interaction of different time-dependent effects such as concrete creep and shrinkage as well as the relaxation of the prestressing steel tendons. Importantly, the FE model incorporated an aging material model proposed by Bofang [285] to describe the dependence of the creep compliance on the loading age. Regarding the relaxation in the tendons, the authors employed the procedure proposed by Hernandez and Gamble [275] by updating the expression proposed by Magura et al. [271] to consider the interaction of the different time-dependent deformations with the relaxation. In this analysis, low relaxation tendons were considered. The rectangular section of the beam has a height and width of 600 mm and 300 mm, respectively, with a reinforcement layout distributed in the section as shown in Fig. 6.25.

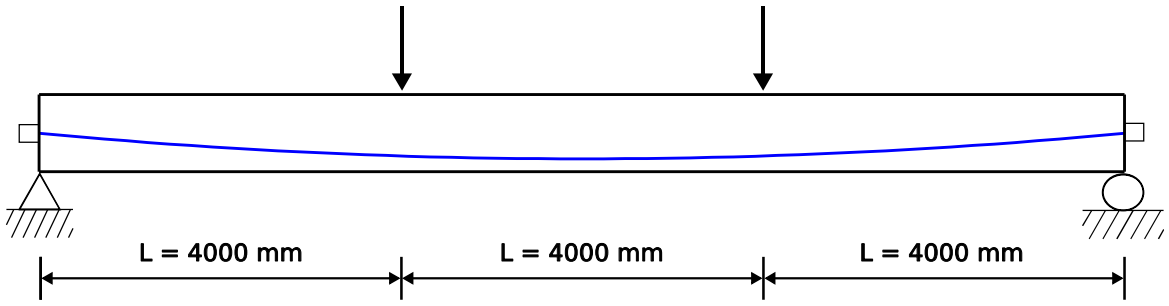


Figure 6.24: Simply-supported post-tensioned RC beam layout.

With regard to the material properties, a concrete cylinder compressive strength and elastic modulus of 35 MPa and 34 GPa at the age of 28 day, respectively, an ordinary reinforcement with a yield strength and elastic modulus of 450 MPa and 200 GPa, respectively, were considerer. Besides, a prestressing steel with a ultimate tensile strength, yield strength and elastic modulus of 1860 MPa, 1674 MPa and 195 GPa, respectively, was used.

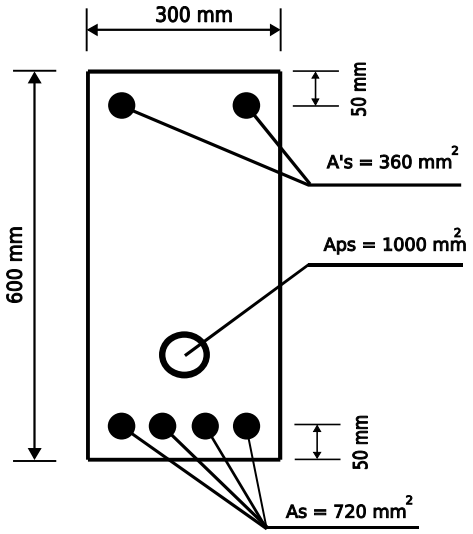


Figure 6.25: Section layout of the post-tensioned simply-supported RC beam.

To perform the long-term analysis, it was assumed a specific weight of 27.2 kN per cubic meter for the beam and a total load of 100 kN for the four-point bending load was considered. In the FE model employed by Lou and Karavasilis [284], the hosting member was discretized into 18 Euler-Bernoulli beam-column elements and its section was subdivided in 10 fibers along the height. For comparison purposes, the same element type and discretization are adopted in the implemented framework. Regarding the modelling of the tendon, both formulations implemented in the framework were employed. The mesh of the FE model used in the analysis is illustrated in Fig. 6.26.

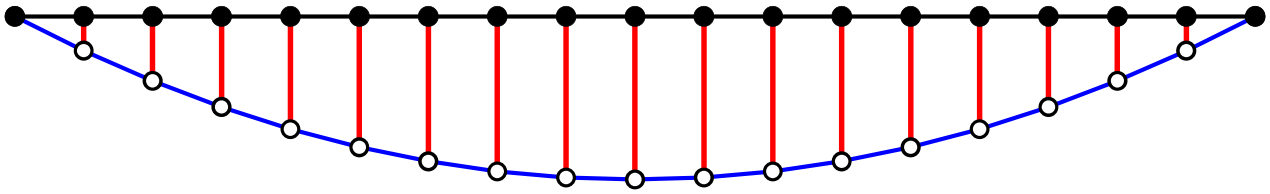


Figure 6.26: FE discretization of the simply-supported post-tensioned RC beam.

To consider the relaxation of the prestressing steel, both procedures described in subsection 6.2.2 are employed for comparison purposes. To this end, the procedures proposed by Hernandez and Gamble [275] and Bažant and Yu [276] are denominated as RP1 and RP2, respectively. The rheological behaviour of the ordinary reinforcement is neglected. In the analysis, two loading scenarios are considered. First, the self-weight is the only force applied to the post-tensioned beam whereas in the second scenario both the self-weight and four-point bending loads are acting on the beam. Both loading scenarios are applied at the age of 28 days along with two effective prestress levels of 800 MPa and 1200 MPa.

The results are shown in Figs. 6.27 to 6.34. It is observed that the results obtained for both

tendon formulations are very similar. However, the computational effort in terms of the total number of iterations performed during the analysis is different. Specifically, the EQL scheme performs twice more iterations than the LRE formulation. In general, satisfactory agreement between the proposed FE model and the numerical benchmark results is observed. Therefore, the implemented framework is capable of taking into account the different time-dependent deformations and their interactions.

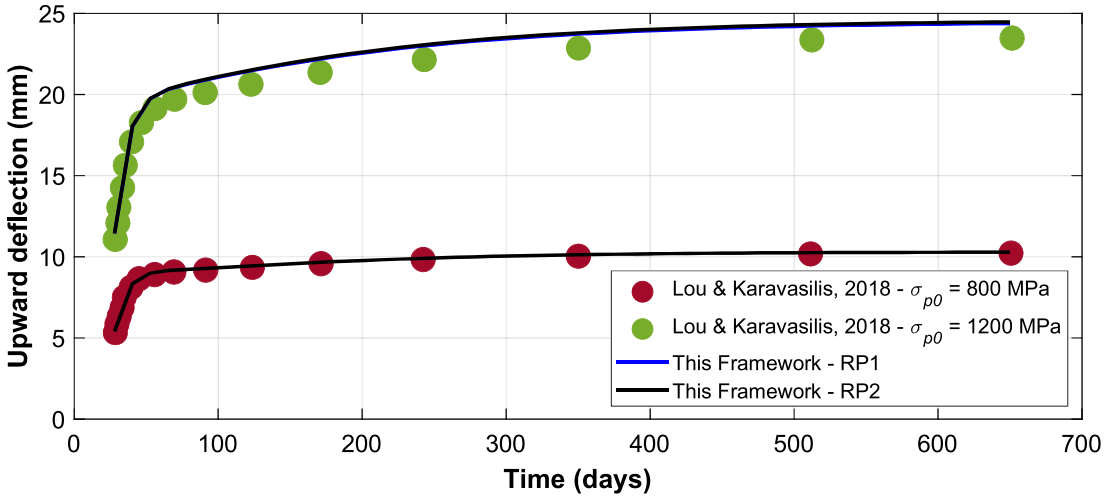


Figure 6.27: Long-term deflections under self-weight loads obtained with the LRE formulation.

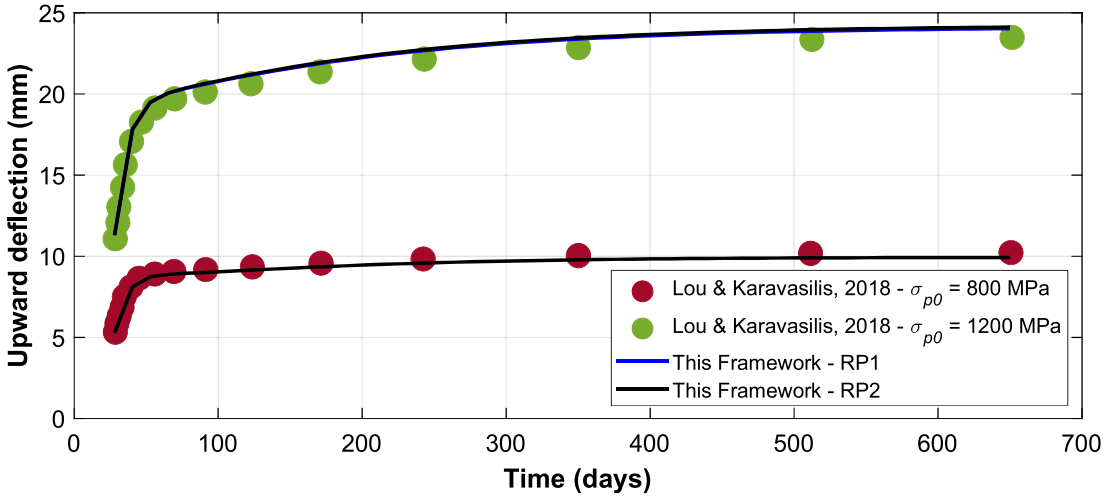


Figure 6.28: Long-term deflections under self-weight loads obtained with the EQL scheme.

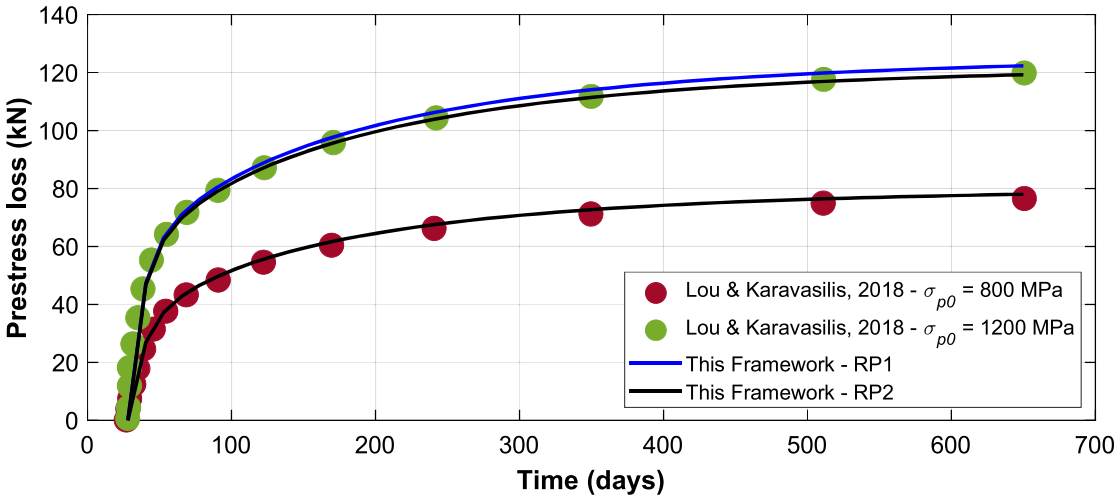


Figure 6.29: Long-term prestress losses under self-weight loads obtained with the LRE formulation.

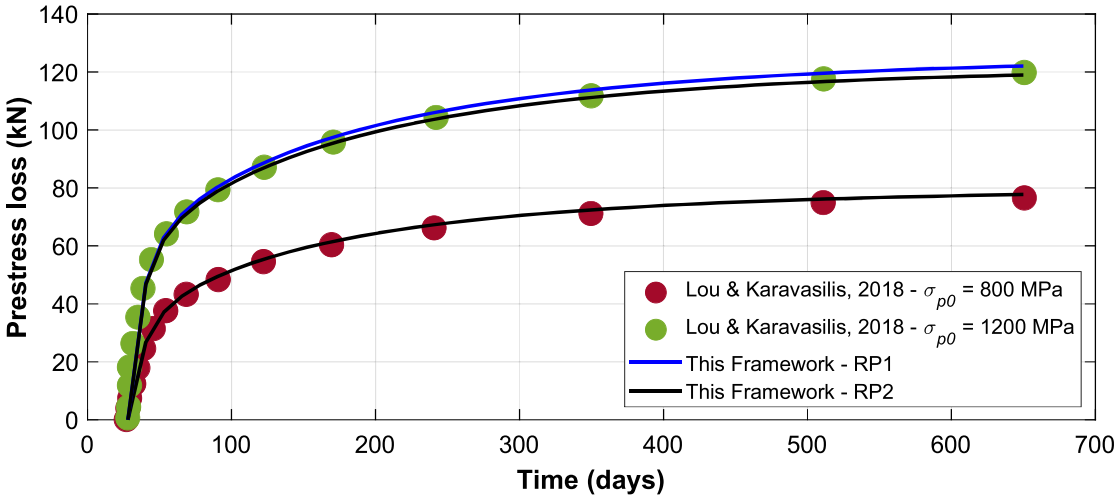


Figure 6.30: Long-term prestress losses under self-weight loads obtained with the EQL scheme.

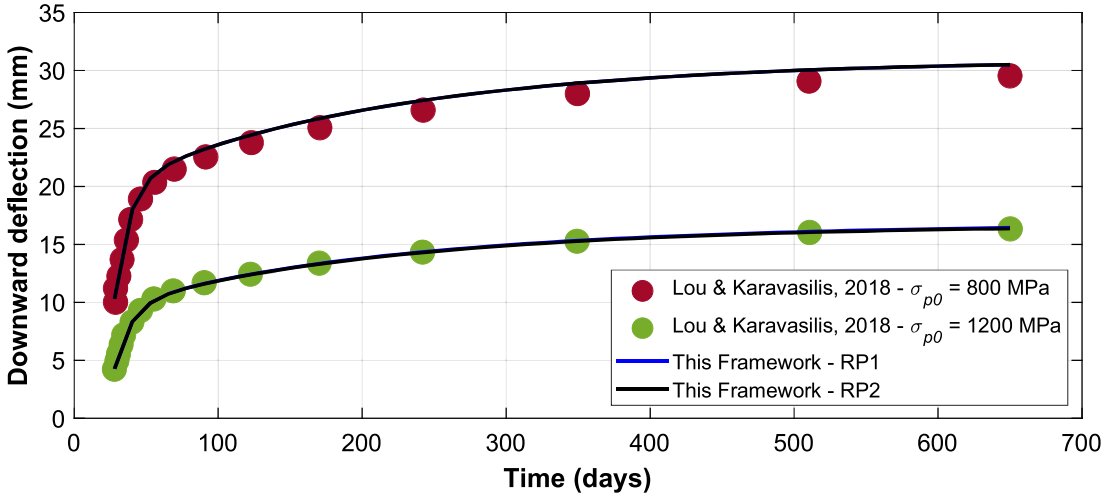


Figure 6.31: Long-term deflection under self-weight and four-point bending loads obtained with the LRE formulation.

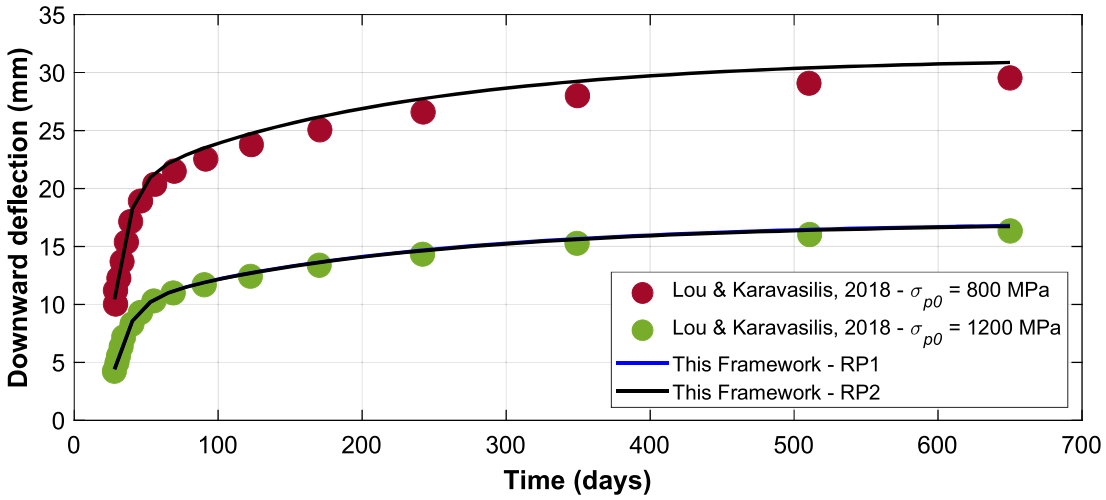


Figure 6.32: Long-term deflection under self-weight and four-point bending loads obtained with the EQL scheme.

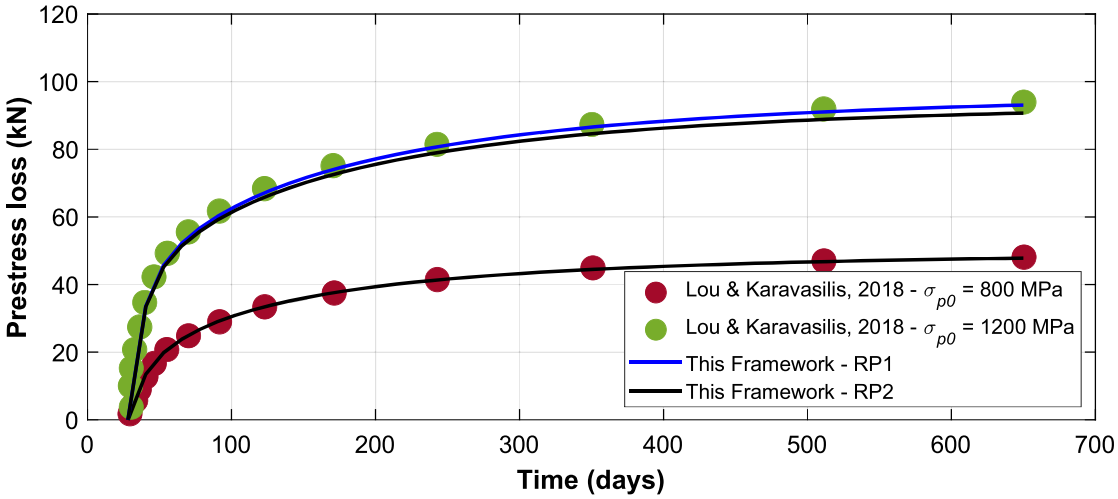


Figure 6.33: Long-term prestress losses self-weight and four-point bending loads obtained with the LRE formulation.

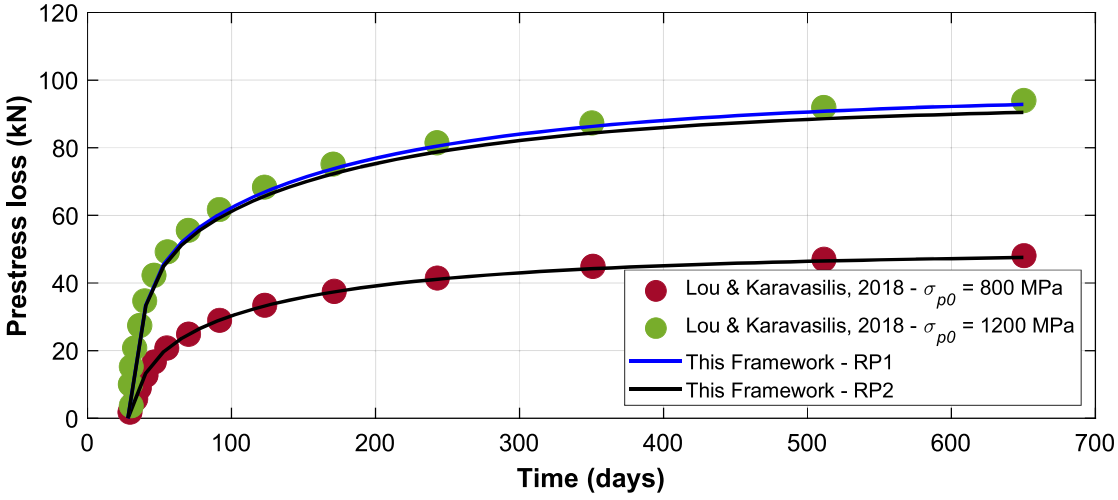


Figure 6.34: Long-term prestress losses self-weight and four-point bending loads obtained with the EQL scheme.

Regarding the relaxation procedures adopted, it can be noticed that the deflections are almost identical whereas in the case of prestress loss the results presents minor differences. It is worth mentioning that the small discrepancies observed between the results can be due to an assumed specific weight of the beam which was not provided by the authors of the original study. As it has been pointed out before, the self-weight of the hosting member is an important parameter to set the right initial conditions after the prestress transfer.

6.5 Concluding Remarks

From the presented methodologies and obtained results in the validation examples, the following conclusions can be offered:

- The equivalent load scheme (described in subsection 6.1.1) to consider strain incompatibility and second order effects in unbonded tendons represents an improvement over the methodology proposed by Lou and Xiang [238]. Specifically, the numerical procedure has been extended to consider a corotational approach instead of an updated Lagrangian approach to describe the large displacements of the hosting member. Moreover, basic end rotations are used instead of the total end rotations. This approach seems to be more appropriate in the derivation of the kinematic equations describing the geometry of the tendons as small approximations for the rotations experienced by the hosting members are considered.

- Similarly, the proposed FE formulation described in subsection 6.1.2 represents an upgraded version of the formulation developed by Moreira et al. [261]. In this specific case, te description of the hosting member is addressed by considering a corotational framework instead of a total lagrangian approach. Furthermore, in the derivation of the kinematic equations of the tendon, the total rotations at the ends of each tendon segment are not simplified or considered small and an inclination of the hosting member is taken into account. As a result, simplified expressions are obtained for the assessment of the force vector and tangent stiffness matrix of the unbonded tendons.

- A robust and efficient numerical procedure to assess the equilibrium state immediately after the prestress transfer process has been adopted. In contrast to an iterative trial-and-error scheme, this numerical procedure increases the computational efficiency of the numerical framework to a greater extent. Furthermore, in case of using an equivalent

load scheme for modelling the unbonded tendons, Quasi-Newton methods are adopted to address the lack of a tangent stiffness for the tendon elements. Last but not least, an initial expression is proposed to start these Quasi-Newton algorithms.

- The results presented attest to the capability of the analysis framework to address the short- and long-term global response of timber members post-tensioned with different tendon profiles as numerical and experimental benchmark results have been reproduced with sufficient accuracy. Furthermore, the framework considers enhanced formulations for the beam-column elements comprising the hosting members allowing the use of coarse discretizations and a better enforcement of equilibrium. As a result, the framework features versatility, numerical robustness and computational efficiency.

- The efficiency of this modelling approach allows carrying out design- oriented parametric studies of post-tensioned timber members where local responses such as strains and internal forces as well as global responses up to the ultimate limit state or during serviceability are of interest.

- Despite of obtaining almost identical results for both tendon formulations, the computational effort differs. In case of assessing the short-term response, it was observed that the numerical performance of both formulations is similar. However, during long-term assessments it was noticed that the resisting element formulation has a superior performance by carrying out less iterations.

- It is worth mentioning that the resisting element formulation offers a less cumbersome algorithm as the tangent stiffness matrix takes into account the change of eccentricities as the hosting member deforms.

- The presented numerical framework allows the consideration of shear deformations in the assessment of the failure load of post-tensioned timber members. It was noticed that these deformations influence the stiffness and deflections of the hosting members. However, in terms of the failure load their impact seems to be not important for the case studies considered.

Chapter 7

Numerical Case Studies

In this chapter, a complementary numerical study is performed to gain insights into the short- and long-term behavior of unbonded post-tensioned timber beams with draped external tendons. To this end, the post-tensioned beam labelled as specimen Beam 3 tested by van Beerschoten et al. [7] and analysed in subsection 6.4.3 is considered as a case study due to the practicality of its deviator layout which could be used frequently in the mainstream engineering practice. In the following analyses, it is assumed that the tensile and compressive strength of the timber material are the same by adopting the highest strength for the reference beam. In the first part of the analysis cases, the ultimate response under short-term loading of the selected post-tensioned specimen beam is analysed by varying the spacing between the deviators defining the profile of the draped tendon. The different beam-column (BC) finite element (FE) formulations described in subsection 4.1.3, subsection 4.1.4, subsection 4.1.5 and subsection 4.1.6 are employed herein. The traditional Euler-Bernoulli and Timoshenko BC elements are referred as EB and TB, respectively, whereas their enhanced formulations are denominated as ENH EB and ENH TB, respectively, in the following analyses. In the same way, the tendon formulations described in subsection 6.1.1 and subsection 6.1.2 are abbreviated as EQL and LRE, respectively. The aim of this comparisons is to show the versatility and efficiency of each finite element modelling approach implemented in the numerical framework. In the second part, only one modelling approach is considered to assess the time-dependent behavior of the generated post-tensioned timber beam layouts.

7.1 Influence of Deviator Spacing on Ultimate Response

In this numerical case study, it is examined the ultimate response of the externally post-tensioned timber Beam 3 by varying the draped profile of the tendon layout. Specifically, the

distance between the two deviators defining the tendon profile of the specimen Beam 3, S_{dev}, is varied while the initial tendon eccentricity is maintained constant. To encompass the influence of the deviator spacing on the ultimate response, the ratio of this distance to the span length of the beam specimen, S_{dev}/L, is defined. This ratio is considered as the main variable to carry out a numerical study of the nonlinear behaviour of post-tensioned timber beams subjected to four-point bending and uniform loads up to failure. On the other hand, according to Lou et al. [246], the spacing between deviators in post-tensioned reinforced concrete beams influences the development of second order effects. To determine if similar effects can take place in post-tensioned timber beams, 10 values of the ratio S_{dev}/L ranging from 0 to 1 were studied for the two loading scenarios. A ratio of zero represents a post-tensioned beam with no deviators whereas a value of one depicts a tendon profile with one deviator at mid-span. Global and local responses such as ultimate loading capacity, midspan displacement, eccentricity variation at the midspan, ultimate stress increase in the tendon, and midspan moment in the beam are analysed to evaluate the influence of deviator spacing on these nonlinear responses.

In this numerical study, the BC and tendon elements described in section 4.1 and section 6.1, respectively, are used to assess the ultimate response of the post-tensioned beams. In the case of the four-point bending loading, four FE models were built. In the first and second FE models, a fine mesh size comprising 18 BC elements was employed along with a EQL scheme for the unbonded tendons. In these models, the traditional EB and TB formulations were used, respectively. Fig. 7.1a shows some of the FE mesh generated for the analysis. On the contrary, the third and forth model employed a coarse mesh size comprising 6 or 4 BC elements depending on the value of the ratio S_{dev}/L adopted. More specifically, for ratios values of 0, 1/3 and 1, a discretization of 4 elements was used, whereas for the remaining values 6 elements were employed as shown in Fig. 7.2. In these coarse-mesh FE models, BC elements with Euler-Bernoulli and Timoshenko enhanced formulations, respectively, were adopted along with LRE formulations for the unbonded tendons with the aim of using the smaller number of elements. In what follows, the previously described FE models are denominated as FE model 1, 2, 3 and 4, respectively. Similarly, the four-point bending and uniform loads applied on the post-tensioned beam reference are denominated as loading scenario 1 and 2, respectively. In the case of loading scenario 2 (uniform loads), only fine-mesh FE models, it means FE model 1 and 2, are used to assess the short-term response of the post-tensioned beams. This discretization is more suitable for this case as the uniform load is represented as equivalent loads along the beam length.

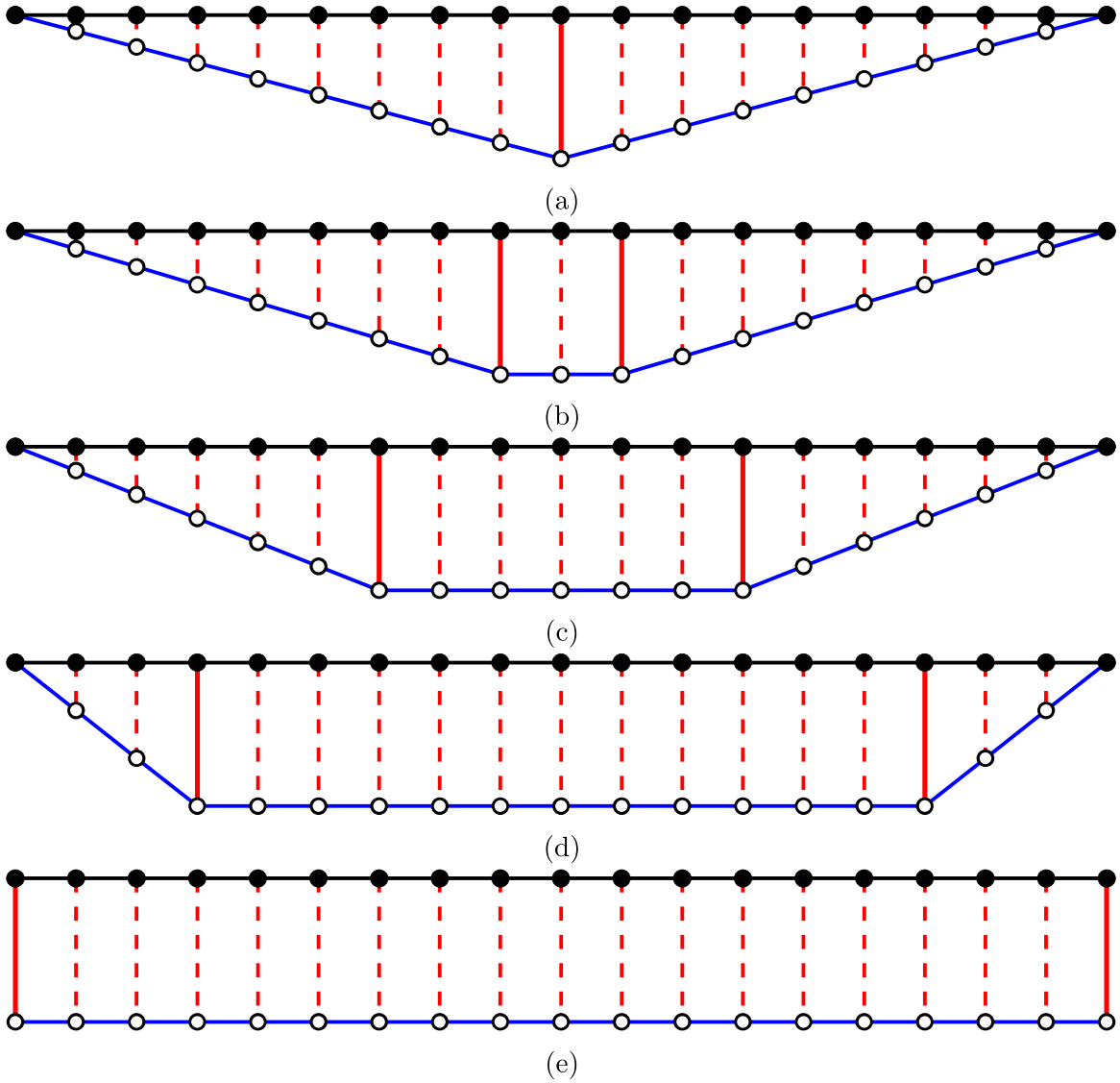


Figure 7.1: Fine mesh discretization adopted for FE models 1 and 2: (a) $S_{dev}/L = 0$; (b) $S_{dev}/L = 1/9$; (c) $S_{dev}/L = 1/3$; (d) $S_{dev}/L = 2/3$; (e) $S_{dev}/L = 1$.

Figs. 7.3 to 7.8 show the global and local responses obtained for the different ratio values S_{dev}/L and FE models described previously. From these figures, it can be observed that the results obtained from the fine- and coarse-mesh FE models with the same section kinematics hypothesis are very similar. By comparing the results obtained for different section kinematics hypothesis, it can be noticed that larger variations of tendon eccentricities and ultimate deflections at the midspan are obtained when the shear deformations are included. From the results, the larger tendon eccentricity variations are obtained for the tendon profile without deviators whereas no variation is obtained when the deviator is located at the midspan.

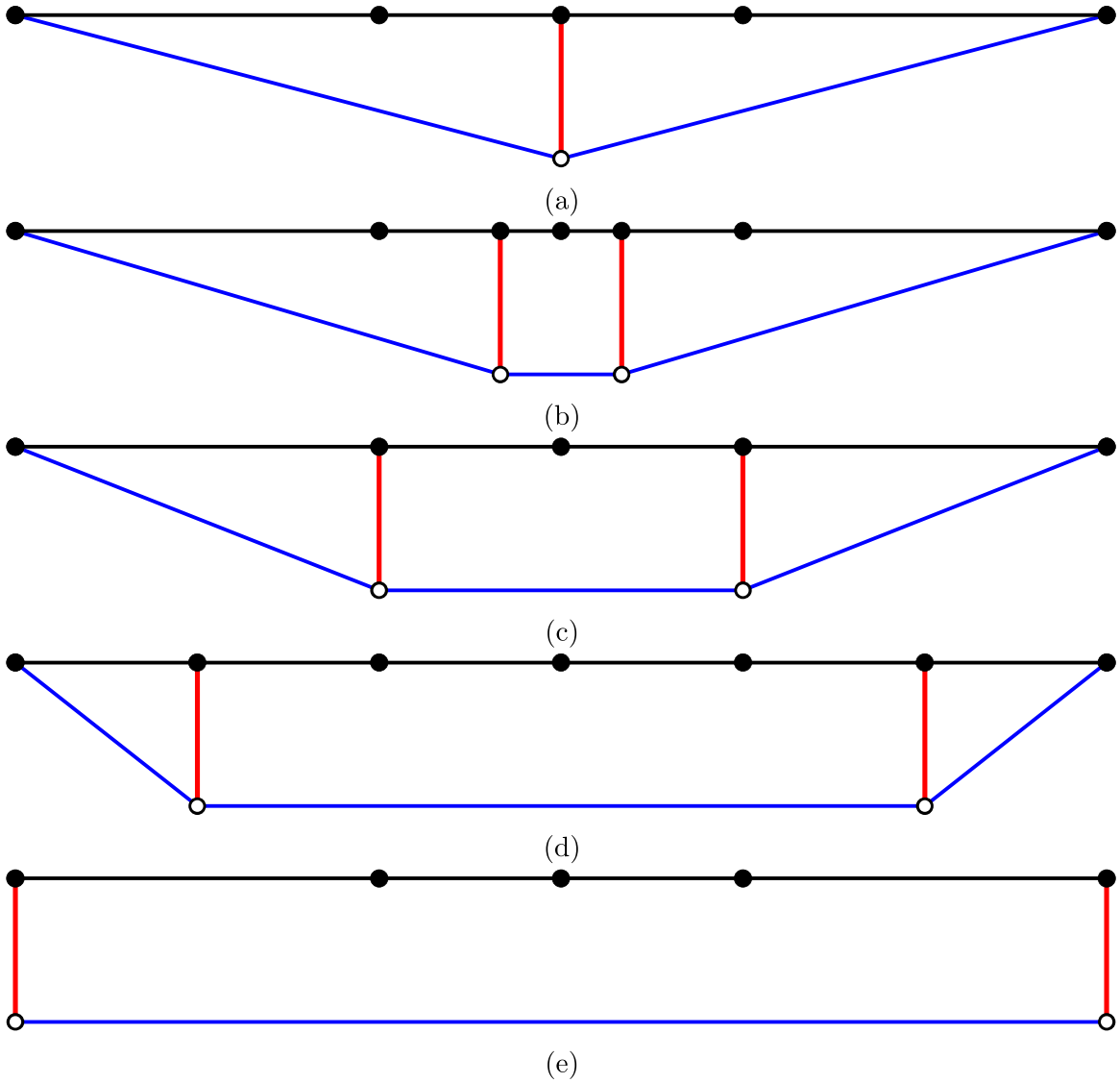
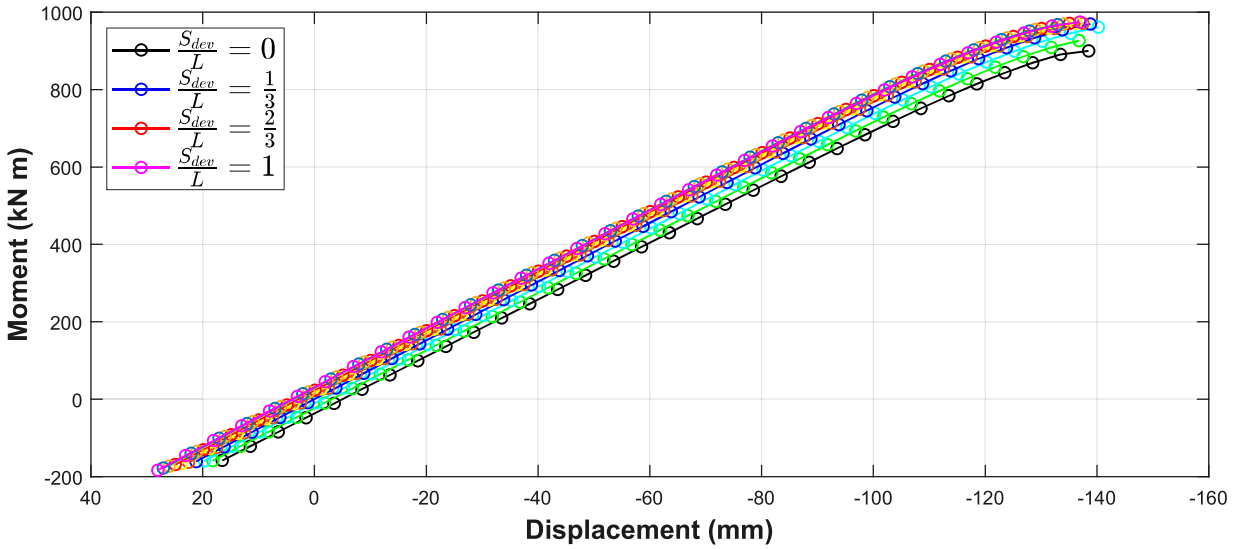
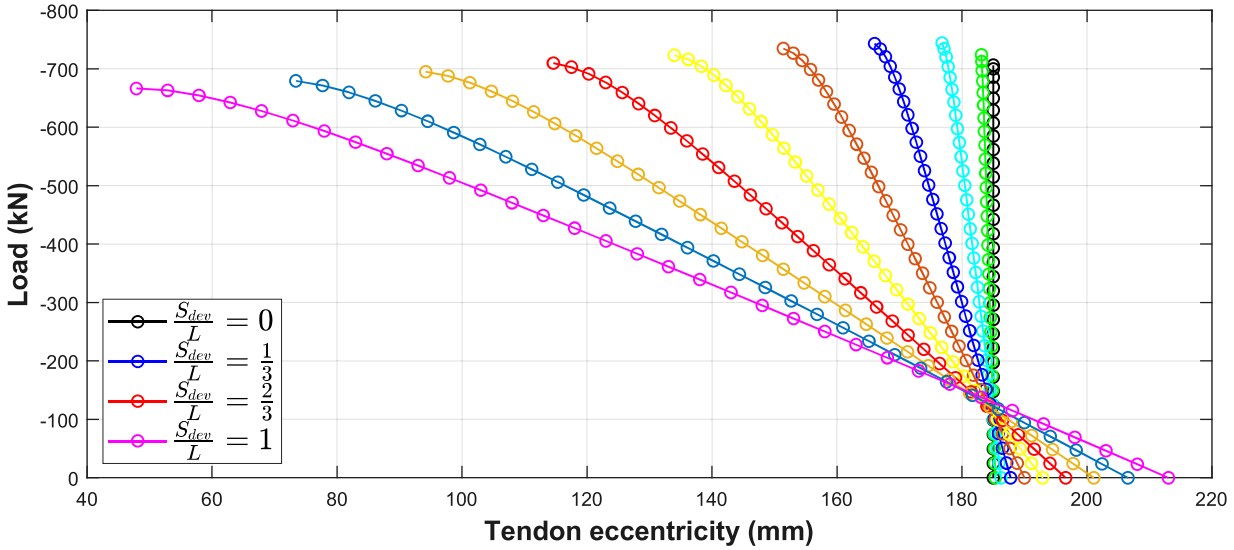


Figure 7.2: Coarse mesh discretization adopted for FE models 3 and 4: (a) $S_{dev}/L = 0$; (b) $S_{dev}/L = 1/9$; (c) $S_{dev}/L = 1/3$; (d) $S_{dev}/L = 2/3$; (e) $S_{dev}/L = 1$.

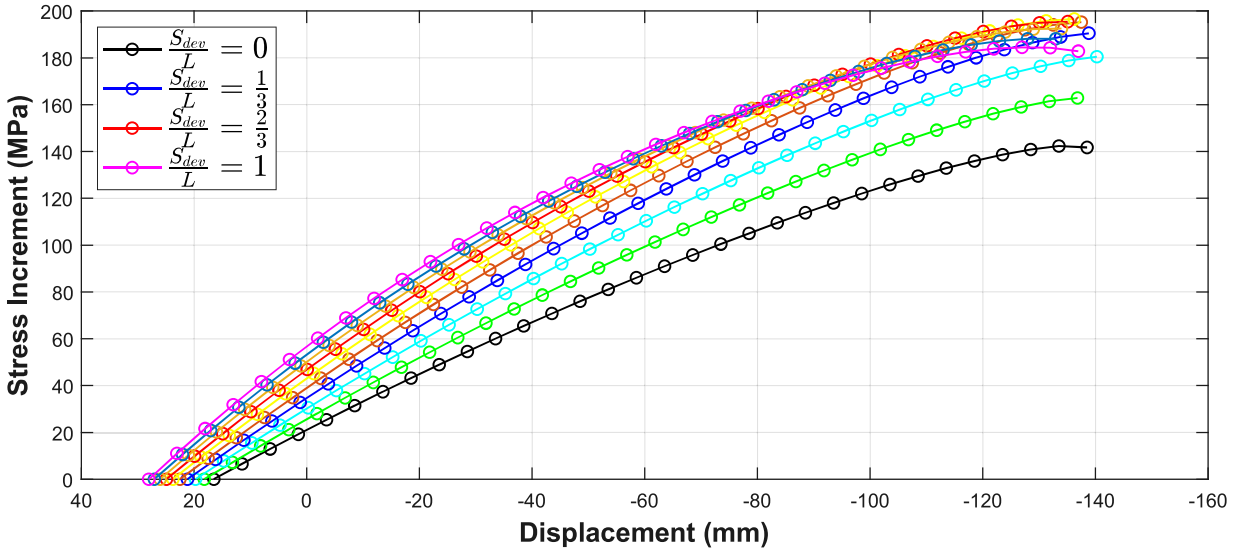
In Fig. 7.9 the ultimate load capacity of the post-tensioned beam is plotted as a function of the deviator spacing ratio S_{dev}/L. From this figure, it can be observed that the obtained results from the fine-mesh and coarse-mesh FE models are very similar and shear deformations has a negligible effect for the four-point bending loading case (loading scenario 1). In this loading scenario, the maximum capacities are attained for span ratios ranging between 2/9 and 4/9. In the case of the uniform distributed loading case (loading scenario 1), higher ultimate loads (up to 28% more) were obtained by including or neglecting shear deformations. In this particular case, the maximum capacity was achieved for the span ratio value of 1/9. Conversely, the post-tensioned beams with no deviators shows the lowest failure loads under both load types.



(a)

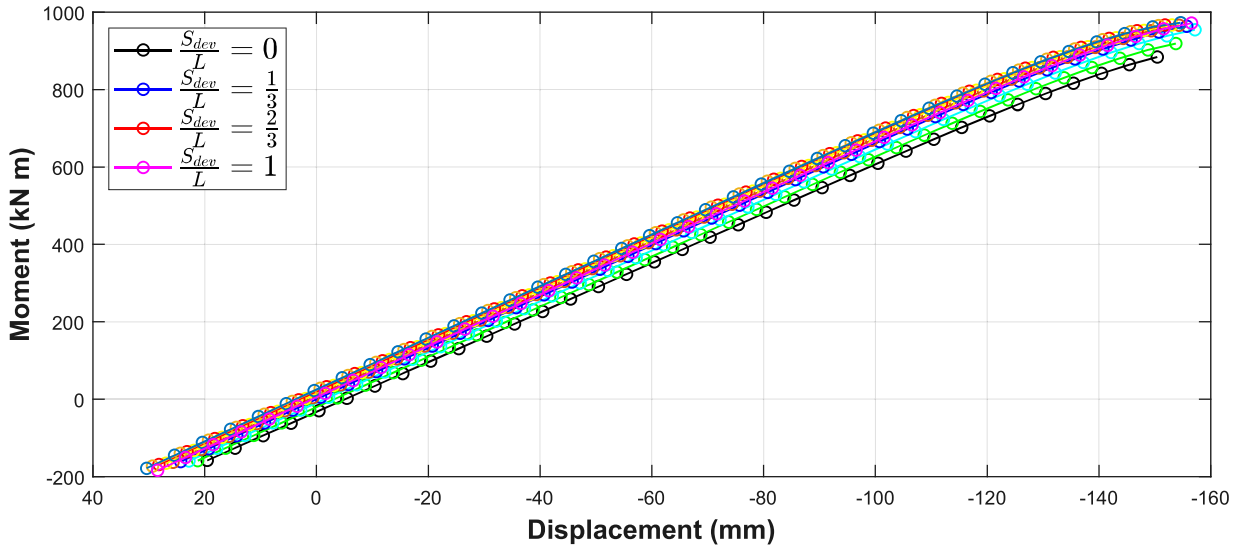


(b)

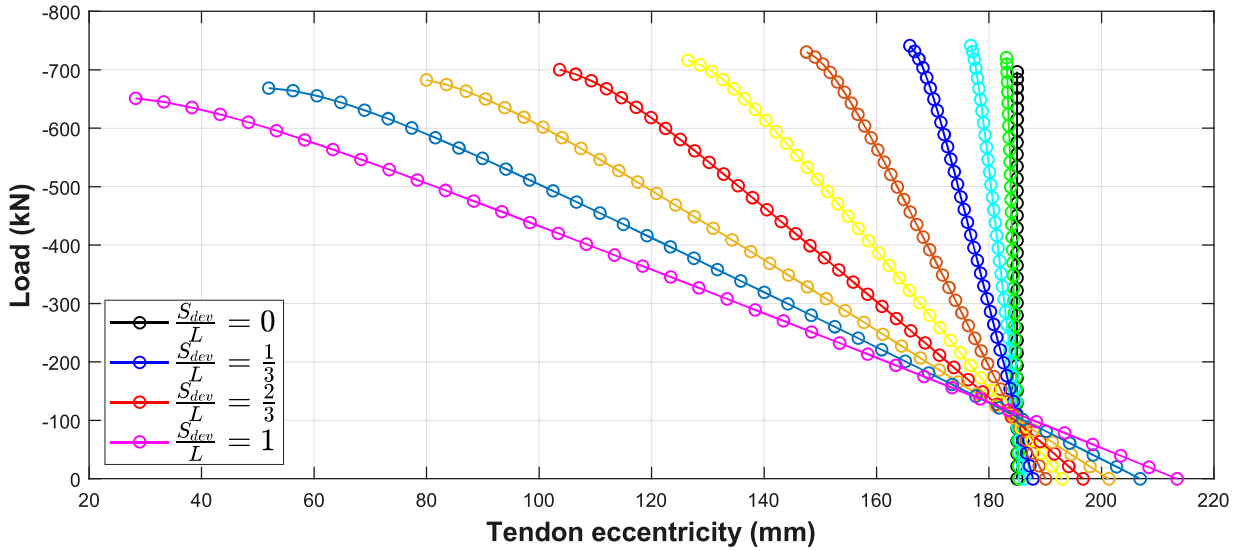


(c)

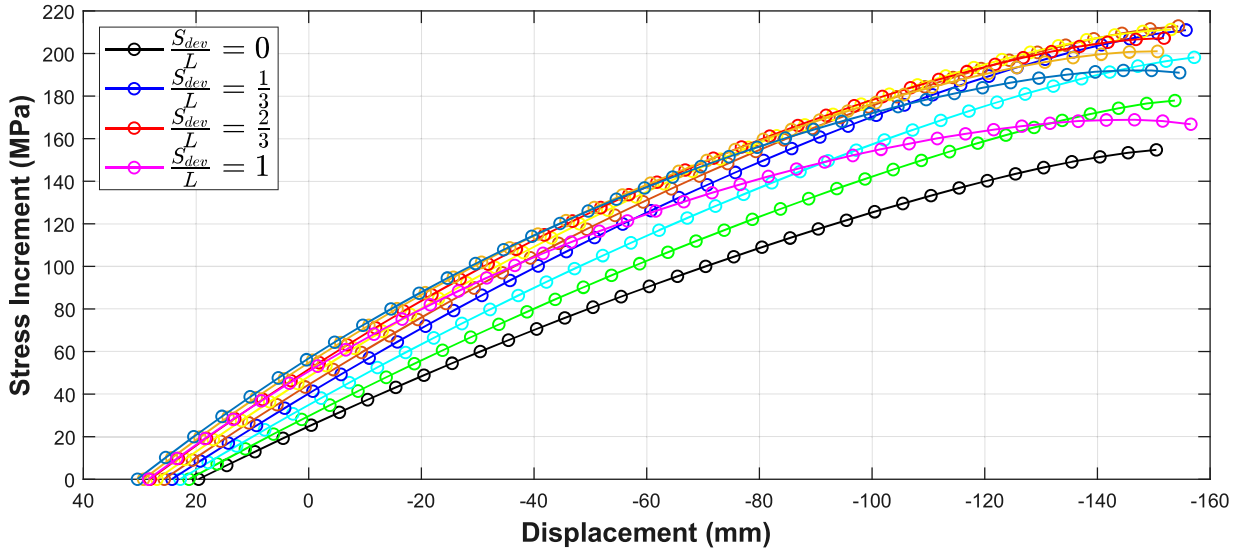
Figure 7.3: Ultimate responses obtained for loading scenario 1 using FE Model 1.



(a)

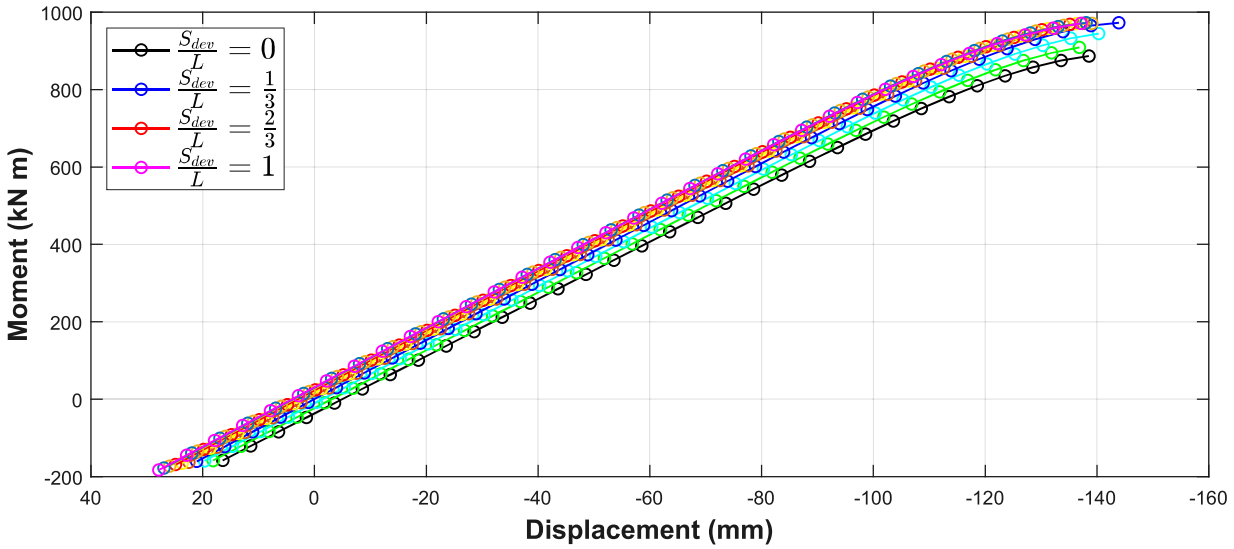


(b)

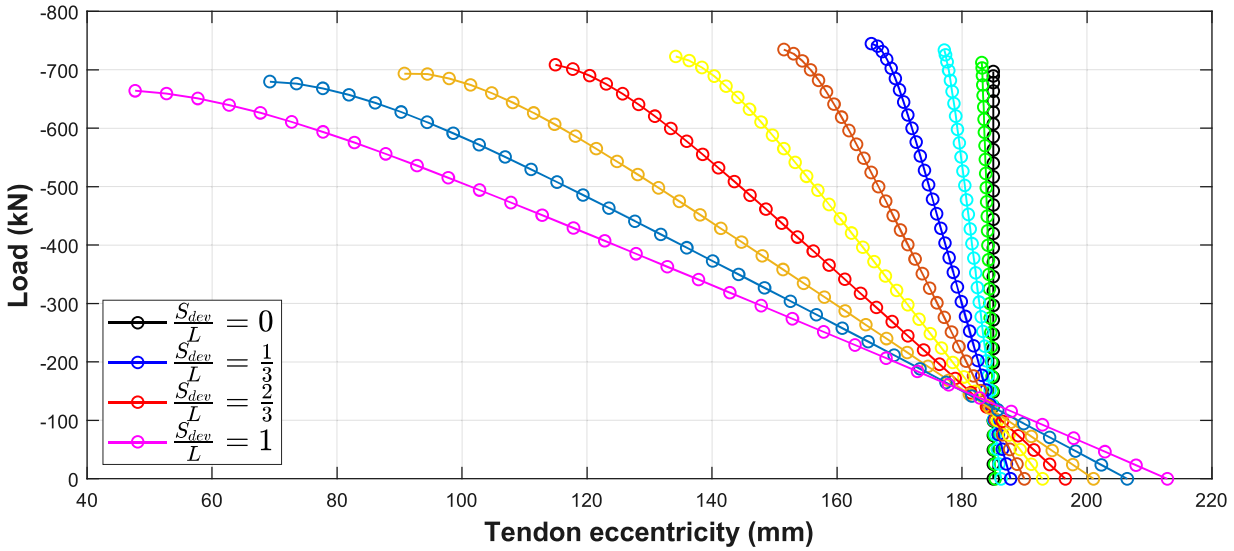


(c)

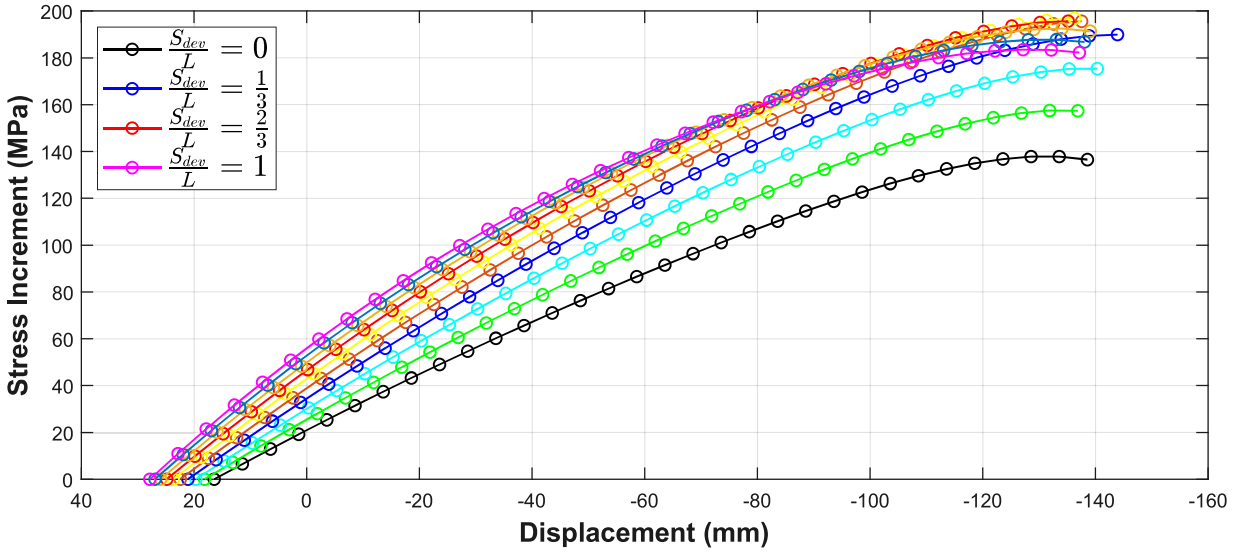
Figure 7.4: Ultimate responses obtained for loading scenario 1 using FE Model 2.



(a)

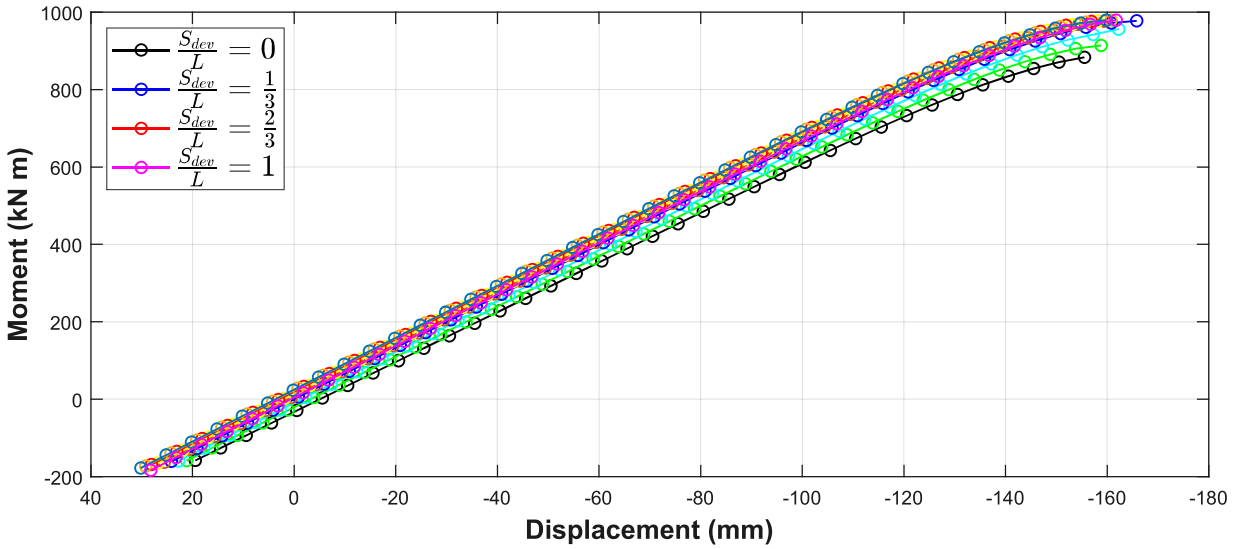


(b)

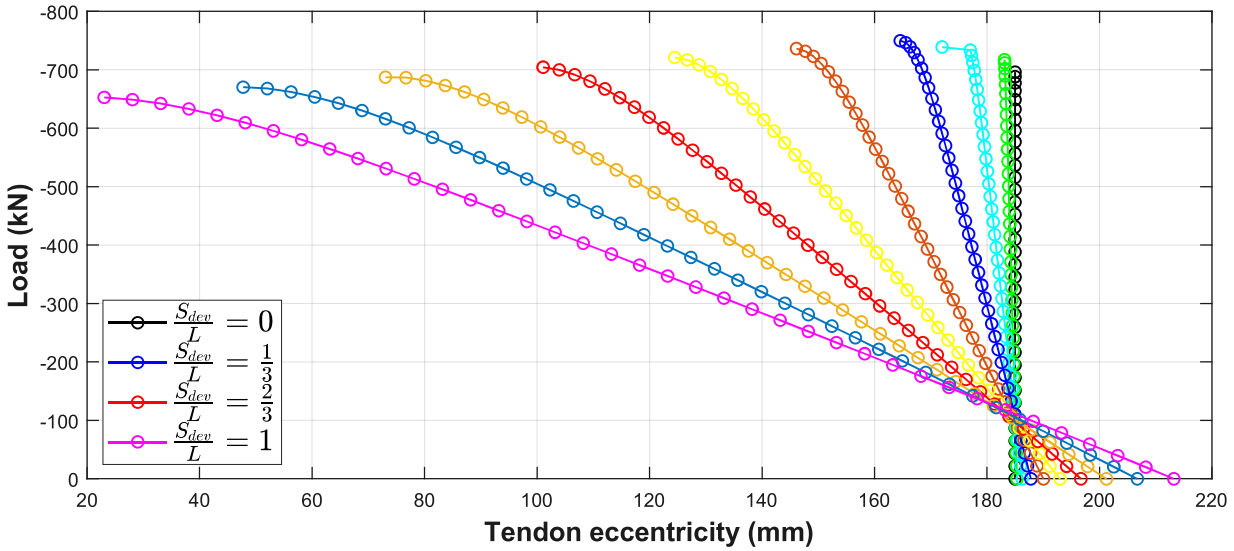


(c)

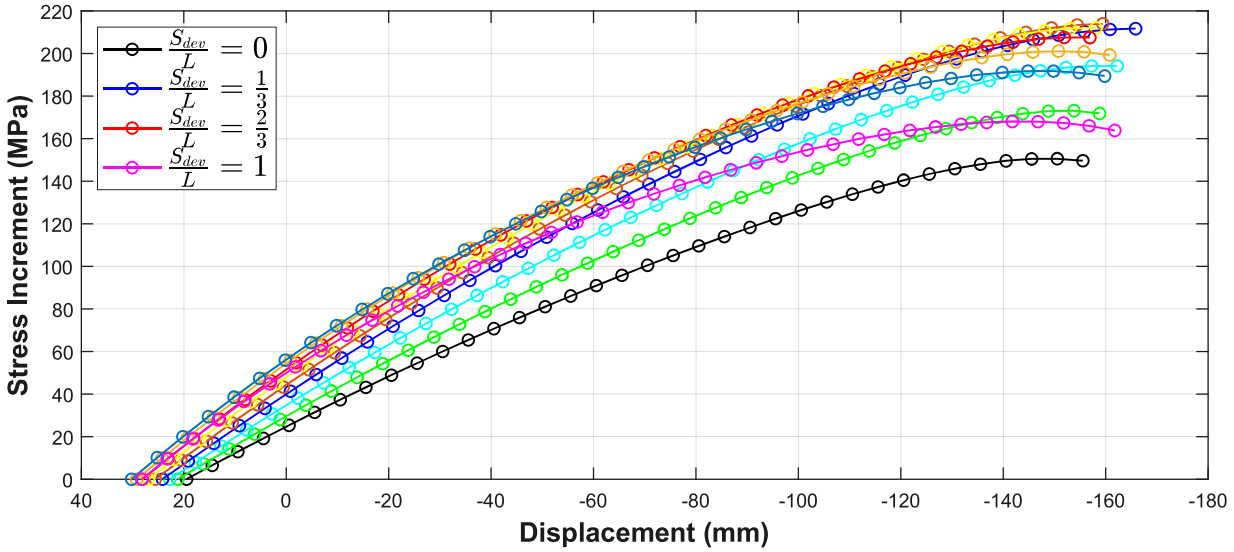
Figure 7.5: Ultimate responses obtained for loading scenario 1 using FE Model 3.



(a)

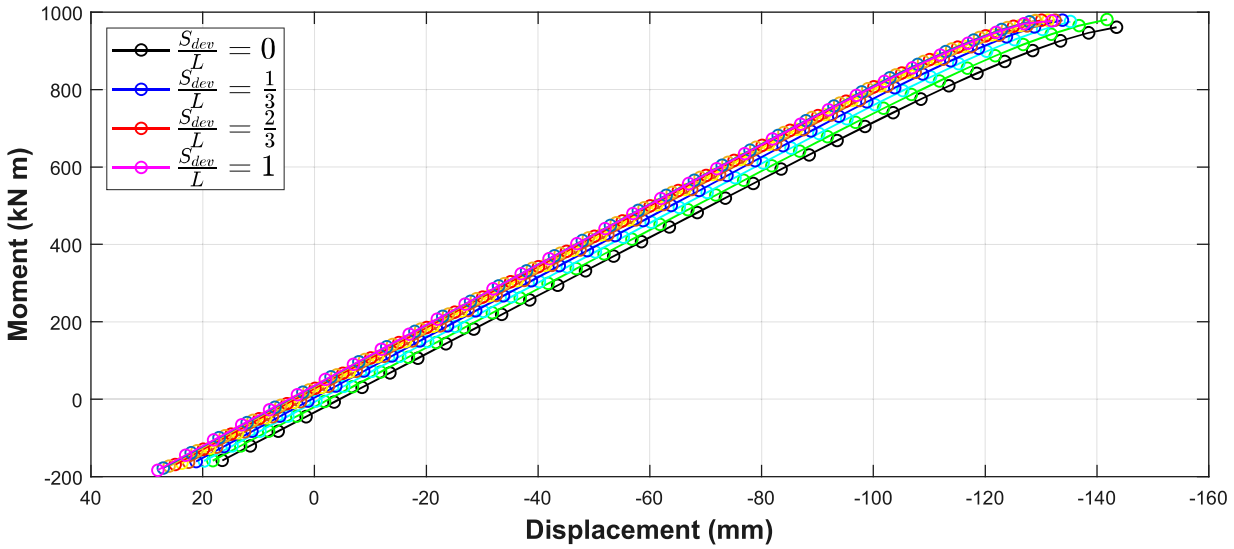


(b)

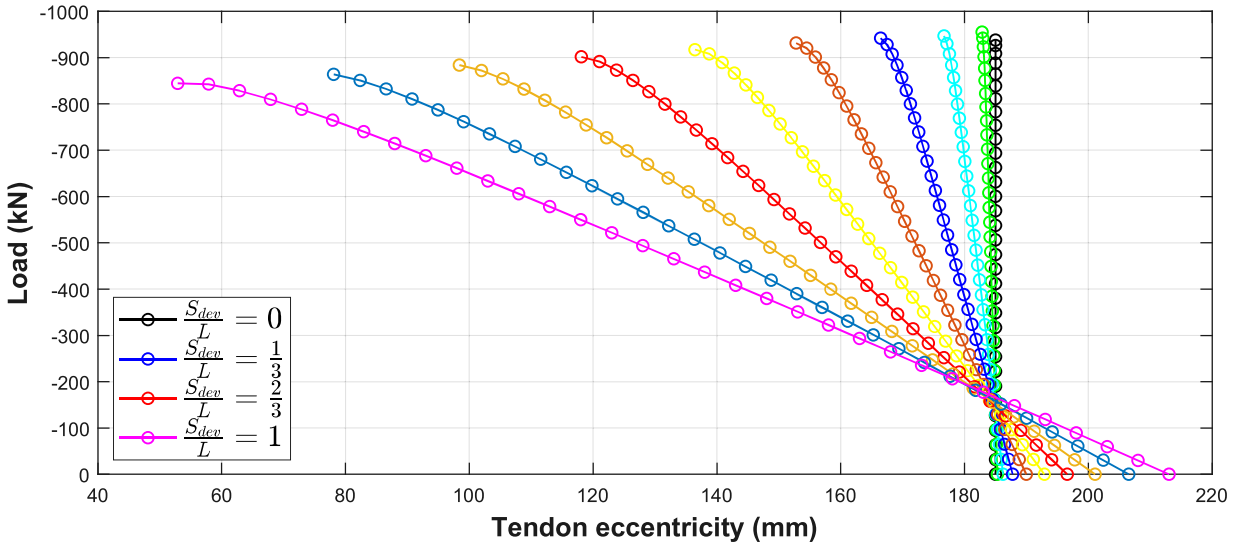


(c)

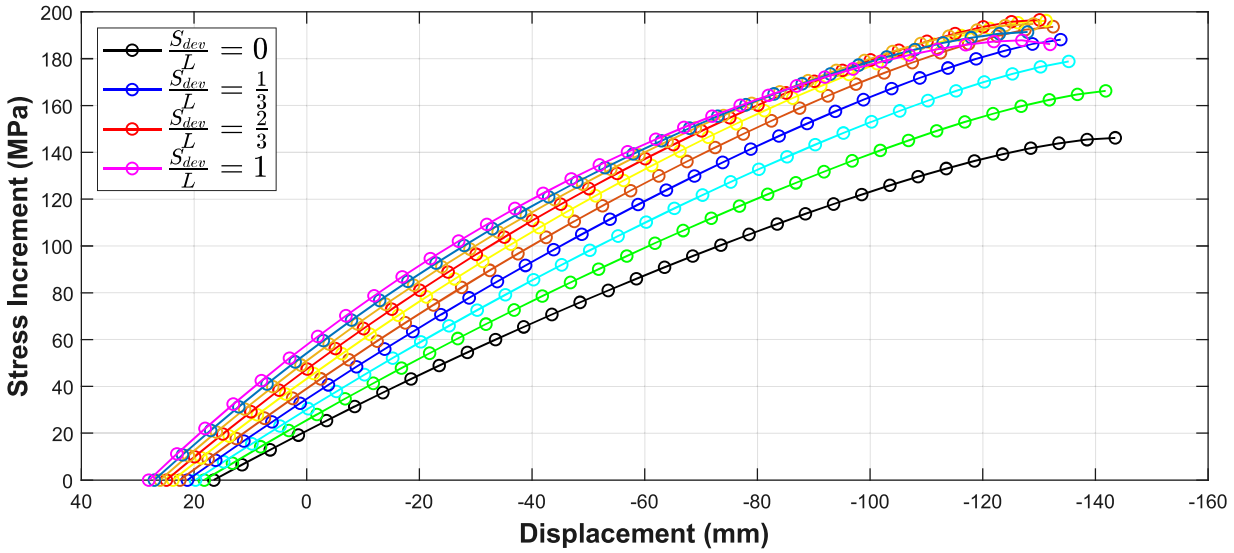
Figure 7.6: Ultimate responses obtained for loading scenario 1 using FE Model 4.



(a)

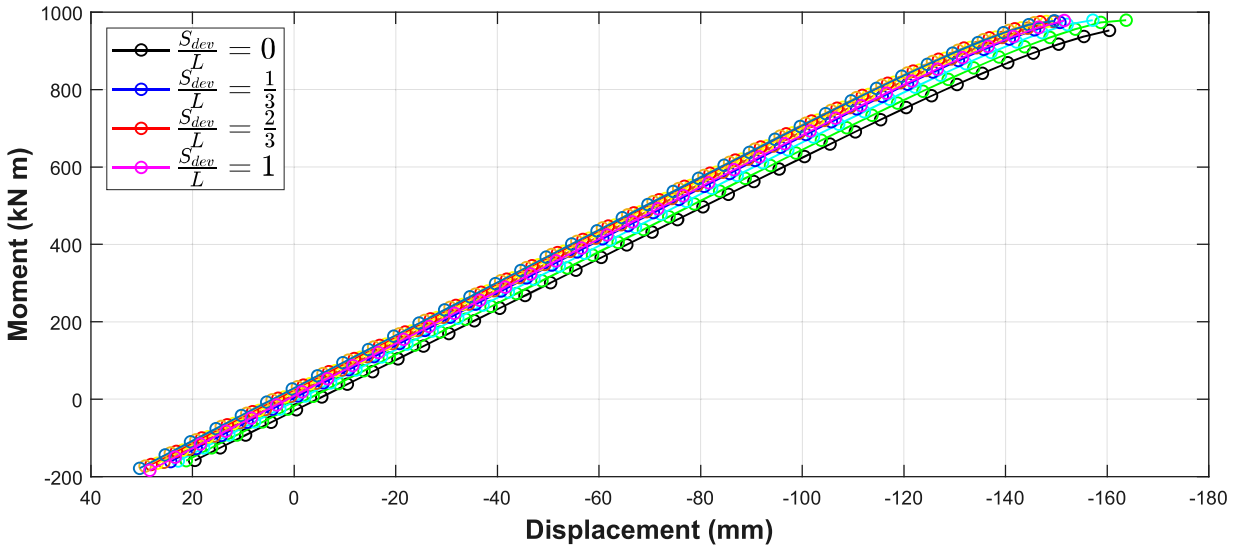


(b)

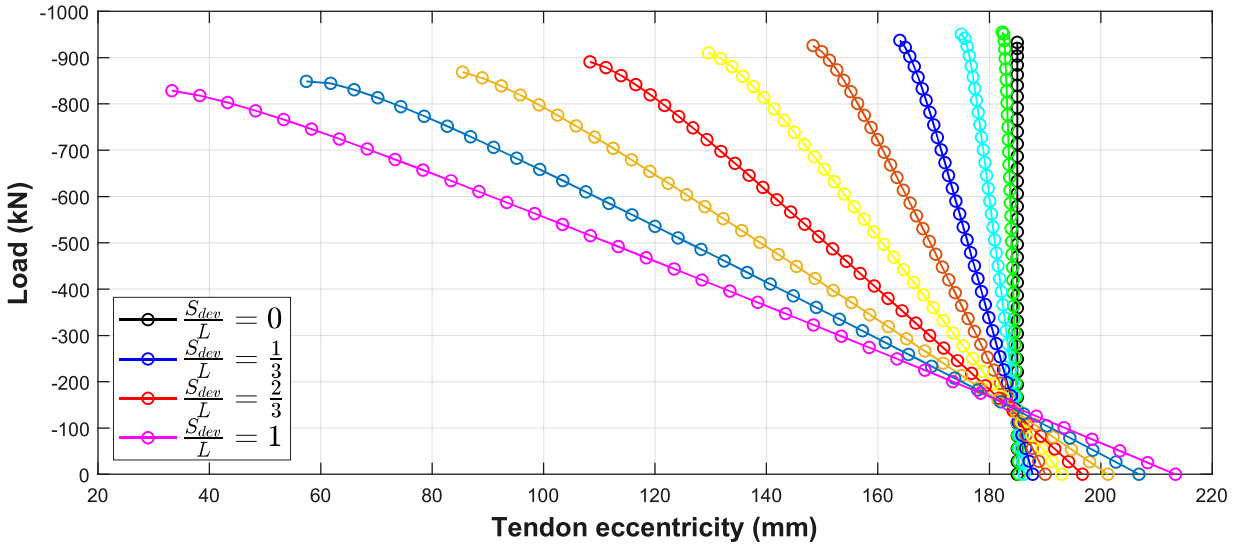


(c)

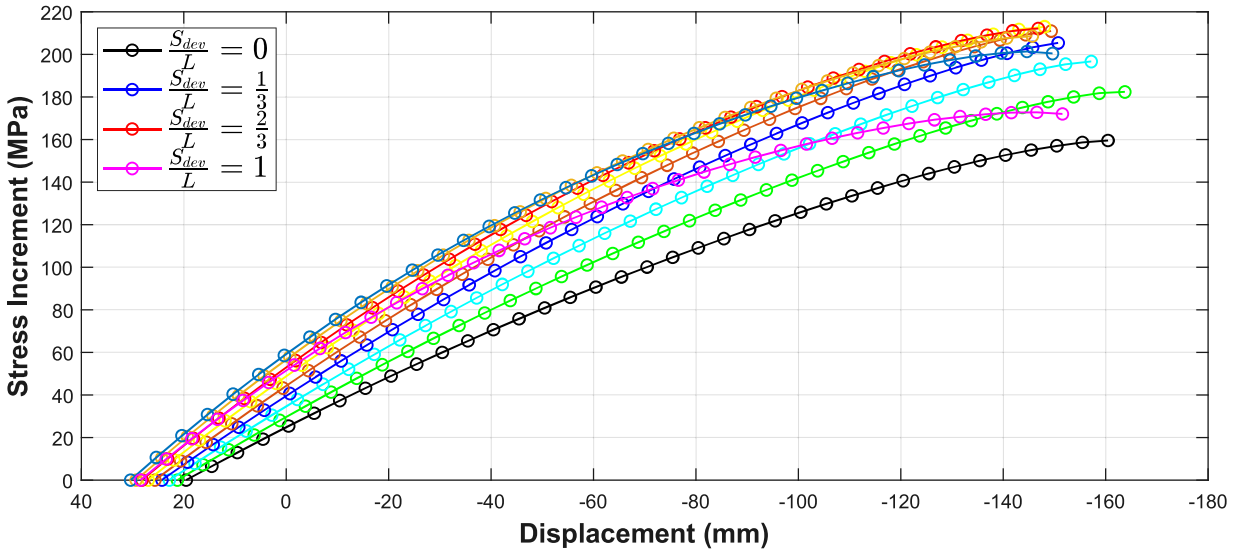
Figure 7.7: Ultimate responses obtained for loading scenario 2 using FE Model 1.



(a)

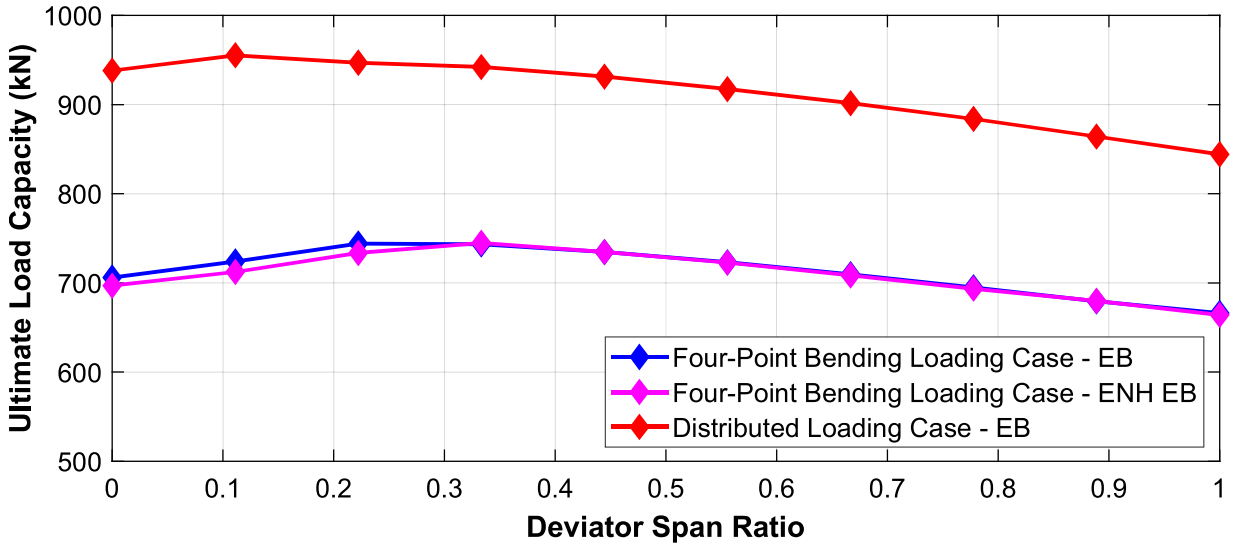


(b)

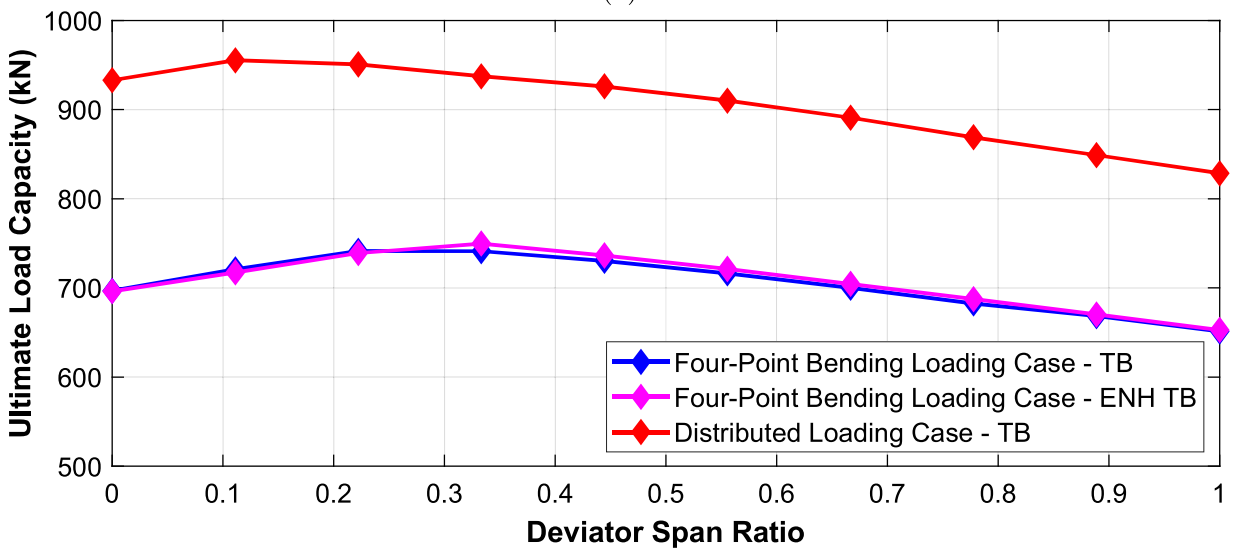


(c)

Figure 7.8: Ultimate responses obtained for loading scenario 2 using FE Model 2.



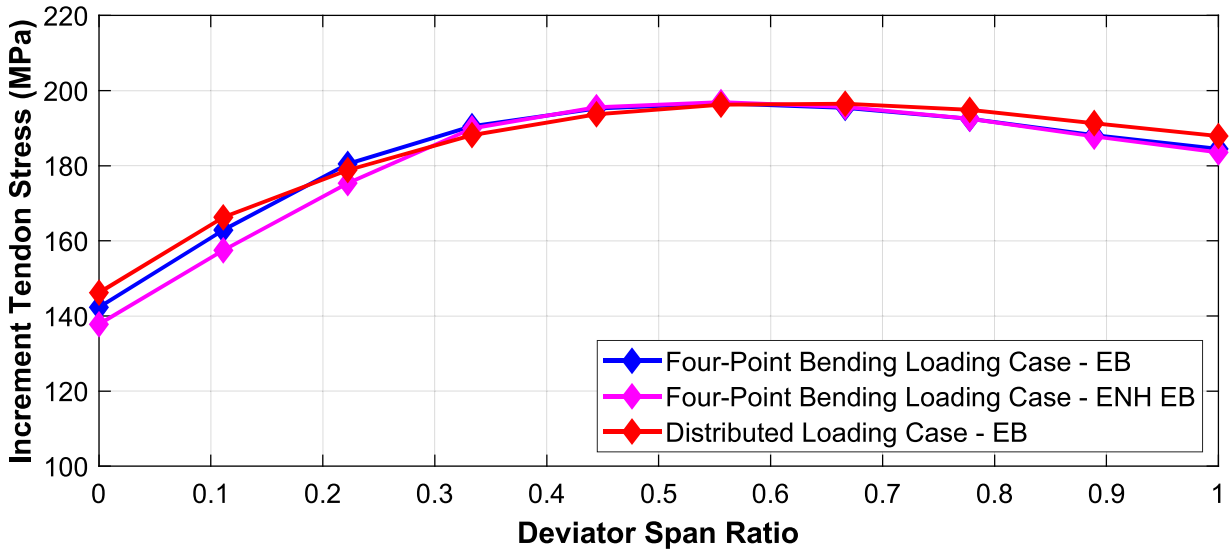
(a)



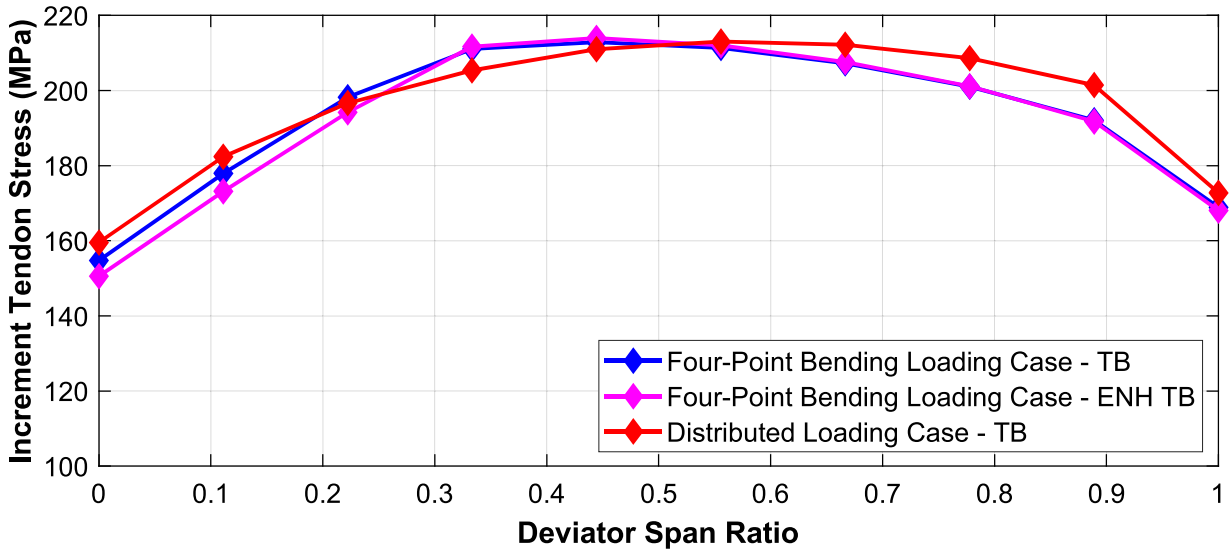
(b)

Figure 7.9: Effects of deviator spacing on ultimate load capacities: (a) Euler-Bernoulli formulations; (b) Timoshenko formulations.

The increase of the ultimate stress in the unbonded tendon is depicted as a function of the deviator spacing ratio S_{dev}/L in Fig. 7.10. From these results, it can be noticed that the loading scenarios considered induces similar trends regarding the stress increments in the tendon at the ultimate states. In the case of including the shear deformations in the hosting member, it can be observed that these deformations incurred in the hosting member induce higher stress increments in the tendon at the ultimate states. The lowest stress increments are registered for the configuration with one deviator at the midspan. In overall, the fine- and coarse-mesh FE models provide similar results for each beam kinematic theory.



(a)



(b)

Figure 7.10: Effects of deviator spacing on ultimate tendon stress increase: (a) Euler-Bernoulli formulations; (b) Timoshenko formulations.

7.2 Influence of Deviator Spacing on Long-Term Response

In this numerical study, the time-dependent behavior of the post-tensioned timber Beam 3 is analysed by considering only three of ratios values, S_{dev}/L, previously used in section 7.1. The considered ratios values in this long-term analysis are: $S_{dev}/L = 0$, $S_{dev}/L = 1/3$ and $S_{dev}/L = 1$. In this analysis, traditional Euler-Bernoulli BC elements are used for modelling the hosting member and the unbonded tendons are simulated by adopting the LRE approach. A mesh of 18 BC elements is used along with one, two or three tendons segments depending on the ratio value as shown in Fig. 7.11.

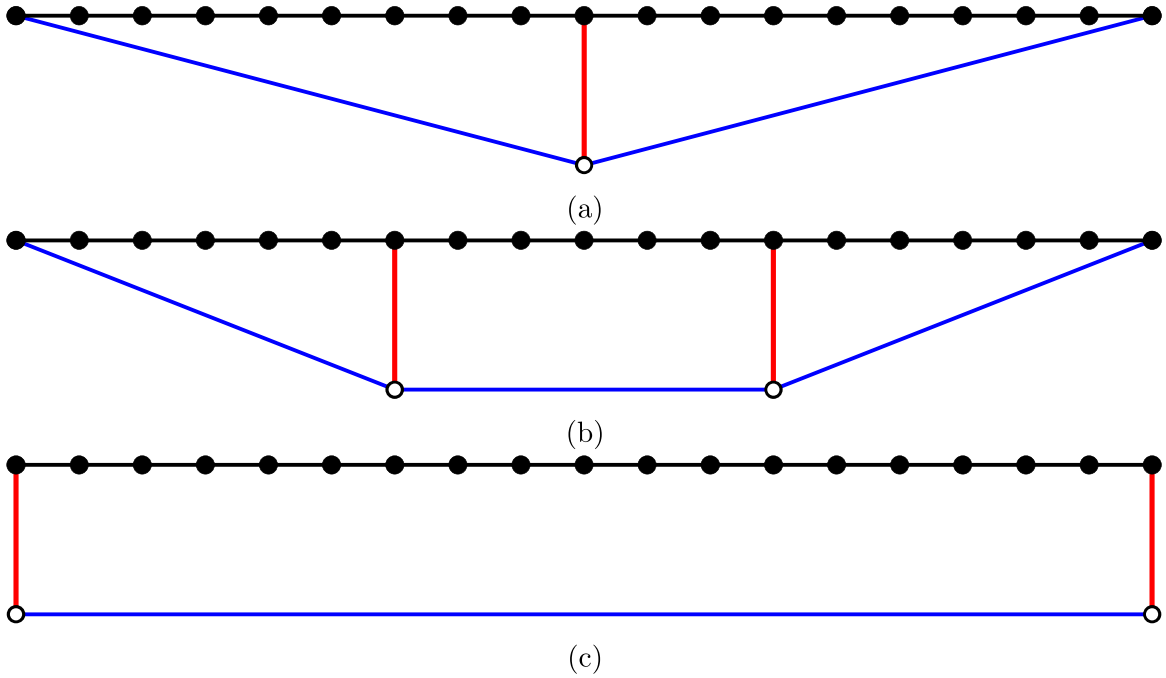


Figure 7.11: FE discretization: (a) $S_{dev}/L = 0$; (b) $S_{dev}/L = 1/3$; (c) $S_{dev}/L = 1$.

For the numerical study, the post-tensioned beam is analysed under two loading scenarios. One scenario consist of only self-weight loads applied whereas the other considers the self-weight along with a four-point bending load. Additionally, as wood posses a hygroscopic behavior, the surrounding environment is also included in the loading scenario. In this particular case analysis, the weekly and daily cyclic humidity variations employed during the test performed by Hoyle et al. [223] are used herein for comparative purposes. These cyclic humidity variations consist of square waves with weekly and daily periods as was described in subsection 4.4.6. By considering a total four-point bending load of 200 kN during the service life of the post-tensioned beam, a maximum stress of 15 MPa at the midspan of the beam is induced meaning that the beam remains in the linear-elastic range. As a result, a viscoelastic model such as the model proposed by Toratti [66] can be used to describe the time-dependent behavior of the beam. As the material comprising the post-tensioned beams tested by van Beerschoten et al. [7] is radiata pine, the parameters used by Toratti [66] can no longer be used as they were obtained for spruce sawn timber. However, Granello et al. [130] proposed a set of values for the mentioned viscoelastic model after performing a calibration based on the creep coefficients proposed by Fragiacomo and Davies [127] which in turn were deduced from the experimental test performed by Davies and Fragiacomo [118] on radiata pine block specimens.

Timber Materials Parameters					
τ_1^{ve}	0.1 days	J_1^{ve}	0.00289	c	6.3
τ_2^{ve}	1 days	J_2^{ve}	0.00492	J_∞^{ms}	0.63
τ_3^{ve}	10 days	J_3^{ve}	0.0088	α^{hyg}	0.00625
τ_4^{ve}	100 days	J_4^{ve}	0.0297	b	1.3
τ_5^{ve}	1000 days	J_5^{ve}	0.0441	m_{ref}	0.108
τ_6^{ve}	10000 days	J_6^{ve}	0.2321	E_0	12.65 GPa

Table 7.1: Adopted material parameters for Toratti's rheological model.

Prior to perform the viscoelastic analysis, a moisture diffusion analysis is performed using the finite difference code OpenMoist (Melchor and Málaga [132]) implemented in the current numerical framework. In a similar way to the viscoelastic model, Granello et al. [130] performed a calibration of the moisture diffusion parameters defining the single Fickian diffusion equations (Eqs. (3.8) and (3.9)) based on the experimental test performed by Davies and Fragiacomo [118]. These values resulted in 0.005 cm^2/day and 1.123 cm/day for the surface emissivity and diffusion coefficient. To perform the moisture diffusion analysis, a grid of 560 elements was generated as illustrated in Fig. 7.12. By considering that the cyclic humidity variations are applied equally to the external perimeter and internal cavity during a period of 120 days, the resulting average moisture content for the weekly and daily variations are depicted in Fig. 7.13. From the results, it can be observed that the weekly variations induced higher variations in the hollow section.

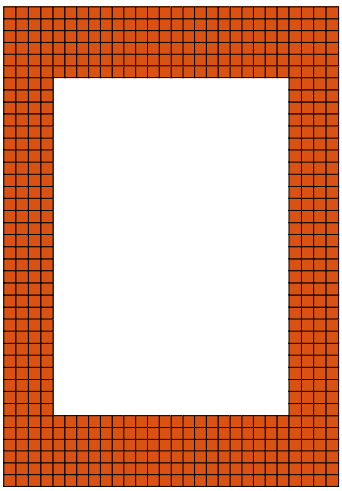


Figure 7.12: Grid generated for the Hollow square section.

In the diffusion analysis, the expression proposed by Toratti [66] to assess the moisture content in equilibrium with the surround environment is employed herein. In relation to the relaxation experienced by the unbonded post-tensioned tendons, the viscoelastic model described by Eq. (6.47) is adopted for the viscoelastic analysis by considering prestressing steel of normal relaxation.

To assess the effects of the different loading scenarios in the time-dependent behavior of the post-tensioned reference beam under three different tendon profile configurations, the tendon eccentricity at the midspan, the midspan displacement of the hosting member and prestress loss in the tendon are evaluated. All these results for the different loading scenarios are depicted in Figs. 7.14 to 7.17. From these figures, it can be observed in overall that the environmental conditions do not have any relevant influence on the long-term deflections in the post-tensioned beam. However, the applied loads induce downward or upward deflections which grow over the time. For the case of inducing precamber in the beam, the eccentric tendon profile ($S_{dev}/L = 1$) led to higher deflections (18% of the elastic deflection). On the contrary, under the combined loading scenario, the draped tendon configuration with one deviator at the midspan ($S_{dev}/L = 0$) provokes larger deflections (29% of the elastic deflection).

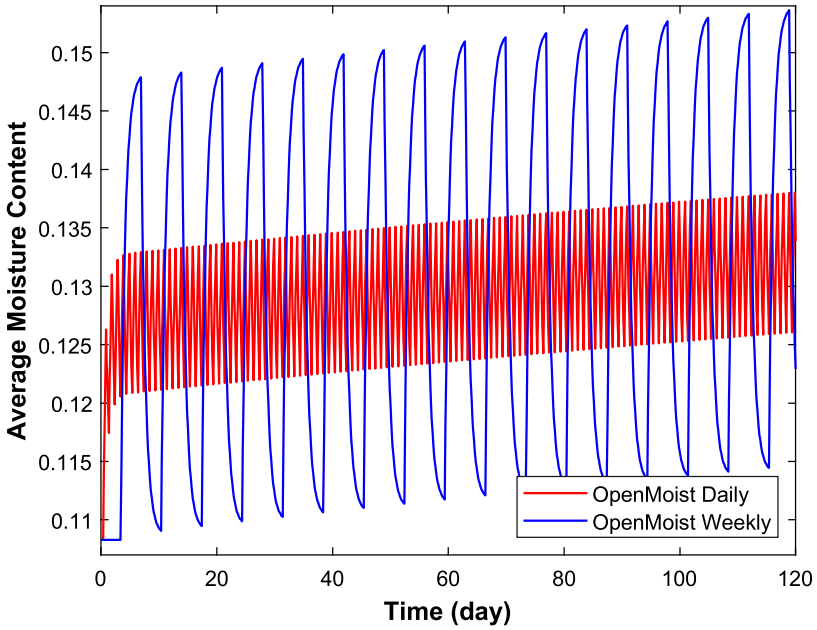
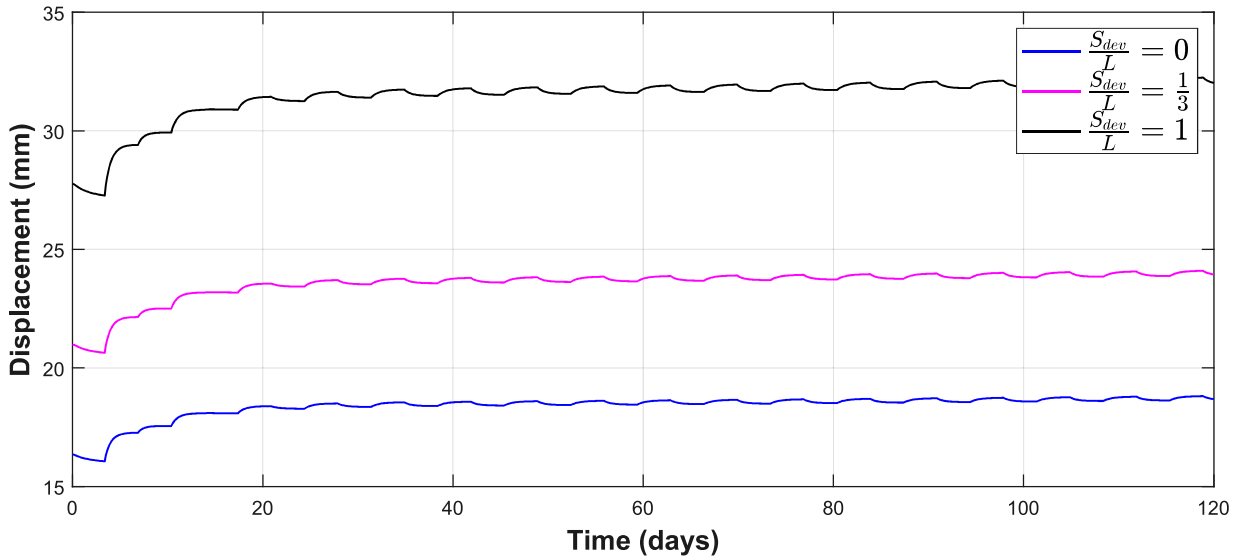
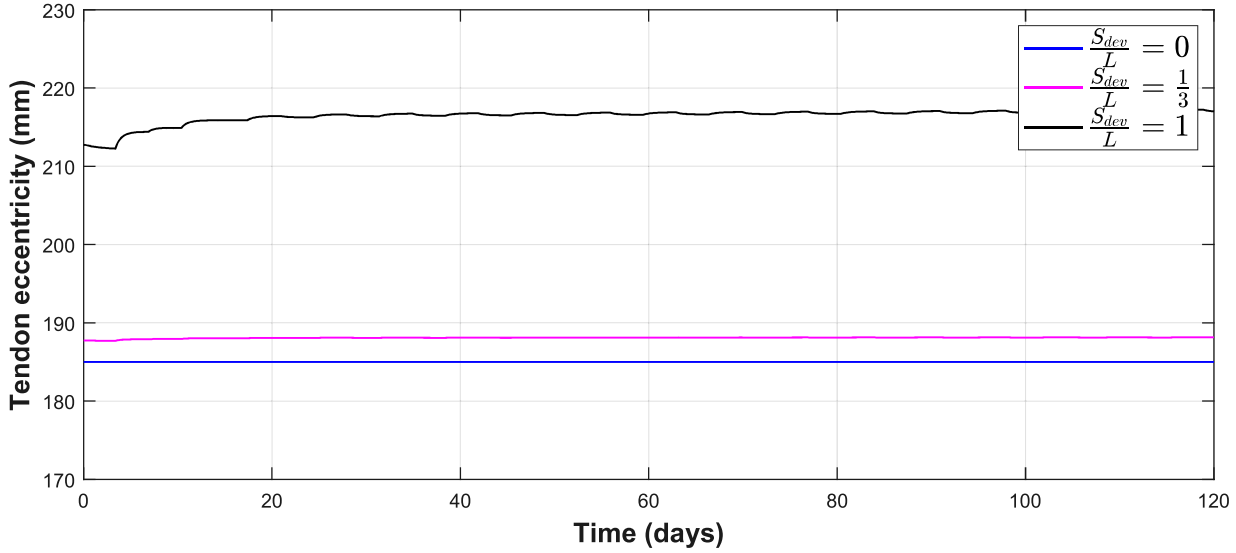


Figure 7.13: Average moisture content under weekly and daily relative humidity cycles.

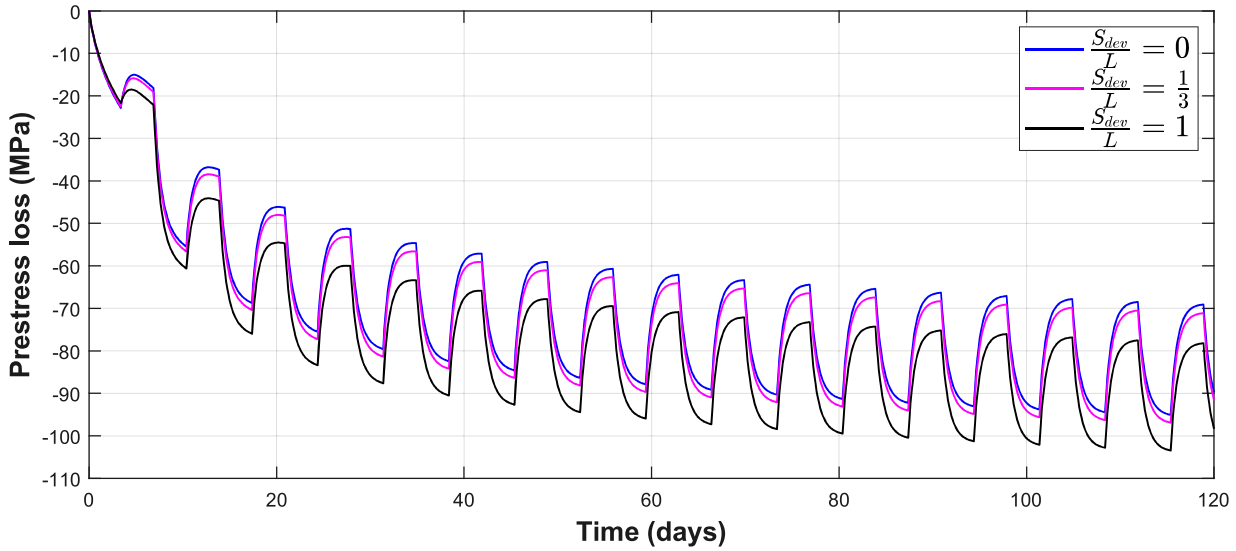
Likewise, from the obtained results for the midspan tendon eccentricity, it can be noticed that under the loading scenario of self-weight loads, the eccentricity for the eccentric profile is the only one having variations (16% increase). Under the combined loading scenario, the eccentric profile presents the highest variations (12% reduction) whereas the draped profile with the ratio value of $S_{dev}/L = 1/3$ has a minor variation. As in the previous case of the deflections, the environmental conditions have negligible effects on the overall eccentricity variations. In the case of the prestress losses, it can be highlighted that under the self-wight loading scenario an average reduction of about 6.9% of the prestress force is experienced whereas for the combined scenario a reduction of about 5.4% can be induced.



(a)

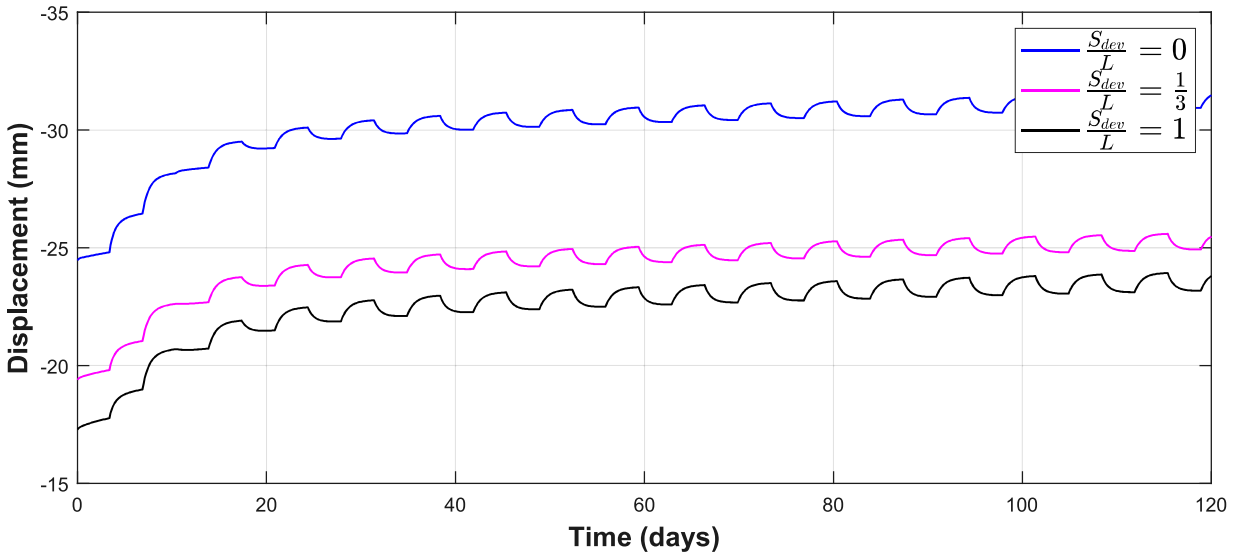


(b)

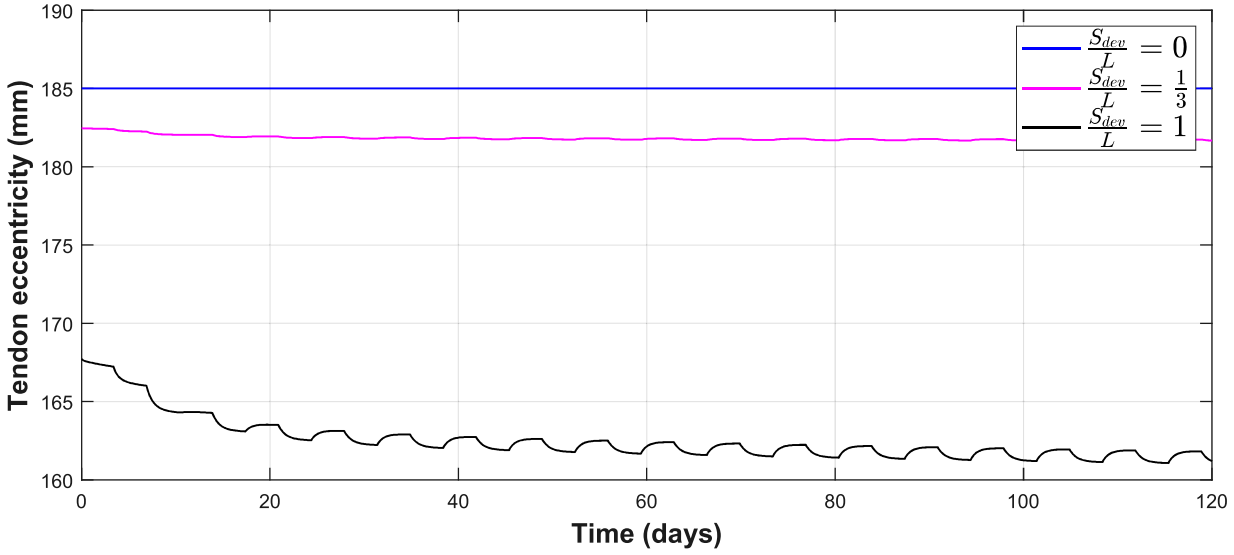


(c)

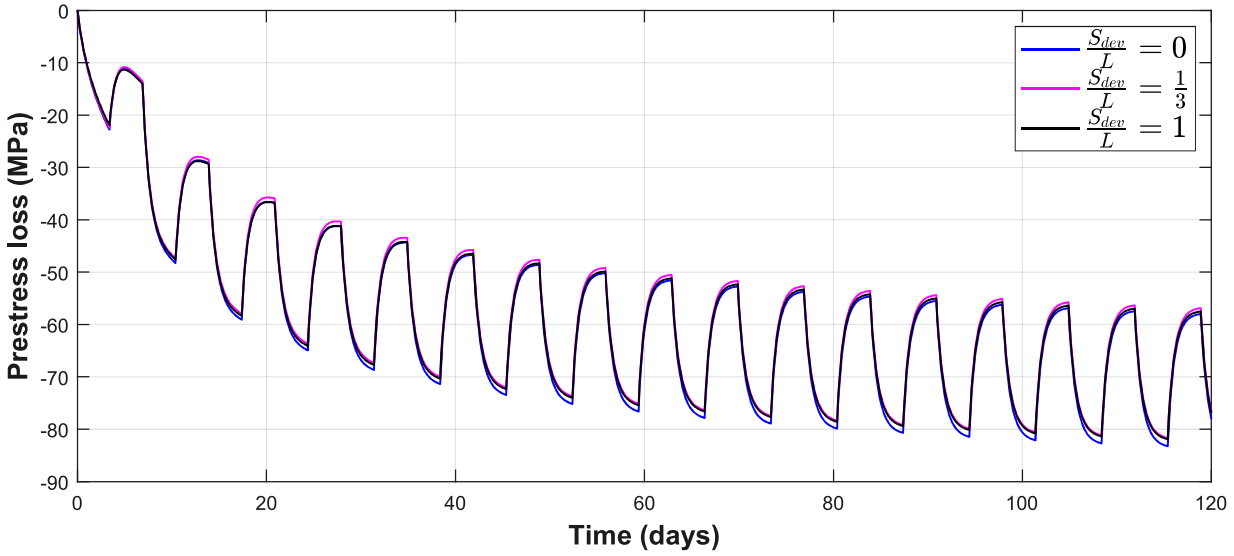
Figure 7.14: Time-dependent responses under self-weight load for weekly climatic variations.



(a)

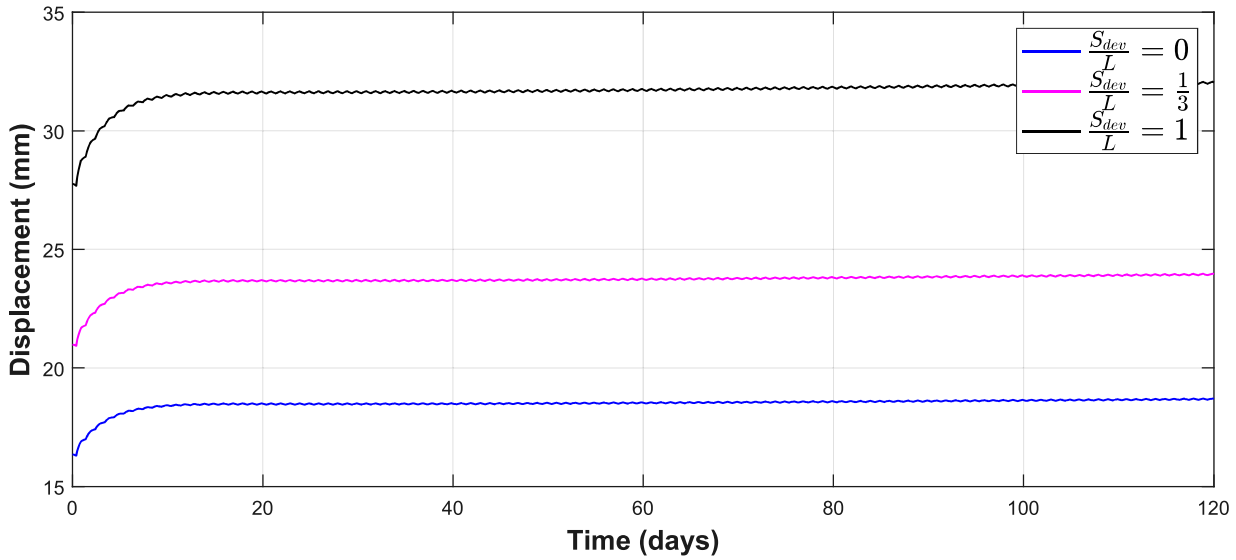


(b)

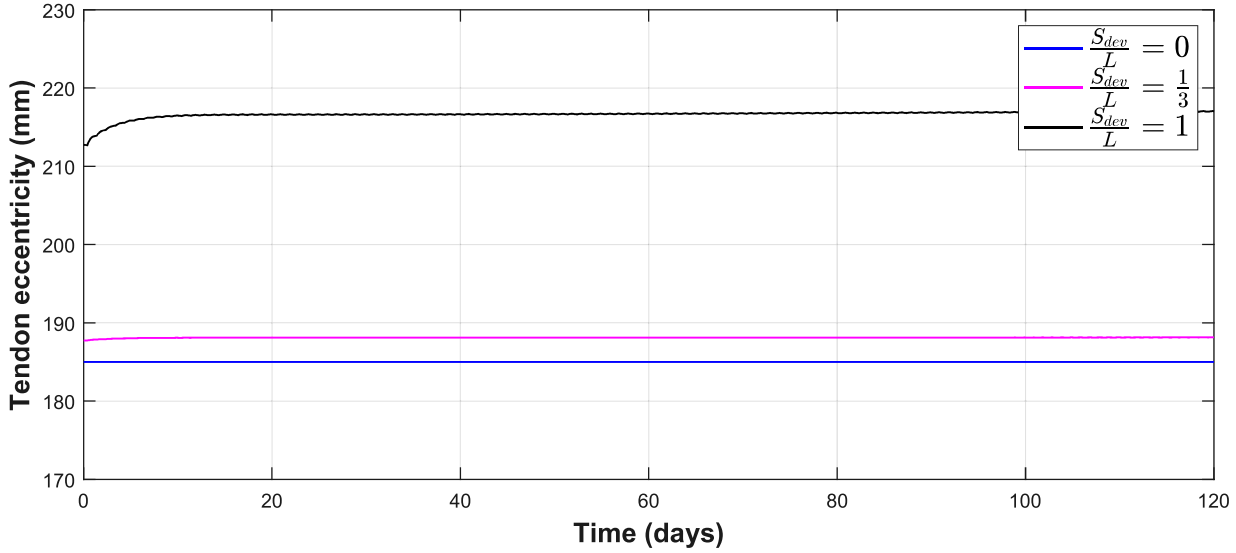


(c)

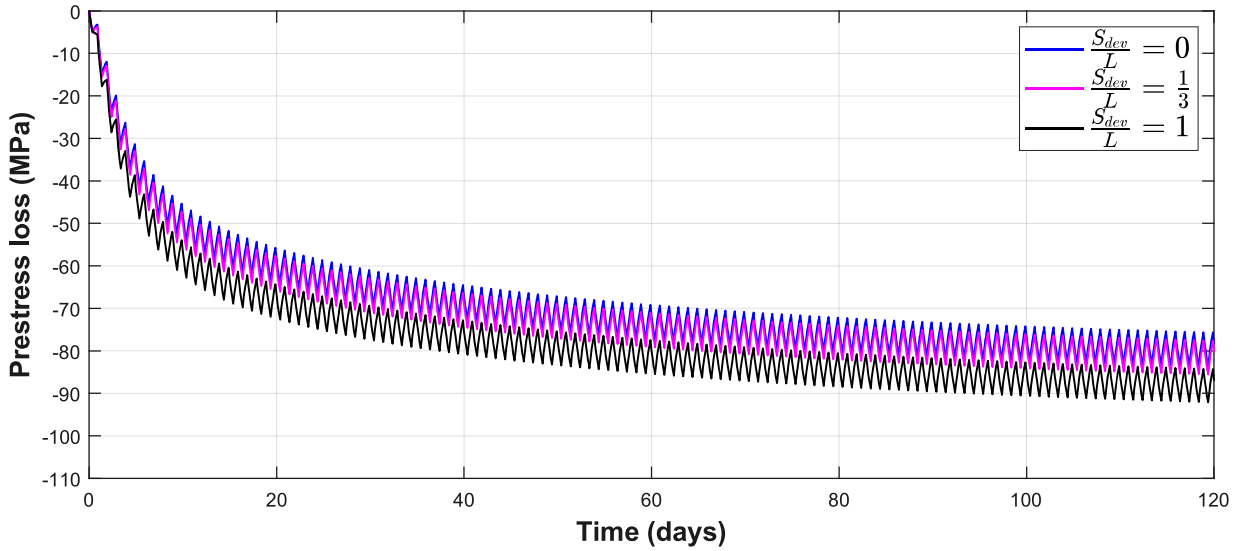
Figure 7.15: Time-dependent responses under self-weight and four-point bending loads for weekly climatic variations.



(a)

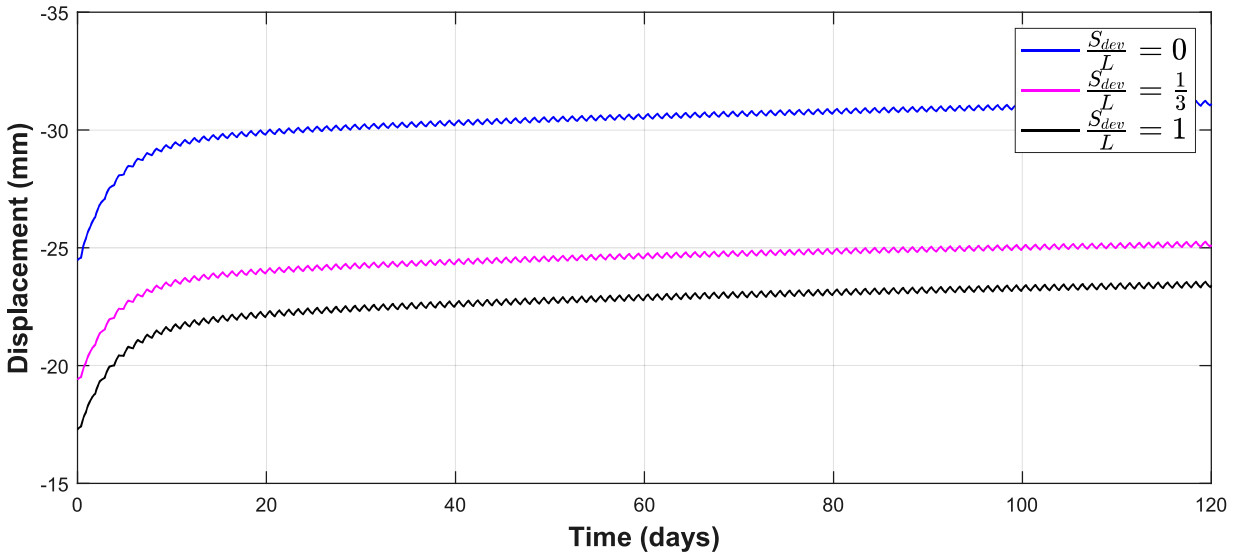


(b)

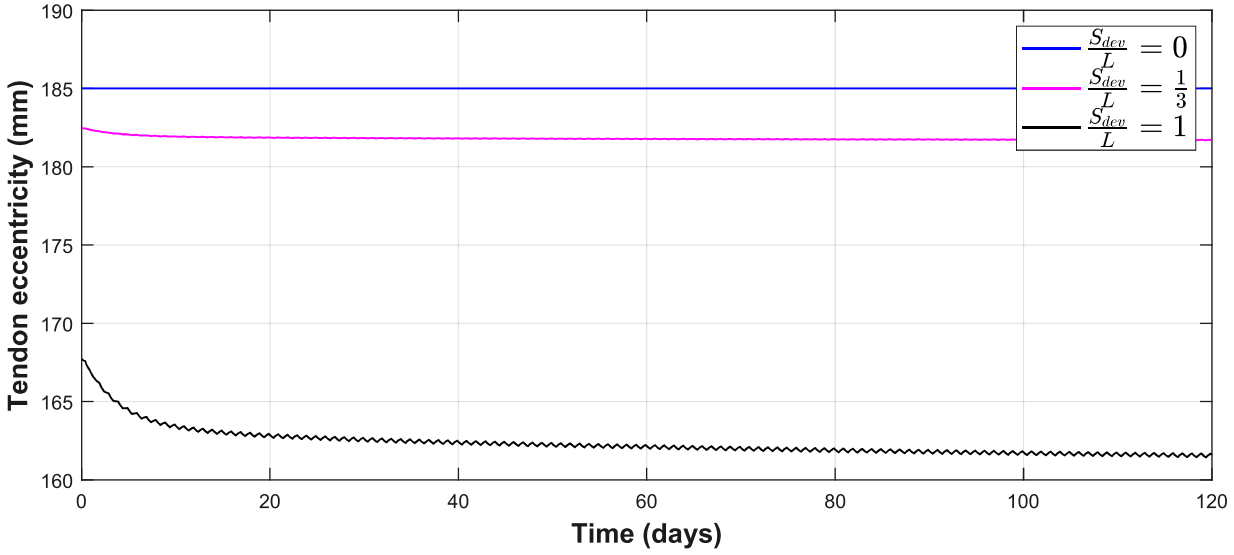


(c)

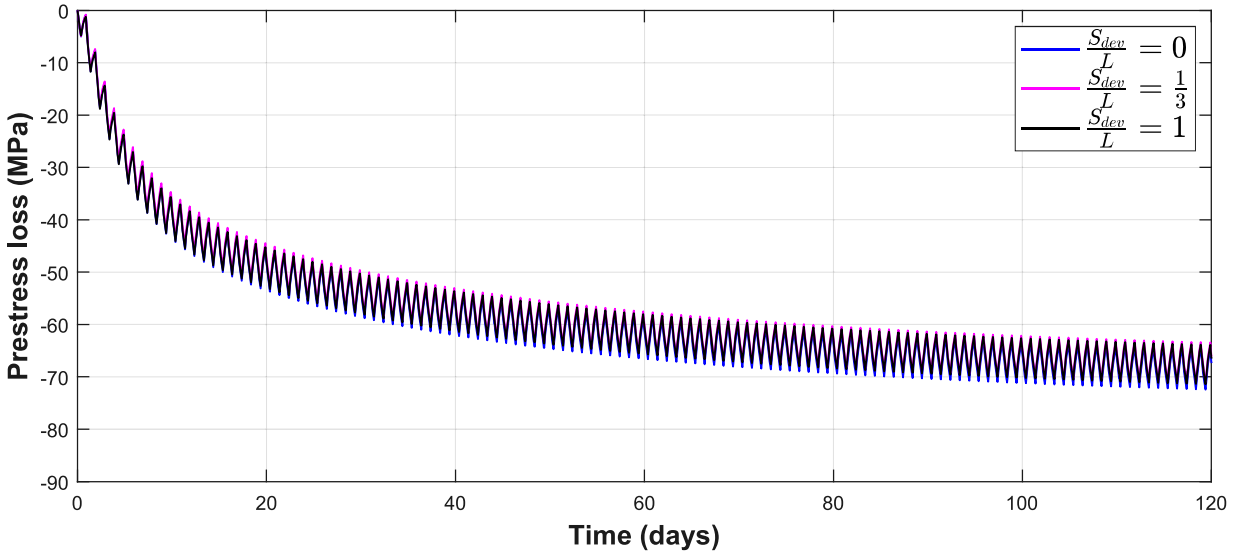
Figure 7.16: Time-dependent responses under self-weight load for daily climatic variations.



(a)



(b)



(c)

Figure 7.17: Time-dependent responses under self-weight and four-point bending loads for daily climatic variations.

7.3 Concluding Remarks

From the obtained results in the numerical case studies, it can be highlighted the following:

- The computational efficiency and numerical robustness of the modelling approach adopted in the numerical framework allows carrying out design-oriented parametric studies of unbonded post-tensioned members to assess the influence of specific parameters in the global and local responses. Intricate features such as material and geometric nonlinearities, the interaction between different time-dependent effects as well as unbonded behavior comprising strain incompatibility and eccentricity variation are taken into account in the parametric study giving a level of accuracy for the obtained results.

- The numerical robustness of beam-column elements with enhanced formulations enables the use of coarse meshes to assess local responses such as stresses and internal forces as well as global responses up to the failure of the post-tensioned member without compromising the accuracy of the results.

- The numerical results indicate that the shear deformations have a negligible effect on the ultimate load capacity of the reference post-tensioned beam. Nevertheless, higher ultimate midspan deflections and eccentricity variations were induced.

- The obtained results related to the short-term response of the post-tensioned beam show that the optimum deviator position depends on the type of loading scenario considered.

- The time-dependent results indicate that higher variations on the midspan displacements depends on the loading scenario applied on the hosting member and the tendon profile. In this specific analysis case, the eccentric profile induces the higher displacements under self-weight loads whereas the draped profile with one deviator at the midspan produces the larger displacements for the loading scenario in which the self-weight and four-point loads are applied at the same time.

Chapter 8

Conclusions and Recommendations for Future Research

This chapter summarizes the main conclusions of the thesis. Additionally, from the contributions made in this thesis, new areas of research have been found and are also discussed below.

8.1 Conclusions

This thesis deals with the numerical simulation of the nonlinear response of post-tensioned timber elements under under short- and long-term loads. A modelling approach is proposed and implemented to predict the short-term ultimate-load and long-term service-load behaviour of post-tensioned timber beams with different tendon profiles. Important features of the response of post-tensioned structures such as strain incompatibility, tendon eccentricity variation, material inelasticity, time-dependent effects and large displacements are all well incorporated. To address the particular behaviour of post-tensioned timber members, shear deformations are included in the formulation of the hosting member and a moisture diffusion analysis is coupled with finite element (FE) framework to simulate the intrinsic wood's hygroscopic behavior. In the proposed modelling approach, the hosting members were simulated using one-dimensional beam-column elements. These elements considered a fibre-based approach along with a corotational formulation to capture the material inelasticity and time-dependent behaviour as well as the undergone large displacements of the hosting member, respectively. Moreover, besides beam-column elements with traditional displacement-based formulations, enhanced-strain formulations were also incorporated within the analysis framework. For the simulation of the

unbonded tendons, two formulations were developed in this thesis by assuming a frictionless slipping behaviour. One formulation consists in an improved version of a constantly updated equivalent load scheme whereas the other involves the consistent derivation of a tangent stiffness matrix for the tendon element. To solve the resulting nonlinear FE equations, traditional Newton–Raphson methods along with more robust numerical solvers were implemented. The proposed modelling approach was extensively validated throughout the thesis after performing several simulations. From the obtained results, the following conclusions can be offered:

- The proposed numerical framework comprising one-dimensional beam-column elements along with sliding tendon element formulations incorporating large displacement effects is capable of capturing the intrinsic and intricate features of post-tensioned structural systems such as strain incompatibility and tendon eccentricity variation. Moreover, including the hygroscopic, inelastic and time-dependent behavior of wood in the numerical framework constitutes a first step to develop a robust, versatile and computationally efficient novel modelling approach to assess the short- and long-term response of post-tensioned timber structures. The numerical robustness and versatility of this novel framework is attested by the accurate simulation of experimental data and benchmark numerical results of post-tensioned timber and reinforced concrete beam specimens having different tendons layouts such as straight, draped and curve profiles. Likewise, the computational efficiency of this framework in contrast to high-fidelity 3D FE models is attested by the lower computation cost involved during the simulations allowing performing parametric finite element analysis for typical design purposes.

- The proposed tendon element formulations implemented in this thesis allowed the inclusion of a frictionless slipping behaviour in the interaction between the tendon and the deviators resulting in the avoidance of modelling rigid arms, multi-freedom constraints, and contact elements. This feature boosted the computational efficiency of the proposed numerical approach as numerical issues associated with these modelling techniques can be alleviated.

- As described in subsection 6.1.1, a novel modelling approach was developed to simulate the intricate behavior of unbonded tendons based on an equivalent load scheme previously developed and widely validated. The novelty of this modelling technique consist in the incorporation of a corotational description for the hosting member and the use of nodal basic rotations instead of nodal total rotations in the derivation of kinematic equations

describing the changing configuration of the unbonded tendons as shown in Eq. (6.1). This modification in considering basic rotations seems to be more suitable and consistent as small rotations assumptions are made in the formulation derivation. From the obtained results, it was demonstrated that these assumptions were capable of representing the response of post-tensioned beam-like structures at ultimate and service states and contributing to the numerical robustness and computational efficiency of the proposed FE model.

- The derived tangent stiffness matrix in subsection 6.1.2 for modelling unbonded tendons constitutes a novel finite element formulation based on the extension and generalization of a previously proposed tendon element formulation. In this development, a corotational description is used to describe the deformed configuration of the hosting member, the nodal rotations employed in the kinematic equations Eq. (6.11) describing the changing configuration of the unbonded tendons are not assumed as small throughout the finite element derivation and an initial inclination of the hosting elements is considered in the element formulation. The simulated results attested the capability of the proposed formulation to assess the short- and long-term response of post-tensioned members. The derived tendon formulation brings numerical robustness and computational efficiency into the proposed modelling approach.

- One-dimensional beam-column elements with traditional displacement-based formulations are capable of capturing the global responses of timber beams and post-tensioned timber beams with an accuracy comparable to the results obtained with nonlinear continuum based FE models as attested in section 4.4 and section 6.4. However, if local responses such as stress resultants and strains need to be assessed, fine FE meshes could be required to obtain accurate results implying higher computational demands. To overcome this, elements with enhanced-strain formulation were also incorporated. The adoption of enhanced beam element formulations constitutes a novel feature among the development of modelling approaches for simulating the short- and long-term response of post-tensioned structural systems. The simulated results demonstrated that elements with enhanced formulations, even with coarse FE meshes, are capable of accurately assessing local responses as satisfaction of equilibrium is enforced. These features translates into more computational efficiency and accurate predictions well suited for structural performance assessments. Nevertheless, it is worth mentioning that this efficiency is lost when relative fine FE meshes are used.

- Timoshenko beam column elements including elastic shear deformations were also incorporated in the developed numerical framework. Herein, bubble or nodeless degrees of freedom were used to formulate a consistent-free-shear locking element. To incorporate a beam-column element that undergoes large displacements and includes shear deformations, an explicit geometric stiffness matrix was derived in this thesis for this element by adopting a corotational approach. The incorporation of consistent-free-shear locking beam elements including large displacements into the development of modelling approaches for simulating post-tensioned structures constitutes a novel attribute into the field. The numerical results in section 4.4 and section 6.4 attested the capabilities of this beam-column element to include the above-mentioned features.

- By comparing the results from both proposed tendon formulations, it can be observed that very similar or almost identical numerically simulated responses are obtained. However, from the computational point of view, the formulation presented in subsection 6.1.2 tend to be more efficient as less lines of code are implemented. Moreover, if beam-column elements with enhanced-strain formulations are combined with this last tendon formulation in building a coarse FE mesh, greater computational efficiency can be achieved as only one tendon segment is required to span the hosting member between consecutive deviators.

- The use of phenomenological material constitutive laws, defined by unsmooth force-deformation relationships, in the implemented framework led to convergence issues during the numerical analysis carried throughout this thesis. Therefore, it was needed the implementation of robust nonlinear solvers such as the Krylov subspace accelerated algorithm, two-level consistent quasi Newton algorithm and Lyapunov-based nonlinear algorithm, to track the whole nonlinear response. However, as the traditional full Newton–Raphson method tend to attain fast convergence, an adaptive solution strategy was adopted to carry out the numerical simulations. This implemented strategy consisted in using the aforementioned nonlinear solvers when convergence issues arise. Once this critical equilibrium point is determined, the solution algorithm returns to use the traditional Newton–Raphson method. In this way, the computational performance of the implemented framework is enhanced.

- As shown in chapter 7, the computational efficiency and versatility of the proposed modelling approach allows carrying out design-oriented parametric studies of post-tensioned

timber members to investigate the influence of specific parameters on the global and local responses.

- A robust and efficient numerical procedure to assess the equilibrium state after the prestress transfer, involving a final stress value in the tendon, has been employed. This methods works well if the tangent stiffness matrix of the tendon is derived as the case presented in subsection 6.1.2. In this case, a traditional Newton-Raphson algorithm can be employed to solve the equations. However, if the tendon formulation does not involve the assessment of an explicit tangent stiffness matrix as the equivalent load scheme presented in subsection 6.1.1, the tangent matrix of the coupled system in Eq. (6.49) can not be directly assessed. As a result, quasi-Newton methods are proposed in this thesis as a numerical strategy to assess the tangent matrix of the system. Moreover, an initial guess of this tangent matrix is also proposed to start the quasi-Newton algorithms. The adoption of this numerical strategy represents a new form of accurately evaluating the equilibrium state after the prestress transfer in post-tensioned structures. From the comparisons and numerical analysis carried out, it was attested that the solution of Eq. (6.49) using Newton-Raphson or quasi-Newton algorithms are almost identical.

- The proposed modelling approach is capable of taking into account the interaction between different time-dependent effects as shown in subsection 6.4.4 and section 7.2. Furthermore, the robustness of the implemented framework has been extended by coupling the finite element framework with a finite difference code (OpenMoist) considering the wood's hygroscopic behavior and modelling the relaxation effects in the prestressing steel. As a result, a more accurate prediction of the long-term response of post-tensioned timber members under different environmental conditions and tendon layouts can be attained. However, it is worth mentioning that the accuracy of the modelling approach depends on the adopted constitutive models and the parameters defining them. The incorporation of the hygroscopic behavior of wood and relaxation phenomenon in prestressing steels constitutes a novel attribute in the proposed modelling approach for assessing the long-term response of post-tensioned timber structures.

- A finite difference code was implemented to solve the transient non-linear moisture diffusion analysis as moisture-dependent diffusion and surface emissivity coefficients were adopted. In the derivation of the finite different equations, variable grid sizes were considered. This feature of the implemented code allowed an accurate discretization of rectangular hollow sections with different web and flange dimensions.

- The versatility of the current numerical framework have been extended to a greater extend as a compartmentalisation strategy have been adopted in the development of the framework. This feature will ease the incorporation of new beam-column elements, tendon formulations, constitutive models and nonlinear equation solvers. This feature also facilitates carrying out analyses under variable loading scenarios.

8.2 Suggestions for Future Work

The capabilities of the proposed modelling approach to assess the response of post-tensioned timber elements under short-term ultimate and long-term service loads has been thoroughly validated in this thesis. This constitutes a first step towards a robust and cost-effective FE modelling of post-tensioned timber structures. however, to achieve this goal further research need to performed in the following areas:

- All the analysis presented in this thesis have adopted phenomenological uniaxial constitutive laws to represent the crushing and fracture behavior of timber under compression and tension solicitations, respectively. Although the adoption of these laws allowed an accurate estimation of the ultimate global responses, the adoption of more sophisticated constitutive models comprising multiaxial stress states would allow the inclusion of shear effects in the assessment of the load carrying capacity of post-tensioned timber elements. Therefore, a wider variety of post-tensioned beam-column structural component configurations can be analysed with the current numerical framework.

- In case of modelling post-tensioned timber beams in composite floors or bridge decks, interfacial slip effects need to be carefully considered to simulate the deformable composite action. The type of mechanical connection employed in composite timber beams influences the shear interaction between the layers. Therefore, to simulate the response of these post-tensioned timber structures in the current numerical framework, shear-slip constitutive relationships in conjunction with beam-column elements incorporating an interlayer slip should be added.

- One limitation of the current modelling approach, is the no incorporation of interface elements to model the decompression and gap opening taking place in contact surfaces. The implementation of this type of elements will allow the modelling of self-centering beam-column connections in post-tensioned timber-framed buildings with seismic rocking

mechanisms and joint discontinuities in post-tensioned segmental bridges. This addition will extent the versatility of the analysis framework and its applicability.

- In this thesis, only one well-known uniaxial constitutive model was used to simulate wood's rheological behavior. However, the extent of this model in capturing all the involved time-dependent effects is limited. Moreover, from experimental campaigns, it was observed that shear effects could present higher rates of deformation. Therefore, more comprehensive constitutive models need to be considered.

- The transport of water in wood consist in a complex coupled process that for the sake of simplicity was modelled in this thesis by adopting a single Fickian diffusion equation to describe the whole process. Nevertheless, multi-Fickian diffusion models seems to be more appropriate as it describe the diffusion of water vapour and bound water in a coupled process. The current finite difference framework could be extended to solve the coupled differential equations defining the multi-Fickian models.

- In this thesis, only numerical studies were carried out to show the capability of the proposed framework to assess the long-term response of post-tensioned timber members. For this reason, it is encouraged to validate the numerical framework against experimental data recorded on post-tensioned timber specimens to attest in a more comprehensive way the capabilities and limitations of the implemented framework.

- The numerical analyses performed to assess the long-term response of post-tensioned timber members only considered limited time intervals of analysis. With the aim of having a better understanding of the service life of these post-tensioned structures, larger periods of analysis such as 50 years or more should be employed. In this way, a more accurate idea of the long-term deflections, post-tensioning force losses and reduced load-carrying capacity that these post-tensioned systems would experience at the end of their service life can be assessed.

Bibliography

[1] Stephen John, Barbara Nebel, Nicolas Perez, and AH Buchanan. Environmental impacts of multi-storey buildings using different construction materials. 2009.

[2] John W Van De Lindt. Evolution of wood shear wall testing, modeling, and reliability analysis: Bibliography. *Practice Periodical on Structural Design and Construction*, 9(1): 44–53, 2004.

[3] Annette M Harte. Mass timber–the emergence of a modern construction material. *Journal of Structural Integrity and Maintenance*, 2(3):121–132, 2017.

[4] Alessandro Palermo, Stefano Pampanin, A Buchanan, and M Newcombe. Seismic design of multi-storey buildings using laminated veneer lumber (lvl). 2005.

[5] Alessandro Palermo, Simona Giorgini, Pampanin Stefano, and Andrew H Buchanan. Potential of longitudinal post-tensioning for short-to-medium span timber bridges. *Structural engineering international*, 21(3):349–355, 2011.

[6] Bruno Dal Lago, Claudio Dibenedetto, Alessandro Palermo, Stefano Pampanin, Simona Giorgini, Andrew H Buchanan, and David Carradine. Structural behavior of longitudinally posttensioned timber beams under serviceability gravity loading. *Journal of Structural Engineering*, 143(8):04017071, 2017.

[7] Wouter van Beerschoten, Gabriele Granello, Alessandro Palermo, and David Carradine. Determining the flexural capacity of long-span post-tensioned lvl timber beams. *Journal of Structural Engineering*, 145(7):04019067, 2019.

[8] Hailey Quiquero, John Gales, Anthony Abu, and Rwayda Al Hamd. Finite element modelling of post-tensioned timber beams at ambient and fire conditions. *Fire Technology*, 56:737–767, 2020.

[9] EE Thybring, M Fredriksson, SL Zelinka, and SV Glass. Water in wood: a review of current understanding and knowledge gaps. forests 13: 2051, 2022.

[10] J Eitelberger, K Hofstetter, and Sergey V Dvinskikh. A multi-scale approach for simulation of transient moisture transport processes in wood below the fiber saturation point. *Composites Science and Technology*, 71(15):1727–1738, 2011.

[11] Franz FP Kollmann and Wilfred A Cote Jr. Principles of wood science and technology. vol. i. solid wood. In *Principles of Wood Science and Technology. Vol. I. Solid Wood*. 1968.

[12] Adolf Fick. Ueber diffusion. *Annalen der Physik*, 170(1):59–86, 1855.

[13] Kristian Krabbenhoft and Lars Damkilde. A model for non-fickian moisture transfer in wood. *Materials and structures*, 37:615–622, 2004.

[14] Stefania Fortino, Florian Mirianon, and Tomi Toratti. A 3d moisture-stress fem analysis for time dependent problems in timber structures. *Mechanics of time-dependent materials*, 13:333–356, 2009.

[15] Francesco Mirko Massaro and Kjell Arne Malo. Modelling the viscoelastic mechanosorptive behaviour of norway spruce under long-term compression perpendicular to the grain. *Holzforschung*, 73(8):715–725, 2019.

[16] HZ Zhou, EC Zhu, Stefania Fortino, and Tomi Toratti. Modelling the hygrothermal stress in curved glulam beams. *The Journal of Strain Analysis for Engineering Design*, 45(2): 129–140, 2010.

[17] Tu T Nguyen, Thang N Dao, Sriram Aaleti, Kobir Hossain, and Kenneth J Fridley. Numerical model for creep behavior of axially loaded clt panels. *Journal of Structural Engineering*, 145(1):04018224, 2019.

[18] Susanne Saft and Michael Kaliske. Numerical simulation of the ductile failure of mechanically and moisture loaded wooden structures. *Computers & structures*, 89(23-24): 2460–2470, 2011.

[19] Susanne Reichel and Michael Kaliske. Hygro-mechanically coupled modelling of creep in wooden structures, part ii: influence of moisture content. *International Journal of Solids and Structures*, 77:45–64, 2015.

[20] Mohammad Masoud Hassani, Falk K Wittel, Stefan Hering, and Hans J Herrmann. Rheological model for wood. *Computer Methods in Applied Mechanics and Engineering*, 283: 1032–1060, 2015.

[21] Thomas Gereke, Per Johan Gustafsson, Kent Persson, and Peter Niemz. Experimental and numerical determination of the hygroscopic warping of cross-laminated solid wood panels. 2009.

[22] Thomas Gereke, Philipp Hass, and Peter Niemz. Moisture-induced stresses and distortions in spruce cross-laminates and composite laminates. 2010.

[23] Thomas Gereke and Peter Niemz. Moisture-induced stresses in spruce cross-laminates. *Engineering Structures*, 32(2):600–606, 2010.

[24] Massimo Fragiacomo, Stefania Fortino, Davide Tononi, Irene Usardi, and Tomi Toratti. Moisture-induced stresses perpendicular to grain in cross-sections of timber members exposed to different climates. *Engineering Structures*, 33(11):3071–3078, 2011.

[25] Vanessa Angst and Kjell A Malo. Moisture induced stresses perpendicular to the grain in glulam: review and evaluation of the relative importance of models and parameters. 2010.

[26] Vanessa Angst and Kjell Arne Malo. Moisture-induced stresses in glulam cross sections during wetting exposures. *Wood science and technology*, 47:227–241, 2013.

[27] Bettina Franke, Steffen Franke, Marcus Schiere, and Andreas Müller. Moisture content and moisture-induced stresses of large glulam members: laboratory tests, in-situ measurements and modelling. *Wood Material Science & Engineering*, 2018.

[28] Nima Khorsandnia, Jörg Schänzlin, Hamid Valipour, and Keith Crews. Coupled finite element-finite difference formulation for long-term analysis of timber–concrete composite structures. *Engineering Structures*, 96:139–152, 2015.

[29] Sigurdur Ormarsson and Óskar V Gíslason. Moisture-induced stresses in glulam frames. *European Journal of Wood and Wood Products*, 74:307–318, 2016.

[30] Gabriele Granello, Claude Leyder, Andrea Frangi, Alessandro Palermo, and Eleni Chatzi. Long-term performance assessment of an operative post-tensioned timber frame structure. *Journal of Structural Engineering*, 145(5):04019034, 2019.

[31] Henrik Lund Frandsen, Lars Damkilde, and Staffan Svensson. A revised multi-fickian moisture transport model to describe non-fickian effects in wood. 2007.

[32] Johannes Eitelberger, Staffan Svensson, and Karin Hofstetter. Theory of transport processes in wood below the fiber saturation point. physical background on the microscale and its macroscopic description. 2011.

[33] Staffan Svensson, Goran Turk, and Tomaz Hozjan. Predicting moisture state of timber members in a continuously varying climate. *Engineering Structures*, 33(11):3064–3070, 2011.

[34] Stefania Fortino, Alessandra Genoese, Andrea Genoese, Lina Nunes, and Pedro Palma. Numerical modelling of the hygro-thermal response of timber bridges during their service life: A monitoring case-study. *Construction and Building Materials*, 47:1225–1234, 2013.

[35] Stefania Fortino, Petr Hradil, Andrea Genoese, Alessandra Genoese, and Anna Pousette. Numerical hygro-thermal analysis of coated wooden bridge members exposed to northern european climates. *Construction and Building Materials*, 208:492–505, 2019.

[36] Maximilian Autengruber, Markus Lukacevic, and Josef Füssl. Finite-element-based moisture transport model for wood including free water above the fiber saturation point. *International Journal of Heat and Mass Transfer*, 161:120228, 2020.

[37] Nima Khorsandnia and K Crews. Application of quasi-brittle material model for analysis of timber members. *Australian Journal of Structural Engineering*, 16(2):99–115, 2015.

[38] M Oudjene and M Khelifa. Finite element modelling of wooden structures at large deformations and brittle failure prediction. *Materials & Design*, 30(10):4081–4087, 2009.

[39] V Karagiannis, C Málaga-Chuquitaype, and AY Elghazouli. Modified foundation modelling of dowel embedment in glulam connections. *Construction and Building Materials*, 102:1168–1179, 2016.

[40] M Gharib, A Hassanieh, H Valipour, and MA Bradford. Three-dimensional constitutive modelling of arbitrarily orientated timber based on continuum damage mechanics. *Finite Elements in Analysis and Design*, 135:79–90, 2017.

[41] Lipeng Zhang, Qifang Xie, Baozhuang Zhang, Long Wang, and Jitao Yao. Three-dimensional elastic-plastic damage constitutive model of wood. *Holzforschung*, 75(6): 526–544, 2021.

[42] Luis Sirumbal Zapata. *Advanced damage modelling for seismic assessment of timber structures*. PhD thesis, Imperial College London, 2019.

[43] V Baño, F Arriaga, A Soilán, and M Guaita. Prediction of bending load capacity of timber beams using a finite element method simulation of knots and grain deviation. *Biosystems engineering*, 109(4):241–249, 2011.

[44] Vanessa Baño, Francisco Arriaga, and Manuel Guaita. Determination of the influence of size and position of knots on load capacity and stress distribution in timber beams of pinus sylvestris using finite element model. *Biosystems engineering*, 114(3):214–222, 2013.

[45] Khaled Saad and András Lengyel. Accurate finite element modelling of knots and related fibre deviations in structural timber. *Journal of King Saud University-Engineering Sciences*, 2022.

[46] ZW Guan and EC Zhu. Finite element modelling of anisotropic elasto-plastic timber composite beams with openings. *Engineering Structures*, 31(2):394–403, 2009.

[47] Nima Khorsandnia, Hamid R Valipour, and Keith Crews. Nonlinear finite element analysis of timber beams and joints using the layered approach and hypoelastic constitutive law. *Engineering Structures*, 46:606–614, 2013.

[48] Hamid Valipour, Nima Khorsandnia, Keith Crews, and S Foster. A simple strategy for constitutive modelling of timber. *Construction and Building Materials*, 53:138–148, 2014.

[49] Amir Karimi-Nobandegani and Hamid Valipour. Timber beams with openings: Laboratory testing and nonlocal finite element modelling. *Engineering structures*, 245:112867, 2021.

[50] Manoochehr Ardalany, Massimo Fragiacomo, and Peter Moss. Modeling of laminated veneer lumber beams with holes using cohesive elements. *Journal of Structural Engineering*, 142(1):04015102, 2016.

[51] Clemens Gebhardt and Michael Kaliske. An xfem-approach to model brittle failure of wood. *Engineering Structures*, 212:110236, 2020.

[52] Elzbieta Lukaszewska, Massimo Fragiacomo, and Helena Johnsson. Laboratory tests and numerical analyses of prefabricated timber-concrete composite floors. *Journal of structural engineering*, 136(1):46–55, 2010.

[53] Hamid R Valipour and Keith Crews. Efficient finite element modelling of timber beams strengthened with bonded fibre reinforced polymers. *Construction and Building Materials*, 25(8):3291–3300, 2011.

[54] P Glos. Zur modellierung des festigkeitsverhaltens von bauholz bei druck. *Zug-und Biegebeanspruchung, Munich, Germany*, 1981.

[55] Nima Khorsandnia, Hamid Valipour, Stephen Foster, and Keith Crews. A force-based frame finite element formulation for analysis of two-and three-layered composite beams with material non-linearity. *International Journal of Non-Linear Mechanics*, 62:12–22, 2014.

[56] Nima Khorsandnia, Hamid Valipour, and Keith Crews. Structural response of timber-concrete composite beams predicted by finite element models and manual calculations. *Advances in Structural Engineering*, 17(11):1601–1621, 2014.

[57] Nima Khorsandnia, Hamid Valipour, and Mark Bradford. Deconstructable timber-concrete composite beams with panelised slabs: Finite element analysis. *Construction and Building Materials*, 163:798–811, 2018.

[58] Haotian Tao, Huifeng Yang, Jin Zhang, Gaoyan Ju, Jiawei Xu, and Benkai Shi. Non-linear finite element analysis on timber-concrete composite beams. *Journal of Building Engineering*, 51:104259, 2022.

[59] Antti Hanhijärvi. Advances in the knowledge of the influence of moisture changes on the long-term mechanical performance of timber structures. *Materials and structures*, 33: 43–49, 2000.

[60] Annika Mårtensson. Mechano-sorptive effects in wooden material. *Wood Science and Technology*, 28(6):437–449, 1994.

[61] Henrik Lund Frandsen. Selected constitutive models for simulating the hygromechanical response of wood. 2007.

[62] RFS Hearmon and JM Paton. Moisture content changes and creep in wood. *Forest Products Journal*, 1964.

[63] Jörg Schänzlin. Modeling the long-term behavior of structural timber for typical serviceclass-ii-conditions in south-west germany. 2010.

[64] P Chassagne, E Bou Saïd, Jean-François Jullien, and P Galimard. Three dimensional creep model for wood under variable humidity-numerical analyses at different material scales. *Mechanics of Time-Dependent Materials*, 9:1–21, 2005.

[65] Rhodel Bengtsson, Mahmoud Mousavi, Reza Afshar, and E Kristofer Gamstedt. Viscoelastic behavior of softwood based on a multiscale computational homogenization. *Mechanics of Materials*, 179:104586, 2023.

[66] Torni Toratti. Modelling the creep of timber beams. *J. Struct. Mech*, 25:12–15, 1992.

[67] Antti Hanhijärvi. Deformation properties of finnish spruce and pine wood in tangential and radial directions in association to high temperature drying part iv. modelling. *Holz als Roh-und Werkstoff*, 58:211–216, 2000.

[68] Staffan Svensson and Tomi Toratti. Mechanical response of wood perpendicular to grain when subjected to changes of humidity. *Wood Science and Technology*, 36(2):145–156, 2002.

[69] Antti Hanhijärvi. Deformation kinetics based rheological model for the time-dependent and moisture induced deformation of wood. *Wood Science and Technology*, 29(3):191–199, 1995.

[70] Elias Bou Said. *Contribution à la modélisation des effets différés du bois et du béton sous conditions climatiques variables: application aux structures mixtes bois-béton.* PhD thesis, Lyon, INSA, 2003.

[71] Antti Hanhijärvi and Peter Mackenzie-Helnwein. Computational analysis of quality reduction during drying of lumber due to irrecoverable deformation. i: Orthotropic viscoelastic-mechanosorptive-plastic material model for the transverse plane of wood. *Journal of Engineering Mechanics*, 129(9):996–1005, 2003.

[72] Emmanuelle Vidal-Sallé and Pierre Chassagne. Constitutive equations for orthotropic nonlinear viscoelastic behaviour using a generalized maxwell model application to wood material. *Mechanics of Time-Dependent Materials*, 11:127–142, 2007.

[73] Taoyi Yu, Ani Khaloian, and Jan-Willem Van De Kuilen. An improved model for the time-dependent material response of wood under mechanical loading and varying humidity conditions. *Engineering Structures*, 259:114116, 2022.

[74] Sabina Huč, Staffan Svensson, and Tomaž Hozjan. Hygro-mechanical analysis of wood subjected to constant mechanical load and varying relative humidity. *Holzforschung*, 72 (10):863–870, 2018.

[75] Kari Santaoja, Tapio Leino, Alpo Ranta-Maunus, and Antti Hanhijärvi. *Mechano-sorptive structural analysis of wood by the ABAQUS finite element program*. VTT Technical Research Centre of Finland, 1991.

[76] Alpo Ranta-Maunus et al. Impact of mechano-sorptive creep to the long-term strength of timber. *Holz als Roh-und Werkstoff*, 48(2):67–71, 1990.

[77] Sigurdur Ormarsson, Ola Dahlblom, and Hans Petersson. A numerical study of the shape stability of sawn timber subjected to moisture variation part 2: Simulation of drying board. *Wood Science and Technology*, 33(5):407–423, 1999.

[78] Sara Florisson, Johan Vessby, and Sigurdur Ormarsson. A three-dimensional numerical analysis of moisture flow in wood and of the wood's hygro-mechanical and visco-elastic behaviour. *Wood Science and Technology*, 55:1269–1304, 2021.

[79] J-G Salin. Numerical prediction of checking during timber drying and a new mechano-sorptive creep model. *Holz als Roh-und Werkstoff*, 50(5):195–200, 1992.

[80] Stefania Fortino, Petr Hradil, and Giovanni Metelli. Moisture-induced stresses in large glulam beams. case study: Vihantasalmi bridge. *Wood Material Science & Engineering*, 14(5):366–380, 2019.

[81] M Yahyaei-Moayyed and F Taheri. Experimental and computational investigations into creep response of afrp reinforced timber beams. *Composite structures*, 93(2):616–628, 2011.

[82] Qingfeng Xu, Lingzhu Chen, Kent A Harries, Fuwen Zhang, Zhuolin Wang, and Xi Chen. Experimental study and numerical simulation of long-term behavior of timber beams strengthened with near surface mounted cfrp bars. *Materials and Structures*, 50:1–13, 2017.

[83] Conan O'Ceallaigh, Karol Sikora, Daniel McPolin, and Annette M Harte. Modelling the hygro-mechanical creep behaviour of frp reinforced timber elements. *Construction and Building Materials*, 259:119899, 2020.

[84] Massimo Fragiacomo, Jeno Balogh, Lam To, and Richard M Gutkowski. Three-dimensional modeling of long-term structural behavior of wood-concrete composite beams. *Journal of Structural Engineering*, 140(8):A4014006, 2014.

[85] Yatong Nie. *Short-and long-term performance of timber-timber composite (TTC) system*. PhD thesis, UNSW Sydney, 2021.

[86] Massimo Fragiacomo. A finite element model for long-term analysis of timber-concrete composite beams. *Structural engineering and mechanics: An international journal*, 20 (2):173–189, 2005.

[87] Massimo Fragiacomo and Ario Ceccotti. Long-term behavior of timber–concrete composite beams. i: Finite element modeling and validation. *Journal of structural engineering*, 132(1):13–22, 2006.

[88] Massimo Fragiacomo. Long-term behavior of timber–concrete composite beams. ii: Numerical analysis and simplified evaluation. *Journal of Structural Engineering*, 132(1): 23–33, 2006.

[89] M Fragiacomo, RM Gutkowski, J Balogh, and RS Fast. Long-term behavior of wood-concrete composite floor/deck systems with shear key connection detail. *Journal of Structural Engineering*, 133(9):1307–1315, 2007.

[90] Massimo Fragiacomo. Experimental behaviour of a full-scale timber-concrete composite floor with mechanical connectors. *Materials and Structures*, 45:1717–1735, 2012.

[91] M Fragiacomo and E Lukaszewska. Time-dependent behaviour of timber–concrete composite floors with prefabricated concrete slabs. *Engineering Structures*, 52:687–696, 2013.

[92] Massimo Fragiacomo and Elzbieta Lukaszewska. Influence of the construction method on the long-term behavior of timber-concrete composite beams. *Journal of Structural Engineering*, 141(10):04015013, 2015.

[93] Nima Khorsandnia, Jörg Schänzlin, Hamid Valipour, and Keith Crews. Time-dependent behaviour of timber–concrete composite members: Numerical verification, sensitivity and influence of material properties. *Construction and Building Materials*, 66:192–208, 2014.

[94] AA Chiniforush, HR Valipour, and A Akbarnezhad. Long-term coupled analysis of steel-timber composite (stc) beams. *Construction and Building Materials*, 278:122348, 2021.

[95] Sigurdur Ormarsson and Ola Dahlblom. Finite element modelling of moisture related and visco-elastic deformations in inhomogeneous timber beams. *Engineering structures*, 49:182–189, 2013.

[96] B Bohannan. Prestressing wood members. *FPJ*, 12(12):596–603, 1962.

[97] G Lantos. Reinforced and post-tensioned glue laminated beams under development at trada laboratories. *Civil Engineering (London)*, 59(690):86–87, 1964.

[98] D Bond and EH Sidwell. Prestressed timber beams. *Civ. Eng.(London)*, 60(705):547–550, 1965.

[99] Raymond J Taylor and P Csagoly. *Transverse post-tensioning of longitudinally laminated timber bridge decks*. Number 665. 1978.

[100] MG Oliva and A Dimakis. Behavior of stress-laminated timber highway bridge. *Journal of Structural Engineering*, 114(8):1850–1869, 1988.

[101] Bruce L Deam, Massimo Fragiacomo, and L Shane Gross. Experimental behavior of prestressed lvl-concrete composite beams. *Journal of Structural Engineering*, 134(5):801–809, 2008.

[102] E McConnell, D McPolin, and S Taylor. Post-tensioning of glulam timber with steel tendons. *Construction and Building Materials*, 73:426–433, 2014.

[103] Emma McConnell, Daniel McPolin, and Su Taylor. Post-tensioning glulam timber beams with basalt frp tendons. *Proceedings of the Institution of Civil Engineers-Construction Materials*, 168(5):232–240, 2015.

[104] Hanan Al-Hayek and Dagmar Svecova. Flexural strength of posttensioned timber beams. *Journal of Composites for Construction*, 18(2):04013036, 2013.

[105] João H Negrão. Preliminary study on wire prestressing methods for timber pieces reinforcement. *Construction and Building Materials*, 102:1093–1100, 2016.

[106] Antonino D'Aveni and Giuseppe D'Agata. Post-tensioned timber structures: new perspectives. *Construction and Building Materials*, 153:216–224, 2017.

[107] Mingfei Li, Mingtao Wu, Nan Guo, Lidan Mei, and Yan Zhao. Analysis of four types of anchorage devices for prestressed glulam beam and experimental research. *Materials*, 14 (21):6494, 2021.

[108] Dolores Otero-Chans, Javier Estévez-Cimadevila, Emilio Martín-Gutiérrez, and Juan Pérez-Valcárcel. Application of a new system of self-tensioning to the design of large-span wood floor framings. *Journal of Structural Engineering*, 142(6):04016012, 2016.

[109] Milad Bazli, Michael Heitzmann, and Hamed Ashrafi. Long-span timber flooring systems: A systematic review from structural performance and design considerations to constructability and sustainability aspects. *Journal of Building Engineering*, 48:103981, 2022.

[110] A Buchanan, A Palermo, D Carradine, and S Pampanin. Post-tensioned timber frame buildings. *The Structural Engineer*, 89(17):24–30, 2011.

[111] Flavio Wanninger and Andrea Frangi. Experimental and analytical analysis of a post-tensioned timber connection under gravity loads. *Engineering structures*, 70:117–129, 2014.

[112] Wouter A van Beerschoten, Alessandro Palermo, and David Carradine. Experimental testing of posttensioned timber frames under gravity loading. *Journal of Structural Engineering*, 141(9):04014210, 2015.

[113] Alessandro Palermo, Stefano Pampanin, David Carradine, Andrew H Buchanan, BRUNO ALBERTO DAL LAGO, Claudio Dibenedetto, Simona Giorgini, Paola Ronca, et al. Enhanced performance of longitudinally post-tensioned long-span lvl beams. In *11th World Conference on Timber Engineering 2010*, pages 1–10, 2010.

[114] Wouter Adrian Van Beerschoten. Structural performance of post-tensioned timber frames under gravity loading. 2013.

[115] Flavio Wanninger. Post-tensioned timber frame structures. *IBK Bericht*, 364, 2015.

[116] Billy Bohannan. Time-dependent characteristics of prestressed wood beams. 1974.

[117] Raymond J Taylor. Prestressed wood bridges. Technical report, 1983.

[118] Matthew Davies and Massimo Fragiacomo. Long-term behavior of prestressed lvl members. i: Experimental tests. *Journal of Structural Engineering*, 137(12):1553–1561, 2011.

[119] Flavio Wanninger, Andrea Frangi, and Massimo Fragiacomo. Long-term behavior of posttensioned timber connections. *Journal of Structural Engineering*, 141(6):04014155, 2015.

[120] Tobias Smith, Felice C Ponzo, Antonio Di Cesare, Stefano Pampanin, David Carradine, Andrew H Buchanan, and Domenico Nigro. Post-tensioned glulam beam-column joints with advanced damping systems: Testing and numerical analysis. *Journal of Earthquake Engineering*, 18(1):147–167, 2014.

[121] Gabriele Granello, Simona Giorgini, Alessandro Palermo, David Carradine, Stefano Pampanin, and Robert Finch. Long-term behavior of lvl posttensioned timber beams. *Journal of Structural Engineering*, 143(12):04017158, 2017.

[122] Gabriele Granello and Alessandro Palermo. Monitoring dynamic properties of a pres-lam structure: Trimble navigation office. *Journal of Performance of Constructed Facilities*, 34(1):04019087, 2020.

[123] Antonio Di Cesare, Felice Carlo Ponzo, Domenico Nigro, Stefano Pampanin, and Tobias Smith. Shaking table testing of post-tensioned timber frame building with passive energy dissipation systems. *Bulletin of Earthquake Engineering*, 15:4475–4498, 2017.

[124] A Di Cesare, FC Ponzo, N Lamarucciola, and D Nigro. Experimental seismic post-tensioning performance and long-term effects of a post-tensioned timber framed model with dissipative systems.

[125] Zheng Li, Xiuzhi Zheng, Minjuan He, Yongliang Sun, and Guirong He. Experimental and analytical investigations into the time-dependent performance in post-tensioned timber beam-column joints under sustained loads and varied environment. *Construction and Building Materials*, 251:118943, 2020.

[126] Xiuzhi Zheng, Minjuan He, Frank Lam, Xiaofeng Sun, Feng Liang, and Zheng Li. Experimental and numerical investigation of long-term loss of prestressing force in posttensioned timber joints with different structural details. *Journal of Structural Engineering*, 148(9): 04022124, 2022.

[127] Massimo Fragiacomo and Matthew Davies. Long-term behavior of prestressed lvl members. ii: Analytical approach. *Journal of Structural Engineering*, 137(12):1562–1572, 2011.

[128] S Giorgini, A Neale, A Palermo, D Carradine, S Pampanin, and A Buchanan. Predicting time dependent effects in unbonded post-tensioned timber beams and frames. In *Proc., CIB-W18 Conf*, number 43-7, page 7, 2010.

[129] Gabriele Granello, Claude Leyder, Alessandro Palermo, Andrea Frangi, and Stefano Pampanin. Design approach to predict post-tensioning losses in post-tensioned timber frames. *Journal of Structural Engineering*, 144(8):04018115, 2018.

[130] G Granello, S Giorgini, A Palermo, and S Pampanin. Post-tensioned lvl beams: Experimental results and numerical modelling. In *Proc., World Conf. on Timber Engineering*, 2016.

[131] Xiuzhi Zheng, Frank Lam, Zheng Li, and Minjuan He. Long-term performance assessment of post-tensioned timber connections under different climates. *Construction and Building Materials*, 368:130360, 2023.

[132] Carlos Melchor and Christian Málaga. Openmoist: A python code for transient moisture transfer analysis. *SoftwareX*, 15:100712, 2021.

[133] Junuthula Narasimha Reddy and David K Gartling. *The finite element method in heat transfer and fluid dynamics*. CRC press, 2010.

[134] Jean-Michel Bergheau and Roland Fortunier. *Finite element simulation of heat transfer*. John Wiley & Sons, 2013.

[135] Suhas V.. Patankar. *Numerical heat transfer and fluid flow*. Hemisphere Publishing Corporation, 1980.

[136] Pradip Majumdar. *Computational methods for heat and mass transfer*. Taylor & Francis, 2005.

[137] Dassault Systemes. Abaqus/standard user's manual; version 6.8 (vols. i-iii). *Simulia Corp., Providence, RI, USA*, 2008.

[138] Zdeněk P Bažant. Thermodynamics of solidifying or melting viscoelastic material. *Journal of the Engineering Mechanics Division*, 105(6):933–952, 1979.

[139] Young-Jin Kang and Alexander C Scordelis. Nonlinear analysis of prestressed concrete frames. *Journal of the structural division*, 106(2):445–462, 1980.

[140] J Hellesland and A Scordelis. Analysis of rc bridge columns under imposed deformations. In *IABSE colloquium*, pages 545–559. Delft the Netherlands, 1981.

[141] Alex C Scordelis. Computer models for nonlinear analysis of reinforced and prestressed concrete structures. *PCI JOURNAL*, 29(6):116–135, 1984.

[142] Enrico Spacone, Filip C Filippou, and Fabio F Taucer. Fibre beam–column model for non-linear analysis of r/c frames: Part i. formulation. *Earthquake Engineering & Structural Dynamics*, 25(7):711–725, 1996.

[143] Ansgar Neuenhofer and Filip C Filippou. Evaluation of nonlinear frame finite-element models. *Journal of structural engineering*, 123(7):958–966, 1997.

[144] Enrico Spacone, Vincenzo Ciampi, and FC Filippou. Mixed formulation of nonlinear beam finite element. *Computers & structures*, 58(1):71–83, 1996.

[145] Marco Petrangeli and VINCENZO Ciampi. Equilibrium based iterative solutions for the non-linear beam problem. *International Journal for Numerical Methods in Engineering*, 40(3):423–437, 1997.

[146] Bulent N Alemdar and Donald W White. Displacement, flexibility, and mixed beam–column finite element formulations for distributed plasticity analysis. *Journal of structural engineering*, 131(12):1811–1819, 2005.

[147] Ioannis Koutromanos and Jeremy Bowers. Enhanced strain beam formulation resolving several issues of displacement-based elements for nonlinear analysis. *Journal of Engineering Mechanics*, 142(9):04016059, 2016.

[148] Danilo Tarquini, João P Almeida, and Katrin Beyer. Axially equilibrated displacement-based beam element for simulating the cyclic inelastic behaviour of rc members. *Earthquake Engineering & Structural Dynamics*, 46(9):1471–1492, 2017.

[149] Giulio Ranzo and Marco Petrangeli. A fibre finite beam element with section shear modelling for seismic analysis of rc structures. *Journal of earthquake engineering*, 2(03): 443–473, 1998.

[150] RL Taylor, FC Filippou, A Saritas, and F Auricchio. A mixed finite element method for beam and frame problems. *Computational mechanics*, 31:192–203, 2003.

[151] Filip C Filippou and A Saritas. A beam finite element for shear-critical rc beams. *ACI Special Publications*, 237:295, 2006.

[152] Alessandra Marini and Enrico Spacone. Analysis of reinforced concrete elements including shear effects. *ACI Structural Journal*, 103:645–655, 2006.

[153] Afsin Saritas and Filip C Filippou. Inelastic axial-flexure–shear coupling in a mixed formulation beam finite element. *International Journal of Non-Linear Mechanics*, 44(8): 913–922, 2009.

[154] V Jafari, SH Vahdani, and M Rahimian. Derivation of the consistent flexibility matrix for geometrically nonlinear timoshenko frame finite element. *Finite Elements in Analysis and Design*, 46(12):1077–1085, 2010.

[155] De-Cheng Feng, Gang Wu, and Chao-Lie Ning. A regularized force-based timoshenko fiber element including flexure-shear interaction for cyclic analysis of rc structures. *International Journal of Mechanical Sciences*, 160:59–74, 2019.

[156] De-Cheng Feng and Xiaodan Ren. Implicit gradient-enhanced force-based timoshenko fiber element formulation for reinforced concrete structures. *International Journal for Numerical Methods in Engineering*, 122(2):325–347, 2021.

[157] De-Cheng Feng, Xin Chen, Frank McKenna, and Ertugrul Taciroglu. Consistent nonlocal integral and gradient formulations for force-based timoshenko elements with material and geometric nonlinearities. *Journal of Structural Engineering*, 149(4):04023018, 2023.

[158] Denise Ferreira, Jesús Bairán, and Antonio Marí. Numerical simulation of shear-strengthened rc beams. *Engineering Structures*, 46:359–374, 2013.

[159] Thomas JR Hughes, Robert L Taylor, and Worsak Kanoknukulchai. A simple and efficient finite element for plate bending. *International Journal for Numerical Methods in Engineering*, 11(10):1529–1543, 1977.

[160] JPSCM Guedes, P Pegon, and AV Pinto. A fibre timoshenko beam element in castem 2000. *special publication Nr. I*, 94:55, 1994.

[161] J Donea and L Gi Lamain. A modified representation of transverse shear in c0 quadrilateral plate elements. *Computer Methods in Applied Mechanics and Engineering*, 63(2): 183–207, 1987.

[162] Junuthula Narasimha Reddy. *Introduction to the finite element method*. McGraw-Hill Education, 2019.

[163] Panagiotis Kotronis and Jacky Mazars. Simplified modelling strategies to simulate the dynamic behaviour of r/c walls. *Journal of earthquake engineering*, 9(02):285–306, 2005.

[164] Renata SB Stramandinoli and Henriette L La Rovere. Fe model for nonlinear analysis of reinforced concrete beams considering shear deformation. *Engineering structures*, 35: 244–253, 2012.

[165] Ning Li, Zhongxian Li, and Lili Xie. A fiber-section model based timoshenko beam element using shear-bending interdependent shape function. *Earthquake Engineering and Engineering Vibration*, 12:421–432, 2013.

[166] Paola Ceresa, Lorenza Petrini, Rui Pinho, and Romain Sousa. A fibre flexure–shear model for seismic analysis of rc-framed structures. *Earthquake Engineering & Structural Dynamics*, 38(5):565–586, 2009.

[167] Huma Khalid. Objective modelling of reinforced concrete structures. 2012.

[168] Miha Jukić, Boštjan Brank, and Adnan Ibrahimbegovic. Failure analysis of reinforced concrete frames by beam finite element that combines damage, plasticity and embedded discontinuity. *Engineering structures*, 75:507–527, 2014.

[169] Denis Caillerie, Panagiotis Kotronis, and Robert Cybulski. A timoshenko finite element straight beam with internal degrees of freedom. *International Journal for Numerical and Analytical Methods in Geomechanics*, 39(16):1753–1773, 2015.

[170] Zhong-Xian Li, Ying Gao, and Qiuhong Zhao. A 3d flexure–shear fiber element for modeling the seismic behavior of reinforced concrete columns. *Engineering Structures*, 117:372–383, 2016.

[171] De-Cheng Feng, Gang Wu, Ze-Yang Sun, and Ji-Gang Xu. A flexure-shear timoshenko fiber beam element based on softened damage-plasticity model. *Engineering Structures*, 140:483–497, 2017.

[172] Jiadaren Liu, Liying Huang, Zhaohan Wu, Douglas Tomlinson, Carlos Cruz-Noguez, John Alexander, Samer Adeeb, and Yong Li. Development of enhanced fiber beam element with multi-axial material constitutive models for reinforced/prestressed concrete beams. *Engineering Structures*, 248:113289, 2021.

[173] De-Cheng Feng and Jian-Ying Wu. Improved displacement-based timoshenko beam element with enhanced strains. *Journal of Structural Engineering*, 146(3):04019221, 2020.

[174] Z Lyu, Christian Málaga-Chuquitaype, and AM Ruiz-Teran. Design of timber-concrete composite (tcc) bridges with under-deck stay cables. *Engineering Structures*, 189:589–604, 2019.

[175] René De Borst, Mike A Crisfield, Joris JC Remmers, and Clemens V Verhoosel. *Nonlinear finite element analysis of solids and structures*. John Wiley & Sons, 2012.

[176] Yeong-Bin Yang and Shyh-Rong Kuo. Theory & analysis of nonlinear framed structures. *(No Title)*, 1994.

[177] William McGuire, Richard H Gallagher, and Ronald D Ziemian. *Matrix structural analysis*. 2000.

[178] Klaus-Jürgen Bathe. *Finite element procedures*. Klaus-Jurgen Bathe, 2006.

[179] Armando Calabrese, Joao Pacheco Almeida, and Rui Pinho. Numerical issues in distributed inelasticity modeling of rc frame elements for seismic analysis. *Journal of Earthquake Engineering*, 14(S1):38–68, 2010.

[180] Joshua S Pugh, Laura N Lowes, and Dawn E Lehman. Nonlinear line-element modeling of flexural reinforced concrete walls. *Engineering Structures*, 104:174–192, 2015.

[181] João Pacheco Almeida, Danilo Tarquini, and Katrin Beyer. Modelling approaches for inelastic behaviour of rc walls: multi-level assessment and dependability of results. *Archives of Computational Methods in Engineering*, 23:69–100, 2016.

[182] D Ehrlich and F Armero. Finite element methods for the analysis of softening plastic hinges in beams and frames. *Computational Mechanics*, 35(4):237–264, 2005.

[183] Ibrahi Bazan. Ultimate bending strength theory for timber beams. 1980.

[184] Andrew H Buchanan. Bending strength of lumber. *Journal of structural engineering*, 116 (5):1213–1229, 1990.

[185] Kay-Uwe Schober, Annette M Harte, Robert Kliger, Robert Jockwer, Qingfeng Xu, and Jian-Fei Chen. Frp reinforcement of timber structures. *Construction and building materials*, 97:106–118, 2015.

[186] Lukas Blank and Andrea Frangi. Design model for the bending resistance of fibre reinforced glulam. *Engineering Structures*, 211:110385, 2020.

[187] Chenyang Cao and Wendel Sebastian. Nonlinear computational framework for hybrid ductile glulam joists. In *Structures*, volume 56, page 104715. Elsevier, 2023.

[188] Frank Lam and Jung-Kwon Oh. Performance of canadian glulam columns with new laminae e requirements. *Engineering Structures*, 172:85–93, 2018.

[189] Roberto Tomasi, Maria Adelaide Parisi, and Maurizio Piazza. Ductile design of glued-laminated timber beams. *Practice Periodical on Structural Design and Construction*, 14 (3):113–122, 2009.

[190] Thomas Ehrhart, René Steiger, Pedro Palma, Ernst Gehri, and Andrea Frangi. Glulam columns made of european beech timber: compressive strength and stiffness parallel to the grain, buckling resistance and adaptation of the effective-length method according to eurocode 5. *Materials and Structures*, 53(4):91, 2020.

[191] Peter Glos. *Zur Bestimmung des Festigkeitsverhaltens von Brettschichtholz bei Druckbeanspruchung aus Werkstoff-und Einwirkungskenngrößen*. PhD thesis, 1978.

[192] Zdeněk P Bažant, Jiaying Pan, and Gilles Pijaudier-Cabot. Softening in reinforced concrete beams and frames. *Journal of Structural Engineering*, 113(12):2333–2347, 1987.

[193] Milan Jirásek and Marco Bauer. Numerical aspects of the crack band approach. *Computers & structures*, 110:60–78, 2012.

[194] Lukas Blank, Gerhard Fink, Robert Jockwer, and Andrea Frangi. Quasi-brittle fracture and size effect of glued laminated timber beams. *European Journal of Wood and Wood Products*, 75:667–681, 2017.

[195] Milan Jirasek and Zdenek P Bazant. *Inelastic analysis of structures*. John Wiley & Sons, 2001.

[196] Gabriele Granello. Long-term behaviour of post-tensioned timber structures. 2018.

[197] Jean-Louis Batoz and Gouri Dhatt. Incremental displacement algorithms for nonlinear problems. *International Journal for Numerical Methods in Engineering*, 14(8):1262–1267, 1979.

[198] EA de Souza Neto and YT Feng. On the determination of the path direction for arc-length methods in the presence of bifurcations andsnap-backs'. *Computer methods in applied mechanics and engineering*, 179(1-2):81–89, 1999.

[199] Marcelo Epstein and David W Murray. Large deformation in-plane analysis of elastic beams. *Computers & Structures*, 6(1):1–9, 1976.

[200] Klaus-Jürgen Bathe and Said Bolourchi. Large displacement analysis of three-dimensional beam structures. *International journal for numerical methods in engineering*, 14(7):961–986, 1979.

[201] LNB Gummadi and AN Palazotto. Large strain analysis of beams and arches undergoing large rotations. *International journal of non-linear mechanics*, 33(4):615–645, 1998.

[202] Pruettha Nanakorn and LN Vu. A 2d field-consistent beam element for large displacement analysis using the total lagrangian formulation. *Finite Elements in Analysis and Design*, 42(14-15):1240–1247, 2006.

[203] Seng-Lip Lee, Francisco S Manuel, and Edwin C Rossow. Large deflections and stability of elastic frame. *Journal of the Engineering Mechanics Division*, 94(2):521–548, 1968.

[204] Czesław Cichoń. Large displacements in-plane analysis of elastic-plastic frames. *Computers & structures*, 19(5-6):737–745, 1984.

[205] Kuo Mo Hsiao, Fang Yu Hou, and KV Spiliopoulos. Large displacement analysis of elasto-plastic frames. *Computers & structures*, 28(5):627–633, 1988.

[206] Z Waszczyszyn and M Janus-Michalska. Numerical approach to the 'exact'finite element analysis of in-plane finite displacements of framed structures. *Computers & structures*, 69(4):525–535, 1998.

[207] MS Park and Byung Chai Lee. Geometrically non-linear and elastoplastic three-dimensional shear flexible beam element of von-mises-type hardening material. *International Journal for Numerical Methods in Engineering*, 39(3):383–408, 1996.

[208] Jean-Marc Battini. *Co-rotational beam elements in instability problems*. PhD thesis, KTH, 2002.

[209] FW Williams. An approach to the nonlinear behavior of the members of a rigidly jointed plane frameworks with finite deformations. *Quarterly Journal of Mechanics and Applied Mathematics*, 17:451–469, 1964.

[210] Alan Jennings. Frame analysis including change of geometry. *Journal of the Structural Division*, 94(3):627–644, 1968.

[211] Richard D Wood and OC Zienkiewicz. Geometrically nonlinear finite element analysis of beams, frames, arches and axisymmetric shells. *Computers & Structures*, 7(6):725–735, 1977.

[212] Siu Lai Chan. Geometric and material non-linear analysis of beam-columns and frames using the minimum residual displacement method. *International Journal for Numerical Methods in Engineering*, 26(12):2657–2669, 1988.

[213] F Tin-Loi and JS Misa. Large displacement elastoplastic analysis of semirigid steel frames. *International Journal for Numerical Methods in Engineering*, 39(5):741–762, 1996.

[214] Lip H Teh and Murray J Clarke. Co-rotational and lagrangian formulations for elastic three-dimensional beam finite elements. *Journal of Constructional Steel Research*, 48 (2-3):123–144, 1998.

[215] Yi-Qun Tang, Yao-Peng Liu, Siu-Lai Chan, and Er-Feng Du. An innovative co-rotational pointwise equilibrating polynomial element based on timoshenko beam theory for second-order analysis. *Thin-Walled Structures*, 141:15–27, 2019.

[216] Yi Qun Tang, Zhi Hua Zhou, and Siu Lai Chan. Nonlinear beam-column element under consistent deformation. *International journal of structural stability and dynamics*, 15(05): 1450068, 2015.

[217] Ted W Buell and Hamid Saadatmanesh. Strengthening timber bridge beams using carbon fiber. *Journal of Structural Engineering*, 131(1):173–187, 2005.

[218] Yail J Kim and Kent A Harries. Modeling of timber beams strengthened with various cfrp composites. *Engineering Structures*, 32(10):3225–3234, 2010.

[219] Chris Gentile, Dagmar Svecova, and Sami H Rizkalla. Timber beams strengthened with gfrp bars: development and applications. *Journal of Composites for Construction*, 6(1): 11–20, 2002.

[220] MA Vaz and M Caire. On the large deflections of linear viscoelastic beams. *International Journal of Non-Linear Mechanics*, 45(1):75–81, 2010.

[221] Farzam Dadgar-Rad and Nasser Firouzi. Large deformation analysis of two-dimensional visco-hyperelastic beams and frames. *Archive of Applied Mechanics*, 91:4279–4301, 2021.

[222] Wilhelm Flügge. *Viscoelasticity*. Springer, 1967.

[223] Robert J Hoyle, Rafik Y Itani, and James J Eckard. Creep of douglas fir beams due to cyclic humidity fluctuations. *Wood and fiber science*, pages 490–497, 1986.

[224] Carl T Kelley. *Iterative methods for linear and nonlinear equations*. SIAM, 1995.

[225] Juan C Simo and Robert Leroy Taylor. Consistent tangent operators for rate-independent elastoplasticity. *Computer methods in applied mechanics and engineering*, 48(1):101–118, 1985.

[226] XH Dai, YC Wang, and CG Bailey. Numerical modelling of structural fire behaviour of restrained steel beam–column assemblies using typical joint types. *Engineering Structures*, 32(8):2337–2351, 2010.

[227] JD Nzabonimpa and Won-Kee Hong. Use of artificial damping factors to enhance numerical stability for irregular joints. *Journal of Constructional Steel Research*, 148:295–303, 2018.

[228] Michael H Scott and Gregory L Fenves. Krylov subspace accelerated newton algorithm: application to dynamic progressive collapse simulation of frames. *Journal of Structural Engineering*, 136(5):473–480, 2010.

[229] Xiaodan Ren and Jie Li. Two-level consistent secant operators for cyclic loading of structures. *Journal of Engineering Mechanics*, 144(8):04018065, 2018.

[230] Hermann Matthies and Gilbert Strang. The solution of nonlinear finite element equations. *International journal for numerical methods in engineering*, 14(11):1613–1626, 1979.

[231] Xiao Liang and Khalid M Mosalam. Lyapunov-based nonlinear solution algorithm for structural analysis. *Journal of Engineering Mechanics*, 144(9):04018082, 2018.

[232] John R Dormand and Peter J Prince. A family of embedded runge-kutta formulae. *Journal of computational and applied mathematics*, 6(1):19–26, 1980.

[233] Andrea Dall'Asta, Laura Ragni, and Alessandro Zona. Analytical model for geometric and material nonlinear analysis of externally prestressed beams. *Journal of engineering mechanics*, 133(1):117–121, 2007.

[234] M Harajli, N Khairallah, and H Nassif. Externally prestressed members: evaluation of second-order effects. *Journal of Structural Engineering*, 125(10):1151–1161, 1999.

[235] Tiejiong Lou and Yiqiang Xiang. Numerical analysis of second-order effects of externally prestressed concrete beams. *Structural engineering and mechanics*, 35(5):631–643, 2010.

[236] Gonzalo Ramos and Angel C Aparicio. Ultimate analysis of monolithic and segmental externally prestressed concrete bridges. *Journal of Bridge Engineering*, 1(1):10–17, 1996.

[237] Bijan O Aalami. Time-dependent analysis of post-tensioned concrete structures. *Progress in Structural Engineering and Materials*, 1(4):384–391, 1998.

[238] Tie-jiong Lou and Yi-qiang Xiang. Finite element modeling of concrete beams prestressed with external tendons. *Engineering structures*, 28(14):1919–1926, 2006.

[239] TJ Lou, AV Lopes, and SMR Lopes. Influence of span-depth ratio on behavior of externally prestressed concrete beams. *ACI Structural Journal*, 109(5), 2012.

[240] Tiejiong Lou, Sergio MR Lopes, and Adelino V Lopes. Flexural response of continuous concrete beams prestressed with external tendons. *Journal of Bridge Engineering*, 18(6): 525–537, 2013.

[241] Tiejiong Lou, Sergio MR Lopes, and Adelino V Lopes. Nonlinear and time-dependent analysis of continuous unbonded prestressed concrete beams. *Computers & Structures*, 119:166–176, 2013.

[242] Tiejiong Lou, Chengming Peng, Di Min, and Wei Sun. Moment redistribution in unbonded prestressed concrete members: Proposed modification of aci equation. *ACI Structural Journal*, 117(6), 2020.

[243] Tiejiong Lou, Sergio MR Lopes, and Adelino V Lopes. Interaction between time-dependent and second-order effects of externally posttensioned members. *Journal of Bridge Engineering*, 20(11):06015003, 2015.

[244] Tiejiong Lou, Sergio MR Lopes, and Adelino V Lopes. Numerical modeling of externally prestressed steel–concrete composite beams. *Journal of Constructional Steel Research*, 121:229–236, 2016.

[245] Tiejiong Lou and Theodore L Karavasilis. Numerical assessment of the nonlinear behavior of continuous prestressed steel-concrete composite beams. *Engineering Structures*, 190: 116–127, 2019.

[246] Tiejiong Lou, Sergio MR Lopes, and Adelino V Lopes. Numerical analysis of behaviour of concrete beams with external frp tendons. *Construction and Building Materials*, 35: 970–978, 2012.

[247] Tiejiong Lou and Theodore L Karavasilis. Numerical evaluation of prestressed steel-concrete composite girders with external frp or steel tendons. *Journal of Constructional Steel Research*, 162:105698, 2019.

[248] Pablo M Páez and Beradi Sensale. Improved prediction of long-term prestress loss in unbonded prestressed concrete members. *Engineering Structures*, 174:111–125, 2018.

[249] Pablo M Páez and Beradi Sensale-Cozzano. Time-dependent analysis of simply supported and continuous unbonded prestressed concrete beams. *Engineering Structures*, 240: 112376, 2021.

[250] Bijan O Aalami. Structural modeling of posttensioned members. *Journal of Structural Engineering*, 126(2):157–162, 2000.

[251] Bilal El-Ariss. Stiffness of reinforced concrete beams with external tendons. *Engineering Structures*, 26(14):2047–2051, 2004.

[252] Nihal Ariyawardena and Amin Ghali. Prestressing with unbonded internal or external tendons: Analysis and computer model. *Journal of structural engineering*, 128(12):1493–1501, 2002.

[253] H Nassif, O Ozkul, and MH Harajli. Flexural behavior of beams prestressed with bonded and unbonded. *PTI Journal*, 1(1):60–71, 2003.

[254] De-Cheng Feng, Hai-Rong Shi, Fulvio Parisi, Emanuele Brunesi, and Chun-Lin Wang. Efficient numerical model for progressive collapse analysis of prestressed concrete frame structures. *Engineering Failure Analysis*, 129:105683, 2021.

[255] Bárbara dos Santos Sánchez, Jorge Palomino Tamayo, Inácio Benvegnu Morsch, and Marcela Palhares Miranda. A nonlinear geometric model for pre-stressed steel–concrete composite beams. *Journal of the Brazilian Society of Mechanical Sciences and Engineering*, 43(5):233, 2021.

[256] Xiao-Han Wu, Shunsuke Otani, and Hitoshi Shiohara. Tendon model for nonlinear analysis of prestressed concrete structures. *Journal of structural engineering*, 127(4):398–405, 2001.

[257] Xiao-Han Wu and Xilin Lu. Tendon model for nonlinear analysis of externally prestressed concrete structures. *Journal of structural engineering*, 129(1):96–104, 2003.

[258] Andrea Dall'Asta and Alessandro Zona. Finite element model for externally prestressed composite beams with deformable connection. *Journal of Structural Engineering*, 131(5): 706–714, 2005.

[259] Andrea Dall'Asta and Luigino Dezi. Nonlinear behavior of externally prestressed composite beams: Analytical model. *Journal of Structural Engineering*, 124(5):588–597, 1998.

[260] Alessandro Zona, Laura Ragni, and Andrea Dall'Asta. Finite element formulation for geometric and material nonlinear analysis of beams prestressed with external slipping tendons. *Finite Elements in Analysis and Design*, 44(15):910–919, 2008.

[261] Leandro S Moreira, João Batista M Sousa Jr, and Evandro Parente Jr. Nonlinear finite element simulation of unbonded prestressed concrete beams. *Engineering Structures*, 170: 167–177, 2018.

[262] Joao Batista M Sousa Jr, Evandro Parente Jr, Esio MF Lima, and Michelle VX Oliveira. Beam-tendon finite elements for post-tensioned steel-concrete composite beams with partial interaction. *Journal of Constructional Steel Research*, 159:147–160, 2019.

[263] Wenjun Gao and Xilin Lu. Modelling unbonded prestressing tendons in self-centering connections through improved sliding cable elements. *Engineering Structures*, 180:809–828, 2019.

[264] Wu-Tong Yan, Bing Han, Hui-Bing Xie, Peng-Fei Li, and Li Zhu. Research on numerical model for flexural behaviors analysis of precast concrete segmental box girders. *Engineering Structures*, 219:110733, 2020.

[265] Wutong Yan, Liangjiang Chen, Bing Han, Huibing Xie, and Yue Sun. Flexural analysis model of externally prestressed steel-concrete composite beam with nonlinear interfacial connection. *Applied Sciences*, 12(9):4699, 2022.

[266] Duong T Tran, Thong M Pham, Hong Hao, and Wensu Chen. Numerical study on bending response of precast segmental concrete beams externally prestressed with frp tendons. *Engineering Structures*, 241:112423, 2021.

[267] Duong T Tran, Thong M Pham, Hong Hao, and Wensu Chen. Numerical investigation of flexural behaviours of precast segmental concrete beams internally post-tensioned with

unbonded frp tendons under monotonic loading. *Engineering Structures*, 249:113341, 2021.

[268] Tan D. Le, Thong M. Pham, and Hong Hao. Numerical study on the flexural performance of precast segmental concrete beams with unbonded internal steel tendons. *Construction and Building Materials*, 248:118362, 2020.

[269] M Menegotto and PE Pinto. Method of analysis for cyclically loaded reinforced concrete plane force and bending. In *Proceedings, IABSE Symposium on Resistance and Ultimate Deformability of Structures Acted on by Well Defined Repeated Loads, Lisbon*, pages 15–22, 1973.

[270] CEB. *CEB-FIP model code 1990: Design code*. Thomas Telford Publishing, 1993.

[271] Donald Dominic Magura, Mete Avni Sozen, and Chester Paul Siess. A study of stress relaxation in prestressing reinforcement. *Civil Engineering Studies SRS-237*, 1962.

[272] Ranier Adonis Barbieri, Francisco de Paula Simões Lopes Gastal, and Américo Campos Filho. Numerical model for the analysis of unbonded prestressed members. *Journal of Structural Engineering*, 132(1):34–42, 2006.

[273] Zdeněk P Bažant and ST Wu. Rate-type creep law of aging concrete based on maxwell chain. *Matériaux et Construction*, 7:45–60, 1974.

[274] Francis TK Au and XT Si. Accurate time-dependent analysis of concrete bridges considering concrete creep, concrete shrinkage and cable relaxation. *Engineering Structures*, 33 (1):118–126, 2011.

[275] HD Hernandez and WL Gamble. Time dependent prestress losses in pretensioned concrete construction, structural research series no. 417. *Urbana, Illinois: Civil Engineering Studies, University of Illinois*, 1975.

[276] Zdeněk P Bažant and Qiang Yu. Relaxation of prestressing steel at varying strain and temperature: Viscoplastic constitutive relation. *Journal of Engineering Mechanics*, 139 (7):814–823, 2013.

[277] Tiejiong Lou, Sergio MR Lopes, and Adelino V Lopes. A finite element model to simulate long-term behavior of prestressed concrete girders. *Finite Elements in Analysis and Design*, 81:48–56, 2014.

[278] John E Dennis, Jr and Jorge J Moré. Quasi-newton methods, motivation and theory. *SIAM review*, 19(1):46–89, 1977.

[279] Eivind Hognestad. Study of combined bending and axial load in reinforced concrete members. Technical report, University of Illinois at Urbana Champaign, College of Engineering, 1951.

[280] YW Chen. The experimental researches on unbonded partially prestressed concrete continuous beams. *master's thesis, Hunan University, Changsha, China*, 2008.

[281] Robert Park, MJ Negel Priestley, and Wayne D Gill. Ductility of square-confined concrete columns. *Journal of the structural division*, 108(4):929–950, 1982.

[282] Wouter A van Beerschoten, David M Carradine, and Alessandro Palermo. Compressive strength and stiffness of radiata pine laminated veneer lumber. *European Journal of Wood and Wood Products*, 71(6):795–804, 2013.

[283] NelsonPine. Specific engineering design guide. *Nelson Pine Industries Limited*, 2016.

[284] Tiejiong Lou and Theodore L Karavasilis. Time-dependent assessment and deflection prediction of prestressed concrete beams with unbonded cfrp tendons. *Composite Structures*, 194:365–376, 2018.

[285] Zhu Bofang. *The finite element method theory and applications*. China Water Power Press, 2009.

Appendix A

In this Appendix, descriptive flowcharts are illustrated in Figs. A.1 to A.8 to show the key features and restrictions of the different implemented developments comprising the numerical framework described throughout this thesis.

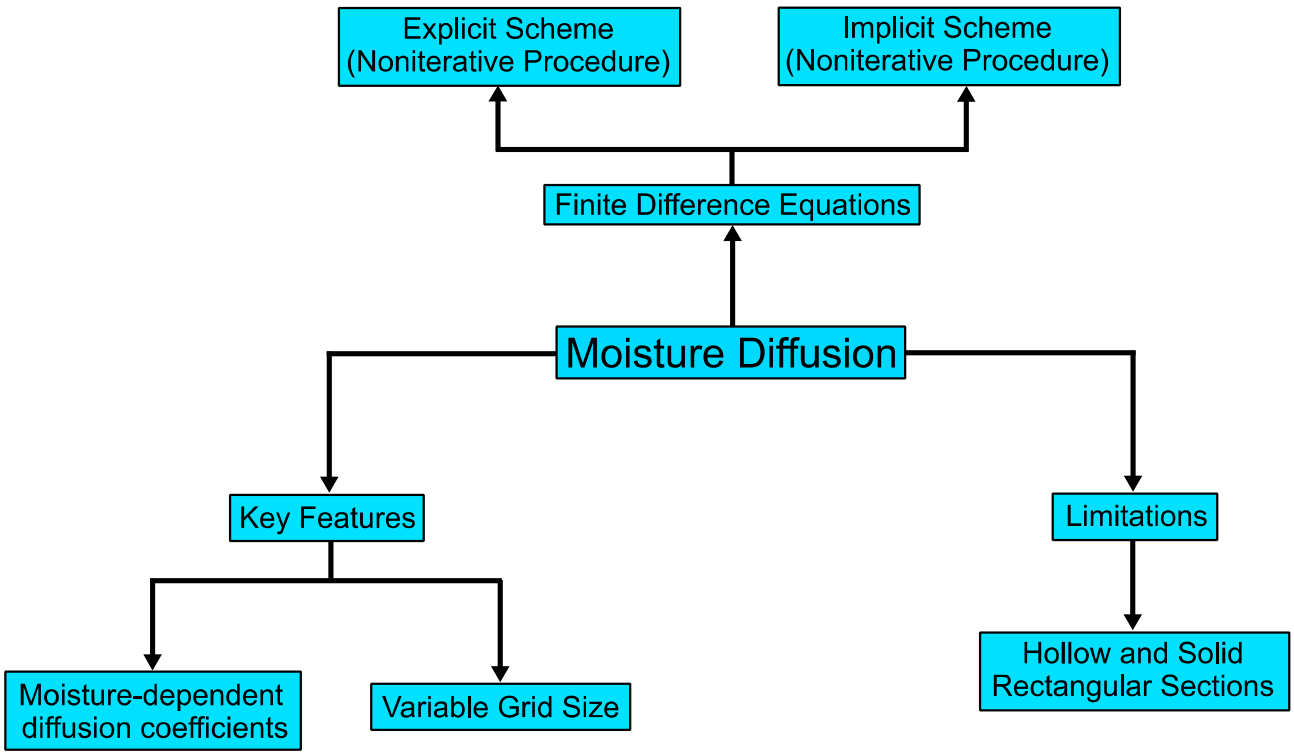


Figure A.1: Descriptive Flow Chart of Finite Difference Framework.

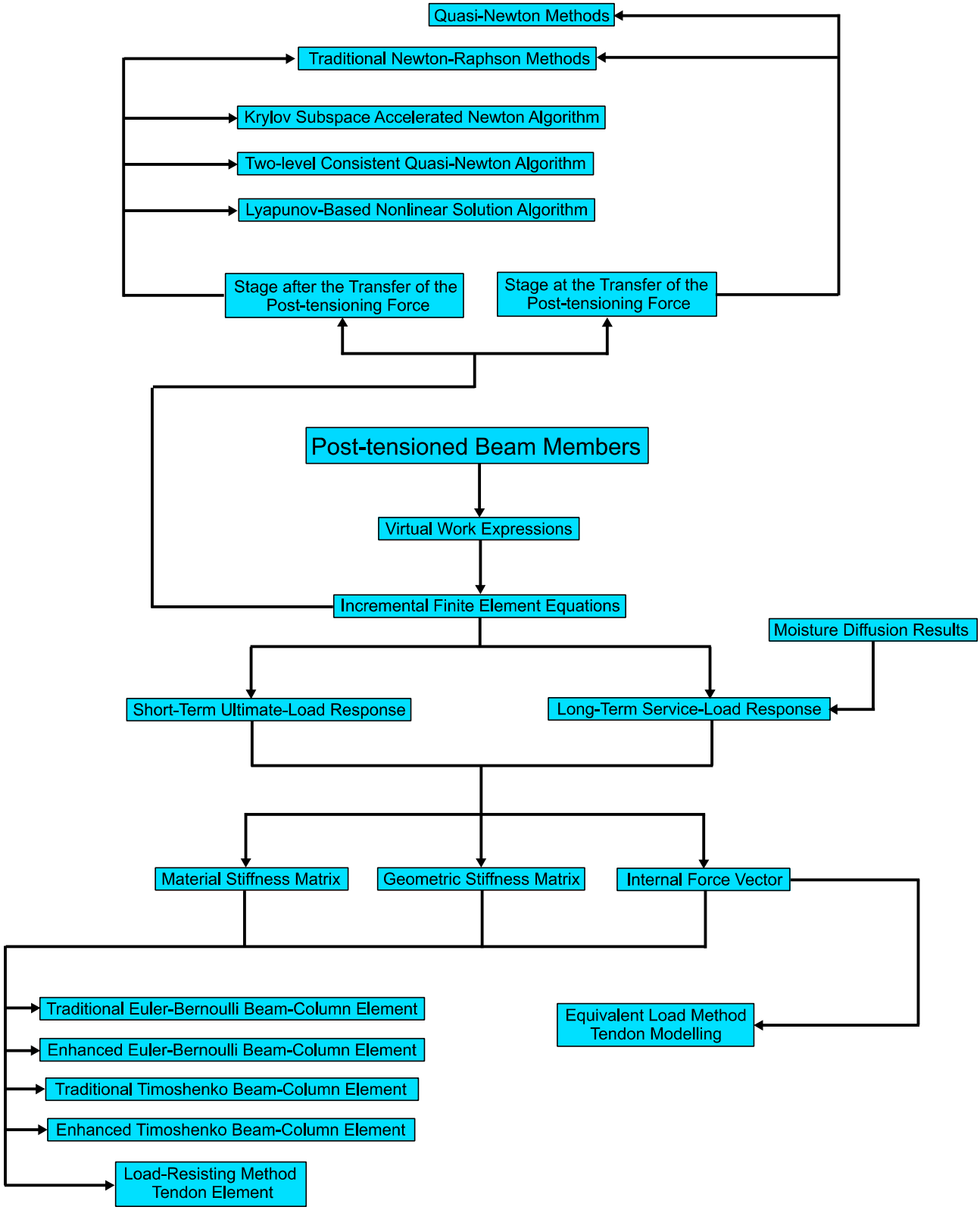


Figure A.2: Descriptive Flow Chart of Finite Element Framework.

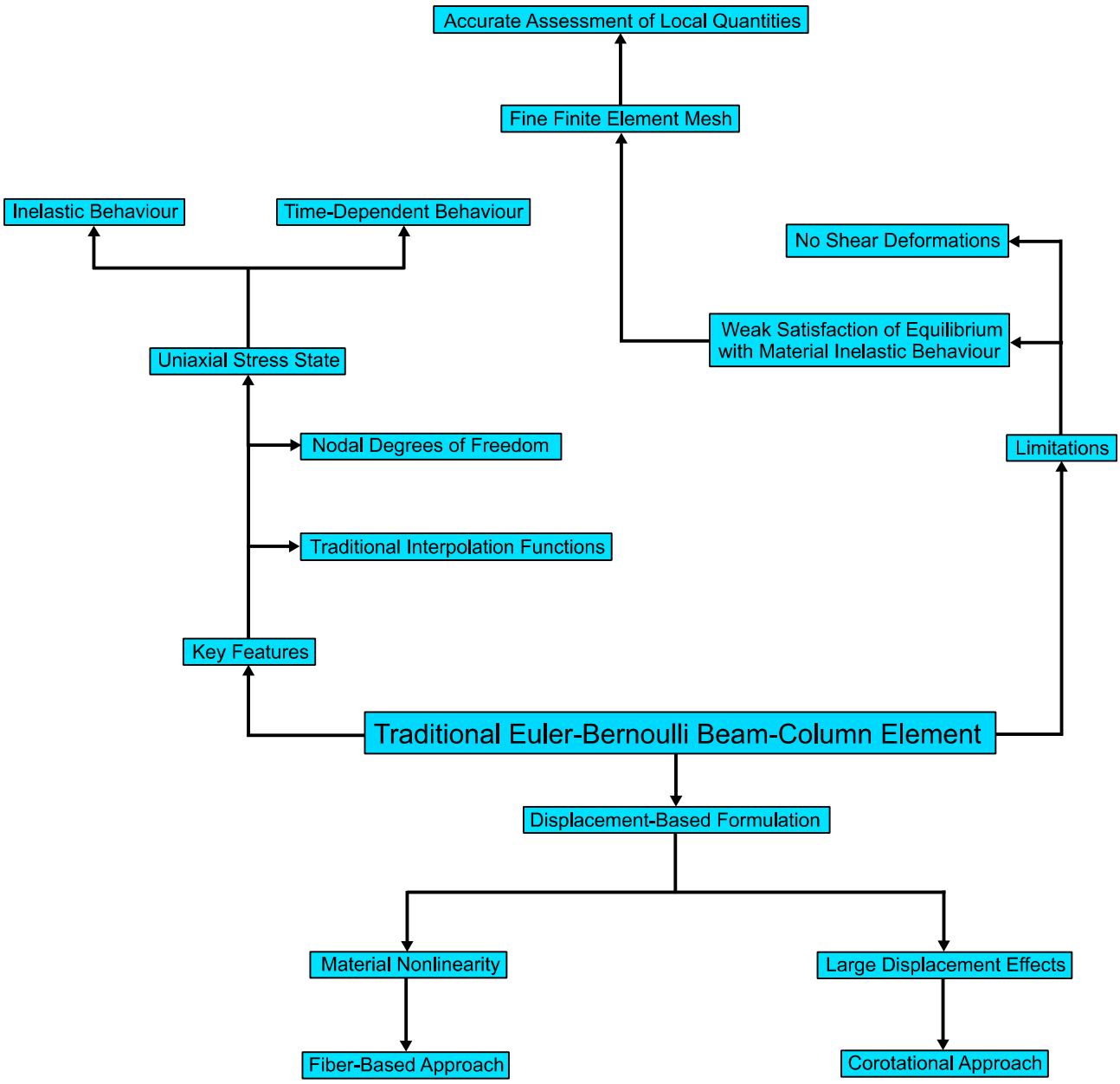


Figure A.3: Descriptive Flow Chart of Traditional Euler-Bernoulli Formulation.

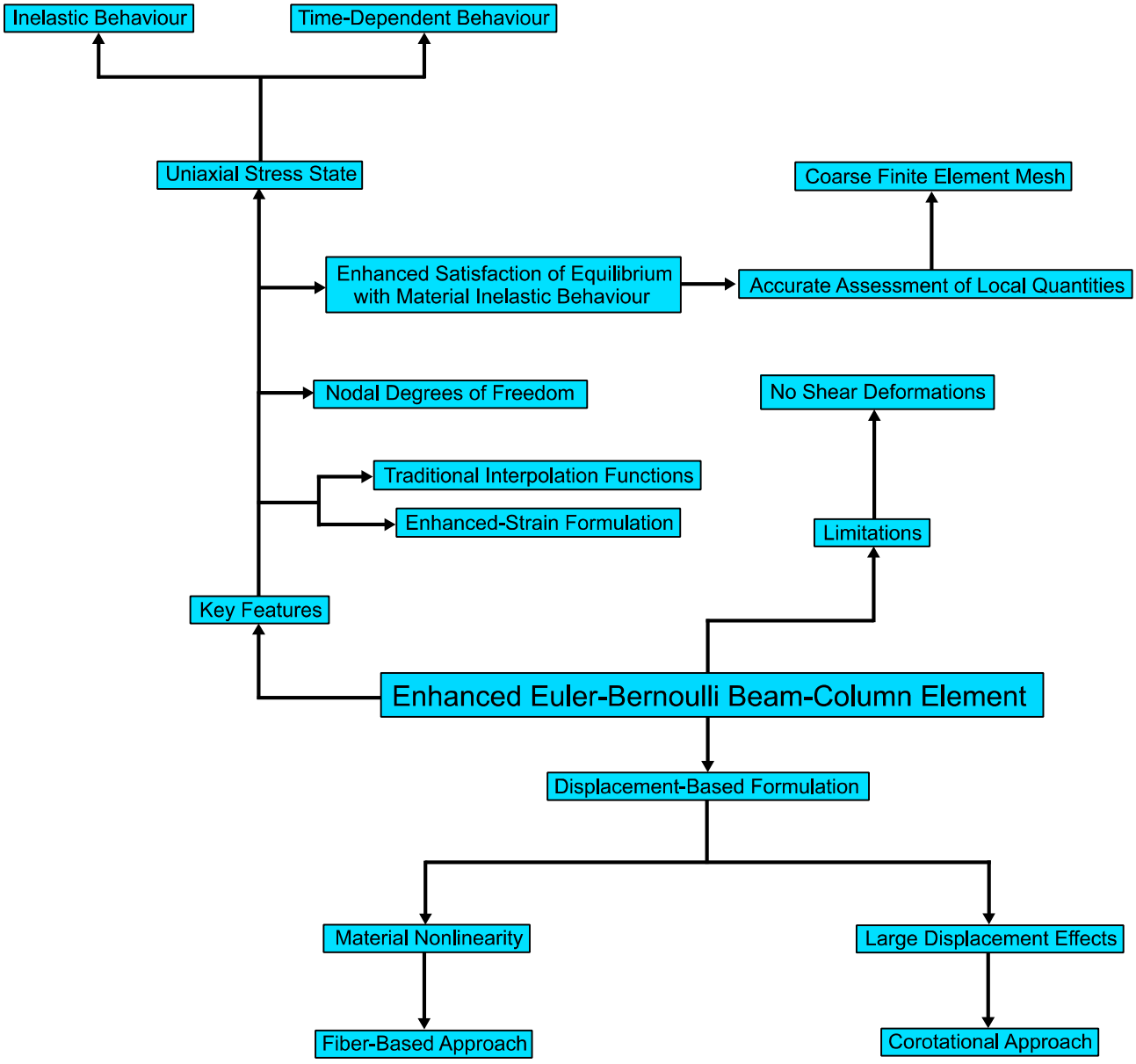


Figure A.4: Descriptive Flow Chart of Enhanced Euler-Bernoulli Formulation.

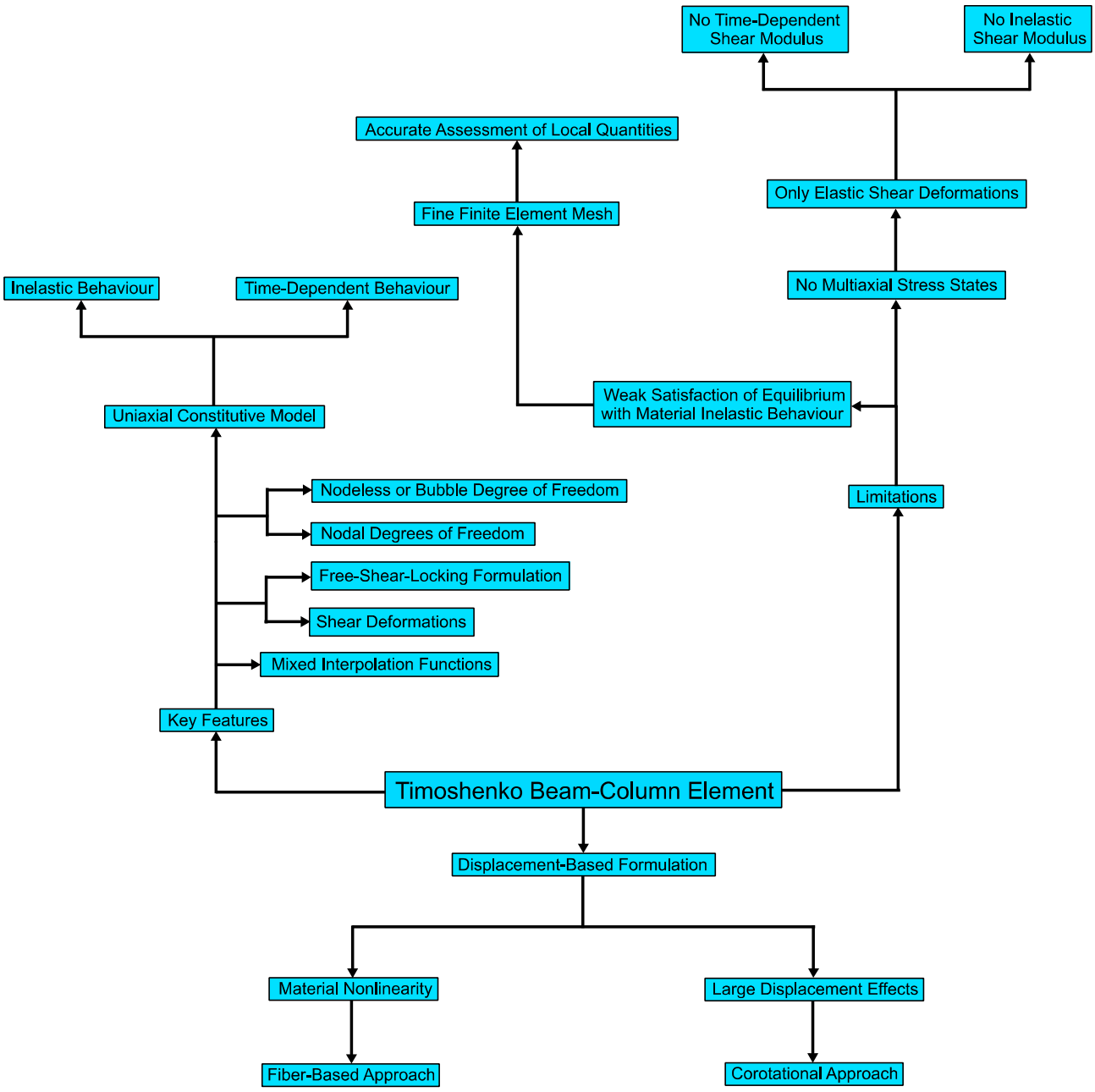


Figure A.5: Descriptive Flow Chart of Timoshenko Formulation.

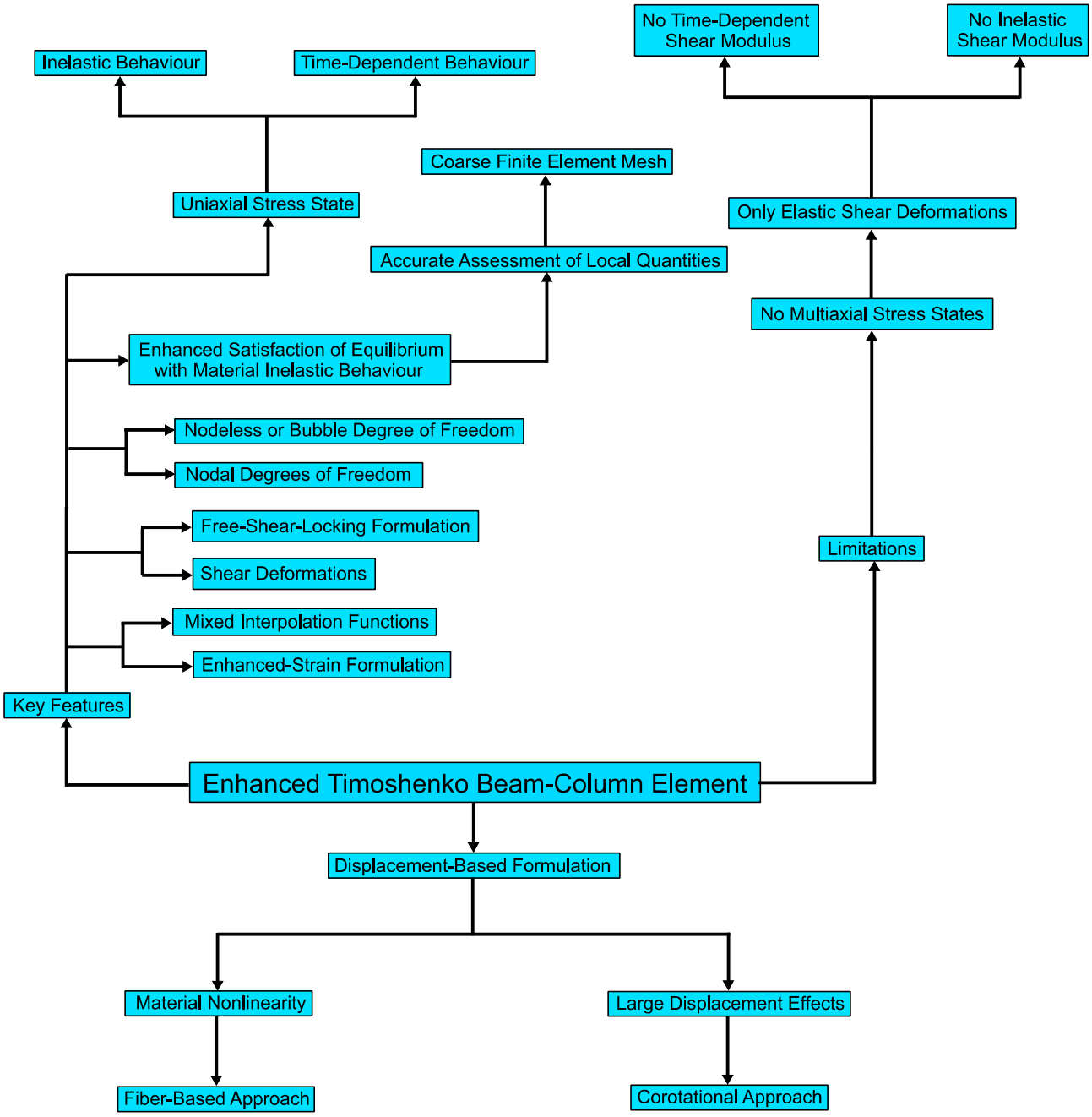


Figure A.6: Descriptive Flow Chart of Enhanced Timoshenko Formulation.

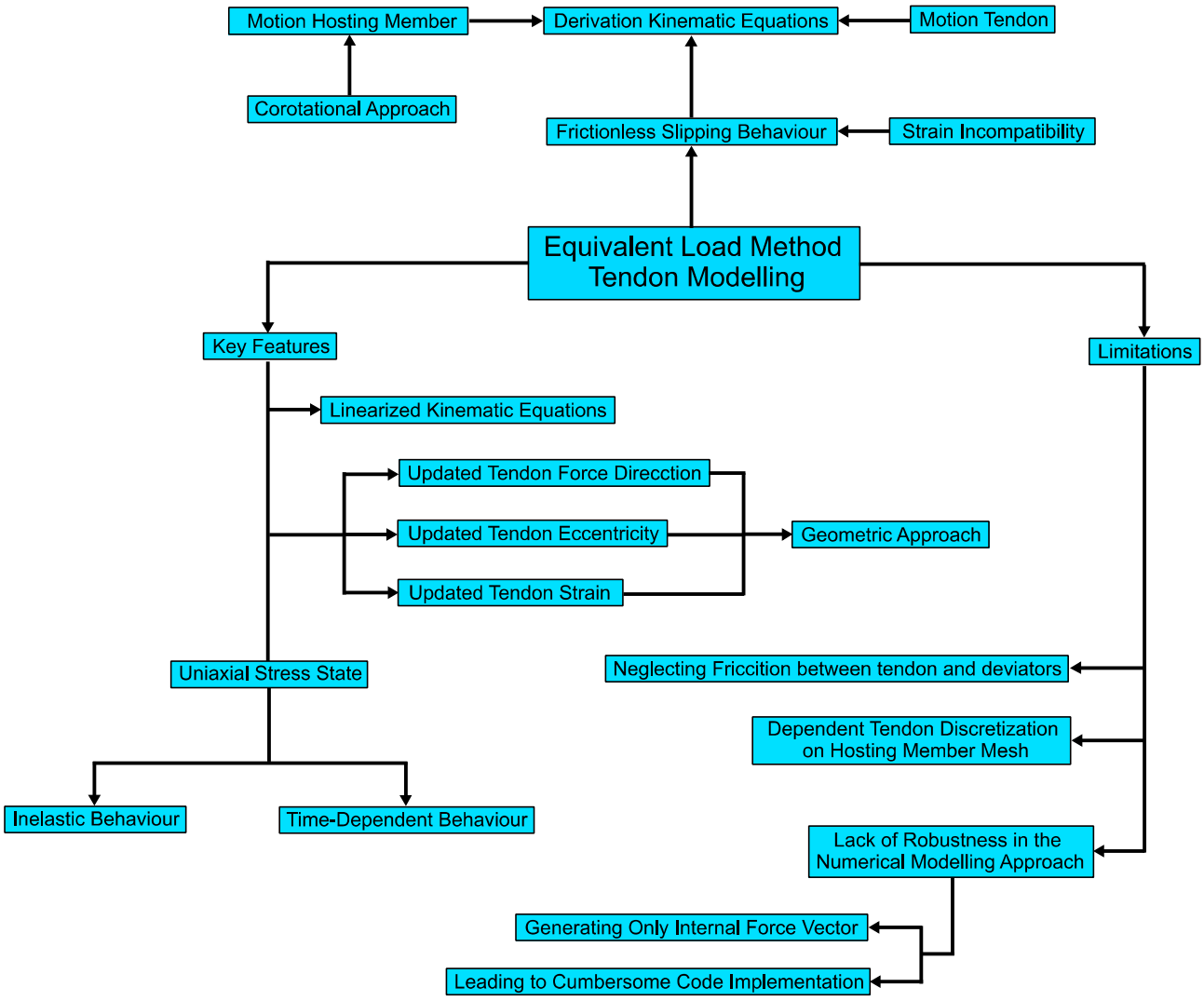


Figure A.7: Descriptive Flow Chart of Tendon Equivalent Load Method.

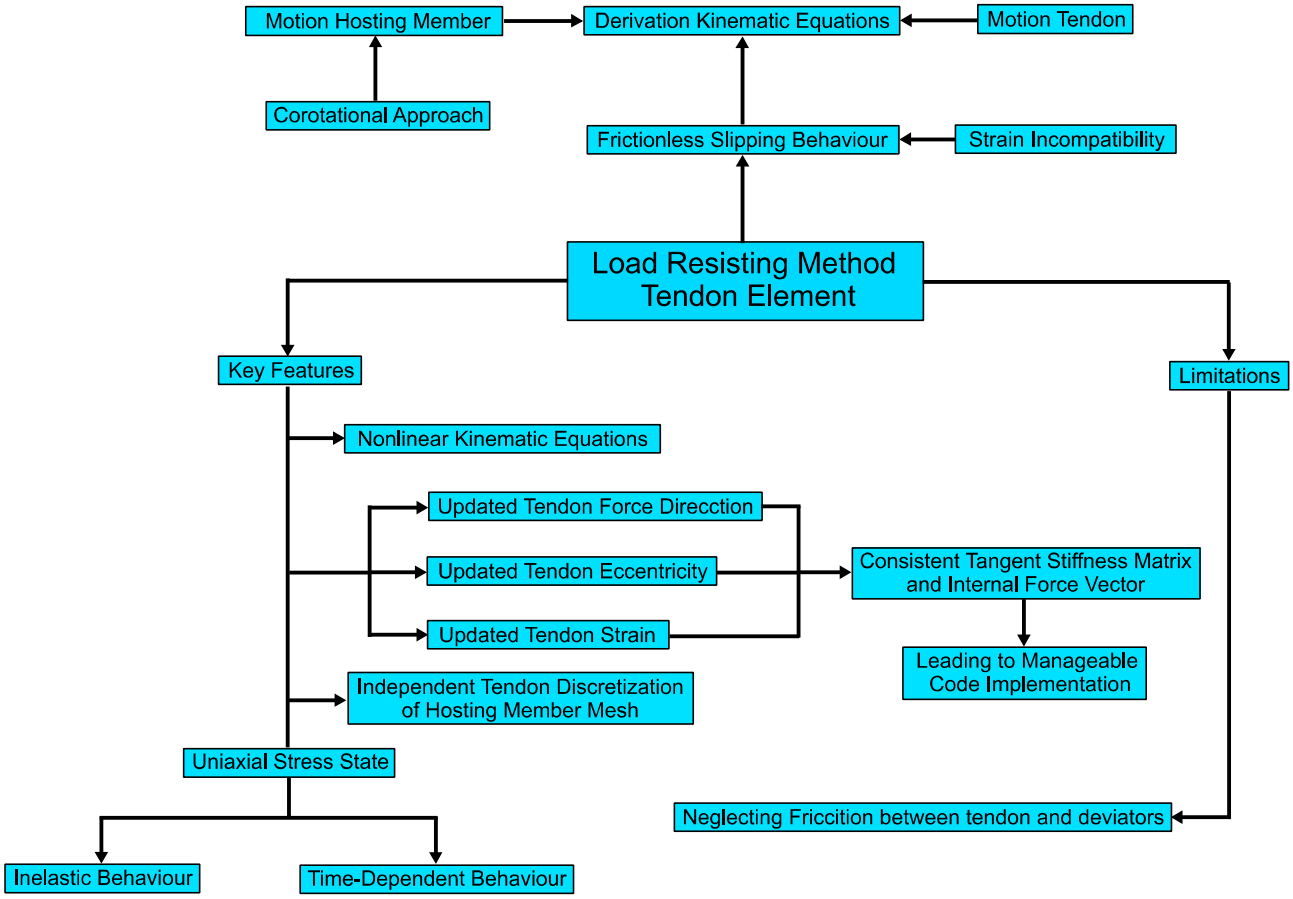


Figure A.8: Descriptive Flow Chart of Tendon Load-Resisting Method.

Appendix B

In this Appendix complementary results related to the validation example in subsection 4.4.4 are presented. In order to compare the numerical performance of the traditional Euler-Bernoulli BC element (EB) with its enhanced version (ENH EB), the obtained history of the basic normal force and bending moment values of one of the most strained elements and the history of the section normal force and bending moment values obtained at the integration Points (IPs) used in each formulation are plotted in Figs. B.1 to B.20. In the case of the EB elements, three integration points were adopted following the Gauss–Legendre quadrature. In contrast, a modified integration rule is adopted for the ENH EB elements in which two integration points located at the two ends points of the element are employed. In this analysis, the third element of the mesh was selected to have a meaningful overview of the results.

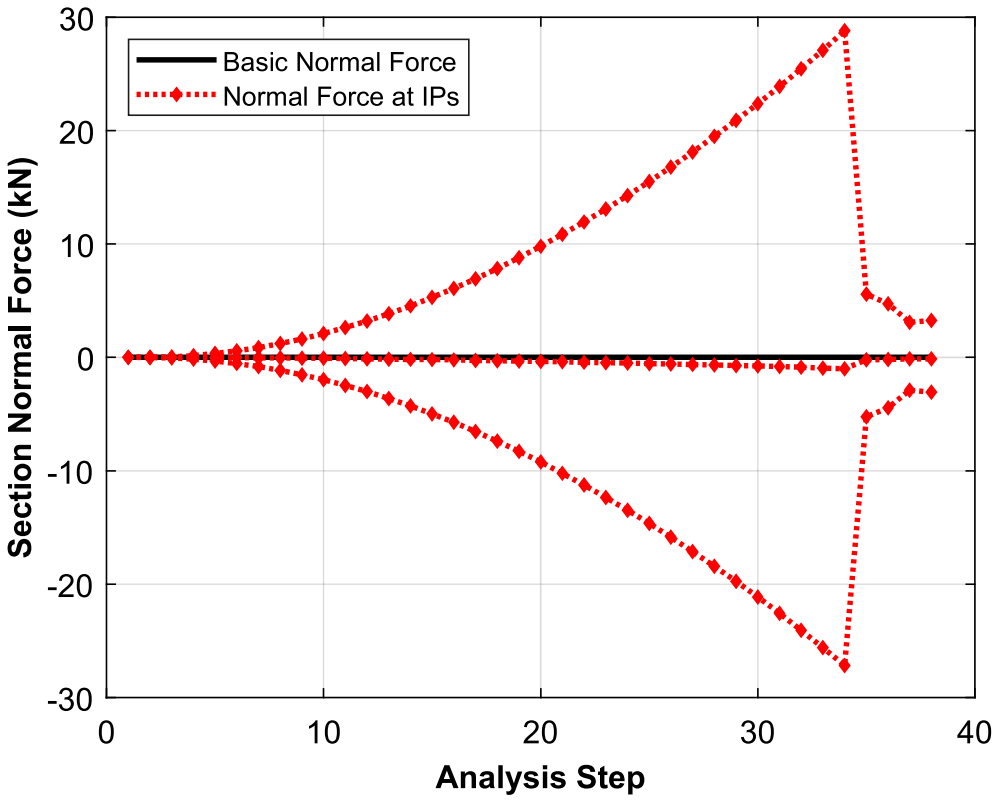


Figure B.1: History of normal forces obtained in the EB elements for Beam B1.

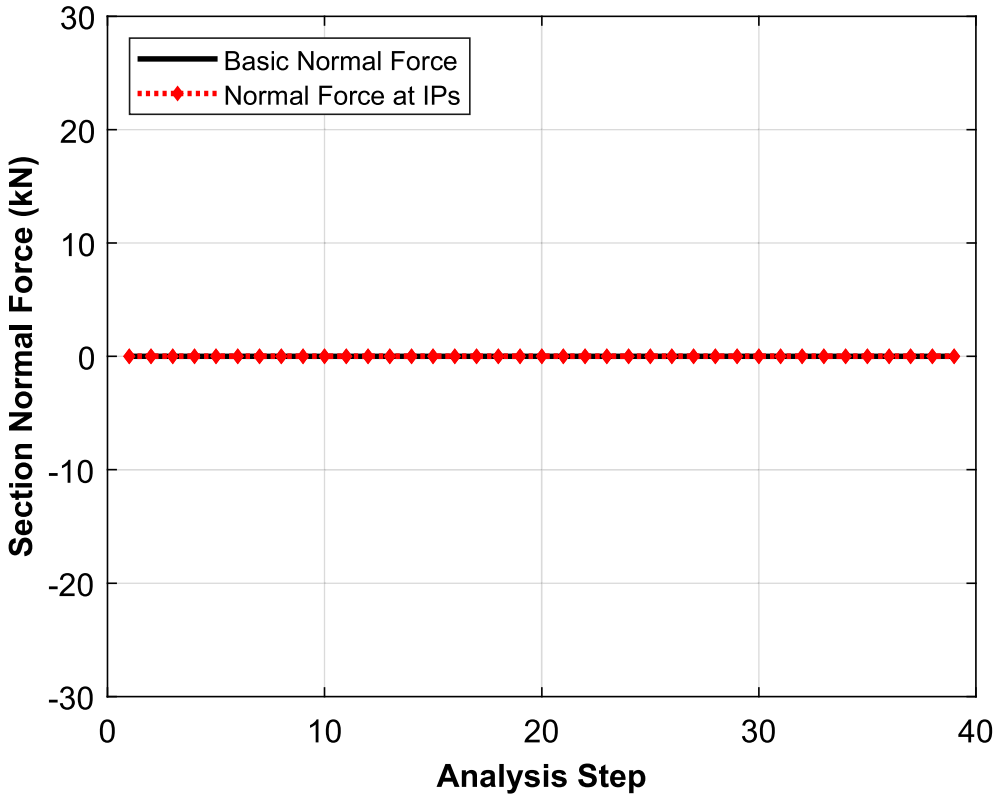


Figure B.2: History of normal forces obtained in the ENH EB elements for Beam B1.

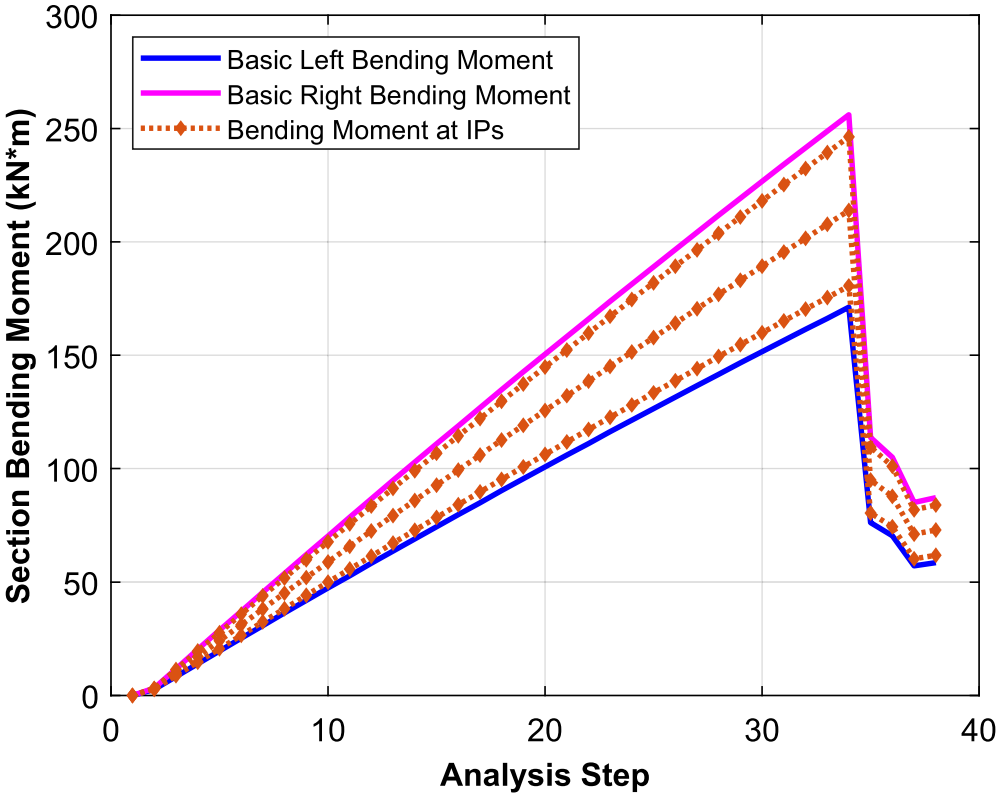


Figure B.3: History of Bending Moments obtained in the EB elements for Beam B1.

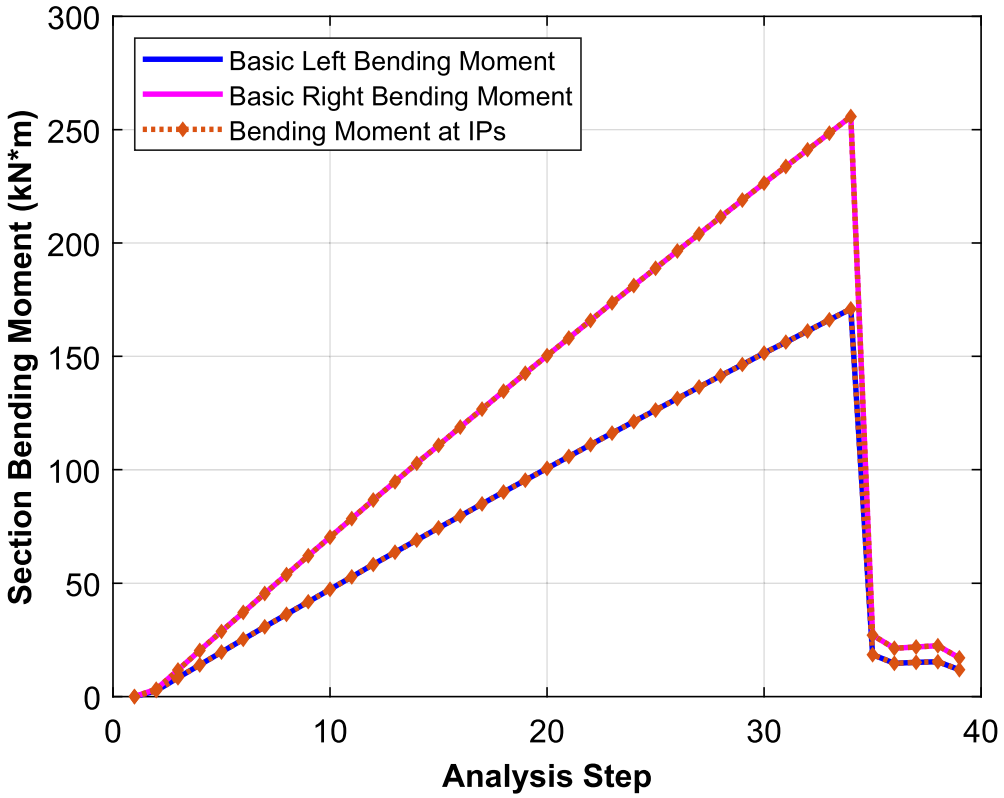


Figure B.4: History of Bending Moments obtained in the ENH EB elements for Beam B1.

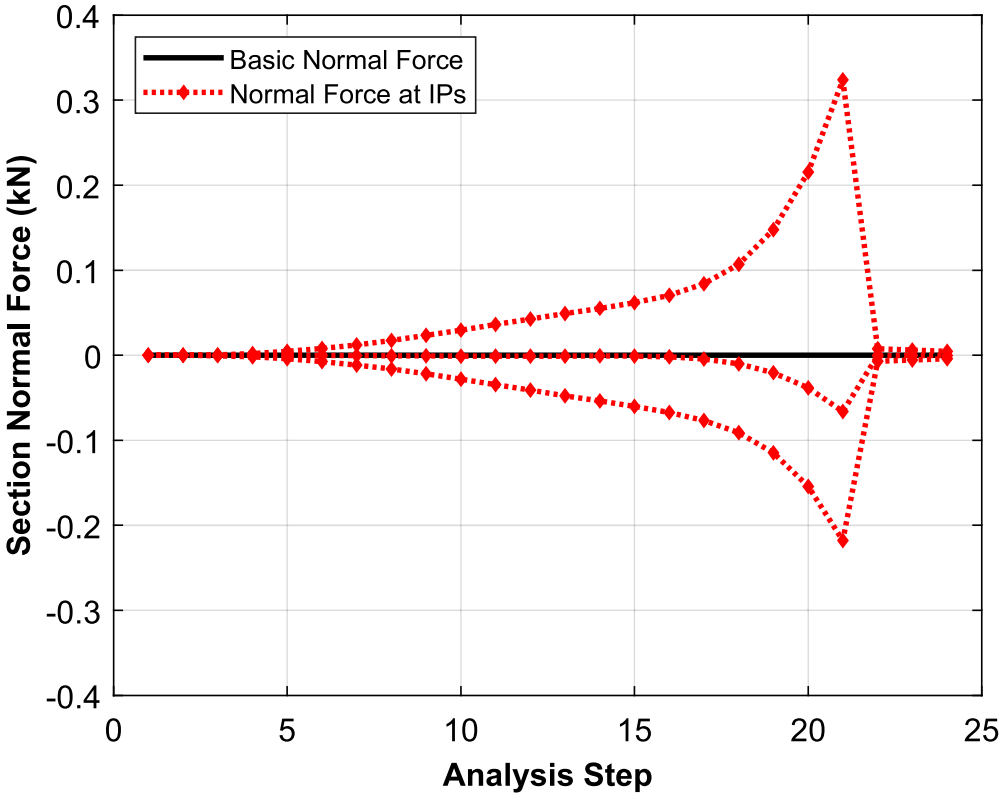


Figure B.5: History of normal forces obtained in the EB elements for Beam DF1.

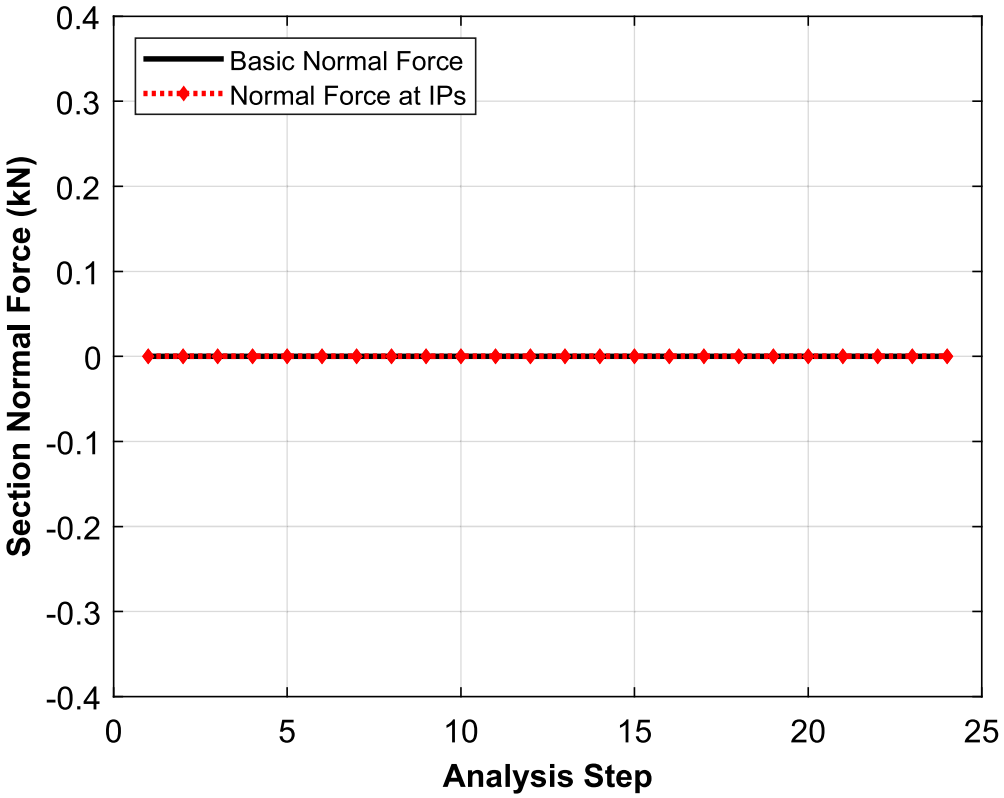


Figure B.6: History of normal forces obtained in the ENH EB elements for Beam DF1.

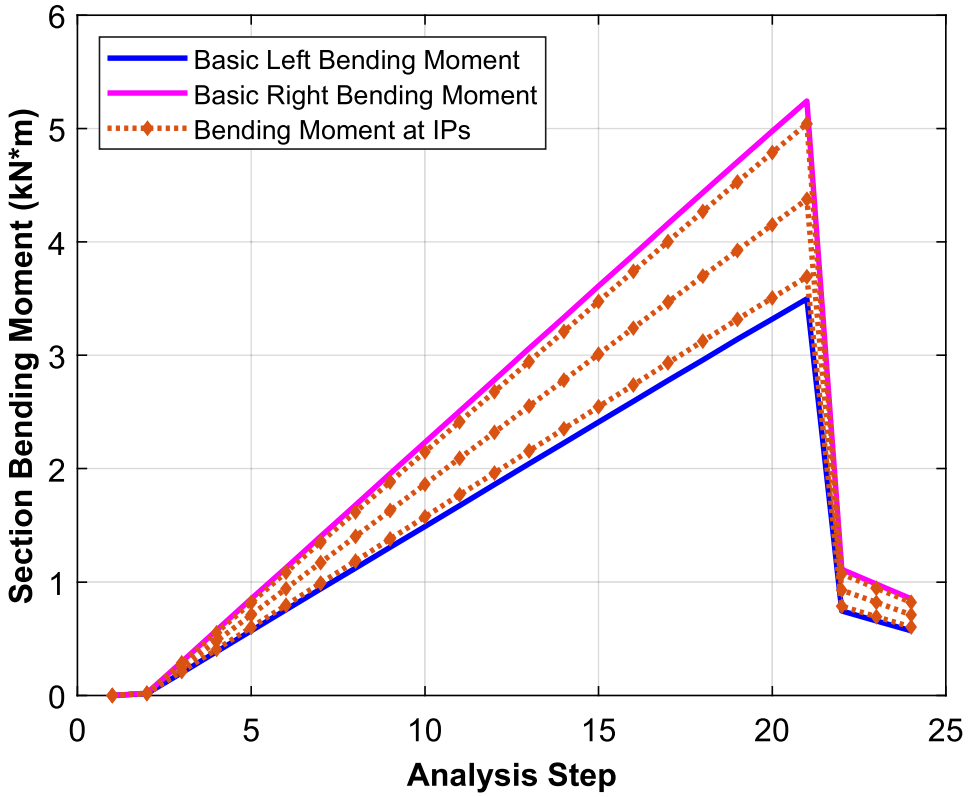


Figure B.7: History of Bending Moments obtained in the EB elements for Beam DF1.

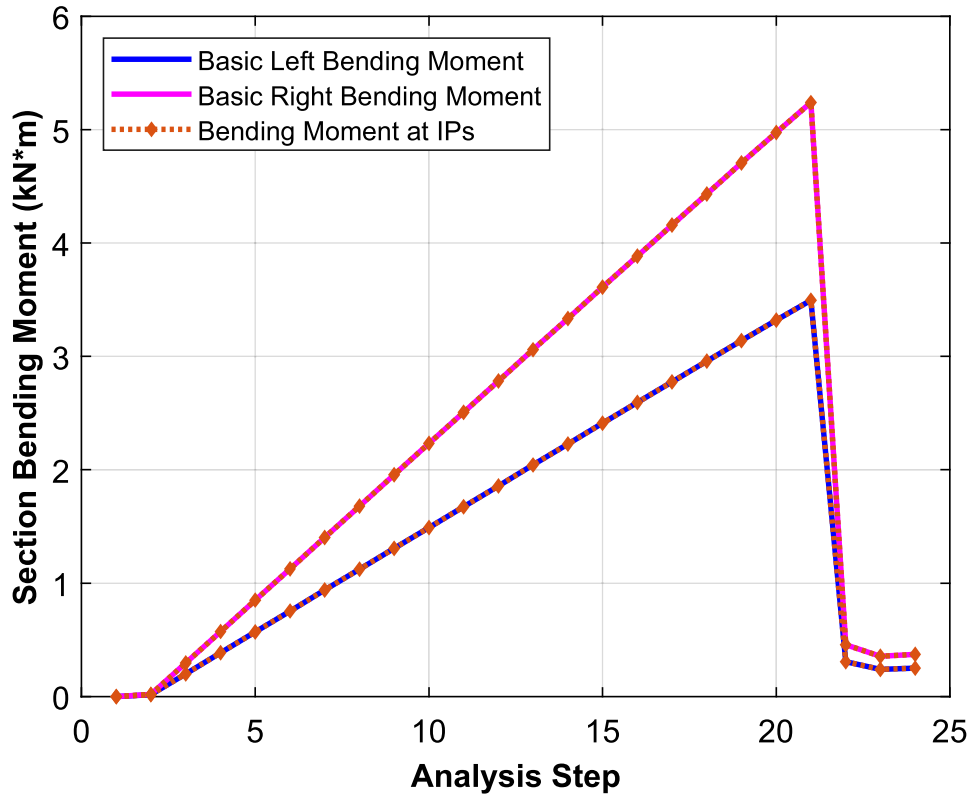


Figure B.8: History of Bending Moments obtained in the ENH EB elements for Beam DF1.

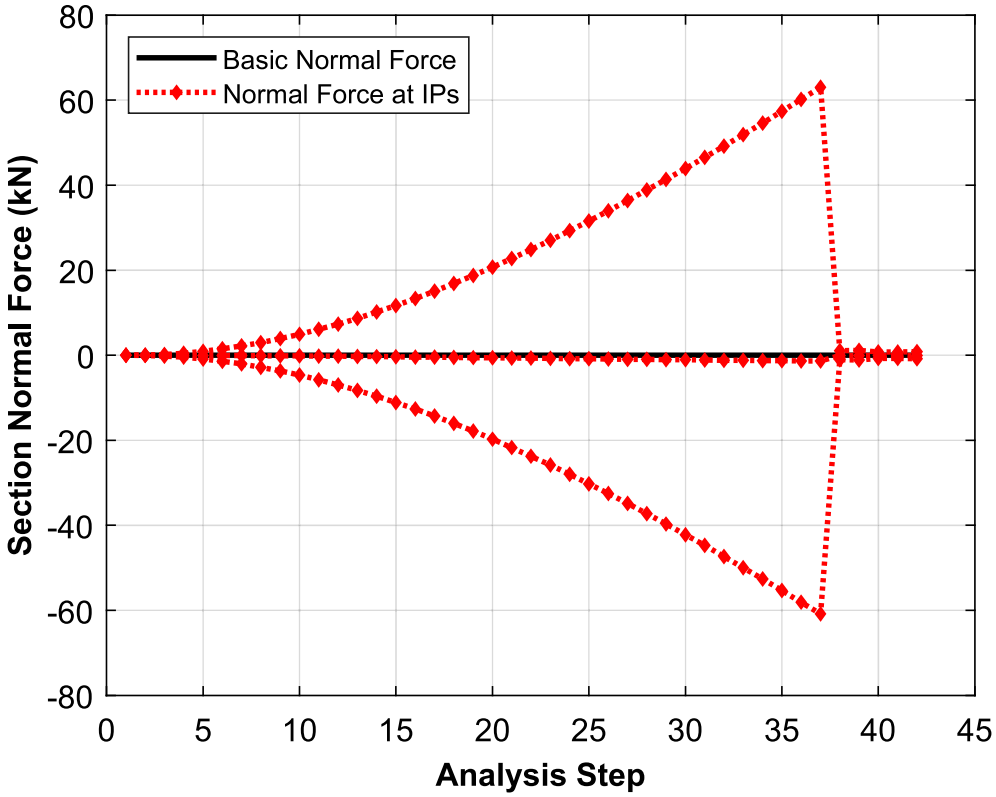


Figure B.9: History of normal forces obtained in the EB elements for Beam FS0.

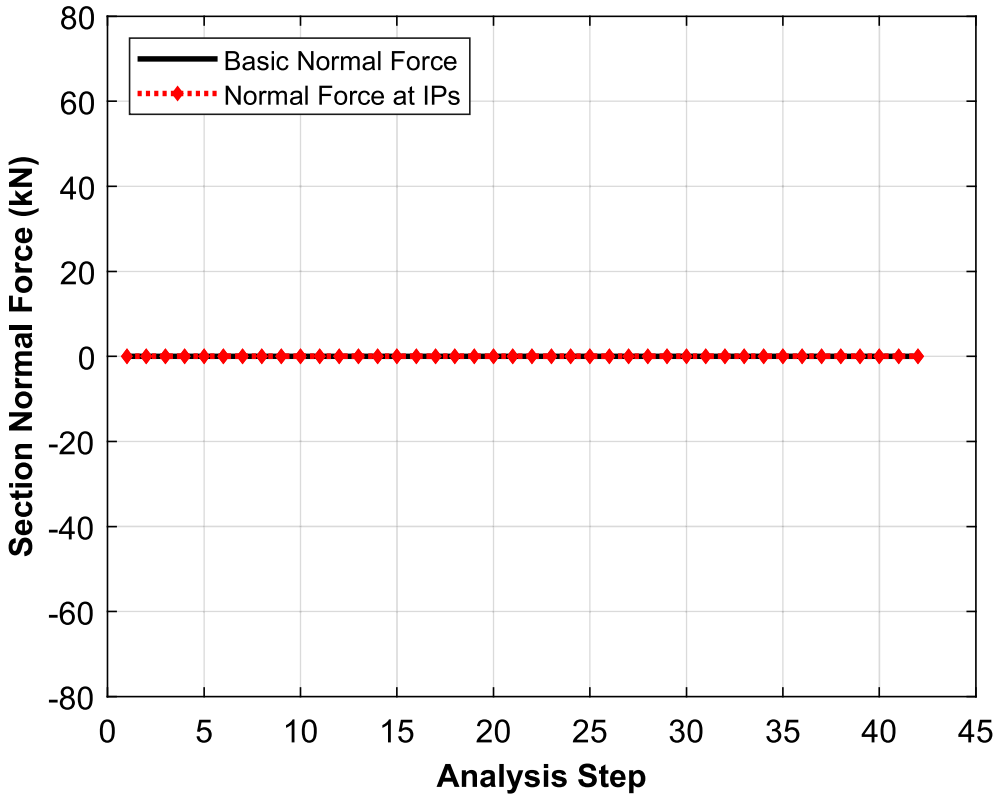


Figure B.10: History of normal forces obtained in the ENH EB elements for Beam FS0.

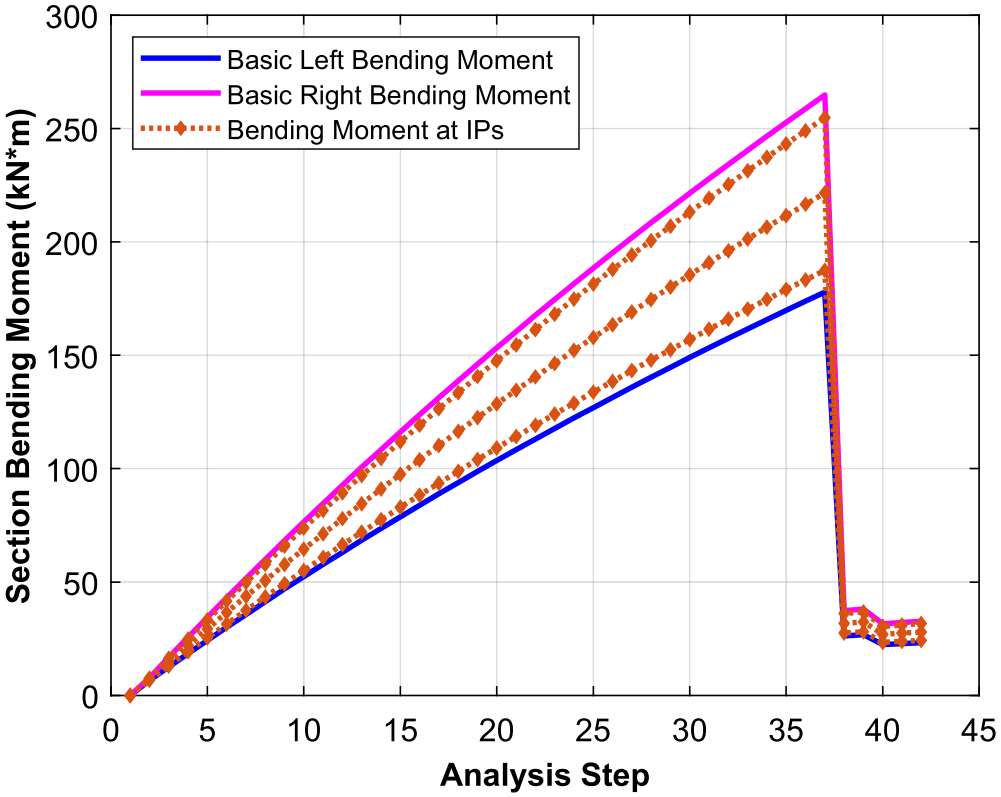


Figure B.11: History of Bending Moments obtained in the EB elements for Beam FS0.

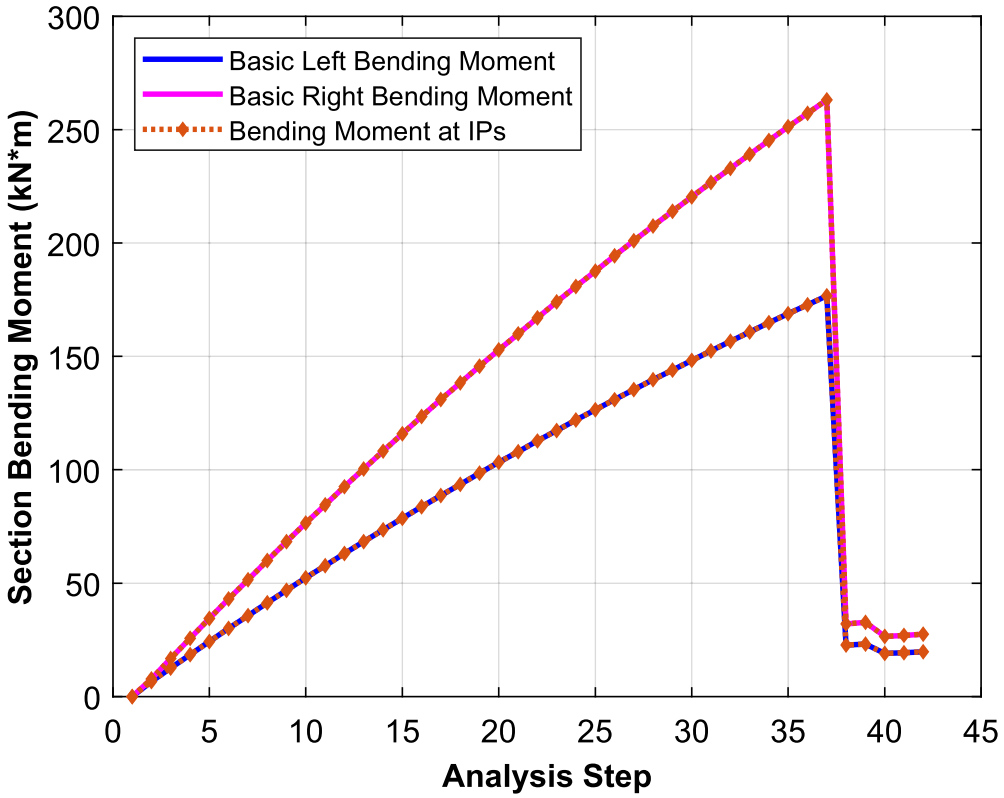


Figure B.12: History of Bending Moments obtained in the ENH EB elements for Beam FS0.

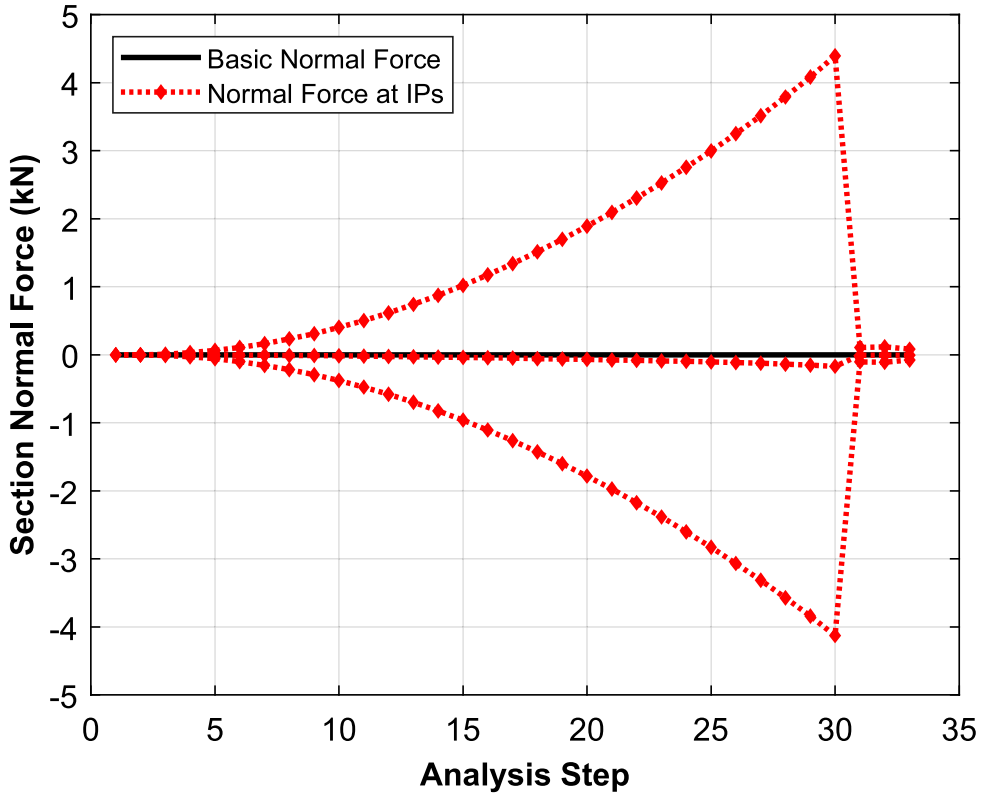


Figure B.13: History of normal forces obtained in the EB elements for Beam HS01.

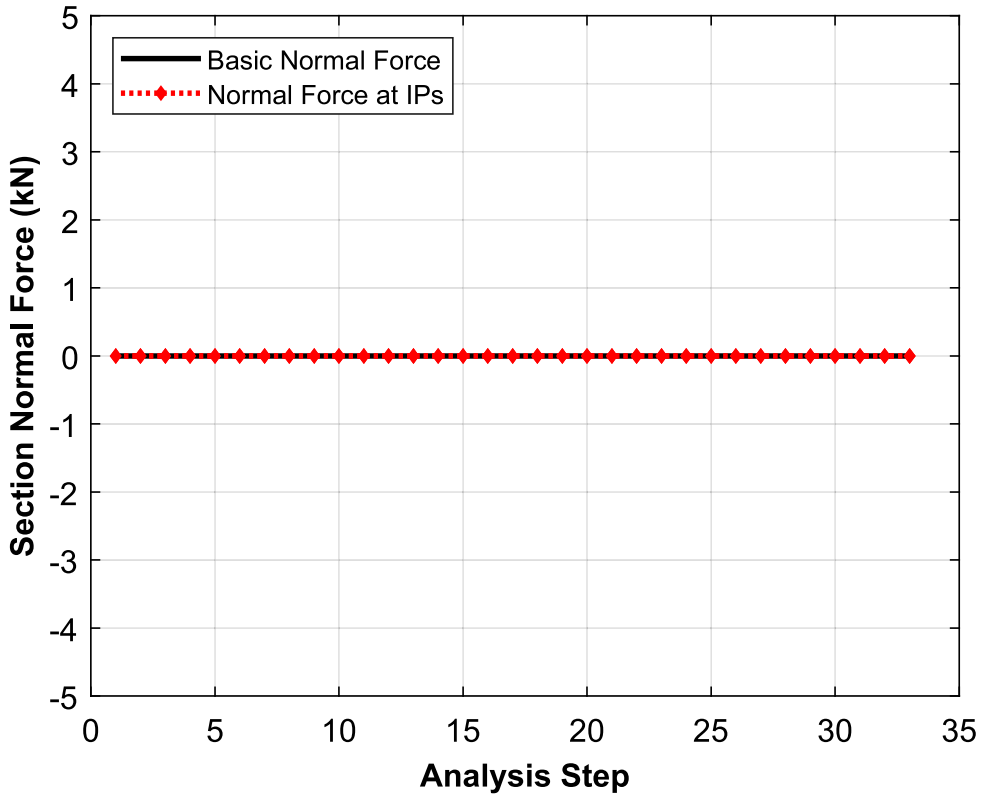


Figure B.14: History of normal forces obtained in the ENH EB elements for Beam HS01.

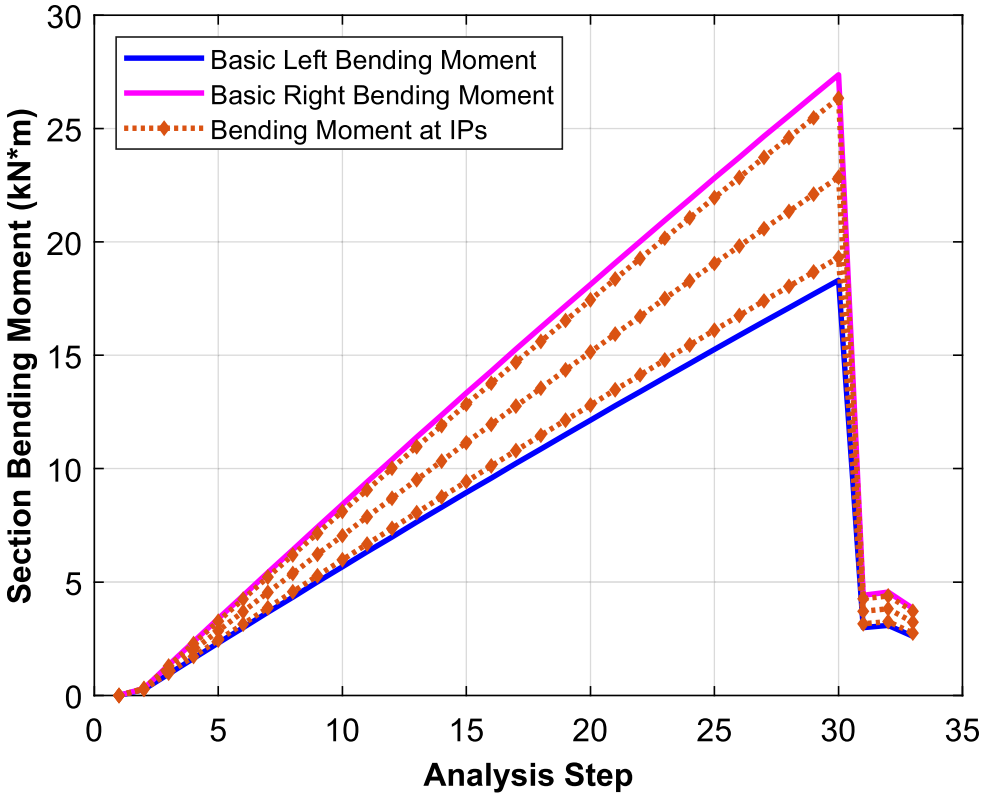


Figure B.15: History of Bending Moments obtained in the EB elements for Beam HS01.

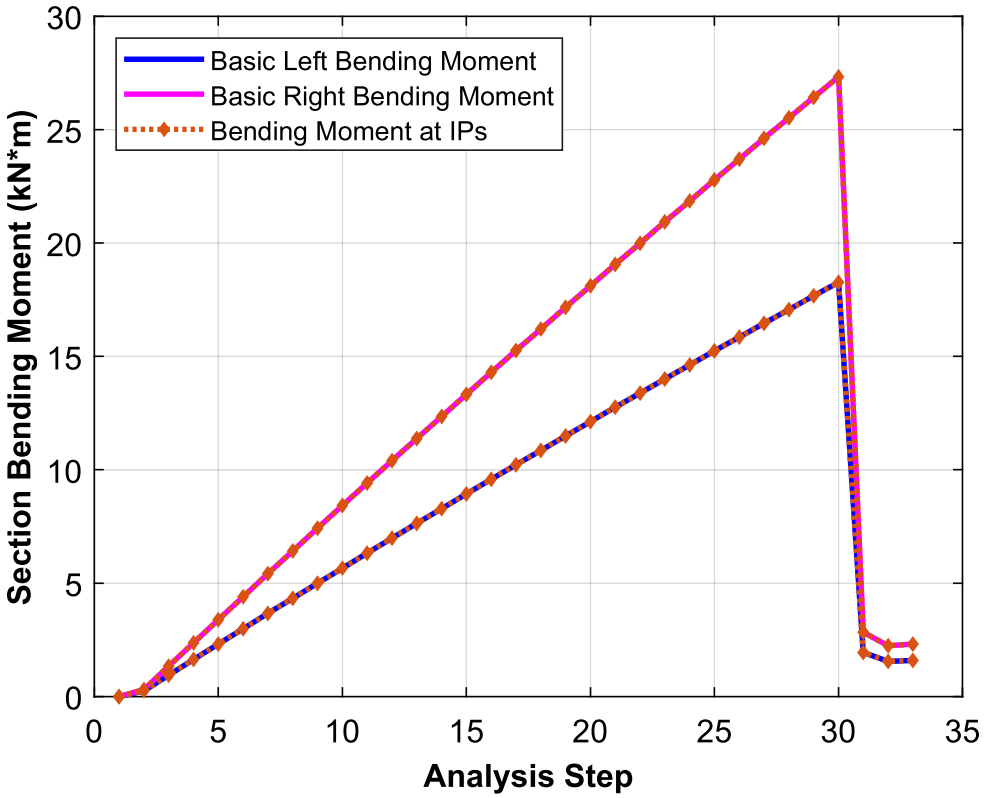


Figure B.16: History of Bending Moments obtained in the ENH EB elements for Beam HS01.

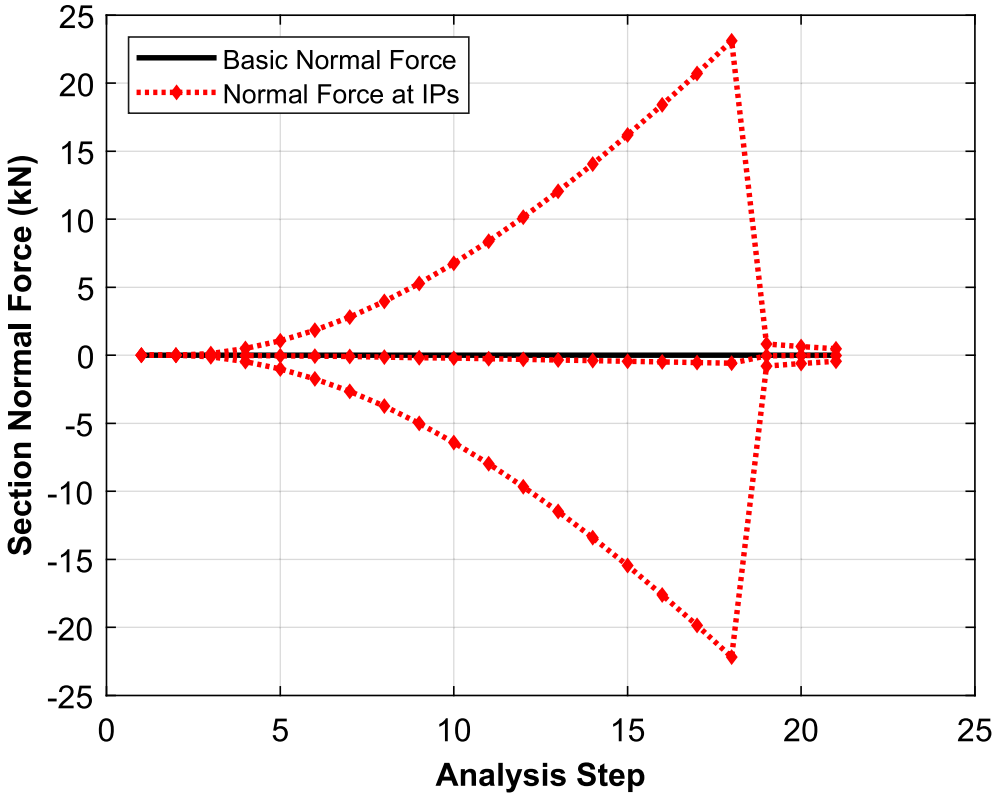


Figure B.17: History of normal forces obtained in the EB elements for Beam HS07.

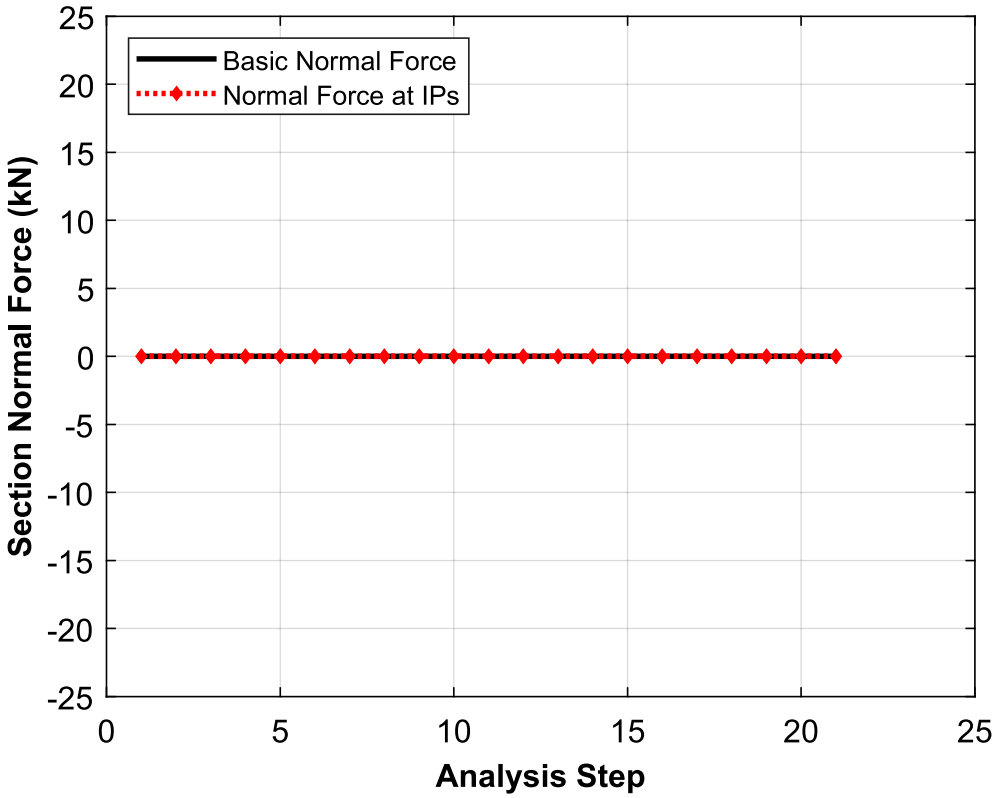


Figure B.18: History of normal forces obtained in the ENH EB elements for Beam HS07.

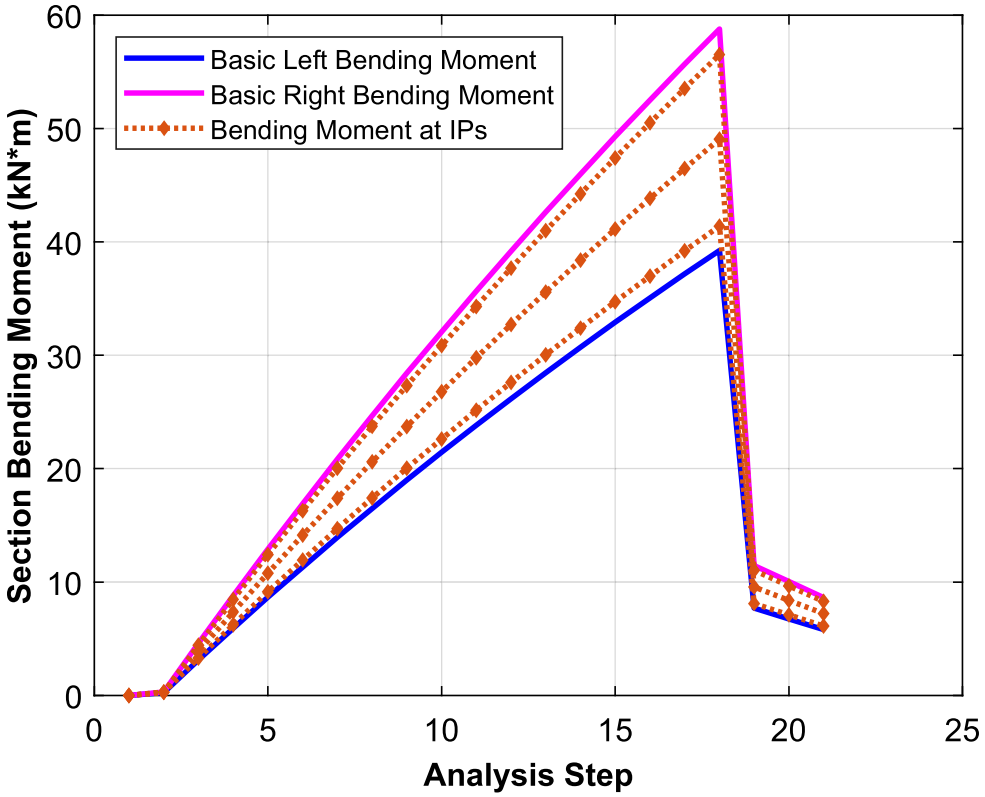


Figure B.19: History of Bending Moments obtained in the EB elements for Beam HS07.

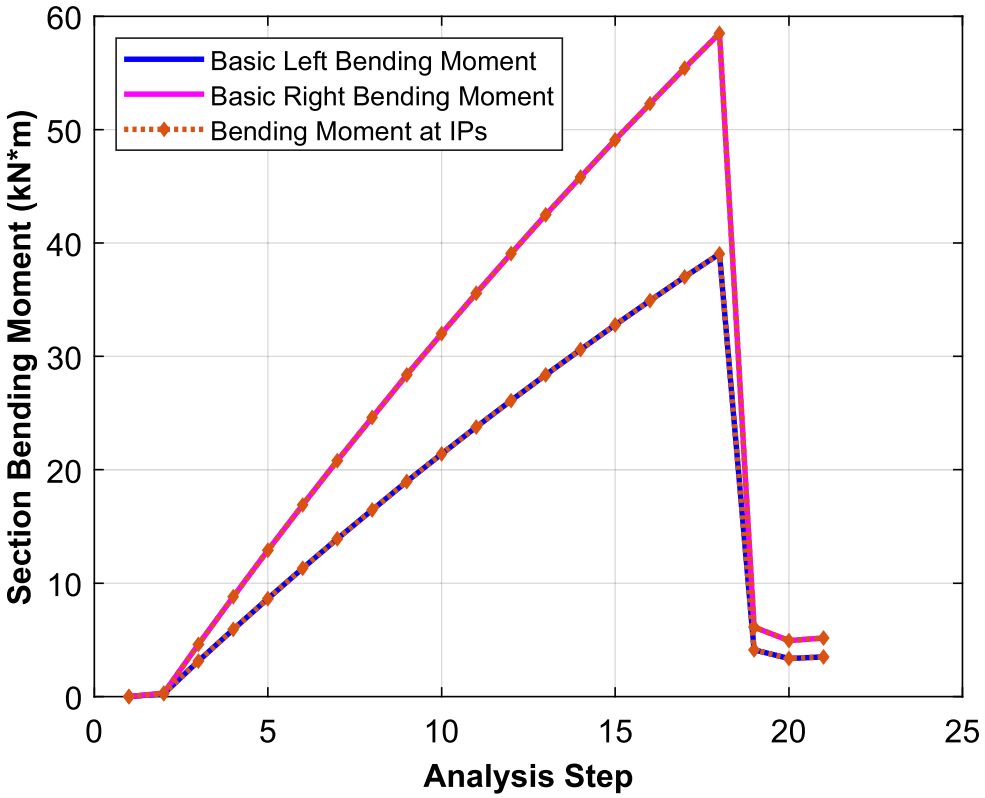


Figure B.20: History of Bending Moments obtained in the ENH EB elements for Beam HS07.

Appendix C

In this Appendix, complementary results related to the study cases analysed in section 5.2 are presented. These results represents the scenario of using well-posed tangent stiffness. The results of using an exponent value of $r = 2$ in the problem described in subsection 5.2.1 are presented in Figs. C.1 to C.6. The results related to the use of a consistent tangent stiffness matrix analysed in subsection 5.2.2 and subsection 5.2.3 are plotted in Figs. C.7 to C.11 and Figs. C.13 to C.17, respectively.

C.1 Single DOF System

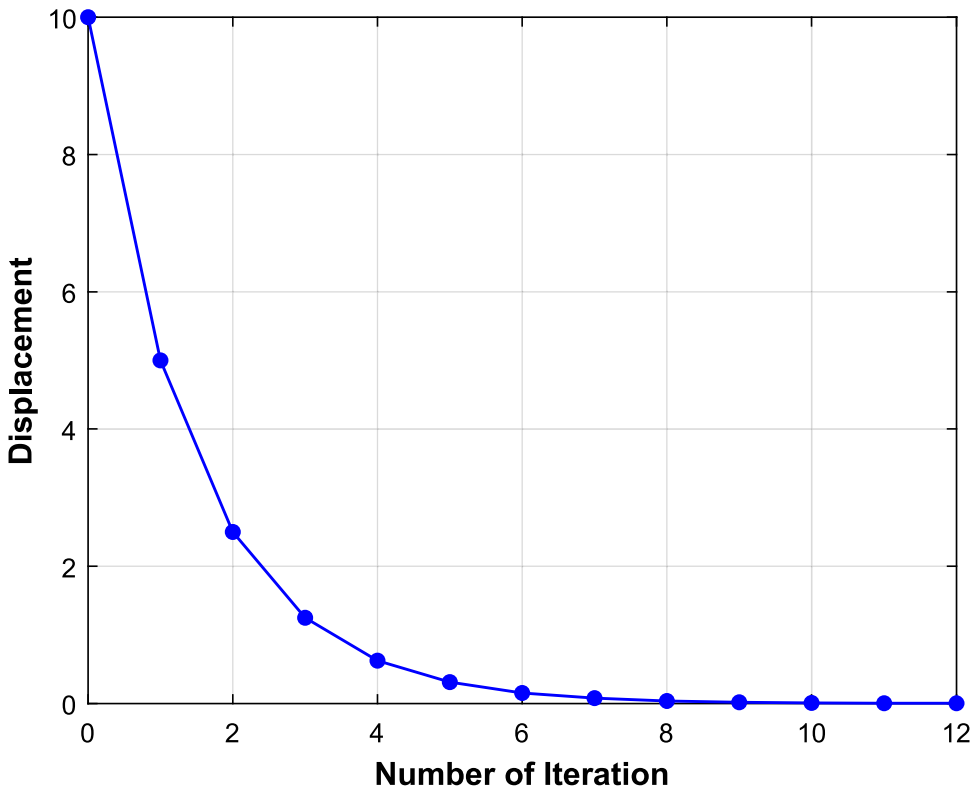


Figure C.1: Newton-Raphson iterative equilibrium search for $r = 2$.

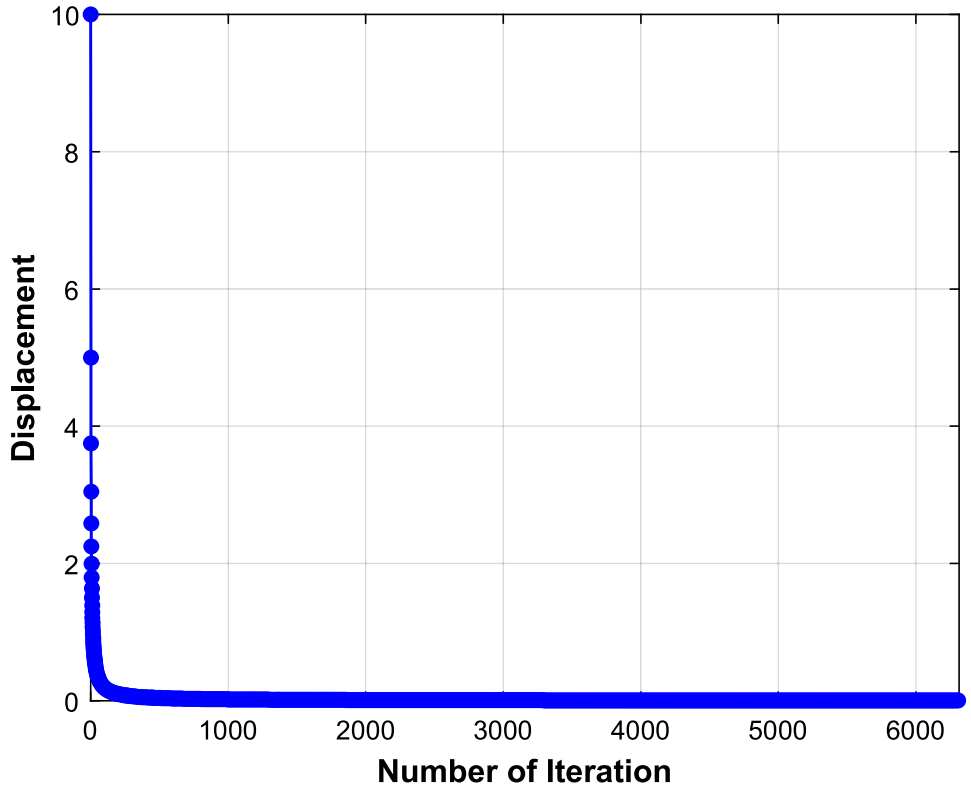


Figure C.2: Modified Newton-Raphson iterative equilibrium search for $r = 2$.

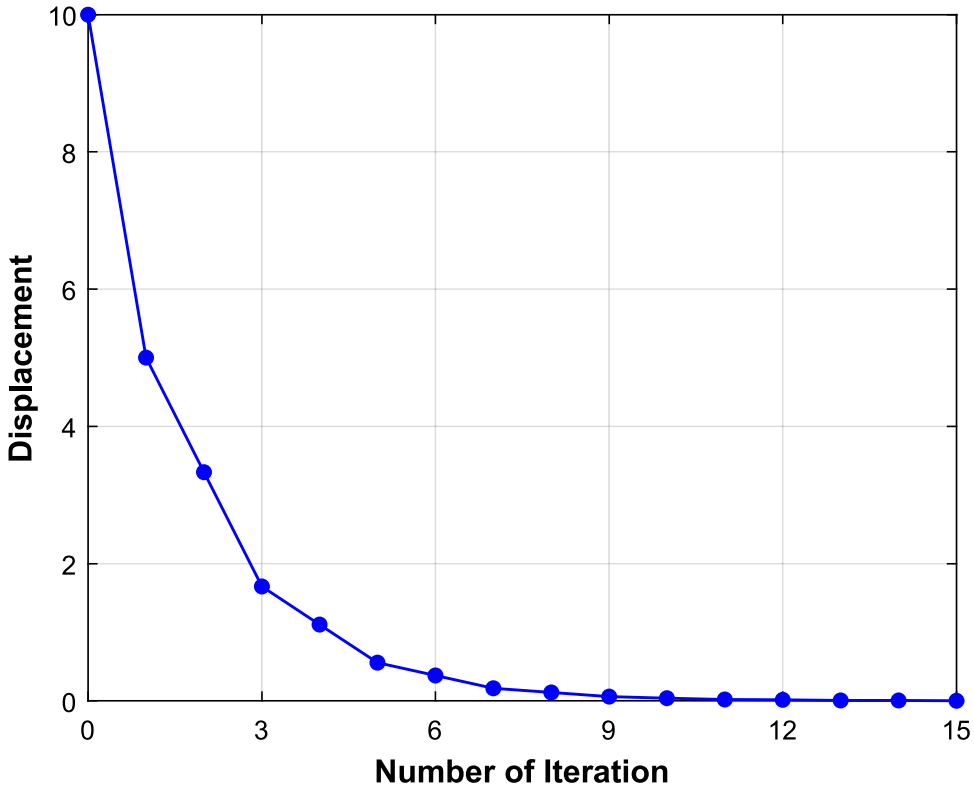


Figure C.3: Krylov-Newton iterative equilibrium search for $r = 2$.

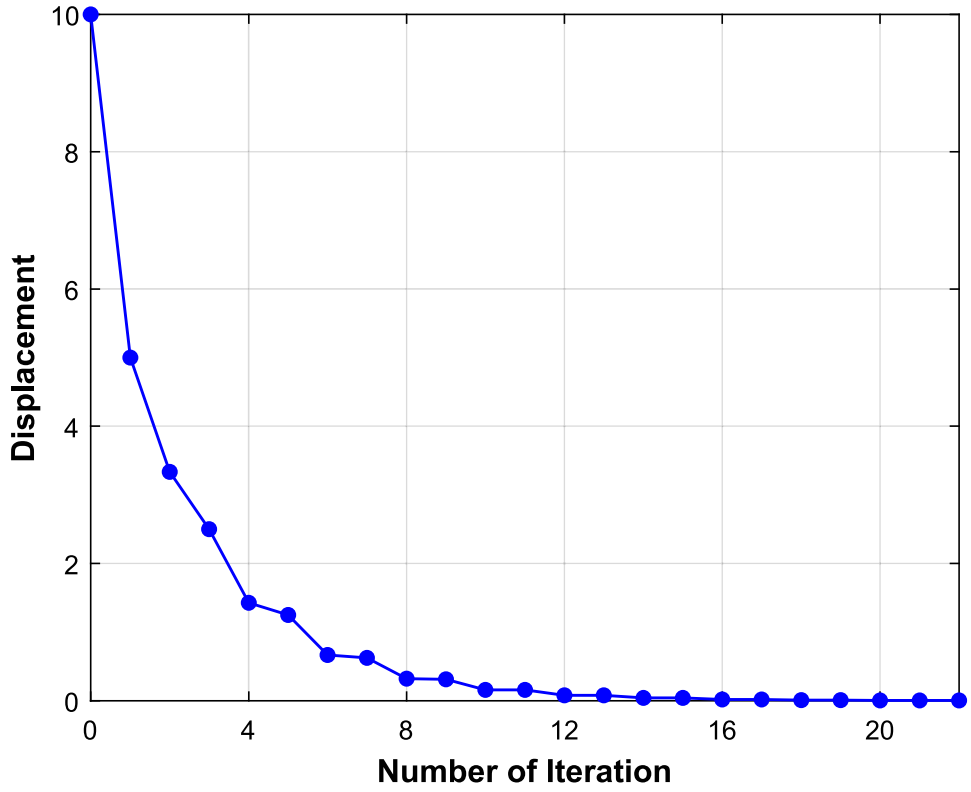


Figure C.4: Quasi Newton iterative equilibrium search with origin operator for $r = 2$.

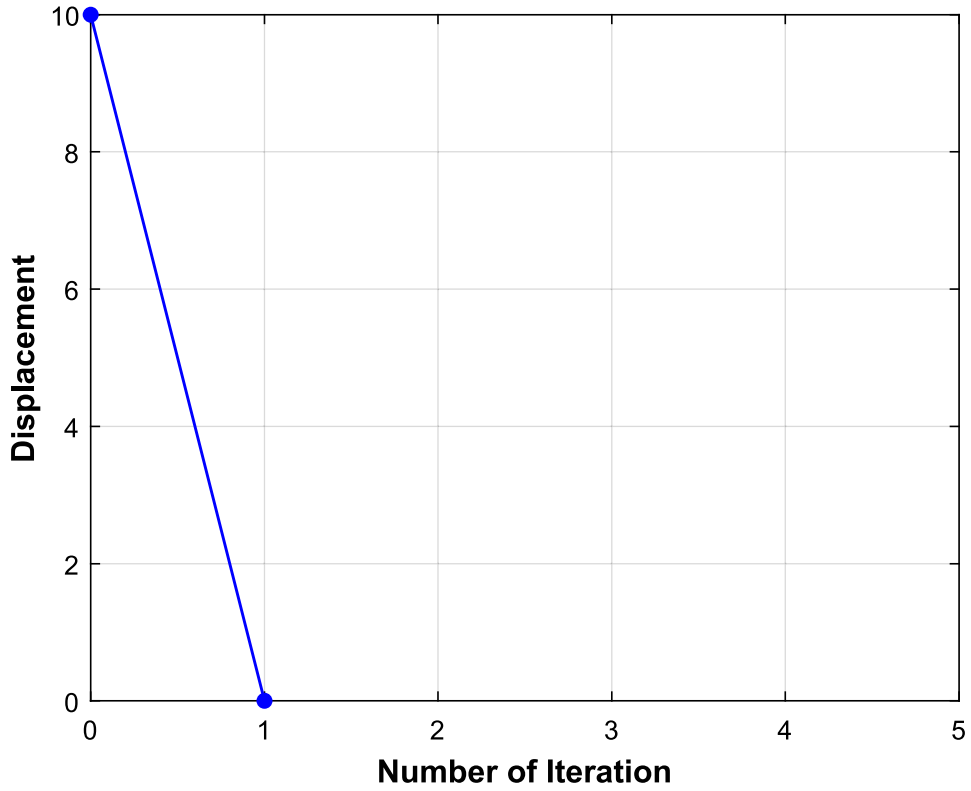


Figure C.5: Quasi Newton iterative equilibrium search with incremental operator for $r = 2$.

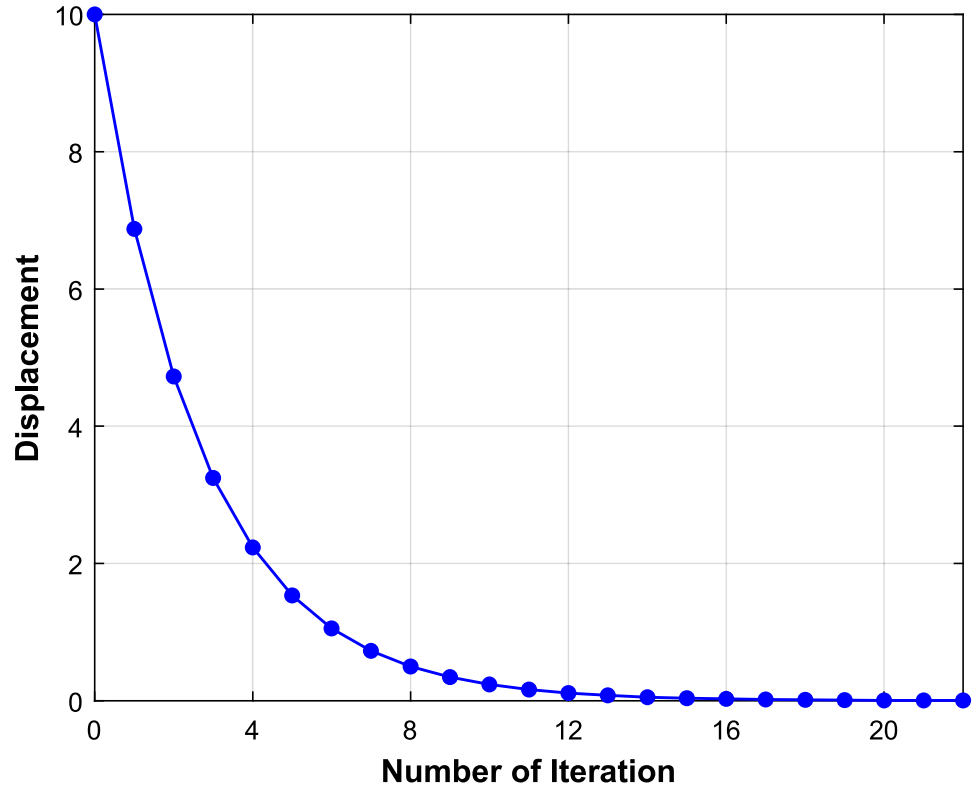


Figure C.6: Lyapunov iterative equilibrium search for $r = 2$.

C.2 Two DOF System with Two Springs

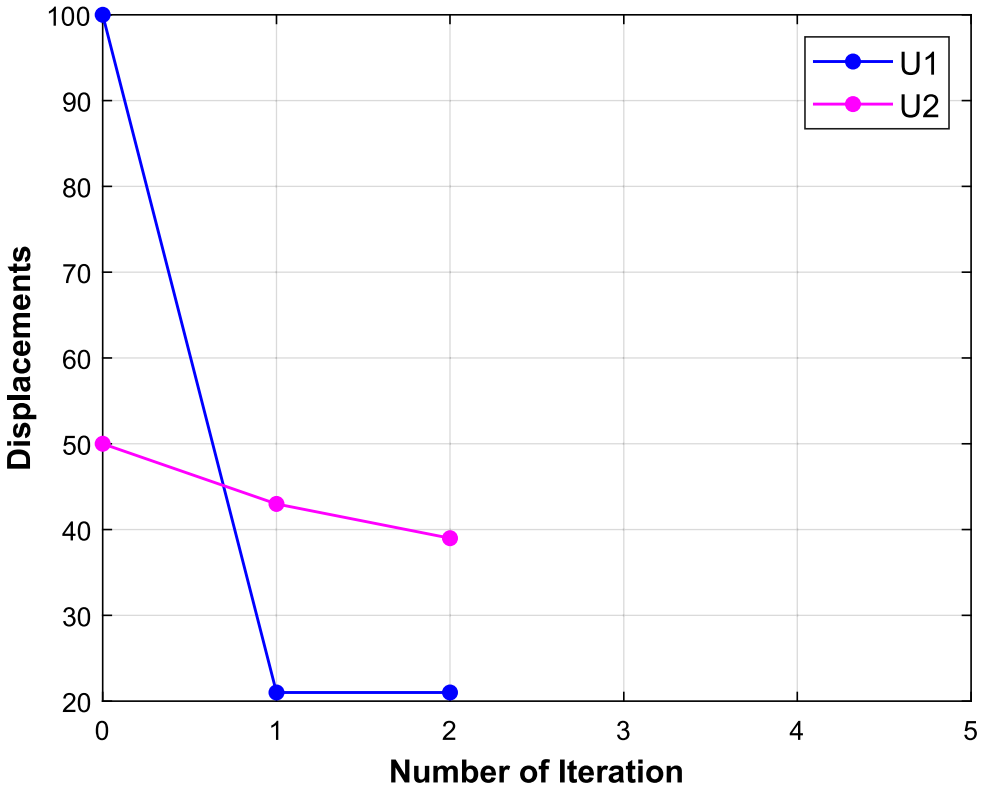


Figure C.7: Newton-Raphson iterative equilibrium search for consistent Jacobian matrix.

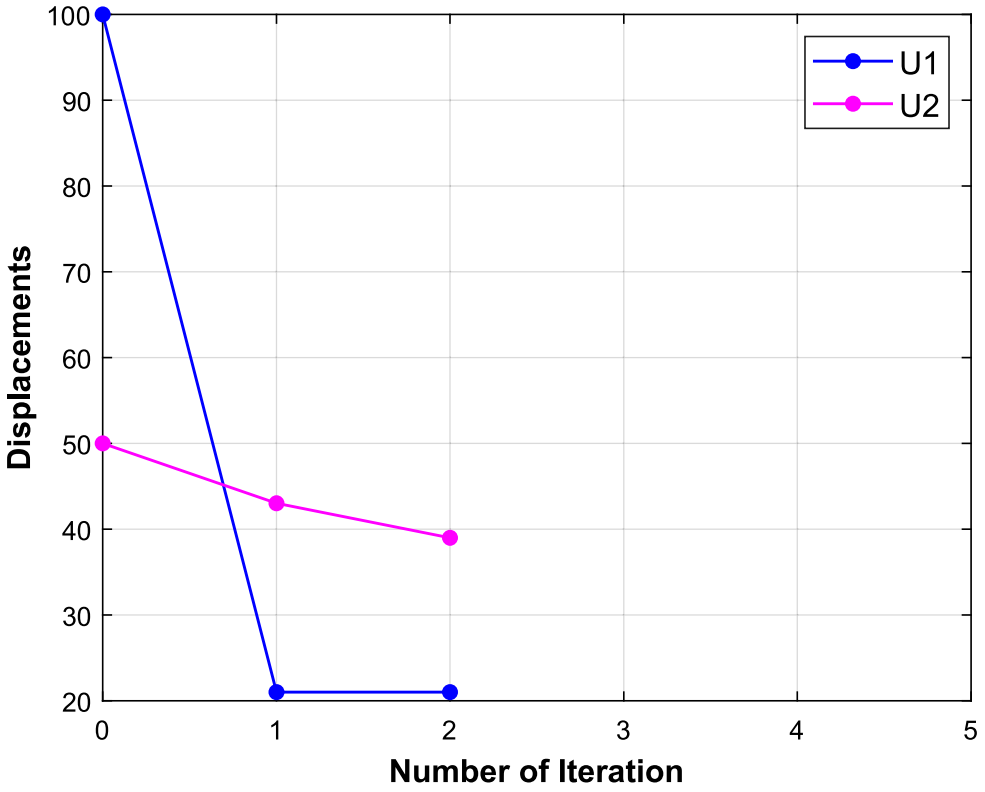


Figure C.8: Modified Newton-Raphson iterative equilibrium search for consistent Jacobian matrix.

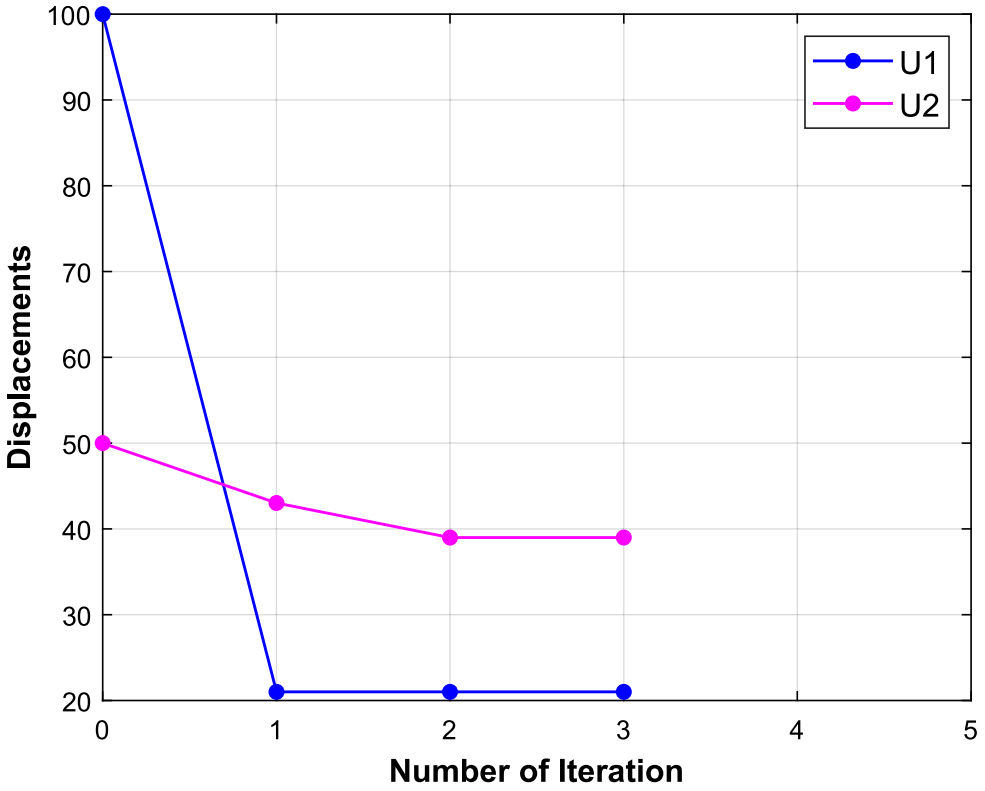


Figure C.9: Krylov-Newton iterative equilibrium search for consistent Jacobian matrix.

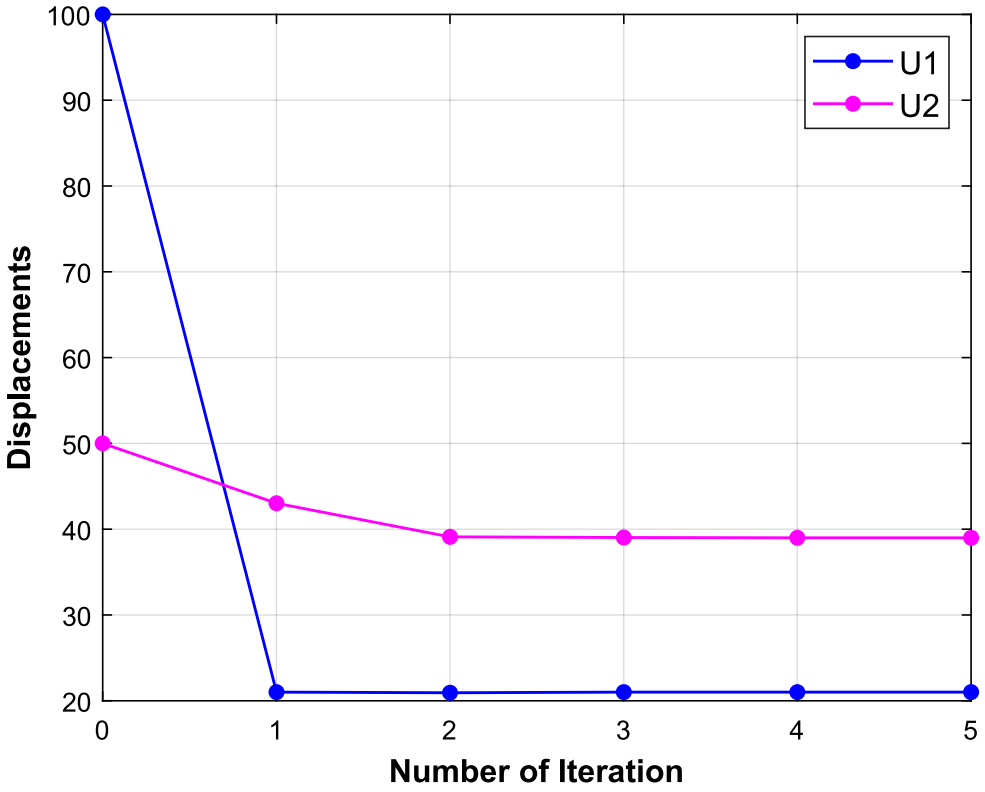


Figure C.10: Quasi Newton iterative equilibrium search with origin operator for consistent Jacobian matrix.

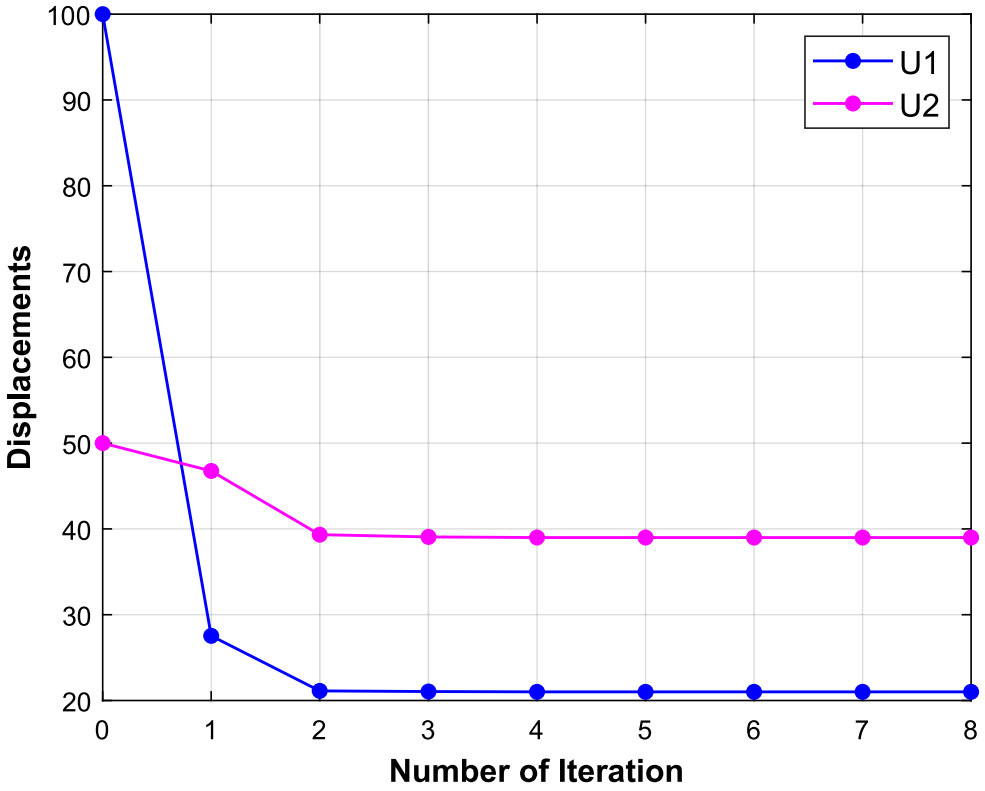


Figure C.11: Quasi Newton iterative equilibrium search with incremental operator for consistent Jacobian matrix.

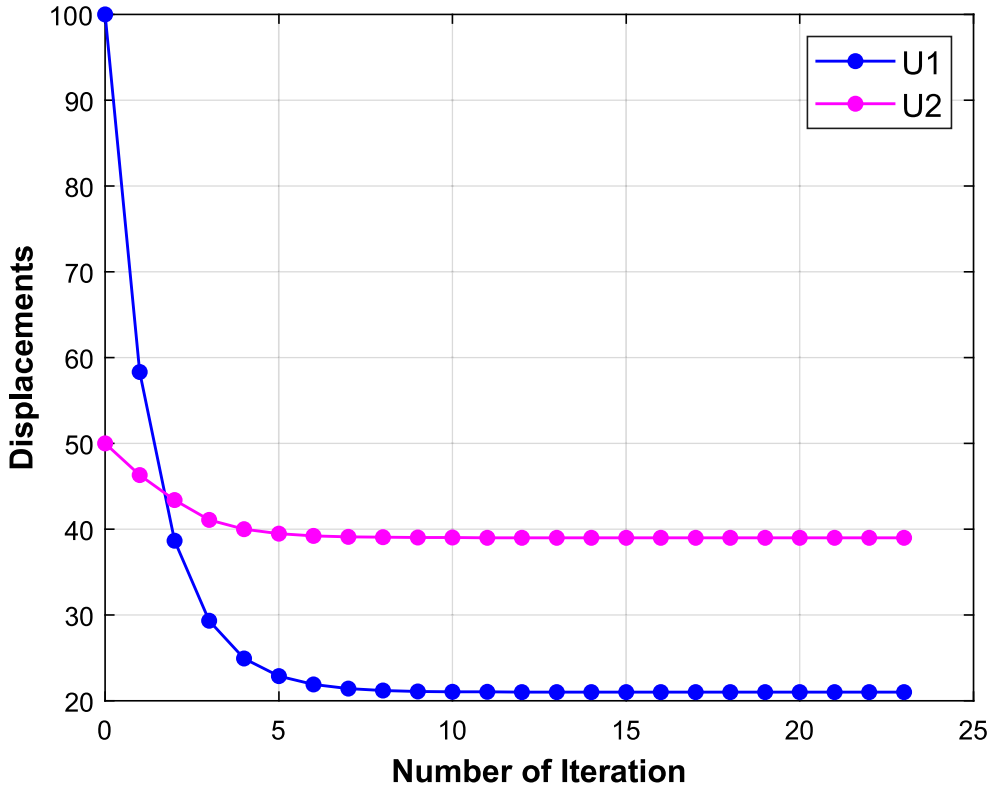


Figure C.12: Lyapunov iterative equilibrium search for consistent Jacobian matrix.

C.3 Two DOF System with Three Springs

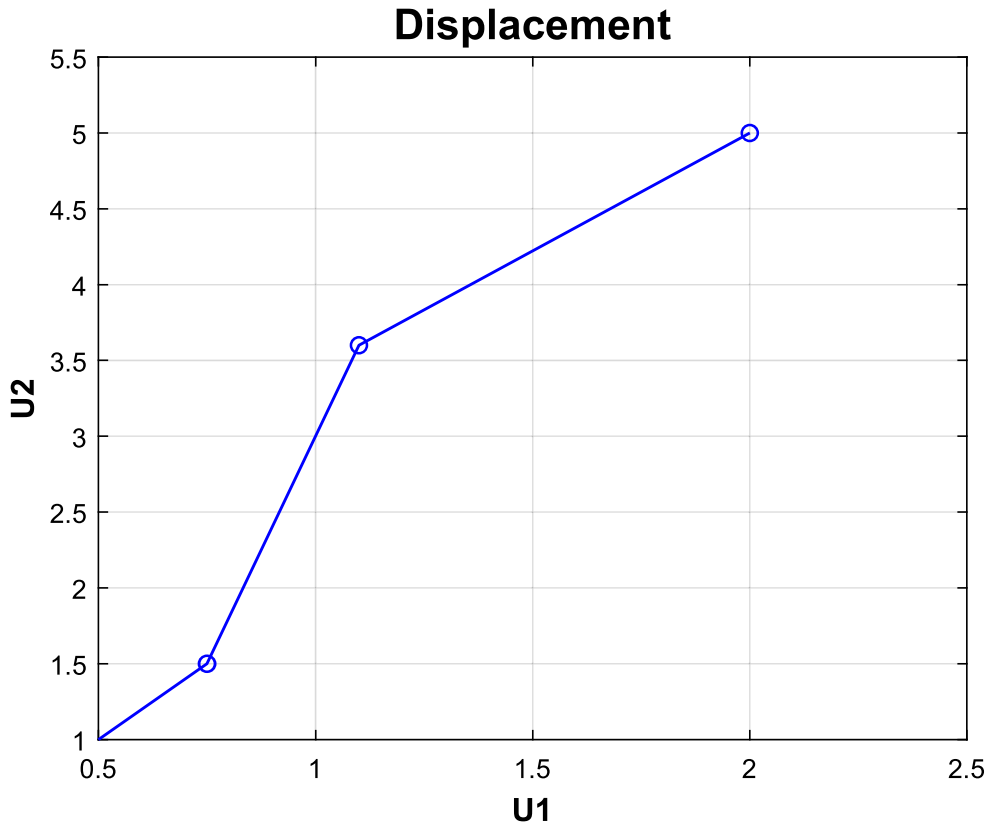


Figure C.13: Newton-Raphson iterative equilibrium search for inconsistent Jacobian matrix.

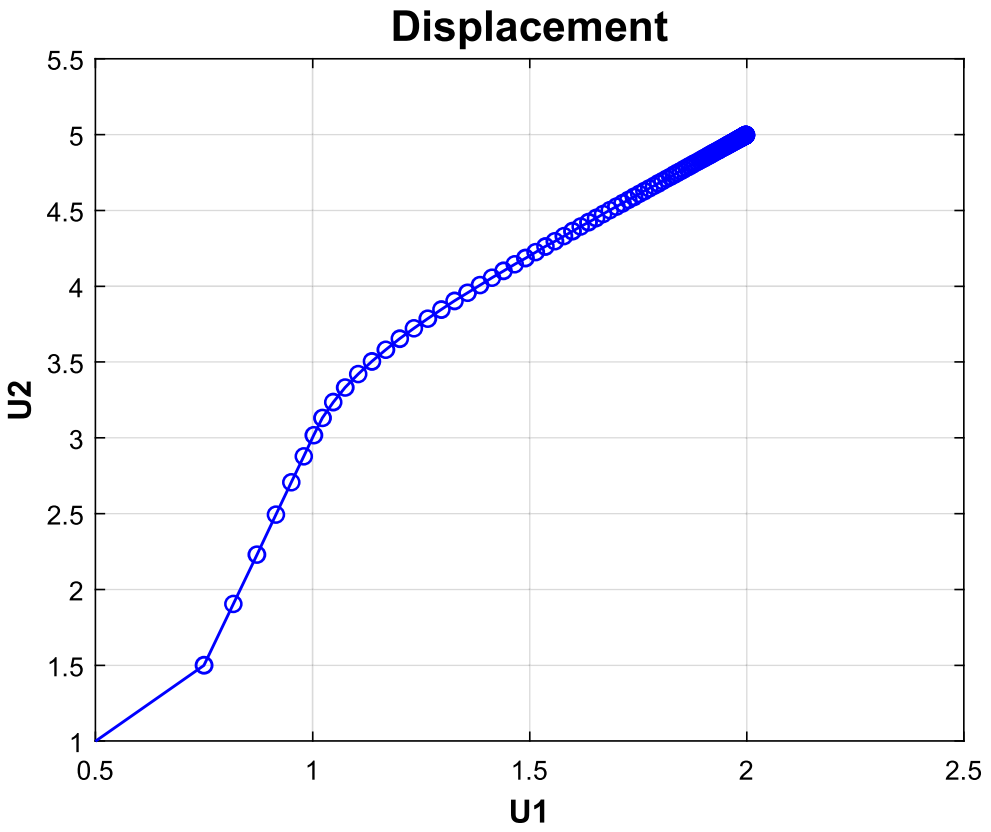


Figure C.14: Modified Newton-Raphson iterative equilibrium search for inconsistent Jacobian matrix.

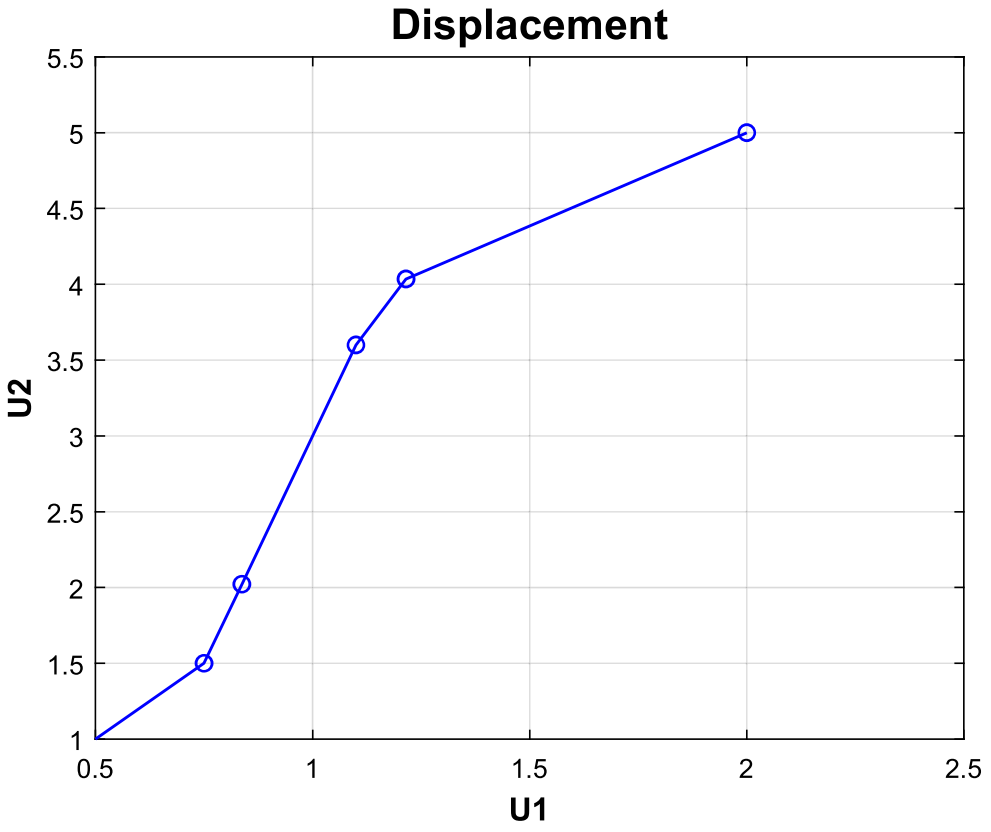


Figure C.15: Krylov-Newton iterative equilibrium search for inconsistent Jacobian matrix.

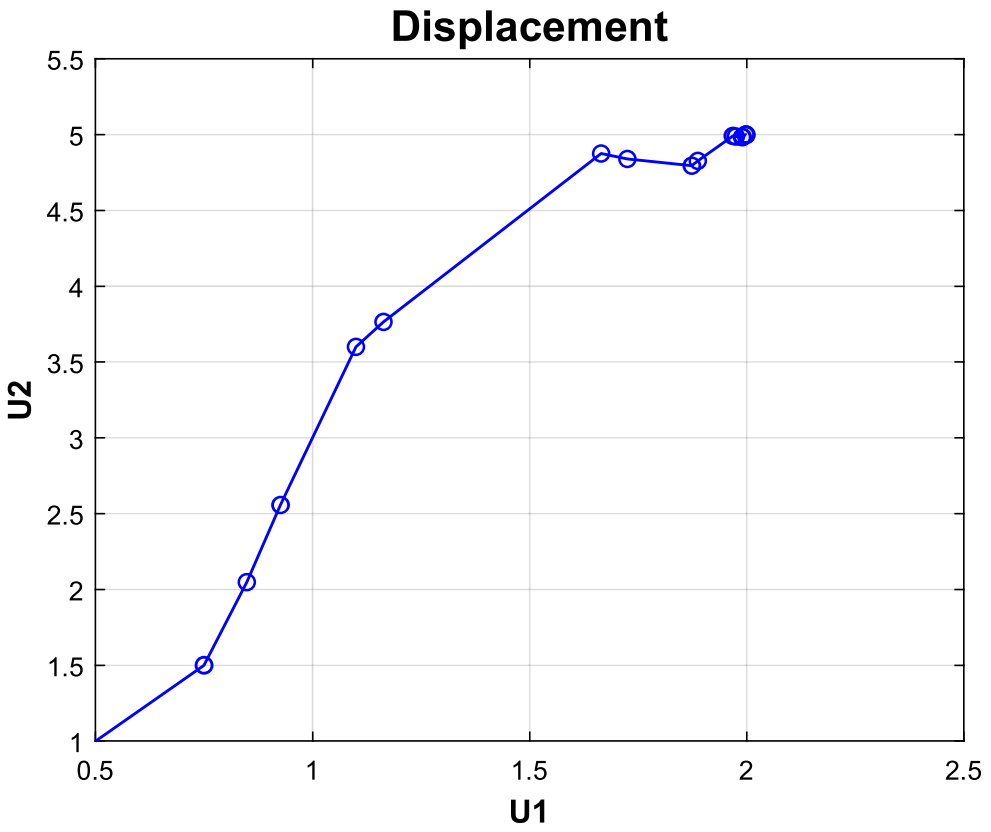


Figure C.16: Quasi Newton iterative equilibrium search with origin operator for inconsistent Jacobian matrix.

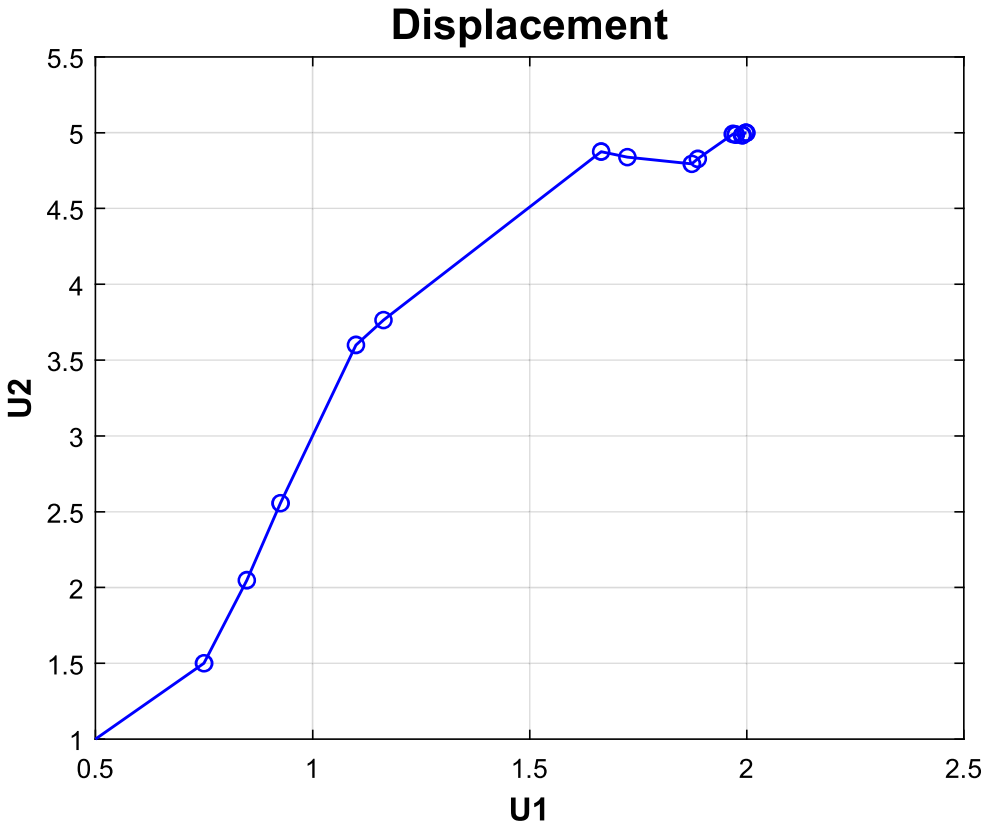


Figure C.17: Quasi Newton iterative equilibrium search with incremental operator for inconsistent Jacobian matrix.

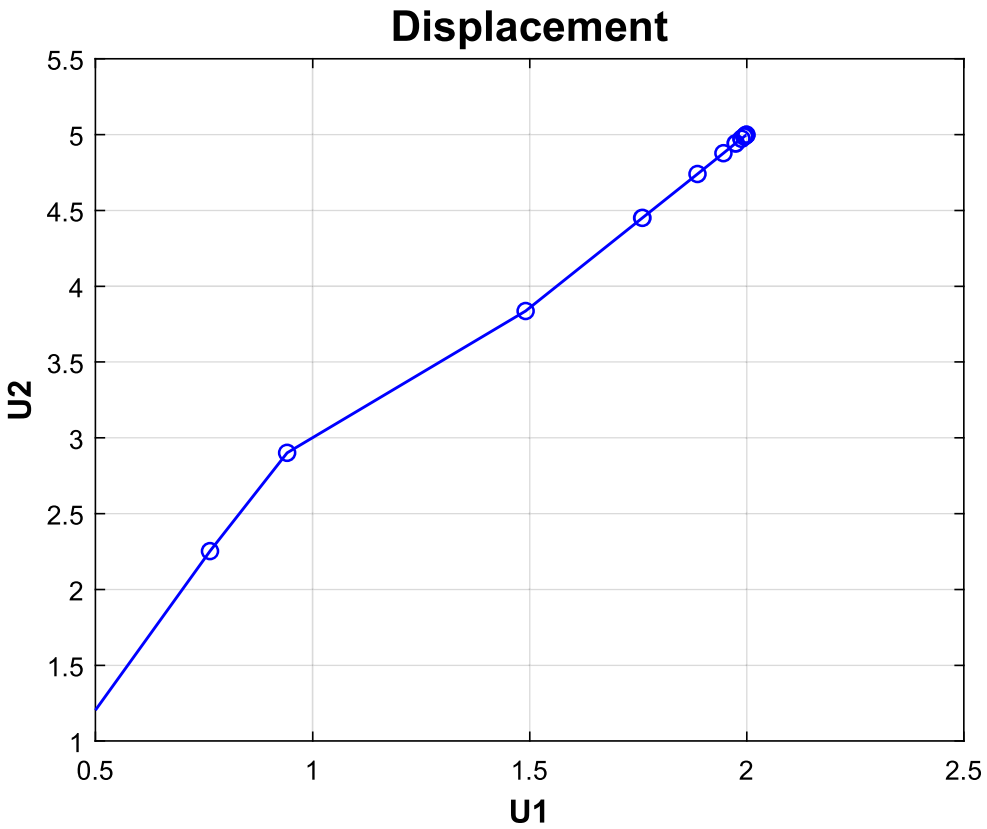


Figure C.18: Lyapunov iterative equilibrium search for inconsistent Jacobian matrix.

Appendix D

Here are presented the complementary results related to the validation example in subsection 6.4.3. To attest the numerical performance offered by the enhanced formulation of the traditional Euler-Bernoulli and Timoshenko beam-column element, denominated as ENH EB and ENH TB, respectively, the obtained history of the basic normal force and bending moment values of one of the most strained elements and the history of the section normal force and bending moment values obtained at the integration Points (IPs) used in each formulation are plotted in Figs. B.1 to B.4. Regarding the modified integration rule adopted for the enhanced strain formulations, two integration points located at the two ends points of the element are employed. In this analysis, the second element of the mesh was selected to have a meaningful overview of the results.

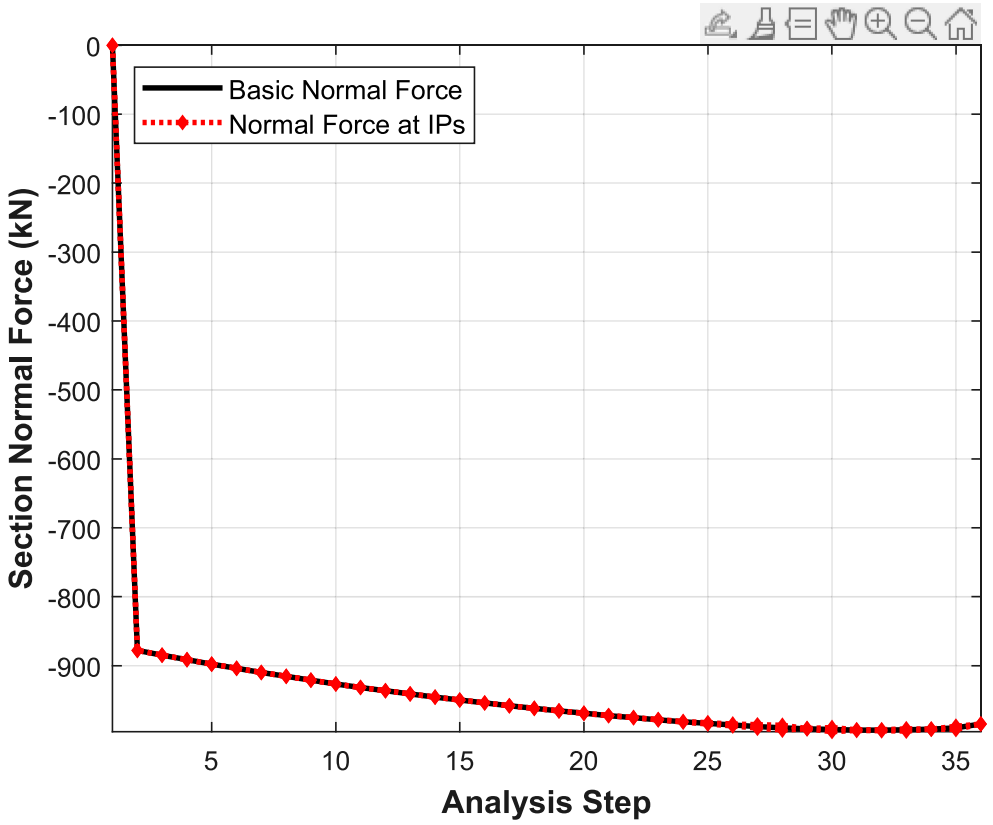


Figure D.1: History of normal forces obtained in the ENH EB elements for Beam B2 and f_{tu} =47.0 MPa.

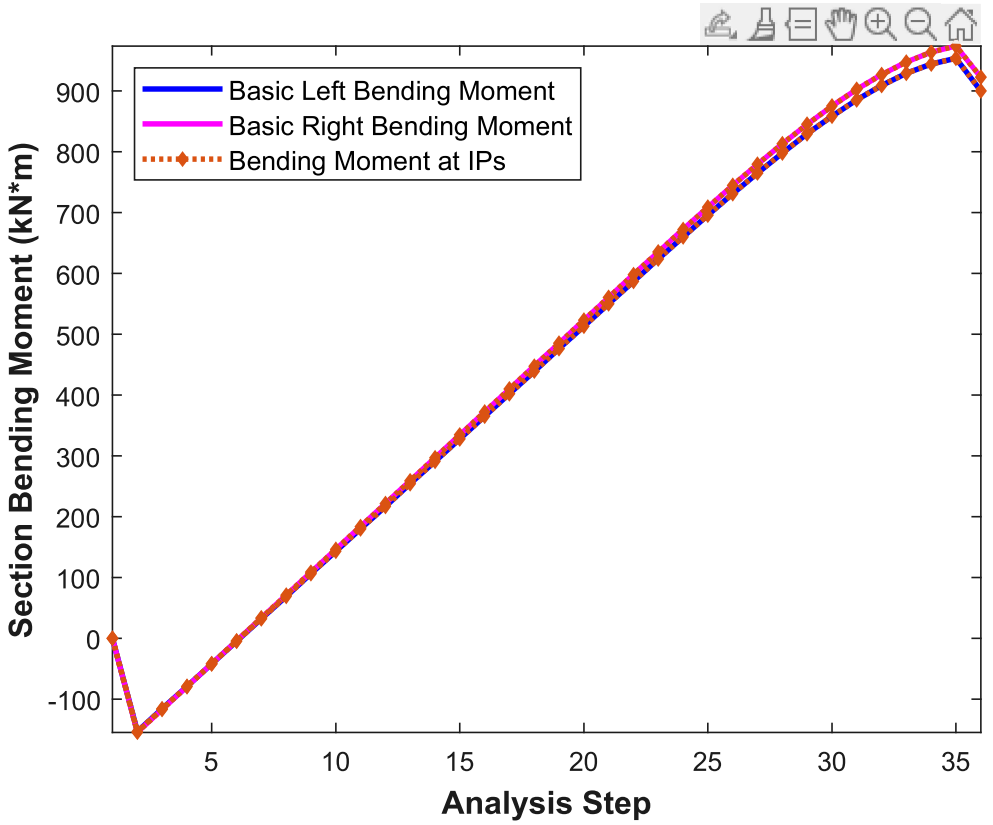


Figure D.2: History of Bending Moments obtained in the ENH EB elements for Beam B2 and f_{tu} =47.0 MPa.

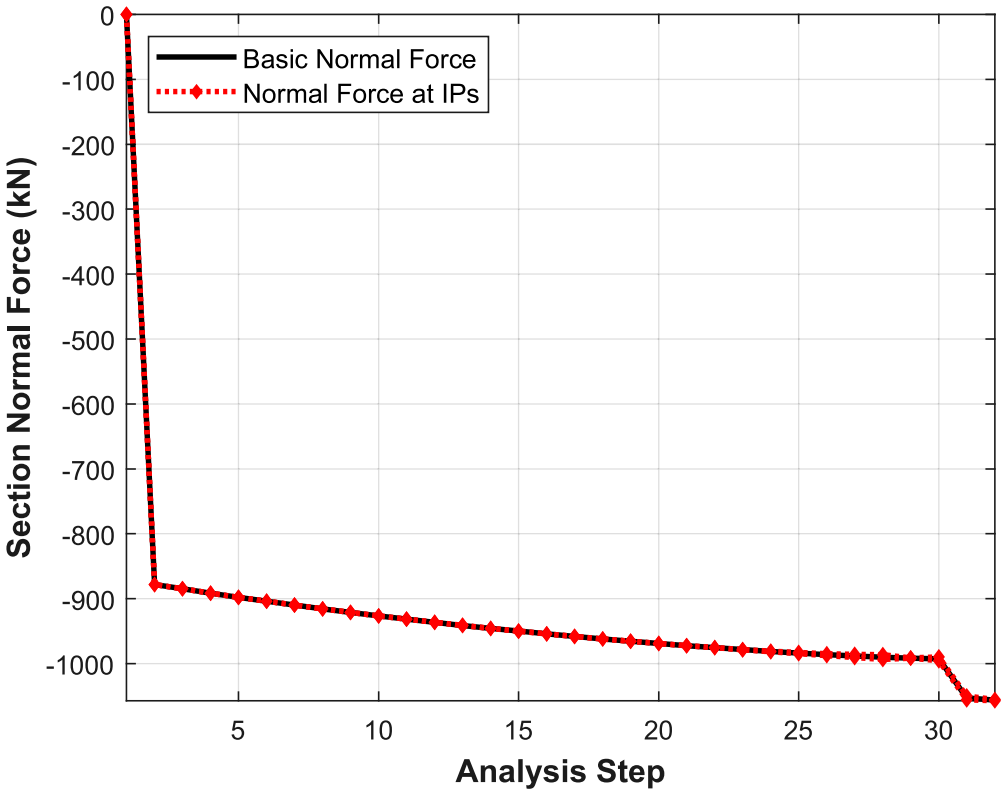


Figure D.3: History of normal forces obtained in the ENH EB elements for Beam B2 and f_{tu} =35.2 MPa.

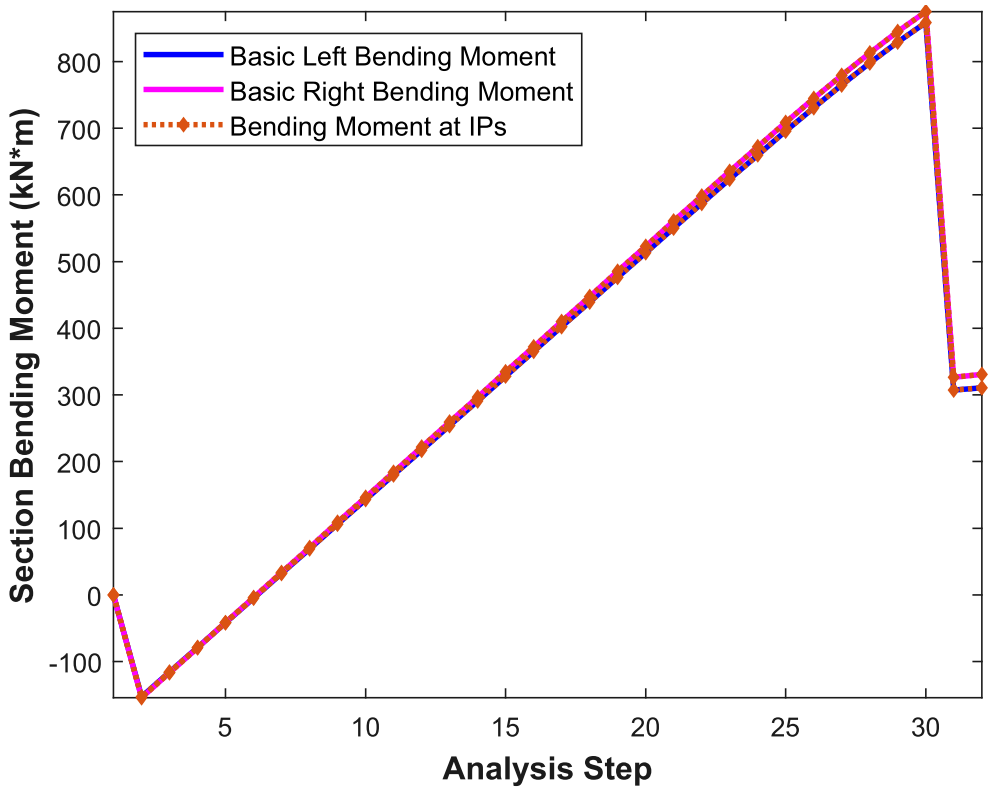


Figure D.4: History of Bending Moments obtained in the ENH EB elements for Beam B2 and f_{tu} =35.2 MPa.

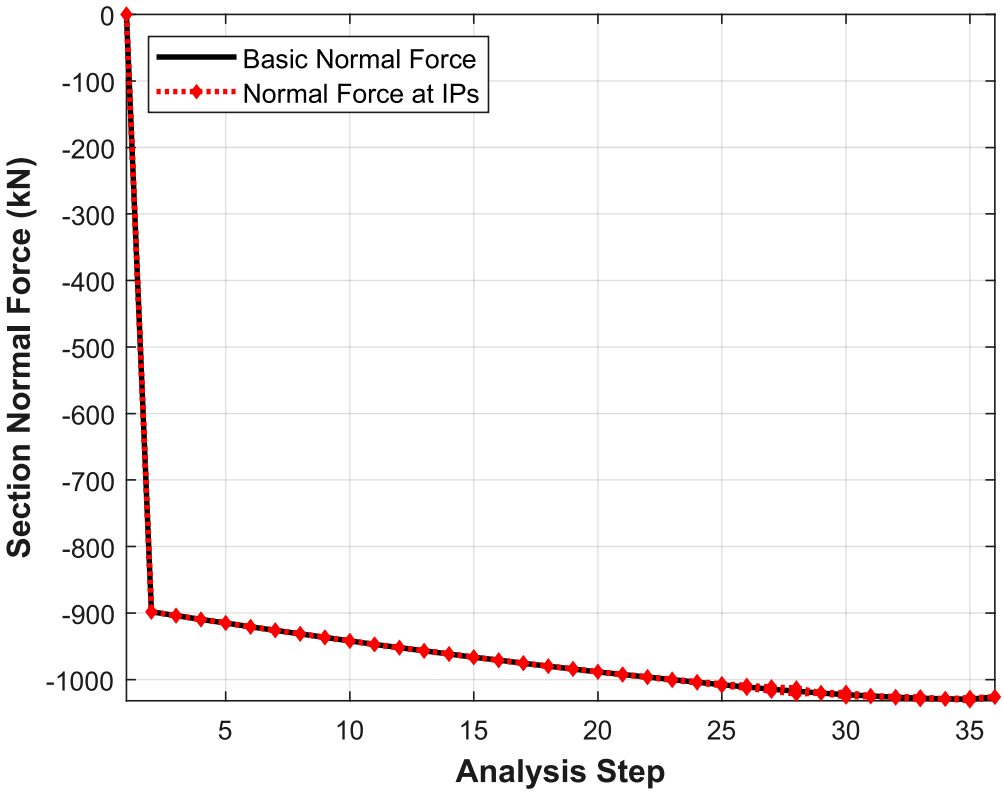


Figure D.5: History of normal forces obtained in the ENH EB elements for Beam B3 and f_{tu} =47.0 MPa.

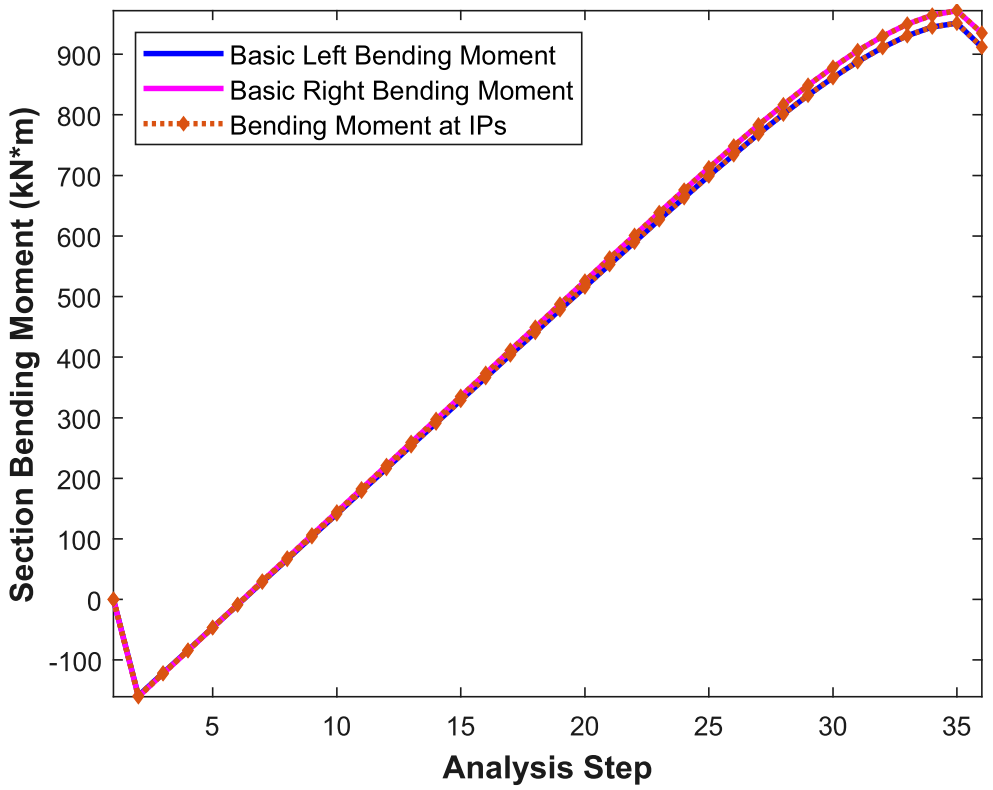


Figure D.6: History of Bending Moments obtained in the ENH EB elements for Beam B3 and f_{tu} =47.0 MPa.

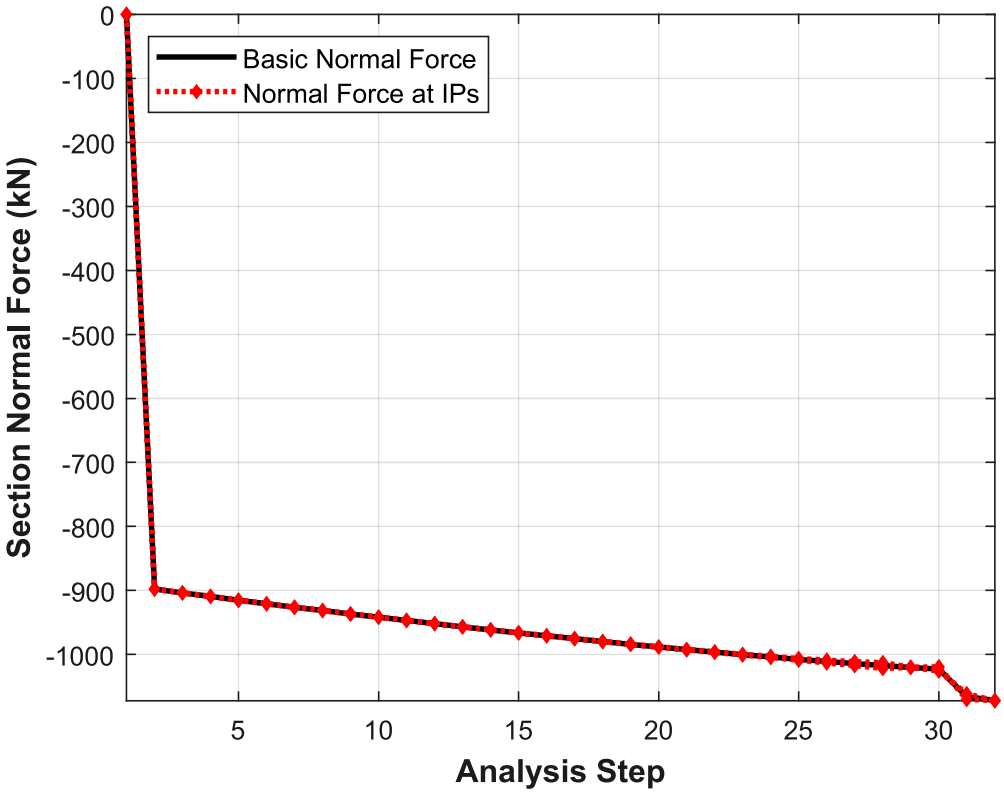


Figure D.7: History of normal forces obtained in the ENH EB elements for Beam B3 and f_{tu} =35.2 MPa.

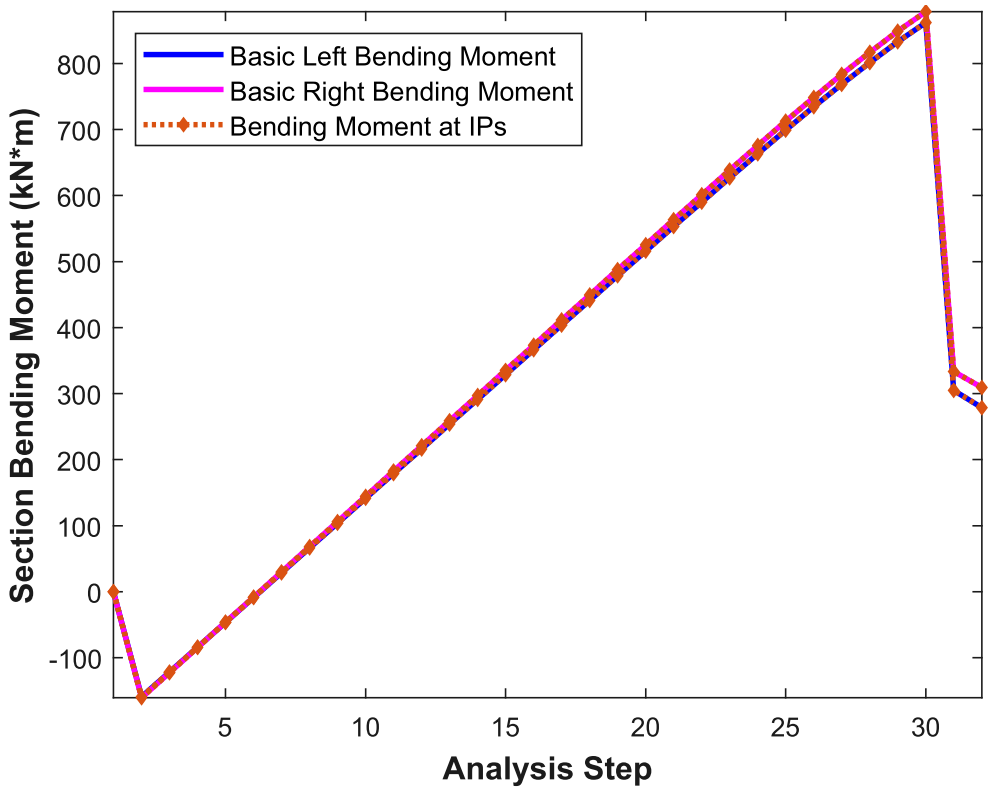


Figure D.8: History of Bending Moments obtained in the ENH EB elements for Beam B3 and f_{tu} =35.2 MPa.

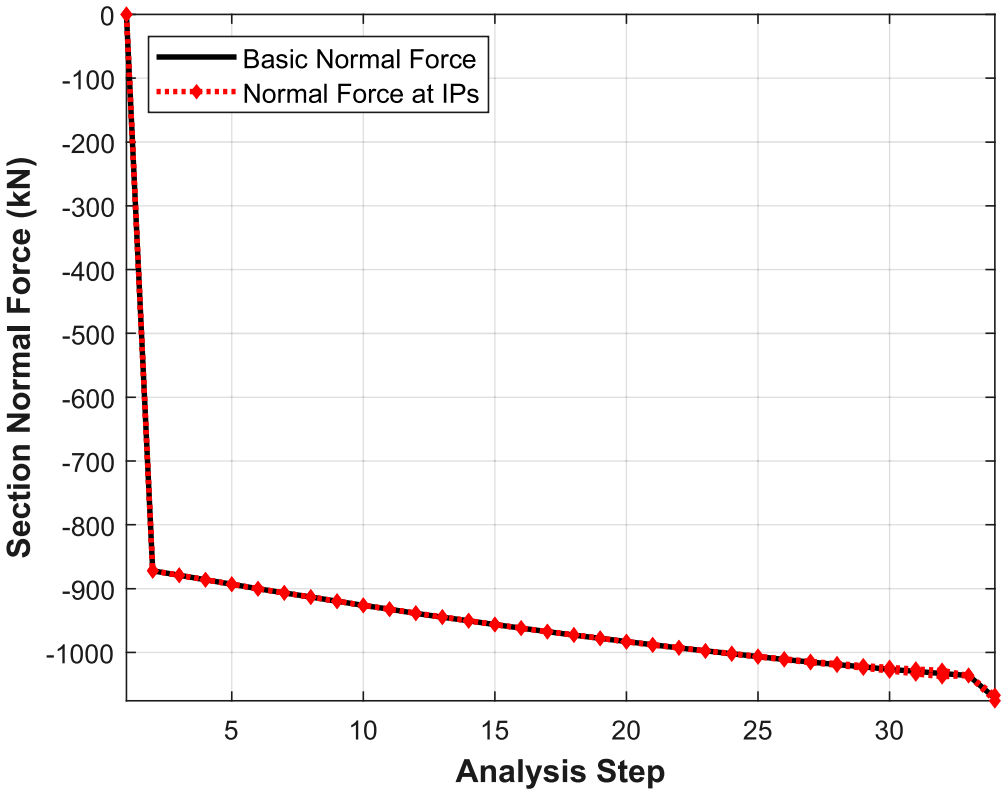


Figure D.9: History of normal forces obtained in the ENH EB elements for Beam B4 and f_{tu} =47.0 MPa.

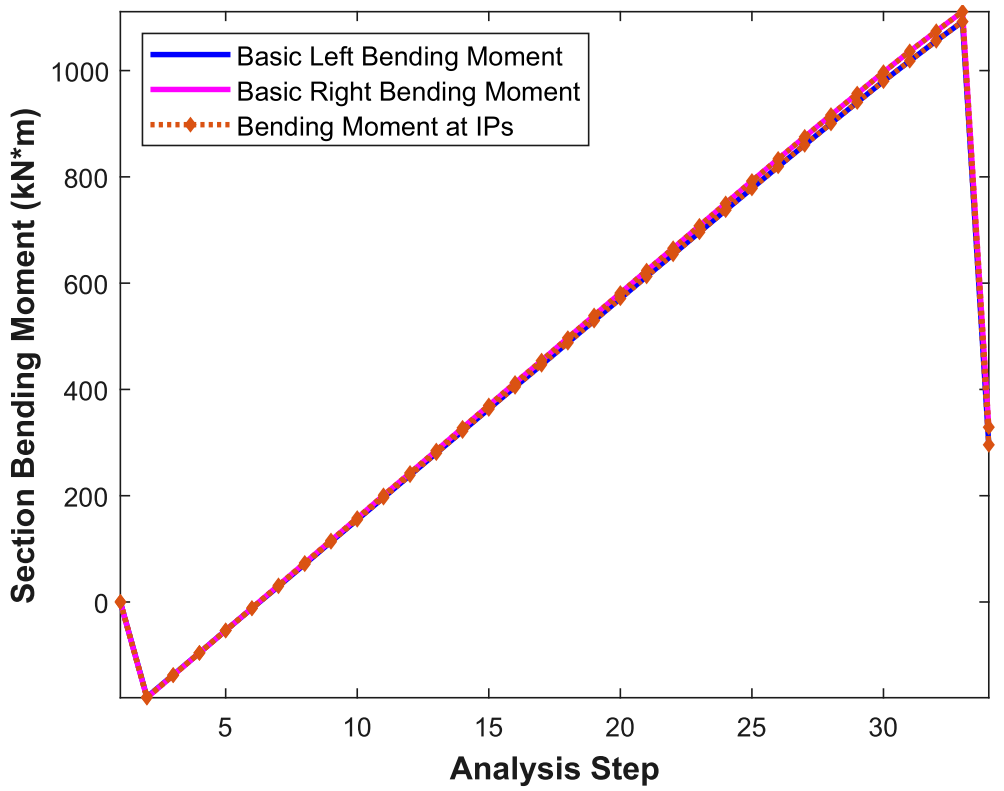


Figure D.10: History of Bending Moments obtained in the ENH EB elements for Beam B4 and f_{tu} =47.0 MPa.

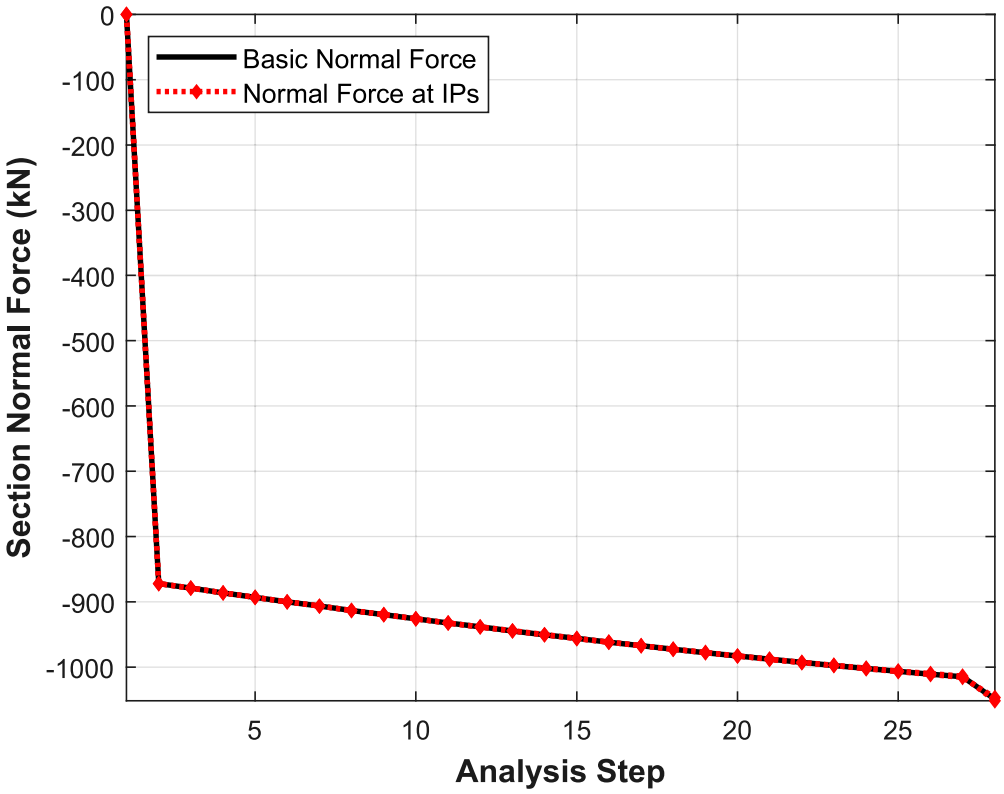


Figure D.11: History of normal forces obtained in the ENH EB elements for Beam B4 and f_{tu} =35.2 MPa.

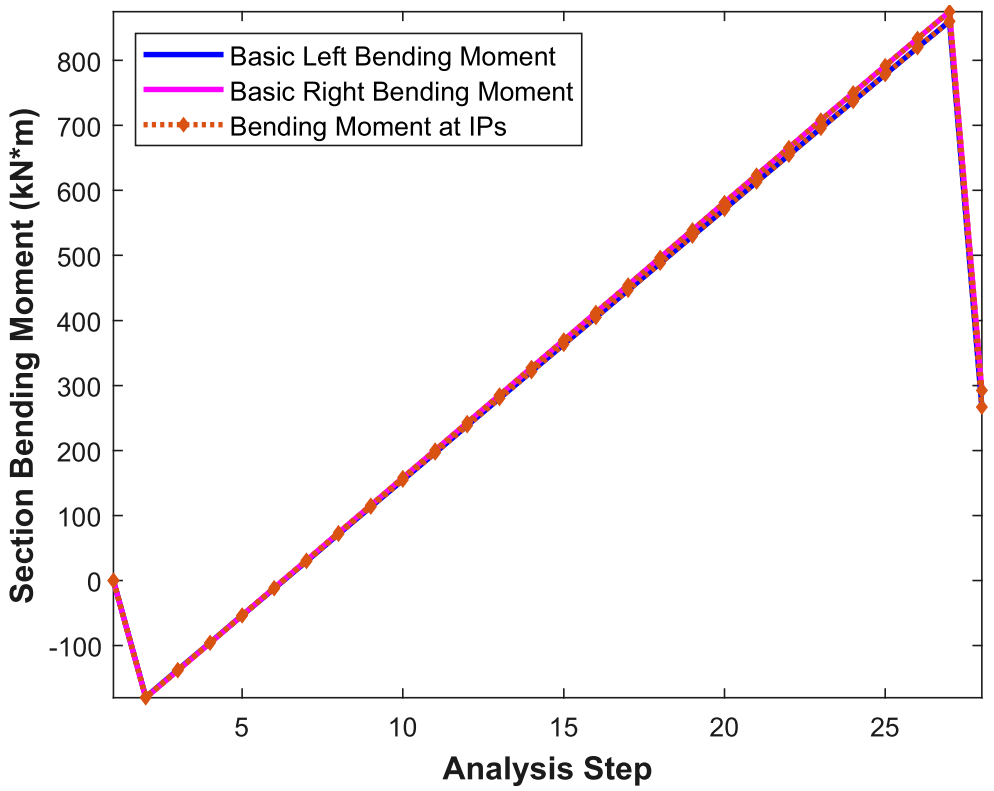


Figure D.12: History of Bending Moments obtained in the ENH EB elements for Beam B4 and f_{tu} =35.2 MPa.

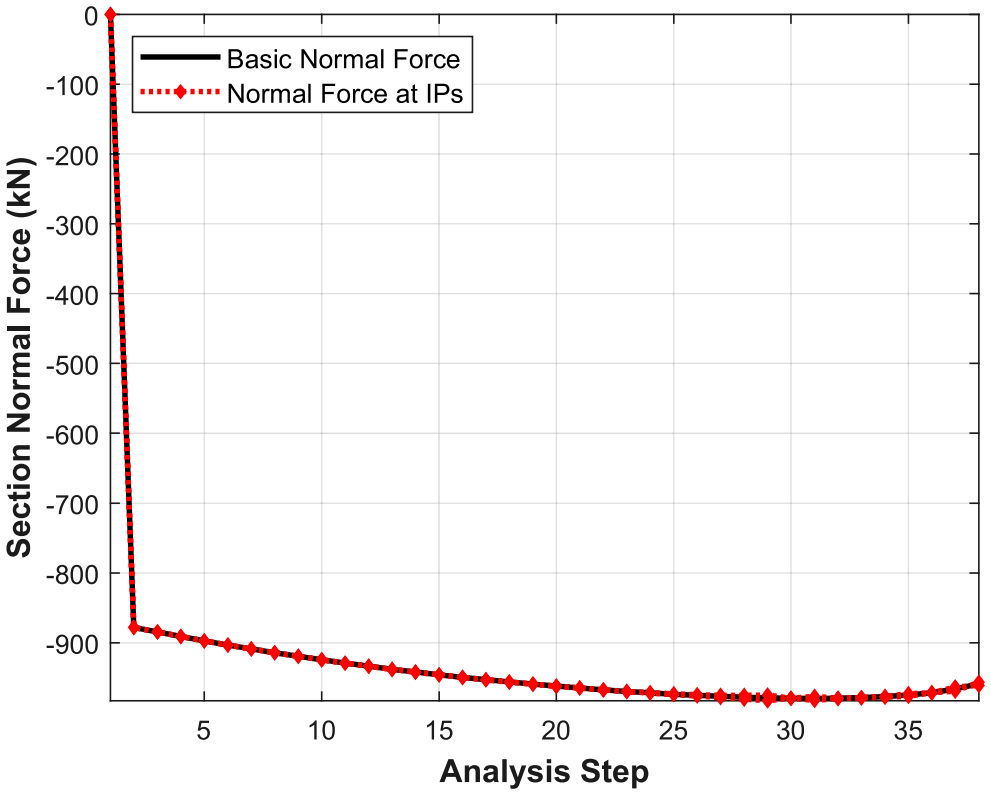


Figure D.13: History of normal forces obtained in the ENH TB elements for Beam B2 and f_{tu} =47.0 MPa.

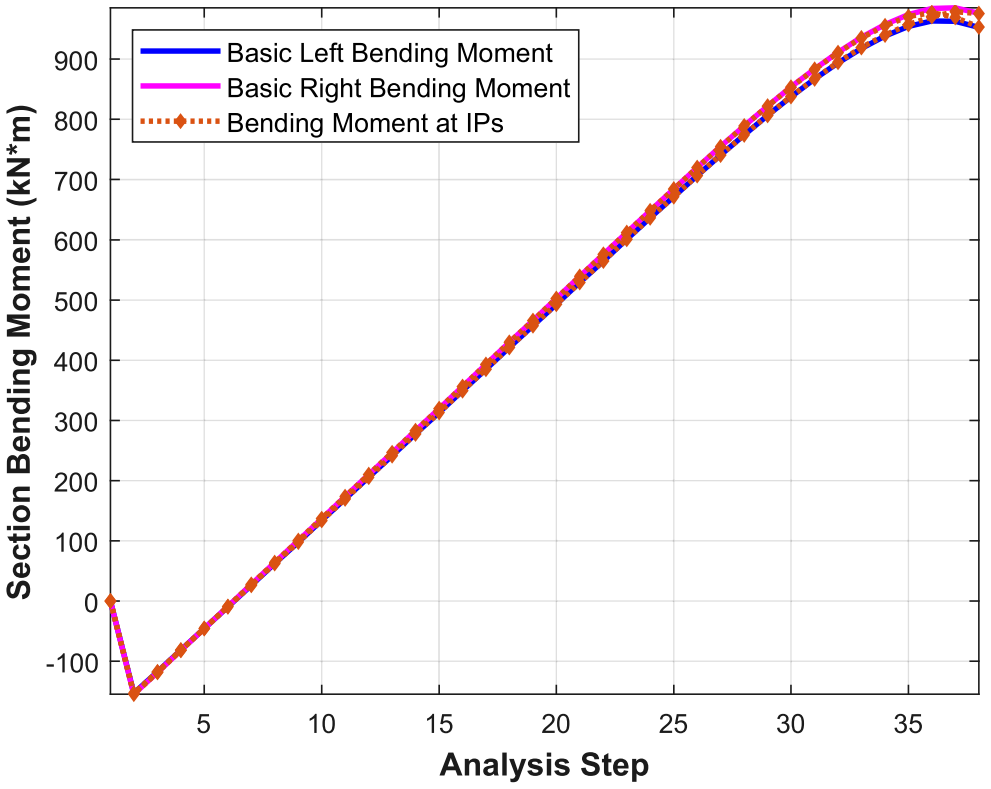


Figure D.14: History of Bending Moments obtained in the ENH TB elements for Beam B2 and f_{tu} =47.0 MPa.

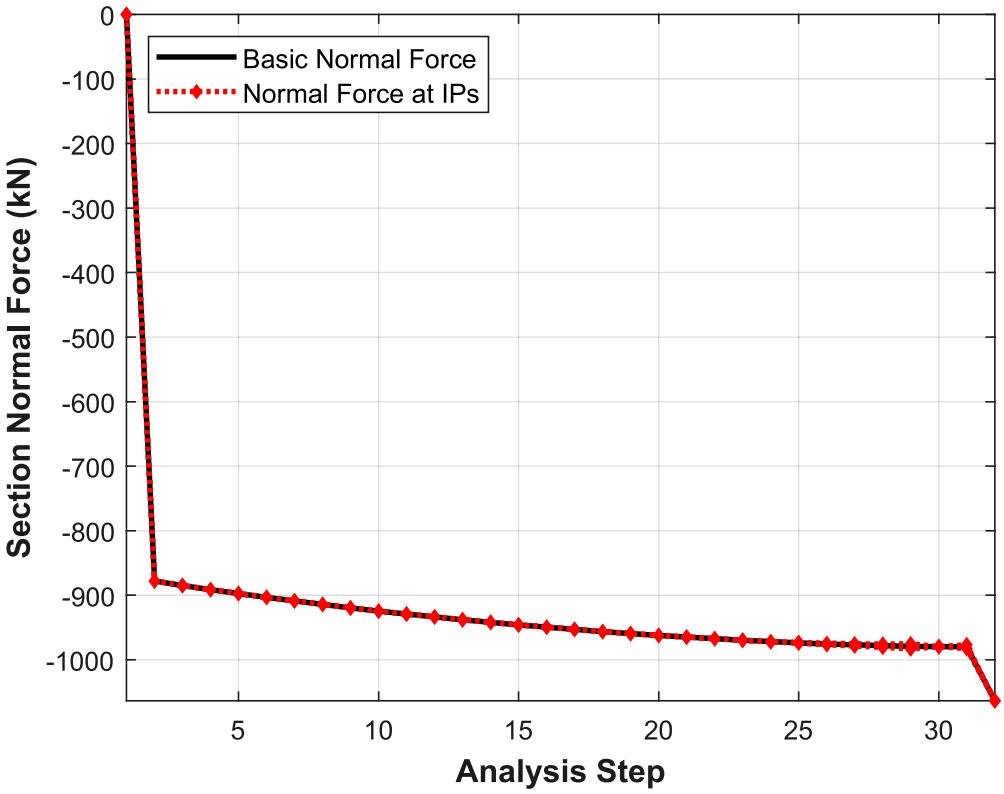


Figure D.15: History of normal forces obtained in the ENH TB elements for Beam B2 and f_{tu} =35.2 MPa.

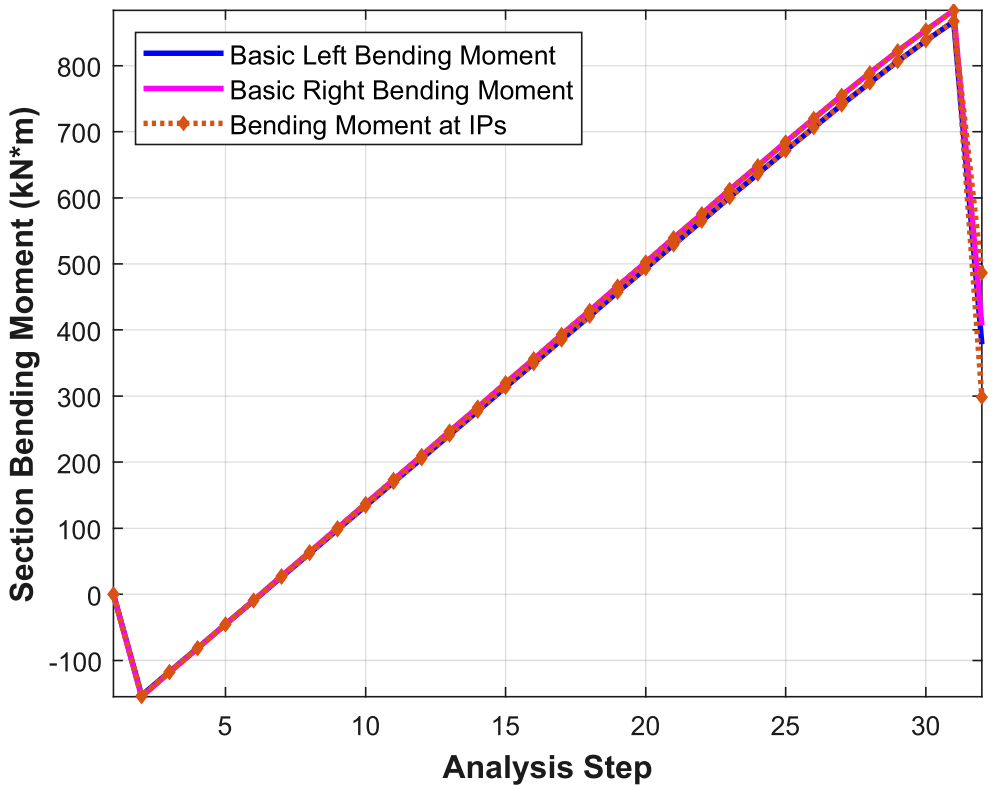


Figure D.16: History of Bending Moments obtained in the ENH TB elements for Beam B2 and f_{tu} =35.2 MPa.

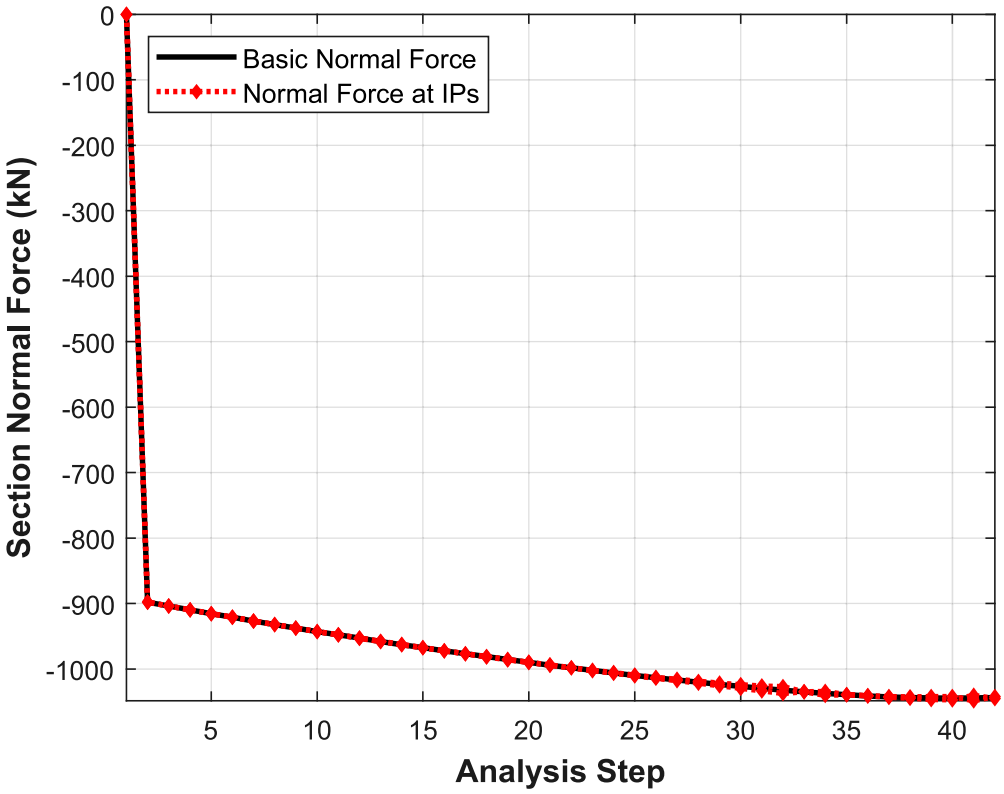


Figure D.17: History of normal forces obtained in the ENH TB elements for Beam B3 and f_{tu} =47.0 MPa.

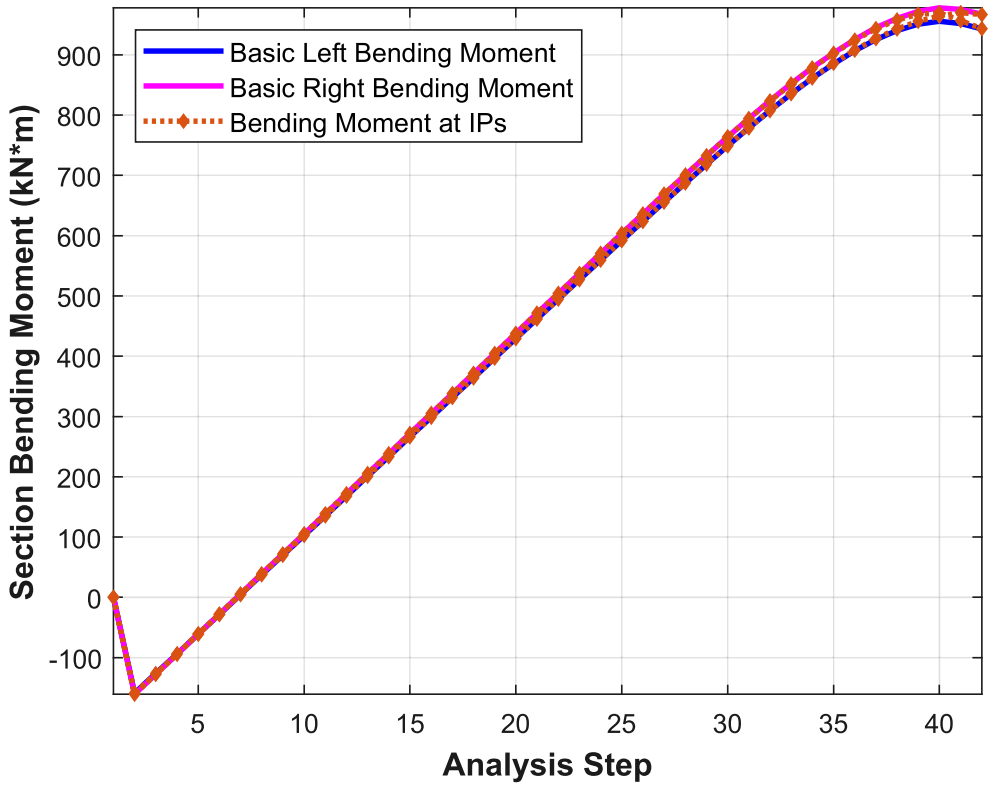


Figure D.18: History of Bending Moments obtained in the ENH TB elements for Beam B3 and f_{tu} =47.0 MPa.

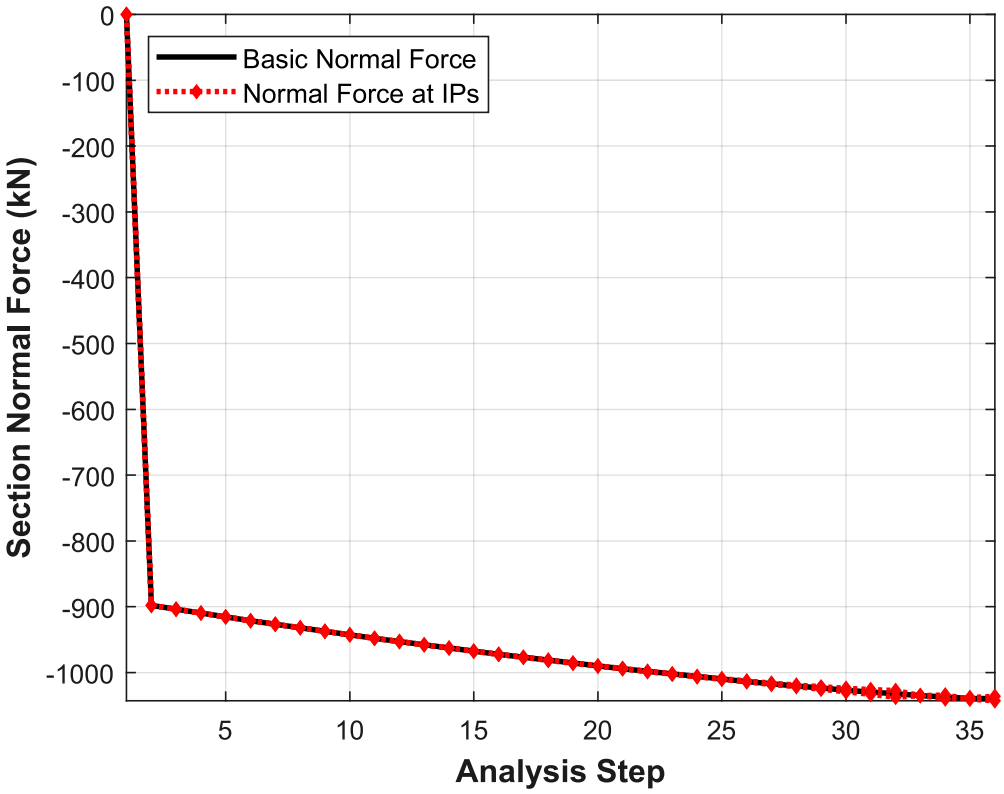


Figure D.19: History of normal forces obtained in the ENH TB elements for Beam B3 and f_{tu} =35.2 MPa.

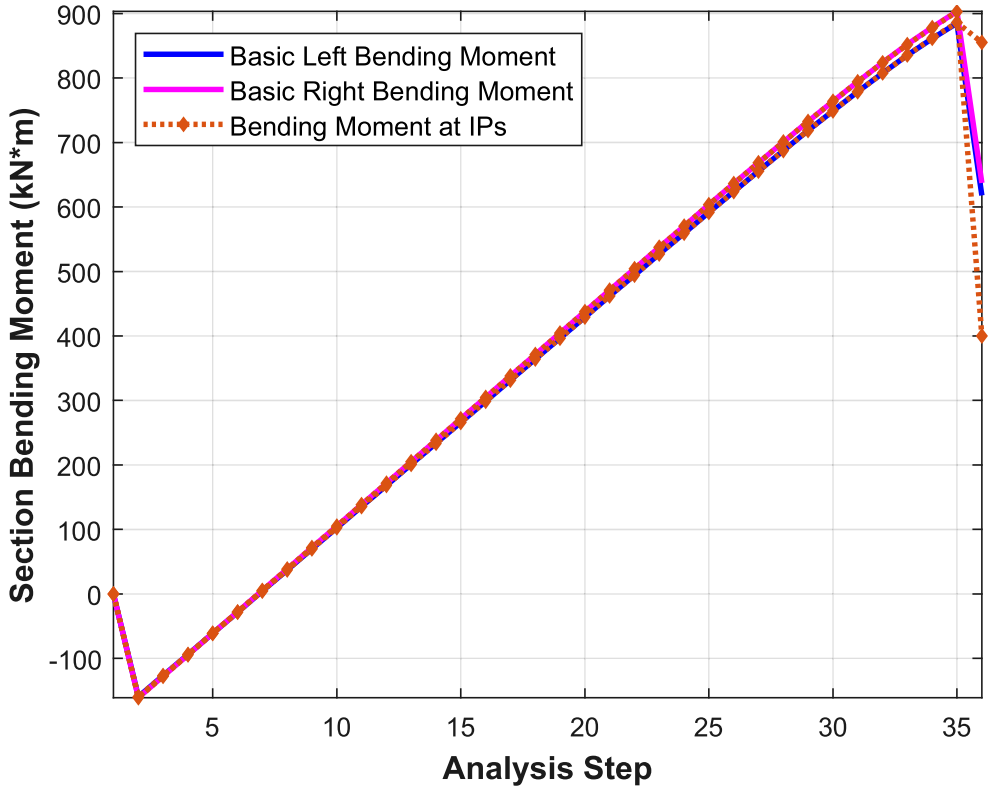


Figure D.20: History of Bending Moments obtained in the ENH TB elements for Beam B3 and f_{tu} =35.2 MPa.

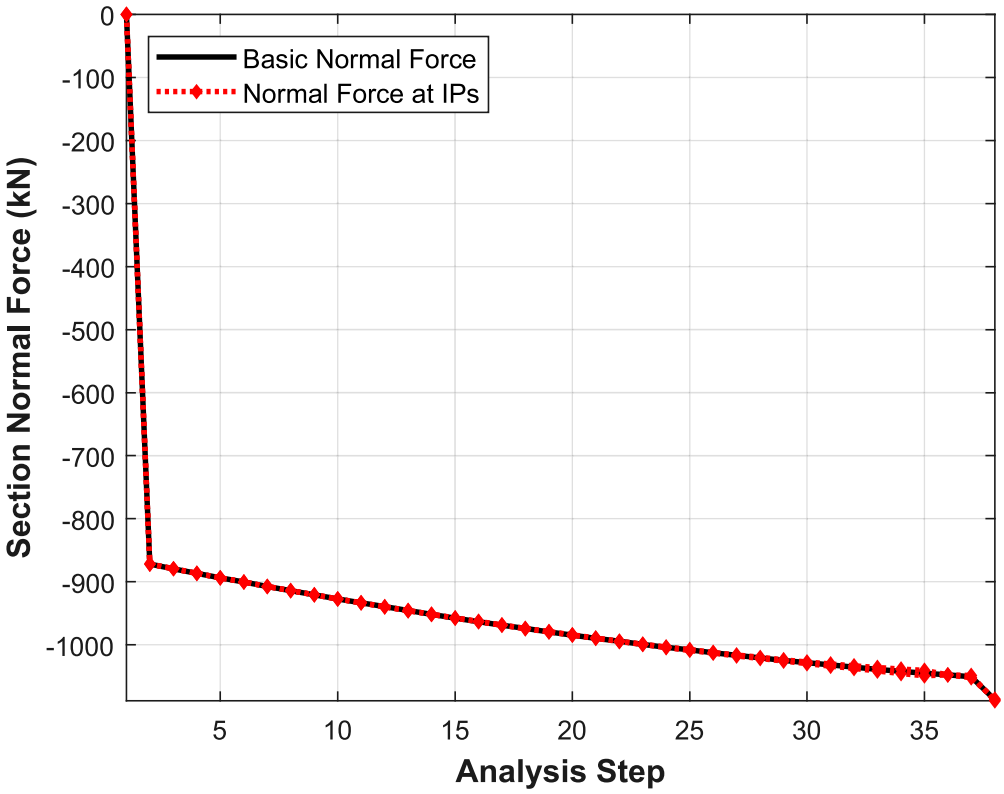


Figure D.21: History of normal forces obtained in the ENH TB elements for Beam B4 and f_{tu} =47.0 MPa.

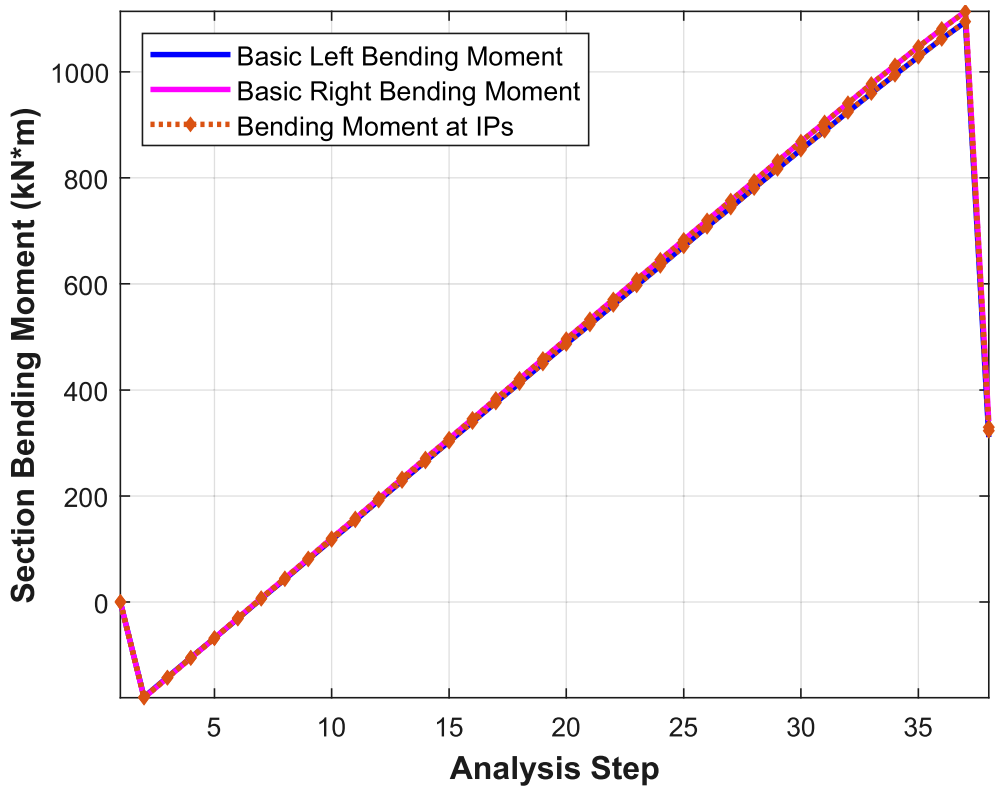


Figure D.22: History of Bending Moments obtained in the ENH TB elements for Beam B4 and f_{tu} =47.0 MPa.

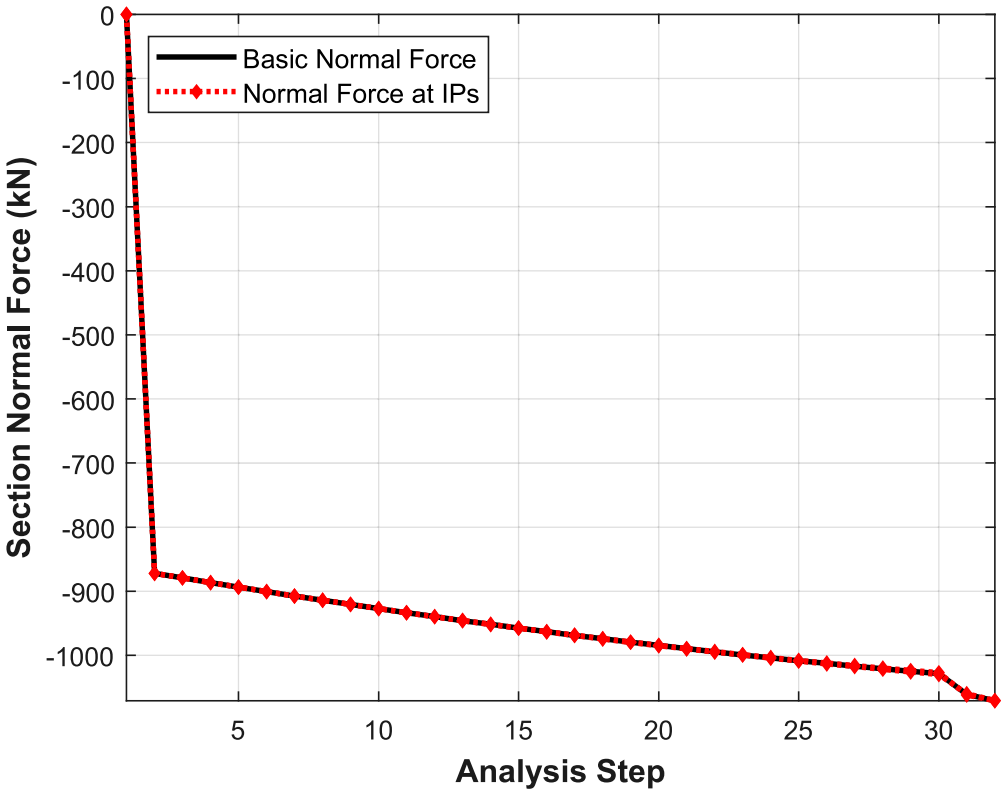


Figure D.23: History of normal forces obtained in the ENH TB elements for Beam B4 and f_{tu} =35.2 MPa.

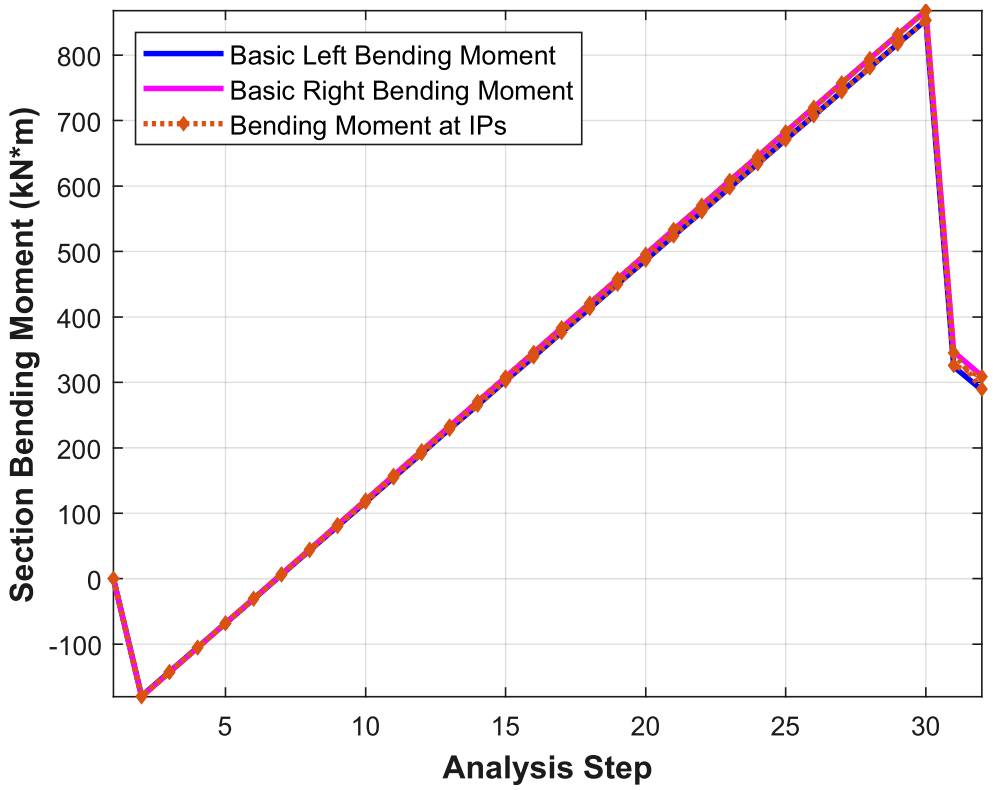


Figure D.24: History of Bending Moments obtained in the ENH TB elements for Beam B4 and f_{tu} =35.2 MPa.